

BIREFRINGENT FABRY-PÉROT SENSORS

A thesis submitted

by

Neil Raymund Yu Caranto

for the degree of

Doctor Of Philosophy



Optical Technology Research Laboratory

Victoria University of Technology

1998

Acknowledgments

Foremost, I thank my supervisor and mentor, Prof. David Booth, OTRL director, for his guidance, support and encouragement during my Ph.D. candidature. I thank him for being available for consultation and for demanding the best from me. I thank him for his wisdom, simplicity and frankness, patience and understanding. I thank him for his kindness and for anticipating and providing for all my needs while I was in Australia.

I thank Dr. Michael M. Murphy, my secondary supervisor, for his guidance during the first two years of my research; Dr. Jakub Sazjman, Dr. Leo Cussen and Kevin Lawlor for sharing their enthusiasm and practical skills in vacuum deposition; Dr. Andrew Stevenson and Dr. Peter Farrell, for the fruitful discussions; and Dr. Stephen Collins, HOD Applied Physics, for his upfront support especially during my recent fellowship at VUT.

I thank the technical staff: Alex Shelamoff, for his help in the design of many of the analogue circuits and also for simply being a great guy; Tibor Kovacs, for his assistance with the computer interface; Mark Kevinin and Donald Ernel, for their high standards of workmanship and efficiency; Hayrettin Arisoy and Durrahman Kuzucu for making available the different components that I needed; and Umit Erturk for providing solutions to challenges in the house and in the laboratory especially when they were most needed.

I thank Cindy Huang, Corinna Sullivan, Mikhail Vasiliev and Dr. Senyemmo Charles Kaddu for being great housemates as well as colleagues. In particular, I thank Kaddu for his simplicity, warm smile, patience and for the work we shared as we developed fusion-spliced sensors.

I thank Darol Garchev for his time and assistance with the fabrication of the fibre Bragg gratings I required. I thank the other graduate students (too many to mention) for their great company.

I thank the Australian Commonwealth Government for their generous support. Without the almost-four-year Equity and Merit Scholarship, I could never have had the fruitful experience of my Ph.D. candidature at Victoria University of Technology. I thank Jill Little who ensured that all went well with my scholarship.

I thank the Philippine Government for a five-month ESEP fellowship to complete this thesis. In particular I thank Undersecretary Dr. Estrella P. Alabastro, Engineering and Science Education Program Director, and her staff Ester Solis, Teody Dayoan, Ulysses Palmones for their prompt support. I thank Dr. Henry Ramos, director of NIP, for his endorsement of my fellowship.

I thank Fr. Bienvenido Nebres, S.J., President of the Ateneo de Manila University, for his generous support and understanding. I thank Dr. Antonette Angeles, head of the Ateneo Faculty Development, for her support of my leave of absence to complete this thesis; the Deans, Dr Mari-Jo Ruiz and Dr. Assunta Cuyegkeng for their patience and encouragement and the Physics Department chairs, Dr. Minella Alarcon, Mr. Nathaniel Libatique, Mr. Carlos Oppus and Dr. John Holdsworth for their understanding.

I thank Fr. Jett Villarin, S.J. and in particular Dr. John L. Holdsworth for taking time to edit as well as re-edit and proof-read my thesis.

I thank Fe Warque for her love, patience and for taking care of my needs especially during the final stages of this thesis writing.

I thank my parents and my brothers who always provided the home to return to come summer breaks.

I like to especially thank Fr. Daniel J. MacNamara, S.J., for his recommendation and moral support throughout my candidature.

Declaration

I, **Neil Raymund Yu Caranto**, declare that the thesis titled,

Birefringent Fabry-Pérot Sensors,

is my own work and has not, been submitted previously, in whole or in part, in respect of any other academic award.

Neil Raymund Yu Caranto,

dated the 14th day of July, 1998

Abstract

This thesis describes the development and performance of short-cavity polarisation-maintaining (birefringent) in-fibre Fabry-Pérot interferometric sensors for the measurement of temperature or strain. By using a highly birefringent optical fibre in their cavity, these sensors form two interferometers - one for each polarisation axis. As in the case of other fibre interferometers, each axial interferometer is extremely sensitive to temperature and strain. But this high sensitivity together with the periodic nature of each interferometer output yields a limited unambiguous measurand range (UMR). However, the differential phase between the axial interferometric phase responses of the birefringent sensors developed in this work can be exploited to provide an extended UMR.

Several approaches in obtaining a large or extended UMR of interferometric sensors are surveyed. In this work the in-fibre birefringent Fabry-Pérot sensor was the chosen sensor configuration primarily because of its high immunity from perturbations in any lead-fibre and its moderately large UMR for both temperature and strain measurements.

Long cavity birefringent fibre Fabry-Pérot sensors have been previously investigated [Farahi *et al.*, 1990] while those with short cavity lengths have not been exploited. The main advantage of short-cavity in-fibre sensors is that they can be deployed in hard-to-reach environments to obtain localised measurements of temperature or strain. Although the maximum possible sensitivity value of short-cavity sensors is lower than that of long-cavity sensors, the former still offer high sensitivity to temperature and strain.

Using short-cavity in-fibre Fabry-Pérot sensors involves challenges both in their fabrication and operation. Crucial to the operation of the sensor is the alignment of the polarisation axes of the lead-in fibre with the polarization axes

of the sensor. In this thesis, the fabrication of two types of short-cavity in-fibre birefringent Fabry-Pérot sensors is described. These sensors employed either fusion-spliced TiO₂ in-line reflectors or in-fibre Bragg gratings and each type of sensor exhibits different mechanical and optical properties. The expected interferometric output and the sensitivity of the cavity phase shift to temperature and strain of the two types of sensors are also discussed.

In this work, to obtain moderately fast measurements, a pseudo-heterodyne signal processing scheme with a modulated laser diode was implemented to detect the interferometric phase shifts of each axial interferometers of the sensors. This scheme primarily requires that the sensors be low finesse whilst the implementation method limits the shortest possible cavity length. Low finesse can be achieved with using low reflectance Fabry-Pérot mirrors.

Measurements made with the different sensors developed are discussed. The axial and differential phase responses of the birefringent sensors were found to exhibit good linear trend with temperature or strain as was expected. However, because of the high phase resolution ($1:10^4$) of the phase recording scheme used in this work, several nonlinear effects were observed. Common to both types of Fabry-Pérot sensors developed were effects associated with the signal processing scheme. Observed only with the grating-based sensors, one of the nonlinear features was subsequently attributed to the dispersion of the “grating” used with the sensor. However there was a large disparity between the magnitude of the dispersion of the “grating” that was experimentally observed and that predicted by coupled-mode theory. This disparity indicates that the “grating” may actually be a complicated structure of several gratings. Such structures is not difficult to imagine since two fibre Bragg gratings have been superimposed in the past [Xu *et al.*, 1994].

Aside for developing an optical fibre sensing arrangement which exhibits high measurand resolution, large UMR and moderate fast sampling rate, and can be assembled in an all-fibre form, the major contribution of this work was the development of a method of directly measuring the dispersion of a “grating” written on optical fibres which may be useful to others investigating the properties of different types of fibre Bragg gratings.

Table of Contents

<i>Acknowledgments</i>	ii
<i>Declaration</i>	iv
<i>Abstract</i>	v
<i>Table of Contents</i>	vii
Chapter 1: Introduction	1–1
1.1 Research Aim and Major Activities.....	1–5
1.2 Thesis Overview.....	1–8
Chapter 2: Temperature Or Strain Interferometric Optical Fibre Sensing Arrangements Exhibiting Large Unambiguous Measurand Range	2–1
2.1 Approaches in Obtaining Large Measurand Range.....	2–2
2.2 Reduced Sensitivity Approaches	2–5
2.2.1 Reduced Sensitivity Via Reduction of the Effective Sensing Length: Ultra-Thin Fabry-Pérot Interferometric Sensors.....	2–6
2.2.2 Reduced Sensitivity Via the Reduction of the Effective Refractive Index	2–7
2.2.2.1 Polarimetric Sensors.....	2–7
2.2.2.2 Dual-Mode Sensors	2–8

2.2.3 Using Direct Physical Techniques.....	2-9
2.3 Direct Extension of Unambiguous Phase Measurement Range Approaches.....	2-10
2.4 Unambiguous Measurement Approaches.....	2-12
2.4.1 Absolute Measurement of Optical Path Difference.....	2-12
2.4.1.1 Coherent Frequency-Modulated Continuous-Wave Interferometry	2-12
2.4.1.2 Low-Coherence or White-Light Interferometry	2-15
2.4.2 Measurement of Optical Path Length, Group-Delay, Dispersion of an Optical Fibre.....	2-17
2.4.2.1 Dispersive Optical Fourier Transform Spectroscopy.....	2-17
2.4.2.2 Measurement of Optical Path Length, Group-Delay, Dispersion of an Optical Fibre	2-19
2.4.3 Spectrally-Encoded Measurements.....	2-20
2.4.3.1 Brillouin Scattering Sensors	2-21
2.4.3.2 In-Fibre Bragg Grating Sensors.....	2-22
2.5 Dual-Measurement Approaches.....	2-25
2.5.1 Two Distinct Sensors	2-25
2.5.1.1 Schemes Not Involving Fabry-Pérot Interferometric Sensors.....	2-26
2.5.1.2 Schemes Involving One Fabry-Pérot Interferometric Sensor	2-27
2.5.1.3 Schemes Involving Effectively Two Distinct Fabry-Pérot Interferometric Sensors.....	2-29
2.5.2 Dual Wavelength Techniques.....	2-30
2.5.2.1 Extending the UMR of Interferometric/Polarimetric Sensors	2-30
2.5.2.2 Extending the UMR of Dual-Evanesciently-Coupled-Core Fibre Sensors.....	2-31
2.5.2.3 More-Than-Two-Wavelength Illumination	2-32
2.5.3 Dual In-Fibre Bragg Grating Sensors.....	2-33
2.5.4 Conventional Interferometry or Polarimetry Combined with Dual-Mode Interference.....	2-39
2.5.4.1 Extending the UMR of Interferometric Sensors.....	2-39
2.5.4.2 Extending the UMR of Polarimetric or Dual-Mode Sensors	2-40
2.5.5 Combined Interferometry and Polarimetry.....	2-41

2.6 Overview Summary	2-43
Chapter 3: Transfer Functions of Optical Fibre Fabry-Pérot Interferometers With Thin-Film or Fibre Bragg Grating Reflectors	3-1
3.1 Intrinsic Fibre Fabry-Pérot Interferometers.....	3-2
3.1.1 Transmission Function of Fibre Fabry-Pérot Interferometers	3-6
3.1.2 Behaviour of the Airy Function, Free Spectral Range and Finesse of Fabry-Pérot Interferometers.....	3-7
3.1.3 Reflection Function of Fabry-Pérot Interferometers	3-10
3.1.4 Low Finesse Fabry-Pérot Interferometers as a Two-Beam Interferometer.....	3-13
3.1.5 Fringe Visibility.....	3-13
3.1.6 Limitations on the Fringe Visibility.....	3-15
3.2 Thin-Film or Bragg-Grating Fabry-Pérot Reflectors	3-16
3.2.1 Dielectric Thin Film	3-16
3.2.2 Fibre Bragg Grating.....	3-19
3.3 The Free Spectral Range of Fibre Fabry-Pérot Interferometers With Either Thin-Film or Fibre Bragg Grating Reflectors.....	3-25
3.3.1 Some Preliminary Calculations	3-25
3.3.1.1 The Case of a Dielectric Thin Film.....	3-25
3.3.1.2 The Case of a Fibre Bragg Grating	3-26
3.3.2 Final Calculations.....	3-28
Chapter 4: Thermal and Strain Sensitivities of Single-Mode Silica Fibre Fabry-Pérot Interferometric Sensors	4-1
4.1 Thermal and Strain Sensitivities of Non-Polarisation-Maintaining Single-Mode Silica Optical Fibre Fabry-Pérot Interferometric Sensors.....	4-1
4.1.1 Stress and Strain Formalisms.....	4-3
4.1.2 Phase-Strain Sensitivity	4-4

4.1.3 Phase-Temperature Sensitivity	4-8
4.1.4 Unified Phase-Strain-Temperature Description	4-10
4.2 Birefringence In Single-Mode Optical Fibres	4-12
4.2.1 Birefringence Mechanisms	4-12
4.2.2 Evolution of the State-of-Polarisation	4-13
4.2.3 Mechanisms for Producing Linear Birefringence	4-13
4.2.4 Characterisation of Linear Birefringence	4-15
4.3 Thermal and Strain Sensitivities of Elliptically-cladded Birefringent Optical Fibres.....	4-16
4.3.1 Stress Distribution In an Elliptically Cladded Birefringent Fibre	4-16
4.3.2 Photo-elastic Effect Constants	4-19
4.3.3 Birefringence of an Optical Fibre with an Internal Elliptical Cladding	4-20
4.3.4 Phase-Strain Sensitivity	4-22
4.3.5 Phase-Temperature Sensitivity	4-23
4.3.6 Cross-Sensitivity of Strain and Temperature	4-25
4.4 Temperature and Strain Sensitivities of a Single-Layer Reflective Thin Film.....	4-27
4.5 Temperature and Strain Sensitivities of an In-Fibre Bragg Grating.....	4-28
4.6 The Phase-Measurand Sensitivity of a Fibre Fabry-Pérot Interferometer with Thin-Film or Bragg-Grating Reflectors.....	4-29
4.7 The Unambiguous Measurand Range of a Fibre Fabry-Pérot Interferometer With Thin-Film or Bragg-Grating Reflectors	4-30
Chapter 5: Development Of Short-Cavity Fibre Fabry-Pérot Interferometers _____	5-1
5.1 Fusion-Spliced Single-Mode Optical Fibre Fabry-Pérot Sensors.....	5-2
5.1.1 Review of the Previous Work on the Construction of Fusion-Spliced In-Fibre Reflectors	5-2
5.1.2 TiO ₂ Reactive Sputter Deposition	5-3
5.1.3 Fabrication Process for Fusion-Spliced Fabry-Pérot Sensors	5-12

5.1.4 Splice Strengthening.....	5-17
5.2 Fusion-Spliced Birefringent Optical Fibre Fabry-Pérot Sensors.....	5-19
5.2.1 Fabrication Process	5-19
5.2.2 Alignment of the Birefringent Axes	5-20
5.3 Grating-Based Birefringent Optical Fibre Fabry-Pérot Sensors.....	5-24
5.3.1 Single-Grating Birefringent FFPSs.....	5-25
5.3.2 Dual-Grating In-line FFPSs	5-29
Chapter 6: A Birefringent Optical Fibre Sensing System for the Measurement of Temperature and Strain	6-1
6.1 The Optical Fibre Sensing Arrangement Compared With Its Closest Fore-Runner	6-1
6.2 Detailed Description of the In-Fibre Birefringent Fabry-Pérot Sensor.....	6-4
6.3 Description of the Optical Fibre Sensing System	6-5
6.4 Jones Calculus Treatment	6-8
6.4.1 In-Fibre Sub-System.....	6-10
6.4.2 Launching Sub-System.....	6-12
6.4.3 Detection Sub-System	6-14
6.4.4 Output Electric Field and System Requirement (reflection)	6-15
6.4.5 Output Electric Field and System Requirement (transmission)	6-17
6.5 Pseudo-Heterodyne Signal Processing Scheme Implemented With A Modulated Laser Diode.....	6-19
6.5.1 The Technique.....	6-19
6.5.2 Implementation.....	6-22
6.5.3 Chirping of the Laser Diode Emission Frequency.....	6-22
6.6 Implementation of the Signal Processing and Phase Detection Scheme.....	6-24
6.6.1 Description of Single Channel.....	6-24
6.6.2 Cumulative Phase Monitoring.....	6-28

Chapter 7: Temperature and Strain Measurements With Fibre Fabry-Pérot Sensors 7-1

7.1 Performance of Non-Polarisation-Maintaining Fusion-Spliced Fibre Fabry-Pérot Sensors	7-2
7.1.1 Characteristics of the NPM Sensors.....	7-2
7.1.2 Temperature Measurements with NPM Sensors	7-4
7.1.3 Static Longitudinal Strain Measurement with NPM Sensors.....	7-8
7.2 Performance of Fusion-Spliced Birefringent Fibre Fabry-Pérot Sensors	7-13
7.2.1 Characteristics of the Fusion-Spliced Birefringent Sensors.....	7-13
7.2.2 Temperature Measurements with Fusion-Spliced Birefringent Sensors.....	7-14
7.3 Performance of Grating-Based Birefringent-Fibre In-Fibre Fabry-Pérot Sensors	7-34
7.3.1 Description of the Sensor	7-34
7.3.2 The Characteristics of In-Fibre Bragg Grating	7-35
7.3.3 Temperature Measurements with Grating-Based Sensors	7-36
7.3.4 Static Longitudinal Strain Measurements with Grating-Based Sensors.....	7-53
7.3.5 Dynamic Strain Measurements with Grating-Based Sensors.....	7-64

Chapter 8: Conclusion 8-1

8.1 Synthesis	8-1
8.2 Further work	8-4

Appendix A: Measurement of the Group Refractive Index of a Single-Mode Optical FibreA-1

Appendix B: Descriptions of the Experimental Circuits and Computer Interfaces B-1

B.1 Experimental Circuits	B-1
B.1.1 Sawtooth Generator Circuit	B-1
B.1.2 Laser Diode Drive Circuit.....	B-4
B.1.3 Temperature Controller Circuit	B-6

B.1.4 Division Circuit.....	B-9
B.1.5 Photodiode Circuit.....	B-9
B.1.6 Band-pass Amplifier Circuit.....	B-12
B.1.7 Squaring Circuit.....	B-14
B.1.8 Phase Determination Circuit.....	B-15
B.2 Computer Interfaces.....	B-20
B.2.1 Measurand Detection Circuits.....	B-22
B.2.1.1 Temperature Detection Circuit.....	B-22
B.2.1.2 Electrical Strain Gauge Amplifier.....	B-23
B.2.2 Continuous Monitoring of the Interferometric Phase Shifts.....	B-25
Appendix C: System Noise and Limitations _____	C-1
C.1 Phase Noise Due to Intensity-Related Noise.....	C-1
C.1.1 Detection Electronics Noise: Electrical Noise in the Photodiode Circuit.....	C-1
C.2 Phase Error in the Detection of the Zero-Crossing Edges.....	C-4
C.3 Phase Noise Due to Some of the Optical Components.....	C-5
C.3.1 Fresnel Reflection From the Proximal Face of the Lead-In Fibre.....	C-5
C.3.2 Lead-In Fibre Insensitivity.....	C-7
C.4 Phase Noise Due to the Characteristics of the Laser Diode.....	C-10
C.4.1 DC Current Characteristics and Noise.....	C-10
C.4.2 Coherence Length of the Laser Diode Operated With A Small-Signal AC Sawtooth Current Modulation.....	C-12
C.4.3 AC Current Characteristics And Noise.....	C-14
C.4.4 Temperature Sensitivity of the Laser Diode and Limitations of the LD Temperature Controller...	C-20
C.5 Phase Noise Due to the Band-Pass Filter.....	C-23
C.6 Overall Phase Noise.....	C-25

Appendix D: Publications Resulting From This Thesis _____ **D-1**

Appendix E: References _____ **E-1**

Appendix F: Symbols Used in This Thesis _____ **F-1**

Appendix G: Abbreviations Used In This Thesis _____ **G-1**

Chapter 1:

Introduction

Optical fibre sensors (OFSs) have been of significant research interest over the last 20 years because of their potential applications in highly sensitive measurements of thermal, mechanical, acoustic, magnetic, electrical or chemical parameters [Giallorenzi *et al.*, 1982; Jackson and Jones, 1986; Kersey, 1990; Jackson, 1994]. The interest in OFSs is principally due to the useful material-dependent properties of optical fibres. In particular, the good electrical isolation, high electromagnetic immunity, high tensile strength, high melting point, great flexibility, high chemical inertness, light weight and small size [Culshaw & Dakin, 1988] of silica-fibre-based OFSs offer the possibility of highly sensitive measurements in hazardous or hard to reach environments [Yeh *et al.*, 1990; Inci *et al.*, 1993]. Although OFS technology is still considered in its infancy, initial commercial successes have been realised [Montgomery & Glasco, 1985; Crossley, 1994; Lequime, 1997] with notably strain and temperature OFS gaining acceptance for use in various fields [Wickersheim & Hyatt, 1990; Mason *et al.*, 1992]. For example in medicine, temperature and pressure OFSs have made a niche as promising alternatives to well-established medical sensors [Martens *et al.*, 1985; Baldini & Mignani, 1994; Rao *et al.*, 1997a]. In aerospace engineering, the development of intrinsic strain sensors has been a major research activity in the fabrication of smart composite structures for aerospace applications [Measures, 1992]. In the operation of nuclear power plants, a multiplexed array of fibre-optic temperature sensors can permit remote monitoring of important thermal parameters of a nuclear reactor with relatively high radiation damage thresholds [Meunier *et al.*, 1994].

OFSs can basically be categorised as either intrinsic or extrinsic. In the extrinsic type, optical fibres serve merely as optical waveguides directing light into and collecting light from a device which is external to the fibres and

where a measurand can modulate one of the optical properties of this external device. In the intrinsic type, the optical fibres are used both as the optical waveguides and the sensing elements themselves. In general, intrinsic sensors are more attractive because they do not suffer from severe optical coupling losses which are common in extrinsic sensors. However intrinsic sensors are limited only to measurands which affect the optical properties of an optical fibre, *e.g.* refractive index, absorption length *etc.* Extrinsic sensors, on the other hand, allow a convergence of optical fibre and other technologies. This convergence of technologies has given rise to several OFSSs measuring a wide variety of measurands.

OFSs can further be classified according to how a measurand affects the optical properties of a sensor. For example a measurand can affect the intensity, the phase, the state of polarisation (SOP) or the optical spectrum of the light beam returning from a sensor. Intensity-modulated sensors exploit the sensitivity of the fibre to measurands which affect loss or attenuation. A measurand can interact with an optical fibre by changing its transmission properties such as scattering loss, macro- and micro-bending loss or evanescent coupling. Phase-modulated or interferometric sensors utilise the dependence on a measurand of the relative optical phase between the beams travelling in the arms of a fibre interferometer. Interferometric sensors can detect changes in their optical path difference which are a fraction of a wavelength of the light source. Polarimetric or SOP-modulated sensors exploit the susceptibility of the SOP of the light guided in an optical fibre to changes in the measurand. For example, Kerr or Faraday effects in optical fibres have been exploited to measure electric and magnetic fields or their related parameters [*e.g.* Tang *et al.*, 1991; Ning *et al.*, 1995]. Spectrally-encoded sensors generally involve measurands which affect the spectral properties of optical processes in an optical fibre. One common example of such sensors is the fibre Bragg grating sensor. Other spectrally-encoded sensors take advantage of nonlinear processes in an optical fibre (*e.g.* Stimulated Raman or Brillouin Scattering).

Of the different combinations of the type and the class of an OFS, an intrinsic interferometric sensor offers a simple, direct and highly sensitive measurement system for temperature, strain or parameters which produce temperature change or strain in an optical fibre. Of the various types of interferometric sensors, an intrinsic in-fibre Fabry-Pérot interferometric sensor (FFPS) offers one of the simplest and most convenient configurations for

incorporation in structures. An FFPS exhibits high lead-fibre phase noise rejection because the interfering beams travel to and from the sensor in the same optical fibre. Such high immunity of the Fabry-Pérot interferometric phase from phase perturbations present in any lead-fibre can facilitate the successful multiplexing of several FFPSs in the same optical fibre. An FFPS addressed in reflection naturally provides single-ended operation of the sensing arrangement without the additional use of other fibres or optical components. Furthermore, with the use of fibre directional couplers and other fibre-optic devices, an all-fibre system can be realised and thereby provide enormous flexibility in deploying FFPSs. For these reasons many research groups have developed measuring systems based on FFPSs. In this present work, FFPSs have been investigated for the measurement of temperature and strain.

FFPSs have properties which limit the variety of possible signal processing schemes that can be employed with them. Only signal processing schemes which are compatible with a non-zero optical path difference can be directly employed with an FFPS. The multi-beam nature of the Fabry-Pérot interference implies that none of the signal processing schemes suitable for two-beam interferometers can be applied unless the combined internal reflectance of the two Fabry-Pérot mirrors is low. Thus the reflectance of the Fabry-Pérot mirrors is an important consideration in the overall design of a measuring system.

Like all other interferometric sensors, an FFPS interrogated with a highly coherent light source provides only relative measurements because interferometric outputs are periodic with respect to the total round-trip cavity optical phase difference. Hence sensing arrangements with FFPSs require re-initialisation after a system reset. On the other hand, after such re-initialisation, the Fabry-Pérot interferometric phase can be continuously monitored such that the total phase excursion can be calculated (fringe counting) or the interferometric phase can be held constant by some suitable feedback control (phase tracking). In either case, the interferometric phase can not instantaneously change by more than 2π . A change in the measurand which produces a 2π interferometric phase change is known as the unambiguous measurand range (UMR).

Temperature or strain directly affects the physical length and refractive index of an optical fibre as will be discussed in Chapter 4. For the measurement of temperature or strain, the corresponding UMR depends on the

absolute length of an FFPS exposed to temperature or strain, the sensing length. On the other hand, the length of the Fabry-Pérot cavity determines the lower bound for the UMR. Both the exposure or sensing length and the cavity length are important considerations in determining the UMR of an FFPS.

Localised measurements of temperature or strain are highly advantageous because these measurands can vary from one location to another even within a small sensing region. Although localised temperature or strain measurements can be achieved by exposing only a portion of an FFPS to either of these measurands, it is generally more beneficial to expose the whole Fabry-Pérot cavity uniformly. This preference can be understood by realising that temperature change or strain can influence areas immediately adjacent to the sensing region (*e.g.* thermal conduction along an optical fibre). The thermal and strain gradients at the ends of the sensing region determine the magnitude of the additional temperature or strain-induced effects and consequently the effective sensing length can vary from one measurement to another. This ambiguity in the sensing length limits the accuracy in determining the measurand or in calibrating the sensor and may be avoided by exposing the whole cavity to the measurand so that the Fabry-Pérot cavity defines the sensing length. Exposing the entire length of a long-cavity FFPS to a measurand yields, however, a narrow UMR sensor. Thus in order to obtain as large as possible UMR while conveniently exposing an FFPS entirely to a measurand, a short-cavity FFPS can be used with the additional advantage that it naturally provides localised measurements.

A short-cavity FFPS is not simple to fabricate in an optical fibre as is outlined in Chapter 6. Some of the earliest attempts to produce these devices involved using fusion-spliced mirrors [Leilabady, 1987; Lee & Taylor, 1988] where it was found that the fusion-splicing unavoidably degrades the tensile strength of the concatenated optical fibres to the point that fusion-spliced FFPSs are not suitable for large strain measurements. To avoid this limitation, FFPSs may be realised by utilising an in-fibre Bragg grating as a Fabry-Pérot reflector. These fibre Bragg gratings can be formed within the core of an optical fibre without significantly compromising the tensile strength of the host fibre [McGarrity & Jackson, 1998]. The thermal sensitivity, the strain sensitivity and the limited optical reflection bandwidth of fibre Bragg gratings define the performance and limitations of grating-

based FFPSs. The performance and limitations of both fusion-spliced and grating-based FFPSs as temperature and strain sensors are assessed and compared in Chapters 3 and 7 of this work.

1.1 Research Aim and Major Activities

This present work began (early in 1992) with the general aim of assembling and assessing the performance and limitations of a reliable optical fibre sensing system capable of accurately measuring moderately fast variations of temperature or strain with high resolution over as wide as possible measurand range and in a localised region.

There were two major inter-related challenges encountered in this work. The first challenge was the fabrication of short-cavity birefringent fibre Fabry-Pérot interferometric sensors and the other challenge was the assembly of a compact optical arrangement with associated signal processing scheme appropriate for interrogating a short-cavity birefringent FFPS.

An FFPS can be operated with either a high-coherence or low-coherence light source. Although low-coherence or white-light interferometry (WLI) offers absolute measurement of a measurand and subsequently a potentially unlimited measurand range, WLI was not an option for this work because of the very slow processing time involved limiting the whole sensing arrangement to quasi-static (< 1 Hz) temperature or strain measurements. In this work, a pseudo-heterodyne signal processing scheme with a carrier of 1 kHz was implemented to extract the Fabry-Pérot interferometric phase shifts [Jackson *et al.*, 1982]. As a result, variations in temperature or strain at a rate of up to 500 Hz can be measured depending on the corresponding phase amplitude. A higher carrier frequency may be used but a 500 Hz signal bandwidth for temperature or strain is more than adequate.

The pseudo-heterodyne signal processing scheme made use of a single-mode laser diode (LD) with a sawtooth modulated drive current. This modulation consequently restricted the parameters of the Fabry-Pérot interferometer as too great an LD drive current may cause the output of the LD to mode-hop. A physical cavity length of at least 10 mm was found compatible with the modulated 785 nm LD as discussed in Chapter 6. This limit in the cavity length specified the minimum width of the sensing region for localised measurements of temperature or strain.

Because of the high sensitivity of an FFPS to either temperature or strain, the temperature and strain UMR even for the case of a 10-mm FFPS at 785 nm are narrow: ~ 1.3 °C and ~ 25 $\mu\epsilon$ for temperature and strain respectively. Clearly such UMR values limit the number of practical applications of an FFPS. However there are numerous schemes that can be employed to extend the UMR of an interferometric sensor as outlined in Chapter 2. This work used a dual FFPS arrangement using a birefringent FFPS. The two fibre Fabry-Pérot interferometers (FFPIs) were manifested along each polarisation axis of a birefringent FFPS. These two axial interferometers were expected to exhibit slightly different temperature and strain sensitivities due to the birefringence of the fibre. Interestingly, the similarity between the axial phase-measurand sensitivities was ideal for producing a birefringent FFPS with a large dynamic range - the ratio between the UMR and the measurand resolution. A birefringent FFPS can be used such that the phase change on one polarisation axis provides high-resolution measurements of temperature change or strain whilst the polarimetric or differential phase change (the difference between the two axial phase change) the fringe order of the chosen axis phase change. Hence the effective UMR of a birefringent FFPS is equivalent to the UMR obtained when only the differential phase sensitivity is considered. In this work, roughly a 16-fold and 64-fold increase in the UMR were generally observed for temperature and strain measurements respectively.

By continuously monitoring the interferometric phase along the two axial interferometers, a birefringent FFPS can still be operated over a measurand range wider than that stipulated by its UMR value. To facilitate such continuous monitoring, the measuring system was interfaced with a personal computer programmed to calculate the total phase excursion along each FFPS between any resetting of the measuring system or any re-initialisation of the sensor. Purpose-designed digital electronic circuits detected the interferometric phase shifts for each axial interferometer and converted these phase measurements into digital signals. These circuits measured each axial phase change with a resolution of $1/10,000^{\text{th}}$ of a fringe (2π radians) at a maximum sampling rate of 1 kHz.

In this work, the largest possible dynamic range for temperature or strain measurements were found to be about 1.6×10^5 and 6.4×10^5 respectively. The actual dynamic range was limited by the level of phase noise in the optical arrangement during a measurement run (Chapter 7). Nevertheless the fabrication of short-cavity birefringent FFPSs was crucial in obtaining a sensing arrangement with extended UMR and dynamic range.

Successful discrimination between the interference along each axial interferometer of a short-cavity birefringent FFPS required a lead-in birefringent fibre whose polarisation axes had been aligned with those of the sensor. Ensuring such alignment of the polarisation axes was laborious with fusion-spliced TiO₂ mirrors because the tolerance for the angular alignment of the polarisation axes is $< 2^\circ$. The alignment of the polarisation axes for grating-based FFPSs was automatic and limited only by the strength of any polarisation cross-coupling and the amount of photo-induced birefringence in the gratings themselves (Chapter 5).

In this work, fusion-spliced FFPSs were initially assessed and were subsequently followed by grating-based FFPSs as soon as fibre Bragg grating technology became available in this laboratory early in 1995. The performance of these two kinds of FFPS to temperature or strain measurements were similar except in their differential phase responses as discussed in Chapter 7.

In this work, a carefully designed optical arrangement was assembled to address a birefringent FFPS in reflection with the least number of components. With minor modification, the same optical arrangement can likewise be used to address a birefringent FFPS in transmission if desired.

By the end of this research, in late 1995, several fibre Fabry-Pérot interferometric sensors were fabricated. These FFPSs used either non-polarisation-maintaining or (birefringent) polarisation-maintaining fibres and either employed fusion-spliced TiO₂ films or in-fibre Bragg gratings as the Fabry-Pérot internal mirrors of these FFPSs. Some of these FFPSs were used as temperature or strain sensors. In the case of a birefringent FFPS, large unambiguous measurand range, high resolution and localised measurements were realised.

Although birefringent FFPSs gave promising performance as strain or temperature sensors, these sensors still suffer from a fundamental drawback – both strain and temperature effects give indistinguishable phase shifts along each axis of the sensor. Hence to effectively measure one of these measurands, the other parameter needs to be kept constant or at least independently monitored so that the corresponding effects of these changes may be subtracted from the total interferometric response.

1.2 Thesis Overview

This thesis is the culmination of an investigation into the fabrication and the performance of fusion-spliced and grating-based short-cavity-length birefringent fibre Fabry-Pérot interferometric sensors with application to temperature or strain measurement. The parameters of the sensors are necessarily, novel. The detailed examination of signal phase and intensity for these sensors and others of similar type, offers a new and complete understanding of the limiting parameters and thus the applicability of these sensor types as measuring devices.

The remainder of this thesis is arranged as follows. Chapter 2 presents an overview of previous work on interferometric optical fibre sensing arrangements which exhibit a large or an extended unambiguous measurand range. This chapter also discusses arrangements which can simultaneously measure temperature and strain because these arrangements are almost identical and can provide single-measurand interferometric sensing arrangements with enlarged dynamic range.

Chapter 3 provides a detailed analysis of the transmission and reflection functions of fibre Fabry-Pérot interferometers. In particular the analysis has taken into account the phase shift upon reflection from thin film mirrors or in-fibre Bragg gratings. This analysis predicts that a fusion-spliced FFPS and a grating-based FFPS exhibit slightly different interferometric phase response. Chapter 4 describes the expected phase sensitivity to temperature and strain of an FFPS fabricated with either non-polarisation-maintaining (ordinary) optical fibres and elliptically-clad birefringent optical fibres.

Chapter 5 discusses the fabrication of fusion-spliced and grating-based Fabry-Pérot interferometric sensors. The last type of sensors fabricated were in-line birefringent FFPSs using two fibre Bragg gratings. This chapter also describes the deposition of a TiO_2 thin film onto either the entire or only around the core-region of the face of a cleaved fibre end, possible schemes to improve or maintain the tensile strength of fusion-spliced fibres, the technique employed to align the polarisation axes of two birefringent fibres to be spliced, and the fabrication processes used to produce fibre Bragg gratings.

Chapter 6 describes in detail the optical and electronic arrangements employed to measure temperature or strain using birefringent fibre Fabry-Pérot interferometric sensors. The details of the electronic circuits implementing the signal processing scheme are described in Appendix B.

Chapter 7 presents and discusses the different experimental temperature, static strain and dynamic strain measurements with some of the FPPSs fabricated. These evaluated sensors were either communications-fibre or birefringent FFPSs fabricated with a fusion-spliced TiO₂ dielectric mirror, or a birefringent FFPS with an in-fibre Bragg grating reflector. These sensors were found to perform well as temperature and strain sensors. For example, one of the sensors can measure slowly-varying temperature between -20 °C to 80 °C with a phase-noise-limited resolution of 7×10^{-3} °C (after removal of systematic effects this resolution can be as high as 2×10^{-4} °C) and a UMR of ~ 34 °C. In Appendix C, the possible sources of phase noise were identified to account for the deviation of the experimentally observed resolution from the maximum possible resolution.

Because of the high resolution phase measurements obtained in this work, two distinct nonlinear features originally believed to be noise were additionally observed in the experimental results. The first of these features was the detection and evaluation of the highly periodic effects on the phase change on each axial interferometers. These effects were subsequently attributed to a nonlinear optical frequency ramp produced by the limited thermal response of a modulated LD. The second feature of the experimental results was a simple and direct observation of the non-linear phase shift in a low-reflectance grating. The effect is normally masked by the linear term but by measuring the differential phase between the two polarisations the resonant part of the phase shift due to the grating is clearly noticeable since it is a significant fraction of the differential phase.

Finally Chapter 8 concludes this thesis and provides suggestions for the future extension of this work.

Chapter 2:

Temperature or Strain Interferometric Optical Fibre Sensing Arrangements Exhibiting Large Unambiguous Measurand Range

In this chapter, techniques to ensure a large or extended unambiguous measurand range (UMR) of temperature or strain interferometric optical fibre sensors (OFSs) are surveyed. A wide measurand range is an important consideration for expanding the practical application of an interferometric OFS. Webb *et al.* [1988a] have previously reviewed the various techniques to extend the UMR of interferometric sensors. These techniques are either based on combining polarimetry with coherent interferometry, dual-wavelength interferometry, white-light interferometry or coherent Frequency-Modulated-Continuous-Wave (FMCW) heterodyne interferometry. Since then several other techniques have been developed. This chapter attempts to present an overview of various UMR-extending techniques reported to date (1998).

An extension of the UMR does not automatically imply an increase in the dynamic range - the ratio between its measurand range and measurand resolution. Whilst a large measurand range increases the practicality of an interferometric sensor, a large dynamic range implies a measuring system exhibiting high precision. Obviously, a measuring system exhibiting both a large measurand range and a high measurand resolution is generally preferred. In this chapter UMR-extending techniques which provide an improved dynamic range receive greater attention.

For this reason, techniques for simultaneous measurement of temperature and strain are also presented because these simultaneous-measurement techniques can easily be adapted to extend the UMR and dynamic range of a sensing arrangement as well.

Although this chapter focuses primarily on temperature or strain interferometric OFS, sensors which measure other parameters such as pressure or displacement, are also included because these type of parameters can be interpreted as indirect manifestations of temperature or strain. This chapter also presents sensors whose output can directly or indirectly be considered similar to that given by an interferometer, *i.e.* an optical output which follows some interference of optical beams. Furthermore, this chapter gives special attention to fibre Fabry-Pérot interferometric sensors (FFPSs) because FFPSs offer many benefits (see Chapter 1) and also because FFPSs have been chosen as the sensor configuration for this present work.

2.1 Approaches in Obtaining Large Measurand Range

There are four possible basic approaches that can be used to obtain a large measurand range for an optical fibre sensing arrangement based on fibre interferometric sensors. The first approach involves reducing the sensitivity of an interferometric OFS to a measurand. In general, reducing the measurand sensitivity increases the UMR but decreases the measurand resolution. The second approach involves directly extending the maximum phase change that can be measured unambiguously. Unlike the first, the second approach provides a direct extension of the dynamic range. The third approach to obtain a large measurand range is to remove any ambiguity in determining the measurand. Such conditions can be accomplished by deriving measurements of some parameter of the optical output of the optical fibre sensor which are not periodic with temperature or strain, *e.g.* absolute measurements of the optical path difference (OPD) of an interferometer. In most cases, the measurand range is essentially unlimited and can be made extremely wide. On the other hand the measurand resolution is limited by the resolution of the instrument or signal processing used to determine the measurand. However if an unambiguous measurement and a high-resolution measurement of the same measurand are combined, an extremely large dynamic range measuring arrangement can be obtained.

The fourth approach describes techniques involving two independent measurements which by themselves exhibit a limited UMR. These two measurements preferably exhibit very similar or else very different sensitivities to temperature or strain. The differential sensitivity of the two measurements provides a measurement with greatly reduced sensitivity. Essentially this dual-measurement approach is similar to the first approach because the effective UMR is determined by the least sensitive among three measurements, the two independent measurements and the difference between these two. Like the second approach, this dual-measurement approach also produces a corresponding increase in the dynamic range. The measurand resolution is determined by the resolution obtained by using the more sensitive of the two independent measurements.

Among these four approaches, the (fourth) dual-measurement approach is of considerable interest because it can potentially provide a greatly extended UMR and dynamic range compared to the others. In such an approach, the sensitivity of the combined interferometric sensing arrangement can be characterised by a sensitivity matrix \tilde{K} which relates two independent measurements, $\bar{\Phi}$, with temperature change ΔT or strain ε by

$$\bar{\Phi} = \tilde{K} \bar{M} , \quad \text{Eq. 2.1}$$

$$\text{where } \tilde{K} = \begin{bmatrix} K_{aT} & K_{a\varepsilon} \\ K_{bT} & K_{b\varepsilon} \end{bmatrix} , \quad \text{Eq. 2.2}$$

$$\bar{M} = \begin{bmatrix} \Delta T \\ \varepsilon \end{bmatrix} , \text{ and} \quad \text{Eq. 2.3}$$

$$\bar{\Phi} = \begin{bmatrix} \Delta\varphi_a \\ \Delta\varphi_b \end{bmatrix} . \quad \text{Eq. 2.4}$$

Basically the matrix \tilde{K} describes a sensing arrangement involving two interferometers. $\Delta\varphi_a$ and $\Delta\varphi_b$ refer to the total phase change which are produced in interferometers a and b respectively when these interferometers simultaneously experience the same temperature change ΔT and strain ε . The matrix elements K_{lM} ($l = a$ or b and $M = T$ or ε) describe the sensitivity of each interferometer l to each measurand M while the other measurand is kept constant. In this chapter, strain ε unless otherwise stated refers to axial longitudinal strain for surface-mounted sensors. When a fibre sensor is embedded within a material, the four-dimensional thermo-strain state of the fibre sensor depends on the composition of and on the interaction between the surrounding materials and the sensor itself [Sirkis, 1993a; 1993b].

Moreover the same sensor configuration described by the characteristic sensitivity matrix \tilde{K} can be employed for the simultaneous measurement of temperature and strain (SMTS). SMTS can be important in some circumstances since both parameters (which produce indistinguishable phase change) can often vary simultaneously in practical measurement environments [Jin *et al.*, 1996; Jones, 1997]. Eq. 2.1 can be re-arranged such that

$$\bar{M} = \tilde{K}^{-1} \bar{\Phi} , \quad \text{Eq. 2.5}$$

where \tilde{K}^{-1} is the inverse of the matrix \tilde{K} . Eq. 2.5 implies that SMTS needs a non-zero determinant $|\tilde{K}|$. In SMTS, the effective UMR of the combined dual-parameter sensor reverts to the smaller UMR of the two interferometers. However, for the operation expressed in Eq. 2.5 to yield an accurate SMTS, the condition number (which is ≥ 1) for the matrix \tilde{K} should approach unity [Atkinson, 1989; Vengsarkar *et al.*, 1990; Ma *et al.*, 1996]. Given $\bar{\Phi}$ with its associated uncertainty, $\delta\bar{\Phi}$, \bar{M} can be obtained using Eq. 2.5 with uncertainty $\delta\bar{M}$. $\delta\bar{M}$ increases as the condition number for the matrix \tilde{K} increases. Mathematically, a condition number for the matrix \tilde{K} that is close to unity implies that the two measurements are highly independent, *i.e.* the two independent measurements are not a linear combination of one another. Physically, a low condition number means that substantially different physical interactions or processes between the sensed parameter of the fibre sensor and the measurand are responsible for producing the phase-measurand sensitivities of the two independent measurements. Interestingly, most of the techniques for SMTS reported in the literature have involved similar physical interactions or processes in obtaining both independent measurements. However these techniques have remained suitable for extending the UMR of the corresponding sensing arrangement.

To compare the various UMR-extending techniques presented in this chapter, it may be useful to define a figure of merit, $E_{UMR,M}$ which describes the ratio by which the UMR of a sensing arrangement is extended by a particular technique compared with the UMR obtained when the technique has not been applied. The greater the value of $E_{UMR,M}$, the greater is the extension of the effective UMR.

For techniques belonging to the dual-measurement approach, the UMR can be extended in two possible ways depending on K_{rM} , the ratio between the sensitivities of the two independent measurements to the same

measurand M . Without any loss of generality, it can be assumed that $|K_{aM}| > |K_{bM}|$ and thus the sensitivity ratio K_{rM} is always greater than unity, *i.e.*

$$K_{rM} \equiv \frac{|K_{aM}|}{|K_{bM}|} > 1. \quad \text{Eq. 2.6}$$

In the extreme case when $|K_{aM}| \approx |K_{bM}|$, the measurements corresponding to the differential sensitivity, $|K_{aM}| - |K_{bM}|$, can be used to extend the UMR whilst in another extreme case when $|K_{aM}| \gg |K_{bM}|$, the measurements obtained with interferometer b can be used. In the case of the former, $K_{rM} \cong 1$,

$$E_{UMR,M} \cong \frac{K_{rM}}{K_{rM} - 1} = \frac{|K_{aM}|}{|K_{aM}| - |K_{bM}|}, \quad \text{Eq. 2.7}$$

whilst in the case of the latter, $K_{rM} \gg 1$,

$$E_{UMR,M} \cong K_{rM} = \frac{|K_{aM}|}{|K_{bM}|}. \quad \text{Eq. 2.8}$$

These two definitions gave the same value for $E_{UMR,M}$ when $K_{rM} = 2$. Thus the boundary for choosing which definition to apply is chosen to be $K_{rM} = 2$. Eq. 2.7 applies for the case $K_{rM} < 2$ whilst Eq. 2.8 applies when $K_{rM} \gg 2$. Furthermore, Eq. 2.7 and Eq. 2.8 show that any arrangement which involves two measurements exhibiting different sensitivities to the same measurand will always provide at least a value of 2 for $E_{UMR,M}$, *i.e.* $E_{UMR,M} \geq 2$. If sufficient data are available, either Eq. 2.7 or Eq. 2.8 is appropriately applied to calculate $E_{UMR,M}$ for the various techniques described in this chapter.

2.2 Reduced Sensitivity Approaches

The change in the interferometric phase φ can be written as

$$\frac{\Delta\varphi}{\Delta M} = 2\pi \frac{n L_M}{\lambda} \varpi_M = 2\pi \frac{n L_M}{c} v \varpi_M \quad \text{Eq. 2.9}$$

where n is the refractive index of a fibre interferometer and L_M the effective physical length of the interferometer exposed to the measurand M , *i.e.* the sensing length. In Eq. 2.9

$$\varpi_M = \left[\frac{1}{\varphi} \frac{\partial \varphi}{\partial M} \right] \quad \text{Eq. 2.10}$$

is the fractional phase-measurand sensitivity of a fibre interferometer. The parameter ϖ_M in Eq. 2.9 tends to be determined by the measurement situation but does not vary substantially for different measurement situations. Eq. 2.9 shows that the phase-measurand sensitivity $\frac{\Delta\varphi}{\Delta M}$ can be reduced by having a lower value for ν , L_M , n , or ϖ_M . Decreasing the effective optical frequency ν can be obtained by simultaneously using two light sources with slightly different optical frequencies, ν_1 and ν_2 . Such technique exploits the beating between the phase measurements at the two optical frequencies or wavelengths (see section 2.5.2). This beating effect implies that the interferometer has been effectively been illuminated by an optical frequency of $|\nu_1 - \nu_2|$. Sensing arrangements which provide a lower value for the effective L_M , n and ϖ_M are described in this section. These descriptions could be found useful in section 2.5.

2.2.1 Reduced Sensitivity Via Reduction of the Effective Sensing Length: Ultra-Thin Fabry-Pérot Interferometric Sensors

For fibre interferometric sensors, their measurand range can be made large by allowing only a narrow segment of one of the arms of the fibre interferometer to be exposed to the measurand (short sensing length). In this regard, only with a Fabry-Pérot interferometer with short cavity length can the sensing length be assured to be both narrow and unambiguous. Furthermore aside from providing a large UMR, a short-cavity Fabry-Pérot interferometric sensor provides remote and localised sensing of a measurand. Unfortunately, the fabrication of an intrinsic all-silica short-cavity Fabry-Pérot interferometric sensor requires highly specialized techniques [Lee *et al.*, 1989; Alcoz *et al.*, 1990; Stone & Stulz, 1993; Kidd *et al.*, 1994]. On the other hand, an extrinsic short-cavity Fabry-Pérot interferometric sensor can be realised by depositing a thin film on an end-face of a fibre [Schultheis, 1988; Schultheis *et al.*, 1988; Beheim *et al.*, 1989], by attaching on to a fibre end-face a micro-cavity Fabry-Pérot fabricated with surface micro-machining techniques [Mitchel, 1989; Kim & Neikirk, 1995], by facing two fibre ends with a short ($< 1\text{mm}$) air-gap [Murphy *et al.*, 1992; Oort & Kate, 1994; Murphy, 1996], by placing a flat diaphragm directly in front of the cleaved surface of a fibre end [Zhou & Letcher, 1995], or by fabricating an in-line fibre etalon (ILFE) [Sirkis *et al.*, 1995]. An ILFE is a Fabry-Pérot etalon assembled by fusion splicing at both ends of a hollow-core fibre to two solid-core fibres which have the same diameter as the hollow-core fibre. Hence a continuous and uniform-diameter fibre sensor is formed. Either the intrinsic or extrinsic short-cavity Fabry-Pérot interferometric sensors have performed well as temperature, strain or vibration sensors.

A short Fabry-Pérot cavity length limits the type of signal processing that can be used. On the other hand such short cavity length allows the use of relatively inexpensive light emitting diodes (LED). If the coherence length of the LED is much greater than the optical path difference (OPD) of an FFPS, the fringe visibility of the interferometric output is constant and thereby gives an interferometric output unambiguous only in an interval of 2π phase change. Otherwise, the fringe visibility decreases with increasing difference between the OPD of the interferometer and the coherence length of the LED, *i.e.* white-light interferometry (WLI) [Rao & Jackson, 1996]. WLI is described with greater depth in section 2.4.1.1 since it is one of the possible signal processing techniques to obtain a large UMR for an interferometric sensor. In either coherent or incoherent interrogation of a short cavity Fabry-Pérot interferometric sensor, the measurand resolution is primarily diminished by the short cavity/sensing length of the interferometer.

2.2.2 Reduced Sensitivity Via the Reduction of the Effective Refractive Index

2.2.2.1 Polarimetric Sensors

Many reasonably wide measurand range temperature, strain, pressure and force sensors have exploited the sensitivity of the state of polarisation (SOP) of a beam launched into a birefringent fibre [Eickhoff, 1981; Corke *et al.*, 1984; Varnham *et al.*, 1983; Franks *et al.*, 1985; Martinelli & De Maria, 1988; Hogg *et al.*, 1989; Domanski *et al.*, 1995; Campbell *et al.*, 1996]. A typical in-fibre polarimetric sensor involves splicing a lead-in and a sensing birefringent fibre such that their polarisation axes are crossed at a 45° angle and the input beam is launched along one of the polarisation axis of the lead-in fibre. A lead-out birefringent fibre can similarly be spliced with the sensing fibre to form an in-line arrangement that can be addressed in transmission. In such cases, the output beam is obtained from either of the two polarisation axes of the lead-out fibre. Alternatively to address a polarimetric sensor in reflection, the distal end of the sensing fibre is made reflective and the beam returning along the unused polarisation axis of the lead-in fibre is subsequently monitored.

A polarimetric sensor can be considered as a two-beam interferometric arrangement. Instead of combining amplitude-divided beams using a directional coupler in a fibre Mach-Zehnder or Michelson interferometer, a linear

polariser can combine two orthogonally polarised beams guided in birefringent fibre. The relevant “interferometric” or polarimetric phase, φ_{pol} , of beam leaving the output polariser is given by

$$\varphi_{pol} = 2\pi \frac{B L_M}{\lambda} \quad \text{Eq. 2.11}$$

where λ is the vacuum wavelength of the input beam and L_M the length of the birefringent fibre exposed to temperature or strain. Clearly, φ_{pol} is proportional to the fibre’s birefringence, B , which is given by

$$B = n_{fast} - n_{slow} \quad \text{Eq. 2.12}$$

where n_{fast} and n_{slow} are the refractive index along the fast and slow axis respectively. Compared with the measurement of the phase of an interferometric sensor over the same physical sensing length L_M and the same wavelength of the light source, φ_{pol} can be expected to vary more slowly with respect to changes in measurand because the ratio $\frac{n}{B}$ is typically large (n is the usual refractive index of a fibre interferometer). However the ratio between the UMR of a polarimetric and an interferometric sensor depends on $\frac{d(n L_M)/dM}{d(B L_M)/dM}$.

2.2.2.2 Dual-Mode Sensors

In weakly-guiding single-mode optical fibres, instead of only guiding the fundamental spatial mode, multiple modes *e.g.* LP_{01} and LP_{11} modes, can be guided by choosing the wavelength of the light source to be above the cut-off wavelength of the next higher-order modes. In a perfectly circular core fibre, these spatial modes are orthogonally polarised and have the same effective refractive index. However this is not the case for a birefringent fibre. In the case of elliptical-core (e-core) birefringent fibres operated at the onset of the two-mode regime, only the two LP_{11}^{even} modes (one for each polarisation) can propagate instead of the usual four LP_{11} modes [Kim *et al.*, 1987]. The elimination of the LP_{11}^{odd} modes can allow stable and well-defined interference between an LP_{01} and an LP_{11} mode.

Just like in a polarimetric sensor, a dual-mode sensor can be considered as a two-beam interferometer whose interferometric arms are manifested by the spatial distribution of the modes. The two spatial modes interfere when their electric fields overlap in a plane transverse to the axis of the fibre. The resulting interference pattern is characterised by their overlapping regions which exhibit an average intensity that varies as the optical phase

difference between the two spatial modes changes. This phase difference can vary because the propagation constants and the common physical path length of the two modes can change with temperature or strain [Wang, A. B. *et al.*, 1991a]. This inter-modal interference can be detected using a variety of methods [Murphy *et al.*, 1990]. A common feature of these methods is the spatial masking of one of the lobes of the inter-modal interference. Spatial filtering can be accomplished with a conventional pin-hole-type spatial filter [Wang G. Z. *et al.*, 1991; Grossman & Costandi, 1992], an elliptical-core fibre fusion-spliced with an ordinary single-mode fibre such that their cores have a slight lateral offset [Berkoff & Kersey, 1992], or with a pair of biconically tapered fibres fused side-by-side [Wang, A. B. *et al.*, 1991b].

The relevant dual-mode phase, φ_{dual} , is given by

$$\varphi_{dual} = 2\pi \frac{(n_1 - n_2) L_M}{\lambda} \quad \text{Eq. 2.13}$$

where L_M is the common physical sensing length of the modes exposed to a measurand. n_1 and n_2 are the effective refractive indices of the two spatial modes guided in the fibre. There is clearly a close similarity between a polarimetric and a dual-mode sensor. However, because n_1 and n_2 are very similar and also depend on the difference between the refractive index of core and cladding, a dual-mode sensor can be expected to exhibit lower measurand sensitivity compared with a polarimetric sensor of the same sensing length and source wavelength.

2.2.3 Using Direct Physical Techniques

Physical techniques can be applied to an OFS to reduce its sensitivity. Wolinski *et al.* [1996] reduced the sensitivity of a polarimetric sensor by covering the sensor with a specially prepared cylindrical epoxy. This epoxy-jacket modified the usual deformation in a highly birefringent (HiBi) fibre caused by temperature, strain or pressure. In their work, Wolinski *et al.* obtained $E_{UMR,P} \cong 5$ for the measurement of pressure P . Their technique can also be applied to interferometric sensors and the corresponding $E_{UMR,M}$ value depends on the thermo-elastic properties of the epoxy and the thermo-mechanical interaction between the epoxy and an optical fibre.

One method of reducing the sensitivity of a polarimetric sensor is to fusion splice two sections of a birefringent fibre such that the fast and slow polarisation axes of the first section are aligned respectively with the slow and fast

axes of the second [Farahi *et al.*, 1988b; Bock *et al.*, 1994]. When a length L_1 of the first fibre and a length L_2 of the second fibre are exposed to the same average amount of measurand change, the effective sensing length for polarimetric phase change is reduced to $L_M = |L_1 - L_2|$. Using this technique which effectively provides an abrupt twist of 90° in a single birefringent fibre polarimetric sensor, $E_{UMR,M} = \left| \frac{L_1 + L_2}{L_1 - L_2} \right|$. Interestingly when $L_1 \cong L_2$, the concatenated fibre exhibits very low temperature or strain sensitivity. Such a configuration becomes ideal in assembling a temperature- or strain-insensitive polarimetric sensor designed to measure other effects, *e.g.* a Faraday-Effect fibre polarimetric current sensor [Noda *et al.*, 1986; Day & Rose, 1988; Tang *et al.*, 1991; Ning *et al.*, 1995].

The discussion in the preceding paragraph implies that some of the techniques intended to produce sensors exhibiting excellent immunity to either temperature or strain can alternatively be considered as techniques to obtain very large UMR since in general the resulting sensors exhibit some residual sensitivity which is ideal for enlarging the UMR. However, these techniques are not further explored in this chapter because unless such temperature- or strain- insensitive sensors are used in conjunction with a more sensitive same-measurand sensor, the dynamic range of such measurand-insensitive sensors is unchanged. UMR-extending techniques which also enlarge the dynamic range of an interferometric fibre sensor are explored in the next three sections.

2.3 Direct Extension of Unambiguous Phase Measurement Range Approaches

The UMR of an interferometric sensor can be extended if the interferometric phase change ($\Delta\varphi$) can be unambiguously determined over a range of more than 2π radians. For example, Chien [1992] has measured unambiguously up to $2N\pi$ radians phase shift in what the author refers to as an “open-loop” Sagnac fibre gyroscope. Similarly, Turner *et al.* [1992] applied the same approach to extend the UMR of a polarimetric strain sensor.

The technique of Chien or Turner *et al.* involves two steps. The first step is modulating the interferometric output (which is typically proportional to $\cos(\varphi)$) at some carrier angular frequency ω_c such that the final electronic (voltage) signal is of the form

$$V_{sig} = A \cos(\omega_c t + \varphi) \quad \text{Eq. 2.14}$$

where A is some constant voltage amplitude, φ the interferometric phase and t time. Any one of a variety of schemes known as “Phase-Generated-Carrier” schemes can be used to obtain an electronic signal described in Eq. 2.14 [see Cole *et al.*, 1982; Jackson *et al.*, 1982; Voges *et al.*, 1982; Dandridge *et al.*, 1983; Kersey *et al.*, 1984; Lewin *et al.*, 1985; Martinelli & De Maria, 1988; Berkoff *et al.*, 1990; Ono *et al.*, 1991; Giulianelli *et al.*, 1994]. In the work of Chien, he used a pseudo-heterodyne signal processing scheme (see Jackson *et al.*, 1982) whilst in the work of Turner *et al.*, they used a “heterodyne-type” signal recovery scheme similar to that reported by Kersey *et al.* [1984]. The details of these two schemes are not critically important in the current discussion and are left to the interested reader to investigate.

The second step involved in the technique of Chien or Turner *et al.* is frequency dividing by N the electronic signal expressed in Eq. 2.14. Both Chien and Turner *et al.* have chosen,

$$N = 2^m \quad \text{Eq. 2.15}$$

where m is a positive integer. Although N can be any integer, frequency division by 2^m can easily be obtained by observing the final output of m cascaded digital toggle flip-flop circuits, *i.e.* a binary counter (hence Eq. 2.15). The result of frequency-down-shifting V_{sig} can be expressed as

$$V'_{sig} = A \cos\left(\frac{\omega_c}{N} t + \frac{\varphi}{N}\right). \quad \text{Eq. 2.16}$$

From the measurement of the electronic phase of V'_{sig} , the effective UMR corresponds to $2\pi = \Delta\left(\frac{\varphi}{N}\right)$ or $2N\pi = \Delta\varphi$. For this frequency-division method, $E_{UMR,M} = N$.

The binary-frequency division method of extending the UMR of an interferometric sensor is certainly very attractive because of the exponential nature in extending the final UMR (see Eq. 2.15). However, besides the method requiring a substantial amount of signal processing, it also reduces the fundamental angular frequency of the sensing arrangement to $\frac{\omega_c}{N}$. This down-shifted fundamental frequency limits the frequency bandwidth of φ (and measurand change as well) to a value reduced by a factor of $\frac{1}{N}$. On the other hand, the effect of this $\frac{1}{N}$ factor can be alleviated by choosing a large carrier frequency (10 MHz as in the case of Chien).

difference f_{beat} is the product of $\frac{L_{OPD}}{c}$, the time delay between the interfering beams, and $f_{saw} \Delta\nu$, the constant rate of change of the optical frequency of the light source; *i.e.*

$$f_{beat} = \frac{L_{OPD}}{c} f_{saw} \Delta\nu. \quad \text{Eq. 2.17}$$

f_{saw} is the frequency of the sawtooth ramp, L_{OPD} the OPD of the interferometer, and $\Delta\nu$ the optical frequency ramp amplitude. Subsequently, the resulting interference beats at a frequency of f_{beat} and such beating effect can be detected by a photodetector. Clearly from Eq. 2.17, variations in L_{OPD} can be determined from variations in the beat frequency. Hence the measurand dynamic range is determined by the characteristics of the measuring system for the beat frequency.

An FMCW-type signal processing scheme can be implemented with a single-longitudinal-mode LD with its drive current modulated in a sawtooth manner [Jacobsen *et al.*, 1982; Giles *et al.*, 1983]. However, this current modulation results in modulation of both the frequency and intensity of the LD output [Kobayashi *et al.*, 1982]. The intensity modulation can be compensated by re-normalisation of the final interferometric output. Several interferometric or polarimetric sensors based on a FMCW technique implemented with a modulated LD have been demonstrated as stress-location [Franks *et al.*, 1986; Zheng *et al.*, 1996] or displacement/strain sensors [Uttam & Culshaw, 1985b; Campbell *et al.*, 1996]. However, because of the limited dynamic range in the measurement of the beat frequency and the limitations attributed to the LD current modulation, the OPD of these sensors has been limited to values between 0.05 m to 10 m. The upper limit is determined by the coherence length of the modulated LD whilst the lower limit by the desired measurand resolution [Uttam & Culshaw, 1985b]. An OPD resolution in the order of 100 μm is not uncommon.

To achieve large dynamic range, the LD needs to be modulated with as large as possible ramp amplitude frequency, $\Delta\nu$. Unfortunately, an ordinary index-guided single-mode LD cannot be modulated with a very large $\Delta\nu$ without driving the LD output to mode-hop [Economou *et al.*, 1986]. Alternatively, distributed feedback (DFB) LD can instead be used. The output of a DFB LD is less susceptible to mode-hop and also exhibits a longer coherence length than a conventional single-mode LD. Hence with a DFB LD, a longer OPD (~ 30 m) can be

measured [Zhou *et al.*, 1996]. A drawback with the use of a DFB LD is its relatively high cost compared with other single-mode LDs.

Recently, Zhou *et al.* [1996] demonstrated a novel technique to extend the measurement range of an FMCW reflectometer based on a modulated DFB LD. In their work, a uni-directional optical fibre loop was introduced into one of the arms of a fibre Michelson interferometer (reference arm) whilst the fibre under investigation was placed in the other (sensing) arm. The optical fibre loop, which employed an acousto-optic modulator (AOM) and an opto-isolator, effectively produced several reference beams for the Michelson interferometer. The N -th reference beam was the beam which had circulated the loop N ($= 0, 1, 2, \dots$) times. Interestingly the N -th reference beam experienced an optical frequency shift of $N \times f_{FS}$ and a relative temporal delay of $N \times \frac{OPL_{loop}}{c}$ which were due to the operation of the AOM and the inherent delay caused by the optical path length of the loop (OPL_{loop}) respectively. f_{FS} ($= 85$ MHz) was the single-pass frequency shift introduced by the AOM. The relative delay $N \times \frac{OPL_{loop}}{c}$ was with respect to the zeroth-order ($N=0$) reference beam which did not traverse the uni-directional loop.

The sensing beam which had traversed the sensing fibre interfered with the N -th reference beam only when the OPD between these beams was less than the LD coherence length. In their arrangement, OPL_{loop} had been chosen to be slightly shorter than the coherence length of the LD output. Consequently, the sensing and the N -th reference beams interfered when OPD_{fibre} was between $N \times OPL_{loop}$ and $(N + 1) \times OPL_{loop}$. OPD_{fibre} was the optical path difference between the sensing arm and the reference arm without the loop. Zhou *et al.* obtained a 3-fold increase ($E_{UMR,M} = N = 3$) in the measurement range which was limited by the transmission loss of the AOM. Nevertheless, their technique overcame the limitation imposed by the coherence length of the modulated laser by utilising a uni-directional optical fibre loop. Unfortunately, the scheme can not be applied to a fibre Fabry-Pérot interferometer which has no spare arm in which to place an optical loop.

The resulting interferometric signal within each ramp period obtained from an interferometer illuminated with an FMCW-type modulated LD exhibits a characteristic phase relative to the ramp. This electrical phase is practically

proportional to the OPD of the interferometer and is unambiguous only for a 2π phase change. Detecting small changes in the OPD can be obtained from the measurements of the changes in this phase. In such instances, the beat frequency remains essentially constant. Essentially, what has just been briefly described is the pseudo-heterodyne phase demodulation scheme [Jackson *et al.*, 1982]. The simultaneous measurement of the beat frequency and phase of an FMCW interferometric signal can provide an absolute measurement of the OPD with coarse resolution together with a high resolution measurement of OPD changes [Campbell *et al.*, 1996].

2.4.1.2 Low-Coherence or White-Light Interferometry

Low-Coherence or White-Light interferometry (WLI) generally refers to a scheme which involves illuminating a (sensing) fibre interferometer with a light source which has a coherence length substantially less than the OPD of the sensing interferometer and interrogating the output of this sensing interferometer with a second (receiving or reference) interferometer or with a spectrometer [Rao & Jackson, 1996].

The receiving or reference interferometer followed by a single photodetector may be used to analyse the output of the sensing fibre interferometer illuminated by a low-coherence source. The photodetector detects interferometric fringes as soon as the difference between the OPD of the receiving and sensing interferometers is similar to or less than the coherence length of the light source. The signal from the photodetector is recorded while the OPD of the receiving interferometer is scanned over a range which surrounds and includes the position of zero path unbalance for the tandem interferometers. For high signal-to-noise ratio and low coherence length, the interferogram recorded above contains a central fringe which is reasonably easily identified. Changes in the OPD of the sensing interferometer can be readily tracked by following the changes in the balancing position of the receiver interferometer. For lower signal-to-noise ratios or long coherence length sources, the identification of the centre of the low coherence fringe pattern is more difficult. The usual method is to fit an equation to the overall fringe pattern to identify the central fringe and then interpolate between data points to find the centre of this fringe. A number of other techniques have been used for recording the low coherence fringe pattern or for enhancing the relative size of the central fringe (*e.g.* recording the whole fringe pattern using a charge-coupled-device (CCD))

array or superimposing a number of low coherence fringe patterns at different wavelengths [Rao & Jackson, 1996] but the principle of the measurement remains the same.

Sensing interferometers with short OPD are more appropriate for WLI using a scanning receiver interferometer (the changes in OPD tend to be small). On the other hand, larger OPD sensing interferometers can still be used. However, an OPD bias generally needs to be introduced in the receiving interferometer and used together with the scanning arrangement in order to cope with large changes in sensing interferometer OPD. Errors in determining the value of this OPD bias limit the accuracy in measuring the OPD of the sensing interferometer.

A major drawback of WLI using a scanning interferometer is slow signal processing time [Kaddu, 1996]. Typically, the scanning process involved mechanical components which are generally slow [*e.g.* Koch & Ulrich, 1991]. On the other hand the scanning time can greatly be reduced by expanding the output beam from the sensing interferometer onto a wedge Fizeau interferometer which has an average OPD similar to the OPD of the sensing interferometer. The resulting output produces an interferogram which can be projected onto a CCD array [Murphy, 1996]. Another contributor to the slow processing time is the determination of the centre of the central fringe. Most low-coherence sources which can launch useful powers into an optical fibre have spectral bandwidths which are much less than is desirable for WLI. Hence the fringe patterns tend to be relatively long and computer processing is generally required to find the centre of the central fringe.

The measurand range for WLI is determined by the scanning range of the receiver interferometer. The measurand resolution is determined by both the scanning resolution of the receiver interferometer and by the signal processing algorithm used to find the centre of the central fringe. Although the resulting measurand range can be extremely wide, the measurand resolution can not rival the best resolution determined from other interferometric signal processing techniques. The centre of the central fringe can be resolved to as high as 1/200 of a fringe and is attainable by employing some intra-fringe interpolation schemes [Kaddu, 1996].

On the other hand, an enhancement of the dynamic range can be achieved by first identifying one of the fringes of the interferogram and following this by tracking a fixed point on this chosen fringe by some active feedback mechanism which suitably adjusts the OPD of the receiving interferometer (enhanced white-light interferometry) [Gerges *et al.*, 1987; McGarrity & Jackson, 1998]. Changes in the OPD of the sensing interferometer can be related to changes in the feedback signal. However, the measurand range in such an arrangement is limited by the tracking range of the feedback system.

The intensity of resulting optical output of the sensing interferometer remains constant even though the OPD has been modulated by a measurand such as temperature or strain. On the other hand the output of the sensing fibre interferometer has an optical spectrum which can be modified by variations in the OPD. In the wavelength domain, the output spectrum of the sensing interferometer exhibits regular spectral peaks which are separated by a wavelength difference inversely proportional to the OPD of the interferometer, *i.e.* a channelled spectrum. Clearly by employing a spectrometer, a measurement of the spectral separation between adjacent peaks is a simple and direct measurement of the OPD [Egorov *et al.*, 1995; Bhatia *et al.*, 1996]. On the other hand, the use of a usually bulky spectrometer is not attractive for practical applications, and such measurements are generally limited to laboratory conditions. Spectrometer measurements usually involve long processing times and give measurand resolution dictated by the spectral resolution of the spectrometer.

White-light interferometry is certainly very attractive because an LED can be used as the light source. LEDs are low cost and easy to operate compared with an LD. Although an LED has low output power, higher power superluminescence LEDs (SLEDs) can also be used.

2.4.2 Measurement of Optical Path Length, Group-Delay, Dispersion of an Optical Fibre

2.4.2.1 Dispersive Optical Fourier Transform Spectroscopy

A closely related technique to WLI is dispersive optical Fourier transform spectroscopy (DFTS). Unlike WLI which requires a sensing interferometer and a receiving interferometer, DFTS requires only one interferometer, the sensing interferometer. The technique involves calculating the phase information from the Fourier transform of

the resulting interferogram as the OPD of the sensing interferometer is scanned. The sensing interferometer effectively filters only the beams with wavelengths simultaneously falling within the spectrum of the light source and the transfer spectrum of the interferometer, *i.e.* a channelled spectrum. The strength of DFTS is its capability to extract the information attributed to the dispersion in the sensing interferometer as the spectral spacing of the channelled spectrum is varied.

Typically in DFTS, a sensing interferometer is illuminated by two light sources, a low-coherence source (*e.g.* an LED) and a high-coherence source (*e.g.* a stabilised HeNe laser). While the OPD of the interferometer is varied to produce the interferogram corresponding to the low-coherence source, the interference fringes corresponding to the high-coherence source can be used to calibrate the scan of the white-light interferogram. This interferogram and the output optical spectrum of the interferometer form a Fourier transform pair.

Flavin *et al.* [1993] have employed DFTS for the simultaneous measurement of temperature and strain (SMTS). They obtained two simultaneous equations to discriminate temperature and strain by measuring the changes in the difference in the group delay and in the difference in the dispersion between the two arms of the interferometer [Flavin *et al.*, 1994]. These differences can be extracted by fitting a cubic polynomial to the phase of the Fourier transform of the resulting white-light interferogram. The linear and quadratic coefficients of the fit represent the change in the difference in the group delay and in the difference in the dispersion respectively.

DFTS was extremely successful in SMTS because the condition number for the corresponding sensitivity matrix \tilde{K} is very close to unity. On the other hand, the technique of Flavin *et al.* does not allow any possibility of increasing the measurand range because the linear and quadratic coefficients of the cubic fit are not periodic with temperature or strain. To increase the dynamic range of the measurement scheme, the dynamic range in obtaining the interferogram needs to be similarly increased.

As in the case with WLI, the requirement to scan the OPD of an interferometer and the need to subsequently calculate the Fourier transform of the interferogram limit the speed of measurement. Scanning the OPD of the

interferometer generally implies mechanical components which may not be suitable in practical measurement environments. Moreover because the OPD of the interferometer needs to be scanned around its zero value, optical Fourier Transform spectroscopy is not suitable for a fibre Fabry-Pérot interferometer which always has a non-zero OPD.

2.4.2.2 Measurement of Optical Path Length, Group-Delay, Dispersion of an Optical Fibre

One of the techniques that can be employed for SMTS is to measure the changes in both the optical path difference and the dispersion of a sensing optical fibre [Gusmeroli & Martinelli, 1994]. In their arrangement, Gusmeroli & Martinelli introduced a sensing fibre into an arm of a nearly balanced fibre Mach-Zehnder interferometer illuminated with 855 nm superluminescent source with a bandwidth of 17 nm. The output of the interferometer was analysed with a bulk-optic Michelson interferometer which had an OPD very similar to that of the sensing fibre Mach-Zehnder interferometer. To recover the phase of the sensing interferometer, the OPD of the Michelson interferometer was further varied in a sawtooth manner in order to produce a periodic (serrodyne) signal, *i.e.* a phase-modulated receiving interferometer (*c.f.* Brady *et al.*, 1995; Rao *et al.*, 1997b).

Instead of directly detecting the output of the Michelson interferometer with a single detector (which can also detect variations in the OPD of the sensing interferometer), Gusmeroli & Martinelli optically filtered the Michelson output beam into three separate beams detected by separate photodiodes. The filters were 5 nm band-pass filters whose peak wavelengths were 845 nm, 855 nm (the central wavelength of the source) and 865 nm. The three resulting signals varied at the same modulation (sawtooth) frequency but had different phase values because of the variations of the OPD of the Mach-Zehnder interferometer with wavelength (*i.e.* dispersion). Gusmeroli & Martinelli subsequently measured the relative phase of the 845-nm and the 865-nm (non-central wavelength) signals with respect to the 855-nm (central wavelength) signal. The sum of these two relative phase measurements was found to be proportional to the optical path difference whilst the difference between them to the dispersion.

The condition number for the corresponding matrix \tilde{K} for the technique of Gusmeroli & Martinelli was far from unity since the two differential phases were expected to have similar sensitivities. On the other hand, their sensing

arrangement would provide $E_{UMR,T} \cong 382$ and $E_{UMR,\varepsilon} \cong 4925$. The relatively large $E_{UMR,M}$ values compared with the $E_{UMR,M}$ values for the other techniques described in this chapter, can be attributed to fact that the sensitivity of the difference between the two differential phase measurements can be expected to be much less than either of the two differential phase measurements. In a sense, the technique of Gusmeroli & Martinelli can be considered as a three-wavelength technique.

Incidentally, DFTS can also measure the change in optical path length of the test fibre by extracting the zeroth order coefficient of the cubic polynomial phase fit. Compared with DFTS, the technique of Gusmeroli & Martinelli does not require the acquisition of an interferogram. However both techniques are similarly complex in terms of the amount of optical components required [*c.f.* Flavin, 1993; Gusmeroli & Martinelli, 1994].

Using a technique with some similarity to that of Gusmeroli & Martinelli, the mean and differential group delays between the fast and slow axis of a (sensing) birefringent fibre illuminated with a broadband source can be used for SMTS [Luke *et al.*, 1996]. In their arrangement, Luke *et al.* analysed the beams from a sensing birefringent fibre using a scanning Michelson interferometer. The scanning interferometer had along one of its arms a reference birefringent fibre with a length chosen in order to balance the OPD and dispersion between the sensing and reference fibres. From the resulting interferogram, the mean and differential group delays were calculated. Both the mean and differential group delays unambiguously measure, with different sensitivities, the temperature-strain state of the sensing fibre. Such unambiguous measurements of temperature or strain imply that the dynamic range of the sensing arrangement can only be increased by improving the resolution in the group delay measurements.

2.4.3 Spectrally-Encoded Measurements

There are several optical fibre sensors which produce an optical output with an optical spectrum that can change with temperature or strain. Because temperature or strain is uniquely encoded with the wavelength, a potentially unlimited measurand range can be obtained. However, the measurand resolution is limited by the resolution of the spectrometer. In the subsequent discussions, several spectrally-encoded sensors which have been reported for SMTS are described and assessed for their suitability for high-resolution and wide-range measurements. In the

discussions below the two most important spectrally-encoded sensor types are discussed. These sensors involve Brillouin scattering and in-fibre Bragg gratings.

2.4.3.1 Brillouin Scattering Sensors

One of the methods reported for SMTS exploits Brillouin scattering in an optical fibre [Parker *et al.*, 1997; Izumita *et al.*, 1997]. The simultaneous measurement of the frequency shift and optical power of a Brillouin scattered beam, which can have different sensitivity to temperature and strain, provide two independent measurements. The determinant of the corresponding sensitivity matrix \tilde{K} is non-zero and hence the technique is suitable for SMTS. However, the extension of measurand range for these sensors is not relevant as neither the scattering frequency nor the scattered power is periodic with respect to temperature or strain. Although Brillouin scattering is not an interference effect, the detection of the frequency shift of a Brillouin scattered beam is obtained interferometrically [Davis & Kersey, 1997].

Davis & Kersey [1997] detected the Brillouin scattering frequency shifts and the wavelength shifts of a fibre Bragg grating in a single fibre for SMTS. For ease of detection, the optical wavelength of the Brillouin beam and the Bragg wavelength were chosen to be substantially different, 1319 nm and 1551 nm respectively. Davis & Kersey expected different temperature and strain sensitivities for the Brillouin scattering frequency shift and the Bragg wavelength shift because Brillouin scattering and the Bragg resonance in an optical fibre are different physical processes. However their arrangement was quite complex because it required one set of equipment to detect Bragg wavelength shifts and another to determine Brillouin scattering frequency shifts. The system described by Davis & Kersey is more suited to measurements in the laboratory rather than in the field.

High resolution Bragg wavelength shift measurements can be achieved using an interferometer (see section 2.4.3.2). In such cases, the Bragg wavelength shifts can provide high resolution measurement whilst the Brillouin scattering frequency can identify the fringe order of the phase change in the interrogating interferometer used to measure the Bragg wavelength shift.

2.4.3.2 In-Fibre Bragg Grating Sensors

In-fibre Bragg gratings (FBGs) are one of the most promising developments in optical fibre sensing technology [Rao, 1997; Kersey *et al.*, 1997]. FBGs are attractive because they can be illuminated by a low-coherence source and a direct measurement of their central Bragg wavelength feature using a spectrometer can determine unambiguously the total shift due to temperature or strain.

However shifts in the Bragg wavelength due to temperature or strain are very small. For example at a Bragg wavelength of $\lambda_b = 785 \text{ nm}$, $\Delta\lambda_b/\Delta T \approx 5 \text{ pm}/^\circ\text{C}$ and $\Delta\lambda_b/\varepsilon \approx 0.6 \text{ pm}/\mu\varepsilon$ for temperature and strain respectively.

Hence to obtain highly resolved measurements, detection of very small shifts in the Bragg wavelength is crucial.

Unfortunately, typical optical spectrometers exhibit low wavelength resolution. Alternatively, an FBG can be interferometrically interrogated by simply directing the reflected beam from an FBG towards an unbalanced interferometer [*e.g.* Kersey *et al.*, 1992; Weis *et al.*, 1994]. The equivalent interferometric phase change, $\Delta\varphi$, due to a Bragg wavelength shift, $\Delta\lambda_b$ is given by

$$\Delta\varphi = 2\pi \frac{L_{OPD}}{\lambda_b^2} \Delta\lambda_b \quad \text{Eq. 2.18}$$

where L_{OPD} is the OPD of the interrogating interferometer. Choosing a large value for L_{OPD} means a large measurand resolution. However L_{OPD} can not be longer than the equivalent coherence length of the FBG beam otherwise no interferometric phase change can be detected. The spectral bandwidth and hence the coherence length of the FBG beam depend on the spectrum of the illuminating light source and the reflectance spectrum of the FBG. For a typical grating with a bandwidth of 0.2 nm, the equivalent coherence length is about 3 mm for $\lambda_b = 785 \text{ nm}$. Likewise the interferometric detection of wavelength is unambiguous only for an interferometric phase change equivalent to 2π . Eq. 2.18 shows that to achieve a UMR that is as large as possible, the OPD of the interferometer L_{OPD} can be chosen to be as short as possible. Hence the choice of the value of L_{OPD} determines both the measurand range and resolution. Obviously issues pertinent to interferometric detection of Bragg wavelength shift are similar to that of a fibre interferometer.

The UMR for the interferometric detection of Bragg wavelength shifts can be extended using two interferometers with OPDs $L_{OPD,1}$ and $L_{OPD,2}$. Assuming $L_{OPD,1} > L_{OPD,2}$, the ratio between the equivalent Bragg-wavelength-phase-measurand sensitivities of the two interferometers is given by

$$K_{rM} = \frac{L_{OPD,1}}{L_{OPD,2}} \geq 1. \quad \text{Eq. 2.19}$$

For a dual-interferometric interrogation of wavelength shifts of a single FBG, $E_{UMR,M}$ is given by Eq. 2.7 or Eq. 2.8 depending on the value of K_{rM} .

Rao *et al.* [1996] employed a dual-cavity interferometric wavelength scanner based on the Michelson interferometer with its OPD sawtooth-modulated [Brady *et al.*, 1995]. The OPD of the interferometers, $L_{OPD,1} = 2.03$ mm and $L_{OPD,2} = 0.71$ mm, were obtained by switching between two different length values of one of the arms of the Michelson interferometer during a measurement run. These OPD values gave $E_{UMR,M} = 2.85$. Clearly, the response time of this arrangement was limited by the rate at which the OPD of the interferometer can be changed.

Alternatively, the wavelength shifts of a single FBG can be detected using two cascaded interferometers with different OPD, $L_{OPD,1}$ and $L_{OPD,2}$. The first interferometer is the usual interferometric wavelength scanner whilst the second interferometer is a phase-modulated (serrodyne) receiving interferometer [Rao *et al.*, 1997b]. Rao *et al.* [1997b] used $L_{OPD,1} = 28$ mm and $L_{OPD,2} = 0.7$ mm to achieve $E_{UMR,M} = 40$. The advantage of this latter arrangement was that the phase of each interferometer can be frequency-multiplexed. Conceptually two interferometers can also be employed in parallel.

There are alternative Bragg-wavelength-detection schemes which can rival interferometric detection of Bragg wavelength shifts. The beam reflected from an FBG can be used as the input beam to an interferometer whose OPD can be varied about the zero-OPD value. If the OPD scan is calibrated with respect to the interferogram for a reference beam (*e.g.* 1.319 μm Nd:YAG beam), the Fourier transform of the interferogram for the FBG beam can be calculated, *i.e.* Fourier transform spectrometer [Davis & Kersey, 1995]. The dominant high frequency component of the FBG interferogram corresponds to the Bragg wavelength of the grating. Interestingly, to obtain

this high frequency component, a short scan of the FBG interferogram is sufficient. Clearly, such method can improve the interrogation/processing time of the FBG. In addition, the method can be used to demultiplex the signals from two FBGs which would exhibit different values for the high frequency component in their corresponding interferograms [Flavin *et al.*, 1997].

Recently Dakin *et al.* [1997] employed a novel scheme to interrogate an FBG. Their scheme was based on pairing the FBG with another grating with similar characteristics. The second grating was introduced into the same fibre to form a fibre Fabry-Pérot interferometer (FFPI). In their arrangement, the FFPI was illuminated using a broadband light source and was exposed to the measurand. The reflection from the FFPI was interrogated using a Michelson interferometer (*i.e.* white-light interferometry). The strength of the technique of Dakin *et al.* was based on changing the OPD of the Michelson interferometer at a fast rate. Subsequently as soon as the OPD of the FFPI and the Michelson interferometer were similar, a burst of interference fringes can be observed at the output of the Michelson interferometer. This burst of fringes was essentially a temporal version of the white-light interferogram for the FFPI. This temporal interferogram manifested a dominant characteristic frequency corresponding to the Bragg wavelength of the grating pair. Shifts in the wavelength of the grating was exhibited as shifts in the dominant frequency of the temporal interferogram. The average velocity in displacing the scanning mirror of the Michelson interferometer had to be high in order to obtain a large dominant frequency in the detector output so that resolution was possible. The scheme can be used to coherently multiplex several gratings which had been paired with similar gratings to form FFPIs with different OPDs. Each grating pair can be differentiated by the different arrival times of the corresponding burst of fringes or temporal interferogram. The different arrival times were due to the different OPD of the FFPIs.

Fibre lasers based on FBGs can be used to measure temperature or strain [Ball *et al.*, 1993; Othonos *et al.*, 1993]. Shifts in lasing wavelength of a fibre laser with FBG reflectors can either be caused by the temperature or strain sensitivity of the gratings or the laser cavity. Likewise, the output of a fibre laser can be detected interferometrically [Koo & Kersey, 1995]. Conceptually, two fibre lasers with different sensitivities to temperature or strain can be multiplexed to provide SMTS or provide an extended dynamic range single-measurand

arrangement [Alavie *et al.*, 1993; Kersey & Morey, 1993; Koo & Kersey, 1995]. The major advantage of a fibre laser is greater signal-to-noise ratio at the detector compared with an FBG illuminated by a broad-band source. However the need to ensure population inversion in the fibre laser cavity increases the complexity of any sensing arrangement based on fibre lasers.

Many sensing arrangements based on two FBGs with different sensitivities to temperature and strain have been exploited for SMTS. One of the earliest of these schemes involved two FBGs, a sensing and reference FBG. [Morey *et al.*, 1992b]. The reference FBG, which is configured to be protected from strain, can be used to measure the temperature of the sensing FBG.

Alternatively, these dual-FBG sensing arrangements can be used to obtain a sensing arrangement with a high measurand resolution. In such cases, these dual-FBG arrangements can either be classified as a dual sensor or a dual-wavelength technique. However because much work has been reported in the use of FBGs for SMTS, these FBG-based schemes are described in a separate sub-section (2.5.3) after schemes involving two distinct sensors or light sources have been described.

2.5 Dual-Measurement Approaches

2.5.1 Two Distinct Sensors

One of the simplest methods of extending the UMR of an interferometric sensing arrangement is to employ two interferometric sensors with either very different or very similar sensitivities. Although a birefringent fibre interferometric sensor described in section 2.5.5 can be considered as a dual interferometer formed at the same location, techniques employing two distinct sensors are described in this present sub-section. An extended dynamic range is exhibited by the combined operation of the two distinct interferometric sensors which by themselves provide a limited UMR. Unfortunately, the improvement in the performance of the combined sensor comes at the cost of two signal demodulation schemes.

2.5.1.1 Schemes Not Involving Fabry-Pérot Interferometric Sensors

Chiang & Tsuchida [1988] demonstrated a dual polarimetric sensor which exhibits an extended temperature range. The two polarimetric sensors employed birefringent fibres of the same type but of slightly different (sensing) lengths, $L_1 (= 520 \text{ cm})$ and $L_2 (= 500 \text{ cm})$, exposed to temperature. Because the same type of fibres was used, $E_{UMR,T} = \frac{L_1}{|L_1 - L_2|}$ (or $E_{UMR,T} = 26$). Experimentally, Chiang & Tsuchida observed slightly higher $E_{UMR,T}$ values for different pairs of sensing length and attributed their results to their under-estimation of the sensing lengths of the fibre. Their underestimation may have been compounded by thermal conduction along the fibres.

Alternatively, a similar result can be obtained by employing two fibres with different characteristics. Herzog & Meyrueis [1990] arranged pairs of single-mode fibres of different physical properties into two fibre Mach-Zehnder interferometers. Each interferometer was fabricated from the same type of fibre and one of the arms of each interferometer was placed in the measurement environment (*e.g.* pressure chamber). Herzog & Meyrueis successfully employed this double interferometric fibre sensing arrangement to measure pressure (P) with good performance for correcting temperature-induced effects. To extend the UMR for either pressure or temperature, $E_{UMR,M}$ is given by Eq. 2.7 and Eq. 2.8, depending on the sensitivity ratio of the two fibres interferometers. For example, using one of their pressure measurement results, $E_{UMR,P} \approx 3$ could be obtained.

Navarette & Bernabeu [1994] proposed a three-branch fibre interferometer based on fibre Mach-Zehnder interferometers for the measurement of two parameters. Their three-branch design involved introducing a (inner) fibre Mach-Zehnder interferometer into one of the arms of the second (outer) Mach-Zehnder interferometer. Essentially this novel arrangement can be considered as a system of two fibre Mach-Zehnder interferometers with a common reference arm and two sensing arms. Navarette & Bernabeu suggested that if the sensing arms have different sensitivities and same temperature and strain, then temperature and strain can be discriminated. On the other hand, as an extended-UMR single-measurand arrangement, $E_{UMR,M}$ depends on the effective lengths of the two arms exposed to the measurand as was the case with the technique of Chiang & Tsuchida [1988].

2.5.1.2 Schemes Involving One Fabry-Pérot Interferometric Sensor

Zhou & Letcher [1995] developed a fibre-optic Fabry-Pérot microphone addressed in reflection. Their sensor measured the displacement of a diaphragm caused by acoustic vibration over an extended (displacement) range. The sensor was based on an extrinsic Fabry-Pérot interferometric sensor and an intensity-modulated sensor placed side by side in a single assembly. The surface of the diaphragm was placed very close and parallel to the end faces of a single-mode and a multimode fibre. The distal end face of the single-mode fibre and the surface of the diaphragm formed an extrinsic Fabry-Pérot sensor whilst that of the multimode fibre and the diaphragm, the intensity-modulated sensor. The intensity coupled back by the diaphragm into the multimode fibre depends inversely proportional to the square of the separation width between the distal end of the multimode fibre and the diaphragm. As the diaphragm vibrated, the variation in intensity received by the multimode fibre can be used to identify the fringe order of the interferometric phase change in the extrinsic Fabry-Pérot sensor. Since the received intensity behaved monotonically with the displacement of the diaphragm, $E_{UMR,M}$ can be large and limited by the minimum change in the received intensity that can be detected. On the other hand, the diaphragm can also be displaced by drifts in temperature. Hence the intensity-modulated signal may only be effective for dynamic displacement, *i.e.* mechanical vibration.

In another arrangement, a fibre Bragg grating (FBG) sensor can be combined with a Fabry-Pérot sensor. For the simultaneous measurement of temperature and micro-displacement, Ferreira *et al.*, [1996] specially designed and fabricated a sensor head which contained a single-mode fibre protruding from one end of the sensor head. The distal end of the single-mode fibre faced a mirror which could be mechanically displaced. Within the section of the fibre dangling inside the sensor head, an FBG was inscribed. Effectively, the sensing arrangement consisted of two sensors in series, an FBG sensor which is affected only by temperature change and an extrinsic Fabry-Pérot interferometer which was affected by both temperature and the displacement of the mirror (relative to the fibre end). For dual-parameter measurements, the Bragg wavelength of the FBG can be used to measure the temperature of the extrinsic Fabry-Pérot sensor. Alternatively to obtain a large dynamic range for temperature measurements, the Bragg wavelength shift can be used to identify the fringe order of the interferometric phase of the extrinsic Fabry-Pérot sensor.

Lui *et al.* [1997] developed a similar sensor head to that of Ferreira *et al.* [1996] which they embedded in a composite material for SMTS. The sensor head of Lui *et al.* involved a multimode fibre facing the end of a single-mode fibre with an FBG. Both the single-mode and multimode fibres were fusion spliced to a hollow capillary tube (128/300 μm) such that the FBG intentionally remained sensitive only to temperature. The sensing arrangement of Lui *et al.* behaved similarly to that of Ferreira *et al.* for simultaneous measurement of temperature and micro-displacement/strain and for extended-range temperature measurements. Unlike Ferreira *et al.*, Lui *et al.* found that their FBG exhibited a residual sensitivity to strain. This residual sensitivity can be attributed to fact that the FBG may not be dangling completely freely inside the capillary tube as intended. The diameter of the fibre was very similar to the inside diameter of the capillary tube which may also had been deformed when the whole sensor was embedded. This residual strain sensitivity of the FBG may be interferometrically detected and the resulting phase sensitivity combined with the phase of the extrinsic Fabry-Pérot sensor to produce an extended UMR strain sensor.

Instead of using a hollow capillary tube, an in-line Fabry-Pérot etalon (ILFE) can be used in tandem with an FBG [Jin *et al.*, 1997]. The advantage of using an ILFE is that a continuous uniform-diameter fibre can be formed and hence the resulting in-fibre sensor is ideal for embedding in composite materials. Jin *et al.* realised that the ILFE was only sensitive to axial strain whilst the FBG to both axial and transverse strain. With their ILFE/FBG hybrid sensor, they were able to simultaneously measure axial and transverse strain. Since axial and transverse strain can not be separated without much difficulty within a composite material, their sensor can not be used solely to measure axial strain in such circumstances. The ILFE/FBG sensor is also sensitive to temperature. A third sensor would be necessary to simultaneously measure all three parameters (*c.f.* the arrangement of Udd *et al.* [1997] described in section 2.5.3).

An intrinsic fibre Fabry-Pérot interferometer can be combined with an FBG to measure several parameters. Rao *et al.* [1997c] employed an FFPI composed of FBG reflectors in tandem with another FBG sensor along the same fibre. In their arrangement, Rao *et al.* were interested in simultaneously measuring temperature, strain and vibration. To measure vibration, the change in the OPD of the FFPI was interferometrically detected whilst the Bragg wavelength shifts in either of the twin FBG reflectors was used to measure temperature. The two FBG

reflectors were both protected from strain whilst the Bragg wavelength shifts of the third FBG was employed to discriminate strain. All three FBGs were placed very close to one another in order to ensure that either of the twin FBGs can measure the temperature of the third grating. Because of the narrow bandwidth of an FBG, several grating-based FFPIs can be wavelength-multiplexed [Henderson *et al.*, 1997].

2.5.1.3 Schemes Involving Effectively Two Distinct Fabry-Pérot Interferometric Sensors

An extrinsic in-line Fabry-Pérot etalon can be followed by an intrinsic fibre Fabry-Pérot interferometer to form a dual Fabry-Pérot sensor [Singh & Sirkis, 1997]. Along an optical fibre, an ILFE was first fabricated [Sirkis *et al.*, 1995]. The distal end of the concatenated fibre was cleaved at some short distance from the ILFE, thereby forming an intrinsic FFPI. The ILFE and the FFPI sensors exhibited different sensitivities to temperature and strain as expected. Singh & Sirkis have interrogated both sensors with two separate interferometers and have been successful in simultaneously measuring temperature and strain.

For extended-UMR measurements, their sensing arrangement would give $E_{UMR,T} \cong 100$ (using Eq. 2.8) and $E_{UMR,\epsilon} \cong 3.8$ (using Eq. 2.7) for temperature and strain respectively. The large value of $E_{UMR,T}$ had been anticipated because the ILFE was expected to exhibit a weaker sensitivity to temperature than the silica-core FFPI. The sensitivity of an ILFE to temperature was attributed to the low thermal expansion of silica ($\sim 0.5 \times 10^{-6}/^{\circ}\text{C}$) and the low thermo-optic coefficient of air ($\sim 0.1 \times 10^{-6}/^{\circ}\text{C}$) whilst the temperature sensitivity of the FFPI was determined by the large thermo-optic coefficient of silica ($\sim 12 \times 10^{-6}/^{\circ}\text{C}$) [Singh & Sirkis, 1997].

An FFPI with identical high-reflectance FBG reflectors which is illuminated with a broad-band source yields a reflection spectrum which exhibits Fabry-Pérot longitudinal mode structures with an amplitude envelope corresponding to the reflection spectrum of the FBG [Shlyagin *et al.*, 1997]. The change in the optical length of the Fabry-Pérot cavity and the FBG pitch can be detected from shifts in the longitudinal mode and the spectral envelope exhibited by the reflection spectrum of a twin-grating FFPI. Typically the shifts in the longitudinal modes are simpler to detect. Potentially two grating-based FFPIs with different sensitivities to temperature and

strain, either operated in parallel or in series, can be used to discriminate between these two parameters or alternatively to obtain a large dynamic range single-measurand sensing arrangement [Dakin *et al.*, 1997].

Earlier, Wosinski *et al.* proposed [1992] and evaluated [1994] a dual Fabry-Pérot sensor with two low-reflectance Bragg grating reflectors written in both cores of a twin-core fibre. In their arrangement, the twin-core fibre was required to have its cores sufficiently separated to avoid any cross-talk between the cores. The two measurements needed for SMTS were obtained by illuminating each core with slightly different wavelength light sources. The novelty of this dual-interferometric sensor was that the two Fabry-Pérot interferometers measure practically the same region. If the light sources have similar wavelengths, the corresponding temperature and strain sensitivities were not expected to be very different unless the materials for the two cores were intentionally chosen to be different [Wosinski *et al.* 1994].

2.5.2 Dual Wavelength Techniques

2.5.2.1 Extending the UMR of Interferometric/Polarimetric Sensors

One of the earliest techniques to extend the UMR of a fibre interferometric sensor was to excite the sensor with two light sources with different but similar wavelengths [Farahi *et al.*, 1988a]. The two wavelengths can be derived from separate sources like two single-mode LDs [Kersey *et al.*, 1986] or from a single laser output, *e.g.* an Argon laser [Gauthier & Turgeon, 1993]. Similarly two equivalent light sources with different wavelengths can be synthesized from the transmission through optical band-pass filters [Webb *et al.*, 1988b].

By using a two-wavelength illumination of a single fibre interferometric sensor, the corresponding phase at each wavelength exhibits slightly different measurand sensitivities. For extended-UMR measurements, the interferometric phase at each wavelength can be measured in the usual manner and the difference between the two interferometric phase measurements, the differential phase, can be used to identify the fringe order of the phase change of either of the two phase measurements [Liu *et al.*, 1991]. If the two (closely-spaced) wavelengths are λ_1 and λ_2 , then

$$E_{UMR,M} \cong \left| \frac{\bar{\lambda}}{\lambda_1 - \lambda_2} \right| \quad \text{Eq. 2.20}$$

where $\bar{\lambda}$ is the average of the two wavelengths. The smaller the wavelength difference, the greater is the value of $E_{UMR,M}$. For example, by using two LDs with $\lambda_1 = 785 \text{ nm}$ and $\lambda_2 = 783 \text{ nm}$, $E_{UMR,M} \cong 390$. The unambiguous phase range for the two wavelengths together corresponds to a 2π phase change for an interferometric sensor illuminated by an effective wavelength of $\frac{\lambda_1 \lambda_2}{\lambda_1 - \lambda_2}$. The minimum wavelength difference

between the light source is determined by the phase noise generated by the light sources [Meggitt *et al.*, 1988].

Alternatively, a suitably scaled electronic version of interferometric signal for each wavelength can become the x- and y-axis inputs of an oscilloscope and thereby tracing a Lissajous figure as the phase for each wavelength varies [McGarrity & Jackson, 1996]. Interestingly, when either of the two wavelengths is not an integral multiple of their wavelength difference, the instantaneous location and slope of the Lissajous figure on the oscilloscope monitor can uniquely identify the relative phase ($< 2\pi$) and fringe order (multiples of 2π) of each wavelength-multiplexed interferometric phase.

Similarly, the UMR of a polarimetric sensor can be extended using a dual-wavelength technique [Kersey *et al.*, 1989; Gauthier & Turgeon, 1993]. The measurand resolution remains that obtained by simply using the smaller wavelength phase measurement.

2.5.2.2 Extending the UMR of Dual-Evanesciently-Coupled-Core Fibre Sensors

Provided that the cores of a dual-core fibre are close enough, optical energy in one of the cores can transfer to the other core and back by evanescent coupling. Changes in coupling are detectable as changes in intensity of the light leaving the fibres. The periodic nature of this coupling can be characterised by a beat length which depends on temperature or strain. Since the coupling length also depends on the wavelength of the light source, SMTS can be achieved by illuminating the twin-core fibre with two light sources with different wavelengths [Meltz & Dunphy, 1988]. For two similar wavelengths, the corresponding coupling-measurand sensitivities are likewise similar and

hence suitable for extending the UMR of a dual-core evanescent sensor. Clearly, a twin-core evanescent sensor is an attractive sensor configuration because both cores can measure a parameter at the same location.

A dual-wavelength technique is very effective in extending the UMR of an interferometric sensor but not for SMTS. This can be expected because the total dispersion in the fibre for a small wavelength difference is extremely small. Mathematically, employing two different but similar wavelengths simply produce two phase measurements which are linear combination of one another unless the total dispersion between the two wavelengths is high. Thus, dual-similar-wavelength arrangements exhibit a very large condition number for the corresponding sensitivity matrix \tilde{K} .

2.5.2.3 More-Than-Two-Wavelength Illumination

More than two wavelength sources can also be utilised to extend the UMR of an interferometric OFS. The effective UMR corresponds to the difference between two measurand values; at each of these values, the modulo- 2π -values for the interferometric phase corresponding to each wavelength, are the same (*i.e.* in-phase condition). Theoretically, compared with two wavelength illumination, more-than-two-wavelength illumination can provide a much wider UMR value for an interferometric sensor provided that the phase-measurand sensitivities of the different wavelengths are not multiples of one another.

Gauthier & Turgeon [1993] have employed the 476 nm, 488 nm and 502 nm output of an Argon ion laser to illuminate a polarimetric temperature sensor. For their purpose, Gauthier & Turgeon have exploited only two of the wavelengths of the output of an Argon ion laser to obtain a large UMR with their polarimetric sensor. Although their arrangement can potentially give a larger UMR, the use of an Argon ion laser can be considered impractical in many circumstances.

Sharma & Posey [1995] demonstrated an extended-range multi-wavelength temperature sensor using the interference at each wavelength between the LP_{02} and LP_{21} modes in a few-mode fibre. Instead of using conventional light sources, Sharma & Posey generated an effective (about 5) multi-wavelength light source in a

few mode fibre. Such a multi-wavelength light source was produced by Stimulated Raman Scattering (SRS) in a few-mode fibre. The scattered beams were predominantly manifested in the LP₀₂ mode and exhibited different characteristic wavelengths. For each wavelength, a simple microbend in the fibre coupled a fraction of the initial LP₀₂ mode SRS light into the LP₂₁ mode which was subsequently allowed to interfere with the remaining light in the LP₀₂ mode. The use of high laser power and SRS in optical fibres is generally not an attractive way to produce multiple wavelengths in a practical sensor.

2.5.3 Dual In-Fibre Bragg Grating Sensors

Many techniques employing two fibre Bragg gratings have been demonstrated for SMTS. These techniques can be used to give an extended-UMR while providing high measurand resolution. High measurand resolution may be achieved by detecting wavelength shifts of the two FBGs using two interferometers (one for each FBG). If K'_{lM} is a wavelength-measurand sensitivity of the l -th FBG with Bragg wavelength $\lambda_{b,l}$, following from Eq. 2.18,

$$K_{lM} = 2\pi \frac{L_{OPD,l}}{\lambda_{b,l}^2} K'_{lM} \quad \text{Eq. 2.21}$$

is the equivalent phase-measurand sensitivity exhibited by an interrogating interferometer with an OPD of $L_{OPD,l}$.

The ratio of the equivalent phase-measurand sensitivities of the two Bragg wavelength shifts is

$$K_{rM} = \frac{K_{1M}}{K_{2M}} = \left(\frac{L_{OPD,1}}{L_{OPD,2}} \right) \left(\frac{\lambda_{b,2}^2}{\lambda_{b,1}^2} \right) \left(\frac{K'_{1M}}{K'_{2M}} \right). \quad \text{Eq. 2.22}$$

By suitably choosing the value of the ratio $\frac{L_{OPD,1}}{L_{OPD,2}}$, either the condition $K_{rM} \cong 1$ or $K_{rM} \gg 2$ can be obtained.

However in most cases, obtaining $K_{rM} \cong 1$ demands less constraints on the choices for the values of $L_{OPD,1}$ and $L_{OPD,2}$ which determine the un-improved UMR and the measurand resolution as in the case of interferometric interrogation of a single FBG (see section 2.4.3.2). The closer K_{rM} is to its unity value, the larger is the value of $E_{UMR,M}$ (using Eq. 2.7). Interestingly, Eq. 2.22 reduced to Eq. 2.20 the case of interrogating a single FBG using two interferometers (see section 2.4.3.2).

On the other hand, the best scheme to obtain an extremely large dynamic range and potentially unlimited UMR is to interferometrically interrogate only one (preferable the more sensitive) of the two gratings simultaneously using

the wavelength shift of the other to identify the fringe order of the interferometer. For example, an arrangement similar to that of Brady *et al.* [1997] could be used to obtain large dynamic range measurements. Brady *et al.* [1997] used a Mach-Zehnder interferometer and a tunable acousto-optic filter to detect Bragg wavelength shifts of two gratings.

The “price” of the above mentioned schemes to improve the dynamic range of a dual-FBG arrangement is the need to employ either two interferometers or one interferometer and a spectrometer. However, especially when the two Bragg wavelengths of the FBGs are far apart, a single interferometer can be used if followed by appropriate wavelength-separating optics. Certainly the use of a single interferometer is an attractive and optimised alternative. In this present sub-section, for the sake of also defining some point of comparison with the other techniques discussed in this chapter, the $E_{UMR,M}$ values for the various dual-FBG arrangements are evaluated assuming the two Bragg wavelength shifts are detected using a single interferometer. The interrogating interferometer is preferably non-dispersive, (*e.g.* the interferometer is composed of air-path-arms). In such cases, the interferometer exhibits the same effective OPD at the two Bragg wavelengths and consequently $E_{UMR,M}$ becomes independent of L_{OPD} , the OPD of the interrogating interferometer (*c.f.* Eq. 2.22). The results of the following discussions also apply for the cases when two interferometers with the same OPD are used.

James *et al.* [1996] fabricated a dual-FBG sensor which was assembled by fusion splicing two fibres which each contained an FBG (spliced grating pair). The separation between the two gratings were as short as possible in order that both gratings can be placed in essentially the same environment. To ensure the suitability of the dual-FBG arrangement for SMTS, the composition of the two fibres, the diameter of the fibres (80 μm and 125 μm) and the Bragg wavelength of the gratings (826 nm and 837 nm) inscribed on each fibre were chosen to be different. When the spliced grating pair was strained, the distribution of strain along the grating pair was not uniform because the fibres forming the splice had different outer diameters. In other words, the amount of strain on each of the FBGs was different. Such difference produced an effect which modified the wavelength-strain sensitivities of the FBGs. This modification enhanced the suitability of the arrangement for SMTS. On the other hand such a

spliced grating pair when employed as a single-measurand extended-range sensor would yield an $E_{UMR,T} \cong 6.0$ and $E_{UMR,\epsilon} \cong 2.1$. The original wavelength-strain sensitivities of the FBGs were very similar and hence a higher $E_{UMR,\epsilon}$ value could have been obtained if the FBGs were not used to form the spliced grating pair.

More recently, Song *et al.* [1997] formed a spliced grating pair sensor which involved two gratings written on optical fibres of the same composition but with different diameters for SMTS. Because the Bragg wavelength of the gratings were chosen to be very similar (1549.3 nm and 1546.4 nm), the wavelength shifts due to temperature of the two gratings were found to be practically the same even for several pairs of fibres with different diameter ratio. Hence, the difference between the Bragg wavelength shifts of the two gratings was only sensitive to strain. The arrangement of Song *et al.* was more suitable for SMTS than that the arrangement of James *et al.* because the differential wavelength shift measurements of Song *et al.* can be used to measure the strain on either of the two FBGs. For extended-UMR strain measurements, their results would give $E_{UMR,\epsilon} \cong 3.0$. As in the case of James *et al.* $E_{UMR,\epsilon}$ would have been higher had the two FBGs were used without being employed in a spliced grating pair. Since the UMR temperature measurements can not be extended, $E_{UMR,T} = 1$ (no improvement). In comparison with the sensor of James *et al.*, the grating-pair produced by the former would exhibit $E_{UMR,T} \cong 6.0$ because the FBGs were formed in two fibres with different composition.

The disadvantage of using two serial Bragg gratings is that the sensing region of the gratings are different. Xu *et al.* [1994] superimposed two gratings whose Bragg wavelengths were different. He chose gratings at 1300 nm and 850 nm for SMTS. The immediate disadvantage of their arrangement was the need to use two light sources. On the other hand this arrangement would allow extended-range sensing with $E_{UMR,T} \cong 2.4$ and $E_{UMR,\epsilon} \cong 3.3$.

Instead of physically writing two gratings at the same location to produce a two-grating system, Brady *et al.* [1997] illuminated a single FBG at its first-order and second-order wavelength (~ 1560 nm and ~ 790 nm) using two light sources for SMTS. This sensing arrangement would provide $E_{UMR,T} \cong 2.2$ and $E_{UMR,\epsilon} \cong 2.0$.

Instead of writing two gratings at the same location on a single fibre, two gratings can simultaneously be formed in a birefringent fibre using a single physical grating. Using an optical spectrum analyser, Sudo *et al.* [1997] measured the Bragg wavelength shifts along the two axial gratings written in a PANDA birefringent fibre and obtained SMTS. This birefringent grating sensor would yield $E_{UMR,T} \cong 16.8$ and $E_{UMR,\epsilon} \cong 162$. Interestingly, these values were large compared with the corresponding values for the other dual grating arrangements. This difference can be attributed to the rather high dependence of the birefringence of the fibre to variation of temperature and its rather low dependence on strain.

Overlaying two gratings of different Bragg wavelengths written on a birefringent fibre produces four gratings in the same location. Udd *et al.* [1996] proposed and demonstrated [1997] the ability of the dual-overlaid-birefringent sensor to determine temperature and strain in three directions in an optical fibre. Udd *et al.* realised that each grating along each polarisation axis of the fibre experiences different strain in the transverse direction. Three dimensional strain and temperature can all be determined by solving the four equations obtained by relating the Bragg wavelength shifts of the four gratings to these parameters. Any two of the four wavelength shifts measurements exhibiting very similar sensitivities can be used to extend the UMR especially for temperature measurements. On the other hand, all four wavelength shifts can be employed to produce an extremely large UMR as described in section 2.5.2.3, more-than-two-wavelengths-illumination techniques.

Instead of exploiting coupling between the forward and backward propagated modes in a single-mode grating, polarisation coupling of the same spatial mode can be exploited in an in-fibre rocking filter written in a birefringent fibre. A rocking filter is essentially a Bragg grating which periodically couples light from one (linear) polarisation state to another within a single-mode birefringent fibre. As in the case of an FBG, a rocking filter is characterised by a resonant coupling wavelength which corresponds to the wavelength at which the electric field of the coupling modes are in phase with the regular spatial perturbation in the fibre, *i.e.* phase match condition. This regular perturbation can be formed in a birefringent fibre by introducing several localised linear birefringence coupling points every beat length of the fibre. These coupling points can be photo-induced in an optical fibre

[Russell & Hand, 1990; Kanellopoulos *et al.*, 1991c; 1992; Hill *et al.*, 1991]. The grating period of a rocking filter is typically a couple of millimeters whilst that of an FBG, a few hundreds of nanometers.

As in the case with an FBG, the resonance wavelength of a rocking filter can shift with temperature change or strain. These wavelength shifts can be measured using an interferometer. However the interferometer needs to have an OPD $< 10 \mu\text{m}$ because of the large bandwidth (*e.g.* 14 nm) of the resonance wavelength exhibited by a rocking filter. On the other hand the wavelength shifts of a rocking filter due to temperature are large and thus the wavelength shifts can be measured using an optical spectrum analyser [Kanellopoulos *et al.*, 1994; 1995]. For example, Kanellopoulos *et al.* [1995] observed that the rocking filter they used had a temperature sensitivity of $-204 \text{ pm}/^\circ\text{C}$ (and resonance wavelength of 837.3 nm).

If a birefringent fibre with a rocking filter is illuminated such that the first few higher order modes can propagate, effectively several rocking filters are manifested, one for each spatial mode. Kanellopoulos *et al.* [1994] utilised the temperature and strain sensitivities of the spectral shifts in the resonance coupling wavelengths of the first- and second-order spatial-modes using the same physical rocking filter for SMTS. Their measurements would yield $E_{UMR,T} \cong 2.5$ and $E_{UMR,\epsilon} \cong 2.2$.

A Bragg grating and a photo-induced rocking filter can be used simultaneously for SMTS. Kanellopoulos *et al.* [1995] superimposed a Bragg grating in the centre of a photo-induced rocking filter on an elliptically cored D-clad fibre. The resonance wavelengths of the FBG and the rocking filter were 798.1 nm and 837.3 nm. Their results revealed that Bragg wavelength shifts of the FBG and the rocking filter with temperature were $7.3 \text{ pm}/^\circ\text{C}$ and $-204 \text{ pm}/^\circ\text{C}$ respectively whilst those with strain were $0.67 \text{ pm}/\mu\epsilon$ and $-1.7 \text{ pm}/\mu\epsilon$ respectively. The strain sensitivities were relatively similar whilst the temperature sensitivities were significantly different. The difference in the temperature sensitivities could be attributed to the fact that the resonance wavelength of an FBG depends on the refractive index of the fibre whilst that of a rocking filter depends on the birefringence of the fibre and that the refractive index and the birefringence of the fibre have substantially different rate of change with respect to temperature (Chapter 4). Their measurement would give $E_{UMR,T} \cong 30$ and $E_{UMR,\epsilon} \cong 2.8$.

One of the disadvantages of an arrangement involving a rocking filter is the need for long sensing length. This requirement arises because a major segment of the rocking filter needs to be exposed to the same average change in the measurand in order to maintain a uniform resonance condition across the filter and thereby avoid unnecessarily broadening the resonance bandwidth of the rocking filter. Since the total length of the rocking filters are large (~25 to ~200 cm) compared with FBG (~1 to ~20 mm), the large sensing region may not be suitable in many applications. Furthermore, since a rocking filter does not exhibit a reflection spectrum (unlike an FBG), only transmission type interrogation is possible with a rocking filter unless somehow the transmitted light is reflected back towards the source.

A long-period fibre grating (LPG) can also be used instead of a normal FBG. A typical LPG usually has a pitch length of the order of 100 μm whilst a typical FBG has a pitch length of the order of 100 nm. In transmission, an LPG exhibits spectral attenuation or resonance bands which correspond to the coupling between the core and cladding modes [Bhatia *et al.*, 1997]. These resonance bands were found to shift with temperature and strain although the corresponding sensitivities differed from band to band and from fibre to fibre. Nevertheless Bhatia *et al.* chose two such bands of an LPG and exploited the measurand sensitivities of these bands for SMTS. Using one of their results, $E_{UMR,T} \cong 14.6$ and $E_{UMR,\epsilon} \cong 4.1$.

Instead of observing two of the resonance bands in a single LPG, shifts in one of the resonance wavelengths of an LPG together with the shift in Bragg wavelength of an FBG can be used for SMTS [Patrick *et al.*, 1996]. Patrick *et al.* have found that the ratio between the wavelength shifts for an LPG and FBG was about seven for temperature whilst about one-half for strain. The difference in the wavelength-shift-to-temperature sensitivities can be attributed to the fact that the resonance wavelength for an FBG depends only on the refractive index of the core whilst that of an LPG depends on the index difference between the core and cladding [Vengsarkar *et al.*, 1996]. As with a rocking filter, an LPG exhibits a wide resonance bandwidth and does not have a reflection spectrum. To achieve a sensing arrangement addressed in reflection, Patrick *et al.* fabricated an LPG followed by two FBGs on a single fibre. The LPG was illuminated first by a broadband LED. The reflection from the two FBGs crossed the LPG before reaching a spectrum analyser. Because the LPG measurand-induced wavelength

shifts were different from those of the FBGs, the instantaneous relative intensity at the two Bragg wavelengths indicated the wavelength shifts of the LPG. The relatively small wavelength shift of the FBGs complicates the analysis but the intensity ratio can still be calibrated and used to sense variations in the measurand.

To obtain an arrangement exhibiting a dynamic range which is as large as possible, the relative intensity measurement could be used to identify the fringe order of the interferometric detection of the Bragg wavelength shifts of one of the FBGs. The measurand range in this case would be determined by the transmission spectrum of the LPG resonance.

2.5.4 Conventional Interferometry or Polarimetry Combined with Dual-Mode Interference

2.5.4.1 Extending the UMR of Interferometric Sensors

One of the arrangements to produce two effective interferometric sensors in the same location without using two physical interferometric sensors is to exploit inter- and intra-spatial-mode interference within a single-mode e-core fibre. An e-core fibre with its first few higher-order spatial modes excited can provide stable and well-defined interference between an LP_{01} and an LP_{11} mode. Using a single 633 nm HeNe laser light source launched into the major-axis of an e-core fibre, Wang G. Z. *et al.* [1991] have exploited the inter-modal (between two different spatial modes of the same polarisation) and intra-modal (between beams of the same spatial mode and of the same polarisation) interference for SMTS. The intra-modal interference can be formed by beams reflected from two cleaved ends of an e-core fibre, *i.e.* Fabry-Pérot interference. Incidentally, this dual-mode and Fabry-Pérot interferometric arrangement gave an ill-conditioned sensitivity matrix \tilde{K} for SMTS. On the other hand, the sensitivity of the inter-modal interference to temperature and strain was lower than that of the intra-modal Fabry-Pérot interference. Clearly, the phase of the inter-mode (dual-mode) interference can be used to identify the fringe order of the phase change in the Fabry-Pérot interference. From the results of Wang G. Z. *et al.* [1991], $E_{UMR,T} \cong 115$ and $E_{UMR,\epsilon} \cong 256$ could be obtained.

2.5.4.2 Extending the UMR of Polarimetric or Dual-Mode Sensors

In an elliptical-core birefringent fibre operated in its two-mode regime, there are actually four non-degenerate guided modes: two types of spatial modes which can be of two orthogonal polarisation states. The propagation characteristics of these four modes are dependent on the wavelength of the light source, temperature and strain [Huang *et al.*, 1990]. Using appropriate polarisation-sensitive optical elements, spatial filters and light sources, polarimetric (interference between beams of the same spatial mode but different polarisation state) and spatial-mode (same polarisation state but different spatial mode) interference can be derived from a single birefringent fibre. A very attractive all-fibre arrangement exploiting this single-wavelength sensing approach has been proposed by Lefèvre *et al.* [1990]. However, the requirement for special polarisation and spatial mode splitting fibre couplers increases the cost of an all-fibre arrangement.

Polarisation-mode and dual-spatial-mode interferences can be used for SMTS even though the corresponding sensitivity matrix \tilde{K} is usually ill-conditioned [Michie *et al.*, 1991; Grossman & Costandi, 1992; Vengsarkar *et al.*, 1990, 1994; Bock & Eftimov, 1994]. On the other hand, depending on the ratio between the phase-measurand sensitivities of polarisation-mode and dual-spatial-mode interferences, a polarimetric or a dual-mode sensor with an extended UMR and dynamic range can be achieved.

Polarimetric and dual-mode interrogation of a birefringent fibre can be achieved using a single wavelength He-Ne laser light source at 633 nm [Grossman & Costandi, 1992; Bock & Eftimov, 1994]. On the other hand preferential excitation of each type of spatial modes can be achieved using two-wavelength interrogation. At the first wavelength, the polarimetric information is derived from the beating LP_{01} modes using a polarisation analyser whilst at the second wavelength, the inter-modal interference of the same polarisation can be obtained [Michie *et al.*, 1991; Vengsarkar *et al.*, 1990; 1994]. Since these two sets of information are spectrally multiplexed, they can be easily separated with appropriate optics. Interestingly, the use of two different wavelength gave a slightly better condition number for the corresponding matrix \tilde{K} when compared with a single wavelength illumination [*c.f.* Wang G. Z. *et al.*, 1991; Vengsarkar *et al.*, 1994].

For the polarimetric and dual-mode sensor, $K_{pol,M}$ and $K_{dual,M}$ (and hence $E_{UMR,M}$) vary according to the construction of birefringent fibres. Bock & Eftimov [1994] have evaluated the practical suitability of several birefringent fibres for LP_{01} and LP_{11} interference of the same polarisation for the simultaneous measurement of pressure and temperature (two inter-spatial-mode-interference sensors). They have concluded that Bow-Tie fibres were more suitable to use for this type of arrangement because their corresponding pressure (hence strain) and temperature sensitivities were relatively constant over a wide range whilst those of elliptical-core fibres varies nonlinearly with the measurand [*c.f.* Kim *et al.*, 1996]. Approximately, $E_{UMR,T} \cong 2$ to 3 and $E_{UMR,\epsilon} \cong 3$ to 13 for an extended range dual-mode or polarimetric sensor [Michie *et al.*, 1991; Grossman & Costandi, 1992; Vengsarkar *et al.*, 1990; 1994; Bock & Eftimov, 1994].

Alternatively, instead of employing two dual-mode-interference sensors as described above, a dual spatially-multiplexed polarimetric sensor can be realised [Thursby *et al.*, 1995]. Thursby *et al.* employed an in-line integrated-optic mode splitter to couple out from a birefringent fibre the LP_{11} modes whilst keeping the LP_{01} modes in the fibre. The dual polarimetric sensor is realised by allowing the pair of polarisation modes of the same spatial mode, LP_{01} or LP_{11} , to interfere after two linear analysers. The resulting matrix \tilde{K} for such a scheme has exhibited a good condition number ensuring SMTS [Thursby *et al.*, 1995]. If the same dual-polarimetric sensing arrangement is to be employed to extend the UMR of either an LP_{01} or LP_{11} polarimetric sensor, then $E_{UMR,T} \cong 180$ and $E_{UMR,\epsilon} \cong 120$.

For dual-mode interference arrangements, the requirement of some spatial-filtering technique to demodulate the two-mode interference limits the practicality of a dual-mode arrangement. Furthermore to obtain excellent visibility, both spatial modes need to be excited equally. Unfortunately equal excitation of the spatial modes can not be guaranteed.

2.5.5 Combined Interferometry and Polarimetry

If a birefringent fibre is introduced into an arm of a fibre interferometer, effectively two fibre interferometers can be simultaneously formed, one along each polarisation axis of the birefringent fibre. Such a configuration provides

both interferometric and polarimetric information. By employing appropriate optical components, the interferometric information can be obtained by determining the phase change for each axial interferometer. On the other hand polarimetric information can be obtained by using a linear analyser or by simply calculating the difference between the phase between the two axial interferometers. This interfero-polarimetric technique has been applied to different fibre interferometers. Examples include a Mach-Zehnder interferometer [Newson *et al.*, 1988], a Michelson interferometer [Corke *et al.*, 1985; Fürstenau *et al.*, 1992; Sirkis & Lo, 1994] or a Fabry-Pérot interferometer [Leilabady *et al.*, 1985; 1986a].

Dual interferometric phase shifts have also been exploited for SMTS. Farahi *et al.* [1990a] used a Bow-Tie birefringent fibre (cleaved at both ends) Fabry-Pérot sensor for SMTS. Instead of a fibre Fabry-Pérot arrangement, Sirkis & Lo [1994] used all-fibre Michelson interfero-polarimetric sensor to measure the axial and transverse strains on a length of a highly birefringent fibre.

Chardon & Huard [1988] demonstrated a novel interferometric-polarimetric configuration for the simultaneous measurement of pressure and temperature. Instead of using a birefringent fibre, Chardon & Huard induced birefringence in a length single-mode fibre by wrapping a section of the fibre around a hollow copper cylinder. When the cylinder radially expands or contracts depending on its temperature or its internal pressure, temperature and pressure can be discriminated. Similar to Farahi *et al.* [1990a], the ends of the fibre were cleaved and thereby formed two low-finesse FFPIs.

With an interferometric-polarimetric sensing arrangement, an interferometric sensor with an extended unambiguous measurand range can be obtained. In this sensing arrangement, the polarimetric information can be used to identify the fringe order of the phase shift along the fast axis [Leilabady *et al.*, 1985; 1986a; Taylor *et al.*, 1987]. $E_{UMR,M}$ depends on the type of birefringent fibre used and also on the measurand. For example $E_{UMR,T} \cong 20$ and $E_{UMR,\epsilon} \cong 100$ (York Bow-Tie fibre) for temperature and strain respectively [Leilabady *et al.*, 1985; 1986a; Taylor *et al.*, 1987; Farahi *et al.*, 1990a; 1990b]; $E_{UMR,\epsilon_{11}} \cong 5$ and $E_{UMR,\epsilon_{22}} \cong 2$ for axial and transverse strains of a surface mounted sensor respectively [Sirkis & Lo, 1994].

Interestingly, the $E_{UMR,M}$ values obtained using an interferometer technique in a bow-tie fibre [Leilabady *et al.*, 1985; 1986a; Taylor *et al.*, 1987; Farahi *et al.*, 1990a; 1990b] were comparable to those obtained from observing the wavelength shifts along the axial gratings which were produced by a single physical grating written in a PANDA birefringent fibre [Sudo *et al.*, 1997].

Compared with an interferometric-dual-mode technique to extend the UMR of an interferometric sensor, the interfero-polarimetric technique provided a lower increase in the measurand range, especially for temperature. This was expected because the birefringence of stress-induced fibres like Bow-Tie fibres is highly temperature dependent.

2.6 Overview Summary

Of all the possible sensing arrangements, either a short-cavity-length fibre Fabry-Pérot interferometric sensor or a fibre Bragg grating (FBG) sensor offer the best alternatives for localised, high resolution and single-ended measurements. Unfortunately FBG technology was not available to this author at the beginning of his research (1992). Thus FFPSs were chosen for this present work. Unless illuminated with a low-coherence source, an FFPS exhibits a limited UMR. In such cases, its UMR can be extended in order to obtain a practical sensor.

Comparing the various techniques for obtaining a large or extended UMR, enhanced white-light interferometry, dual-wavelength illumination, dual-spatial mode technique, combined polarimetry and interferometry, and binary-frequency-division technique are compatible with a short-cavity FFPI. Enhanced white-light interferometry gives the highest dynamic range extension whilst binary-frequency-division technique (for $N < 20$) the lowest for either temperature or strain measurements. A dual-FFPI configuration using a birefringent FFPS similar to that of Farahi *et al.* [1990a] can be considered to perform relatively well in many situations. Its benefits include simplicity, immunity from polarisation induced signal fading (inherent in the use of polarisation-maintaining fibres), the same physical placement for the two effective FFPI, adequately large improvement in dynamic range for both temperature or strain and the potential for simultaneous measurement of temperature and strain.

This thesis concentrates on the development and evaluation of a dual FFPS based on birefringent fibres with relatively small variation in refractive index for the two polarisations. In this way the sensor can be used to extend the UMR. The sensor developed in this work was also designed to have a simple, computer-compatible method of demodulating the phase information of the two interferometers.

The next two chapters investigate in detail the optical characteristics and the sensitivity to temperature and strain of FFPS that were fabricated with either thin-film or fibre Bragg grating Fabry-Pérot reflectors. These FFPIs were fabricated using both non-polarisation-maintaining and elliptically-cladded birefringent fibre.

Chapter 3:

Transfer Functions of Optical Fibre Fabry-Pérot Interferometers With Thin- Film or Fibre Bragg Grating Reflectors

This chapter analyses the transmission and reflection transfer functions of fibre Fabry-Pérot interferometers (FFPIs) illuminated with a monochromatic light source. The analyses can be considered an extension of those found in the literature in two aspects [Born & Wolf, 1980; Vaughan, 1989]. First, the analyses include the contributions of the phase change upon transmission through or reflection from the Fabry-Pérot reflectors to the total interferometric phase. Secondly, they use simplifications applicable to propagation of light in a single-mode weakly-guiding optical fibre. Subsequently, the transfer functions obtained can be used to determine the expected fringe visibility. Since the fringe visibility is an important consideration to achieve good signal-to-noise ratio for a photodetector, effects which influence the fringe visibility of an FFPI are briefly discussed.

The optical properties of the Fabry-Pérot mirrors fundamentally determine the behaviour of the interferometric transfer functions of an FFPI and thus these properties can influence the choice of an appropriate signal processing scheme for the FFPI. This chapter also describes the optical properties of in-fibre dielectric mirrors and in-fibre Bragg gratings, both of which have been used with the FFPIs fabricated in this work (Chapter 5).

In the latter part of this chapter, the free spectral range (FSR) of an FFPI with in-fibre thin-film or Bragg-grating reflectors is described in detail since the FSR is an important parameter in the pseudo-heterodyne signal processing scheme used in this work (Chapter 6).

3.1 Intrinsic Fibre Fabry-Pérot Interferometers

Fabry-Pérot interferometers were first conceptualised in 1898 by Charles Fabry and Alfred Pérot who at that time were interested in measuring micro-displacements with precision. They described the interference resulting from the multiple reflections from two closely separated parallel mirrors. The region between these (Fabry-Pérot) mirrors is commonly referred to as the Fabry-Pérot cavity. In a Fabry-Pérot interferometer each light beam approaching either Fabry-Pérot mirror is partially transmitted by the mirror and partially recirculated back into the Fabry-Pérot cavity. The end result of this Fabry-Pérot arrangement is a set of beams leaving the cavity in the forward direction (transmitted beams) and in the backward direction (reflected beams). (The adjectives “forward” and “backward” are defined relative to the propagation direction of the initial incident beam). If these transmitted or reflected beams are temporally coherent and allowed to combine, the resulting interference varies periodically with the total round-trip phase change in the Fabry-Pérot cavity. This phase change is determined by the optical length of the Fabry-Pérot cavity, the optical frequency of the light source and the phase change introduced by the Fabry-Pérot mirrors.

Fabry-Pérot interferometers can be characterised by properties describing their spectral filtering capabilities. These characteristics are the free spectral range (FSR), the bandwidth of each Fabry-Pérot fringe and the finesse. The wavelengths at which maximum transmission (reflection) occur are the transmission (reflection) longitudinal modes of the cavity. Adjacent longitudinal modes are separated in the optical frequency domain by an amount known as the FSR. Each longitudinal mode can be characterised by its full width at half maximum (FWHM) bandwidth. This bandwidth narrows with increasing value of the combined internal reflectance of the mirrors (R). The quality or the finesse of a Fabry-Pérot interferometer is defined as the ratio between the FSR and the FWHM bandwidth of the transmission longitudinal modes.

In the derivations below, the ideal FSR, bandwidth and finesse are calculated for interferometric arrangements used. These derivations include the effects of phase changes on transmission and reflection and the use of some simplifying assumptions which are appropriate for Fabry-Pérot interferometers formed in weakly-guiding optical fibres. These assumptions are:

- i. *No inter-modal coupling or interference.* The use of single-mode optical fibre greatly simplifies the resulting interferometric output (single-mode propagation). In addition, it can be safely assumed that there is no coupling between the cladding and core (guided) modes provided that the lead-in fibre has a substantial length or a mode-stripping jacket (as with the birefringent fibres used).
- ii. *No polarisation coupling effects.* Coupling between the polarisation modes can be safely neglected as long as the physical state of the fibre is not greatly perturbed or the fibre is polarisation maintaining (as in this present work).
- iii. *Plane wave approximation.* For weakly-guiding single-mode fibres, the propagated mode can be considered to approximately have no electric-field component in the propagation direction [Snyder & Love, 1983]. Thus the propagated mode can be approximately described as a plane wave propagating in the optical fibre.
- iv. *Normal incidence.* The effective transverse surface of either a fusion-spliced thin film or fibre Bragg grating as Fabry-Pérot mirrors can be made perpendicular to the propagation axis of the fibre without much difficulty.
- v. *Loss-less cavity.* A short cavity length fibre Fabry-Pérot cavity is essentially expected not to introduce any loss except at the mirrors. If necessary, the effects of any absorption, diffraction or scattering losses in the cavity can be incorporated in the reflection and transmission coefficients of the mirrors.
- vi. *Monochromatic light source.* The input beam is assumed to be highly coherent.

Figure 3.1 shows a Fabry-Pérot interferometer formed within the core of an optical fibre. The two Fabry-Pérot mirrors \mathfrak{M}_1 and \mathfrak{M}_2 divide the core into three regions: the left-most region called region 1, is the incident region; region 2 is the cavity region and region 3 is the transmission region. The refractive indices of these regions are n_1 , n_2 and n_3 respectively. For the simplest fibre Fabry-Pérot interferometer (Figure 3.1)

$$n_1 = n_2 = n_c ,$$

Eq. 3.1

where n_c is the refractive index of the core. ($n_3 = n_c$ for an in-line FFPI). Using the above convention, m_1 can be called the proximal mirror and m_2 the distal mirror (with respect to the incident beam).

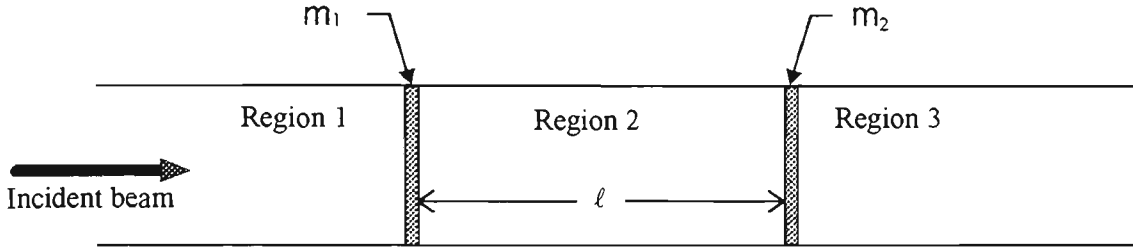


Figure 3.1: A Fabry-Pérot interferometer formed along the core of an optical fibre.

In general, mirrors m_1 and m_2 can be any reflector with finite thicknesses. However in the following discussions, m_1 and m_2 are assumed to be infinitely thin without any loss of generality. This assumption holds even with in-fibre Bragg gratings as Fabry-Pérot reflectors. Interestingly, Legoubin *et al.* [1995] derived the transmission function of an FFPI composed of two identical Bragg gratings by applying coupled mode theory to the whole fibre Fabry-Pérot etalon. The results of Legoubin *et al.* are the same with those obtained using the treatment in this chapter.

The time-varying electric field of the beam incident on the fibre Fabry-Pérot etalon can be described as a plane wave:

$$\tilde{\mathbf{E}}_o = \tilde{E}_o \exp(-i\omega t), \quad \text{Eq. 3.2}$$

where \tilde{E}_o is the time-independent complex electric field, ω is the angular optical frequency and t is the time. The irradiance or the time-average intensity of the field $\tilde{\mathbf{E}}_o$ is given by

$$I_o = \frac{\epsilon_{EM} c}{n} \left\{ \lim_{\tau \rightarrow \infty} \frac{1}{\tau} \int_{-\tau/2}^{\tau/2} \tilde{\mathbf{E}}_o (\tilde{\mathbf{E}}_o)^* dt \right\} = \frac{\epsilon_{EM} c}{n} |\tilde{E}_o|^2, \quad \text{Eq. 3.3}$$

where ϵ_{EM} and n are the electric permittivity and refractive index of the medium, c is the speed of light in vacuum, τ is some multiple of the optical period $2\pi/\omega$, and $(\tilde{\mathbf{E}}_o)^*$ is the complex conjugate of $\tilde{\mathbf{E}}_o$. For dielectric materials such as optical fibres, the relation

$$n \cong \sqrt{\varepsilon_{EM}} \quad \text{Eq. 3.4}$$

can be used.

The Fabry-Pérot mirrors can be described by complex electric field reflection and transmission coefficients. The complex electric field reflection coefficient of the mirror between regions b and d , \tilde{r}_{bd} ($b, d = 1, 2, 3$), is defined as

$$\tilde{r}_{bd} \equiv \frac{\tilde{\mathbf{E}}_d^r}{\tilde{\mathbf{E}}_b} = r_{bd} \exp(i\theta_{bd}^r). \quad \text{Eq. 3.5}$$

$\tilde{\mathbf{E}}_b$ is the complex electric field strength of the beam incident from region b travelling towards region d and $\tilde{\mathbf{E}}_d^r$ the complex electric field strength of the reflected beam. r_{bd} is the amplitude reflection coefficient whilst θ_{bd}^r is the relative phase of the reflected electric field with respect to the incident electric field. Since the time varying electric field is given by Eq. 3.2, a positive value for phase, *e.g.* θ_{bd}^r , physically corresponds to the electric field of the reflected beam, $\tilde{\mathbf{E}}_d^r$, lagging that of incident beam, $\tilde{\mathbf{E}}_b$. Similarly, the complex transmission coefficient \tilde{t}_{bd} is defined as

$$\tilde{t}_{bd} \equiv \frac{\tilde{\mathbf{E}}_d^t}{\tilde{\mathbf{E}}_b} = t_{bd} \exp(i\theta_{bd}^t) \quad \text{Eq. 3.6}$$

where $\tilde{\mathbf{E}}_d^t$ is the complex electric field of the transmitted beam, t_{bd} is the transmission amplitude coefficient while θ_{bd}^t is the (transmission) optical phase change resulting from traversing the mirror between regions b and d . As in the reflection case, θ_{bd}^t is defined relative to the phase of the incident beam at the proximal edge of the mirror. Without loss of generality, r_{bd} and t_{bd} can be assumed to be positive real numbers, *i.e.* $r_{bd} \equiv |\tilde{r}_{bd}|$ and $t_{bd} \equiv |\tilde{t}_{bd}|$.

The intensity transmission coefficient or transmittance \mathbf{T} , and the intensity reflection coefficient or reflectance \mathbf{R} , of a Fabry-Pérot interferometer are defined as

$$\mathbf{T} = \frac{I_t}{I_o}, \quad \text{and} \quad \text{Eq. 3.7}$$

$$\mathbf{R} = \frac{I_r}{I_o}. \quad \text{Eq. 3.8}$$

I_t and I_r are the transmission and reflection intensities of a Fabry-Pérot interferometer, computed from their corresponding time-varying electric field strength $\tilde{\mathbf{E}}_t$ and $\tilde{\mathbf{E}}_r$, respectively.

3.1.1 Transmission Function of Fibre Fabry-Pérot Interferometers

The transmission electric field $\tilde{\mathbf{E}}_t$ is composed of several beams. The first of these beams traverses both Fabry-Pérot mirrors and the Fabry-Pérot cavity once and is described by

$$\tilde{\mathbf{E}}_t^1 = t_{12}t_{23}\tilde{\mathbf{E}}_o \exp\left[i(-\omega t + \theta_{12}^t + \beta + \theta_{23}^t)\right], \quad \text{Eq. 3.9}$$

$$\text{where } \beta = 2\pi \frac{n_2 \ell}{\lambda} = 2\pi \frac{n_2 \ell \nu}{c} \quad \text{Eq. 3.10}$$

is the phase shift introduced by a single pass of the cavity; λ and ν are the wavelength and frequency of the incident beam in vacuum; n_2 ($= n_c$) and ℓ are the refractive index and physical length of the optical fibre cavity respectively. The other beams can be derived by following additional reflections from the mirrors and round trips across the cavity. For example the second and third beams are

$$\tilde{\mathbf{E}}_t^2 = t_{12}t_{23}\tilde{\mathbf{E}}_o \exp\left[i(-\omega t + \theta_{12}^t + \beta + \theta_{23}^t)\right] r_{23}r_{21} \exp\left[i(\theta_{23}^r + \theta_{21}^r + 2\beta)\right], \text{ and} \quad \text{Eq. 3.11}$$

$$\tilde{\mathbf{E}}_t^3 = t_{12}t_{23}\tilde{\mathbf{E}}_o \exp\left[i(-\omega t + \theta_{12}^t + \beta + \theta_{23}^t)\right] \left(r_{23}r_{21} \exp\left[i(\theta_{23}^r + \theta_{21}^r + 2\beta)\right]\right)^2. \quad \text{Eq. 3.12}$$

Thus, the total transmitted electric field is

$$\tilde{\mathbf{E}}_t = t_{12}t_{23}\tilde{\mathbf{E}}_o \exp\left[i(-\omega t + \theta_{12}^t + \beta + \theta_{23}^t)\right] \left\{ \sum_{m=0}^{\infty} \left(r_{23}r_{21} \exp\left[i(\theta_{23}^r + \theta_{21}^r + 2\beta)\right] \right)^m \right\}, \quad \text{Eq. 3.13}$$

which when simplified using the binomial expansion of $\frac{1}{1-x}$ is

$$\tilde{\mathbf{E}}_t = \frac{t_{12}t_{23}\tilde{\mathbf{E}}_o \exp\left[i(-\omega t + \theta_{12}^t + \beta + \theta_{23}^t)\right]}{1 - r_{23}r_{21} \exp\left[i(\theta_{23}^r + \theta_{21}^r + 2\beta)\right]}. \quad \text{Eq. 3.14}$$

Using Eq. 3.3 to Eq. 3.7, the transmitted irradiance and the transmittance of a Fabry-Pérot interferometer are

$$I_t = \frac{n_3 c}{2} \left\{ \frac{(t_{12}t_{23})^2 |\tilde{\mathbf{E}}_o|^2}{1 + (r_{23}r_{21})^2 - 2r_{23}r_{21} \cos(\theta_{23}^r + \theta_{21}^r + 2\beta)} \right\}, \text{ and} \quad \text{Eq. 3.15}$$

$$T = \frac{n_3}{n_1} \left\{ \frac{(t_{12}t_{23})^2}{1 + (r_{23}r_{21})^2 - 2r_{23}r_{21} \cos(\theta_{23}^r + \theta_{21}^r + 2\beta)} \right\}. \quad \text{Eq. 3.16}$$

By setting $R \equiv r_{23}r_{21}$, Eq. 3.17

$$T_{fwd} \equiv t_{12}t_{23}, \quad \text{Eq. 3.18}$$

$$\theta_c \equiv \theta_{23}^r + \theta_{21}^r, \text{ and} \quad \text{Eq. 3.19}$$

$$\phi \equiv 2\beta + \theta_c, \quad \text{Eq. 3.20}$$

Eq. 3.16 can be written as

$$T = T_{\max} A(\phi), \quad \text{Eq. 3.21}$$

$$\text{where } T_{\max} = \frac{n_3}{n_1} \left\{ \frac{T_{fwd}^2}{(1-R)^2} \right\} \quad \text{Eq. 3.22}$$

is the maximum transmittance value whilst

$$A(\phi) = \frac{1}{1 + F \sin^2(\phi/2)} \quad \text{Eq. 3.23}$$

is a normalised function known as the (Fabry-Pérot) Airy function. The Airy function depends on the coefficient of

$$\text{finesse } F = \frac{4R}{(1-R)^2}, \quad \text{Eq. 3.24}$$

and the total round-trip cavity phase change, ϕ . The coefficient of finesse F approximately varies linearly for small values of R whilst F approaches infinity as R approaches unity. The phase change ϕ includes the round-trip phase shift 2β which is contributed only by the cavity and the phase shifts resulting from the two successive internal reflections (within the cavity), θ_c (Eq. 3.19). It is worth noting that θ_c is a combined constant of the mirrors. In addition, R can be interpreted as the combined internal reflectance of the Fabry-Pérot mirrors whilst T_{fwd} is the combined forward transmittance of the mirrors.

3.1.2 Behaviour of the Airy Function, Free Spectral Range and Finesse of Fabry-Pérot Interferometers

Figure 3.2 shows the behaviour of the Airy function with respect to the phase ϕ for different values of F . The figure also shows that the Airy function is periodic for $\Delta\phi = 2m\pi$ ($m = 1, 2, 3, \dots$) and that the width of each of its modes becomes narrower with increasing value of F . This periodicity is equivalent to the FSR, $\Delta\nu_{\text{FSR}}$, in the frequency domain. In this domain, $\Delta\nu_{\text{FSR}}$ is the separation between adjacent longitudinal modes. On the other hand in the time domain, optical beams having frequencies which differ by $\Delta\nu_{\text{FSR}}$ overlap and therefore are indistinguishable. Thus, $\Delta\nu_{\text{FSR}}$ can be interpreted as the range of optical frequencies that a Fabry-Pérot interferometer can unambiguously address.

Assuming that the refractive index of the Fabry-Pérot cavity is independent of the optical frequency of the light source ν , the FSR of a Fabry-Pérot interferometer can be calculated as follows. Eq. 3.20 can be differentiated with respect to ν :

$$\frac{\partial \phi}{\partial \nu} = \left(2 \frac{\partial \beta}{\partial \nu} + \frac{\partial \theta_c}{\partial \nu} \right). \quad \text{Eq. 3.25}$$

Since $\frac{\partial \beta}{\partial \nu} = 2\pi \frac{2n_2 l}{c} = \frac{\beta}{\nu}$, Eq. 3.26

and using Eq. 3.25,

$$\Delta \phi \cong \left(\frac{2\beta}{\nu} + \frac{\partial \theta_c}{\partial \nu} \right) \Delta \nu. \quad \text{Eq. 3.27}$$

Therefore the free spectral range (FSR) $\Delta \nu_{\text{FSR}}$ is

$$\Delta \nu_{\text{FSR}} \cong \frac{2\pi}{\overline{\left(\frac{2\beta}{\nu} + \frac{\partial \theta_c}{\partial \nu} \right)}}. \quad \text{Eq. 3.28}$$

The line above the denominator in Eq. 3.28 means averaging the terms under the line over some optical frequency interval ($= \Delta \nu_{\text{FSR}}$) which includes the ν .

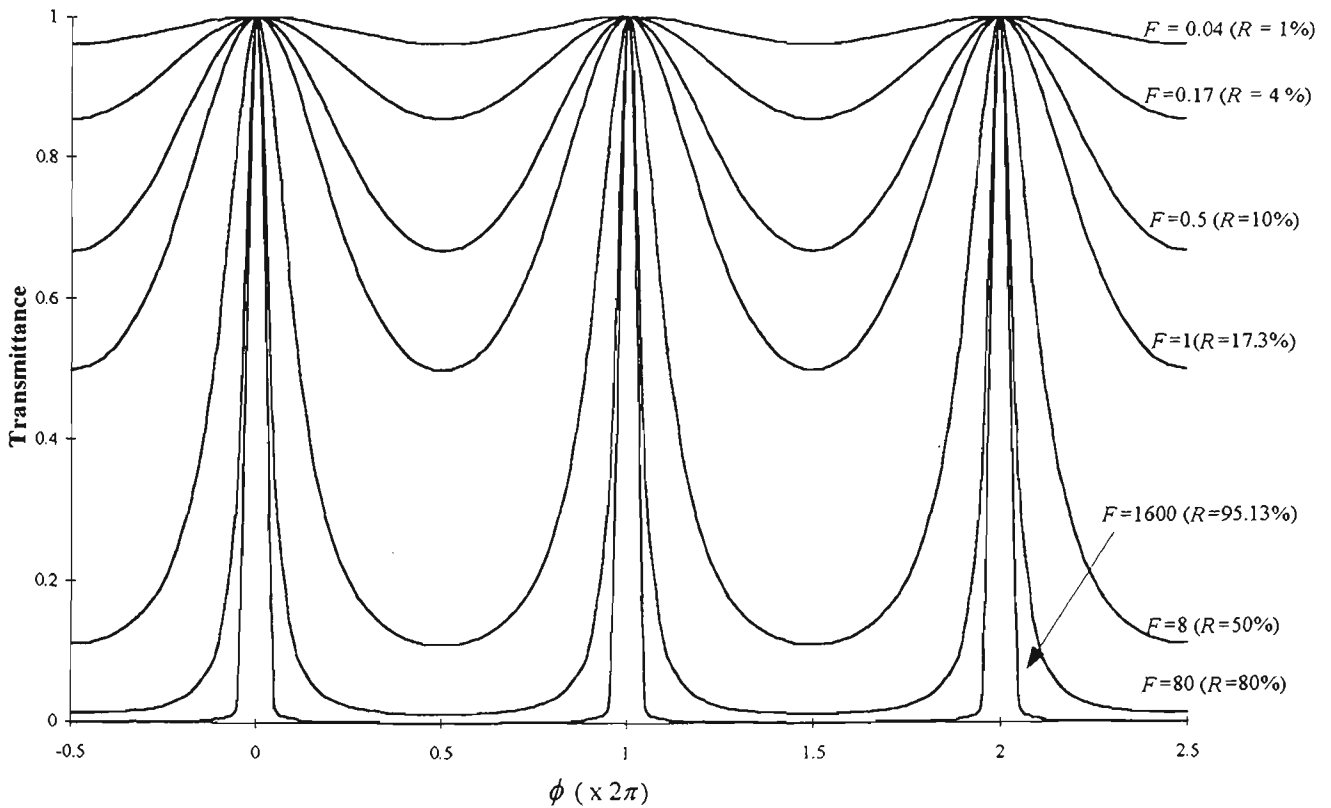


Figure 3.2: The (Fabry-Pérot) Airy function as a function of the total round-trip cavity phase ϕ and the coefficient of finesse F .

If

$$2 \frac{\overline{\beta}}{\nu} = 2 \frac{\beta}{\nu} = \frac{4\pi n_2 \ell}{c} \gg \frac{\partial \theta_c}{\partial \nu}, \quad \text{Eq. 3.29}$$

for example, when θ_c is independent of ν ($\frac{\partial \theta_c}{\partial \nu} = 0$), then

$$\Delta \nu_{\text{FSR}} = \frac{2\pi\nu}{2\beta} = \frac{c}{2n_2\ell}, \quad \text{Eq. 3.30}$$

which is the familiar formula for the FSR.

Each of the transmission longitudinal modes (plotted in the ϕ domain) is symmetric about its centre (Figure 3.2).

The (FWHM) bandwidth of the m th mode is determined from the half-maximum points of the mode which symmetrically occur at

$$\phi = 2\pi m \pm \phi_{1/2}, \quad \text{Eq. 3.31}$$

where
$$\frac{T_{\text{max}}}{1 + F \sin^2(\phi_{1/2} / 2)} = \frac{T_{\text{max}}}{2}. \quad \text{Eq. 3.32}$$

Thus
$$\phi_{1/2} = 2 \sin^{-1} \left(\frac{1}{\sqrt{F}} \right). \quad \text{Eq. 3.33}$$

Hence the finesse F is

$$F \equiv \frac{\Delta \nu_{\text{FSR}}}{\Delta \nu_{\text{FWHM}}} = \frac{2\pi}{2\phi_{1/2}} = \pi \left[2 \sin^{-1} \left(\frac{1}{\sqrt{F}} \right) \right]^{-1}, \quad \text{Eq. 3.34}$$

and the FWHM frequency bandwidth $\Delta \nu_{\text{FWHM}}$ is

$$\Delta \nu_{\text{FWHM}} = 2\phi_{1/2} \frac{\Delta \nu_{\text{FSR}}}{2\pi} = 2 \frac{\Delta \nu_{\text{FSR}}}{\pi} \sin^{-1} \left(\frac{1}{\sqrt{F}} \right). \quad \text{Eq. 3.35}$$

Figure 3.3 graphically shows the FSR and FWHM bandwidth of an FFPI.

For large values of F ($F \gg 1$) the argument of the inverse sine function in Eq. 3.35 becomes small.

Consequently for highly reflecting Fabry-Pérot mirrors, the finesse can be approximately written as

$$F \cong \frac{\pi\sqrt{R}}{1-R}. \quad \text{Eq. 3.36}$$

Aside from the narrowing of the bandwidth when $F \gg 1$, the transmission function around the m th mode exhibits an interesting behaviour. Setting $\phi = 2\pi m + \phi'$ where $|\phi'|$ is close to zero, the transmission function can be approximately written as

$$T = \pi \delta \phi' T_{\max} \left\{ \frac{\delta \phi'}{\pi (\delta \phi')^2 + \phi'^2} \right\} \quad \text{Eq. 3.37}$$

where $\delta \phi' = \frac{2}{\sqrt{F}}$. Eq. 3.38

The term between the curly brackets in Eq. 3.37 is the normalised Lorentzian function whose FWHM bandwidth is $2\delta\phi'$. Eq. 3.38 is identical to the expression for the half-bandwidth ($\phi_{1/2}$) derived from Eq. 3.33 with large F values.

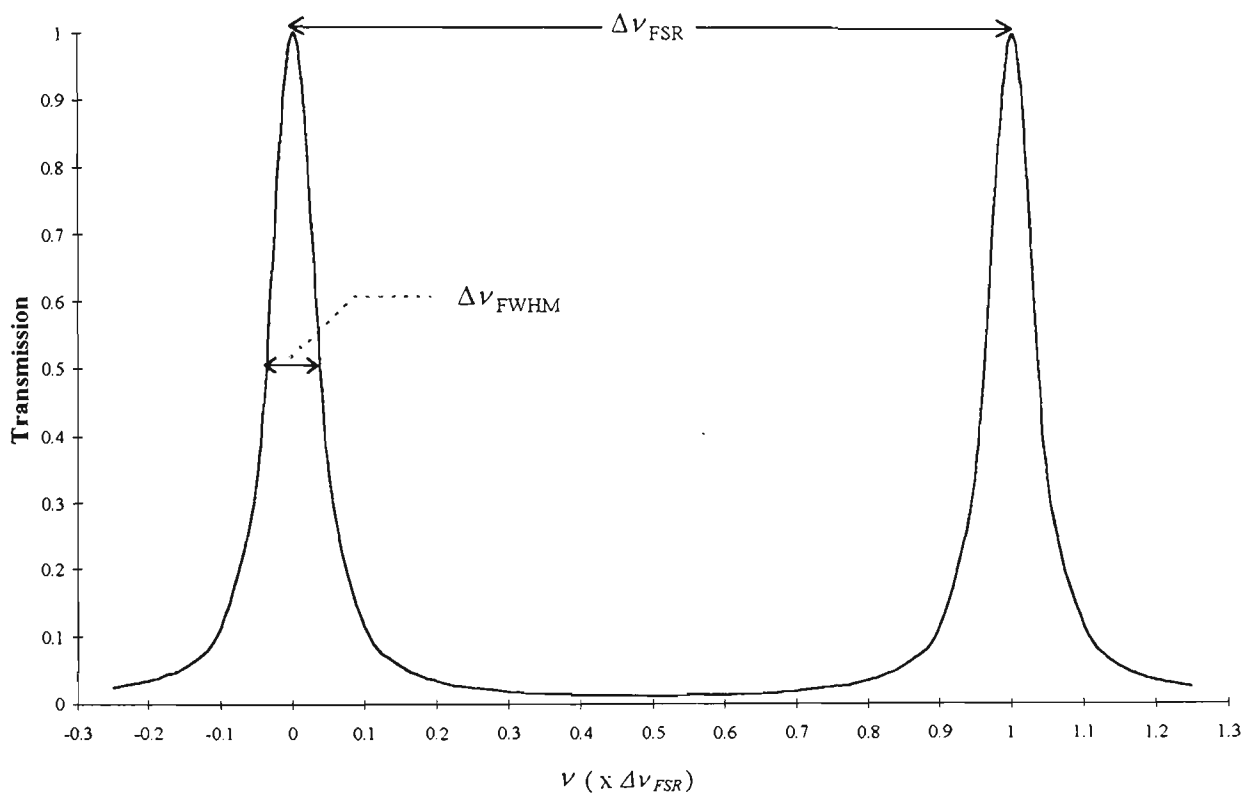


Figure 3.3: Graph of the free spectral range ($\Delta \nu_{FSR}$) and FWHM bandwidth ($\Delta \nu_{FWHM}$) of the modes of Fabry-Pérot interferometer.

3.1.3 Reflection Function of Fabry-Pérot Interferometers

The reflection electric field, $\tilde{\mathbf{E}}_r$, can be obtained in a similar manner to the transmitted field (Eq. 3.14) as

$$\tilde{\mathbf{E}}_r = \tilde{\mathbf{E}}_o \exp(-i\omega t) \left\{ r_{12} \exp(i\theta_{12}^r) + r_{23} t_{12} t_{21} \exp[i(\theta_{23}^r + \theta_{12}^i + \theta_{21}^i + 2\beta)] \sum_{n=0}^{\infty} [r_{23} r_{21} \exp[i(\theta_{23}^r + \theta_{21}^r + 2\beta)]]^n \right\}. \quad \text{Eq. 3.39}$$

The equation can be further simplified to

$$\tilde{\mathbf{E}}_r = \tilde{E}_o \exp(-i\omega t) \left\{ r_{12} \exp(i\theta_{12}^r) + \frac{r_{23} t_{12} t_{21} \exp[i(\theta_{23}^r + \theta_{12}^i + \theta_{21}^i + 2\beta)]}{1 - r_{23} r_{21} \exp[i(\theta_{23}^r + \theta_{21}^r + 2\beta)]} \right\}, \quad \text{Eq. 3.40}$$

which can be subsequently expressed as a single fraction

$$\tilde{\mathbf{E}}_r = \tilde{E}_o \exp(-i\omega t) \left\{ \frac{r_{12} \exp(i\theta_{12}^r) + r_{23} \tilde{G} \exp[i(\theta_{23}^r + 2\beta)]}{1 - r_{23} r_{21} \exp[i(\theta_{23}^r + \theta_{21}^r + 2\beta)]} \right\} \quad \text{Eq. 3.41}$$

$$\text{where } \tilde{G} \equiv t_{12} t_{21} \exp[i(\theta_{12}^i + \theta_{21}^i)] - r_{12} r_{21} \exp[i(\theta_{12}^r + \theta_{21}^r)]. \quad \text{Eq. 3.42}$$

Eq. 3.42 can be written as

$$\tilde{G} = -\exp[i(\theta_{12}^r + \theta_{21}^r)] \left\{ r_{12} r_{21} - t_{12} t_{21} \exp[i\phi_r] \right\} \quad \text{Eq. 3.43}$$

$$\text{where } \phi_r = \theta_{12}^i + \theta_{21}^i - \theta_{12}^r - \theta_{21}^r \quad \text{Eq. 3.44}$$

is the difference between the combined transmission and reflection phase shifts of the proximal mirror.

Using Eq. 3.19, Eq. 3.20 and Eq. 3.43, Eq. 3.41 can be written as

$$\tilde{\mathbf{E}}_r = E_o \exp(-i\omega t + i\theta_{12}^r) \left\{ \frac{r_{12} - r_{23} G \exp[i(\phi + \phi_G)]}{1 - r_{23} r_{21} \exp[i\phi]} \right\} \quad \text{Eq. 3.45}$$

$$\text{where } G = |r_{12} r_{21} - t_{12} t_{21} \exp[i\phi_r]|, \text{ and} \quad \text{Eq. 3.46}$$

$$\phi_G = \arg(r_{12} r_{21} - t_{12} t_{21} \exp[i\phi_r]). \quad \text{Eq. 3.47}$$

The reflected intensity I_r can be calculated using Eq. 3.3 and Eq. 3.45 and

$$I_r = \frac{n_1 c}{2} \left\{ \frac{(r_{12})^2 + (r_{23} G)^2 - 2r_{23} r_{12} G \cos(\phi + \phi_G)}{1 + R^2 - 2R \cos(\phi)} \right\}. \quad \text{Eq. 3.48}$$

Hence from Eq. 3.8

$$R = \frac{(r_{12})^2 + (r_{23} G)^2 - 2r_{23} r_{12} G \cos(\phi + \phi_G)}{1 + R^2 - 2R \cos(\phi)}. \quad \text{Eq. 3.49}$$

The reflectance R of a Fabry-Pérot interferometer is complicated by ϕ_G and G . One can plot R against ϕ for different values of ϕ_G , G and R . The general conclusions from the plots are that for low-finesse Fabry-Pérot interferometers, R and T vary sinusoidally and are not 180° out of phase whilst for high-finesse Fabry-Pérot

interferometers, R is characterised by asymmetric modes. One of the cases for which asymmetric reflection modes are evident is that of a Fabry-Pérot interferometer with a metallic thin-film proximal mirror.

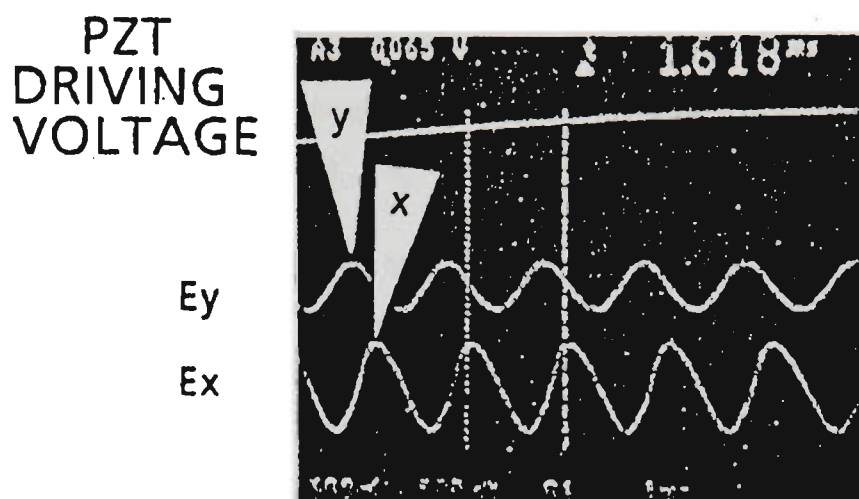


Figure 3.4: Reflection signals from a Fabry-Pérot interferometer with a metallic thin film as its Fabry-Pérot proximal mirror [Kitajima *et al.*, 1990].

Figure 3.4 shows the interferometric output from an extrinsic FPS using a birefringent lead fibre, an Au thin film proximal mirror and an air-spaced cavity [Kitajima *et al.*, 1990]. In their work, Kitajima *et al.* had illuminated their FPS with two orthogonally polarised beams (along the x- and y-axis) with a 90° relative phase difference in order to produce two competing interferometric outputs. Although Kitajima *et al.* did not indicate it in their paper, the asymmetry in the x- and y-axis signals (Figure 3.4) (as the cavity length was varied) can be attributed to the phase change upon reflection from a metallic thin-film. Interestingly, this asymmetry can be used to determine the direction of measurand change.

On the other hand, if the Fabry-Pérot reflectors are Fresnel interfaces between two dielectrics, a single-layer dielectric thin film or an in-fibre Bragg grating, $\phi_G = 0$ and subsequently Eq. 3.49 becomes

$$R = \frac{(r_{12})^2 + (r_{23}G)^2 - 2r_{12}r_{23}G \cos(\phi)}{1 + R^2 - 2R \cos(\phi)}. \quad \text{Eq. 3.50}$$

3.1.4 Low Finesse Fabry-Pérot Interferometers as a Two-Beam Interferometer

For low-finesse Fabry-Pérot interferometers (obtained when roughly $F < 0.5$ or $R < 10\%$), the transmission and reflection functions of a Fabry-Pérot interferometer can also be calculated by using only the first two beams composing the entire resultant electric field. Using relations defined in previous discussions,

$$\tilde{\mathbf{E}}_t^{1+2} = RT\tilde{E}_o \exp\left[i(-\omega t + \theta_{12}^i + \theta_{23}^i + \theta_{23}^r + \theta_{21}^r + \beta)\right] \left[1 + R \cdot \exp(i\phi)\right], \text{ and} \quad \text{Eq. 3.51}$$

$$\tilde{\mathbf{E}}_r^{1+2} = \tilde{E}_o \exp\left[i(-\omega t + \theta_{12}^r)\right] \left\{r_{12} + r_{23}t_{12}t_{21} \exp\left[i(\phi + \phi_r)\right]\right\}, \quad \text{Eq. 3.52}$$

are the two-beam approximations of the transmission and reflection electric fields respectively. The transmittance and reflectance for the two-beam approximations are

$$\mathbf{T}_{1+2} = \frac{n_3}{n_1} (RT)^2 \left[1 + R^2 + 2R \cdot \cos(\phi)\right], \text{ and} \quad \text{Eq. 3.53}$$

$$\mathbf{R}_{1+2} = (r_{12})^2 + (r_{23}t_{12}t_{21})^2 + 2r_{12}r_{23}t_{12}t_{21} \cos(\phi + \phi_r). \quad \text{Eq. 3.54}$$

These equations demonstrate sinusoidally-varying transmission and reflection transfer functions with the latter function being out of phase from the former by ϕ_r . Such behaviour implies that for low values of the combined internal reflectance, signal processing schemes which are suitable for two-beam interferometers can be applied to low-finesse Fabry-Pérot interferometers.

3.1.5 Fringe Visibility

The fringe visibility of an interferometric output is defined as the ratio between the difference and sum of the maximum and minimum intensity values of the interferometric output:

$$V = \frac{I_{\max} - I_{\min}}{I_{\max} + I_{\min}}. \quad \text{Eq. 3.55}$$

The fringe visibility V can vary between 0 and 1 where a value of 1 means excellent visibility ($I_{\min} = 0$).

Physically, the fringe visibility describes the contrast or ease of identifying an interferometric fringe.

I_{\max} and I_{\min} may include some additional common background irradiance which contribute only to the denominator of the right-hand side of Eq. 3.55. Such additional intensity reduces the experimental fringe visibility value of V . In addition, the experimental fringe visibility can decrease when the optical path difference of an interferometer approaches the coherence length of the light source. However, since in this work, a highly

coherent source has been employed, such effects due to coherence degradation are ignored. In the following discussions, the fringe visibility V is calculated with the assumption that the light source is essentially monochromatic and that there is no background intensity signal.

The fringe visibility of the transmission function of a Fabry-Pérot interferometer can readily be shown to be

$$V_T = \frac{F}{2 + F}. \quad \text{Eq. 3.56}$$

Clearly for high finesse Fabry-Pérot interferometers, the transmission fringe visibility is approximately equal to 1. The reflection fringe visibility V_R for the reflection function gives a more complicated expression compared with the transmission case (Eq. 3.56). However, the reflection fringe visibility becomes unity when

$$r_{12} = r_{23}G. \quad \text{Eq. 3.57}$$

Excellent reflection fringe visibility can be achieved because R (Eq. 3.49) can become zero at some value of $\phi + \phi_G$ when Eq. 3.57 is satisfied. The quantity $r_{23}G$ can be interpreted as the effective amplitude reflectance of the distal Fabry-Pérot mirror. Hence, Eq. 3.57 implies that the reflection fringe visibility is a maximum when the effective reflectance values of both Fabry-Pérot mirrors are similar.

If $\phi_G = 0$, Eq. 3.50 can be used to compute for the reflection fringe visibility V_R . In such case,

$$V_R = \frac{2r_{12}r_{23}G(1 + (r_{12})^2(r_{23})^2) - 2r_{12}r_{23}((r_{12})^2 + (r_{23}G)^2)}{((r_{12})^2 + (r_{23}G)^2)(1 + (r_{12})^2(r_{23})^2) - 4(r_{12})^2(r_{23})^2G}. \quad \text{Eq. 3.58}$$

It can easily be shown that $V_R = 1$ when Eq. 3.57 holds.

The transmission fringe visibility for the two-beam approximation case is also given by Eq. 3.56 and is approximately

$$V_T^{1+2} = \frac{F}{2 + F} = \frac{2R}{1 + R^2} \cong 2R. \quad \text{Eq. 3.59}$$

Consequently, the transmission fringe visibility is low since R needs to be small for the two-beam approximation case. On the other hand, the reflection fringe visibility for the two-beam approximation case is expressed as

$$V_R^{1+2} = \frac{2r_{12}r_{23}t_{12}t_{21}}{(r_{12})^2 + (r_{23}t_{12}t_{21})^2}. \quad \text{Eq. 3.60}$$

As in the multiple-beam case, V_R^{1+2} approaches unity when

$$r_{12} = r_{23}t_{12}t_{21}, \quad \text{Eq. 3.61}$$

i.e. when the mirrors have similar effective front reflectance. In the current case, the effective reflectance of the distal mirror is modified instead by $t_{12}t_{21}$, the round-trip transmittance of the proximal mirror. Alternatively, this result can be obtained by assuming that the transmission amplitude coefficients dominate in Eq. 3.45 to Eq. 3.47.

3.1.6 Limitations on the Fringe Visibility

The fringe visibility of a Fabry-Pérot interferometer can be limited by scattering, absorption and coupling losses in the Fabry-Pérot mirrors. Light propagating within the Fabry-Pérot mirrors that are either fusion-spliced thin film or in-fibre Bragg gratings can be scattered or absorbed due to some inhomogeneity in these reflector regions. In the case of reflective thin films, these losses arise from the impurities in the material of the film and imperfections attributed to the deposition or fabrication process employed. Scattering loss is more pronounced near optical boundaries because there is usually migration of ionic species across the boundaries thereby increasing the inhomogeneity around these optical interfaces. On the other hand, scattering losses within the film can be generally neglected due to the narrow thickness of the film.

Absorption losses can be minimised by using a light source whose frequency is far from any resonant absorption region in the deposited material. This implies that the thin film behaves as a dielectric at the source wavelength.

In the fabrication of in-fibre fusion-spliced dielectric reflectors, aside from the deposition and fusion processes themselves contributing to the inhomogeneity of the refractive index of the film (scattering losses), non-alignment of the core of the fibres on either side of the film can give significant coupling losses. In fact, this is a major loss contribution for the fusion-spliced dielectric mirrors used in fabricating fusion-spliced fibre Fabry-Pérot interferometers (Chapter 5).

In-fibre Bragg gratings also suffer from losses due to the inefficient coupling of the incident propagating mode to the forward and backward propagating beams (insertion losses) and the scattering from the ultraviolet irradiated regions [Krug *et al.*, 1993]. Furthermore when the Bragg grating planes are not normal to the axis of the core,

light can be lost into the cladding and eventually leaves the side of the fibre [St. Russell *et al.* 1994]. Experimentally the aggregate loss in in-fibre Bragg gratings was found to be significantly less than that of fusion-spliced reflectors since the core of the fibre is still intact. Interestingly, losses in a grating can be used to locate the position of the grating along an optical fibre (Chapter 5).

The losses attributed to the Fabry-Pérot mirrors can easily be incorporated in the electric field reflection \tilde{r}_{bd} and transmission \tilde{t}_{bd} coefficients. For the ideal case of a loss-less mirror, conservation of energy requires [Born & Wolf, 1980]

$$|\tilde{r}_{bd}|^2 + \frac{n_d}{n_b} |\tilde{t}_{bd}|^2 = 1. \quad \text{Eq. 3.62}$$

On the other hand, real mirrors which exhibit some loss deviate from this relation and for real mirrors

$$|\tilde{r}_{bd}|^2 + \frac{n_d}{n_b} |\tilde{t}_{bd}|^2 = 1 - L_{bd}, \quad \text{Eq. 3.63}$$

where the term L_{bd} incorporates all the energy losses in the mirror.

3.2 Thin-Film or Bragg-Grating Fabry-Pérot Reflectors

In this section, the optical properties of ideal single-layer dielectric thin films and fibre Bragg gratings are discussed.

3.2.1 Dielectric Thin Film

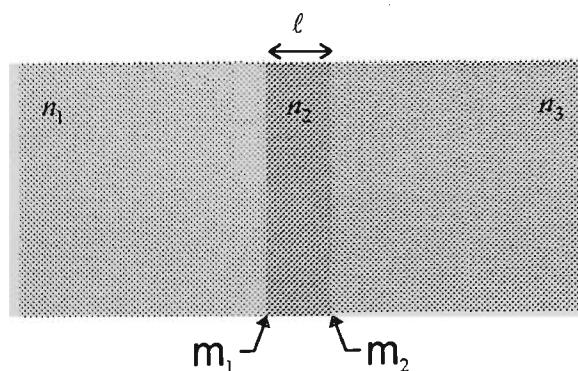


Figure 3.6: A single-layer optical thin film sandwiched between two optical media of refractive indices n_1 and n_3 , with refractive index n_2 and physical thickness ℓ .

A single-layer thin film is essentially a Fabry-Pérot etalon with Fresnel optical interfaces as the Fabry-Pérot reflectors (Figure 3.6) and hence the discussions in section 3.1 can be applied with a single-layer thin film. In the present case, the electric field transmission and reflection coefficients of the Fabry-Pérot mirrors are those given by the Fresnel formula for normal incidence:

$$\tilde{t}_{12} = \frac{2n_1}{n_1 + n_2}, \text{ and} \quad \text{Eq. 3.64}$$

$$\tilde{r}_{12} = \frac{n_1 - n_2}{n_1 + n_2}. \quad \text{Eq. 3.65}$$

Also, the following replacements are used:

$$\beta \rightarrow \beta_f = 2\pi \frac{n_f \ell_f}{\lambda} = 2\pi \frac{n_f \ell_f \nu}{c} \quad \text{Eq. 3.66}$$

$$n_2 \rightarrow n_f \quad \text{Eq. 3.67}$$

$$\ell \rightarrow \ell_f \quad \text{Eq. 3.68}$$

$$n_1, n_3 \rightarrow n_c \quad \text{Eq. 3.69}$$

where n_f and ℓ_f are the refractive index and the physical thickness of the film respectively. Following the discussions outlined in section 3.1 and assuming that $n_c < n_f$, the electric field transmission and reflection coefficients of the thin film embedded in an optical fibre are

$$\tilde{t}_{film} = \frac{T_f \exp[i\beta_f]}{1 - R_f \exp[i2\beta_f]} = \frac{T_f \exp[i(\beta_f + \theta_f^{nl})]}{\sqrt{1 + R_f^2 - 2R_f \cos[2\beta_f]}}, \text{ and} \quad \text{Eq. 3.70}$$

$$\tilde{r}_{film} = \left(\frac{n_c - n_f}{n_c + n_f} \right) \left(\frac{1 - \exp[i2\beta_f]}{1 - R_f \exp[i2\beta_f]} \right) = \frac{2\sqrt{R_f} \sin[\beta_f] \exp[i(\beta_f + \theta_f^{nl} + \frac{\pi}{2})]}{\sqrt{1 + R_f^2 - R_f \cos[2\beta_f]}}, \quad \text{Eq. 3.71}$$

(c.f. Eq. 3.14 and Eq. 3.45) where

$$T_f = \frac{4n_c n_f}{(n_c + n_f)^2}, \quad \text{Eq. 3.72}$$

$$R_f = \left(\frac{n_c - n_f}{n_c + n_f} \right)^2, \text{ and} \quad \text{Eq. 3.73}$$

$$\theta_f^{nl} = \tan^{-1} \left(\frac{R_f \sin[2\beta_f]}{1 - R_f \cos[2\beta_f]} \right). \quad \text{Eq. 3.74}$$

T_f and R_f are the transmittance and reflectance of the Fresnel optical interfaces. The superscript nl in θ_f^{nl} indicates that θ_f^{nl} behaves nonlinearly with β_f (and also with the optical frequency of the light source, the refractive index and physical length of the film). This nonlinear behavior of θ_f^{nl} can be understood by realising that the transmitted or reflected beam is the superposition of several beams which are out of phase with one another by an integral multiple of $2\beta_f$.

The transmittance (Eq. 3.16) and reflectance (Eq. 3.49) of a dielectric thin film embedded in an optical fibre are

$$T_{film} = \frac{(T_f)^2}{1 + (R_f)^2 - 2R_f \cos(2\beta_f)}, \text{ and} \quad \text{Eq. 3.75}$$

$$R_{film} = \frac{2R_f [1 - \cos(2\beta_f)]}{1 + (R_f)^2 - 2R_f \cos(2\beta_f)}. \quad \text{Eq. 3.76}$$

Clearly these functions are periodic with respect to the optical thickness of the film. Also,

$$T_f + R_f = 1, \text{ and} \quad \text{Eq. 3.77}$$

$$T_{film} + R_{film} = 1. \quad \text{Eq. 3.78}$$

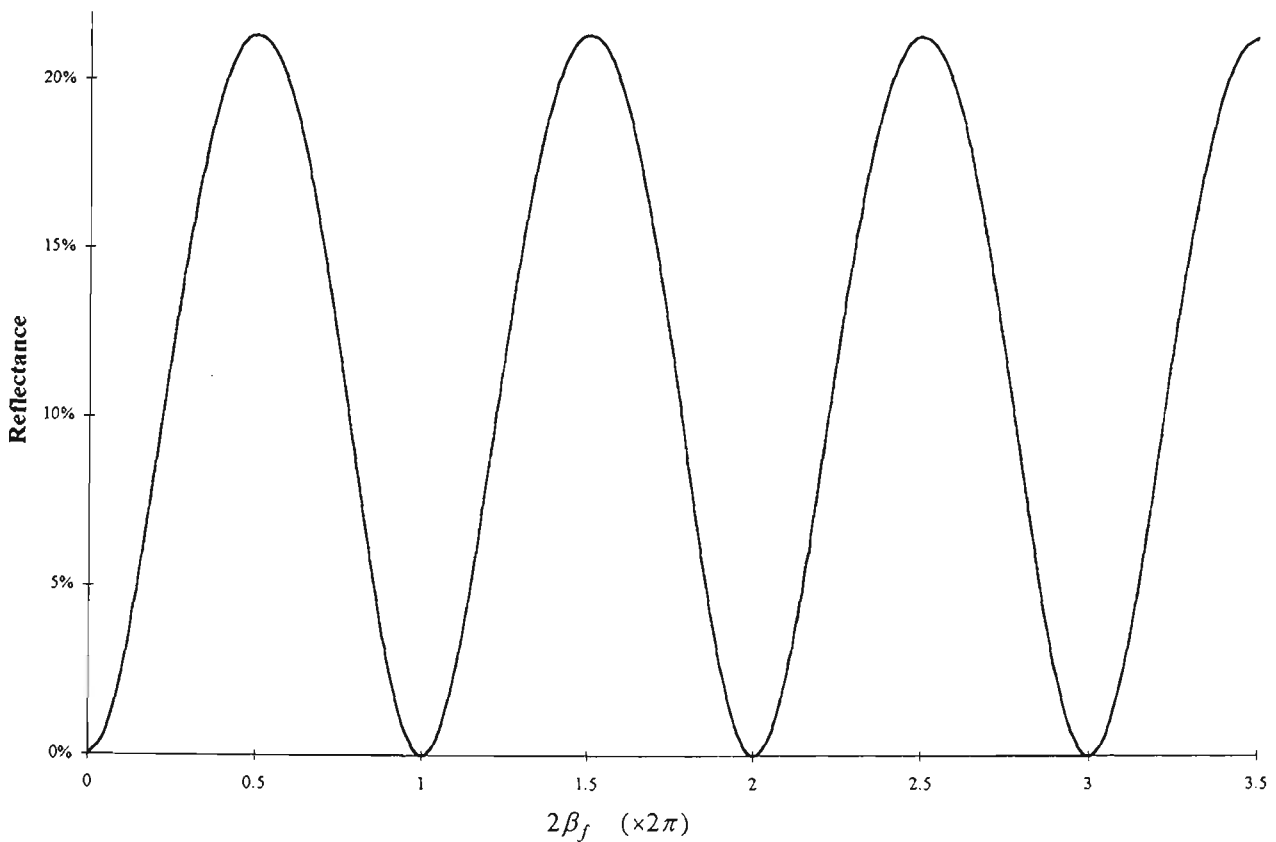


Figure 3.6: The reflectance of a single-layer TiO₂ thin-film ($n_f \approx 2.4$) embedded in an optical fibre ($n_c \approx 1.46$) plotted against the round-trip phase change $2\beta_f$ associated with the film.

The extrema of R_{film} , derived from differentiating the right-hand side of Eq. 3.76, occur when

$$2\beta_f = m\pi \quad \text{Eq. 3.79}$$

where m is an integer. For odd-multiples of the quarter-wave optical thicknesses (m is odd), R_{film} is at maximum value of

$$R_{film}^{\lambda/4} = \left(\frac{(n_c)^2 - (n_f)^2}{(n_c)^2 + (n_f)^2} \right)^2 \quad \text{Eq. 3.80}$$

whilst for even multiples of quarter-wave optical thickness (m is even), R_{film} is zero (minimum value). Figure 3.6 shows the reflectance of a single-layer TiO_2 thin-film embedded in an optical fibre ($n_c \approx 1.46$) plotted against $2\beta_f$. The refractive index of TiO_2 is about $n_f \approx 2.4$ giving $R_f \cong 6.0\%$ and $R_{film}^{\lambda/4} \cong 21\%$.

From Eq. 3.70 and Eq. 3.71, the transmitted and reflected electric fields from a thin film generally exhibit a phase shift after encountering the thin film. The total phase shifts are

$$\theta_{film}^i = \beta_f + \theta_f^{nl}, \text{ and} \quad \text{Eq. 3.81}$$

$$\theta_{film}^r = \beta_f + \theta_f^{nl} + \frac{\pi}{2}. \quad \text{Eq. 3.82}$$

Since the optical properties of the thin film are the same whether the incident beam is travelling from the left or from the right the film as shown in Figure 3.6, the values of ϕ_r , G and ϕ_G can be calculated (using Eq. 3.44, Eq. 3.46 and Eq. 3.47) from Eq. 3.81 and Eq. 3.82:

$$\phi_r = -\frac{\pi}{2} - \frac{\pi}{2} = -\pi, \quad \text{Eq. 3.83}$$

$$\phi_G = 0, \text{ and} \quad \text{Eq. 3.84}$$

$$G = 1. \quad \text{Eq. 3.85}$$

3.2.2 Fibre Bragg Grating

Bragg gratings in optical waveguides can be formed by producing periodic variations either in the refractive index or in the waveguide physical structure [Yariv & Nakamura, 1977]. Figure 3.7 illustrates a refractive-index-type fibre Bragg grating (FBG) embedded with the core of an optical fibre. These variations are usually not large but

extend over a section of the waveguide. The effect of these variations is a preferred reflection at a particular wavelength. At this wavelength, the grating is on-resonance, coupling light to propagate in the opposite direction to the incident beam. Although a Bragg grating can be considered as a multi-layer film stack, such an approach leads to a cumbersome analysis. Alternatively, Bragg gratings resonance can be best treated by coupled-mode theory which considers coupling between modes of an optical waveguide in the presence of some waveguide perturbations [Yariv, 1973]. Maximum coupling occurs when the phase-matching condition is achieved. This condition can be expressed as (the Bragg resonance condition)

$$\lambda_b = 2n_b \Lambda , \quad \text{Eq. 3.86}$$

where λ_b is the Bragg resonance wavelength, n_b the average effective refractive index of the mode guided within the grating and Λ the spatial period of the grating (pitch length).

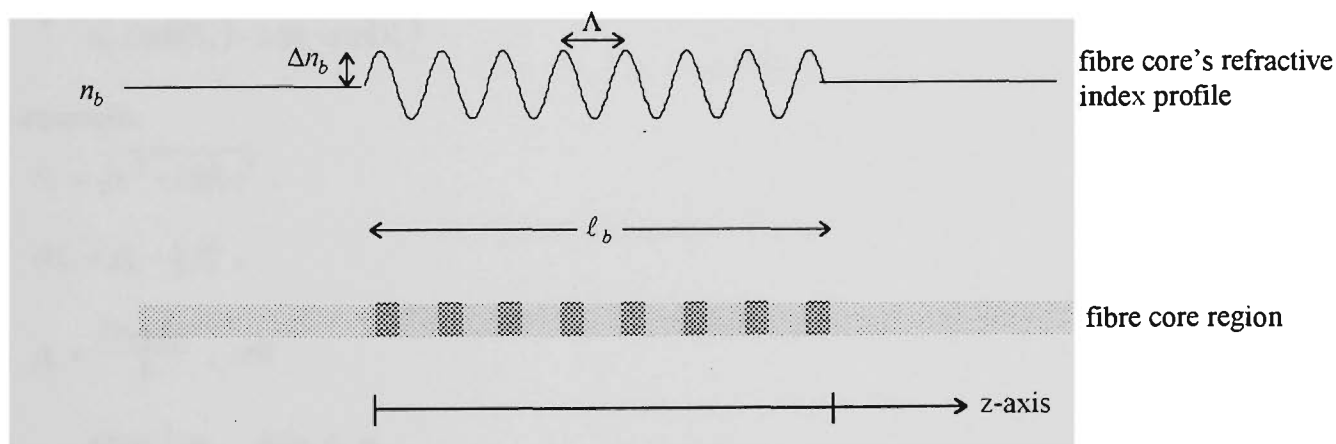


Figure 3.7: Schematic of a fibre Bragg grating embedded along the core of an optical fibre.

Figure 3.7 shows the refractive index distribution corresponding to a sinusoidal modulation of electric permittivity in the core of a Ge-doped fibre. Such modulation of length l_b in the electric permittivity can be described as [Yariv, 1973]

$$\epsilon_{EM} = \begin{cases} n_b^2 + \Delta(n_b^2) \sin\left(\beta_b^0 \frac{z}{l_b}\right), & 0 \leq z \leq l_b \\ n_b^2, & z \leq 0 \text{ or } z \geq l_b \end{cases} \quad \text{Eq. 3.87}$$

where $\beta_b^0 = \frac{2\pi}{\Lambda} l_b$. Eq. 3.88

z is measured along the longitudinal axis of the fibre beginning from the proximal end of the grating. In Eq. 3.87, the relation $n_b \cong \sqrt{\epsilon_{EM}}$ was used and hence the amplitude modulation of the electric permittivity is described as

$$\Delta\epsilon_{EM} = \Delta(n_b^2) = 2n_b \Delta n_b. \quad \text{Eq. 3.89}$$

Δn_b refers to the amplitude of the refractive index modulation (Figure 3.7).

By employing Eq. 3.87, coupled-mode theory predicts that the electric field transmission and reflection coefficients of an FBG are [Yariv, 1973; Yariv & Nakamura, 1977; Lam & Garside, 1981]

$$t_b = \frac{S_b \exp\left(i \frac{\beta_b^0}{2}\right)}{S_b \cosh(S_b) - i \delta\beta_b \sinh(S_b)}, \text{ and} \quad \text{Eq. 3.90}$$

$$r_b = \frac{i \kappa \sinh(S_b)}{S_b \cosh(S_b) - i \delta\beta_b \sinh(S_b)}. \quad \text{Eq. 3.91}$$

In these equations,

$$S_b = \sqrt{\kappa^2 - (\delta\beta_b)^2}, \quad \text{Eq. 3.92}$$

$$\delta\beta_b = \beta_b - \frac{1}{2} \beta_b^0, \quad \text{Eq. 3.93}$$

$$\beta_b = \frac{2\pi n_b \ell_b}{\lambda}, \text{ and} \quad \text{Eq. 3.94}$$

$$\kappa = \frac{\pi \Delta(n_b^2) \eta_b}{2n_b \lambda} = \frac{\pi \Delta n_b \ell_b \eta_b}{\lambda}. \quad \text{Eq. 3.95}$$

In the last equation, η_b is the fraction of the total power of the mode guided in the core. In deriving Eq. 3.90 and Eq. 3.91, it was assumed that no energy gain or loss occurs at the grating and that the coupling is only between the forward and backward propagating modes of the same polarisation. In the case where cross-polarisation coupling occurs, additional coupled equations are required. The electric field transmission and reflection coefficients of an FBG used in this work (Eq. 3.90 and Eq. 3.91) are the complex conjugates of the corresponding expressions typically found in the literature [Yariv, 1973; Yariv & Nakamura, 1977; Lam & Garside, 1981]. This choice was made in order to remain consistent with the convention for phase change (a positive electric field phase of the output beam signifies a phase lag with respect to the input beam) and electric field variation ($e^{-i\omega t}$).

Eq. 3.90 and Eq. 3.91 can be rewritten as

$$t_b = \frac{S_b \exp\left(i\left(\theta_b + \frac{\beta_b^0}{2}\right)\right)}{\sqrt{(\delta\beta_b)^2 \sinh^2(S_b) + (S_b)^2 \cosh^2(S_b)}}, \text{ and} \quad \text{Eq. 3.96}$$

$$r_b = \frac{\kappa \sinh(S_b) \exp\left(i\left(\theta_b + \frac{\pi}{2}\right)\right)}{\sqrt{(\delta\beta_b)^2 \sinh^2(S_b) + (S_b)^2 \cosh^2(S_b)}}, \quad \text{Eq. 3.97}$$

$$\text{where } \theta_b = \tan^{-1}\left(\frac{\delta\beta_b}{S_b} \tanh(S_b)\right). \quad \text{Eq. 3.98}$$

The transmittance and reflectance of a fibre grating can be computed as in Section 3.1:

$$T_b = \frac{(S_b)^2}{(\delta\beta_b)^2 \sinh^2(S_b) + (S_b)^2 \cosh^2(S_b)} = \frac{(S_b)^2}{(S_b)^2 + \kappa^2 \sinh^2(S_b)}, \text{ and} \quad \text{Eq. 3.99}$$

$$R_b = \frac{\kappa^2 \sinh^2(S_b)}{(\delta\beta_b)^2 \sinh^2(S_b) + (S_b)^2 \cosh^2(S_b)} = \frac{\kappa^2 \sinh^2(S_b)}{(S_b)^2 + \kappa^2 \sinh^2(S_b)}. \quad \text{Eq. 3.100}$$

$$\text{Clearly, } T_b + R_b = 1 \quad \text{Eq. 3.101}$$

which confirms the conservation of energy as originally assumed.

When the phase-matching condition

$$\delta\beta_b = 0 \quad \text{Eq. 3.102}$$

occurs, the Bragg condition (Eq. 3.86) is obtained and

$$S_b = \kappa_b = 2\pi \frac{n_b \ell_b}{\lambda_b} \eta_b \quad \text{Eq. 3.103}$$

where κ_b is the value of κ at λ_b .i.e. (Bragg) coupling phase. The Bragg transmittance and reflectance of an FBG

(T_b and R_b at λ_b) are

$$T_b^0 = \text{sech}^2(\kappa_b) \quad \text{and} \quad \text{Eq. 3.104}$$

$$R_b^0 = \tanh^2(\kappa_b). \quad \text{Eq. 3.105}$$

For typical FBGs,

$$\kappa \approx \kappa_b \quad \text{Eq. 3.106}$$

and thus κ_b can be considered as a constant of the grating.

From Eq. 3.96 the phase change upon transmission is

$$\theta_b^t = \theta_b + \frac{\beta_b^0}{2} \quad \text{Eq. 3.107}$$

whilst from Eq. 3.97 the phase change upon reflection is

$$\theta_b^r = \theta_b + \frac{\pi}{2}. \quad \text{Eq. 3.108}$$

The phase shift upon reflection or transmission across a grating thus depends on θ_b . It is therefore important to determine the behaviour of θ_b . When the phase mismatch $\delta\beta_b$ is substantially larger than the coupling phase κ ,

$$\delta\beta_b \gg \kappa, \quad \text{Eq. 3.109}$$

$$S_b \approx i\delta\beta_b \quad \text{Eq. 3.110}$$

$$\text{and } \tanh(S_b) \approx i \tan(\delta\beta_b). \quad \text{Eq. 3.111}$$

Hence when Eq. 3.109 holds, Eq. 3.98 becomes

$$\theta_b \approx \delta\beta_b. \quad \text{Eq. 3.112}$$

Alternatively, the approximation in Eq. 3.112 can be removed such that Eq. 3.98 can be written as

$$\theta_b = \delta\beta_b + \theta_b^{nl} \quad \text{Eq. 3.113}$$

where θ_b^{nl} can be considered as the (residual) nonlinear phase component of θ_b as opposed to the phase-mismatch $\delta\beta_b$ which behaves linearly with the optical frequency of the light source, the refractive index and physical length of the grating.

Figure 3.8 shows the R_b , θ_b^r and θ_b^{nl} of an FBG plotted against $\delta\beta_b$ for the case when $\kappa_b = 0.446$. This value of κ_b corresponds to that of the grating used in this work (*Grating1*). Bragg reflectance of $R_b^0 = 17.5\%$. Since the range of the \tan^{-1} function is between $-\frac{\pi}{2}$ and $\frac{\pi}{2}$, only the relative phase value of θ_b^r (modulo π) is plotted. The exact value of θ_b^r requires that its half-fringe be determined in order to unwrap its behaviour when $\delta\beta_b$ is varied by more than π . In addition, the figure also shows that $\delta\beta_b$ and θ_b^r are proportional to each other in regions far from the central Bragg wavelength ($\delta\beta_b = 0$) consistent with Eq. 3.112. By subtracting this linear trend from θ_b^r , θ_b^{nl} is obtained. Figure 3.8 also illustrates that the behaviour of θ_b^{nl} is similar to that of the anomalous dispersion in the region of an optical absorption band in a material. θ_b^{nl} is also referred to in this thesis as the anomalous dispersion of a fibre Bragg grating.

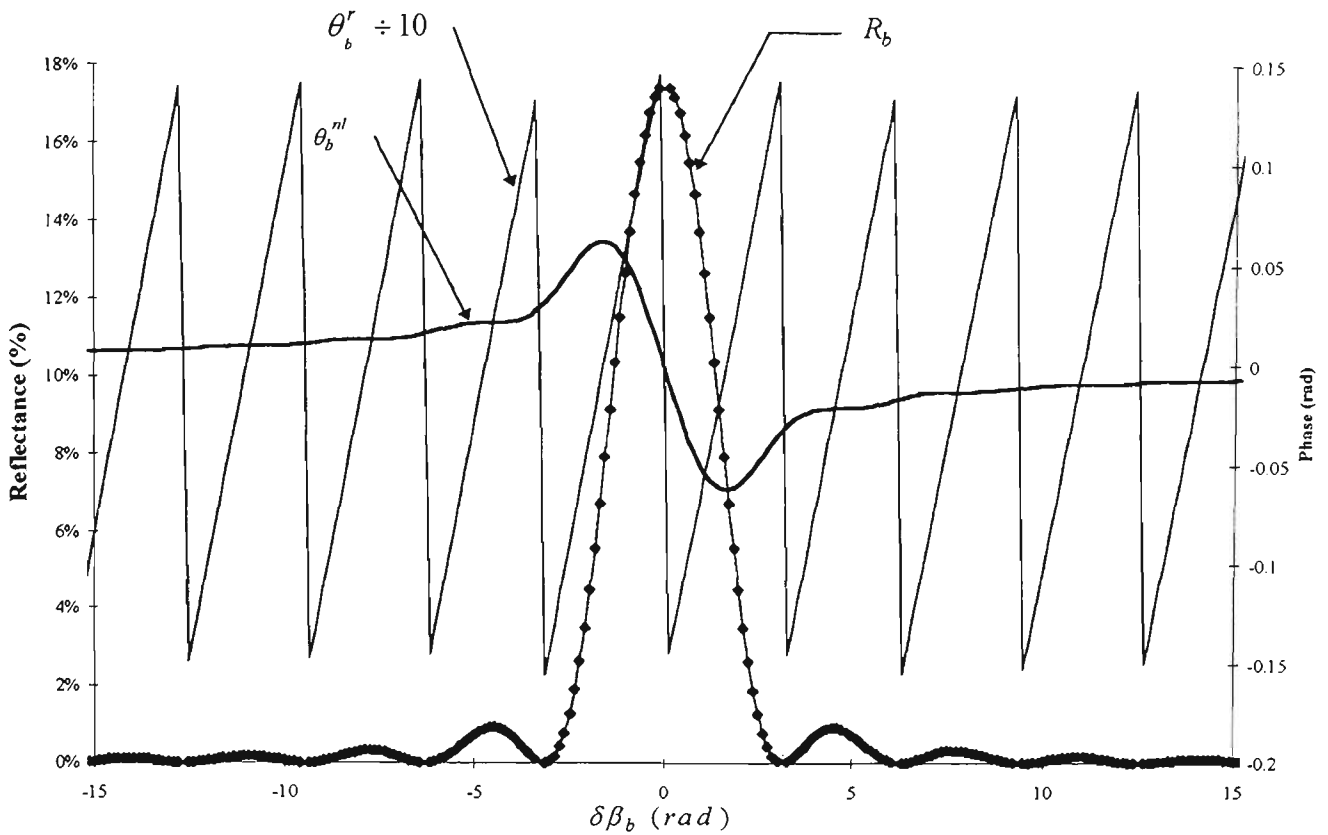


Figure 3.8: The reflectance (R_b), the electric field phase change upon reflection (θ_b^r) and the nonlinear phase component of θ_b^r (θ_b^{nl}) of a Bragg grating plotted against the phase mismatch $\delta\beta_b$ for the case when $\kappa_b = 0.446$ (and Bragg reflectance of $R_b^0 = 17.5\%$). In the figure, the values of θ_b^r are divided by 10 ($\theta_b^r \div 10$) in order that the behaviour of θ_b^{nl} can be easily shown (when $\theta_b^r \div 10$ and θ_b^{nl} are plotted on the same scale).

As with a thin film, an FBG exhibits reciprocal optical properties. When a fibre grating is used as the proximal Fabry-Pérot mirror of an FFPI, the value of ϕ_r is (substituting Eq. 3.107 and Eq. 3.108 into Eq. 3.44)

$$\phi_r = \beta_b^0 \ell_b - \pi = 2\pi N_b - \pi, \quad \text{Eq. 3.114}$$

$$\text{where } N_b = \frac{\ell_b}{\Lambda}, \quad \text{Eq. 3.115}$$

is the number of periodic refractive index (grating) planes composing the Bragg grating. Subsequently ϕ_G and G (using Eq. 3.46 and Eq. 3.47) are

$$\phi_G = 0, \text{ and} \quad \text{Eq. 3.116}$$

$$G = 1. \quad \text{Eq. 3.117}$$

Therefore, as was the case with a thin film mirror, the reflection function of an FFPI with a proximal FBG mirror can be simplified and is given by equation 3.49.

3.3 The Free Spectral Range of Fibre Fabry-Pérot Interferometers With Either Thin-Film or Fibre Bragg Grating Reflectors

In this section, the free spectral range (FSR) of FFPIs with either thin-film or fibre Bragg grating reflectors is described. Eq. 3.28 can be rewritten and the chain rule for differentiation can be applied so that,

$$\frac{2\pi}{\Delta\nu_{\text{FSR}}} = 2 \frac{\beta}{\nu} + \frac{\partial\theta_{m_1}^r}{\partial\beta_{m_1}} \frac{\partial\beta_{m_1}}{\partial\nu} + \frac{\partial\theta_{m_2}^r}{\partial\beta_{m_2}} \frac{\partial\beta_{m_2}}{\partial\nu}. \quad \text{Eq. 3.118}$$

For a dielectric thin-film embedded in a fibre or an FBG reflector, θ_X^r ($X = m_1$ or m_2) refers to the phase change upon reflection on either surface of the reflector (*i.e.* the reflector is assumed to have the same phase change from either propagation direction). β_X is the phase change associated with the optical length of the mirror X . Assuming that the optical length associated with β_X does not depend on the optical frequency ν ,

$$\frac{2\pi}{\Delta\nu_{\text{FSR}}} = 2 \frac{\beta}{\nu} + \frac{\partial\theta_{m_1}^r}{\partial\beta_{m_1}} \frac{\beta_{m_1}}{\nu} + \frac{\partial\theta_{m_2}^r}{\partial\beta_{m_2}} \frac{\beta_{m_2}}{\nu}. \quad \text{Eq. 3.119}$$

The corresponding functions for a thin-film or an FBG reflector, $\frac{\partial\theta_{\text{film}}^r}{\partial\beta_f}$ and $\frac{\partial\theta_b^r}{\partial\beta_b}$ respectively, are described in the following discussions.

3.3.1 Some Preliminary Calculations

3.3.1.1 The Case of a Dielectric Thin Film

Using Eq. 3.82,

$$\frac{\partial\theta_{\text{film}}^r}{\partial\beta_f} = \frac{\partial\left(\beta_f + \theta_f^{nl} + \frac{\pi}{2}\right)}{\partial\beta_f} = 1 + \frac{\partial\theta_f^{nl}}{\partial\beta_f}. \quad \text{Eq. 3.120}$$

On the other hand,

$$\frac{\partial\theta_f^{nl}}{\partial\beta_f} = \frac{-2R_f[R_f - \cos(2\beta_f)]}{1 + (R_f)^2 - 2R_f \cos(2\beta_f)}. \quad \text{Eq. 3.121}$$

Using only the first two terms of the Taylor's series expansion of $\frac{\partial\theta_f^{nl}}{\partial\beta_f}$ in R_f about $R_f = 0$, the right-hand side

of Eq. 3.121 yields

$$\frac{\partial \theta_f^{nl}}{\partial \beta_f} \approx 2R_f \cos(2\beta_f) + 2 \left[2 \cos^2(2\beta_f) - 1 \right] (R_f)^2. \quad \text{Eq. 3.122}$$

for small values of R_f ($R_f \approx 0$). The maximum value of $\left| \frac{\partial \theta_f^{nl}}{\partial \beta_f} \right|$ is roughly

$$\left| \frac{\partial \theta_f^{nl}}{\partial \beta_f} \right|_{\max} \approx 2(R_f)^2 \quad \text{Eq. 3.123}$$

for films with odd-multiples of $\lambda/4$ optical thicknesses. Hence when R_f is small, this equation means that Eq.

3.120 can be expressed as

$$\frac{\partial \theta_{film}^r}{\partial \beta_f} \approx 1. \quad \text{Eq. 3.124}$$

3.3.1.2 The Case of a Fibre Bragg Grating

$\frac{\partial \theta_b^r}{\partial \beta_b}$ can be computed in a similar manner to the thin-film case:

$$\frac{\partial \theta_b^r}{\partial \beta_b} = \frac{\partial(\delta\beta_b + \theta_b^{nl} + \frac{\pi}{2})}{\partial \beta_b} = 1 + \frac{\partial \theta_b^{nl}}{\partial \beta_b}. \quad \text{Eq. 3.125}$$

Figure 3.9 shows R_b and $\frac{\partial \theta_b^r}{\partial \beta_b}$ for the grating shown in Figure 3.8. The maximum value of $\frac{\partial \theta_b^r}{\partial \beta_b}$ occurs when

$$\delta\beta_b = 0.$$

$$\left| \frac{\partial \theta_b^{nl}}{\partial \beta_b} \right|_{\max} = 1 - \frac{\tanh(\kappa_b)}{\kappa_b}. \quad \text{Eq. 3.126}$$

Figure 3.10 shows the Bragg reflectance R_b^0 and $\left| \frac{\partial \theta_b^{nl}}{\partial \beta_b} \right|_{\max}$ as functions of κ_b . The figure indicates that

$\left| \frac{\partial \theta_b^{nl}}{\partial \beta_b} \right|_{\max} < 0.035$ when $\kappa_b < 0.32$ rad or $R_b^0 < 10\%$. Alternatively, expanding the right-hand side of Eq. 3.126

as a Taylor's series in κ_b about $\kappa_b = 0$ and using only the first two terms of the series yields

$$\left| \frac{\partial \theta_b^{nl}}{\partial \beta_b} \right|_{\max} \approx \frac{\kappa_b^2}{3} \left(1 - \frac{2\kappa_b^2}{5} \right). \quad \text{Eq. 3.127}$$

For the special case when $\kappa_b \approx 0$ (which implies the Bragg reflectance R_b^0 is also small), Eq. 3.125 reduces to

$$\frac{\partial \theta_b^r}{\partial \beta_b} \left(= \frac{\partial \theta_b}{\partial \beta_b} \right) \approx 1. \quad \text{Eq. 3.128}$$

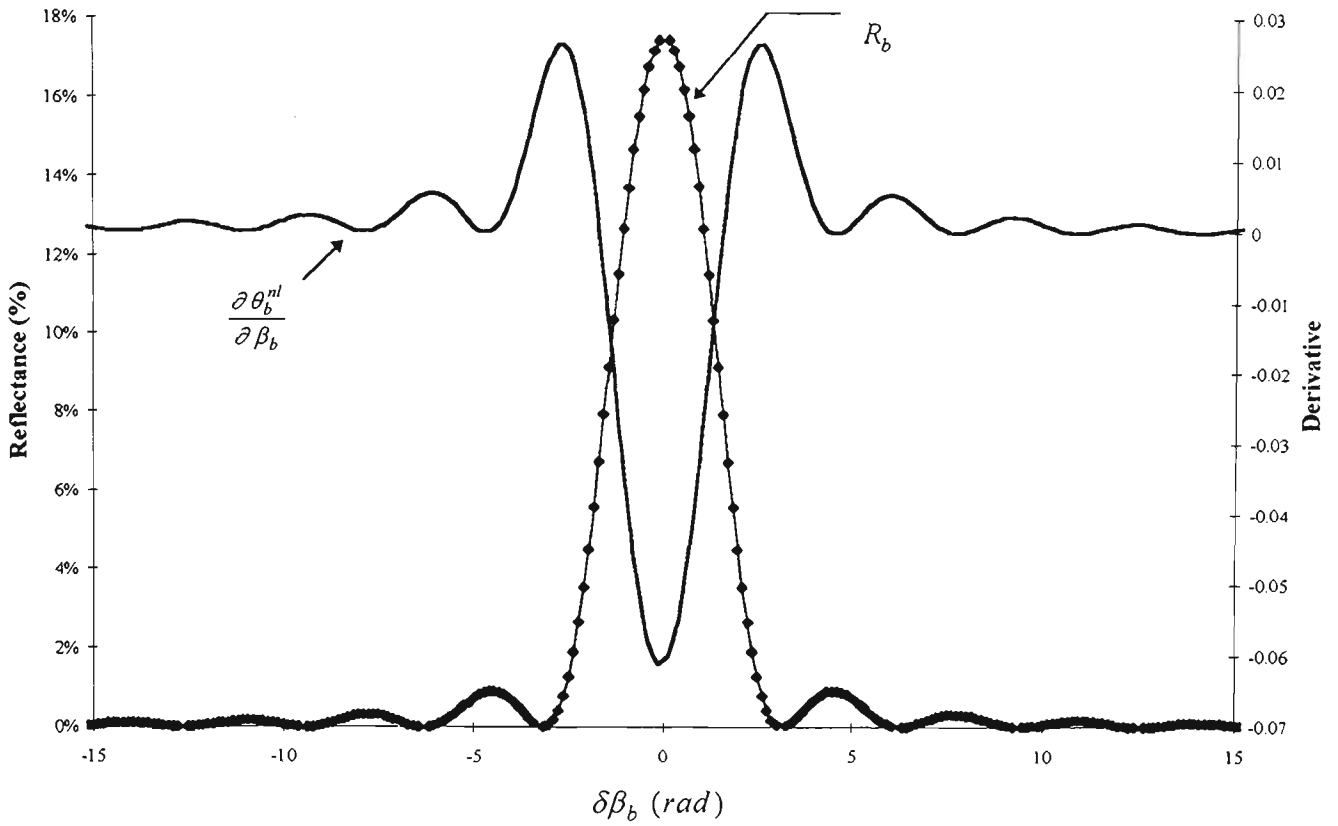


Figure 3.9: The behaviour of R_b and $\frac{\partial \theta_b^r}{\partial \beta_b}$ of a fibre Bragg grating plotted against the phase mismatch $\delta \beta_b$ for the case when $\kappa_b = 0.446$ (and Bragg reflectance of $R_b^0 = 17.5\%$).

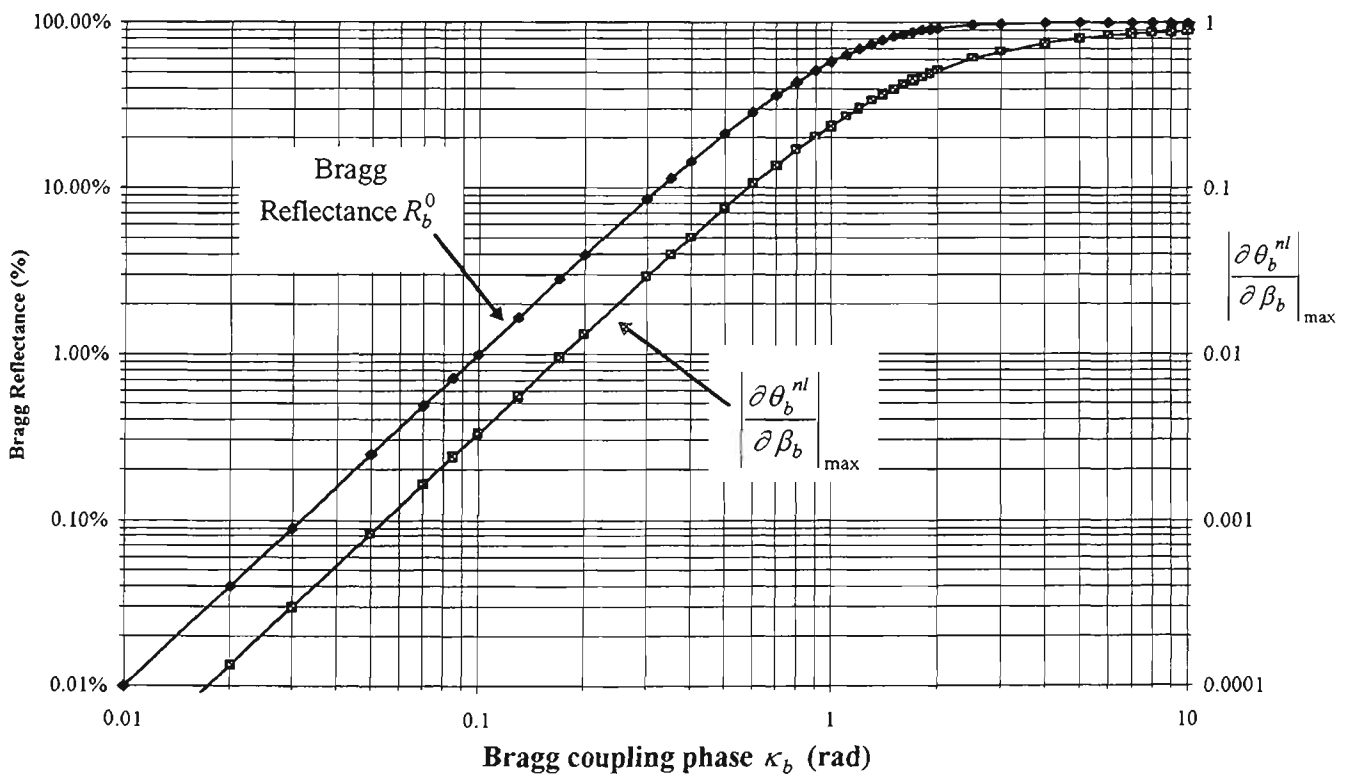


Figure 3.10: The Bragg reflectance R_b^0 and $\left. \frac{\partial \theta_b^{nl}}{\partial \beta_b} \right|_{\max}$ of a grating plotted against Bragg coupling phase κ_b .

3.3.2 Final Calculations

Eq. 3.124 and Eq. 3.128, imply that $\frac{\partial \theta_X^r}{\partial \beta_X} \approx 1$ when mirror X is either an in-fibre single-layer thin-film or an

FBG with low Bragg reflectance. Hence Eq. 3.119 becomes

$$\frac{2\pi}{\Delta \nu_{\text{FSR}}} \approx 2 \frac{\beta}{\nu} + \frac{\beta_{m_1}}{\nu} + \frac{\beta_{m_2}}{\nu}, \text{ or} \quad \text{Eq. 3.129}$$

$$\Delta \nu_{\text{FSR}} \approx \frac{2\pi\nu}{2 \left(\beta + \frac{\beta_{m_1}}{2} + \frac{\beta_{m_2}}{2} \right)}. \quad \text{Eq. 3.130}$$

By comparing Eq. 3.130 and Eq. 3.29, the FSR of an FFPI with either in-fibre single-layer thin-film or low-reflectance FBG Fabry-Pérot reflectors is approximately equal to an FSR corresponding to an effective optical cavity length measured between the middle of both Fabry-Pérot reflectors. The maximum fractional error in $\Delta \nu_{\text{FSR}}$ can be expressed as

$$\left| \frac{\Delta \nu_{\text{FSR, max error}}}{\Delta \nu_{\text{FSR}}} \right| \approx \frac{\frac{\beta_{m_1}}{\nu} \left| \frac{\partial \theta_{m_1}^{nl}}{\partial \beta_{m_1}} \right|_{\text{max}} + \frac{\beta_{m_2}}{\nu} \left| \frac{\partial \theta_{m_2}^{nl}}{\partial \beta_{m_2}} \right|_{\text{max}}}{2 \frac{\beta}{\nu} + \frac{\beta_{m_1}}{\nu} + \frac{\beta_{m_2}}{\nu}}, \text{ or} \quad \text{Eq. 3.131}$$

$$\left| \frac{\Delta \nu_{\text{FSR, max error}}}{\Delta \nu_{\text{FSR}}} \right| \approx \frac{\beta_{m_1} \left| \frac{\partial \theta_{m_1}^{nl}}{\partial \beta_{m_1}} \right|_{\text{max}} + \beta_{m_2} \left| \frac{\partial \theta_{m_2}^{nl}}{\partial \beta_{m_2}} \right|_{\text{max}}}{2\beta + \beta_{m_1} + \beta_{m_2}}. \quad \text{Eq. 3.132}$$

$\left| \frac{\partial \theta_{m_1}^{nl}}{\partial \beta_{m_1}} \right|_{\text{max}}$ and $\left| \frac{\partial \theta_{m_2}^{nl}}{\partial \beta_{m_2}} \right|_{\text{max}}$ are given by Eq. 3.123 or Eq. 3.126 depending on whether the mirrors are (quarter-

wave) thin-films or FBGs. Eq. 3.132 implies that the errors in the approximation for the FSR (Eq. 3.130) depends on R_f and R_b .

In obtaining the FSR, $\frac{\partial \theta_{\text{film}}^r}{\partial \beta_f}$ and $\frac{\partial \theta_b^r}{\partial \beta_b}$ are useful quantities. Similarly, $\frac{\partial \theta_{\text{film}}^r}{\partial \beta_f}$ and $\frac{\partial \theta_b^r}{\partial \beta_b}$ will be found useful in

calculating the unambiguous measurand range (UMR) of a fibre Fabry-Pérot sensor (Chapter 4).

In summary, this chapter has investigated the transmission and reflection transfer functions of a fibre Fabry-Pérot interferometer for both the exact and two-beam approximation cases. In addition to the phase change due to a round-trip of the cavity, these transfer functions are also dependent on the phase change upon reflection and transmission from the Fabry-Pérot reflectors. In particular, the phase changes due to the proximal mirror can produce asymmetric reflection longitudinal modes (high-finesse case) or modes in which the transmission and reflection are not 180° out of phase (low-finesse case). For most reflectors, these phase changes due to the mirrors depend on the optical frequency of the light source (ν) and consequently contribute to the value of the free spectral range of the interferometer. In the case of single-layer dielectric thin film or fibre Bragg grating reflector, the relation between its transmission or reflection phase change and the optical frequency of the light source, has a linear and nonlinear component. If only the linear component is considered, the FSR is constant and can be calculated by using an effective optical cavity length measured from the centres of the Fabry-Pérot mirrors. If in addition the nonlinear component is taken into account, the FSR depends on ν . The FSR of the sensors developed in this work is an important parameter for the pseudo-heterodyne signal processing scheme used with them.

If low-reflectance ($< 10\%$) dielectric thin films or fibre Bragg gratings are used as Fabry-Pérot reflectors, then the two-beam approximation for the transfer functions can be applied. The phase changes due to the proximal mirror give symmetric modes which are anti-phase with the transmission modes, and the corresponding phase changes upon transmission through and reflection from the mirrors essentially depend linearly with ν . These characteristics were expected from the output of the individual interferometers of low-finesse birefringent fibre Fabry-Pérot sensors developed in this work.

Chapter 4:

Thermal and Strain Sensitivities of Single-Mode Silica Fibre Fabry-Pérot Interferometric Sensors

This chapter primarily describes the expected phase-temperature and phase-strain sensitivities of a single-mode silica fibre Fabry-Pérot interferometric sensor (FFPS). The first part of the chapter focuses on the phase-measurand sensitivities of a non-polarisation-maintaining (NPM) FFPS. In particular, the phase-strain sensitivity of an NPM FFPS is extremely useful in describing the birefringence and the phase-measurand sensitivities of a polarisation-maintaining (birefringent) fibre having an internal stress-inducing elliptical cladding similar to that used in this work. This chapter also explores the effects of temperature and strain variations on the amplitude and phase response of dielectric thin film and in-fibre Bragg gratings. In addition, the chapter discusses the unambiguous measurand range (UMR) of an FFPS with either an in-fibre thin-film or Bragg-grating Fabry-Pérot reflectors.

4.1 Thermal and Strain Sensitivities of Non-Polarisation-Maintaining Single-Mode Silica Optical Fibre Fabry-Pérot Interferometric Sensors

Butter and Hocker [1978] were the first to describe a fibre optic strain gauge which exploited the strain-optic effect in silica optical fibres. Subsequently Hocker [1979] suggested the use of fibre optic sensors for the measurement of temperature or pressure. In his work, Hocker used a simple fibre Mach-Zehnder interferometer composed of two

fibres with their distal ends placed side by side. The emerging beams were made to interfere in the far field. One of the arms was exposed to temperature or pressure variations which modulated the intensity of the far-field interference. Following this pioneering work, many have produced fibre temperature or strain sensors using these basic principles [*e.g.* Giallorenzi *et al.*, 1982; Tseng & Chen, 1988; Measures, 1992].

The expressions for the phase-temperature and the phase-strain sensitivity of an optical fibre obtained by Hocker apply to a fibre Fabry-Pérot interferometer (FFPI). In the case of an FFPI, the corresponding sensitivities are twice that of a fibre Mach-Zehnder interferometer for the same sensing length. The round-trip optical phase change contributed only by the Fabry-Pérot cavity of an FFPI is

$$\varphi = 2\beta = 2\pi \frac{2n\ell}{\lambda} = 2\pi \frac{2n\ell}{c} \nu, \quad \text{Eq. 4.1}$$

where n and ℓ are the effective refractive index and the physical length of the fibre-optic cavity. Furthermore, λ , ν and c are the wavelength, the optical frequency and the speed of light in vacuum respectively. β is the (single-pass) phase shift associated with the optical length of the Fabry-Pérot cavity (Eq 3.10). (To simplify the notation, the symbol for the refractive index of the core of the fibre used in this chapter is simply n instead of n_c used in Chapter 3). Shifts in φ can be expressed as

$$\Delta\varphi = 2\pi \left\{ \frac{\Delta\nu}{\Delta\nu_{FSR}} + \frac{\Delta(n\ell)}{\lambda/2} \right\} \quad \text{Eq. 4.2}$$

Eq. 4.2 implies that a complete fringe shift occurs whenever the optical frequency changes by an amount equivalent to the FSR or when the cavity optical length ($n\ell$) varies by half the wavelength of the light source. In general, the FSR depends on three factors: the optical frequency of the light source, the cavity optical length and the phase change due to the Fabry-Pérot mirrors (section 3.3). The relations involving the FSR in Eq. 4.2 can be useful in the discussions on signal processing (Chapter 6). Variations resulting from strain or temperature change are examined further in the following sections.

4.1.1 Stress and Strain Formalisms

The force per unit area or stress $\bar{\sigma}$ and the fractional change in the dimensions of a material, (total) strain $\bar{\varepsilon}$, can be described as second-rank tensors [Timoshenko & Goodier, 1970]. Ascribing a cartesian coordinate system to an optical fibre where the z-axis refers to the longitudinal axis of the fibre, the stress and strain can be described as follows:

$$\bar{\sigma} = [\sigma_{ij}] = \begin{bmatrix} \sigma_{xx} & \sigma_{xy} & \sigma_{xz} \\ \sigma_{yx} & \sigma_{yy} & \sigma_{yz} \\ \sigma_{zx} & \sigma_{zy} & \sigma_{zz} \end{bmatrix}, \quad \text{Eq. 4.3}$$

$$\bar{\varepsilon} = [\varepsilon_{ij}] = \begin{bmatrix} \varepsilon_{xx} & \varepsilon_{xy} & \varepsilon_{xz} \\ \varepsilon_{yx} & \varepsilon_{yy} & \varepsilon_{yz} \\ \varepsilon_{zx} & \varepsilon_{zy} & \varepsilon_{zz} \end{bmatrix}, \quad \text{Eq. 4.4}$$

where the indices are the coordinate values. The diagonal and off-diagonal elements of $\bar{\sigma}$ are the normal and shear stresses respectively. In addition, the diagonal and off-diagonal elements of $\bar{\varepsilon}$ are the longitudinal and shear strains respectively. Since these second-rank tensors are symmetric, Voigt's contracted notation can be employed to simplify the tensor operations to vector algebra as shown in Table 4.1 [Weber, 1986].

Old notation	ij	zz	xx	yy	xy,yx	yz,zy	zx,xz
Voigt's notation	m	1	2	3	4	5	6
Alternative Voigt's notation	m	z	x	y	xy	yz	zx

Table 4.1: Voigt's contracted index notations for symmetric tensor indices.

Using Voigt's notation, the stress and strain "vectors" are related as follows

$$\sigma_i = c_{ij} \varepsilon_j, \text{ and} \quad \text{Eq. 4.5}$$

$$\varepsilon_i = s_{ij} \sigma_j, \quad \text{Eq. 4.6}$$

where $\bar{c} = [c_{ij}]$ is the elastic compliance tensor and $\bar{s} = [s_{ij}]$ is the elastic stiffness tensor. The repeated indices imply a summation over all their possible values (Einstein convention).

The elements of the stiffness and compliance matrices are determined from Hooke's law. Since silica optical fibres can be considered as isotropic material, $\bar{s} = [s_{ij}]$ and $\bar{c} = [c_{ij}]$ are [Weber, 1986]

$$\bar{s} = \frac{1}{Y} \begin{bmatrix} 1 & -\mu & -\mu & 0 & 0 & 0 \\ -\mu & 1 & -\mu & 0 & 0 & 0 \\ -\mu & -\mu & 1 & 0 & 0 & 0 \\ 0 & 0 & 0 & 2(1+\mu) & 0 & 0 \\ 0 & 0 & 0 & 0 & 2(1+\mu) & 0 \\ 0 & 0 & 0 & 0 & 0 & 2(1+\mu) \end{bmatrix}, \text{ and} \quad \text{Eq. 4.7}$$

$$\bar{c} = \frac{Y}{(1+\mu)(1-2\mu)} \begin{bmatrix} 1-\mu & \mu & \mu & 0 & 0 & 0 \\ \mu & 1-\mu & \mu & 0 & 0 & 0 \\ \mu & \mu & 1-\mu & 0 & 0 & 0 \\ 0 & 0 & 0 & \frac{1-2\mu}{2} & 0 & 0 \\ 0 & 0 & 0 & 0 & \frac{1-2\mu}{2} & 0 \\ 0 & 0 & 0 & 0 & 0 & \frac{1-2\mu}{2} \end{bmatrix}, \quad \text{Eq. 4.8}$$

where Y is the Young modulus and μ is the Poisson's ratio of the fibre.

4.1.2 Phase-Strain Sensitivity

Consider an optical fibre experiencing an externally applied tensile stress along its axis, then

$$\sigma_z = \varepsilon Y, \quad \text{Eq. 4.9}$$

where ε is the axial (or longitudinal) strain. Using Eq. 4.9, the total strain on the fibre due to the axial strain ε is

$$\bar{\varepsilon} = \begin{bmatrix} \varepsilon & -\mu\varepsilon & -\mu\varepsilon & 0 & 0 & 0 \end{bmatrix}^t, \quad \text{Eq. 4.10}$$

where the notation $[]^t$ represents the transpose matrix of $[]$. Eq. 4.10 describes changes in lateral strain which is opposite in sign to that of the axial strain (Poisson's effect). Furthermore consider an axial strain ε affecting a segment L_ε of the cavity, i.e. $L_\varepsilon \leq \ell$. The phase change $\Delta\varphi$ due to ε is given by [Butter & Hocker, 1978]

$$\Delta\varphi = \frac{4\pi n L_\varepsilon}{\lambda} \left\{ \varepsilon + \frac{1}{n} \frac{\partial n}{\partial V_{fb}} \frac{\partial V_{fb}}{\partial r_{co}} \Delta r_{co} + \frac{1}{n} (\Delta n)_\varepsilon \right\}, \quad \text{Eq. 4.11}$$

where V_{fb} (Eq. 4.21) is the normalised frequency of the fibre with radius r_{co} and $(\Delta n)_\varepsilon$ is the elasto-optic change in the effective refractive index of the mode. In Eq. 4.11, $\Delta(n\ell) = \Delta(nL_\varepsilon)$ and the assumption $\Delta\nu = 0$ were used.

The first term in Eq. 4.11 is due to the physical effect of strain on the gauge length L_ε . The second term allows for the contribution to the total refractive index change by variations in the waveguide properties of the fibre caused by changes in the radius of the core Δr_{co} . This change in the radius is due to the Poisson's effect,

$$\Delta r_{co} = -\mu \varepsilon r_{co}. \quad \text{Eq. 4.12}$$

Subsequently Eq. 4.11 can be written as

$$\Delta \varphi = \frac{4\pi n L_\varepsilon}{\lambda} \left\{ \varepsilon (1 - \mu \chi_{co}) + \frac{1}{n} (\Delta n)_\varepsilon \right\}, \quad \text{Eq. 4.13}$$

$$\text{where } \chi_{co} = \frac{r_{co}}{n} \frac{\partial n}{\partial V_{fib}} \frac{\partial V_{fib}}{\partial r_{co}} \quad \text{Eq. 4.14}$$

describes the waveguide effect due to Δr_{co} .

Since for weakly-guiding single-mode fibres, the core and the cladding are made from very similar materials, it can be assumed that the elasto-optic variations in the refractive indices of the core (n_{co}) and cladding (n_{cl}) are essentially the same. Subsequently, the elasto-optic variations in the effective refractive index of the propagated mode (n) follow those of n_{co} and n_{cl} . $(\Delta n)_\varepsilon$ can be derived from

$$\begin{aligned} \bar{B} = [B_i] &= \Delta \left[\left(\frac{1}{n^2} \right)_i \right] = \Delta \left[\left(\frac{1}{n_{co}^2} \right)_i \right] \\ \bar{B} &= \left[\Delta \left(\frac{1}{n^2} \right)_i \right] = \left[\Delta \left(\frac{1}{n_{co}^2} \right)_i \right], \end{aligned} \quad \text{Eq. 4.15}$$

the change in the fibre's optical indicatrix tensor $\left[\left(\frac{1}{n^2} \right)_i \right]$ (which is assumed to be the same as that of the core,

i.e. $\left[\left(\frac{1}{n^2} \right)_i \right] = \left[\left(\frac{1}{n_{co}^2} \right)_i \right]$) [Butter & Hocker, 1978; Weber, 1986; Bertholds & Dändliker, 1987]. \bar{B} is related to

strain by

$$B_i = \rho_{ij} \varepsilon_j, \quad \text{Eq. 4.16}$$

where $\bar{\rho} = [\rho_{ij}]$ is the fourth-rank elasto-optic tensor. For an isotropic medium like fused silica fibre,

$$\bar{\bar{p}} = \begin{bmatrix} p_{11} & p_{12} & p_{12} & 0 & 0 & 0 \\ p_{12} & p_{11} & p_{12} & 0 & 0 & 0 \\ p_{12} & p_{12} & p_{11} & 0 & 0 & 0 \\ 0 & 0 & 0 & p_{44} & 0 & 0 \\ 0 & 0 & 0 & 0 & p_{44} & 0 \\ 0 & 0 & 0 & 0 & 0 & p_{44} \end{bmatrix}, \quad \text{Eq. 4.17}$$

where $p_{44} = \frac{p_{11} - p_{12}}{2}$. The Pockels strain-optic coefficients p_{11} and p_{12} completely describe the strain-optic

effect for an isotropic fibre. Using Eq. 4.17,

$$B_x = B_y = \varepsilon(p_{12} - \mu(p_{11} + p_{12})). \quad \text{Eq. 4.18}$$

From Eq. 4.15, the refractive index change $(\Delta n)_\varepsilon$ perpendicular to the axial strain is

$$(\Delta n)_\varepsilon = -\frac{n^3}{2} \Delta\left(\frac{1}{n^2}\right) = -\frac{n^3}{2} B_x. \quad \text{Eq. 4.19}$$

The factor χ_{co} is determined from the normalised propagation constant b_{fib} and frequency V_{fib} [Jeunhomme, 1990]:

$$b_{fib} = \frac{n^2 - n_{co}^2}{n_{co}^2 - n_{cl}^2}, \quad \text{and} \quad \text{Eq. 4.20}$$

$$V_{fib} = k_o r_{co} \sqrt{n_{co}^2 - n_{cl}^2}, \quad \text{Eq. 4.21}$$

$$\text{where } k_o = \frac{2\pi}{\lambda}. \quad \text{Eq. 4.22}$$

The factor χ_{co} can be easily evaluated as follows:

$$\chi_{co} = \frac{r_{co}}{n} \frac{\partial n}{\partial V_{fib}} \frac{\partial V_{fib}}{\partial r_{co}} = \frac{r_{co}}{n} \frac{\partial n}{\partial b_{fib}} \frac{\partial b_{fib}}{\partial V_{fib}} \frac{\partial V_{fib}}{\partial r_{co}}, \quad \text{or} \quad \text{Eq. 4.23}$$

$$\chi_{co} = \frac{V_{fib}^3}{2n^2 k_o^2 r_{co}^2} \frac{\partial b_{fib}}{\partial V_{fib}} = \frac{V_{fib}^3 (n_{co}^2 - n_{cl}^2)}{2n^2} \frac{\partial b_{fib}}{\partial V_{fib}}. \quad \text{Eq. 4.24}$$

For a weakly-guiding single-mode fibre, *i.e.*

$$\delta n = \frac{n_{co} - n_{cl}}{n} \cong 10^{-2}, \quad \text{and} \quad \text{Eq. 4.25}$$

$$n \cong n_{co} \cong n_{cl}. \quad \text{Eq. 4.26}$$

Eq. 4.24 becomes

$$\chi_{co} \approx V_{fib} (\delta n)^2 \frac{\partial b_{fib}}{\partial V_{fib}}. \quad \text{Eq. 4.27}$$

At around the single-mode cut-off of a single-mode fibre,

$$V_{fib} \approx 2.405, \text{ and} \quad \text{Eq. 4.28}$$

$$\frac{\partial b_{fib}}{\partial V_{fib}} \approx 0.5 \quad [\text{Snyder \& Love, 1983}]. \quad \text{Eq. 4.29}$$

$$\text{Thus } \chi_{co} \approx 10^{-4} \ll 1. \quad \text{Eq. 4.30}$$

Clearly Eq. 4.30 means that the waveguide effect due to a change in the radius of the fibre can be omitted in Eq.

4.13. Using this approximation together with Eq. 4.18 and Eq. 4.19, Eq. 4.13 becomes

$$\frac{\Delta \varphi}{\varepsilon} \cong \frac{4\pi n L_\varepsilon}{\lambda} \left\{ 1 - \frac{n^2}{2} (p_{12} - \mu(p_{11} + p_{12})) \right\}. \quad \text{Eq. 4.31}$$

Eq. 4.31 implies that the phase-strain sensitivity increases with the sensing length L_ε and that its maximum value can be obtained when the whole cavity is exposed to strain; *i.e.* $L_\varepsilon = \ell$. Alternatively, Eq. 4.31 implies that the effective Fabry-Pérot cavity length during axial strain measurements is simply the gauge length L_ε .

A strain sensitivity expression independent of the sensing length can be obtained by normalising Eq. 4.31 with respect to the phase change due to a round-trip of the gauge length L_ε ,

$$\varphi_\varepsilon \equiv 2\pi \left[\frac{2nL_\varepsilon}{\lambda} \right]. \quad \text{Eq. 4.32}$$

The fractional strain sensitivity ϖ_ε is given by

$$\frac{\Delta \varphi_\varepsilon}{\varphi_\varepsilon \varepsilon} = \varpi_\varepsilon \cong 1 - \frac{n^2}{2} (p_{12} - \mu(p_{11} + p_{12})). \quad \text{Eq. 4.33}$$

Eq. 4.33 can be called the optical gauge factor for an FFPI [Fürstenau *et al.*, 1992] similar to the definition for the gauge factor of resistive strain gauges [Window, 1992]. The unity value in Eq. 4.33 refers to the physical effect of strain whilst the other term describes the strain-optic effect. In general, ϖ_ε depends on λ primarily because n can depend on λ as well.

Symbol	Description	Value	Comments	Reference
α	Linear thermal expansion coefficient of silica fibre	$+5.5 \times 10^{-7} / ^\circ\text{C}$	Silica	Lagakos <i>et al.</i> [1981]
n	Effective core refractive index	1.458 1.462 (group)	Ge-doped @633 nm @785 nm	Lagakos <i>et al.</i> [1981] Experimental results
$\frac{dn}{dT}$	Thermo-optic coefficient	$+10.93 \times 10^{-6} / ^\circ\text{C}$	@1 μm , Bulk silica	Barlow & Payne [1983]
μ	Poisson's ratio	0.16	optical fibre	Bertholds & Dändliker [1988]
γ	Young's modulus	64.1 GPa	optical fibre	Bertholds & Dändliker [1987]
p_{11}	Pockels strain-optic coefficients	+0.113	@633 nm, fibre	Bertholds & Dändliker [1988]
p_{12}		+0.252	@633 nm, fibre	Bertholds & Dändliker [1988]

Table 4.2: Some relevant thermal and strain constants for silica fibres at wavelengths close to 780 nm.

Table 4.2 summarises the relevant thermal and strain related constants for silica optical fibres at wavelengths near 780 nm. Using the values in the table, the strain-optic contribution has a net opposite effect compared with the physical effect of strain. This condition gives an optical gauge factor less than unity (for λ close to 780 nm):

$$\frac{\Delta\varphi_\varepsilon}{\varphi_\varepsilon \varepsilon} = \varpi_\varepsilon \approx 0.80. \quad \text{Eq. 4.34}$$

4.1.3 Phase-Temperature Sensitivity

If a segment L_T of the cavity is exposed to a temperature change ΔT and if the cavity can freely expand, the resulting phase change can be calculated in a manner similar to the case of strain measurements. Differentiating

Eq. 4.1 with respect to temperature T ,

$$\frac{d\varphi}{dT} = \frac{4\pi}{\lambda} \left\{ \frac{\partial(nL_T)}{\partial n} \frac{dn}{dT} + \frac{\partial(nL_T)}{\partial L_T} \frac{dL_T}{dT} \right\}. \quad \text{Eq. 4.35}$$

Again $d(n\ell) = d(nL_T)$ are used. Subsequently,

$$\frac{\Delta\varphi}{\Delta T} \equiv \frac{4\pi n L_T}{\lambda} \left\{ \frac{1}{n} \frac{\partial n}{\partial T} + \frac{(\Delta n)_{\varepsilon T}}{n \Delta T} + \frac{1}{n} \frac{\partial n}{\partial V} \frac{\partial V}{\partial r_{co}} \frac{dr_{co}}{dT} + \frac{1}{L_T} \frac{dL_T}{dT} \right\}. \quad \text{Eq. 4.36}$$

The first three terms in Eq. 4.36 involve changes in n whilst the fourth changes in ℓ . The first term is the fractional change in n per unit temperature change and is a result of any direct dependence of n with temperature T . The second term involves $(\Delta n)_{\bar{\epsilon}^T}$ which is the change in n produced by thermal strain $\bar{\epsilon}^T$ (see Eq. 4.39 below). The third term describes the change in the waveguide properties of the fibre due to thermal expansion. Finally, the fourth term is the linear thermal expansion coefficient α of the fibre.

Since the radius of the core expands thermally at the same rate as the sensing length, *i.e.*

$$\alpha = \frac{1}{r_{co}} \frac{dr_{co}}{dT} = \frac{1}{L_T} \frac{dL_T}{dT}, \quad \text{Eq. 4.37}$$

by using Eq. 4.23 and Eq. 4.37, Eq. 4.36 can be written as

$$\frac{\Delta\varphi}{\Delta T} = \frac{4\pi n L_T}{\lambda} \left\{ \frac{1}{n} \frac{\partial n}{\partial T} + \frac{(\Delta n)_{\bar{\epsilon}^T}}{n \Delta T} + \alpha(1 + \chi_{co}) \right\}. \quad \text{Eq. 4.38}$$

As in the case of strain measurements, χ_{co} can also be omitted in Eq. 4.38 for weakly-guiding fibres.

The thermal expansion of the fibre can be described by the following strain state, *i.e.* thermal strain:

$$\bar{\epsilon}^T = \begin{bmatrix} \alpha \Delta T & \alpha \Delta T & \alpha \Delta T & 0 & 0 & 0 \end{bmatrix}^T, \quad \text{Eq. 4.39}$$

Thus a refractive index change

$$(\Delta n)_{\bar{\epsilon}^T} = -\frac{n^3}{2} \alpha (p_{11} + 2p_{12}) \Delta T \quad \text{Eq. 4.40}$$

is produced via the elasto-optic effect. Thus, Eq. 4.36 can now be written (without any waveguide term) as

$$\frac{\Delta\varphi}{\Delta T} \cong \frac{4\pi n L_T}{\lambda} \left\{ \frac{1}{n} \frac{dn}{dT} + \alpha \right\}, \quad \text{Eq. 4.41}$$

where
$$\frac{dn}{dT} = \frac{\partial n}{\partial T} - \frac{n^3}{2} \alpha (p_{11} + 2p_{12}) \quad \text{Eq. 4.42}$$

is interpreted as the total rate of change of the refractive index with temperature. Eq. 4.41 is the phase-temperature sensitivity as derived by Butter & Hocker [1979] and Hughes & Priest [1979]. This equation is a more practical expression because $\frac{dn}{dT}$ (Eq. 4.42) can readily be measured unlike the expression $\frac{\partial n}{\partial T}$.

Defining an effective round-trip optical phase shift similar to Eq. 4.32, Eq. 4.41 can be normalised as

$$\frac{\Delta\varphi_T}{\varphi_T \Delta T} = \varpi_T \cong \frac{1}{n} \frac{dn}{dT} + \alpha. \quad \text{Eq. 4.43}$$

Clearly ϖ_T is the sum of all the significant terms inside the curly brackets in Eq. 4.36. ϖ_T describes the temperature sensitivity of the fractional optical length of an optical fibre independent of the sensing length. As in the case of strain measurements, ϖ_T depends on λ because n can depend on λ as well. Using the values in Table 4.2, the more dominant term in Eq. 4.43 is $\frac{1}{n} \frac{dn}{dT}$ which is about an order of magnitude larger than α . The expected value for ϖ_T for wavelengths near 780 nm is

$$\frac{\Delta\varphi_T}{\varphi_T \Delta T} = \varpi_T \approx 8.04 \times 10^{-6} / ^\circ C. \quad \text{Eq. 4.44}$$

4.1.4 Unified Phase-Strain-Temperature Description

The analyses above have assumed that the change in the refractive index n is attributed only to strain transversely symmetric and uniformly distributed along the sensing length. However in many cases this symmetric and uniform distribution can be broken when a fibre is surface-bonded on or embedded in a structure.

Sirkis & Haslach [1990] described a unified phase-strain-temperature model for optical fibres in any physical environment. This model focuses on the actual strain and temperature experience by the core which can be affected by the strain and temperature state of the immediate environment of the fibre. In general, the total phase of the fibre is described as an integral over the sensing length [Sirkis, 1991,1993]:

$$\varphi_j = 2 \int_{\Gamma} \beta(\varepsilon_j, \Delta T) (1 + \varepsilon_z) d\Gamma, \quad j = x, y, \quad \text{Eq. 4.45}$$

where $\beta(\varepsilon_j, \Delta T) = \frac{2\pi}{\lambda} n(\varepsilon_j, \Delta T)$ Eq. 4.46

is the effective propagation constant of an electro-magnetic wave polarised along the j -axis (either x -axis or y -axis) when a (sensing) length Γ of the fibre is exposed to a temperature change ΔT and total strain $\bar{\varepsilon}$ (with ε_z as the axial strain along the fibre's axis). Compared with the equations of Sirkis & Haslach, Eq. 4.45 involves the additional factor of 2 which accounts for a round trip across a Fabry-Pérot cavity. The integral approach in

Eq. 4.45 is the proper description for the change in the optical length of the because temperature or strain can vary along the sensing region.

Following a Taylor's series expansion about some initial strain-temperature state (*e.g.* $\bar{\varepsilon} = \bar{0}$ and $\Delta T = 0$) and keeping only the first-order terms in $\bar{\varepsilon}$ and ΔT , the phase change is given by

$$\Delta\varphi_j = 2\beta(0,0) \int_{\Gamma} \left(\varepsilon_z - \frac{n^2}{2} (p_{jk} \varepsilon_k) + \frac{\partial n}{\partial T} \frac{\Delta T}{n} \right) d\Gamma, \quad j = x, y, \quad \text{Eq. 4.47}$$

where $\beta(0,0) = \frac{2\pi n}{\lambda}$. Eq. 4.48

In Eq. 4.47, no distinction is made between mechanical and thermal strains. Hence the strain $\bar{\varepsilon}$ is the algebraic sum of these two types of strain. In Eq. 4.47 (and also in Eq. 4.49 below), the refractive index n is the average value over the cross-section of the fibre.

Kim *et al.* [1993a] derived an equation similar to Eq. 4.47 but employed experimentally measurable parameters.

Their final equation can be expressed as

$$\Delta\varphi_j = 2\beta(0,0) \int_{\Gamma} \left(\varepsilon_z - \frac{n^2}{2} p_{jk} (\varepsilon_k - \varepsilon_k^T) + \frac{dn}{dT} \frac{\Delta T}{n} \right) d\Gamma, \quad \text{Eq. 4.49}$$

where $\bar{\varepsilon}^T$ is the thermal strain expressed in Eq. 4.39.

Eq. 4.47 and Eq. 4.49 are two models of a unified phase-strain-temperature description of temperature or strain FFPS. Clearly, these models describe the interferometric phase change for any arbitrary strain-temperature state of the core. For embedded sensors, the strain state of the core is determined by the interaction between the fibre and its host environment [Sirkis, 1993a]. However, when the stiffness ratio between the fibre and its host is greater than 10 (*e.g.* surface-bonded sensors), the strain in the core is approximately that in the host material [Matthews & Sirkis, 1990].

The two models average the effect of any asymmetry in the refractive index due to an asymmetric strain distribution. This simplification does not produce significant error with measurements which allow the fibre to

experience unimpeded thermal expansion or symmetric transverse strains (*e.g.* measurement of transverse pressure, axial strain) [Butter & Hocker, 1978; Sirkis & Haslach, 1990; Egalon & Rogowski, 1992]. However, the induced birefringence as a result of asymmetric strain distributions in the core remains to be important especially in the operation of polarisation-maintaining or birefringent FFPS.

4.2 Birefringence In Single-Mode Optical Fibres

To appreciate the performance of birefringent FFPS, it may be useful to describe briefly the birefringence of a single-mode silica fibre. Theoretically, an optical fibre with perfectly circular core and homogeneous core refractive index distribution guides light which can be polarised either along two orthogonal directions, *e.g.* *x*- or *y*-axis. Intrinsically or extrinsically induced imperfections in the fibre which produced inhomogeneity either in the geometry or in the propagation constant can lift the (polarisation) degeneracy of the fundamental mode [Norman *et al.*, 1979]. These effects do not pose any problem when the desired output does not depend on the state of polarisation (SOP) of the resulting beams. On the other hand in interferometric sensors, such effects produce unwanted polarisation-induced signal-fading or dispersion. However if the birefringence of a fibre is enhanced, the light can be propagated in an optical fibre with a relatively constant SOP.

4.2.1 Birefringence Mechanisms

Birefringence mechanisms in an optical fibre can be linear, circular, elliptical or dichronic. Fibres exhibiting linear birefringence can be considered a retarder and hence can guide linearly polarised light throughout the fibre if this beam is launched along one of the principal polarisation axes (polarisation-maintaining fibres). Different methods of producing linear birefringence will be presented shortly.

Circular birefringence refers to the retardation of left- and right-circularly polarised light. The end results of such retardation is a rotation of the polarisation azimuth of the propagating beam. Such birefringence can be produced by twisting the fibre about its longitudinal axis [Smith, 1980] or by immersing the fibre in a strong magnetic field (Faraday effect) [Day & Rose, 1988]. Magneto-optic and also electro-optic properties of fibres have been exploited

to measure current [Ren & Robert, 1989; Yu & Siddiqui, 1994], voltage [Kuroda *et al.*, 1985; Bohnert & Nehring, 1989], magnetic field [Rashleigh, 1981; Suzuki *et al.*, 1988] amongst others. In general fibres which exhibit both linear and circular birefringence can be described as elliptically birefringence fibres.

Dichronism refers to a preferred propagation of a single polarisation mode regardless of the initial state of the input beam. The basic principle of dichronic mechanisms in fibre is to force one of the polarisation modes to exhibit higher propagation loss than the other [Simpson *et al.*, 1983]. Hence such fibres are referred to as single-polarisation fibres or polarising fibres [Kaminow & Ramaswamy, 1979].

4.2.2 Evolution of the State-of-Polarisation

The evolution of the SOP of a light propagated in a single-mode fibre follows a complicated pattern resulting from the interplay of linear and circular birefringence (optical activity) in the fibre [Simon & Ulrich, 1977]. The output SOP may appear to behave randomly since the coupling between polarisation modes may be easily induced by internal and external perturbations in the fibre waveguide [Yariv, 1973; Okamoto *et al.*, 1982; Tsubokawa *et al.*, 1985, 1989; Feng *et al.*, 1990; Shlyagin *et al.*, 1994]. Incidentally, when externally induced birefringence is introduced to the fibre using some feedback arrangement, the output SOP can be stabilised [Ulrich, 1979].

On the other hand with highly birefringent (Hi-Bi) polarisation-maintaining fibres, such feedback arrangement is unnecessary to maintain a linear SOP. Linearly polarised beam can be propagated along one polarisation axis of the fibre for as long as the fibre does not experience any great external perturbation [Katsuyama *et al.*, 1983]. Twists in Hi-Bi fibres need to be minimised as well since twists can produce optical activity coupling light between the polarisation modes [Ulrich & Simon, 1979].

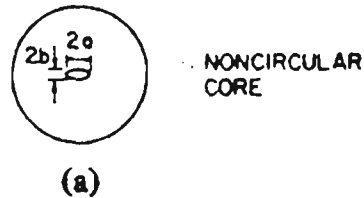
4.2.3 Mechanisms for Producing Linear Birefringence

Figure 4.1 shows the different mechanisms to produce linear birefringence in fibres. Methods of producing linear birefringence fall under two major forms: asymmetry in the cross-sectional geometry or stress in the core of the

fibre. The common configuration of the latter form involves additional inclusions in the cladding, *e.g.* an inner elliptical cladding similar to the fibres used whilst the former is an elliptical-core fibre. The inclusions usually have higher thermal expansion coefficients compared with those of the substrate cladding and the core. Hence thermal compressive stress is produced when the fibre cools during its drawing from the fibre preform [Rashleigh, 1983].

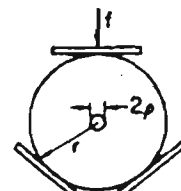
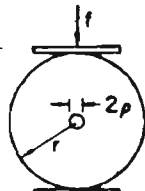
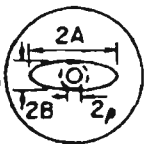
Other methods of stress-induced birefringence are by an application of transverse pressure or by bending [Ulrich *et al.*, 1980]. In general, the birefringence is directly proportional to the difference in the asymmetric stress with the fast-axis aligned along the direction of maximal compressive stress.

I GEOMETRICAL



II MATERIAL

ASYMMETRICAL LATERAL STRESS



BENDING

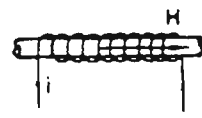
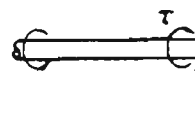
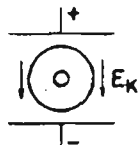
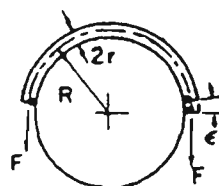
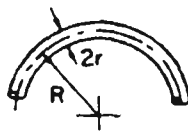


Figure 4.1: Basic birefringence mechanisms in a single-mode fibre due to internal deformation or external action [Rashleigh, 1983].

4.2.4 Characterisation of Linear Birefringence

The (linear) birefringence B of a fibre refers to the difference in the refractive indices of the fast-and slow-axis.

Setting the y -axis as the fast-axis,

$$B = n_x - n_y, \quad \text{Eq. 4.50}$$

where n_x and n_y are the slow- and fast-axis refractive indices respectively. B can be expressed as

$$B = B_G + B_{S_0} + B_S, \quad \text{Eq. 4.51}$$

where B_G is the birefringence due to geometry (*i.e.* asymmetry in the core), B_{S_0} is the self-induced birefringence due to the difference in the thermal expansion of an asymmetric core and its surrounding cladding and B_S is the stress-induced birefringence due to the stress-applying components in the cladding [Noda *et al.*, 1986]. In the case of an elliptical-core fibre, $B_S = 0$ whilst B_G and B_{S_0} are non-zero. B_G and B_{S_0} increase with the ellipticity of the core and the difference between the refractive indices and thermal expansion coefficients of the core and cladding [Sakai & Kimura, 1981]. In the case of a stress-induced birefringent fibre with a circular core, $B_G \approx 0$.

Linearly birefringent fibres are characterised by their polarisation-holding parameter h , beat length L_B and birefringence (polarisation) coherence length L_c [Kaminow, 1981]. h refers to the (intensity) cross-talk between the polarisation modes per unit coupling length z and is related to the extinction ratio $\langle \eta \rangle$ between them, *i.e.*

$$\langle \eta \rangle = \frac{\langle I_y \rangle}{\langle I_x \rangle} = hz, \quad \text{Eq. 4.52}$$

where $\langle I_y \rangle$ and $\langle I_x \rangle$ are the average irradiance along each axis. L_B is the distance between two locations along the fibre whereby the incident beam has the same SOP and is related to the birefringence B as follows

$$L_B = \frac{\lambda}{B} = \frac{\lambda}{n_x - n_y}. \quad \text{Eq. 4.53}$$

whilst L_c refers to the distance within which the incident light remains polarised and depends on the optical bandwidth $\Delta\lambda$ of the light source. The relative phase between the polarised beams is given by

$$\vartheta = \frac{2\pi B}{\lambda} z. \quad \text{Eq. 4.54}$$

Thus for the orthogonal beams to interfere coherently when they are coupled, *e.g.* with an analyser, the corresponding time delay between the modes in Eq. 4.54 must be less than the coherence time τ_c of the light source. Hence the birefringence coherence length is

$$L_c = \frac{\tau_c c}{B} \approx \frac{\lambda^2}{B\Delta\lambda}. \quad \text{Eq. 4.55}$$

4.3 Thermal and Strain Sensitivities of Elliptically-cladded Birefringent Optical Fibres

Figure 4.2 illustrates a polarisation-maintaining fibre which has an internal elliptical cladding (IEC-fibre) similar to those used in this work. The stress distribution inside the core region needs to be established in order to determine the refractive index and the phase-measurand sensitivities along each polarisation axis of an IEC-fibre. It can be assumed that the components of an IEC-fibre exhibit similar elasto-optic properties but different thermal expansion coefficients (α , α_e and α_s for the core, inner elliptical and outer cladding respectively). The thermal expansion coefficients can be chosen by selecting the doping concentration of these components [Ramaswamy *et al.*, 1979].

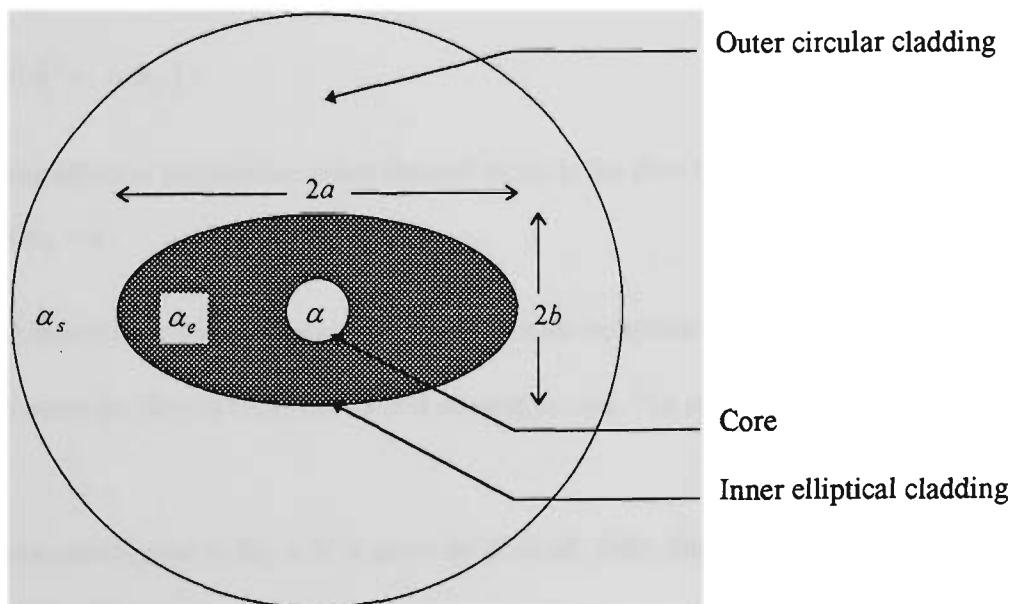


Figure 4.2: Cross-section of an elliptically-cladded birefringent fibre.

4.3.1 Stress Distribution In an Elliptically Cladded Birefringent Fibre

Assuming that an IEC-fibre is an infinitely long cylinder, then the thermally induced stress in the core is reduced to a plane-strain problem [Timoshenko & Goodier, 1970]. The plain strain problem implies that

$$\varepsilon_z = \varepsilon_{yz} = \varepsilon_{xz} = 0 \quad \text{Eq. 4.56}$$

and hence the resulting stress and strain are only a function of the transverse plane coordinates.

The aggregate stress distribution inside the core is given by the sum of two contributions [Tsai *et al.*, 1991]; *i.e.*

$$\bar{\sigma} = {}^1\bar{\sigma} + {}^2\bar{\sigma}. \quad \text{Eq. 4.57}$$

The first contribution in Eq. 4.57 arises from the thermal stress between the core and the inner cladding whilst the second contribution is from the thermal stress between the outer circular and the inner elliptical cladding. In the subsequent discussions, for each contribution the inner cladding/outer cladding is assumed to radially extend to infinity as far as the core/inner cladding is concerned. These assumptions result in a uniform stress distribution along each axis (x -axis and y -axis as the case maybe).

Using Eq. 4.5, Eq. 4.8 and Eq. 4.39, the first stress contribution is given by

$${}^1\sigma_x = {}^1\sigma_y = \frac{Y\delta\alpha_1(T - T_s)}{1 - 2\mu}, \text{ and} \quad \text{Eq. 4.58}$$

$${}^1\sigma_z = \mu({}^1\sigma_x + {}^1\sigma_y), \quad \text{Eq. 4.59}$$

where T_s is some effective temperature when thermal stress in the fibre has began to build up and

$$\delta\alpha_1 = \alpha_e - \alpha. \quad \text{Eq. 4.60}$$

T_s is difficult to determine experimentally because of the wide transition from the viscous state to the fused state of an optical fibre when the fibre is being drawn and allowed to cool. The other stress elements in ${}^1\bar{\sigma}$ are zero.

The second stress contribution in Eq. 4.57 is given by [Eickoff, 1982; Stolen, 1983]

$${}^2\sigma_x = \frac{Y\delta\alpha_2(T - T_s)}{1 - \mu} \left(\frac{a}{a+b} \right), \quad \text{Eq. 4.61}$$

$${}^2\sigma_y = \frac{Y\delta\alpha_2(T - T_s)}{1 - \mu} \left(\frac{b}{a+b} \right), \text{ and} \quad \text{Eq. 4.62}$$

$${}^2\sigma_z = \mu({}^2\sigma_x + {}^2\sigma_y). \quad \text{Eq. 4.63}$$

a and b are the semi-major and semi-minor axis of the inner cladding and

$$\delta\alpha_2 = \alpha_s - \alpha_e. \quad \text{Eq. 4.64}$$

The other stress elements in ${}^1\bar{\sigma}$ are zero.

The parameters $\delta\alpha_1$ and $\delta\alpha_2$ depend on α , α_e and α_s (Figure 4.2). These coefficients can be estimated from the weighted average of the linear expansion coefficients of its composing materials [Kaminow & Ramaswamy, 1979]. Assuming that d_g is the molar concentration of each doping material g , the resulting expansion coefficient can approximately be given by

$$\alpha_x = \sum d_g \alpha_g + \left(1 - \sum d_g\right) \alpha_{SiO_2}, \quad \text{Eq. 4.65}$$

where fused silica is the host material. Table 4.3 shows the expansion coefficients of typical dopants.

Symbol	Description	Values	Comments	Reference
α α_{SiO_2}	Linear thermal expansion coefficient of silica fibre	$+5.5 \times 10^{-7} / ^\circ\text{C}$	Silica	Lagakos <i>et al.</i> [1981]
$\alpha_{B_2O_3}$	of boron oxide	$+10 \times 10^{-6} / ^\circ\text{C}$		Rashleigh & Marrone [1983]
α_{GeO_2}	of germanium dioxide	$+4.5 \times 10^{-6} / ^\circ\text{C}$		Ballard & Browder [1986]
$\alpha_{P_2O_5}$	of phosphate	$+14 \times 10^{-6} / ^\circ\text{C}$		Rashleigh & Marrone [1983]
$T - T_s$	T_s is on-set temperature of thermal stress	800°C	About room temperature	Rashleigh & Marrone [1983]
C_ϵ	Strain-optic coefficient	0.2733	@850 nm	Rashleigh [1983]
C_σ	Stress-optic Coefficient	$-3.367 \times 10^{-3} / \text{GPa}$	@633 nm, silica	Barlow & Payne [1983]

Table 4.3: Relevant thermal and strain constants for birefringent silica optical fibres at λ near 780 nm.

Combining all the stress contributions identified above in Eq. 4.57, the expected stress components in the core are

$$\sigma_x = Y(T - T_s)D_1, \quad \text{Eq. 4.66}$$

$$\sigma_y = Y(T - T_s)D_2, \text{ and} \quad \text{Eq. 4.67}$$

$$\sigma_z = \mu(\sigma_x + \sigma_y), \quad \text{Eq. 4.68}$$

where $D_1 = \frac{\delta\alpha_1}{1-2\mu} + \frac{\delta\alpha_2}{1-\mu} \left(\frac{a}{a+b} \right)$, and Eq. 4.69

$$D_2 = \frac{\delta\alpha_1}{1-2\mu} + \frac{\delta\alpha_2}{1-\mu} \left(\frac{b}{a+b} \right). \quad \text{Eq. 4.70}$$

Unfortunately, the characteristics of the different components of the IEC-fibre used in this research, 3M FS-HB-4211, were not available. To appreciate D_1 and D_2 , the following assumptions were used:

$$\frac{a}{b} = 3 \quad [\text{for an ellipticity constant of } 0.5 \text{ (c.f. Eq. 4.94)}], \quad \text{Eq. 4.71}$$

$$\delta\alpha_1 \approx 1 \times 10^{-6} / ^\circ C \quad [\text{an order of magnitude estimate only}] \quad \text{and} \quad \text{Eq. 4.72}$$

$$\delta\alpha_2 \approx -2.5 \times 10^{-6} / ^\circ C \quad [\text{Rashleigh \& Marrone, 1983}]. \quad \text{Eq. 4.73}$$

Using these values and the values found in Table 4.2 and Table 4.3,

$$D_1 \approx -0.8 \times 10^{-6} / ^\circ C, \quad \text{and} \quad \text{Eq. 4.74}$$

$$D_2 \approx +0.7 \times 10^{-6} / ^\circ C. \quad \text{Eq. 4.75}$$

4.3.2 Photo-elastic Effect Constants

The photo-elastic effect in an optical fibre is important in determining the refractive index along each polarisation axis of an IEC-fibre. From Eq. 4.6, Eq. 4.7 and Eq. 4.17, the photo-elastic refractive index changes are given by

$$\delta n_i = -\frac{n^3}{2} p_{ij} s_{jk} \sigma_k, \quad \text{Eq. 4.76}$$

where n refers to the refractive index of mode guided in the un-stressed core, Eq. 4.76 can be written as

$$\delta n_i = C_{ik} \sigma_k, \quad \text{Eq. 4.77}$$

where $C_{ik} = -\frac{n^3}{2} p_{ij} s_{jk}$. Eq. 4.78

Eq. 4.77 describes the photo-elastic effect, *i.e.* the stress description of the strain-optic effect.

For an isotropic medium, two constants are sufficient to completely describe the photo-elastic effect [Borrelli and Miller, 1968]:

$$C_1 = -\frac{n^3}{2Y}(p_{11} - 2\mu p_{12}) = C_{ik} : \forall i = k = 1,2,3, \text{ and} \quad \text{Eq. 4.79}$$

$$C_2 = -\frac{n^3}{2Y}(p_{12} - \mu(p_{11} + p_{12})) = C_{ik} : \forall i \neq k = 1,2,3. \quad \text{Eq. 4.80}$$

These constants are known as the photo-elastic stress constants and their difference is called the stress-optic (opto-elastic) constant:

$$C_\sigma = C_1 - C_2 = -\frac{n^3}{2Y}(1 + \mu)(p_{11} - p_{12}). \quad \text{Eq. 4.81}$$

This constant describes the birefringence as well as the optical activity since

$$C_\sigma = C_{ik} : \forall i = k = 4,5,6. \quad \text{Eq. 4.82}$$

The other C_{ik} coefficients not defined by Eq. 4.79, Eq. 4.80 and Eq. 4.82 are zero.

Using the parameters in Table 4.2,

$$C_1 \approx -0.8 \times 10^{-3} / GPa, \quad \text{Eq. 4.83}$$

$$C_2 \approx -4.6 \times 10^{-3} / GPa, \text{ and} \quad \text{Eq. 4.84}$$

$$C_\sigma \approx 3.8 \times 10^{-3} / GPa. \quad \text{Eq. 4.85}$$

These values are similar to those reported in the literature [Barlow & Payne, 1983; Namihira, 1985].

4.3.3 Birefringence of an Optical Fibre with an Internal Elliptical Cladding

Expanding Eq. 4.77, the refractive index change along the x - and y -axes of an IEC-fibre are

$$\delta n_x = C_1 \sigma_x + C_2 \sigma_y + C_2 \sigma_z, \text{ and} \quad \text{Eq. 4.86}$$

$$\delta n_y = C_2 \sigma_x + C_1 \sigma_y + C_2 \sigma_z. \quad \text{Eq. 4.87}$$

By using Eq. 4.58 to Eq. 4.63, Eq. 4.79 and Eq. 4.80,

$$\delta n_x = -\frac{n^3}{2}(T - T_s)(1 + \mu) \left\{ D_1 (p_{11} - \mu(p_{11} + p_{12})) + D_2 (p_{12} - \mu(p_{11} + p_{12})) \right\} \text{ and} \quad \text{Eq. 4.88}$$

$$\delta n_y = -\frac{n^3}{2}(T - T_s)(1 + \mu) \left\{ D_2(p_{11} - \mu(p_{11} + p_{12})) + D_1(p_{12} - \mu(p_{11} + p_{12})) \right\}. \quad \text{Eq. 4.89}$$

These two equations show that the induced refractive index change along each polarisation axis is proportional to temperature. Consequently this establishes the strong temperature dependence of the birefringence of an IEC-fibre.

The refractive index along the x - and y -axes are

$$n_x = n + \delta n_x = n + C_1 \sigma_x + C_2 \sigma_y + C_2 \sigma_z, \text{ and} \quad \text{Eq. 4.90}$$

$$n_y = n + \delta n_y = n + C_2 \sigma_x + C_1 \sigma_y + C_2 \sigma_z \quad \text{Eq. 4.91}$$

whilst the birefringence of an IEC-fibre is

$$B = \delta n_x - \delta n_y = (C_1 - C_2)(\sigma_x - \sigma_y) = C_\sigma(\sigma_x - \sigma_y), \text{ or} \quad \text{Eq. 4.92}$$

$$B = \delta n_x - \delta n_y = -\frac{n^3}{2}(p_{11} - p_{12})\delta\alpha_2(T - T_s)\left(\frac{1 + \mu}{1 - \mu}\right)e_{ic}, \quad \text{Eq. 4.93}$$

where $e_{ic} = \frac{a - b}{a + b}$ Eq. 4.94

is the ellipticity of the inner cladding. From Eq. 4.93, the strength of the birefringence B increases with the ellipticity e_{ic} , the thermal coefficient mismatch $\delta\alpha_2$ and the temperature difference from the thermal stress on-set temperature T_s . Eq. 4.93 also implies that the birefringence depends only on the thermal stress produced between the inner and outer claddings (Equation 4.58). This is because the stress between the core and the elliptical cladding is radially symmetric. Eq. 4.93 can be rewritten as

$$B = \delta n_x - \delta n_y = C_\epsilon \delta\alpha_2(T - T_s)\left(\frac{1}{1 - \mu}\right)e_{ic}, \quad \text{Eq. 4.95}$$

where $C_\epsilon = C_\sigma Y = -\frac{n^3}{2}(p_{11} - p_{12})(1 + \mu)$ Eq. 4.96

is known as the strain-optic constant for an isotropic fibre.

Using the parameters in Table 4.2 and Table 4.3, the estimated values for δn_x , δn_y and B for the IEC-fibres used are

$$\delta n_x \approx +14 \times 10^{-4}, \quad \text{Eq. 4.97}$$

$$\delta n_y \approx -16 \times 10^{-4}, \text{ and} \quad \text{Eq. 4.98}$$

$$B \approx 3 \times 10^{-4}. \quad \text{Eq. 4.99}$$

These estimates indicate that the core of the fibre experiences extensive stress parallel to the x -axis of the ellipse and compressive stress along the y -axis. In addition, the values indicate that the y -axis is clearly the fast-axis of the fibre. The birefringence B is lower than the expected value of 4×10^{-4} for the birefringent fibre used.

However,

$$C_\varepsilon \approx 0.24 \quad \text{Eq. 4.100}$$

is similar to those reported in the literature [Rashleigh, 1983].

4.3.4 Phase-Strain Sensitivity

The calculation for the phase-strain sensitivities of an FFPS employing IEC-fibres is slightly different from that of the non-polarisation-maintaining fibre case (section 4.1.2). The different transverse stress due to an axial strain needs to be distinguished. The additional stress caused by an axial strain ε along a length L_ε , εY (Eq. 4.9) can be expressed as

$$\Delta \sigma_k = \varepsilon Y \delta_{kz}, \quad \text{Eq. 4.101}$$

where δ_{kz} is the Kronecker delta function:

$$\delta_{kz} = \begin{cases} 1 & , k = z \\ 0 & , k \neq z \end{cases}. \quad \text{Eq. 4.102}$$

The axial refractive index change is given by the difference between refractive index values at two different stress states: $[\sigma_k + \varepsilon Y \delta_{kz}]$ and $[\sigma_k]$. $[\sigma_k]$ is the initial stress producing the birefringence. The refractive index change can be described as

$$\Delta n_{i,\varepsilon} = \Delta(n + \delta n_i) = (n + C_{ik}(\sigma_k + \varepsilon Y \delta_{kz})) - (n + C_{ik} \sigma_k) = C_{iz} \varepsilon Y. \quad \text{Eq. 4.103}$$

For the change along the x - and y -axis,

$$\Delta n_{x,\varepsilon} = \Delta n_{y,\varepsilon} = C_\sigma \varepsilon Y = -\frac{n^3}{2} \varepsilon (p_{12} - \mu(p_{11} + p_{12})). \quad \text{Eq. 4.104}$$

Assuming that an IEC-fibre is weakly guiding then the waveguide effects can be neglected as in the NPM fibre case. The strain-induced phase change along each polarisation axis of a birefringent FFPS is:

$$\Delta\varphi_{i,\varepsilon} \cong \frac{4\pi n_i L_\varepsilon}{\lambda} \left\{ \varepsilon + \frac{1}{n_i} \Delta n_{i,\varepsilon} \right\}, \quad i = x \text{ or } y. \quad \text{Eq. 4.105}$$

Although from Eq. 4.104, the refractive index changes due to the additional stress along each polarisation axis are the same, the total change in the optical length of the slow-axis cavity would be slightly larger than that of the fast-axis simply because $n_x > n_y$. This relationship has been observed experimentally (Chapter 7).

The corresponding optical gauge factors are

$$\frac{\Delta\varphi_{i,\varepsilon}}{\varphi_{i,\varepsilon}\varepsilon} = \varpi_{i,\varepsilon} \cong 1 - \frac{n^3}{2n_i} \left(p_{12} - \mu(p_{11} + p_{12}) \right) \quad \text{Eq. 4.106}$$

assuming no thermally induced stress effects affect the initial birefringence of the fibre. Using the values in Table 4.2 and the results in section 4.3.3,

$$\frac{\Delta\varphi_{x,\varepsilon}}{\varphi_{x,\varepsilon}\varepsilon} = \varpi_{x,\varepsilon} = 0.7937, \text{ and} \quad \text{Eq. 4.107}$$

$$\frac{\Delta\varphi_{y,\varepsilon}}{\varphi_{y,\varepsilon}\varepsilon} = \varpi_{y,\varepsilon} = 0.7936. \quad \text{Eq. 4.108}$$

These values are very similar to one another and for the case of NPM FFPSs (Eq. 4.34).

4.3.5 Phase-Temperature Sensitivity

The refractive index change due to temperature of an elliptically clad fibre is given by the difference of the refractive indices at two temperature states. This thermal refractive index change can be described as

$$\Delta n_{i,T} = \Delta(n + \delta n_i) = \left(n(T + \Delta T) - \frac{(n(T + \Delta T))^3}{2} p_{ij} s_{jk} \sigma_k(T + \Delta T) \right) - \left(n(T) - \frac{(n(T))^3}{2} p_{ij} s_{jk} \sigma_k(T) \right), \quad \text{Eq. 4.109}$$

where $n(T + \Delta T)$ is the refractive index of the un-stress core at temperature $T + \Delta T$. $\vec{\sigma}(T + \Delta T)$ is the thermally-induced stress. Expanding Eq. 4.109 as a Taylor series in ΔT and subsequently keeping only the ΔT terms and adding the contribution of the thermal strain $\vec{\varepsilon}^T$,

$$\Delta n_{i,T} \cong \frac{\partial n}{\partial T} \left(1 - \frac{3n^2}{2} p_{ij} s_{jk} \sigma_k \right) \Delta T - \frac{n^3}{2} p_{ij} s_{jk} \frac{\partial \sigma_k}{\partial T} \Delta T - \frac{n^3}{2} p_{ij} \varepsilon_j^T. \quad \text{Eq. 4.110}$$

The first term in Eq. 4.110 is the refractive index change due to direct dependence of n_i ($i=x,y$) with temperature.

The last two terms are the contributions of the thermally induced stress and strain respectively. Together they give the elasto-optic refractive index change due to variations in temperature. From Eq. 4.58 to Eq. 4.64,

$$\frac{\partial \sigma_k}{\partial T} = \frac{\sigma_k}{T - T_s}. \quad \text{Eq. 4.111}$$

Thus, Eq. 4.110 can be rewritten as

$$\Delta n_{i,T} \cong \frac{dn_i}{dT} \Delta T, \quad \text{Eq. 4.112}$$

where $\frac{dn_i}{dT} = \frac{\partial n_i}{\partial T} - \frac{n^3}{2} (p_{11} + 2p_{12}) \alpha$, and Eq. 4.113

$$\frac{\partial n_i}{\partial T} = \frac{\partial n}{\partial T} + \delta n_i \left(\frac{3}{n} \frac{\partial n}{\partial T} + \frac{1}{T - T_s} \right). \quad \text{Eq. 4.114}$$

Alternatively,

$$\frac{dn_i}{dT} = \frac{dn}{dT} + \delta n_i \left[\frac{3}{n} \left(\frac{dn}{dT} + \frac{n^3}{2} \alpha (p_{11} + 2p_{12}) \right) + \frac{1}{T - T_s} \right], \quad \text{Eq. 4.115}$$

where $\frac{dn}{dT}$ is that given by Eq. 4.42 - the total refractive index change due to temperature of the un-stress core. Of

the terms inside the square brackets in Eq. 4.115, the dominant term is $\frac{1}{T - T_s}$ which can be interpreted as the

fractional change in the internal stress experienced by the core (Eq. 4.111). In fact the product $\delta n_i \frac{1}{T - T_s}$ has the

same order of magnitude as $\frac{dn}{dT}$. Using the values in Table 4.2, Table 4.3 and the results in section 4.3.3

$$\frac{dn_x}{dT} \approx 10.8 \times 10^{-6} / ^\circ C, \quad \text{and} \quad \text{Eq. 4.116}$$

$$\frac{dn_y}{dT} \approx 111 \times 10^{-6} / ^\circ C. \quad \text{Eq. 4.117}$$

These are the total refractive index change due to temperature along each polarisation axis of the IEC-fibre.

Hence from Eq. 4.11, the phase-temperature sensitivities due to temperature change along each polarisation axis

are:

$$\Delta\varphi_{i,T} \cong \frac{4\pi n_i L_T}{\lambda} \left\{ \alpha + \frac{1}{n_i} \frac{dn_i}{dT} \right\} \Delta T, \quad i = x \text{ or } y, \quad \text{Eq. 4.118}$$

and the corresponding fractional temperature sensitivities are

$$\frac{\Delta\varphi_{i,T}}{\varphi_{i,T} \Delta T} = \varpi_{i,T} \cong \alpha + \frac{1}{n_i} \frac{dn_i}{dT}. \quad \text{Eq. 4.119}$$

Using the values in Table 4.2, Eq. 4.116 and Eq. 4.117, the estimated values along each axis are

$$\varpi_{x,T} = 7.9 \times 10^{-6} / ^\circ C, \text{ and} \quad \text{Eq. 4.120}$$

$$\varpi_{y,T} = 8.2 \times 10^{-6} / ^\circ C. \quad \text{Eq. 4.121}$$

As in the case of NPM fibres, the thermo-optic effect dominates the thermal linear expansion effect for an IEC-fibre. However, $\varpi_{x,T}$ and $\varpi_{y,T}$ are significantly different from the non-birefringent case (Eq. 4.44). Furthermore, compared with the case of strain for IEC-fibres, the phase-temperature sensitivity of the fast-axis is greater than that of the slow-axis. This prediction can be explained by the greater relaxation rate of the compressive stress along the fast-axis with an increase in temperature [Rashleigh, 1983]. In this work, $\varpi_{x,T} < \varpi_{y,T}$ was observed in Chapter 7.

4.3.6 Cross-Sensitivity of Strain and Temperature

By examining the expressions for phase-strain and phase-temperature sensitivities (Eq. 4.106 and Eq. 4.119), these sensitivities may be dependent on one another (cross-sensitivity between strain and temperature). Using Eq. 4.106 and Eq. 4.119, the optical phase difference of a birefringent Fabry-Pérot cavity can be expressed as

$$\varphi_i(\varepsilon, \Delta T) = \frac{4\pi n_i \ell}{\lambda} \left[1 + \varpi_{i,\varepsilon} \varepsilon + \varpi_{i,T} \Delta T \right]. \quad \text{Eq. 4.122}$$

Alternatively this expression can be obtained from a first-order Taylor expansion of the optical phase with respect to ε , ΔT and $\varepsilon \Delta T$. By including the cross-sensitivity term, the total cavity phase difference can be written as

$$\varphi_i(\varepsilon, \Delta T) = \frac{4\pi n_i \ell}{\lambda} \left[1 + \varpi_{i,\varepsilon} \varepsilon + \varpi_{i,T} \Delta T + \varpi_{i,\varepsilon T} \varepsilon \Delta T \right]. \quad \text{Eq. 4.123}$$

Interestingly,

$$\frac{4\pi n_i \ell}{\lambda} \varpi_{i,\varepsilon T} = \frac{\partial}{\partial \varepsilon} \left[\frac{4\pi n_i \ell}{\lambda} \varpi_{i,T} \right], \text{ or} \quad \text{Eq. 4.124}$$

$$\frac{4\pi n_i \ell}{\lambda} \varpi_{i,\varepsilon T} = \frac{\partial}{\partial T} \left[\frac{4\pi n_i \ell}{\lambda} \varpi_{i,\varepsilon} \right]. \quad \text{Eq. 4.125}$$

Substituting Eq. 4.106 into Eq. 4.125 and evaluating the partial derivative gives

$$\frac{4\pi n_i \ell}{\lambda} \varpi_{i,\varepsilon T} \cong \frac{4\pi n_i \ell}{\lambda} \left[\varpi_{i,\varepsilon} \varpi_{i,T} - \left(\frac{3n^2}{2n_i} \frac{dn}{dT} - \frac{n^3}{2n_i^2} \frac{dn_i}{dT} \right) (p_{12} - \mu(p_{11} + p_{12})) \right]. \quad \text{Eq. 4.126}$$

Since for an IEC-fibre, it can be shown that $n_i \approx n$ and $\frac{dn_i}{dT} \approx \frac{dn}{dT}$, Eq. 4.126 becomes

$$\varpi_{i,\varepsilon T} \approx \varpi_{i,\varepsilon} \varpi_{i,T} - n_i \frac{dn_i}{dT} (p_{12} - \mu(p_{11} + p_{12})). \quad \text{Eq. 4.127}$$

Using the values in Table 4.1 and estimates (see Eq. 4.97, Eq. 4.98, Eq. 4.107, Eq. 4.108, Eq. 4.116, Eq. 4.117, Eq. 4.120 and Eq. 4.121) of the different parameters required in Eq. 4.127,

$$\varpi_{x,\varepsilon T} \approx 3.2 \times 10^{-6} / ^\circ\text{C}, \text{ and} \quad \text{Eq. 4.128}$$

$$\varpi_{y,\varepsilon T} \approx 3.3 \times 10^{-6} / ^\circ\text{C}. \quad \text{Eq. 4.129}$$

Farahi *et al.* [1990b] used a Bow-Tie birefringent fibre and experimentally determined the corresponding cross-sensitivity factor for their fibre. This factor was obtained by determining the phase-temperature sensitivities at different strain state of the fibre. Their technique can easily be appreciated from a simple rearrangement of Eq. 4.123:

$$\varphi_i(\varepsilon, \Delta T) = \frac{4\pi n_i \ell}{\lambda} \left[1 + \varpi_{i,\varepsilon} \varepsilon + \left\{ \varpi_{i,T} + \varpi_{i,\varepsilon T} \varepsilon \right\} \Delta T \right]. \quad \text{Eq. 4.130}$$

For their fibre, the slow-axis sensitivity changed from 8.0 to 3.8 rad/°C as a 7 cm segment was stretched from 0 to 30 μm . This ~50 % change gave (slow-axis) $\varpi_{x,\varepsilon T} \approx 4.8 \times 10^{-3} / ^\circ\text{C}$ using $n=1.46$ and $\lambda=633$ nm. This value is several orders of magnitude higher than the expected value for an IEC-fibre similar to that used in this work (*c.f.* Eq. 4.128). This can only be attributed to the birefringence mechanisms in a Bow-Tie fibre although even with the much higher birefringence of this structure, the measurements give a surprisingly large value. Others [Smith, 1980; Barlow & Payne, 1983] had indirectly measured this cross-sensitivity effect. In characterising bend-induced retardation and twist-induced rotation in optical fibres, they observed the temperature dependence of the stress-optic coefficient of $\frac{dC_\sigma}{dT} \approx -4.398 \times 10^{-7} / (\text{GPa} \cdot ^\circ\text{C})$ in the case of Barlow & Payne.

Cross-sensitivity between strain and temperature arises because of the temperature dependence of the stress-induced birefringence in an optical fibre. However, this cross-sensitivity effect can be neglected when either temperature or strain is kept constant or when moderate excursions in strain or temperature are involved.

4.4 Temperature and Strain Sensitivities of a Single-Layer Reflective Thin Film

The optical properties of the thin film introduced in an optical fibre depend on the phase change associated with the optical thickness of a thin film (see chapter 3):

$$\beta_f = \frac{2\pi n_f \ell_f}{\lambda}, \quad \text{Eq. 4.131}$$

where n_f and ℓ_f are the refractive index and the (physical) thickness of the film respectively. The fractional temperature or strain sensitivities of β_f , ω_T^{film} and $\omega_\varepsilon^{film}$, can be obtained as in the optical-fibre case (Eq. 4.33 and Eq. 4.43),

$$\frac{\Delta\beta_f}{\Delta M} = \beta_f \omega_M^{film}, \quad \text{Eq. 4.132}$$

where $M =$ temperature T or strain ε . The values of ω_T^{film} and $\omega_\varepsilon^{film}$ are expected to be of the same order of magnitude as in the optical fibre case. (At most the order of magnitude of the values can be expected to be about $\omega_T^{film} \approx 10^{-5}$ and $\omega_\varepsilon^{film} \approx 1$). Thus,

$$\frac{\Delta\beta_f}{\Delta T} = \frac{2\pi(\lambda/4)}{\lambda} \omega_T^{film} = \frac{\pi}{2} \omega_T^{film} \approx \frac{\pi}{2} \times 10^{-5} \text{ rad}/^\circ\text{C}, \text{ and} \quad \text{Eq. 4.133}$$

$$\frac{\Delta\beta_f}{\varepsilon} = \frac{2\pi(\lambda/4)}{\lambda} \omega_\varepsilon^{film} = \frac{\pi}{2} \omega_\varepsilon^{film} \approx \frac{\pi}{2} \times 10^{-6} \text{ rad} / \mu\varepsilon \quad \text{Eq. 4.134}$$

for temperature change and strain respectively. In either case, a change of about $1,100^\circ\text{C}$ or $11,000\mu\varepsilon$ change is required to induce the equivalent of 1° phase change in β_f . Hence, the optical properties of the thin film can be considered invariant to moderate thermal or strain variations.

4.5 Temperature and Strain Sensitivities of an In-Fibre Bragg Grating

The Bragg wavelength of a fibre grating can easily be shown to be sensitive to strain and temperature change. Since a fibre Bragg grating (FBG) and a fibre Fabry-Pérot sensor have similar refractive indices, the fractional change in Bragg wavelength of a fibre Bragg grating with respect to strain and temperature change can be expressed similar to those found in Eq. 4.33 and Eq. 4.43:

$$\frac{\Delta\lambda_b}{\lambda_b \varepsilon} = \varpi_\varepsilon = 1 - \frac{n_b^2}{2} \left(p_{12} - \mu(p_{11} + p_{12}) \right), \text{ and} \quad \text{Eq. 4.135}$$

$$\frac{\Delta\lambda_b}{\lambda_b \Delta T} = \varpi_T = \frac{1}{n_b} \frac{dn_b}{dT} + \alpha \quad \text{Eq. 4.136}$$

for strain and temperature change respectively.

When an FBG is used as a Fabry-Pérot reflector of an FFPI, the temperature- or strain-induced change in the reflectance and transmittance of the FBG implies changes in the fringe visibility. Such changes are important considerations in determining the overall measurand range of the Fabry-Pérot sensor. These intensity variations do not, however, directly affect the measurements of the phase shifts as long as the interferometric signals can be detected with reasonable signal-to-noise ratio.

On the other hand, shifts in the spectrum of the FBG are accompanied with a corresponding phase change. At a fixed wavelength of the light source, the electric field reflection and transmission coefficients can vary with the phase β_b . As in the Bragg wavelength shifts, it can easily be shown that

$$\frac{1}{\beta_b} \frac{d(\beta_b)}{dM} = \varpi_M, \quad \text{Eq. 4.137}$$

where M refers to temperature T or strain ε . The phase change due to reflection from an FBG (θ_b^r) can contribute to the interferometric phase of an FFPI (ϕ),

$$\frac{\partial \theta_b^r}{\partial M} = \frac{\partial \theta_b^r}{\partial \beta_b} \frac{\partial \beta_b}{\partial M}. \quad \text{Eq. 4.138}$$

Using Eq. 3.125 and Eq. 4.137

$$\frac{\partial \theta_b^r}{\partial M} = \frac{\partial \theta_b^r}{\partial \beta_b} \frac{\partial \beta_b}{\partial M} = \left(1 + \frac{\partial \theta_b^{nl}}{\partial \beta_b} \right) \beta_b \varpi_M. \quad \text{Eq. 4.139}$$

As was the case in section 3.2.3, $\frac{\partial \theta_b^{nl}}{\partial \beta_b}$, can be neglected for low Bragg reflectance values (Eq. 3.128). Hence

$$\frac{\partial \theta_b^r}{\partial M} \approx \beta_b \varpi_M. \quad \text{Eq. 4.140}$$

4.6 The Phase-Measurand Sensitivity of a Fibre Fabry-Pérot Interferometer with Thin-Film or Bragg-Grating Reflectors

The transmittance and reflectance of an FFPS have been shown to depend on either ϕ or $\phi + \phi_r$ (Chapter 3). For a dielectric thin-film or an FBG, ϕ_r is a constant. The change in ϕ is given by

$$\Delta \phi = \Delta(\phi + \phi_r) = \Delta(2\beta) + \Delta\theta_c. \quad \text{Eq. 4.141}$$

Using the chain rule for differentiation,

$$\Delta \phi \cong \left(2 \frac{\partial \beta}{\partial M} + \frac{\partial \theta_c}{\partial M} \right) \Delta M. \quad \text{Eq. 4.142}$$

θ_c is the sum of the phase change upon internal reflection of the cavity (Eq. 3.19). Using Eq. 4.140,

$$\Delta \phi \cong \left(2\beta \varpi_M + \frac{\partial \theta_c}{\partial M} \right) \Delta M. \quad \text{Eq. 4.143}$$

Subsequently similar to the steps introduced in section 3.3, it follows from Eq. 4.143

$$\frac{\Delta \phi}{\Delta M} \cong 2\beta \varpi_M + \frac{\partial \theta_{m_1}^r}{\partial \beta_{m_1}} \frac{\partial \beta_{m_1}}{\partial M} + \frac{\partial \theta_{m_2}^r}{\partial \beta_{m_2}} \frac{\partial \beta_{m_2}}{\partial M}, \quad \text{Eq. 4.144}$$

where \mathbf{m}_1 and \mathbf{m}_2 are the Fabry-Pérot mirrors which in this work are either dielectric thin films or FBGs. θ_X^r refers to the phase change upon reflection from either surface of the reflector (assuming reciprocal properties) and β_X is the phase associated with the optical length of the mirror X ($= \mathbf{m}_1$ or \mathbf{m}_2). Using Eq. 4.132 or Eq. 4.137,

$$\frac{\Delta \phi}{\Delta M} \cong 2\beta \varpi_M + \frac{\partial \theta_{m_1}^r}{\partial \beta_{m_1}} \beta_{m_1} \varpi_M^{m_1} + \frac{\partial \theta_{m_2}^r}{\partial \beta_{m_2}} \beta_{m_2} \varpi_M^{m_2}. \quad \text{Eq. 4.145}$$

Using Eq. 3.120 and Eq. 3.125,

$$\frac{\Delta \phi}{\Delta M} \cong 2\beta \varpi_M + \left(1 + \frac{\partial \theta_{m_1}^{nl}}{\partial \beta_{m_1}} \right) \beta_{m_1} \varpi_M^{m_1} + \left(1 + \frac{\partial \theta_{m_2}^{nl}}{\partial \beta_{m_2}} \right) \beta_{m_2} \varpi_M^{m_2}. \quad \text{Eq. 4.146}$$

$\frac{\partial \theta_X^{nl}}{\partial \beta_X} \approx 0$ if the mirrors are quarter-wave thick thin films or low-reflectance Bragg gratings (Eq. 3.123 and Eq.

3.127). With these types of reflectors, Eq. 4.145 becomes

$$\frac{\Delta \phi}{\Delta M} \approx 2\beta \varpi_M + \beta_{m_1} \varpi_M^{m_1} + \beta_{m_2} \varpi_M^{m_2}. \quad \text{Eq. 4.147}$$

Since the right-hand side of this equation is constant, this equation implies that the interferometric phase shift varies linearly with measurand change ΔM . Strictly, slight error or nonlinear variations can be expected in $\Delta \phi$.

This nonlinear variations are given by

$$\frac{\Delta \phi^{nl}}{\Delta M} \cong \frac{\partial \theta_{m_1}^{nl}}{\partial \beta_{m_1}} \beta_{m_1} \varpi_M^{m_1} + \frac{\partial \theta_{m_2}^{nl}}{\partial \beta_{m_2}} \beta_{m_2} \varpi_M^{m_2}, \quad \text{Eq. 4.148}$$

the difference between Eq. 4.146 and Eq. 4.147.

4.7 The Unambiguous Measurand Range of a Fibre Fabry-Pérot Interferometer With Thin-Film or Bragg-Grating Reflectors

Using only the linear trend in $\Delta \phi$ (Eq. 4.147), the unambiguous measurand range, ΔM_{UMR} can be estimated to be

$$\Delta M_{\text{UMR}} \approx \frac{2\pi}{2\beta \varpi_M + \beta_{m_1} \varpi_M^{m_1} + \beta_{m_2} \varpi_M^{m_2}}. \quad \text{Eq. 4.149}$$

In the case of thin-film mirrors, the temperature or strain induced variations in the reflection phase change can be neglected since in most cases $\beta_f \varpi_M^{\text{film}} \ll \beta \varpi_M$ (section 4.4). For subsequent discussions, an FPPS with two

FBGs (m_1 and m_2) is considered. Thus,

$$\Delta M_{\text{UMR}} \approx \frac{2\pi}{2\beta \varpi_M + \beta_{m_1} \varpi_M^{m_1} + \beta_{m_2} \varpi_M^{m_2}}, \text{ or} \quad \text{Eq. 4.150}$$

$$\Delta M_{\text{UMR}} \approx \frac{2\pi}{2\varpi_M \left(\beta + \frac{\beta_{m_1}}{2} + \frac{\beta_{m_2}}{2} \right)}. \quad \text{Eq. 4.151}$$

Eq. 4.151 implies that the effective optical length of the Fabry-Pérot cavity with FBGs is equivalent to the distance between the centres of the two FBG reflectors. This approximation assumes that the Fabry-Pérot cavity and the Fabry-Pérot reflectors experience the same amount of measurand change.

In summary, this chapter has presented the expected phase-temperature and phase-strain sensitivities of fibre Fabry-Pérot sensors fabricated with two types of fibres: non-polarisation-maintaining and polarisation-maintaining (with an internal elliptical stress-producing cladding) fibres. In the latter case, the phase-temperature sensitivity

for the fast axis is expected to be greater than that of the slow axis whilst the phase-strain sensitivity for the slow-axis is expected to be greater than that of the fast axis. The temperature- and strain-induced variations to the properties of thin-film and Bragg grating reflectors were also investigated. The intensity variations determined the fringe visibility. For quarter-wave thick thin films and low-reflectance Bragg gratings, the associated phase change with these reflectors can be neglected. In addition, the phase-measurand sensitivity, the UMR and the FSR of the sensor can be calculated by using the distance between the centres of the Fabry-Pérot mirrors as the effective optical length of the cavity.

Chapter 5:

Development Of Short-Cavity Fibre Fabry-Pérot Interferometers

A fibre Fabry-Pérot sensor (FFPS) may be easily constructed from a piece of single-mode optical fibre with cleaved ends, however the long cavity length and ancillary bulk optics necessary for signal analyses limit the application of this sensor in the field. An alternative is an in-fibre FFPS. It is possible to have short cavity lengths and therefore potential for localised measurements, the incorporation of bulk optics functions into an all-fibre arrangement, the possibility of multiplexing several sensors and the incorporation of those sensors into structures [Lee *et al.*, 1989; Alcoz *et al.*, 1990; Valis *et al.*, 1990b; Lee *et al.*, 1992b; Mason *et al.*, 1992].

This chapter describes the development of in-fibre FFPSs with short-cavity length and enlarged unambiguous measurand range (UMR). The latter property is realised with the use of a birefringent FFPS which has its polarisation axes aligned with those of a lead-in fibre forming essentially a dual-interferometer sensor. The large UMR arises from the differential phase shift between the dual interferometers and the more-sensitive axial phase shift to obtain high measurand resolution. In this research, in-fibre short-cavity birefringent FFPSs were developed using either reflective fusion splices [see Lee *et al.*, 1987] or in-fibre Bragg gratings [see Morey *et al.*, 1992a].

Initially fusion-spliced FFPSs were made with single-mode non-polarisation-maintaining (NPM) fibres in order to gain familiarity with fabricating fusion-spliced devices before birefringent sensors were produced. Both the NPM or birefringent sensors involved an in-line (proximal) fusion-spliced titanium oxide (TiO₂) mirror and a coated

cleaved distal end. Unfortunately, these fusion-spliced sensors are inherently fragile because the regions around the fusion splices are mechanically weak. To fabricate mechanically stronger sensors suitable for strain measurements, the fusion-spliced reflectors were replaced with in-fibre gratings. Both single-grating- and dual-grating based birefringent FFPSs were fabricated.

5.1 Fusion-Spliced Single-Mode Optical Fibre Fabry-Pérot Sensors

5.1.1 Review of the Previous Work on the Construction of Fusion-Spliced In-Fibre Reflectors

In-fibre reflective mirrors can be fabricated using various techniques. Reflective fusion splices can be formed by lowering the fusion current such that only the cladding regions were joined whilst forming an air bubble in the core region [Leilabady, 1987; Leilabady & Corke, 1987]. These intentionally bad splices exhibited reasonable reflectance but were found to be weak. The tensile strength of the splices may be increased by using some metal rods to brace the splice region.

To increase the reflectance of a reflective fusion splice, prior to fusion, a thin film [Lee *et al.*, 1987; Yeh *et al.*, 1990; Valis *et al.*, 1990a; Inci *et al.*, 1992; Kaddu *et al.*, 1993] can be coated on end-faces of either NPM [Lee & Taylor, 1988b; Inci *et al.*, 1992; Kaddu *et al.*, 1993] or polarisation-maintaining fibres [Mason *et al.*, 1992; Valis *et al.*, 1990b]. Metallic (*e.g.* silver [Valis *et al.*, 1990a], aluminium [Valis *et al.*, 1990b]) and dielectric (titanium dioxide (TiO₂) [Lee & Taylor, 1988b; Inci *et al.*, 1992]) thin films were found to survive the violent fusion-arc process provided that the fusing current and duration were reduced. These fusion conditions gave weak tensile strength, high loss and low reflectance splices. The transmission loss can be minimised by ensuring good core-to-core alignment whilst absorption loss by using dielectric rather than metallic films. Although the reflectance of a single layer of dielectric thin film can be sufficient in some applications, the reflectance can be further increased with the use of multi-layer dielectric coatings incorporating silicon dioxide (SiO₂) and TiO₂ film. Seven-layer quarter-wave TiO₂/SiO₂ stacks were successfully used to form an in-line high-finesse Fabry-Pérot sensor [Lee *et al.*, 1992a].

Measures' group at the University of Toronto had suggested coating only the core-region of a fibre face comprising only 1% of the total surface area [Hogg *et al.*, 1991; Measures, 1992]. This procedure was believed to have enhanced the strength of the splice since much of the cladding can fuse without any intermediate thin film. In their work, they coated only the core-region of a fibre end with a thin layer of aluminum ("core-coated"). They also reported that there was no need to reduce the ordinary fusion current with core-coated fusion splices [Hogg *et al.*, 1991]. However in this work, fusion splicing with normal fusing parameters of core-coated TiO₂ fibre faces destroyed the TiO₂ film. Thus, both (entire-)face-coated and core-coated fusion-spliced TiO₂ reflectors were fabricated using reduced fusion current.

Table 5.1 summarises the reported procedures in fabricating reflective fusion splices. These splices were made at Texas A & M University, University of Toronto, Herriot-Watt University and Victoria University of Technology.

5.1.2 TiO₂ Reactive Sputter Deposition

TiO₂ was used in order to obtain reflective fusion splices because of its strong adherence on silica fibre faces, high melting temperature, low absorption and high refractive index. The melting temperature TiO₂ is 1820 °C [Ballard & Browder, 1986] which is higher than the liquid-to-glass state transition temperature of silica (1175 °C [Fleming, 1986]). It is also highly transparent and has low-absorption at wavelengths between 0.45 μm to 6 μm, *i.e.* the visible and the near infra-red [Weber, 1986]. TiO₂ has a relatively high refractive index ranging from 2.2 to 2.6 depending on the deposition method. The refractive index of TiO₂ not only varies with different deposition processes but also depends on deposition rates, substrate temperature, chamber conditions and operators [Bennett *et al.*, 1989]. An earlier study on reactive deposition of TiO₂ from sputtered titanium to yield the TiO₂ and Ti₂O₅ gave similar conclusions [Pulker *et al.*, 1976].

TiO₂ exists in several forms: rutile, anatase, octahedite, brookite, ilmenite and perovskite [Richardson & Gangolli, 1994]. However, vacuum-deposited TiO₂ films are either rutile or anatase [Pulker *et al.*, 1976]. Rutile which exhibits a stable tetragonal structure is generally formed when pure titanium is used [Pulker *et al.*, 1976] as was the case in this work.

Researchers	Sensor type	Mirror type	Deposition method	Typical fusing parameters	Optical properties	Tensile strength	Features/ comments
Measures' Group:							
a) Valis <i>et al.</i> , 1990a	Single-splice sensor	Single-layer Ag film	Dipping fibre ends in a silver rochelle solution	Splicer: Ericsson FSU 850 Fusion cycle : 5.7 mA (0.1 s), 4.4 mA (0.1 s), 7.7 mA (1.0 s) overrun: 5 μ m	Typical R:T:L ratio: 10:10:80 Best R:T:L ratio: 10:40:50	~1 N	Surface-mounted strain measurements
b) Hogg <i>et al.</i> , 1991	Single-splice sensor	Single-layer Al film	Vacuum evaporation of Al core-region-only deposition	No change in normal fusion parameters			Surface-mounted strain measurements Embedded fibre strain rosette
c) Valis <i>et al.</i> , 1990b							
Lee & Taylor's Group:							
a) Lee <i>et al.</i> , 1987	Multi-tap splices		DC magnetron reactive sputter Deposition.	Splicer: Siecor M-67	L = 0.1 - 0.05 dB R = 0.5-5%		Graded-index multimode fibre
b) Lee & Taylor, 1988b	In-line sensor	Single-layer TiO ₂ film	Sputtered Ti in 70% argon and 30% oxygen atmosphere	Fusing parameter: 5mA (0.3 s) [normally 14 mA (1.5s)] 1-30 pulses	L = 0.5- 1 dB R = 1-2%		Temperature measurements
c) Lee <i>et al.</i> , 1988	In-line sensor					~3.5 N (360 g)	Embedded sensor temperature measurements
d) Lee & Taylor, 1988a	In-line sensor	TiO ₂ + SiO ₂ stack			L = 0.1-0.2 dB R = ~5%		Embedded sensor ultra-sound measurements
e) Lee <i>et al.</i> , 1989	In-line sensor	Seven-layer $\lambda/4$ TiO ₂ /SiO ₂ stack			L = ~0.33 dB R = ~86%		Temperature measurements
f) Alcoz <i>et al.</i> , 1990	In-line sensor						
g) Lee <i>et al.</i> , 1992a	In-line sensor						

Table 5.1: Summary of the fusion-splicing parameters used to fabricate fusion-spliced fibre Fabry-Pérot interferometers.

Researchers	Sensor type	Mirror type	Deposition method	Typical fusing parameters	Optical properties	Tensile strength	Features/ comments
Jones' Group:							
a) Inci <i>et al.</i> , 1992 b) Inci <i>et al.</i> , 1993	Single-splice sensor	Single-layer TiO ₂ film	Electron beam evaporation	Splicer: BIT BFS-50 Fusing Parameters: Initial: 30 μm (5 mA) Final: 10 μm (6 - 12mA) Overrun: 4 μm Total Duration: (0.5 - 0.7 s) 8 - 20 pulses @ 6-12mA, 0.5 s	R = 1-2.5% Average R = ~12% Fringe visibility = 66-92% (second R=4%)	2-9 N Average = ~5 N	Temperature measurements
Booth's Group:							
a) Kaddu <i>et al.</i> , 1993	Single-splice sensor	Single-layer TiO ₂ film	DC magnetron reactive sputter deposition. Sputtered Ti in 80% argon and 20 % oxygen atmosphere	Splicer: BIT BFS-50 Fusing Parameters: Initial: 30 μm (10 mA) Final: 10 μm (10 mA) Overrun: 2 μm Duration: (0.5 s) 7-15 pulses	R = ~1-10% L = ~50%	Proof tested with 2 N tension	Temperature or surface mounted strain measurements

Table 5.1 (continued): Summary of the fusion-splicing parameters used to fabricate fusion-spliced fibre Fabry-Pérot interferometers.

TiO₂ films used in this work were formed by reactive sputter deposition. In this method relatively heavy argon (Ar) atoms are ionised and accelerated towards a Ti target. Subsequently, the Ti atoms from the target are sputtered and can combine with other free molecules in the sputtering chamber. For example, if deposition chamber contains oxygen, TiO₂ can be synthesised. At low reactive gas partial pressure and high sputtering rate, most of the chemical reactions occur at the substrate rather than at the target [Vossen & Coumo, 1978]. The stoichiometric ratio of the film depends on the relative arrival rates of the molecular species to compose the film. In the case of TiO₂ deposited onto cleaved fibre ends, the partial pressure of oxygen (O₂) is maintained at a level such that for approximately every Ti atom arriving at the fibre a single O₂ molecule is available. It is critical to maintain this balance because it has been experimentally observed that deficiency in oxygen molecules produced a bluish-tint film (due to a resonance absorption at 1.2 μm [Beals, 1970]) whilst abundance is accompanied by a decrease in the deposition rate. In the case of the latter, an increase in the partial pressure of O₂ produces a more stringent threshold condition to ionise the Ar atoms [Vossen & Coumo, 1978]. Hence the partial pressure of O₂ critically determines the composition and formation of TiO₂ and consequently the optical properties of the film as well.

TiO₂ was reactively deposited using a DC magnetron sputtering system (Figure 5.1). Prior to deposition, the vacuum chamber was initially evacuated using a diffusion and rotary-vane vacuum pumps in tandem to a pressure of $\sim 1.5 \times 10^{-5}$ mbar. A liquid Nitrogen cold trap at the entrance of the diffusion pump reduced the partial pressure of water vapour in the chamber. The typical ultimate pressure achieved was $\sim 2 \times 10^{-6}$ mbar. The chamber was filled with Ar and O₂ mixture with a molar ratio of 4:1 and had a US Inc. sputtering gun diode with a 99.95% Ti target. The sputtering gun used was a circular planar magnetron sputtering device (Figure 5.2). The gun was operated at 108 W at a sputtering pressure of $\sim 2 \times 10^{-3}$ mbar. A DC potential difference was applied between an annular anode outer ring (at ground potential) and a Ti cathode disk (the target). This difference maintained a glow discharge which ionised the Ar atoms, at an ambient pressure of $\sim 10^{-2}$ mbar. Permanent disk magnets situated under the cathode formed donut-shaped magnetic field lines on top of the cathode. These annular magnetic field lines trapped the electrons within the plasma discharge and hence increased the ionisation

efficiency of the sputtering Ar ions. Because the sputtering ions were positive, they were accelerated towards the negative-potential cathode, and thereby sputtered Ti upon impact.

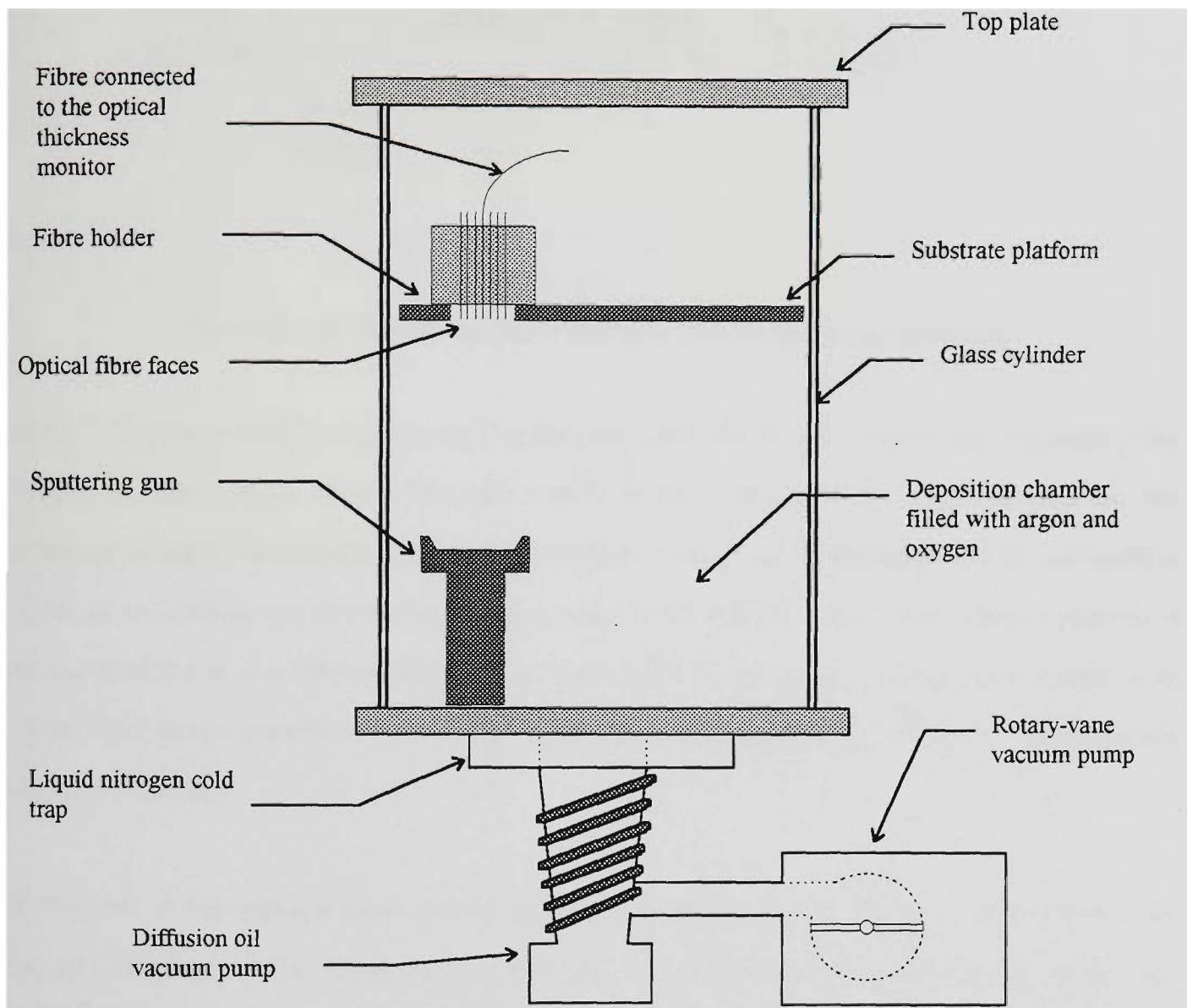


Figure 5.1: Schematic diagram of the sputtering chamber used to deposit TiO_2 on fibre end-faces.

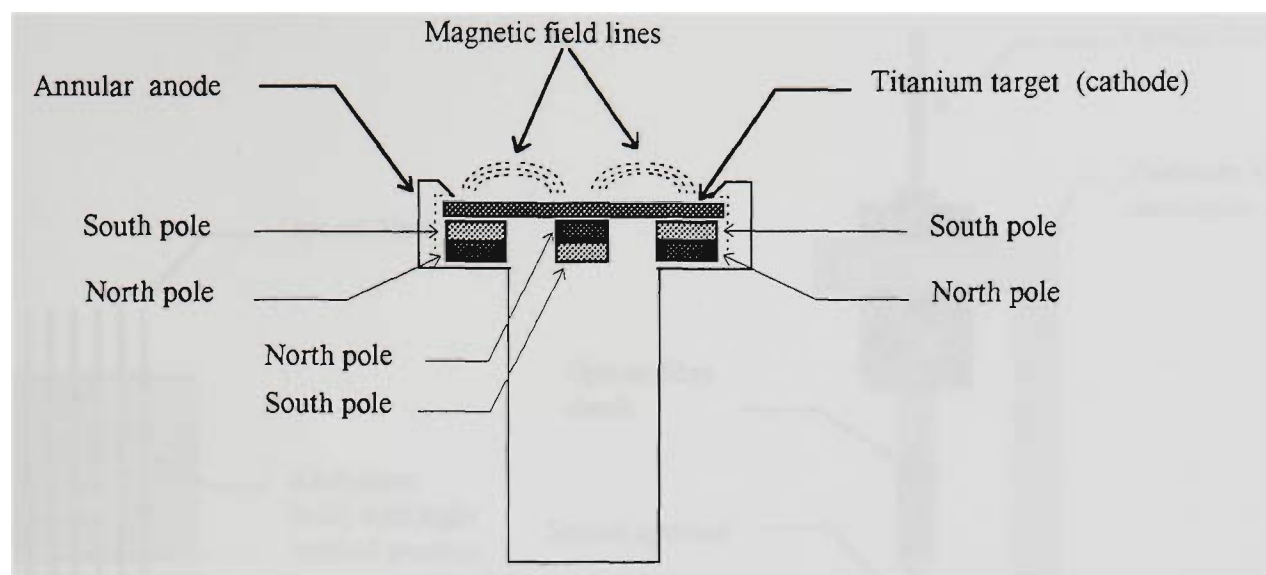


Figure 5.2: Schematic diagram of a circular planar magnetron sputtering gun.

In this work, fibre ends facing parallel to the Ti target were coated with TiO_2 either only on the core-region or the entire face. One or several (at most) fibre ends could be coated simultaneously in a single deposition run. The fibres were arranged side-by-side in a simple aluminum holder (Figure 5.3a). During deposition, the multiple-fibre holder sat on a platform such that the fibres were at a suitable location that ensured relatively similar thicknesses of the deposited film on each fibre [see Waits, 1978]. For each fibre, the thickness of the film can be assumed to be uniform over the core since the cross-sectional area of the core is very small. Figure 5.4a shows a micrograph of a face-coated fibre end.

Coating only the core region of a fibre end-face was achieved by placing a $25\text{-}\mu\text{m}$ aperture directly in front of the core of a fibre (Figure 5.3b). The aperture and fibre were held fixed to a special assembly after the aperture and the core had been optically aligned. The alignment was achieved by maximising the transmission of light from the core through the aperture. The light source employed was an 840 nm LED, the same LED that was used for the real-time monitoring of the reflectance of the deposited film (Figure 5.5). Figure 5.4b shows a micrograph of a core-coated fibre end.

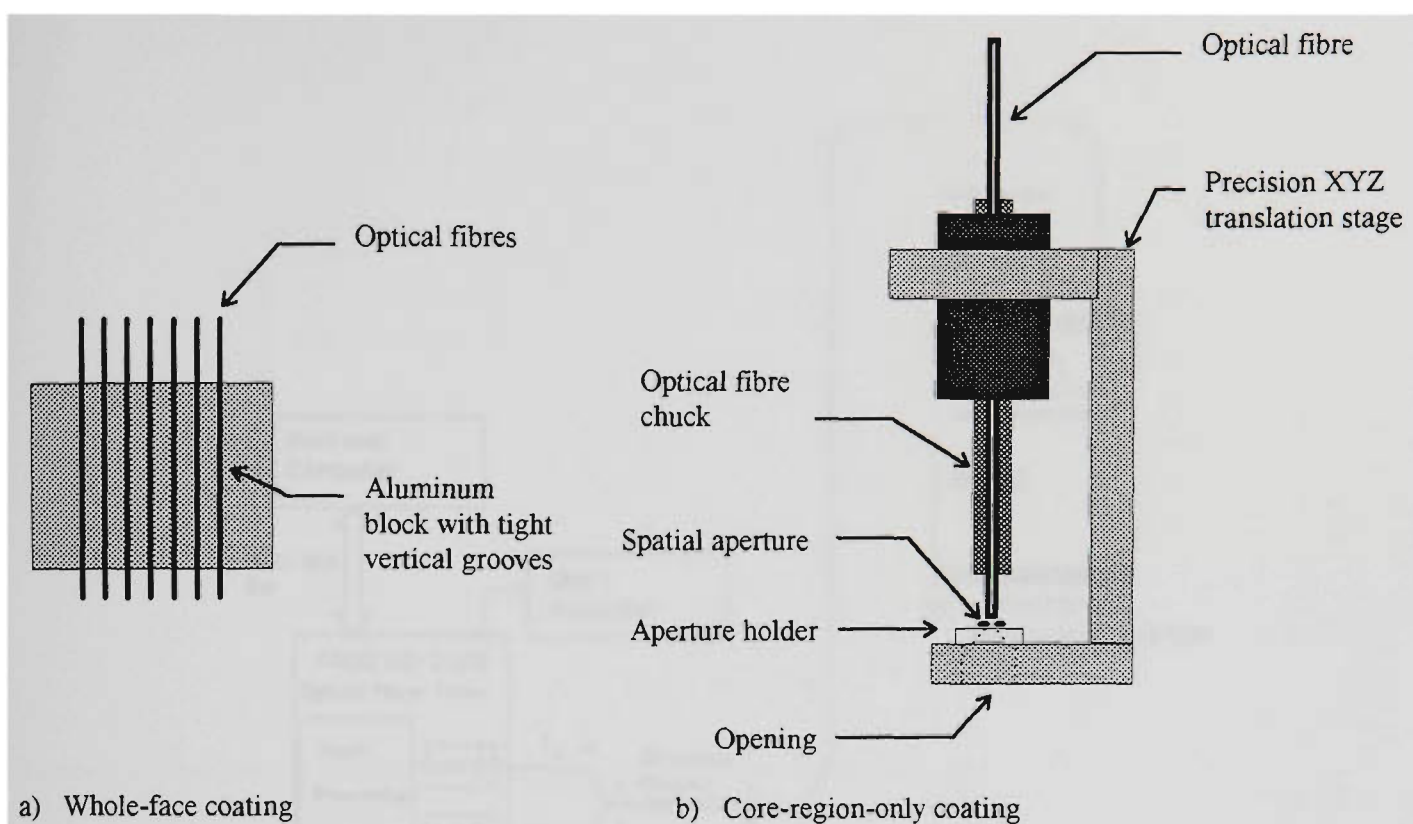
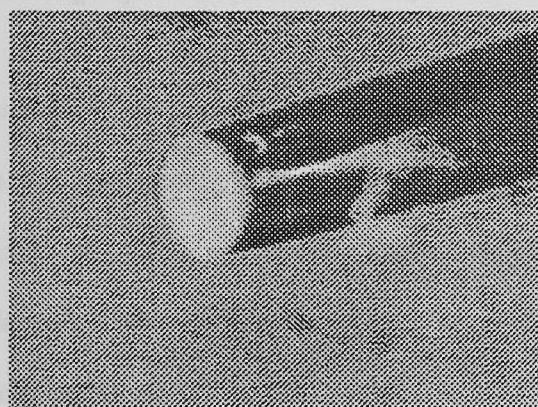


Figure 5.3: Schematic diagrams of the special fibre holders for a) entire-face or b) core-region-only deposition.



a) face-coated



b) core-coated

Figure 5.4: Micrographs of a fibre end-face coated entirely with TiO_2 or only around its core-region.

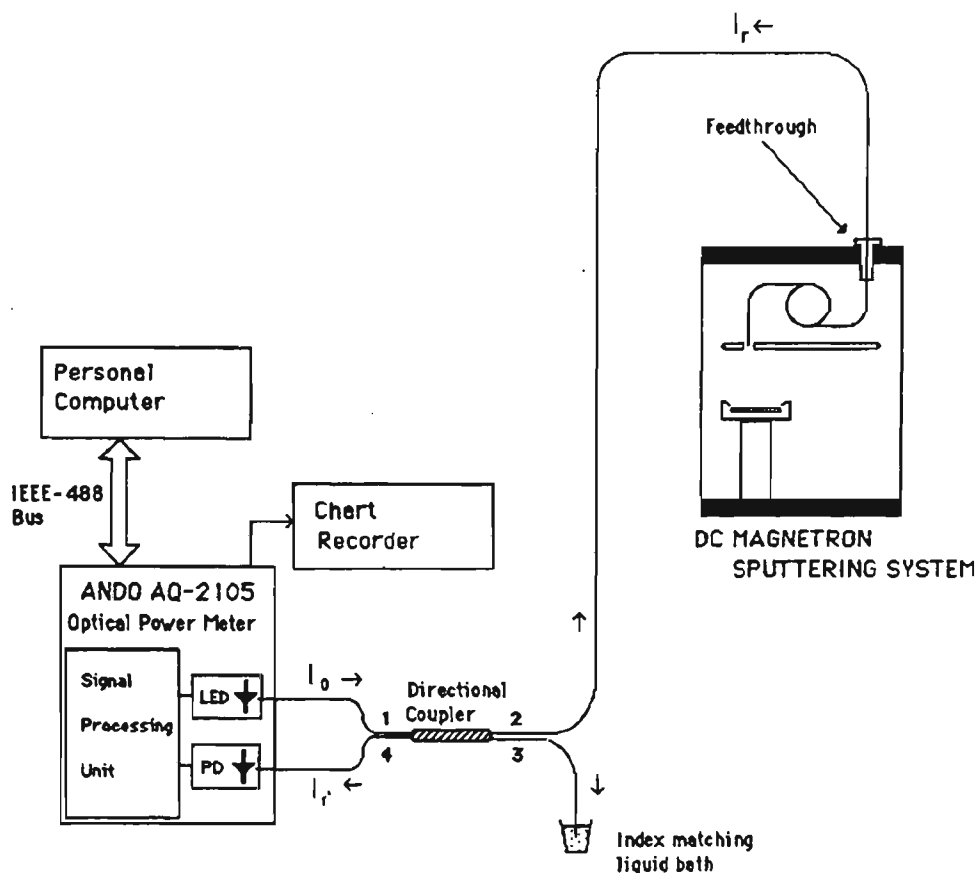


Figure 5.5: Schematic diagram of an optical fibre arrangement used to monitor the reflectance of the TiO_2 film during deposition [Caranto *et al.*, 1993].

The reflectance of the TiO_2 film deposited onto the fibre ends was optically monitored during deposition. Figure 5.5 shows the schematic of an optical fibre monitoring system [Caranto *et al.*, 1993]. This all-fibre optical thickness monitoring arrangement avoided any use of optical components which can also be inadvertently coated inside the vacuum chamber [*c.f.* Pitt *et al.*, 1975; Thomas, 1986; Severin & Severijns, 1990]. Light from an intensity-stabilised 840 nm LED was launched into one leg of a fibre directional coupler. On one of the opposite legs of the coupler, a lead fibre was fused while the other opposite leg was index-matched to avoid any reflection. The lead fibre was introduced into the deposition chamber using a special feedthrough whilst its distal end directly faced the sputtering gun [Caranto *et al.*, 1993]. During deposition, the reflectance of this end varied with thickness of the film and a fraction of the reflected beam reached a PD coupled to the remaining unused leg of the fibre directional coupler. The intensity of the detected beam was directly proportional to the reflectance of the film. Hence this return signal can be calibrated from two intensity-reflectance pair measurements.

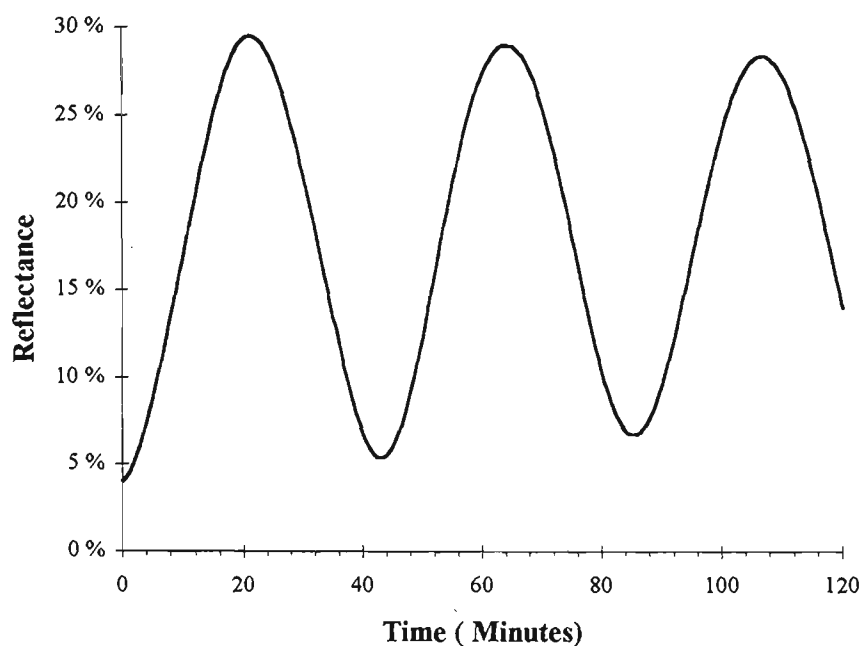


Figure 5.6: Monitored reflectance of a fibre end-face deposited with TiO_2 film.

Figure 5.6 shows the reflectance of a fibre end as it was coated with TiO_2 during one of the deposition runs. Assuming a constant deposition rate, the thickness of the film can be inferred from the deposition time. Clearly, the reflectance varies periodically with the optical thickness of the film as expected (Chapter 3). The decaying feature in the figure was due to the short coherence length of the LED ($\sim 7 \mu\text{m}$). Figure 5.6 also shows that integral multiples of quarter-wave optical thicknesses can be easily determined. For optical thicknesses less than a quarter-wave, the uncertainty in determining the physical thickness depends on the uncertainty in the refractive index of the film used with the calculations. Unfortunately, the refractive index of the deposited TiO_2 film varies with the sputtering conditions and parameters. For films of more than a quarter-wave thickness, the reflectance at the quarter-wave condition can be used to determine the refractive index of the film. However the effect due to the coherence length of the light source needs to be accounted for. In this work, it was more critical to determine the reflectance rather than the physical thickness of the film. Hence no major effort was made to determine the refractive index. If desired, the refractive index of the film can be measured using other optical techniques [Stagg & Charalampopoulos, 1992; del Pozo & Díaz, 1992; Kihara & Yokomori, 1992].

5.1.3 Fabrication Process for Fusion-Spliced Fabry-Pérot Sensors

Figure 5.7 describes the step-by-step procedures in fabricating fusion-spliced either for a single reflector sensor or for an in-line sensor, if desired. The same procedures can be used for the fabrication of the birefringent sensors with the added requirement prior to fusion splicing that the fibres have their polarisation axes aligned.

Preparing an uncontaminated fibre end is the first step for successful thin-film deposition and fusion splicing. Although fibre surfaces may be cleaned using solvents (acetone or isopropyl alcohol), freshly cleaved ends placed immediately inside the deposition chamber yield good-adhering films.

To produce low-loss fusion splices, the end faces need to be perpendicular with respect to the longitudinal axis of the fibre so that no lateral shift in the cores occurs during splicing. Perpendicularly cleaved end faces may be readily obtained by scribing the side of the fibre while under tension. This method is used by the YORK FK11 cleaver which applies a 2N tension along the fibre and has a vibrating diamond blade scribe the taut fibre from the side. Highly repeatable perpendicular cleaves are obtainable and depend on the applied tension. In this work, the tension was 210 grams (0.17 GPa) for 125 μm communications-grade 1300-nm fibres.

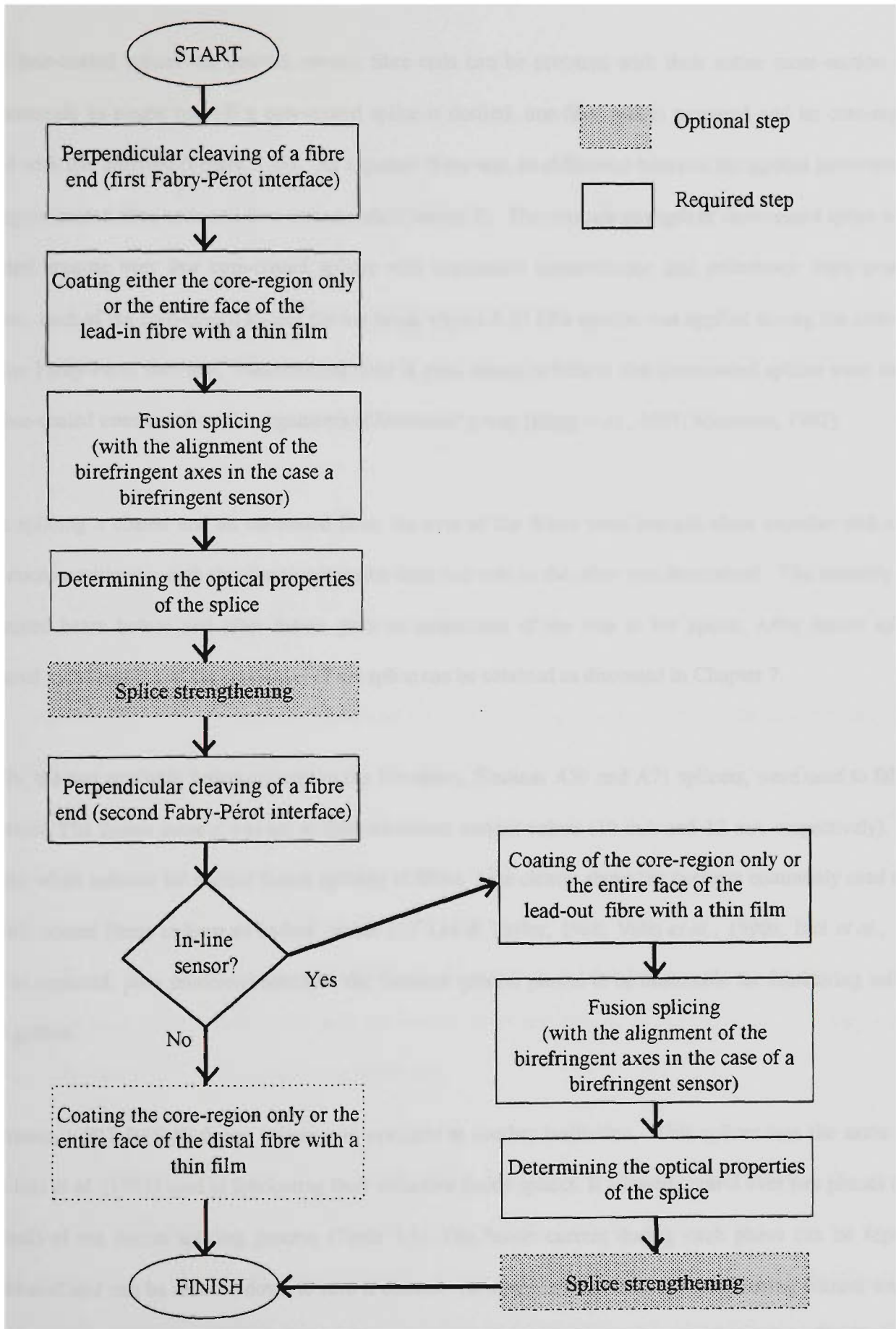


Figure 5.7: Flow diagram in the fabrication of fusion-spliced optical fibre Fabry-Pérot interferometers.

If only face-coated splices are desired, several fibre ends can be prepared with their entire cross-section coated simultaneously in single run. If a core-coated splice is desired, one fibre end is prepared and its core-region is aligned with the aperture (Figure 5.3b). As expected there was no difference between the optical performance of core-region coated fibre ends and face coated ends (Chapter 7). The ultimate strength of core-coated splice was not evaluated because very few core-coated splices with reasonable transmittance and reflectance were produced. However, each of the core-coated splices did not break when a 0.17 GPa tension was applied during the cleaving of the other Fabry-Pérot interface. Nevertheless there is good reason to believe that core-coated splices were stronger than face-coated ones based on the arguments of Measures' group [Hogg *et al.*, 1991; Measures, 1992].

Before splicing a coated and an un-coated fibre, the core of the fibres were brought close together and aligned using micro-positioners such that the transmission from one core to the other was maximised. The intensity of the transmitted beam before and after fusion gave an assessment of the loss at the splice. After fusion splicing, additional measurement of the properties of the splice can be obtained as discussed in Chapter 7.

Initially, the two available fusion-splicers in the laboratory, Siemens A30 and A71 splicers, were used to fabricate the splices. The fusion current was set to their minimum current values (10 mA and 12 mA respectively). These currents, while suitable for normal fusion splicing of fibres, were clearly above the currents commonly used to fuse dielectric coated fibres to form an in-line mirror [*c.f.* Lee & Taylor, 1988; Valis *et al.*, 1990a; Inci *et al.*, 1993]. Thus, as expected, after numerous attempts, the Siemens splicers proved to be unsuitable for fabricating reflective fusion splices.

Fortunately, a BIT BFS-50 fusion splicer was available at another institution. This splicer was the same model which Inci *et al.* [1993] used in fabricating their reflective fusion splices. It allowed control over two phases (initial and final) of the fusion splicing process (Table 5.1). The fusion current during each phase can be separately programmed and can be reduced down to zero if desired. However in this work, the same fusing current was used for both the initial and final arc phases since experimentally there was no significant benefit obtained by distinguishing between the two fusing currents.

The fusion current of the BIT splicer was initially set at 5 mA, the typical value used by other researchers (Table 5.1). However, this current did not fuse the fibres. Thus, it was increased to 10 mA, the maximum current which would fuse the fibres without ablating the TiO₂ mirrors. This difference in the settings may indicate that the built-in current meter may not be properly calibrated. The duration of the arc discharge was 0.5 second.

Fusion-splicing parameters	Normal	Fusing arc	Sub-arc
Initial separation	15 μm	30 μm	0 μm
Fusing current	20 mA	10 mA	10 mA
Fusing time	3.5 seconds	0.5 second	0.5 second
Overrun	5 μm	2 μm	0 μm

Table 5.2: Typical fusing parameters for a BIT BFS-50 fusion splicer used in fabricating reflective fusion splices.

There were two sets of fusion-splicing parameters utilised. These parameters were similar to those used by Inci *et al.* [1993] and are summarised in Table 5.2. The first set (fusing arc) was used to fuse the coated and un-coated fibre faces. Just before the arc discharged, the fibres were separated (initial separation). The fibre ends were then brought together and compressed into each other (overrun) while the arc was still on. The second set were those for subsequent arc discharges (sub-arcs). These parameters were similar to the fusing-arc parameters except that they do not involve any mechanical movement of the fibres. The purpose of these sub-arcs was to anneal the splice and strengthen the bond. The technique had been empirically developed [Inci *et al.*, 1993] and in this case at least 10 sub-arcs were used to give adequate splice strengthening.

The sub-arcs also generally decreased the reflectance of the splice. This could be monitored during the fabrication with a 2x2 coupler arrangement similar to that used in determining the reflectance of thin film during deposition, and the number of sub-arcs may be varied to tune the reflectance. This decrease would suggest that the thin film diffused into the fibre. However in other cases, there was an initial increase in the reflectance attributed to the optical thickness of the film decreasing from an initial thickness greater than a quarter-wave to a final thickness less than a quarter-wave.

The reflective TiO₂ splices fabricated with the NPM fibres were mechanically weak. The axial tensile strength of these splices were determined by applying tension to the fibre. To provide points of comparison, the tensile strength of the NPM fibres with a section of their jacket chemically removed and standard fusion-spliced NPM fibres were determined. The chemically stripped fibres broke at the edges of the bare section of the fibres when a stress of ~1.05 GPa (or strain of ~15,600 $\mu\epsilon$) was applied. The standard spliced fibres exhibited tensile strength of about ~0.5 GPa (~8,000 $\mu\epsilon$) some 50% lower than the bare fibre case. The reflective TiO₂ splices exhibited strengths between ~0.2 to 0.25 GPa (~3,000 $\mu\epsilon$ to ~4,000 $\mu\epsilon$), about 25 % of the original strength of the fibres. Although these strength values are adequate for moderate strain applications, these strength values do not meet the standards of some applications, *e.g.* a typical aerospace structure may require $\pm 5,000 \mu\epsilon$ [Dunphy *et al.*, 1993]. In the beginning of this work, an effort was made to determine ways of improving the tensile strength of the reflective splices. Unfortunately it was not possible to make concrete conclusions from the investigation except that the best way not to compromise the tensile strength of the splices was to minimise the amount of handling of the fibres. A summary of this investigation is given below in section 5.1.4.

The next step in the fabrication of an FFPS was cleaving the fused fibre to form the surface of the second mirror. For a single-in-line-reflector sensor, this cleaved end may be coated if desired to compensate for the high transmission loss of the reflective splice. In addition, coating this end is important when the sensor is to be immersed in bonding epoxy or other material used to bond the sensor on to a cantilever beam. For an in-line sensor, which is suitable for serial multiplexing several sensors, the distal cleaved end can be fused with a coated end of a (lead-out) fibre (Figure 5.7).

The fabrication process described above gave reflective fusion splices of reflectance 1 % to 10 % and a single-pass transmission loss of about 1 to 3.5 dB. The high transmission loss was attributed to scattering loss and to the misalignment of the fibre cores after fusion. Out of the 98 reflective fusion splices made, only 19 (~20%) were successful as gauged by an adequate splice strength, reasonable transmission and reflection properties. There was no attempt to fabricate in-line fusion-spliced NPM FFPSs due to this poor yield determining a likely 6% yield of the more complex devices.

5.1.4 Splice Strengthening

The mechanical weakness of reflective splices stimulated an effort to reinforce or strengthen these splices. Using ordinary fusion splices as the test material, the techniques investigated were chemically-stripping the fibre jacket using highly concentrated sulfuric acid [Krause *et al.*, 1981a], heating close and to either side of the splice using an additional fusion arc [Tachikura & Haibara, 1985] and heating the splice using a CO₂ laser beam [Kaddu *et al.*, 1993].

As in the case of ordinary glass plates, a stressed optical fibres can easily break when cracks on its surface grow [Michalske & Bunker, 1984]. The rate of crack growth increases in the presence of water molecules [Krause *et al.*, 1981b]. Clearly avoiding any mechanical flaw can reduce the risk of any crack formation. One of the methods of reducing mechanical flaws is etching the surface of the fibre with hydrofluoric acid [Miyajima *et al.*, 1981]. Alternatively the fibre jacket can be chemically stripped using highly concentrated sulfuric acid. As high as a three-fold improvement in the strength of the spliced fibre has been reported [Krause *et al.*, 1981a].

In this work, chemically-stripped non-spliced fibres broke at the edges of the bare section of the fibres when a stress of ~ 1.05 GPa (or strain of $\sim 15,600 \mu\epsilon$) was applied. Mechanically-stripped ordinary fibres splices exhibited tensile strength of about ~ 0.5 GPa ($\sim 8,000 \mu\epsilon$) whilst chemically-stripped splices exhibited a strength of about 0.4 GPa ($\sim 6,250 \mu\epsilon$). No obvious improvement in the strength of the spliced fibre was observed, hence chemically stripping was not used further.

Fibre splices fused using the recommended parameters don't break at the splice. The weakest regions are those about few millimetres away from the splice [Tachikura & Haibara, 1985]. In these regions, crystal grains which tend to be large around contaminants (*e.g.* OH) can be formed and the silica devitrify. Devitrification refers to the crystallisation of the fibre from its vitreous state and is attributed to the rapid heating and cooling of the regions around the splice during the fusion process. Tachikura & Haibara heated about 1 mm on either side of a splice for 0.5 sec using normal fusion current in order to reverse the devitrification effect. This technique was also investigated in this work. However, no improvement in the strength of ordinary fusion splices were observed.

Alternatively, the splice region can be heated in a path of a CW CO₂ beam [Kaddu *et al.*, 1993]. This novel technique was expected to “anneal” the devitrified regions of a spliced fibre. In this work, the splices were exposed in the path of a 10-mm beam with different beam intensity and for different exposure time. Heating the splices with a 200 W beam even for 0.5 second softened the fibre enough for it to sag due to its own weight. On the other hand, heating the splices with a 100W for about 10 seconds gave slight improvement in the strength of the splice. The suitability of this treatment with face-coated reflective fusion splices was subsequently investigated.

After the initial experiments with ordinary fusion splices, the strength of face-coated TiO₂ reflective splices were assessed. The initial experiments involved reflective splices which were fabricated either with 10 or 15 additional sub-arcs after the fusing arc discharge and which were either heat-treated or not with the CO₂ laser. Both the CO₂-laser treated and untreated splices broke at the splice indicating the splice remains the weakest region of the spliced fibre. The preliminary results are presented in Table 5.3. Although the number of samples is small, the table indicates that about 10 sub-arcs was sufficient to provide adequate splice strengths. On the other hand, Table 5.3 shows that the strength of the reflective splices did not improved with the CO₂ laser treatment unlike the case of normally splices fibres. From these preliminary results, there was no gain in using the CO₂ laser treatment with reflective fusion splices.

Treatment of fusion splices	10 Sub-arcs	15 Sub-arcs
Untreated	0.254 GPa	0.220 GPa
Heat treated with a 100 W CO ₂ laser	0.218 GPa	0.224 GPa

Table 5.3: Average tensile strength of TiO₂ reflective (face-coated) splices fabricated with either 10 or 15 sub-arcs and heat treated with a 100 W CO₂ laser. The fibres were mechanically stripped. Each entry in the table is the average of 5 samples.

Of the various techniques investigated to improve the strength of ordinary fusion splices, only the CO₂ laser treatment indicated the possibility of any improvement. However, the CO₂ laser treatment when applied to the reflective fusion splices did not give any improvement. Although the number of ordinary and reflective splices

evaluated were not significantly large to yield any acceptable conclusion, we observed that splices with the least amount of handling or treatment was consistently stronger. Thus, it was concluded that extra care in handling the fibres rather than using any special and sometimes elaborate technique is the most prudent method of obtaining maximum splice strength.

5.2 Fusion-Spliced Birefringent Optical Fibre Fabry-Pérot Sensors

5.2.1 Fabrication Process

Birefringent fibre Fabry-Pérot sensors were fabricated following the procedures similar to that of ordinary single-mode fibres (Figure 5.7) except for the additional requirement of aligning the polarisation axes of a lead-in fibre and sensor. The fusing parameters used were the same as that given in Table 5.2. As discussed in the previous section, there was no significant difference observed between a face-coated and a core-coated in-line mirror in their optical properties or possibly even in their mechanical characteristics. Thus, for simplicity, the entire end-face of the birefringent fibres was coated with TiO_2 .

The tension of the York FK-11 cleaver had to be modified to 150 grams (stress of 0.29 GPa) because the 80- μm -diameter birefringent fibre broke when the tension value recommended for 125 μm fibre was used. This new tension value was experimentally determined to give excellent perpendicularly cleaved ends without inadvertently breaking the fibre.

After fusion, the polarisation axes of the fibres sections had to be aligned in order to simultaneously detect the phase shifts of the individual interferometers of the sensor. The error in the angular alignment of the polarisation axes must be less than 2° . In this work the alignment technique used was time-consuming because the splicer had no provisions for rotating the fibres about its axis. Good angular alignment of the polarisation axes and excellent alignment of the cores after fusion needed to be achieved. Unfortunately, these splice characteristics were difficult to attain simultaneously. Consequently, the success rate in fabricating reflective splices with birefringent fibres was low, about 11% of the 56 attempts. Subsequently, no tensile strength evaluation were made on the successful reflective fusion splices because they were not simple to fabricate. In addition to the coupling loss due to core-to-

core misalignment, the lateral misalignment of the cores after fusion can result in undesirable coupling between polarisation modes (crosstalk) via the cladding modes [Noda *et al.*, 1983].

The fusing arc produced very weak splices. Hence several sub-arcs were applied to the splices to further strengthen them. Nevertheless the splices were still weak. For this reason, the splice were not placed under tension during the cleaving of the concatenated fibre to form the second distal mirror. This choice meant that the minimum cavity length was about 35 mm in order to avoid straining the splice.

5.2.2 Alignment of the Birefringent Axes

There are a couple of physical and optical methods of aligning the polarisation axes of birefringent fibres. Once the polarisation axes can be identified, *e.g.* as in the case of D-type birefringent fibres, the axes can appropriately aligned. For circular cross-section birefringent fibres, the polarisation axes can be marked on the fibre by dipping the fibre ends in a solution of hydrofluoric acid [Noda *et al.*, 1983]. This method relies on the differential etching rate of the stress-producing parts and the core of the fibre. The method involves dangerous chemicals and also produced a fibre with a non-uniform cladding diameter since part of the cladding is also etched.

The simplest optical method involves launching linearly polarised light along only one axis of the two fibres (a proximal and a distal fibre) to be fused. The alignment is determined when maximum extinction can be obtained after an analyser placed after the distal end of distal fibre [Watanabe *et al.*, 1988]. The fibre ends placed inside the fusing assembly of the splicer and the analyser can be rotated such that the maximum extinction ratio value is obtained. The effectiveness of this method is limited by the polarisation crosstalk in the fibre and the inherent extinction ratio of the analyser.

Polarisation cross-coupling can be induced by squeezing the birefringent fibres [Carrara *et al.*, 1986; Carrara, 1990]. Interestingly if the fibre is squeezed parallel to one of its polarisation axes, no cross-coupling is induced and this method may identify one polarisation axis.

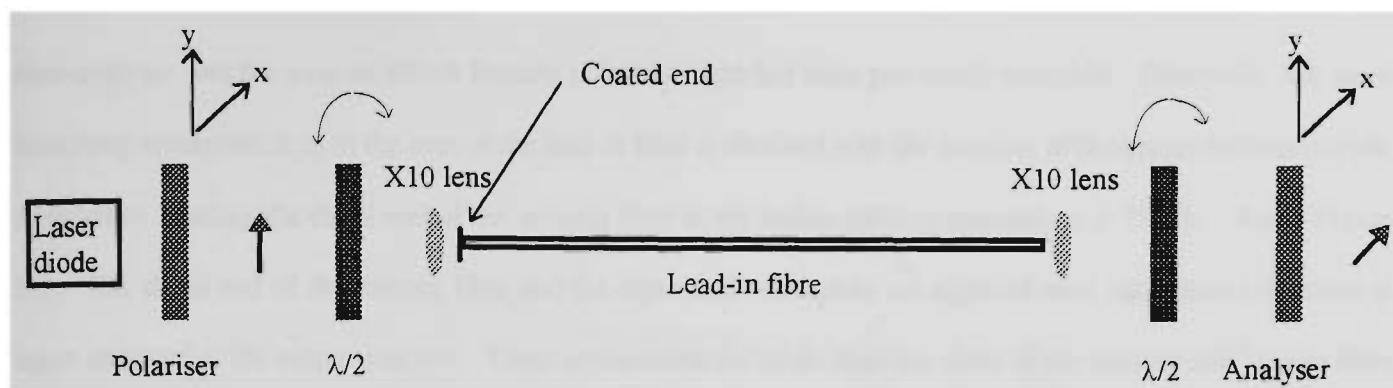


Figure 5.8: Schematic diagram of the arrangement to launch linearly polarised light along one polarisation axes of the lead-in fibre.

The procedure in aligning the polarisation axes of a birefringent FFPS and its lead-in fibre is a two-step process. These steps involve launching linearly polarised light into the two birefringent fibres to be fused. Figure 5.8 shows the experimental arrangement used to launch linearly polarised light from a 785 nm LD into one of the polarisation axis of one of the birefringent fibres. This fibre with its proximal end pre-coated with TiO_2 (as shown in Figure 5.8) eventually becomes the lead-in fibre of the sensor. Effectively the figure describes the fibre behaving like a linearly birefringent wave-plate between two crossed polarisers. In Figure 5.8, the polariser in front of the LD refers to the output polariser of the opto-isolator. The half-wave plates are used to rotate the polarisation azimuth of the input and output beams (Figure 5.8) such that maximum extinction through the output analyser is achieved. When maximum extinction has been determined, the fibre is gently tapped to verify that the extinction was not due to any destructive interference of any cross-coupled components. The gentle taps slightly strain the fibre and thereby slightly change its optical length. These optical-length perturbations are manifested as intensity variations at the output analyser if the linearly polarised light is not launched only into one of the polarisation axes and this axis and the axis of the output polariser are not perpendicular to one another.

When linearly polarised light has been satisfactorily launched into the lead-in fibre, the output half-wave plate is held fixed and the proximal coated end of the fibre (see Figure 5.8) is then placed on the right-hand side of the fusion splicing assembly (Figure 5.10). Subsequently, another fibre with perpendicularly cleaved and uncoated end-faces is used. The distal end of the fibre is placed on the left-hand side of the fusion splicing assembly whilst the proximal end in front of the input half-wave plate (Figure 5.9). This fibre will become the cavity of the sensor. At this stage the lead-in fibre behaved like an analyser as far as the sensing fibre was concerned. The axis of this

fibre-analyser was the axis on which linearly polarised light has been previously launched. Effectively, the same launching arrangement as in the case of the lead-in fibre is obtained with the function of the output half-wave-plate replaced by rotating the distal end of the sensing fibre at the fusion splicing assembly (*c.f.* Figure 5.8 and Figure 5.9). The distal end of the sensing fibre and the input half-wave-plate are adjusted until maximum extinction is again observed at the output analyser. These adjustments are made after the cores of the sensing and lead-in fibre have been aligned and brought close to another. Gentle taps are applied to the sensing fibre to ensure maximum extinction has been obtained.

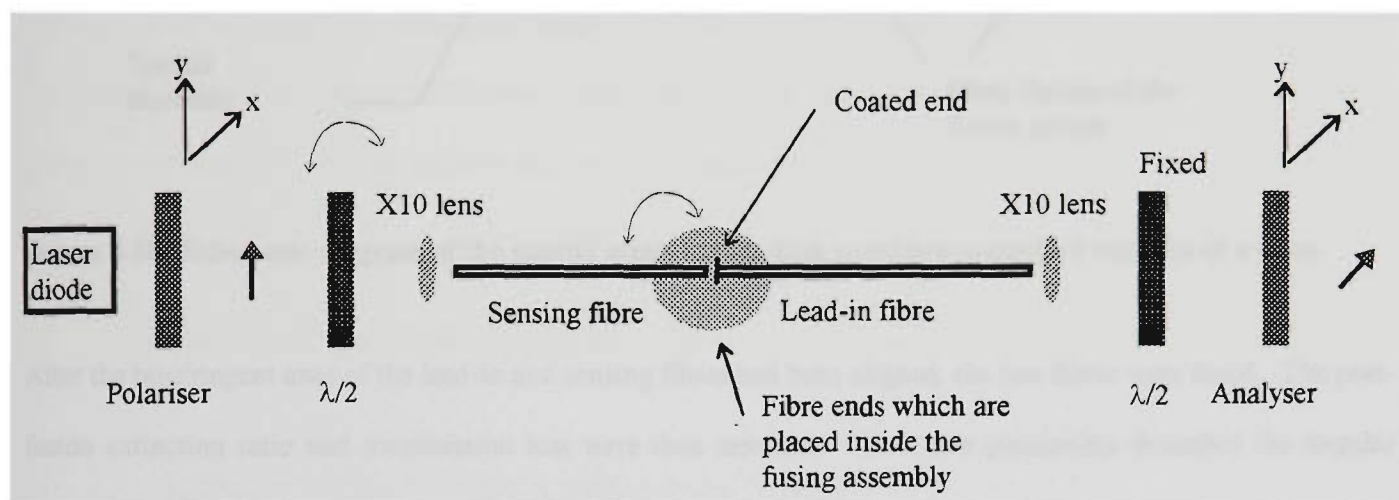


Figure 5.9: Schematic diagram of the basic arrangement to launch linearly polarised light along one polarisation axis of a birefringent fibre.

Since the BIT splicer had no provision for rotating a fibre about its axis, a special assembly was fabricated (Figure 5.10). This assembly was placed on top of the splicer and supported a cylindrical fibre chuck which can be rotated. A section of the sensing fibre was held fixed within the centre of the chuck and may be rotated by rotating the chuck. The rotation angle was determined from an angular scale marked on the chuck handle (Figure 5.10).

The estimated pre-fusion angular accuracy of the aligning the birefringent axes was about $\pm 3^\circ$. This value was based on the measured extinction ratio of 1% for the bulk-optic analysers and polarisers. Although the chuck can be rotated with an accuracy of $\pm 1^\circ$, the repeatability of the aligning the axes of the sensing and lead-in fibre was very poor because the sensing fibre had to be clamped and unclamped each time it was rotated. In a sense there is some element of luck involved in obtaining a good alignment of the axes.

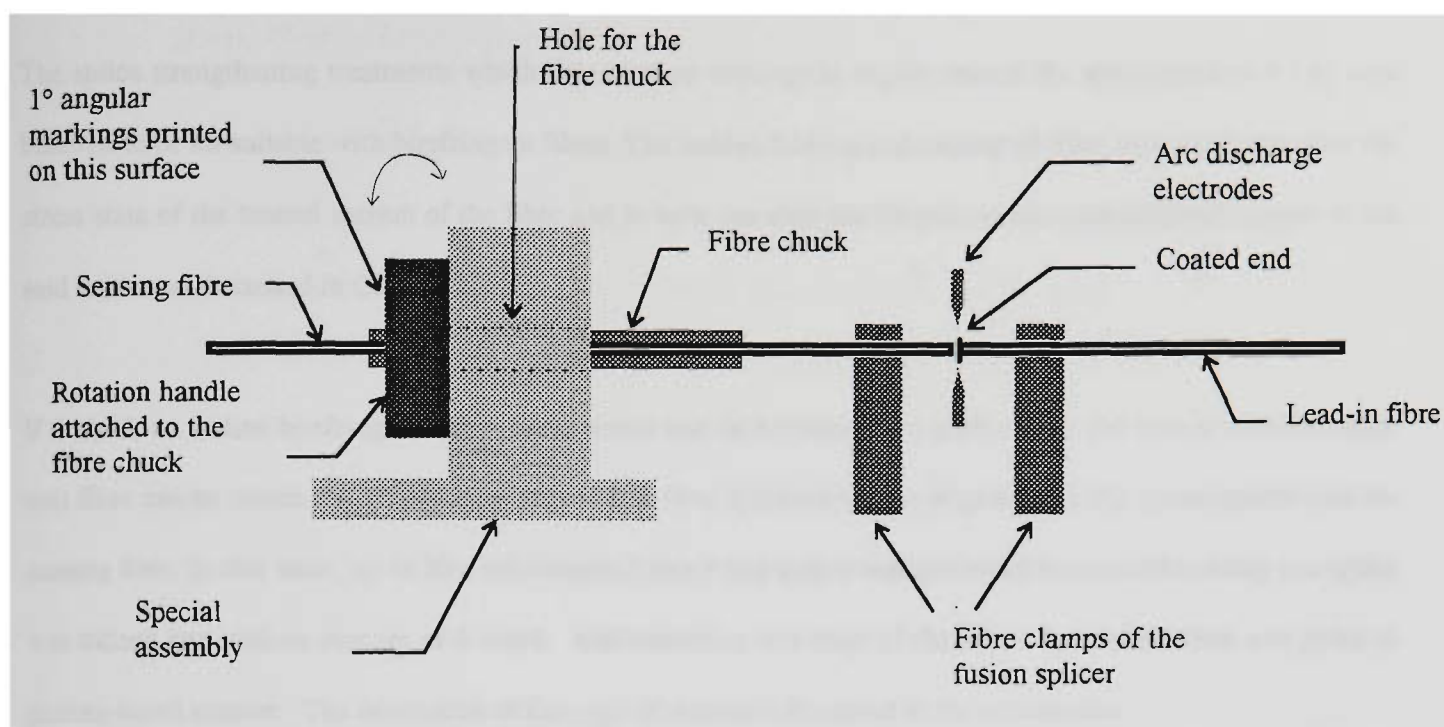


Figure 5.10: Schematic diagram of the special attachment which provided controlled rotation of a fibre.

After the birefringent axes of the lead-in and sensing fibres had been aligned, the two fibres were fused. The post-fusion extinction ratio and transmission loss were then assessed. These two parameters describe the angular alignment of the polarisation axes and the lateral alignment of the fibre cores respectively.

The fast-axes of the lead-in and sensing fibres need not correspond to one another (Chapter 3). The function of each polarisation axis of the lead-in fibre is to guide light into and out of each polarisation axis of the Fabry-Pérot cavity (sensing fibre). In other words the relative angle between the fast axes of the lead-in and sensing fibres can either be 0° or 90° .

The highly coherent LD output can affect the accuracy of the launching parameter because any cross-coupled beam can coherently interfere with the originally-guided beam on a polarisation axis. However, intrinsically-induced polarisation cross-coupling was assumed to be negligible because of the short length of the fibres involved. The extrinsically-induced cross-coupling can be minimised by eliminating sharp bends and reducing the magnitude of any external force squeezing on the fibre.

The splice strengthening treatments which depended on heating the region around the splice (section 5.1.4) were believed to be un-suitable with birefringent fibres. The sudden heating and cooling of these treatments can alter the stress state of the treated section of the fibre and in turn can alter the thermal-stress-induced birefringence of the said section as discussed in Chapter 4.

If desired, an in-line birefringent Fabry-Pérot sensor can be fabricated. In such a case, the face of another (lead-out) fibre can be coated. A polarisation axis of this fibre is then similarly aligned with the concatenated lead-in-sensing fibre. In this work, no in-line birefringent Fabry-Pérot sensor was fabricated because fabricating one splice was tedious and took an average of 3 hours. Additionally at this stage of the research, consideration was given to grating-based sensors. The fabrication of this type of sensors is discussed in the next section.

5.3 Grating-Based Birefringent Optical Fibre Fabry-Pérot Sensors.

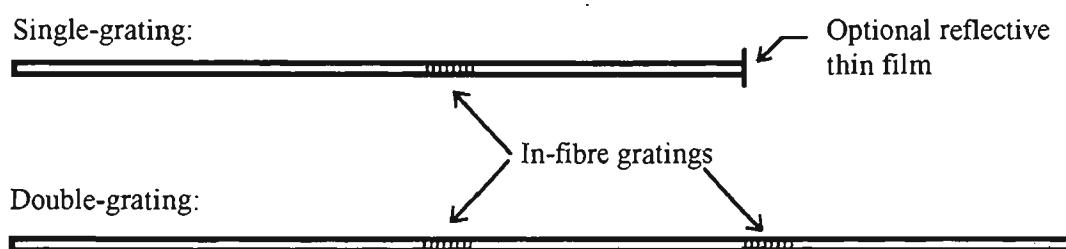


Figure 5.11 Schematic diagram of the grating-based Fabry-Pérot sensors.

In this work two types of birefringent Fabry-Pérot sensors with fibre Bragg gratings (FBGs) were fabricated (Figure 5.11). The first type involved one FBG and a coated distal end whilst the second involved two FBGs. In the case of the single-grating sensor, after the grating has been written, the fibre is further cleaved to form the second Fabry-Pérot mirror. The reflectance of this cleaved end can be increased with a deposited thin film. In the case of the double-grating sensor, each of the FBGs needs to be written separately. One of the advantages of the double-grating sensor is its suitability for serially-multiplexing several fibre Fabry-Pérot sensors.

5.3.1 Single-Grating Birefringent FFPSs

Optical Fibre Technology Centre (OFTC) in Sydney, Australia was contracted to fabricate two gratings, *Grating1* and *Grating2*, written on supplied 3M FS-HB-4211 birefringent fibres. The actual fabrication method they used was not known. Presumably they used a two-beam interference fabrication method similar to that of Meltz *et al.* [1989]. These gratings were initially used to develop single-grating sensors while our grating fabrication facility was in the process of being assembled. Figure 5.12 and Figure 5.13 show the transmission spectra of these Bragg gratings. The noise in the spectra is due to the fact that the optical signal from the Bragg grating was near the noise floor of an ANDO AQ3610B optical spectrum analyser (OSA). Naturally, the gratings exhibit two Bragg resonances, one along each polarisation axis. The resonance in the lower end of the spectrum is that along the fast axis of the birefringent fibre. The FWHM bandwidth of the axial gratings in Figure 5.12 and Figure 5.13 was about 0.17 ± 0.1 nm. The average Bragg wavelengths of *Grating1* and *Grating2* are 783.41 nm and 784.37 nm respectively.

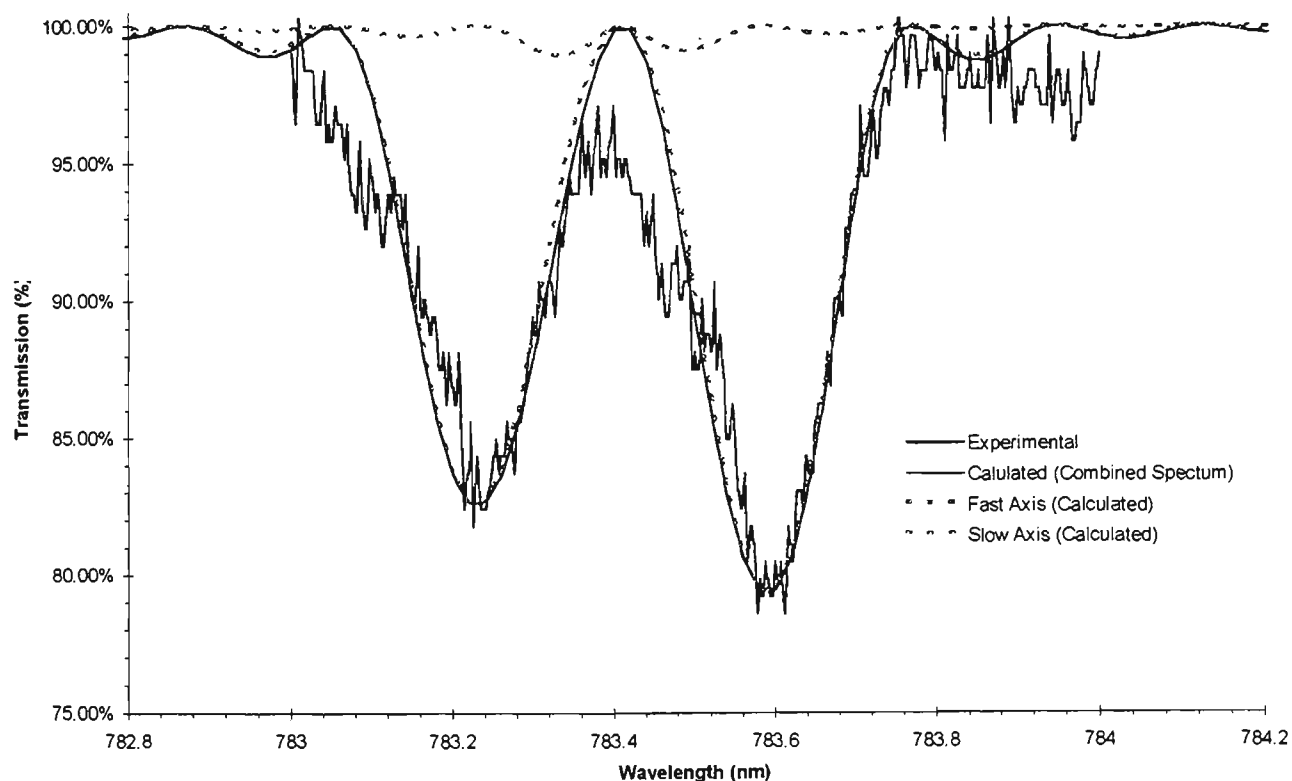


Figure 5.12: Experimental and calculated transmission spectra of a fibre Bragg grating written in birefringent fibre single-mode at 785 nm (*Grating1*). The dotted lines are the calculated spectra for each polarisation axis grating.

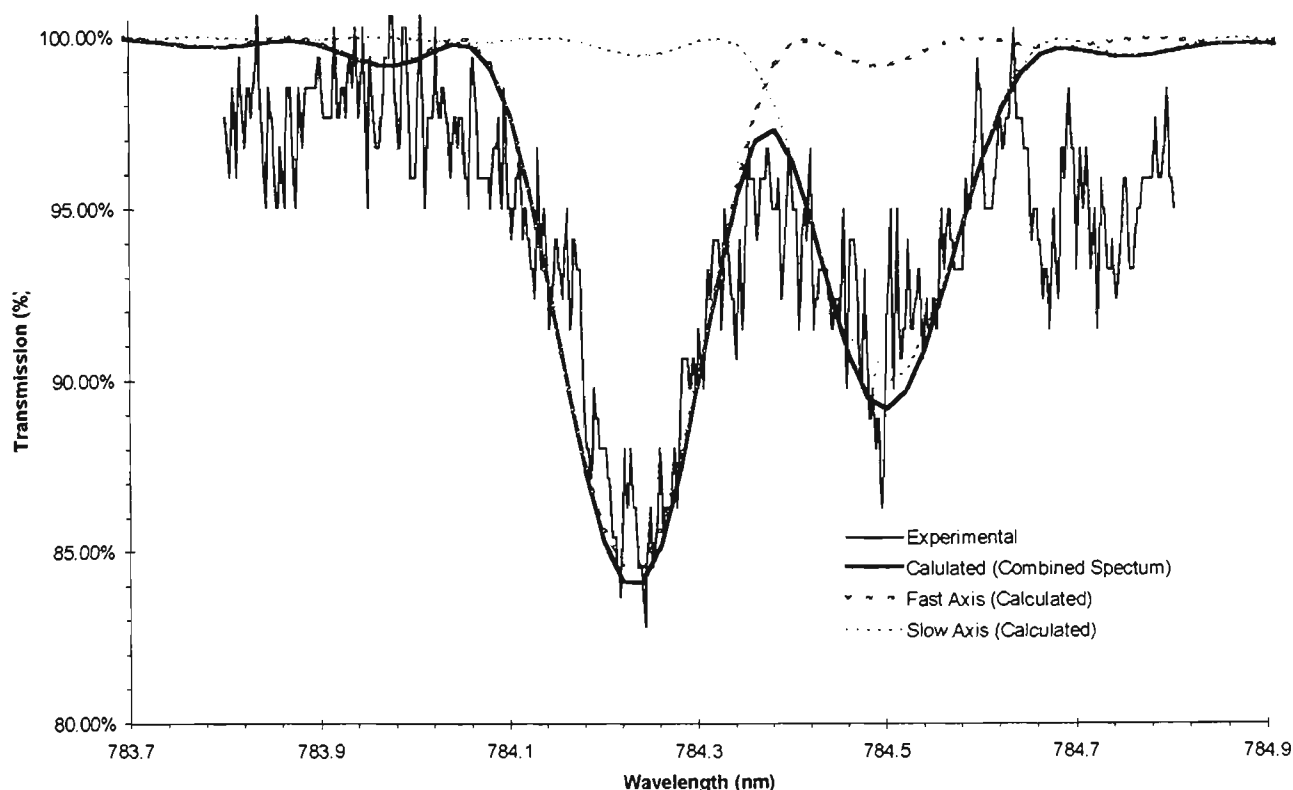


Figure 5.13: Experimental and calculated transmission spectra of a fibre Bragg grating written in birefringent fibre single-mode at 785 nm (*Grating2*). The dotted lines are the calculated spectra for each polarisation axis grating.

The spectra shown in Figure 5.12 and Figure 5.13 describe the combined transmission spectrum of the two axial grating as white light source used was unpolarised and hence excited both axes of the birefringent in-fibre grating with equal intensities, the spectra in Figure 5.12 and Figure 5.13 show the 50:50 combination of the transmission spectra of the axial Bragg gratings. In Chapter 7, a high-resolution spectrum of *Grating1* was obtained by employing a novel real-time method of monitoring the fringe visibility of *HibiGrat*, the sensor fabricated with *Grating1* as its proximal mirror.

The effective cavity length of *HibiGrat* is 15 mm. To measure this cavity length, a 637 nm LD was used to illuminate the sensor. The 6 mm section of the sensor which subsequently glowed identified the location of the grating. The centre of this glow was assumed to be the centre of the grating. The distance from the centre of the grating to the cleaved distal end of the sensor was measured to be 15 mm. The temperature and strain sensitivities of the sensor are presented Chapter 7.

Several parameters of the grating are required in order to predict the performance of the grating-based sensors. Unfortunately the parameters of the gratings were not supplied by OFTC. Thus, a Mathematica program was written to determine these parameters by fitting the experimental transmission spectra with theoretical spectra. Figure 5.12 and Figure 5.13 also show the calculated transmission spectra of *Grating1* and *Grating2*. Table 5.4 shows the parameters determined by the Mathematica program.

Parameter		<i>Grating1</i>		<i>Grating2</i>	
		Fast axis	Slow axis	Fast axis	Slow axis
Coupling coefficient	η_b	0.782141			
Pitch length	Λ	267.86 nm		268.20 nm	
Length	ℓ_b	1.172 mm		1.165 mm	
Refractive index	n_b	1.462	1.46267	1.462	1.46250
Apparent birefringence	$B' =$ $\Delta n_{sf} =$ $n_s - n_f$	6.7×10^{-4}		5.0×10^{-4}	
Bragg wavelength	λ_b	783.23 nm	783.59 nm	784.23 nm	784.50 nm
Bragg separation	$\Delta \lambda_b^{sf}$	0.36 nm		0.27 nm	
FWHM bandwidth	$\Delta \lambda_b$	0.170 nm	0.172 nm	0.170 nm	0.166 nm
Bragg reflectance	R_b	17.5 %	20.7 %	15.5 %	10.0 %
Index modulation	Δn_b	1.21×10^{-4}	1.34×10^{-4}	1.14×10^{-4}	0.90×10^{-4}
Index modulation birefringence	$\Delta n_b^{sf} =$ $\Delta n_b^s - \Delta n_b^f$	1.2×10^{-5}		-2.4×10^{-5}	

Table 5.4: Calculated parameters for the gratings shown in Figure 5.12 and Figure 5.13.

The value used in the calculation for coupling coefficient η_b was $\eta_b = 0.782141$. This value was determined from the dimensions of the birefringent fibre (see Chapter 4). Practically the same value of η_b was used for both polarisation axes because of the slight difference in the corresponding axial refractive index values. The average refractive index of the core employed in the calculations, $n_b = 1.462$, was the experimentally determined group core refractive index value (Appendix A). Although this value was not correct to be used with gratings, it was

nevertheless believed to be the best value available to be used in the calculations. The actual average core refractive index within the grating was different from that of the usual effective core refractive index due to the DC photo-induced refractive index change.

The apparent birefringence of the fibre, Δn_{sf} , can be inferred from the Bragg wavelength separation of the axial gratings. From Figure 5.12, Figure 5.13 and the theoretical calculations, Δn_{sf} was about 6.7×10^{-4} and 5.0×10^{-4} for *Grating1* and *Grating2* respectively. These values were different from the expected value of $\Delta n_{sf} = 4 \times 10^{-4}$ which was calculated from the beat-length of 1.6 mm at 633 nm (measured by the manufacturer).

The slow-axis Bragg grating was expected to exhibit a greater reflectance assuming that both axes experienced the same index modulation following the couple-mode theory of FBGs. This expectation was observed in *Grating1* but not in *Grating2*. The photo-induced refractive index change in germano-silicate fibre has both a DC (slowly-varying) and an AC component. The AC component was responsible for the resonance effect whilst the DC component and the pitch length of the grating determined the Bragg resonance wavelength. Figure 5.13 then suggests that the slow-axis of *Grating2* experienced both a greater AC and DC refractive index change than its fast-axis compared with those of *Grating1*. Clearly, the writing conditions in the fabrication of the two Bragg gratings (*Grating1* and *Grating2*) were different.

Aside from illustrating that the fast-axis grating had a greater peak reflectance value, Figure 5.12 and Figure 5.13 show that the Bragg wavelength separation of the axial gratings for *Grating2* (0.27 nm) was shorter compared with that of *Grating1*. Having different refractive index change induced on the same type of birefringent fibre implied that the photo-induced refractive index change has a birefringent character. Poirier *et al.* [1993] had described the model of the defect centres associated with 245 nm absorption band of germano-silicate fibres are preferentially excited and bleached by UV light polarised along the dipole moment of the defect centres, *i.e.* the orientation of the polarisation of the writing beam determines the orientation of the photo-induced birefringence. In addition, this photo-induced birefringence may enhance or relieve the intrinsic birefringence of an optical fibre [Bardal *et al.*,

1992]. This enhancement or relief of the total birefringence can explain the difference between the Bragg wavelength separation of *Grating1* and *Grating2* (Figure 5.12 and Figure 5.13).

The significant difference of $\sim 25\%$ between the Bragg wavelength separation of the two gratings implies that the photo-induced birefringence was about an order of magnitude less than the birefringence of the fibre. The calculated (absolute) photo-induced birefringence for *Grating1* and *Grating2* are 1.2×10^{-5} and 2.4×10^{-5} respectively (Table 5.4). These conclusions agreed with the results of Erdogan and Mizrahi [1994] who had measured photo-induced birefringence between 1×10^{-5} to 6×10^{-5} in different photosensitive fibres.

5.3.2 Dual-Grating In-line FFPSs

In this work several gratings were inscribed in a birefringent fibre with the intention of fabricating in-line FFPSs. This ability to write gratings in-house allowed us to determine the grating parameters and to tailor-design gratings. The fabrication of these gratings and the in-line sensors are described in the following discussions.

Of all the methods for fabricating FBGs (see review in Rao [1997] and Kersey *et al.* [1997]), the phase-mask method is the simplest approach (Figure 5.14). It offers greater immunity from mechanical vibration and requires less optical components to implement. This method exploits the diffraction interference pattern impressed on a fibre produced by a UV beam through a phase mask [Anderson *et al.*, 1993; Hill *et al.*, 1993]. The novelty of this scheme (Figure 5.14) is that the in-fibre grating spacing depends only on the pitch of the phase-mask and not on the wavelength or the angle of incidence of the UV beam [Anderson *et al.*, 1993]. Hence the method is less sensitive to vibration as long as the relative position of the fibre and the mask was maintained. Long-length and hence narrow-bandwidth gratings had been achieved by translating either the UV beam [Rourke *et al.*, 1994] or the fibre-phase-mask assembly [Martin & Ouellette, 1994]. On the other hand, short-length grating can be envisioned with spatial apertures. The disadvantage of the phase-mask method was a fixed pitch length. Unfortunately the grating spacing of the phase mask can only be slightly tuned thermally or mechanically or alternatively pre-straining the fibre during grating inscription [Zhang *et al.*, 1994b].

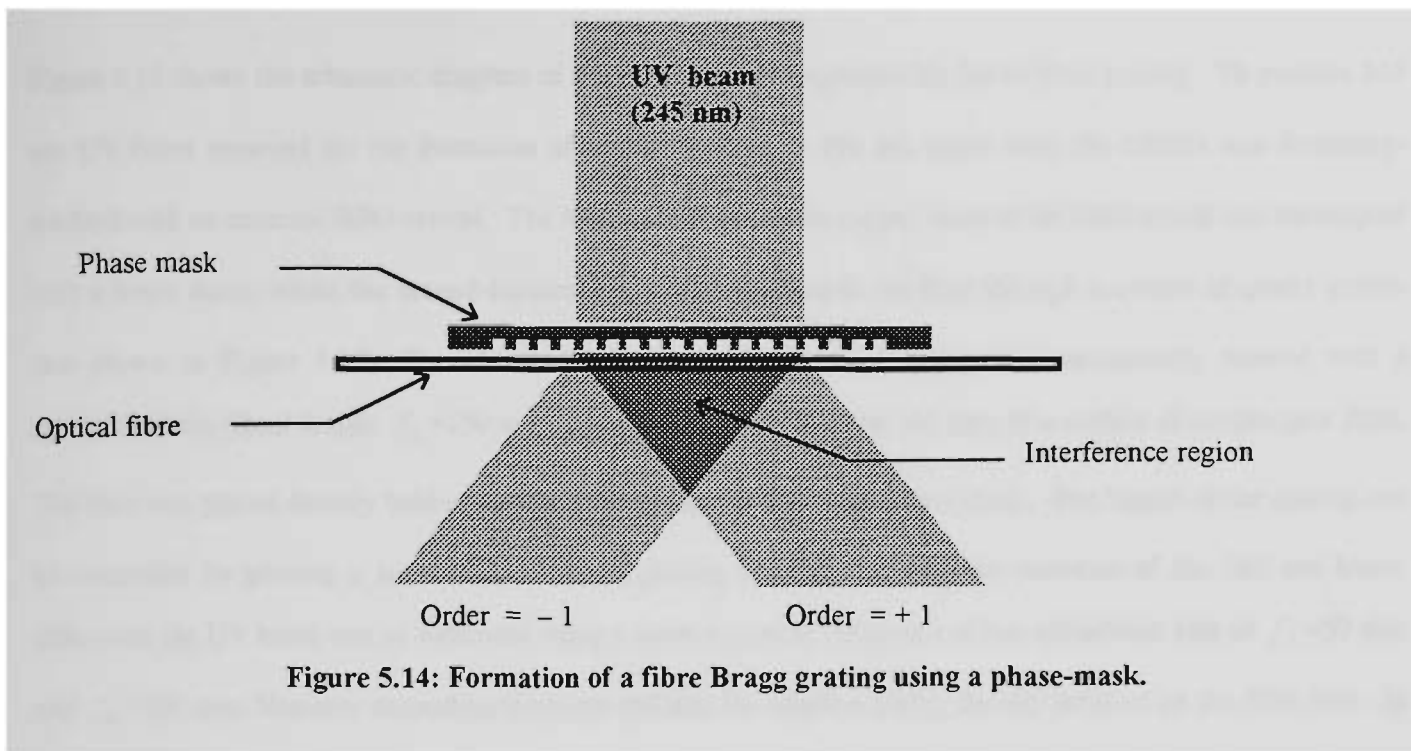


Figure 5.14: Formation of a fibre Bragg grating using a phase-mask.

The FBGs fabricated at the Optical Technology Research Laboratory (OTRL) used a transmission-type phase-mask and a Spectra-Physics MOPO light source. The MOPO light source consists of a Quanta-Ray GCR-230 Q-switched Nd:YAG laser (Master Oscillator) coherently seeding a Quanta-Ray MOPO-730 OPO (Optical Parametric Oscillator) module which has an internal Beta Barium Borate (BBO) nonlinear crystal. The MO-OPO (or MOPO) tandem system produced widely tunable and highly intense pulses with pulse-width less than 10 ns at a maximum repetition rate of 10 Hz.

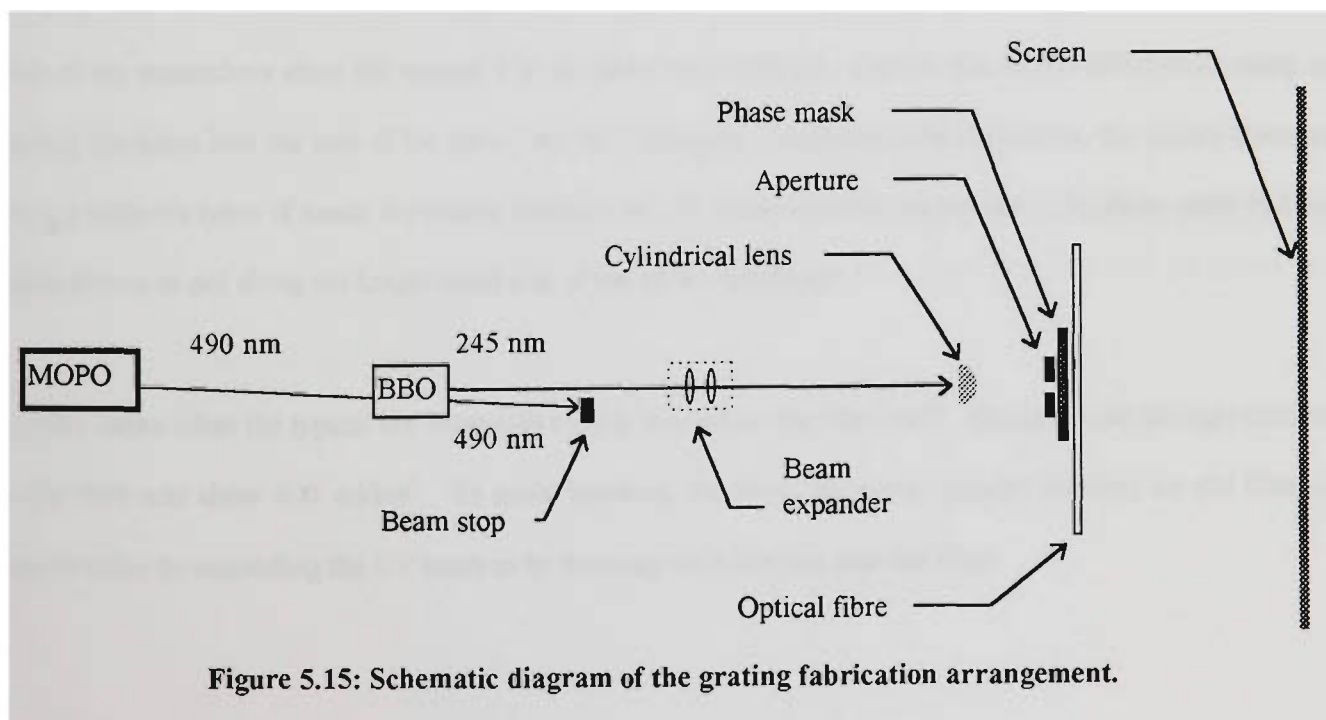


Figure 5.15: Schematic diagram of the grating fabrication arrangement.

Figure 5.15 shows the schematic diagram of the fabrication arrangement for the in-fibre grating. To produce 245 nm UV beam required for the formation of in-fibre grating, a 490 nm beam from the MOPO was frequency-doubled with an external BBO crystal. The fundamental-harmonic output beam of the BBO crystal was interrupted with a beam dump whilst the second-harmonic was directed towards the fibre through a system of quartz prisms (not shown in Figure 5.15). The 245 nm beam with a diameter of 3 mm was subsequently focused with a cylindrical lens (focal length $f_L=150$ mm) into a thin optical line near the core of a section of birefringent fibre. The fibre was placed directly behind the transmission side of the quartz phase-mask. The length of the grating can be controlled by placing a suitable aperture for grating lengths less than the diameter of the 245 nm beam. Otherwise the UV beam can be expanded using a beam expander composed of two cylindrical lenses of $f_L=50$ mm and $f_L=100$ mm. However expanding the beam reduced the effective energy density incident on the fibre core. In practice, such reduction in the incident energy density were sometimes necessary in order to avoid the 1 J/cm^2 damage threshold for the phase-mask or the fibre. The inscription was monitored by determining the transmission spectrum of the fibre using an ANDO AQ3610B optical spectrum analyser whilst the fibre was illuminated with a white-light source.

Made of thick white cardboard and placed after the phase-mask-fibre assembly (Figure 5.15), the screen served a dual purpose. First it acted as an absorber of UV radiation not absorbed by the optical fibre. This ensured the safety of the researchers since the unused UV radiation was captured. Second, the screen aided in focusing and aligning the beam into the side of the fibre. As the UV beams were absorbed by the screen, the screen fluoresced showing different types of bands depending whether the UV interferometric pattern from the phase-mask had been projected onto or not along the longitudinal axis of the fibre respectively.

The fibre broke when the typical UV beam was exactly focused on the fibre itself. The measured damage threshold for the fibre was about 600 mJ/cm^2 . To avoid breaking the fibre, the energy density incident on the fibre was reduced either by expanding the UV beam or by focusing the beam just near the fibre.

The photo-induced refractive index change in germanium-doped silica fibre required exposure to relatively large energy density of UV beam. However, the photo-sensitivity of the fibres can be enhanced when the fibres had been previously exposed to high pressure of hydrogen or deuterium [Lemaire *et al.*, 1993; Mizrahi *et al.*, 1993]. These hydrogen-treated fibres then required much lower energy density to induce photo-refractive index change.

The birefringent fibres used were hydrogenated. They were inserted inside a specially designed capsule which was filled with 70 atm of hydrogen. The capsule which contained the fibres was kept at a temperature of 100 °C for about 16 hours. Subsequently the internal pressure of the capsule at this temperature reached about 100 atm. The elevated temperature and pressure enhanced the permeability of hydrogen into the core of the fibres and thus accelerated the enhancement of the photo-sensitivity of the fibre. Typically, the fibres were left inside the pressurised capsule until the fabrication of the grating was about to commence.

The spectrum of one of the initial gratings written on birefringent fibres, *Grating3*, is shown in Figure 5.16. The spectrum of *Grating3*, as expected exhibited two Bragg wavelengths as a consequence of the birefringence of the fibre. The parameters of the grating were deduced from the theoretical fit of the spectrum. Table 5.5 summarised the results of the fit. The phase-mask employed had grooves spaced 536.2 nm apart, This means that the grating pitch was 268.1 nm. From the axial Bragg wavelengths, the effective core refractive indices of the fast and slow axis are 1.4578 and 1.45845 respectively. These values imply the earlier refractive index value used in the earlier calculations in this work, $n_b = 1.462$, gave an error of at most 0.3% and thus the previous calculations based on $n_b = 1.462$ were not re-calculated. The separation of the two Bragg wavelengths was about 0.35 nm and indicated a birefringence Δn_f of about 6.7×10^{-4} . On the other hand, the photo-induced birefringence was calculated to be 2×10^{-5} in agreement with the results from the earlier gratings.

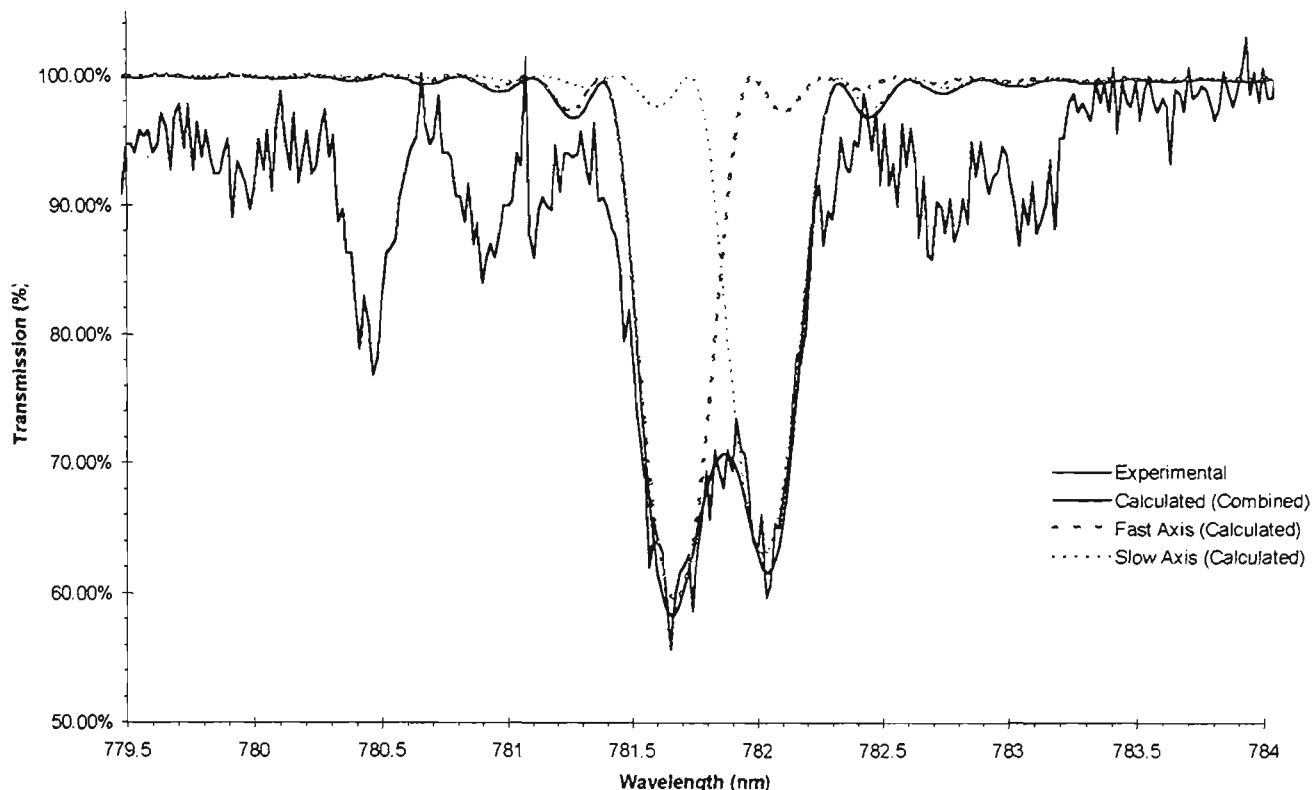


Figure 5.16: Transmission spectrum of a Bragg grating written on birefringent fibre (*Grating3*).

Figure 5.16 shows side-lobes which were not accounted for by the theoretical fit and hence their origin maybe a result of other effects. It is most likely that coupling between the two polarised core modes may have been induced as well. This effect is similar to the effect exploited to fabricate photo-induced rocking filters [Russel & Hand, 1990; Kanellopoulos *et al.*, 1991c; 1992; Hill *et al.*, 1991].

The calculated grating length of 0.72 mm for *Grating3* was about 4 times less than the diameter of the UV writing beam (3 mm). This value may denote an effective beam width of the writing beam. In general the spatial intensity distribution of the writing beam was not always uniform. In fact, on some occasions the writing beam had “hot-spots” which broke the fibre during the initial few seconds of exposure. Certainly this condition was avoided and only beams with good profile were used in fabricating the gratings. The non-uniform distribution may explain the effective writing beam width lower than the diameter of the beam. This effective width implies a limited grating length. However, for the wide-bandwidth gratings envisioned in this work, this apparent upper limit to the length of the grating was more than adequate.

Parameter		Grating3	
		Fast axis	Slow axis
Coupling coefficient	η_b	0.782141	
Pitch length	Λ	268.1 nm	
Length	ℓ_b	0.717 mm	
Refractive index	n_b	1.4578	1.45845
Apparent birefringence	$B' =$ $\Delta n_{sf} =$ $n_s - n_f$	6.5×10^{-4}	
Bragg wavelength	λ_b	781.67 nm	782.02 nm
Bragg separation	$\Delta \lambda_b^{sf}$	0.35 nm	
FWHM bandwidth	$\Delta \lambda_b$	0.310 nm	0.3044 nm
Bragg reflectance	R_b	40.5 %	37.0 %
Index modulation	Δn_b	3.33×10^{-4}	3.13×10^{-4}
Index modulation birefringence	$\Delta n_b^{sf} =$ $\Delta n_b^s - \Delta n_b^f$	-2.0×10^{-5}	

Table 5.5: Calculated parameters for *Grating3* (Figure 5.16).

After fabricating several gratings on birefringent fibres, an in-line dual-grating birefringent FFPSs was attempted. The ideal parameters for the in-fibre Bragg gratings are presented in Table 5.6. These parameters assume that the average Bragg wavelength is 790.4 nm. This wavelength is the centre of the range of emission wavelengths which give stable single-longitudinal output of the modulated LD. A reflectance of 3% and bandwidth of 2 nm were desired for each axial grating. These values easily produce low-finesse interferometers along each axis of the sensor and also give a small magnitude for the anomalous dispersion over the bandwidth of the grating. To obtain a large bandwidth, the grating length must be very short, 0.1 mm.

The in-line sensors were produced using a double-slit aperture placed between the UV light source and the phase-mask. The double-slit aperture was specially crafted using a 0.3 mm thick cardboard paper. The slit width and separation were 0.2 mm and 10 mm respectively. These conditions imply grating lengths slightly smaller than 0.2 mm and a Fabry-Pérot cavity length of 10 mm. Although the ideal grating length desired was about 0.1 mm,

for an initial grating length, 0.2 mm was chosen in order to lower the refractive index modulation value required to produce some reflectance and to provide at least a bandwidth of 1 nm. The 245 nm UV beam was found not to diverge significantly through the 0.2 mm slits. The aperture nevertheless was placed immediately in-front of the phase-mask to minimise the diffraction of the UV beam (Figure 5.15).

Parameter		<i>Ideal Grating</i>	
		Fast axis	Slow axis
Coupling coefficient	η_b	0.782141	
Pitch length	Λ	271 nm	
Length	ℓ_b	0.1 mm	
Refractive index	n_b	1.458	1.45863
Apparent birefringence	$B' =$ $\Delta n_{sf} =$ $n_s - n_f$	6.3×10^{-4}	
Bragg wavelength	λ_b	790.225 nm	790.575 nm
Bragg separation	$\Delta \lambda_b^{sf}$	0.35 nm	
FWHM bandwidth	$\Delta \lambda_b$	2 nm	2 nm
Bragg reflectance	R_b	3 %	3 %
Index modulation	Δn_b	5.864×10^{-4}	5.867×10^{-4}
Index modulation birefringence	$\Delta n_b^{sf} =$ $\Delta n_b^s - \Delta n_b^f$	3×10^{-7}	

Table 5.6: Ideal parameters for gratings written on a birefringent fibre to form a Fabry-Pérot sensor.

There were initial attempts to write the two gratings simultaneously. The 245 nm beam was expanded to a diameter wider than the separation of the slits. However, no grating was formed even after 30 minutes of exposure. This may be due to the weaker energy density at the wings of the expanded UV beam compared at its

centre. Thus, each of the grating was then written one after the other by directing the unexpanded UV beam through each of the corresponding slits. Figure 5.17 shows the transmission spectra of the gratings which formed an in-line fibre Fabry-Pérot sensor (*InLineFPI*). The two gratings were each written for about 15 minutes with an effective incident energy density of 120 mJ/cm^2 . The spectrum of the first grating (Grating-Mirror 1) was obtained at conditions near the noise floor of the optical spectrum analyser. In hindsight, the noise in the spectrum could have been reduced by applying some averaging routine.

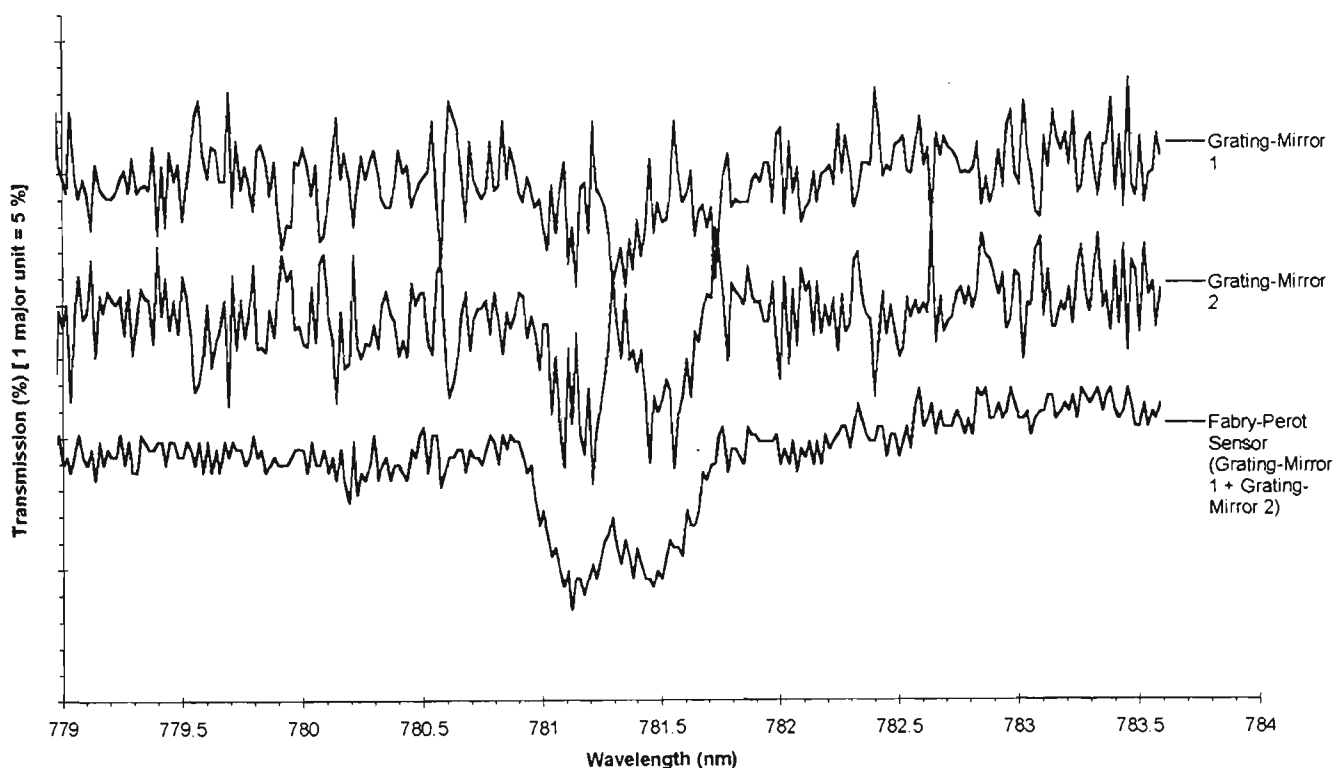


Figure 5.17: Transmission spectra of the two grating-mirrors written on a birefringent fibre to produce an in-line fibre Fabry-Pérot sensor (*InLineFPI*). For clarity, each spectrum has been vertically shifted in order to separate itself from the other spectra. Each data point composing the spectrum for the in-line sensor (labeled “Fabry-Pérot Sensor”) is the average of 20 samples. No averaging routine was performed with the spectrum of the first grating (labeled “Grating-Mirror 1”).

In Figure 5.17, the spectrum of the second mirror was derived by subtracting the spectrum of the first mirror from combined spectrum of the in-line sensor. Figure 5.17 shows that the spectrum of the second mirror exhibited evidently two Bragg resonances unlike that of the first mirror. This double-resonance feature was unexpected because the features of the wide-bandwidth axial gratings are not suppose to be distinguishable when the combined transmission spectrum of the axial gratings is obtained using an unpolarised white-light source. Ocular inspection of the slits after the fabrication of the second grating revealed that the focused UV beam had gradually cut

perpendicularly across the slits. This cut implies a longer length for the second grating and thus explains the narrower bandwidth properties of the second grating as shown in Figure 5.17. The reflectance of the axial gratings of the first mirror was about 2.5 % whilst those of the second mirror, about 4%. This means that the sensor is low finesse.

Other in-line double-grating FFPSs were fabricated with an improved double-slit aperture. As in the earlier case, the new double-slit aperture had a slit-width of 0.2 mm and a separation of 10 mm. Each of the slits consists of two layers of cardboard paper sandwiching stainless steel razor blades. The sharp edges of the razor blades defined the edges of the slits. The cardboard paper were employed primarily for safety since steel can reflect UV light. Thus the cardboard paper absorbed the unused UV beam and thereby fluoresced.

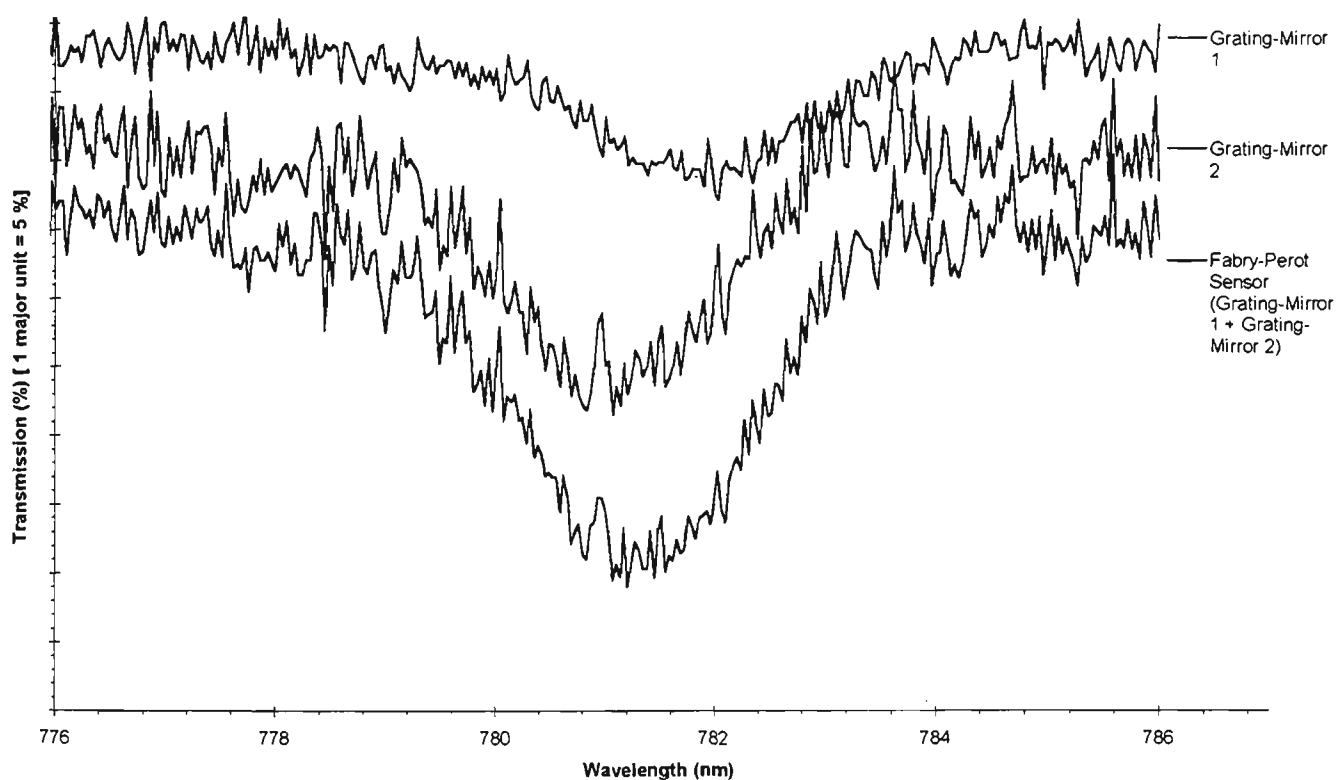


Figure 5.18: Transmission spectra of the two gratings written on a birefringent fibre to produce an in-line fibre Fabry-Pérot sensor (*InLineFP*).

Figure 5.18 shows the transmission spectra of the gratings employed to fabricate one of the in-line fibre Fabry-Pérot sensors using the new double-slit aperture (*InLineFP2*). The first grating written had an exposure time of about 10 minutes whilst the second 20 minutes. The effective incident energy density was about 60 mJ/cm^2 . The

estimated reflectance and bandwidth of the axial gratings are 4 % and 1.8 nm respectively for the first mirror, 8 % and 2.2 nm for the second mirror. The grating formation rate of *InLineFP2* was faster than that of *InLineFP1*. This greater value can be attributed to the better focusing of the UV interference patterns into the core of the fibre.

The spectra of *InLineFP1* and *InLineFP2* show that the average Bragg wavelength of their Fabry-Pérot mirrors do not coincide. In fact Figure 5.17 and Figure 5.18 show that the spectral location of the second grating-mirror was to the left of the first grating-mirror of the in-line sensors. This condition means the overall measurand range of the sensor is smaller than when the averaged Bragg wavelength of their Fabry-Pérot mirrors coincided. The overall range is still large though because of the large bandwidth of the axial gratings.

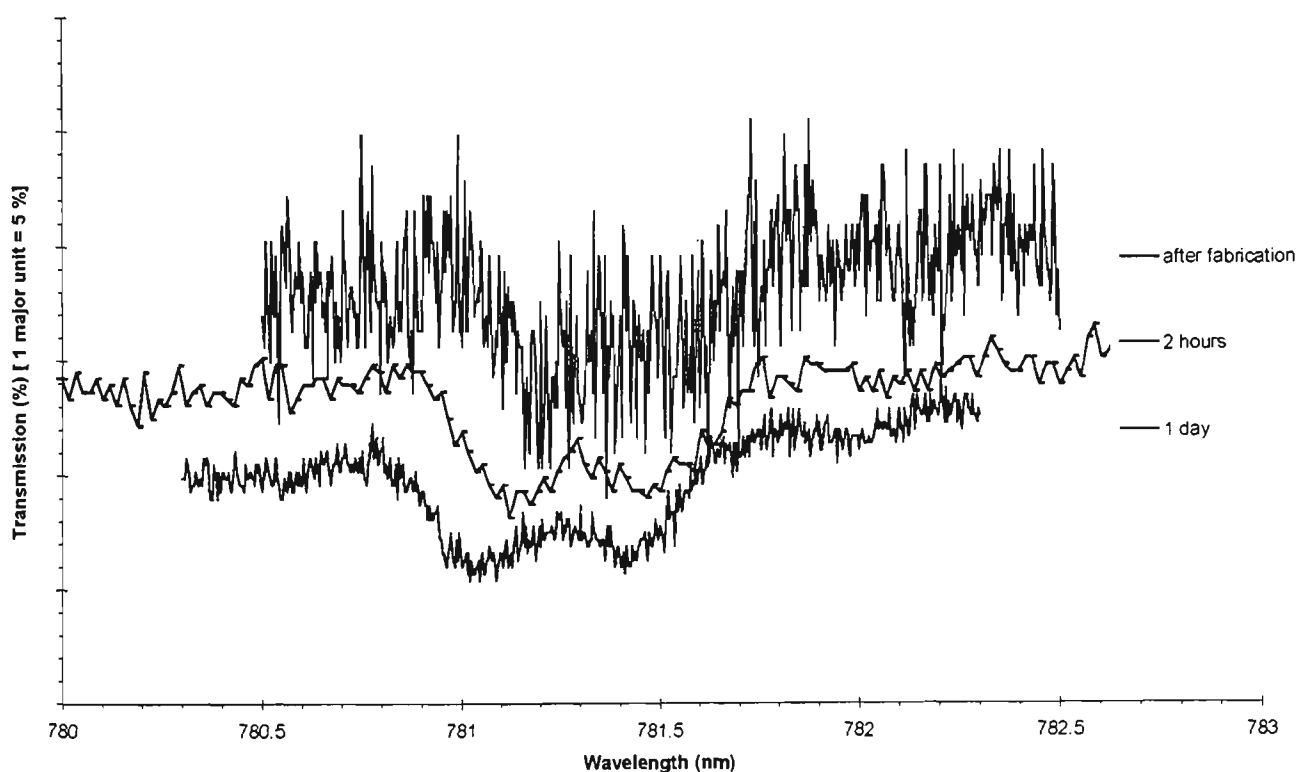


Figure 5.19: Transmission spectra of the two gratings written on a birefringent fibre to produce an in-line fibre Fabry-Pérot sensor (*InLineFP1*).

There is a slight complication with hydrogenating the birefringent fibres. When the combined transmission spectrum of the in-line Fabry-Pérot sensors was recorded after fabrication, the spectrum had shifted to lower wavelength values. For example, Figure 5.19 shows the shifts in the transmission spectrum of *InLineFP1*. *InLineFP1* shifted by 0.1 nm after 24 hours since fabrication. This was due to the fact that when hydrogen was

introduced into the core of the fibre, the effective core refractive index had increased. Thus when the hydrogen molecules outgas themselves from the core, the refractive index of the core decreased. Hence this wavelength shifts must be considered when the sensors are finally used.

No temperature or strain measurements were made with the in-line Fabry-Pérot interferometers fabricated including the two described in this section. This was because the LD output could not be tuned to the actual Bragg wavelength of the gratings without causing the LD output to mode-hop. Replacing the LD with another similar device gave similar results most probably because all the LDs were fabricated in the same batch. Had the wavelength of the LD fallen within the spectrum of the gratings, interferometric signals would have been expected even when the spectra of the first and second grating-mirrors did not exactly coincide because low optical signal can still be detected (Appendix B).

The measurements made with the sensors developed in this work are discussed in the Chapter 7. In the next chapter, the measurement arrangement used with the birefringent sensor is described.

Chapter 6:

A Birefringent Optical Fibre Sensing System for the Measurement of Temperature and Strain

This chapter describes an optical fibre sensing arrangement employing a birefringent fibre Fabry-Pérot sensor for the measurement of temperature and strain. The arrangement has four major components: the sensor, optical detection arrangement, signal processing and phase recording system. In this work, these components have been chosen such that localised measurement of temperature or strain can be obtained with high-resolution, large UMR and at a moderately fast rate.

6.1 The Optical Fibre Sensing Arrangement Compared With Its Closest Fore-Runner

In terms of operation principles, the arrangement described in this chapter (Figure 6.1) is similar to that employed by Farahi *et al.* [1990] (Figure 6.2). In this work, we have extended their arrangement in many aspects. A brief comparison is worthwhile. The chosen sensor configuration of this work and that of Farahi *et al.* was a Fabry-Pérot sensor formed in a birefringent single-mode fibre with thermally induced stress production parts. We used a fibre with an internal elliptical cladding (IEC-fibres) whilst Farahi *et al.* used a bow-tie fibre. In both cases, two Fabry-Pérot interferometers are formed, one along each polarisation axis.

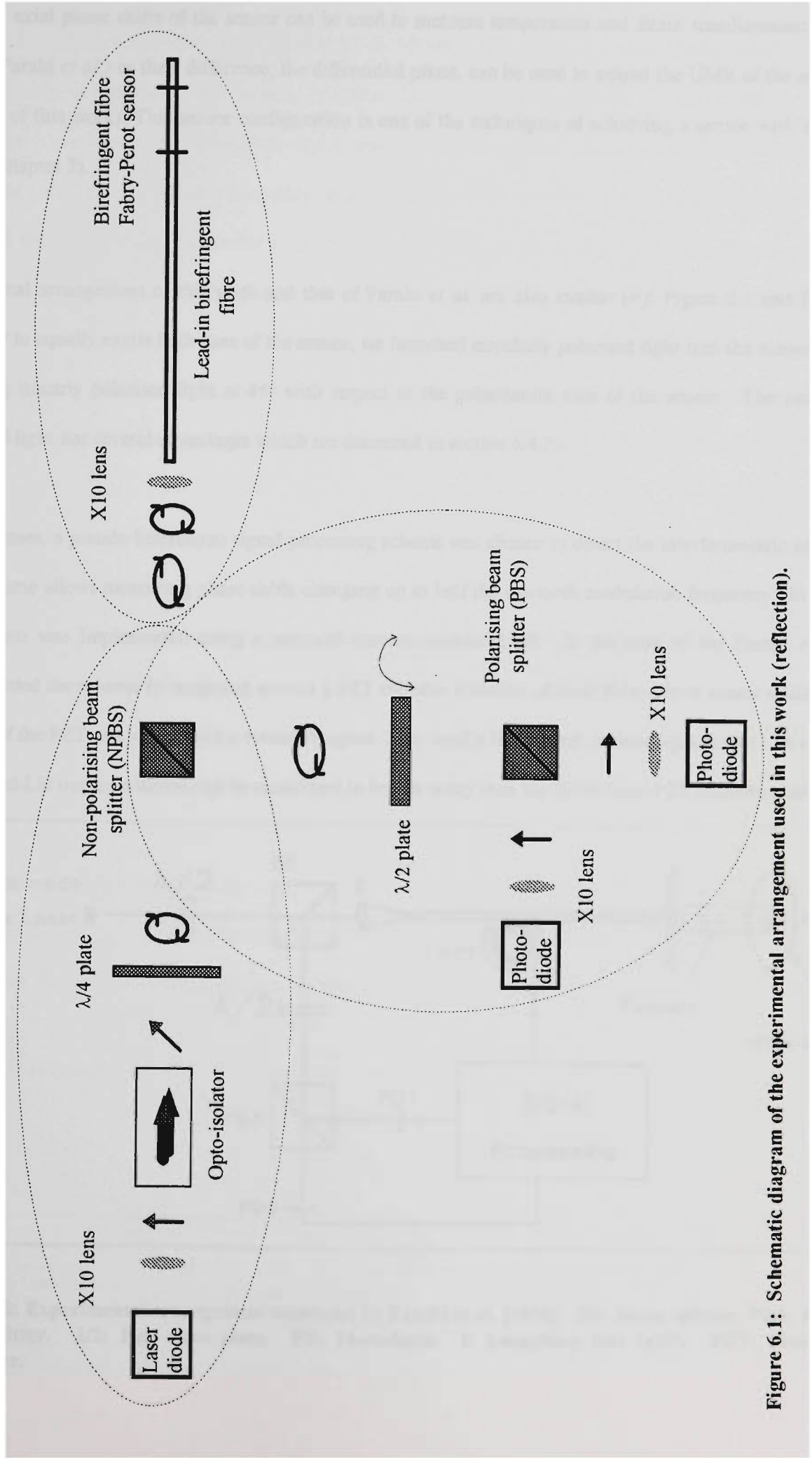


Figure 6.1: Schematic diagram of the experimental arrangement used in this work (reflection).

The two axial phase shifts of the sensor can be used to measure temperature and strain simultaneously (as in the case of Farahi *et al.*) or their difference, the differential phase, can be used to extend the UMR of the sensor (as in the case of this work). This sensor configuration is one of the techniques of achieving a sensor with an extended UMR (Chapter 2).

The optical arrangement of this work and that of Farahi *et al.* are also similar (*c.f.* Figure 6.1 and Figure 6.2). However to equally excite both axes of the sensor, we launched circularly polarised light into the sensor instead of orienting linearly polarised light at 45° with respect to the polarisation axes of the sensor. The use circularly polarised light has several advantages which are discussed in section 6.4.2.

In both cases, a pseudo-heterodyne signal processing scheme was chosen to detect the interferometric phase shifts. This scheme allows measuring phase shifts changing up to half the sawtooth modulation frequency. In this work, the scheme was implemented using a sawtooth-current-modulated LD. In the case of the Farahi *et al.*, they implemented the scheme by wrapping around a PZT cylinder a section of their Fabry-Pérot sensor while the input voltage of the PZT was varied with a sawtooth signal. They used a HeNe laser as their light source. In a sense, the modulated-LD implementation can be considered to be less bulky than the HeNe-laser-PZT implementation.

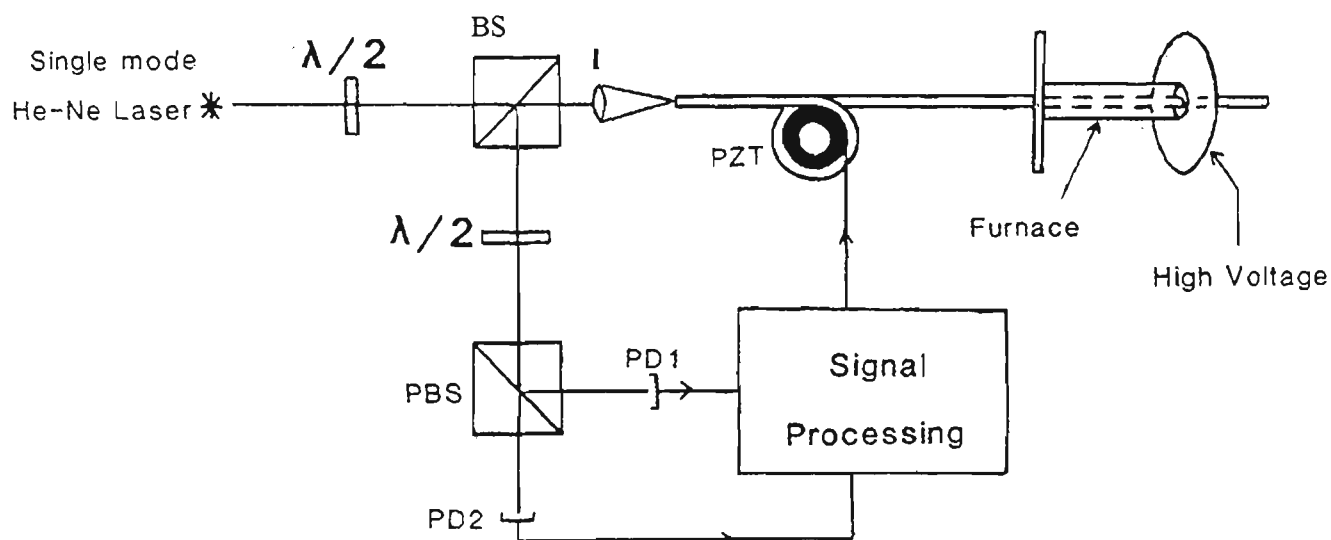


Figure 6.2: Experimental arrangement employed by Farahi *et al.* [1990]. BS: Beam splitter. PBS: Polarising beam splitter. $\lambda/2$: Half-wave plate. PD: Photodiode. l: Launching lens (x10). PZT: Piezo-electric transducer.

The implementation of Farahi *et al.* is suited to a Fabry-Pérot sensor with a long cavity within which only a section of their sensor is exposed to the measurand limiting its sensitivity to reasonable values. In this work, we have chosen to investigate short-cavity Fabry-Pérot sensors. The minimum cavity length was determined by the maximum chirp in the emission frequency of the modulated LD without any accompanying mode-hop effect. Although the phase-measurand sensitivity is proportional to the exposure length, these short-cavity sensors are still highly sensitive to measurands like temperature or strain (Chapter 4). In addition, short-cavity sensors can provide localised measurements which are desirable in many applications. They use a lead-in fibre which eliminates the interference involving the cladding or leaky modes. Moreover, the lead-in fibre naturally provides the first step in assembling an all-fibre arrangement and if desired, several sensors can be serially multiplexed on the same fibre line.

In this work, we investigated birefringent FFPSs either fabricated with fusion-spliced TiO_2 mirrors or in-fibre Bragg gratings. The fabrication of these sensors was one of the major challenges of this work (Chapter 5). These fabricated sensor were designed to be low-finesse because low-finesse FFPSs approximately give sinusoidal interferometric outputs (Chapter 3). This type of output is required by the pseudo-heterodyne signal processing scheme.

The digital electronic circuits we employed to measure the interferometric phase shifts with a resolution of $1:10^4$ enabled us to observe effects attributed to the non-ideal adjustments of the pseudo-heterodyne signal processing scheme and the dispersion of a Bragg grating reflector written in an optical fibre (Chapter 7).

6.2 Detailed Description of the In-Fibre Birefringent Fabry-Pérot Sensor

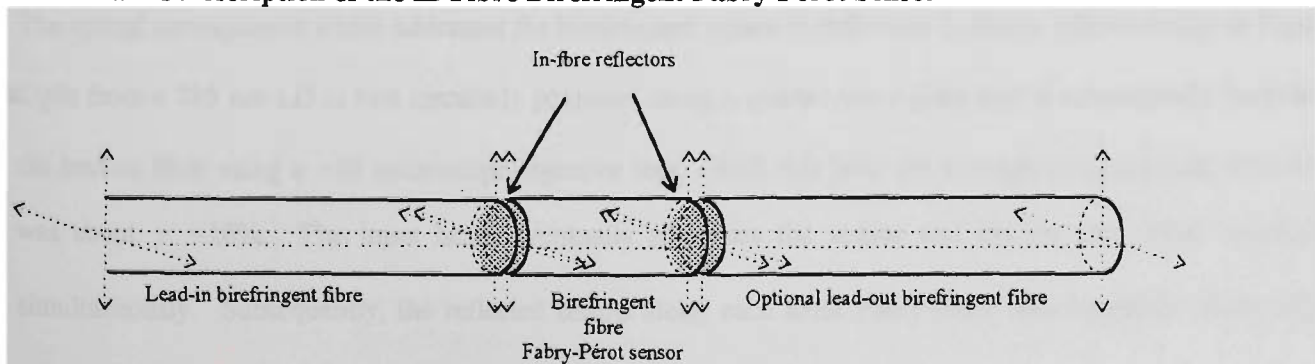


Figure 6.3: An in-fibre birefringent Fabry-Pérot sensor.

Figure 6.3 shows the in-fibre arrangement used a birefringent FFPS. The lead-in fibre waveguide and the Fabry-Pérot cavity are composed of the same type of polarisation-maintaining fibre. The polarisation axes of this lead-in fibre are aligned with those of the birefringent Fabry-Pérot cavity in order that each axial interferometer can be independently addressed in reflection. Optionally, the sensor can be concatenated with a lead-out fibre which provided a waveguide to address the sensor in transmission or to multiplexed with other Fabry-Pérot sensors.

The lead-in fibre provides the simplest mechanism for remote sensing and single-ended operation of the sensor without any additional optical components. The length of this fibre can be as long as desired to the upper limit determined by the crosstalk between the polarisation axes of the fibre as described by the parameter h , the coupling ratio per unit length of the fibre. With the specifications given by the manufacturer for the polarisation-maintaining fibre used (Table 6.1), a crosstalk of more than 1% appears only after a length of 1 km assuming no sharp bends are present along the fibre.

To avoid any inter-modal interference, the sensor needs to be operated in the single-mode regime. This is ensured by using a suitable light source. In this work, the LD used was chosen because its emission wavelength is greater than that of the 700 nm single-mode cut-off wavelength of the fibre. In addition, the lead-in fibre can also act as a mode filter. By using a sufficiently long lead-in fibre, any initial cladding and leaky modes is dissipated and only the fundamental-mode beam eventually reaches the sensor. Fortunately, the fibre used is a mode-stripping acrylic jacket. A length of about two meters is sufficient to remove any unwanted cladding modes.

6.3 Description of the Optical Fibre Sensing System

The optical arrangement which addresses the birefringent sensor in reflection is shown schematically in Figure 6.1. Light from a 785 nm LD is first circularly polarised using a quarter-wave plate and is subsequently launched into the lead-in fibre using a $\times 10$ microscope objective lens. With this lens, the average coupling ratio into the fibre was about $\gamma = 10\%$. The input beam eventually addresses the sensor and excites each axial interferometer simultaneously. Subsequently, the reflected beams along each axial Fabry-Pérot interferometer return following the reverse path taken by the initial input axial beams.

Component	Manufacturer and Part Number	Specifications	
LD	Hitachi HL7806G	Lasing wavelength Description Lasing material Structure Longitudinal-mode spacing Feature Monitor responsivity Maximum power Threshold current Slope efficiency Coherence length	~ 785 nm Single longitudinal mode AlGaAs Index-guided channel-substrate-planar (CSP) ~ 0.3 nm with built-in photodiode ~0.5 A/W 5 mW 45 mA @ 20 °C 0.28 mW/mA (measured) ~ 2 m (modulated)
Photodiodes	Optex OPF480	Material Collecting area Flux responsivity Rise time Peak wavelength	Silicon 1 mm x 1 mm ~ 0.5 A/W @780 nm 1 ns ($V_R = 15$ V, $R_L = 50 \Omega$, 10%-90%) 820 nm
Polarisation Maintaining Fibres	3M FS-HB-4211	Type Single-mode cut-off core/fibre/jacket radius Feature Estimated Delta Numerical aperture Beat length Attenuation Crosstalk parameter h Proof test level	Stress-induced elliptical cladding 700 nm 2.25/40/100 μ m Mode-stripping outer acrylic jacket 0.47 % 0.12 1.6 mm @ 633 nm 4.2 db/km @ 850 nm 10^{-5} / m 50 kpsi
Microscope objective lens	ELIZA	Magnification Numerical aperture	+10 0.25
Wave plates: half-wave quarter-wave	Melles Griot 02WRQ021/785 02WRQ001/785	Type Central wavelength Aperture Retardation tolerance	Quartz, multi-order Designed @ 785 nm 10 mm diameter $\lambda/500$
Polarisation beam splitter cube	Newport 05FC16PB.5	Operation wavelength Extinction ratio (experimental) Length of side	620 - 1000 nm s -beam = 0.6 % (-22.2 dB) p -beam = 3.3 % (-14.8 dB) 12.7 mm (0.5 in.)
Non-polarising beam splitter cube	Newport 05BC16NP.6	Operation wavelength Spectral tolerance Splitting ratio Length of side	780 nm \pm 3% 50/50 12.7 mm (0.5 in.)
Optical isolator	Optics for Research (OFR) IO-2-NIR2	Operating wavelength Transmittance Isolation Aperture	780 nm 94 % (test results) -40 dB (test results) 5 mm

Table 6.1: Specifications for the components comprising the sensing system.

To prevent any reflection from this face, the proximal end of the lead-in fibre can be polished at an angle of about 7° with respect to the plane perpendicular to the longitudinal axis of the fibre. This reflection is not desired for two main reasons. First, this reflection can otherwise coherently interfere with the returning beams and hence exhibit another Fabry-Pérot interference between this proximal face and the mirrors of the Fabry-Pérot sensor. This additional Fabry-Pérot effect occurs only when the length of the lead-in fibre is shorter than the coherence length of input beam. Although the lead-in fibre can be chosen to be long, this approach was not implemented because of the limited amount of the birefringent fibres available for this work. Secondly the intensity of the reflected beam from this end is greater than that of the beam coming from the sensor, this reflection contributes to an additional background intensity detected by the photodiodes (PDs). Thus, minimising the contribution of this reflection improves the electronic fringe visibility.

The returning beams from the sensor are diverted towards a polarising beam splitter (PBS) cube using a non-polarising beam splitter (NPBS) cube. The non-polarising properties of the NPBS is due to a specially designed thin-film deposited at the reflecting interface of the NPBS cube. This film exhibits equal reflectance of the *s*- and *p*-polarised beams. Since the properties of the thin-film are wavelength-dependent, the NPBS was fabricated to operate at a wavelength of about 785 nm.

The polarisation axes of the sensor were aligned with those of the PBS using a half-wave plate. In general the combined beam returning from the birefringent FFPS is elliptically polarised. However, the PBS conveniently decomposed this elliptically polarised beam into tangential beams which are the outputs of the two polarised interferometers. The intensities of these tangential beams were detected by silicon PDs.

The light source is a 5 mW Hitachi HL7806G LD lasing at a single longitudinal mode of ~ 785 nm. This mode of operation occurs if the LD is driven well above its lasing threshold. To prevent any undesirable optical feedback into the laser cavity, an opto-isolator was inserted between the LD device and the quarter-wave plate. The opto-isolator is composed of a Faraday rotator between two crossed polarisers. Hence the output beam is linearly polarised. This linearly polarised beam was converted into a circularly polarised light using a quarter-wave plate.

The quarter-wave and half-wave waveplates used were of the multi-order type and were designed to operate at ~ 785 nm with a tolerance of about 1.6 nm.

6.4 Jones Calculus Treatment

The overall optical system described in the last two sections can be analysed using Jones calculus [Jones, 1941; Hurwitz & Jones, 1941; Klinger *et al.*, 1990]. In such an analysis, the evolution of the amplitude and phase of the electric field of two perpendicular electromagnetic waves as these waves pass through a sequence optical elements are determined. Alternatively, these waves can be treated together as a single wave with two independent components. Hence in general the tip of the electric field of the combined wave follows an elliptical helix as the beam propagates. The ellipticity and orientation of the ellipse describe the state of polarisation of the light beam. Such a beam can be expressed as a Jones vector

$$\mathbf{E}_{in} = \begin{bmatrix} E_x \\ E_y \end{bmatrix}. \quad \text{Eq. 6.1}$$

When the beam expressed in Eq. 6.1 travels through an optical element, the emerging beam can be expressed as

$$\mathbf{E}_{out} = \mathbf{J} \cdot \mathbf{E}_{in} = \begin{bmatrix} J_{xx} & J_{xy} \\ J_{yx} & J_{yy} \end{bmatrix} \begin{bmatrix} E_x \\ E_y \end{bmatrix} \quad \text{Eq. 6.2}$$

where \mathbf{J} is the characteristic Jones matrix for the optical element. The diagonal elements in \mathbf{J} can be interpreted as direct transformation of each polarised beam whilst the off-diagonal elements the cross-coupling between the two orthogonal input beams. Eq. 6.2 completely describes the resulting beam due to an input beam incident on the optical element. It follows therefore that an optical system comprising of several optical elements can equivalently be described as a single (total) Jones matrix \mathbf{J}_t , the matrix product of the Jones matrices of the individual optical elements, *i.e.*

$$\mathbf{E}_{out} = \mathbf{J}_t \cdot \mathbf{E}_{in} = \mathbf{J}_n \cdot \mathbf{J}_{n-1} \cdot \dots \cdot \mathbf{J}_2 \cdot \mathbf{J}_1 \cdot \mathbf{E}_{in} \quad \text{Eq. 6.3}$$

where \mathbf{J}_1 and \mathbf{J}_n are the first and last optical element encountered by the beam respectively.

The components of the total electric field are spatially orthogonal and hence do not interfere. However, these components can interfere when they are brought together. The light beam is said to be unpolarised if its two orthogonal components do not interfere when brought together and polarised if they interfere. In practice no beam

is perfectly unpolarised or polarised and hence in general most beams are partially polarised. Since Jones calculus operates only on electric fields, it is inadequate for partially polarised beams. An intensity treatment is more appropriate and the corresponding analysis is known as Mueller calculus [Jerrard, 1982]. However since the coherence length of the LD used in this work is much longer than the OPD of the sensors, the Jones calculus treatment suffices.

For the optical arrangement described in Figure 6.1, the total electric field emerging either from the side ($b = y$) or the straight-through ($b = x$) beams of the polarising beam splitter can be described as follows

$$\mathbf{E}_{out,b} = \mathbf{J}_t \cdot \mathbf{E}_{in} = \mathbf{J}_{detection,b} \cdot \left\{ \mathbf{J}_{Fresnel} + \mathbf{J}_{in-fibre} \right\} \cdot \mathbf{J}_{launching} \cdot \mathbf{E}_{in} \quad \text{Eq. 6.4}$$

where $\mathbf{J}_{Fresnel}$ describes the Fresnel reflection from the proximal face of the lead-in fibre while the other three Jones matrices are the launching, in-fibre and detection sub-systems of the experimental arrangement. The input beam in Eq. 6.4 is the output beam of the opto-isolator. This beam is linearly polarised. For the rest of the analysis, this input beam (normalised) is defined to be along the x-axis, *i.e.*

$$\mathbf{E}_{in} = \begin{bmatrix} 1 \\ 0 \end{bmatrix}. \quad \text{Eq. 6.5}$$

The other three Jones matrices in Eq. 6.4 are given by

$$\mathbf{J}_{launching} = \mathbf{R}(S) \cdot \mathbf{J}_{NPt} \cdot \mathbf{R}(Z) \cdot \mathbf{J}_{quarter} \cdot \mathbf{R}(Q), \quad \text{Eq. 6.6}$$

$$\mathbf{J}_{in-fibre} = \sqrt{\gamma} \cdot \mathbf{J}_{lead} \cdot \mathbf{R}(U) \cdot \mathbf{J}_{FP} \cdot \mathbf{R}(U) \cdot \mathbf{J}_{lead}, \text{ and} \quad \text{Eq. 6.7}$$

$$\mathbf{J}_{detection,b} = \mathbf{J}_{P,b} \cdot \mathbf{R}(H) \cdot \mathbf{J}_{half} \cdot \mathbf{R}(W) \cdot \mathbf{J}_{NPr} \cdot \mathbf{R}(S). \quad \text{Eq. 6.8}$$

γ is the intensity coupling efficiency into the fibre and is assumed to be equal for both polarisation axes. The polarisation coordinate system of the left-hand side in Eq. 6.6, Eq. 6.7 and Eq. 6.8 is that of the distal optical element (described by the first matrix element in the right-hand side of each equation). The Jones matrices are those for the individual optical elements in the optical detection system and are presented in Table 6.2. $\mathbf{R}(Q)$, the transformation due to an angular rotation of Q , accounts for the relative angular orientation of the polarisation axes of two adjacent optical elements and is measured anti-clockwise from the positive x-axis from the first element. Q is the angle between the x-axis of the input beam and that of the quarter-wave plate, Z between the x-axis of quarter-wave plate and that of the NPBS, S between the x-axis of the NPBS and that of the lead-in fibre,

U between the x-axis of the lead-in fibre and that of the Fabry-Pérot sensor, W between the x-axis of the NPBS and that of the half-wave plate and H between the x-axis of the half-wave plate and that of the PBS.

Eq. 6.6, Eq. 6.7 and Eq. 6.8 divides Eq. 6.4 into three major groups of optical components comprising the entire optical arrangement. $\mathbf{J}_{in-fibre}$ determines the resulting electric field after an initial field has transverse the lead-in fibre and reflected from the sensor, $\mathbf{J}_{launching}$ determines the degree each polarisation axis of the sensor will be excited, and $\mathbf{J}_{detection,b}$ determines the electric field detected by each PD b . In general these matrices can be complicated. However, if certain assumptions and the design considerations are taken into effect, the final expressions for the output beams are simple. These final expressions are described in the of following discussions.

6.4.1 In-Fibre Sub-System

The role of the in-fibre sub-system in the whole sensing system is to guide the incident light towards and the subsequent reflected light from a birefringent Fabry-Pérot sensor. The resulting Jones matrix for the optical arrangement with a single in-fibre sensor in general can be complicated if the optical energy can cross-couple between the polarisation axes in the lead-in fibre and the birefringent Fabry-Pérot sensor. Fortunately, because the small cross-coupling ratio of the fibre used in this research, the off-diagonal terms in \mathbf{J}_{lead} can be neglected. Likewise, \mathbf{J}_{FP} can be written to have only the diagonal terms if it is assumed that there is no cross-coupling between the axes of the cavity and also no cross-illumination of the axes during reflections from the two Fabry-Pérot mirrors. Hence, calculating Eq. 6.7, the Jones matrix for the in-fibre sub-system is

$$\mathbf{J}_{in-fibre} = \sqrt{\gamma} \begin{bmatrix} -\exp(i2k_x z) \{F_{xx} \cos^2(U) + F_{yy} \sin^2(U)\} & -\exp(ik_x z + ik_y z) \sin(2U) \{F_{xx} - F_{yy}\} \\ \exp(ik_x z + ik_y z) \sin(2U) \{F_{xx} - F_{yy}\} & \exp(i2k_y z) \{F_{xx} \sin^2(U) + F_{yy} \cos^2(U)\} \end{bmatrix} \quad \text{Eq. 6.9}$$

Eq. 6.9 implies that in order for F_{xx} and F_{yy} to be distinguishable, the off-diagonal elements must be zero. This condition occurs when

$$U = 0^\circ, \text{ or} \quad \text{Eq. 6.10}$$

$$U = \pm 90^\circ. \quad \text{Eq. 6.11}$$

Optical Element	Jones Matrix	Definitions/Comments
Non-polarising beam splitter: transmission	$\mathbf{J}_{NPt} = \begin{bmatrix} t_x & 0 \\ 0 & t_y \end{bmatrix}$	t_x and t_y are electric field transmission coefficients along the x- and y-axis.
Non-polarising beam splitter: reflection	$\mathbf{J}_{NPr} = \begin{bmatrix} r_x & 0 \\ 0 & r_y \end{bmatrix}$	r_x and r_y are electric field reflection coefficients along the x- and y-axis.
Polarising beam splitter	$\mathbf{J}_{P,b} = \begin{bmatrix} \delta_{xb} + \varepsilon_{xy}\delta_{yb} & 0 \\ 0 & \delta_{yb} + \varepsilon_{yx}\delta_{xb} \end{bmatrix}$ $\mathbf{J}_{P,x} = \begin{bmatrix} 1 & 0 \\ 0 & \varepsilon_{yx} \end{bmatrix}$ $\mathbf{J}_{P,y} = \begin{bmatrix} \varepsilon_{xy} & 0 \\ 0 & 1 \end{bmatrix}$	<p>The x- and y-axis beams emerge as straight-through ($b = x$) and side ($b = y$) beams, respectively. The diagonal elements involve the Kronecker delta functions $\delta_{b,b}$.</p> <p>ε_{xy} and ε_{yx} are the residual electric field extinction ratio for a polariser oriented along the y-axis and x-axis respectively.</p>
Lead-in fibre	$\mathbf{J}_{lead} = \begin{bmatrix} L_{xx} & L_{xy} \\ L_{yx} & L_{yy} \end{bmatrix} = \begin{bmatrix} \exp(ik_x z) & L_{xy} \\ L_{yx} & \exp(ik_y z) \end{bmatrix}$ <p>where $k_{x,y} = \frac{2\pi n_{x,y}}{\lambda}$ and</p> $ L_{xy} = L_{yx} = \sqrt{hz}$	<p>The cross-coupling coefficients are assumed not to have any phase dependence.</p> <p>h is the cross-coupling per unit length.</p> <p>z is the length of the lead-in fibre.</p>
Half-wave plate	$\mathbf{J}_{half} = \begin{bmatrix} 1 & 0 \\ 0 & -1 \end{bmatrix}$	x-axis is the fast axis.
Fabry-Pérot sensor	$\mathbf{J}_{FP} = \begin{bmatrix} -F_{xx} & -F_{xy} \\ F_{yx} & F_{yy} \end{bmatrix}$	F_{xx} and F_{yy} are the electric field interferometric reflection coefficients as derived in Chapter 4. The negative sign in the matrix accounts for the effect of reflection.
Transformation matrix describing the rotation of eigen-polarisation axes	$\mathbf{R}(Q) = \begin{bmatrix} \cos(Q) & \sin(Q) \\ -\sin(Q) & \cos(Q) \end{bmatrix}$	Q is the angular rotation of the polarisation axis measured <i>relative to the original x-axis</i> . Positive values of Q is in the anti-clockwise direction.
Fresnel reflection from the proximal end of the lead-in fibre	$\mathbf{J}_{Fresnel} = \begin{bmatrix} -r_f & 0 \\ 0 & r_f \end{bmatrix}$	r_f is the Fresnel reflection at normal incidence to the proximal face of the lead-in fibre. The negative sign accounts for mirror inversion of the polarisation axes.

Table 6.2: Jones matrix representation of each optical element of the sensing system.

Eq. 6.10 refers to the case when the fast axis of the lead-in fibre and that of the sensor are aligned. Eq. 6.11 refers to the case when the fast axis of the lead-in fibre and the slow axis of the sensor are aligned. Subsequently Eq. 6.9 becomes

$$\mathbf{J}_{in-fibre} = \sqrt{\gamma} \begin{bmatrix} -\exp(i2k_x z)F_{xx} & 0 \\ 0 & \exp(i2k_y z)F_{yy} \end{bmatrix} \quad \text{or} \quad \text{Eq. 6.12}$$

$$\mathbf{J}_{in-fibre} = \sqrt{\gamma} \begin{bmatrix} -\exp(i2k_x z)F_{yy} & 0 \\ 0 & \exp(i2k_y z)F_{xx} \end{bmatrix} \quad \text{Eq. 6.13}$$

after Eq. 6.10 or Eq. 6.11 has been used respectively. The negative sign in the first diagonal element in the matrices signifies the effect of reflection. For other values of U other than 0° and 90° , the electric field of each interferometer can coherently interfere resulting in a complicated electric field.

6.4.2 Launching Sub-System

The launching sub-system determines the intensity of light coupled into each polarisation axis of the birefringent FFPS. The launching optical arrangement was basically designed such that circularly polarised light is launched into the lead-in fibre using the linearly polarised light coming from an opto-isolator. However, launching circularly polarised is not a strict requirement but rather is the simplest method to equally excite the two axial Fabry-Pérot interferometers. In general, the effect of an elliptically polarised beam incident on the lead-in fibre is unequal excitation along the polarisation axes of the sensor.

Circularly polarised light can be produced from linearly polarised light using a quarter-wave plate oriented such that the fast axis of the quarter-wave makes a 45° angle with respect to the input beam, *i.e.*

$$Q = \pm 45^\circ. \quad \text{Eq. 6.14}$$

Because circularly polarised light has no polarisation azimuth state, it is invariant under any rotational transformation. To maintain this rotational invariance, the electric field transmission coefficients of the NPBS must be equal, *i.e.*

$$t_x = t_y = t^+. \quad \text{Eq. 6.15}$$

Substitution Eq. 6.14 and Eq. 6.15 into Eq. 6.6, the resulting Jones matrix for the launching arrangement is

$$\mathbf{J}_{launching} = \frac{t^+}{\sqrt{2}} \begin{bmatrix} \exp(i(Z+S)) & \exp(-i(Z+S)) \\ i \exp(i(Z+S)) & -i \exp(-i(Z+S)) \end{bmatrix}. \quad \text{Eq. 6.16}$$

Hence the beam launched into the lead-in fibre is

$$\mathbf{E}'_{in} = \mathbf{J}_{launching} \cdot \mathbf{E}_{in} = \frac{t^+}{\sqrt{2}} \exp(\pm i(Z+S)) \begin{bmatrix} 1 \\ \pm i \end{bmatrix}, \quad \text{Eq. 6.17}$$

is always circularly polarised and does not depend on either the angular alignment of the polarisation axes between the NPBS and quarter-wave plate nor that between the NPBS and the lead-in fibre. Hence, the use of circularly polarised light considerably simplifies the optical measuring system.

On the other hand, when the beam splitter is polarising in transmission, *i.e.*

$$t_x \neq t_y, \quad \text{Eq. 6.18}$$

the launching sub-system will need a half-wave plate in order to launch circularly polarised light. Figure 6.4 the alternative arrangement which uses the half-wave plate. The quarter-wave plate converts linearly polarised light into an elliptically polarised light of any ellipticity. Subsequently, the azimuth of this elliptically polarised light is rotated such that the resulting beam when it traverse the NPBS (which is no longer non-polarising) will be circularly polarised.

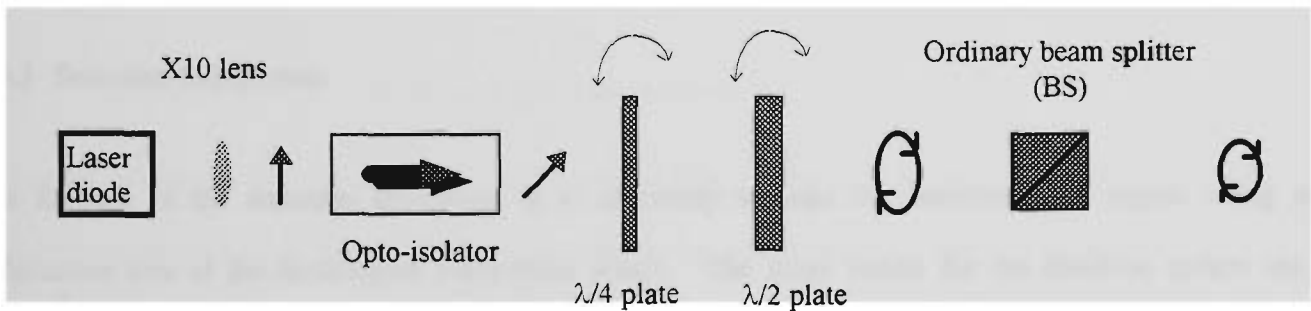


Figure 6.4: Alternative launching optical arrangement.

Besides the advantage of the rotational invariance of circularly polarised light, the launching arrangement enhances the optical isolation between the rest of the experimental arrangement and the LD. In particular, the Fresnel reflection at the proximal face of the lead-in fibre is effectively attenuated. This reflected beam returning to the LD passes through the launching arrangement in reverse order, *i.e.*

$$\mathbf{E}_{returning, Fresnel} = \mathbf{R}(Q) \cdot \mathbf{J}_{quarter} \mathbf{R}(Z) \cdot \mathbf{J}_{NPi} \cdot \mathbf{R}(S) \cdot \mathbf{J}_{Fresnel} \cdot \mathbf{E}'_{in}. \quad \text{Eq. 6.19}$$

Evaluating Eq. 6.19,

$$\mathbf{E}_{\text{returning,Fresnel}} = \pm r_f t^+ t^+ \begin{bmatrix} 0 \\ 1 \end{bmatrix} \quad \text{Eq. 6.20}$$

which is cross-polarised with respect to the input beam (Eq. 6.5). As previously mentioned, this input beam is produced by the opto-isolator output linear polariser which will not allow $\mathbf{E}_{\text{returning,Fresnel}}$ to reach the LD. Effectively, the input beam \mathbf{E}_{in} is rotated by 90° which is not surprising since the double pass through the quarter-wave plate makes the arrangement a half-wave plate oriented at 45° . This opto-isolation property of the launching arrangement holds for any reflection of the circularly polarised beam from other optical elements. This property of the optical launching sub-system is in addition to that provided by the opto-isolator.

However, the opto-isolator is still an important component of the optical sensing system. Without its use, the LD has been experimentally observed to be affected by back reflection from the Fabry-Pérot sensor. This situation occurs because the beam returning from the sensor and traveling towards the LD, in general can be elliptically polarised which will not be isolated by the quarter-wave-plate-linear-polariser tandem arrangement described above. Thus the suitable attenuation of this returning beam is depended solely on the isolation properties of the opto-isolator.

6.4.3 Detection Sub-System

The function of the detection sub-system is to effectively separate the interferometric signals along each polarisation axis of the birefringent Fabry-Pérot sensor. The Jones matrix for the detection system can be simplified if it can be assumed that the half-wave plate is suitably adjusted such that the axes of the polarising beam splitter and those of the in-fibre sub-system (hence those of the sensor) are aligned. This means

$$W = H - S \quad \text{or} \quad W = H - S \pm 90^\circ. \quad \text{Eq. 6.21}$$

Just like with the components of the in-fibre sub system, the fast and slow axes of the PBS and those of the in-fibre system do not need to correspond. Using Eq. 6.21, Eq. 6.8 becomes,

$$\mathbf{J}_{\text{detection,b}} = \begin{bmatrix} (\delta_{xb} + \varepsilon_{xy} \delta_{yb}) \{r_x \cos^2(S) + r_y \sin^2(S)\} & (\delta_{xb} + \varepsilon_{xy} \delta_{yb}) \sin(2S) \{r_x - r_y\} \\ -(\delta_{yb} + \varepsilon_{yx} \delta_{xb}) \sin(2S) \{r_x - r_y\} & -(\delta_{yb} + \varepsilon_{yx} \delta_{xb}) \{r_x \sin^2(S) + r_y \cos^2(S)\} \end{bmatrix}. \quad \text{Eq. 6.22}$$

Eq. 6.22 implies that in order for the detection arrangement to separately analyse each axial interferometer of the sensor, the diagonal elements (in Eq. 6.22) needs to be zero. This condition means that either the axes of NPBS and the lead-in fibre are aligned in the beginning on one hand, *i.e.*

$$S = 0^\circ \quad \text{or} \quad S = \pm 90^\circ; \quad \text{Eq. 6.23}$$

or the beam splitter is non-polarising in reflection, *i.e.*

$$r_x = r_y = r^+ \quad \text{Eq. 6.24}$$

on the other. The former situation though achievable can not be guaranteed always especially when the sensor under investigation is replaced with another. Thus, the latter condition may be more practical and using the latter condition, Eq. 6.22 becomes

$$\mathbf{J}_{detection,b} = \begin{bmatrix} (\delta_{xb} + \varepsilon_{xy}\delta_{yb})r^+ & 0 \\ 0 & -(\delta_{yb} + \varepsilon_{yx}\delta_{xb})r^+ \end{bmatrix} \quad \text{Eq. 6.25}$$

Interestingly, $\mathbf{J}_{detection,b}$ is not dependent on angle S as Eq. 6.22 has implied. Clearly, the condition expressed in Eq. 6.24 simplifies the whole optical arrangement. This condition implies that NPBS needs to be effectively non-polarising both in transmission and reflection. Eq. 6.25 depends on the fact that Eq. 6.21 and Eq. 6.24 hold. With the NPBS exhibiting the properties expressed in Eq. 6.24, Eq. 6.21 can be ensured by using a rotatable half-wave plate between the PBS and the NPBS (Figure 6.1).

6.4.4 Output Electric Field and System Requirement (reflection)

The beam arriving at the PD has two main component beams. The first beam is the beam reflected from the proximal end of the lead-in fibre and the second beam is that coming from the Fabry-Pérot sensor (Eq. 6.4). The detection sub-system cannot discriminate between these two components. Taking into consideration all the conditions described above, the output beam can be written as

$$\mathbf{E}_{out,b} = \frac{-r^+t^+ \exp(\pm i(Z+S))}{\sqrt{2}} \begin{bmatrix} (\delta_{xb} + \varepsilon_{xy}\delta_{yb})(r_f + \sqrt{\gamma} \exp(i2k_x z)F_{xx}) \\ \pm i(\delta_{yb} + \varepsilon_{yx}x\delta_{xb})(r_f + \sqrt{\gamma} \exp(i2k_y z)F_{yy}) \end{bmatrix} \quad \text{or} \quad \text{Eq. 6.26}$$

$$\mathbf{E}_{out,b} = \frac{-r^+t^+ \exp(\pm i(Z+S))}{\sqrt{2}} \begin{bmatrix} (\delta_{xb} + \varepsilon_{xy}\delta_{yb})(r_f + \sqrt{\gamma} \exp(i2k_x z)F_{yy}) \\ \pm i(\delta_{yb} + \varepsilon_{yx}x\delta_{xb})(r_f + \sqrt{\gamma} \exp(i2k_y z)F_{xx}) \end{bmatrix} \quad \text{Eq. 6.27}$$

Unfortunately, the contribution of the Fresnel reflection can be as great or even greater than the returning Fabry-Pérot beams. This situation occurs because of the intensity loss in the in-fibre sub-system especially at the

proximal Fabry-Pérot mirror and also because the limited value of γ . When the output intensity is obtained, Eq. 6.26 and Eq. 6.27 indicate that the Fresnel reflection can interfere with the beam returning from the sensor if the length of the lead-in fibre is less than the coherence length of the light source. Effectively this means additional Fabry-Pérot-type effects between the proximal end of lead-in fibre and the Fabry-Pérot mirrors of the sensor. To minimise these effects either the length of the lead-in fibre is made sufficiently long or the reflection of proximal end of the lead-in fibre is reduced. The latter was a more feasible approach in this work because of the scarcity of birefringent fibre.

When the Fresnel beam has been eliminated, the expected electric field output beams can be expressed as

$$\mathbf{E}_{out,b} = \frac{-r^+ t^+ \exp(\pm i(Z+S))}{\sqrt{2}} \begin{bmatrix} (\delta_{xb} + \varepsilon_{xy} \delta_{yb}) \sqrt{\gamma} \exp(i2k_x z) F_{xx} \\ \pm i (\delta_{yb} + \varepsilon_{yx} x \delta_{xb}) \sqrt{\gamma} \exp(i2k_y z) F_{yy} \end{bmatrix} \quad \text{or} \quad \text{Eq. 6.28}$$

$$\mathbf{E}_{out,b} = \frac{-r^+ t^+ \exp(\pm i(Z+S))}{\sqrt{2}} \begin{bmatrix} (\delta_{xb} + \varepsilon_{xy} \delta_{yb}) \sqrt{\gamma} \exp(i2k_x z) F_{yy} \\ \pm i (\delta_{yb} + \varepsilon_{yx} x \delta_{xb}) \sqrt{\gamma} \exp(i2k_y z) F_{xx} \end{bmatrix} \quad \text{Eq. 6.29}$$

The resulting intensity resulting from either Eq. 6.28 or Eq. 6.29 are given by

$$I_{out,b} \propto \gamma \frac{|r^+|^2 |t^+|^2}{2} \left[(\delta_{xb} + \varepsilon_{xy} \delta_{yb}) |F_{xx}|^2 + (\delta_{yb} + \varepsilon_{yx} x \delta_{xb}) |F_{yy}|^2 \right] \quad \text{or} \quad \text{Eq. 6.30}$$

$$I_{out,b} \propto \gamma \frac{|r^+|^2 |t^+|^2}{2} \left[(\delta_{xb} + \varepsilon_{xy} \delta_{yb}) |F_{yy}|^2 + (\delta_{yb} + \varepsilon_{yx} x \delta_{xb}) |F_{xx}|^2 \right] \quad \text{Eq. 6.31}$$

respectively. The two components in either Eq. 6.28 or Eq. 6.29 do not interfere when the intensity relation is obtained because these components are perpendicularly oriented.

For an ideal PBS, the expected intensity function detected by each PD is simply proportional to one of intensity reflection function of one of the interferometers. For a real PBS which have a finite extinction ratio, the intensity detected by the PD additionally includes the interferometric reflection function of the other axial interferometer multiplied by the corresponding extinction ratio. Although this additional term is generally small, this term may not be negligible for the case when the fringe visibility of the dominant interferometer decreases whilst that of the other interferometer increases such that their net intensity values are similar. Such conditions can occur with grating-based birefringent sensors.

In summary, the capability of the optical arrangement to successfully interrogate separately the two axial interferometric information from a birefringent Fabry-Pérot with the least number of optical components critically depends on the following:

- 1) All the optical elements should have negligible cross-coupling between the beams travelling along each polarisation axes. This implies the wave plates give the correct amount of retardation and the birefringent material used in them has low cross-coupling constant.
- 2) The polarisation axes of the lead-in fibre and the cavity needs to be aligned in order to avoid any cross-polarisation interference effect.
- 3) The beam reflected from the proximal end of the lead-in fibre needs to be minimised. This can be achieved by coating this end with an anti-reflection film or to appropriately angle-polishing it.
- 4) The NPBS needs to be at least be non-polarising in reflection to be able the detection optical arrangement to separate the two Fabry-Pérot interferometers. In this minimal case, the two axes are not necessarily equally excited since in general the lead-in fibre is excited with an elliptically polarised light. The ideal case is when the NPBS is non-polarising both in transmission and in reflection. This further implies that circularly polarised light at the input end of the system can be produced with the least number of components.
- 5) The use of circularly polarised light at the input end aside from exciting both axes of the sensor equally also means that after the initial assembly of the optical detection system, the only adjustment to be made is aligning the polarisation axes of the PBS and the Fabry-Pérot sensor using a half-wave plate.

6.4.5 Output Electric Field and System Requirement (transmission)

If desired, the birefringent Fabry-Pérot sensor can be addressed in transmission. The transmission arrangement is shown in Figure 6.5. This arrangement is simpler than the reflection case because the NPBS is not required. This simplification means that the total power throughput across the system is increased at least 4 times because no beams are unnecessary diverted as in the reflection case (*c.f.* Figure 6.1 and Figure 6.5).

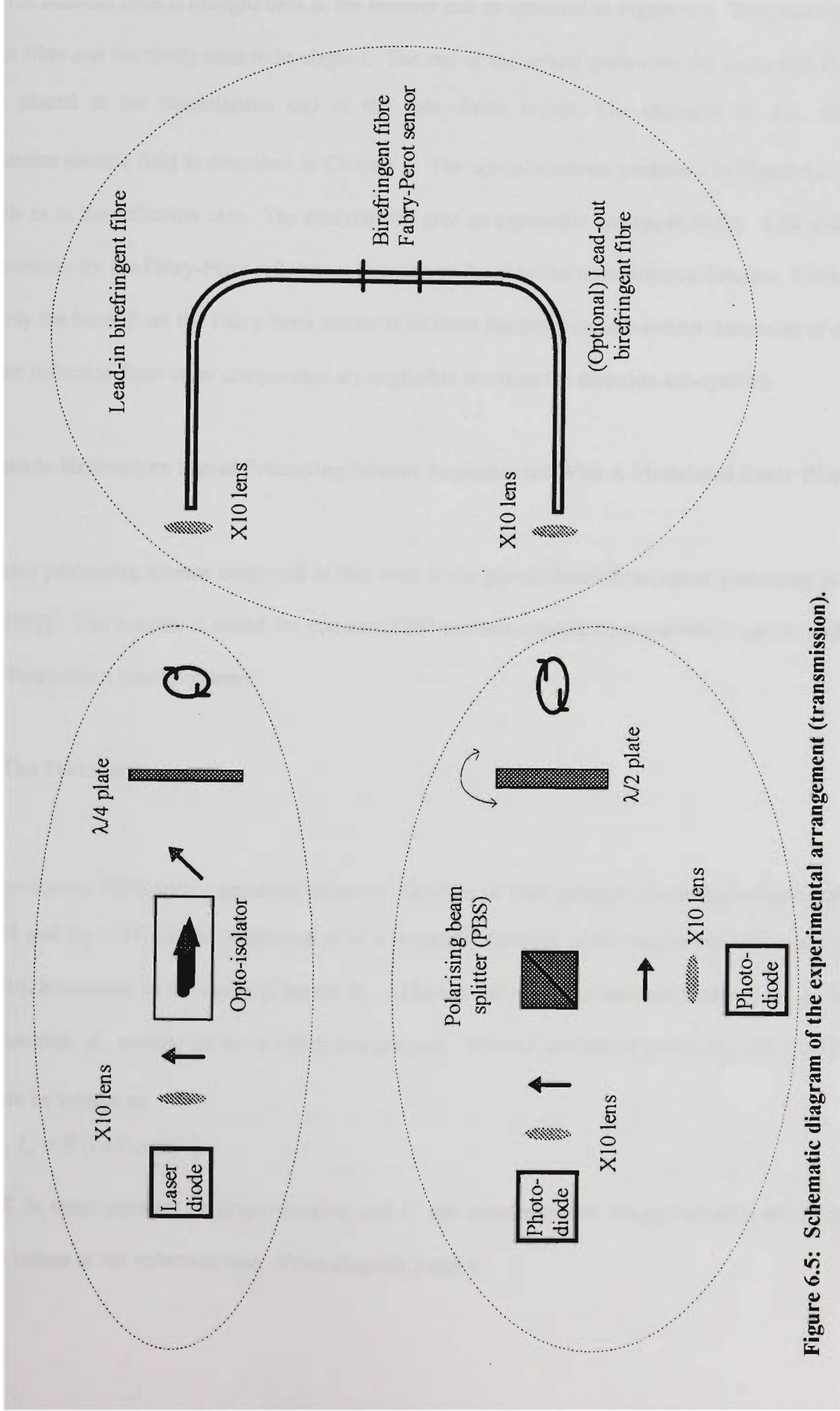


Figure 6.5: Schematic diagram of the experimental arrangement (transmission).

Inherently, the transmission arrangement does not provide single-ended operation. However, if single-ended operation is required, an (optional) lead-out fibre can be additionally concatenated with the sensor and the distal end of the lead-out fibre is brought back at the receiver end as indicated in Figure 6.5. The polarisation axes of the lead-out fibre and the cavity need to be aligned. The rest of the optical system are the same with the detection sub-system placed at the transmission end of the Fabry-Pérot sensor. The elements of \mathbf{J}_{FP} are the complex transmission electric field as described in Chapter 3. The optical elements presented in Figure 6.5 can be analysed similarly as in the reflection case. The analysis will give an expression analogous to Eq. 6.28 and Eq. 6.29 with the expression for the Fabry-Pérot reflectance function replaced by the transmittance function. Unlike the reflection case, only the beam from the Fabry-Pérot sensor is incident the detection sub-system (assuming of course there are not other reflection from other components are negligible reaching the detection sub-system).

6.5 Pseudo-Heterodyne Signal Processing Scheme Implemented With A Modulated Laser Diode

The signal processing scheme employed in this work is the pseudo-heterodyne signal processing scheme [Jackson *et al.*, 1982]. The scheme is suited for non-zero OPD two-beam interferometers which can be realised with low-finesse Fabry-Pérot interferometers.

6.5.1 The Technique

For a low-finesse FFPS with a proximal dielectric thin-film or FBG reflector, the reflection/transmission intensity (Eq. 3.53 and Eq. 3.54) can be considered to be a sinusoidal function of the total round trip optical phase shift, ϕ (Eq. 3.20), introduced by the cavity (Chapter 3). Although the reflection function involves the ϕ_r term inside the cosine function, ϕ_r modulo 2π is $-\pi$ which is a constant. Without any loss of generality, the ideal interferometric signal can be written as

$$I_r = K\{1 + V \cos(\phi)\} \quad \text{Eq. 6.32}$$

where K is some constant of proportionality and V the interferometric fringe visibility which is allowed take negative values in the reflection case. From chapters 3 and 4,

$$\Delta\phi = 2\pi \left\{ \frac{\Delta\nu}{\Delta\nu_{FSR}} + \frac{\Delta M}{\Delta M_{UMR}} \right\}. \quad \text{Eq. 6.33}$$

Eq. 6.33 implies that a complete fringe shift occurs when the optical frequency (ν) changes by an amount equivalent to the FSR or when a measurand (M) which affects the interferometric phase changes by an amount equivalent to the corresponding UMR (ΔM_{UMR}). The temperature and strain UMR have been described in Chapter 4. In chapters 3 and 4, it has been shown that $\Delta\nu_{FSR}$ and ΔM_{UMR} are essentially constant for low-finesse interferometers. However $\Delta\nu_{FSR}$ and ΔM_{UMR} strictly depends ν and M since the Fabry-Pérot mirrors in general are dispersive (see chapters 3 and 4).

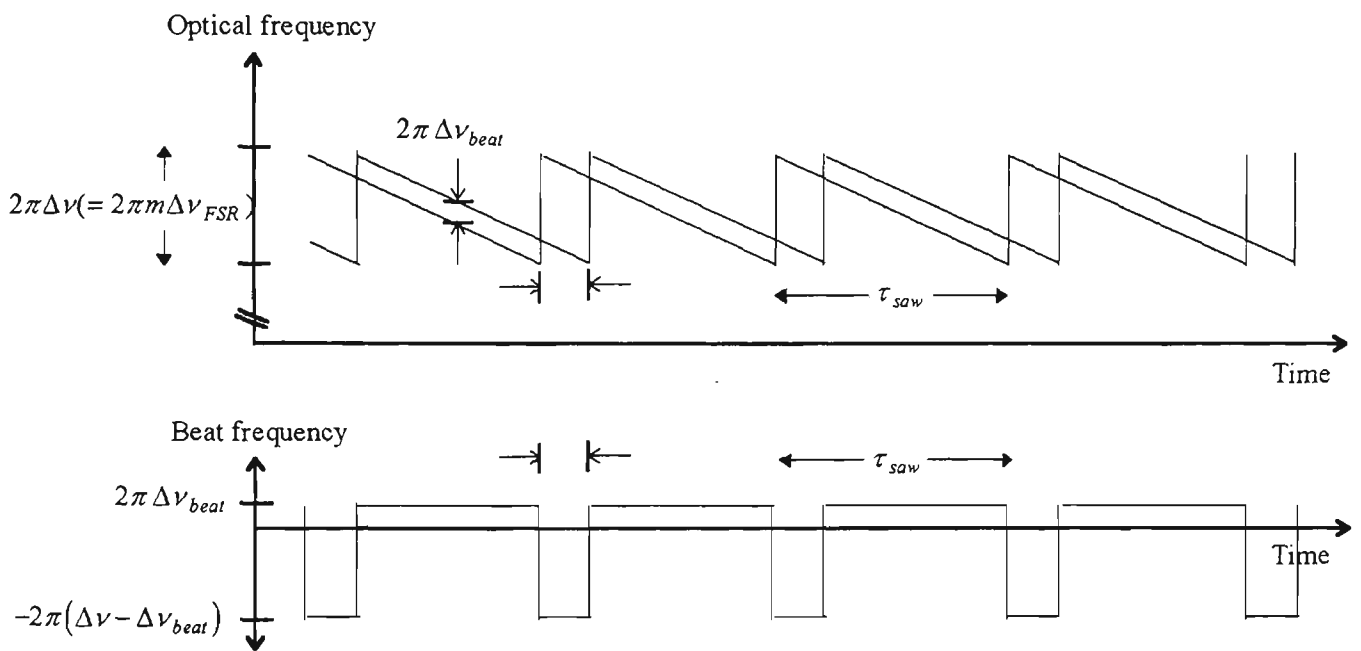


Figure 6.7: Generation of the beat frequency in a pseudo-heterodyne/FMCW-type signal.

In pseudo-heterodyne the optical frequency of the light source is linearly ramped periodically in a sawtooth manner (Figure 6.7). Furthermore, the total optical frequency chirp $\Delta\nu$ is chosen such that it is an integral multiple of the FSR of the interferometer, *i.e.*

$$\Delta\nu = -m \cdot \Delta\nu_{FSR} \quad \text{Eq. 6.34}$$

where m is some integer. The negative sign in Eq. 6.34 refers to a negatively sloping optical frequency ramp as was the case in this work. The Eq. 6.34 implies that the sawtooth modulation takes the interferometer over m number of fringes during each ramp period in time. Using Eq. 6.34, the interferometric signal can be written as

$$I_r = K \left[1 + V \cos(\phi_{\text{int}} - \omega_m t) \right] \quad \text{Eq. 6.35}$$

$$\text{where } \omega_m = 2\pi \frac{m}{\tau_{saw}},$$

Eq. 6.36

and ϕ_{int} is the interferometric phase less the phase change due to $\Delta\nu$ (sawtooth modulation). Eq. 6.35 implies that the interferometric signal is now a continuous sinusoidal function of time t with an effective angular frequency of ω_m and with an electronic phase of ϕ_{int} . ϕ_{int} can be measured with a phase meter. Subsequently, temperature- or strain-induced shifts in ϕ_{int} can be measured to determine the variations in these measurands.

In this work, ϕ_{int} is measured from the location of the zero-crossings during each ramp period. Consequently in order that the shifts in zero-crossings have the same sense as the change in temperature or strain, a negatively sloping optical frequency ramp was chosen. Eq. 6.35 can alternatively be written as

$$I_r = K \left[1 + V \cos(\omega_m t - \phi_{int}) \right].$$

Eq. 6.37

In Chapter 4, ϕ_{int} has been established to linearly change with temperature or strain with a positive and linear rate. Eq. 6.37 clearly indicates that when temperature or strain increases, the continuous sinusoidal function shifts to the right in time relative to the sawtooth ramp when viewed using an oscilloscope. This situation also results in an increase in the temporal position of the zero-crossings (relative to the start of the ramp).

The continuity of the resulting pseudo-heterodyne signal in time obviously depends on how short the fly-back period can be made. During the fly-back period, the value of the beat frequency is larger compared with that during the rest of the ramp (Figure 6.7). This fly-back beat frequency approaches the FSR value of the cavity and needs to be removed to form a continuous temporal signal. However such high frequency signals are immediately filtered out by the photodetectors which can not change quickly at this high frequency value.

For the pseudo-heterodyne scheme to be suitable for a birefringent FFPS, it is impossible for the integral condition expressed in Eq. 6.34 be strictly satisfied simultaneously by the axial interferometers. Interestingly the fraction difference between the FSR of the axial interferometers is about the same as the fractional birefringence:

$$\frac{\Delta\nu_{FSR,s} - \Delta\nu_{FSR,f}}{\Delta\nu_{FSR,sf}} = \frac{\Delta n_{sf}}{n_{sf}}$$

Eq. 6.38

where $\Delta\nu_{FSR, sf}$ and n_{sf} are the average FSR and refractive index along each polarisation axis. Fortunately with a fractional birefringence $\frac{\Delta n_{sf}}{n_{sf}}$ of $\sim 3 \times 10^{-4}$ for the polarisation-maintaining fibre used in this work, the FSR of the two interferometers can practically be taken to be the same. Thus a single sawtooth-modulated LD can be used to illuminate each axial interferometer of the sensor. By optically separating the signals from each interferometer, the axial pseudo-heterodyne signals are two sinusoidal signals which have the same angular frequency of ω_m but have different phase values.

6.5.2 Implementation

The pseudo-heterodyne signal processing scheme can be implemented by modulating the optical frequency of an LD and can be accomplished by either modulating the current or the temperature of an LD. These various methods are discussed in the next sub-section. Alternatively, pseudo-heterodyne signal processing can be implemented by stretching the Fabry-Pérot cavity in a linear sawtooth manner [Farahi *et al.*, 1990]. This approach which does not introduce any amplitude modulation as in the case of modulation the LD drive current. Since this implementation is typically accomplished with a PZT cylinder, it can not be employed for short cavity Fabry-Pérot sensors.

6.5.3 Chirping of the Laser Diode Emission Frequency

There are several ways to frequency-modulate the output of an LD. The frequency chirp is a consequence of variations in the carrier density [Dandridge & Goldberg, 1982] or the temperature of the lasing region [Ohba *et al.*, 1989; Chen *et al.*, 1988]. The frequency shift can be expressed as [Ito & Kimura, 1980]

$$\Delta\nu = \nu \left\{ \frac{1}{n_{LD}} \frac{\partial n_{LD}}{\partial \rho_c} \Delta\rho_c + \frac{1}{n_{LD}} \frac{\partial n_{LD}}{\partial T} \Delta T + \alpha_{LD} \Delta T \right\} \quad \text{Eq. 6.39}$$

where ν is the emission frequency and ρ_c the carrier density. n_{LD} and α_{LD} are the refractive index and thermal expansion coefficient of cavity respectively.

Direct current modulation is the most convenient method of frequency modulating the output of an LD but exhibits several drawbacks. The modulation of the LD drive current (inevitably) modulates the intensity of the LD output as well [Peterman, 1988]. In this case the raw interferometric signal can be described as

$$I_{raw} = K' [1 + r(t)] [1 + V \cos(\omega_m t - \phi_{int})]. \quad \text{Eq. 6.40}$$

where K' is a constant of proportionality which includes the quantum efficiency of the PD and the gain of the trans-impedance amplifier used with the PD and $r(t)$ is the ratio between the AC component (with respect to time t) of the sawtooth ramp and the DC component of the ramp. The factor $[1 + r(t)]$ in Eq. 6.40 describes the sawtooth modulation in the intensity of the LD output. Clearly, this additional complication needs to be addressed before any subsequent processing can be useful.

There are two possible schemes used in this work to isolate $V \cos(\omega_m t - \phi_{int})$ term in I_{raw} . One of these schemes involved dividing I_{raw} by the intensity of the LD output. This scheme can easily be implemented with an electronic division circuit. The second scheme involves subtracting from I_{raw} the term $K' r(t)$ giving

$$I_{raw,sub} = K' \left\{ 1 + V [1 + r(t)] \cos(\omega_m t - \phi_{int}) \right\}. \quad \text{Eq. 6.41}$$

When $r(t) \ll 1$, then Eq. 6.41 becomes similar to Eq. 6.37. Subsequently, $I_{raw,sub}$ can be band-pass filtered about a narrow range centred at the sawtooth modulation frequency giving

$$I'_{raw} \approx K' V \cos(\omega_m t - \phi_{int}). \quad \text{Eq. 6.42}$$

The division scheme was used with grating-based birefringent FFPSs whilst the subtraction-band-pass-filtering scheme with the fusion-spliced birefringent FFPSs.

Direct small-signal modulation of the LD current is dependent on the modulation frequency [Peterman, 1988]. The frequency response of direct small-signal current modulation can limit the performance of the pseudo-heterodyne signal processing scheme since a sawtooth waveform is composed of (at least 10) higher harmonics signals. Although for modulation frequencies < 1 kHz, this frequency response is expected not to introduce any significant complication since the frequency response is relatively flat for frequency < 10 kHz (see Appendix C). Effects associated with this frequency response have been observed in the experimental results (Chapter 7).

The temperature of the LD can be modulated to produce a frequency chirp. However, in most LD devices it is difficult to rapidly change the temperature of the LD cavity due to the intrinsic thermal resistance and capacitance of the cavity and the casing for the LD. Furthermore, this approach is similarly accompanied with an intensity modulation.

Alternatively, the LD cavity can be heated preferentially by a focused beam from an external LD. [Anderson & Jones, 1992]. Subsequently, the intensity of this external beam can be modulated and thereby controlling the amount of heat introduced in the laser cavity in the technique known as opto-thermal modulation. To avoid any instability in the output of the LD to be modulated, the wavelength of this heating beam is chosen to fall substantially away from the gain spectrum of the LD. This method offers the advantage of faster modulation rate compared with varying the temperature of the entire LD. Because only the temperature of the cavity is perturbed, the method involves substantially less intensity modulation compared with either direct current or temperature modulation. Although this method appears to be an attractive alternative, its implementation demands a high level of mechanical stability because of the requirement to precisely focus the modulation beam into the laser cavity itself.

The direct-current modulation is the most practical approach despite its drawbacks of mode-hopping, temperature dependence, coherence length, intensity-modulation, modulation frequency response, non-linear thermal response and line broadening, amplitude phase noise [Economou *et al.*, 1986]. Some of these limitations will be discussed in Appendix C.

6.6 Implementation of the Signal Processing and Phase Detection Scheme

6.6.1 Description of Single Channel

This subsection discusses the electronic circuits employed to implement the pseudo-heterodyne signal processing scheme and the determination of the resulting interferometric phases. The details of the circuits are described in Appendix B. In subsequent discussions, the optical beam from a Fabry-Pérot birefringent sensor is assumed to have been successfully decomposed by the optical arrangement discussed previously into two beams which represent the two axial interferometric signals of the sensor. Signal processing of the sensor involves the simultaneous processing of these two axial signals. However, in the following discussion, processing for a single axis/channel (Channel b where $b = 1$ or 2) is discussed since the operation of the other channel is equivalent.

Figure 6.8 shows the schematic of the pseudo-heterodyne signal processing scheme and the phase recording scheme employed in this work. Figure 6.9 shows the corresponding output waveforms for a typical experimental measurement for a birefringent FFPS addressed in reflection. A 976.5625 Hz (~ 1 kHz) sawtooth generator produces a negatively-sloping voltage ramp (similar to Figure 6.9: Divisor). This voltage ramp is generated using a Digital-to-Analog-Converter with its input connected to a free-running 12-bit counter clocked by a 4.000 MHz crystal oscillator. The voltage ramp is used to modulate the drive current of a temperature-controlled LD. Due to the design of the LD drive circuit (Appendix B), the resulting sawtooth LD current ramp yields a positively-sloping sawtooth LD intensity signal (Figure 6.9: LD Intensity). This current modulation also induces the emission frequency of the LD output to decrease during the ramp.

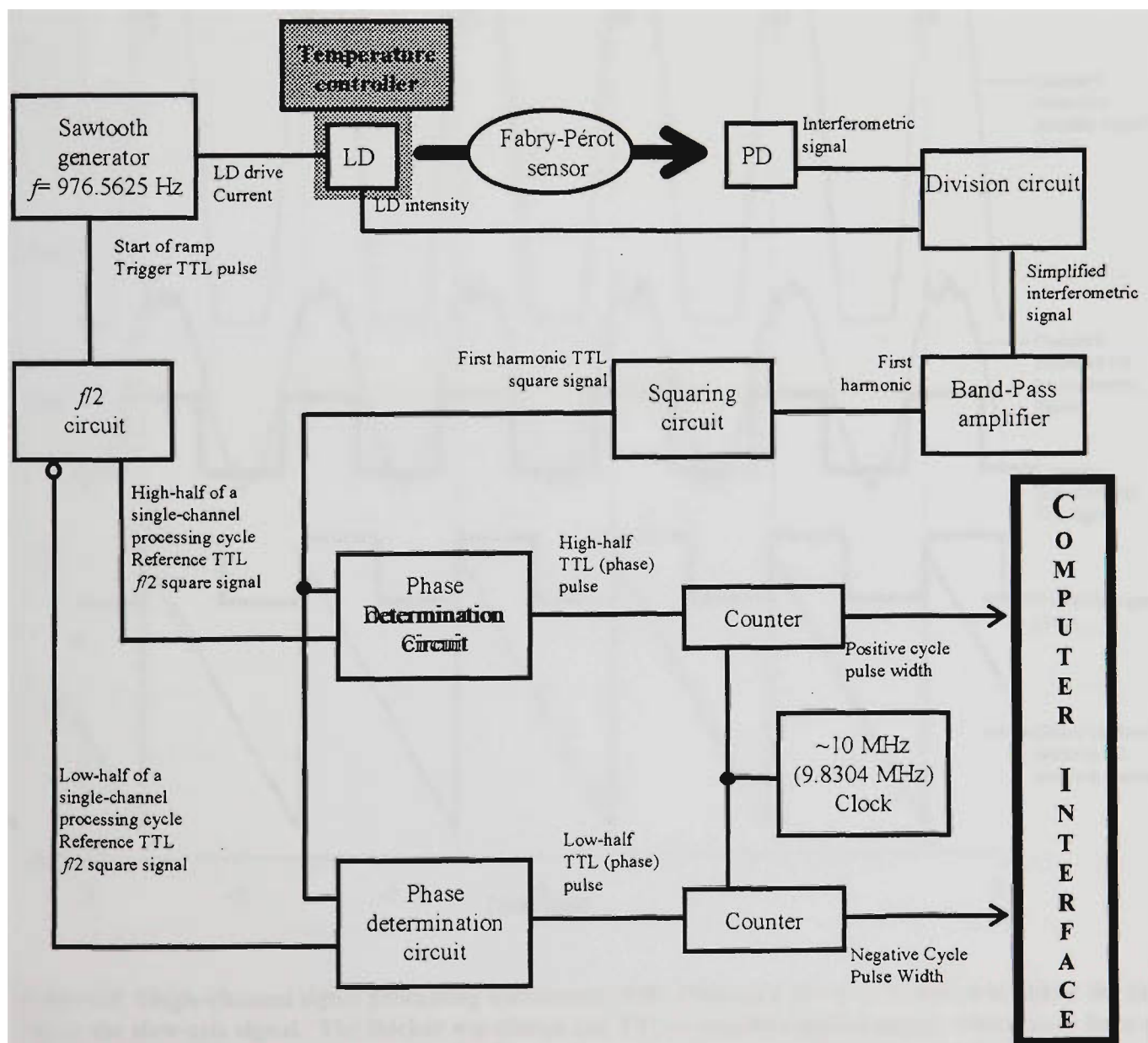


Figure 6.8: Schematic diagram of the pseudo-heterodyne signal processing and phase recording scheme.

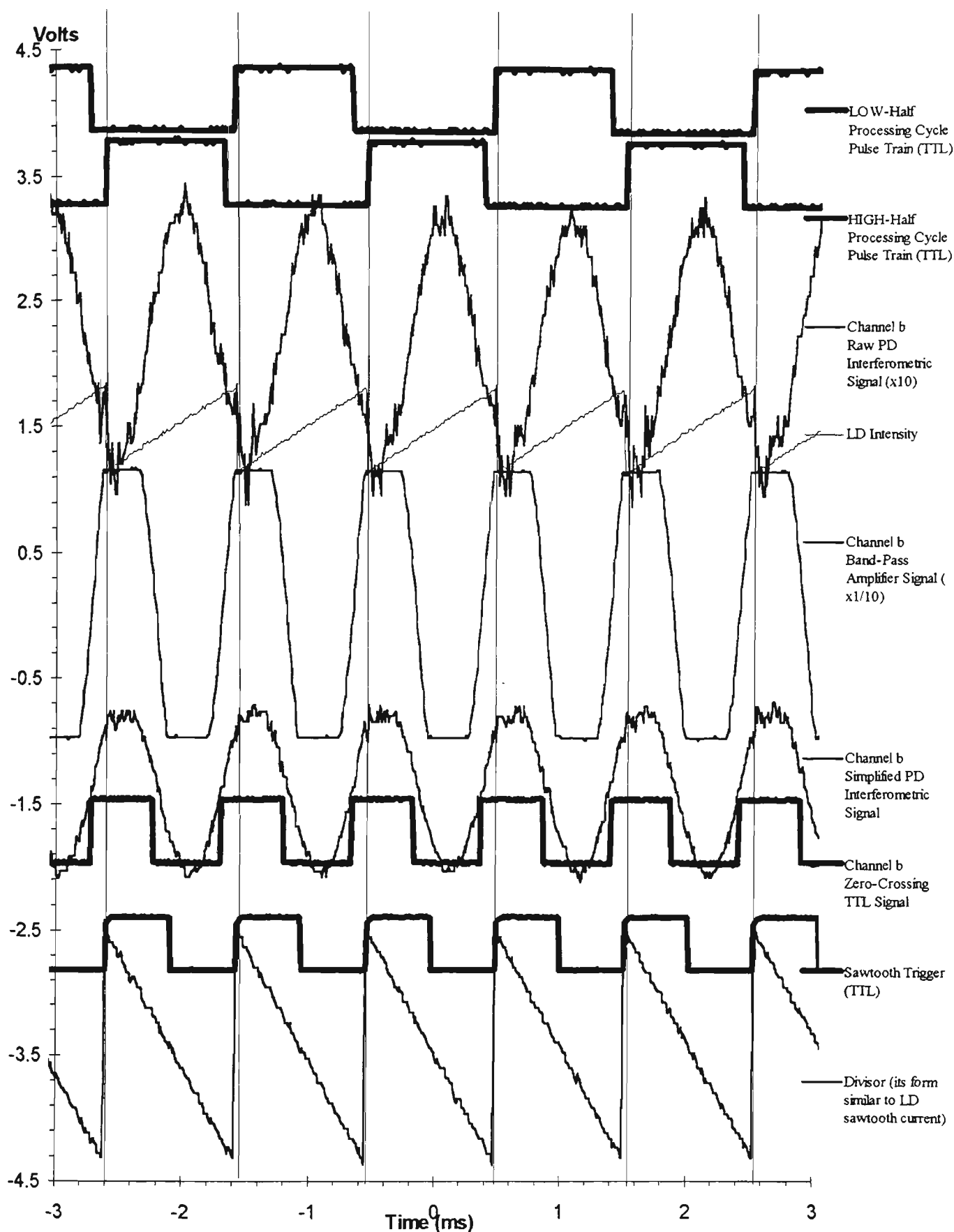


Figure 6.9: Single-channel signal processing waveforms. *NB*: Channel b ($b = 1$ or 2) refers to either the fast-axis or the slow-axis signal. The thicker waveforms are TTL-compatible digital signals which have been re-scaled and were given appropriate vertical offsets in order that they do not overlap with the other analogue signals. The vertical scale refers to the voltage axis for the analogue signals.

This intensity and frequency modulated LD output addresses the birefringent Fabry-Pérot cavity and the resulting interferometric outputs are detected by the PDs. As expected, these PD outputs show that the interferometric outputs exhibit features attributed to an interference signal together with some intensity modulation (compare Figure 6.9: Channel *b* Raw PD Interferometric Signal and Eq. 6.40). The intensity modulation produces discontinuities in the PD output during the fly-back (Figure 6.9: Channel *b* Raw PD interferometric signal).

The intensity modulation is eliminated by dividing this raw interferometric signal by a signal proportional to LD output intensity (Figure 6.9: Divisor) and providing a purely interferometric signal for subsequent processing (Figure 6.9: Channel *b* Simplified PD Interferometric Signal). This “simplified” signal, (Eq. 6.37) is adjusted to behave as a continuous sinusoid by suitably adjusting the amplitude of the LD current ramp. Interestingly this simplified signal as shown in Figure 6.9 is in anti-phase with the raw PD signal because the divisor signal had to be restricted to negative voltage values to avoid positive feedback in the division circuit.

The simplified interferometric signal is subsequently band-pass filtered and amplified (Figure 6.9: Channel *b* Band-Pass Amplified Signal). This filtered signal is then converted into a TTL-compatible square wave whose edges signified its zero-crossing (Figure 6.9: Channel *b* Zero-Crossing TTL Signal). The amplified signal exhibits less noise than the raw interferometric signal simply because of the narrow bandwidth of the filter. This TTL version of the interferometric signal exhibits a relative phase difference with respect to the sawtooth Trigger signal (Figure 6.9), a symmetric TTL signal with the same frequency as the sawtooth modulation. The shifts in this relative phase is the same as the shifts in the interferometric phase of the axial interferometer. Thus since phase shift is the parameter of interest, for all practical purposes, the relative phase is considered to be the “phase” of the corresponding axial interferometer.

The measurement of the relative phase is accomplished with a digital phase-determination processing technique. The technique involved producing a pulse train whose width of each pulse was proportional to interferometric phase. The rising edge of each pulse corresponds to the start of the ramp whilst its falling edge to the negatively-sloping zero-crossing of the original interferometric signal (or the positively-sloping zero-crossing of the TTL-

version of the interferometric signal). The width of each pulse is measured accurately with a digital counter based on a 9.8304 MHz (~ 10 MHz) crystal clock oscillator. The phase resolution is determined by the frequency ratio of sawtooth modulation and the high-frequency clock. In this work, this ratio is 1:10,066 (or $\sim 1:10^4$). The processing cycle for each channel involves producing two pulse trains such that the pulses of each train are interleaved in time (HIGH- and LOW-half pulse trains). This convenient arrangement allows a computer program to fetch the value of one counter while the other counter can be busy determining the width of the next pulse.

6.6.2 Cumulative Phase Monitoring

Using a computer program, the phase of each axial interferometer of a birefringent FFPS can be continuously monitored and the differential phase can be calculated as well. High-resolution measurement of the measurand is obtained from the axial phase measurements. The fringe order of the axial phase measurements is determined the value of the differential phase. The sensitivity of the differential phase determines the UMR of the sensor (Chapter 4). If between successive measurements, the differential phase can vary as much as 2π , then the overall measurand range is limited to the UMR.

The overall measurand range is not limited to the UMR if it can be assumed that the differential phase varies only up to π between successive measurements. For this special case, the overall measurand range can be increased as long as the interferometric signal can be received by the PDs. The assumption of this special case is equivalent to the knowing the directionality of the differential phase change. Because the direction of change is known the fringe order of the differential phase can be determined. In this special case, the axial phase change can be more than 2π .

In another special case, fringe order of each axial-interferometer phase change can also be inferred if it can be assumed that the axial phase does not change by more than π between successive measurements. This was the case with the measurements made with the sensors developed in this work and for this reason the overall measurand range of the measurements was large than the UMR of the sensor (Chapter 7). This alternative method of determining the fringe order of the axial phase can be verified with the value of the differential phase.

Figure 6.10 shows the algorithm to calculate the fringe order of the j -th interferometric phase ϕ_j (either that of the fast-axis, slow-axis or differential phase responses) with the assumption that successive values of ϕ_j do not differ by more than π . The algorithm determines the occurrence of a fringe jump when the apparent change between two successive modulo 2π measurements is greater than π rad. If the current phase measurement ${}^{2\pi}\phi_{j,current}$ is greater than the previous ${}^{2\pi}\phi_{j,previous}$, the interferometric fringe order $\phi_{j,Order}$ has decreased and vice versa. The cumulative phase change is simply

$$\phi_j = 2\pi\phi_{j,Order} + {}^{2\pi}\phi_j.$$

Eq. 6.43

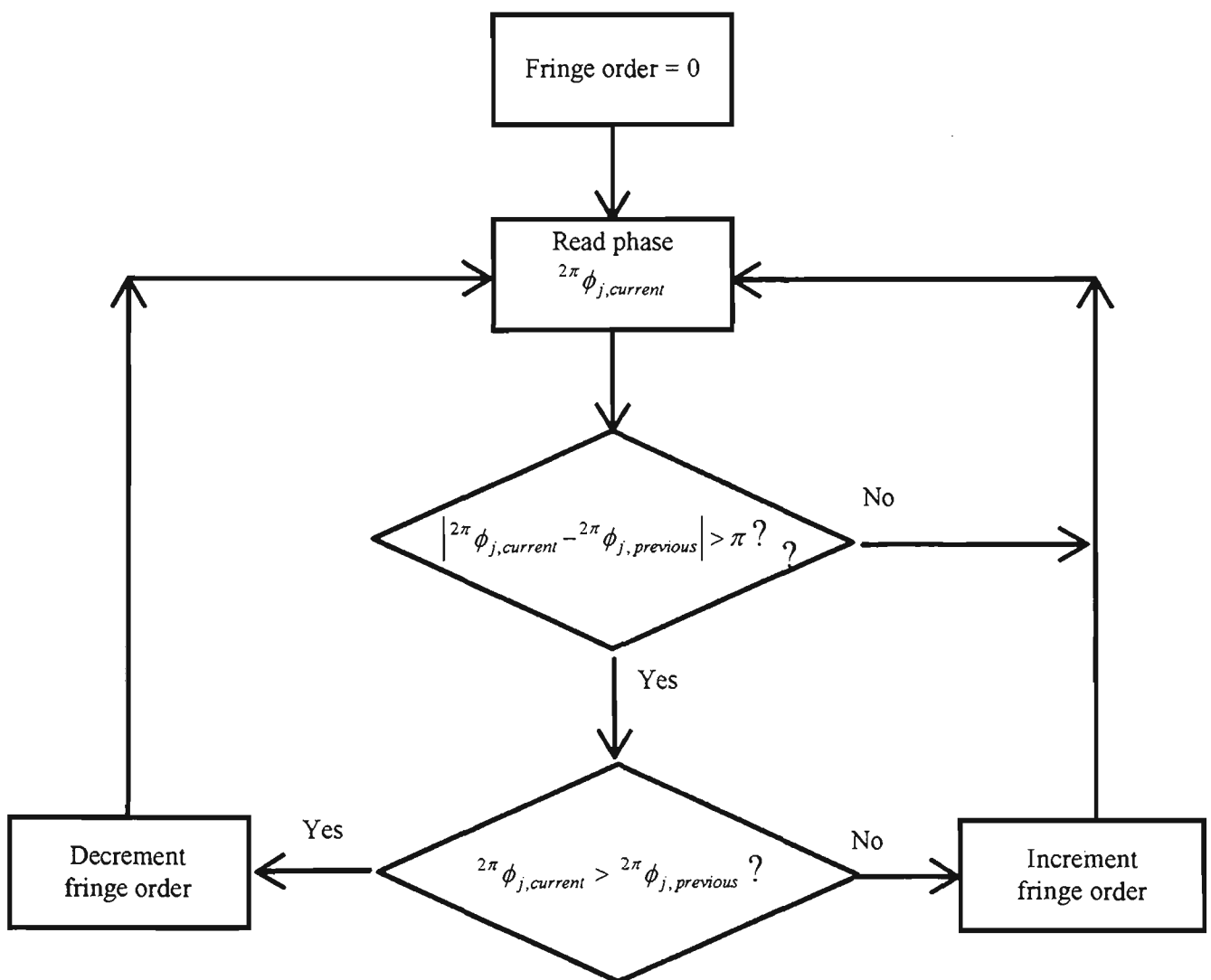


Figure 6.10: Flow diagram to determine the fringe order of the j -th interferometric phase ϕ_j

The assumption that successive values of ϕ_j do not differ by more than π implies certain properties of the measurand-induced phase shifts $\Delta\phi_{j,M}$ which can be described in general as

$$\Delta\phi_{j,M} = \phi_{j,M}^A \sin(\omega_{j,M} t). \quad \text{Eq. 6.44}$$

where $\phi_{j,M}^A$ and $\omega_{j,M}$ are the amplitude (depth of modulation) and angular frequency of the induced phase shifts due to the measurand M . The derivative of $\Delta\phi_{j,M}$ with respect to time gives

$$\frac{d(\Delta\phi_{j,M})}{dt} = \phi_{j,M}^A \omega_{j,M} \cos(\omega_{j,M} t). \quad \text{Eq. 6.45}$$

For the assumption described above to be valid,

$$\left| \frac{d(\Delta\phi_{j,M})}{dt} \right|_{\max} = |\phi_{j,M}^A| \omega_{j,M} < \frac{\pi}{\tau_{\text{Sampling}}} \quad \text{Eq. 6.46}$$

where τ_{Sampling} is the sampling period. Alternatively,

$$|\phi_{j,M}^A| < \frac{\omega_{\text{Sampling}}/2}{\omega_{j,M}} = \frac{\omega_{\text{Nyquist}}}{\omega_{j,M}} \quad \text{Eq. 6.47}$$

where ω_{Nyquist} is the angular Nyquist frequency. Since

$$\omega_{j,M} \leq \omega_{\text{Nyquist}}, \quad \text{Eq. 6.48}$$

the minimum $|\phi_{j,M}^A|$ is unity for the assumption to hold. Interestingly, when the signal frequency $\omega_{j,M}$ approaches zero, $|\phi_{j,M}^A|$ increased without bound. This conclusion simply mean that the measuring system can accommodate larger swings in the total phase excursions induced by the measurand as its maximum frequency decreases. On the other hand, an infinite $|\phi_{j,M}^A|$ value is meaningless because it meant that there is no measurand-induced phase shifts (*i.e.* DC case: $\omega_{j,M} = 0$). For the temperature or strain measurements obtained in this work, $\omega_{\text{Nyquist}} = 2\pi \times 500$ Hz was adequate that Eq. 6.47 holds.

In Chapter 7, the cumulative phase axial shifts of several short-cavity birefringent FFPSs were measured against variations in temperature or strain using the arrangement described in this chapter. The arrangement gave moderately fast and high resolution measurements of temperature or strain and as well revealed several insights on the performance of these sensors.

Chapter 7:

Temperature and Strain Measurements With Fibre Fabry-Pérot Interferometric Sensors

This chapter discusses the temperature and strain performance of several fibre Fabry-Pérot interferometric sensors which were developed. The first generation of fabricated sensors employed non-polarisation-maintaining single-mode fibres and used face-coated or core-region-only-coated fusion-spliced TiO_2 reflectors as their proximal mirrors. The second generation of sensors were birefringent FFPSs with face-coated fusion-spliced TiO_2 proximal mirrors. The third generation were birefringent FFPSs which involved in-fibre Bragg gratings as their proximal mirrors. Each of these FFPSs exhibited slightly different performance characteristics. The limitations of the final UMR-extended sensing arrangement used with birefringent FFPSs are presented.

The data from a single sensor, or from a single polarisation axis of a birefringent sensor, behaved very much as expected. However, with the birefringent sensors, the differential phase allowed measurements with high sensitivity and resolution. Close examination of these differential phase results showed a number of interesting features which were not expected. A considerable part of this chapter is devoted to modeling and explaining these features. The results reveal some problems with the LD source which arose during the experiment. The most significant of these was a nonlinear optical frequency ramp which produced periodic phase modulation at the UMR of the individual polarisation axis. This “noise” is not a fundamental limitation of the sensor and could be very greatly reduced by careful adjustment of the LD current modulation waveform. In addition to LD-related phase

effects, we also observed a further phase effect which was clearly produced in the Bragg grating mirror. This effect was consistent in position and shape with an anomalous dispersion phase change associated with the Bragg reflection peak. However the magnitude was about 0.35 fringe which is about 20 times larger than the figure for this phase change which was calculated in Chapter 3.

7.1 Performance of Non-Polarisation-Maintaining Fusion-Spliced Fibre Fabry-Pérot Sensors

The aim of fabricating sensors using NPM single-mode fibres was to gain familiarisation before fabricating birefringent FFPSs without the need for the extra step of alignment of polarisation axes. Subsequently, these NPM FFPSs were calibrated as either temperature or strain sensors.

7.1.1 Characteristics of the NPM Sensors

Two types of low finesse NPM FFPSs were fabricated in this work. The proximal mirror of the NPM FFPSs was an in-fibre fusion-spliced TiO_2 reflector deposited either on the entire cross-sectional face (*face-coated*) or only around the core region (*core-coated*) of a fibre. In the subsequent discussions, the results from one of the face-coated sensors (labeled “*ComFace*”) and one of the core-coated sensors (labeled “*ComCore*”) are presented. The characteristics of these sensors are summarised in Table 7.1.

The proximal Fabry-Pérot mirrors were formed by fusion splicing a fibre end pre-coated with TiO_2 film to an uncoated fibre end. There was no significant benefit in choosing a particular initial thickness for a film since the ultimate thickness of the fusion-spliced thin film depended on how much of the film survived during the fusion arc discharge. The coating thickness chosen corresponded to about a quarter-wave optical thickness at 840 nm, the wavelength of the light source used to optically monitor the thickness of the film during its deposition [Caranto *et al.*, 1993]. In most cases, films with an initial thickness of 92 nm were sufficient to give useful post-fusion reflectance of the spliced reflectors.

The optical properties of the fusion-spliced TiO_2 mirrors were obtained prior to cleaving the distal end of the concatenated fibre to form a fibre Fabry-Pérot sensor. The arrangement used to determine these parameters is

schematically shown in Figure 7.1. The reflected beam from a fusion-spliced mirror was detected using a 2×2 coupler arrangement operated at 1300 nm. The light source used was an ANDO AQ-1338 intensity-stabilised 1300 nm laser diode whilst the detector was an ANDO AQ-2715 InGaAs photodiode connected to an ANDO AQ-2105 power meter unit. Both ends of the spliced fibre were alternately fused to one of the legs of the directional coupler to evaluate the forward- and backward-direction properties of the spliced mirror. The unused fibre leg of the directional coupler was immersed in a pool of index matching liquid to prevent unwanted reflections.

The excess losses of the proximal mirrors presented in Table 7.1 allowed for all loss mechanisms including transmission and scattering loss terms at the splice. These losses implied that the effective reflectance of the distal mirrors was reduced by a factor of 5.5 dB and 3.4 dB for the face-coated and core-coated sensors, respectively. To compensate for this loss, the reflectance of the distal mirror was increased. The thickness chosen was a half-wave at 840 nm as this was very convenient for the monitoring system. This thickness gave a (fibre-film-air) reflectance of about 30% at the measurement wavelength of 1300 nm. This reflectance was close to the maximum possible (quarter-wave optical thickness) and this was desirable as the reflectivity was later decreased when the film was covered with epoxy in bonding it to a cantilever. The effective (fibre-film-air) reflectance of the distal Fabry-Pérot mirror for the face-coated sensor was about 8.4 % whilst that of the core-coated sensor was 10.4 % (Table 7.1).

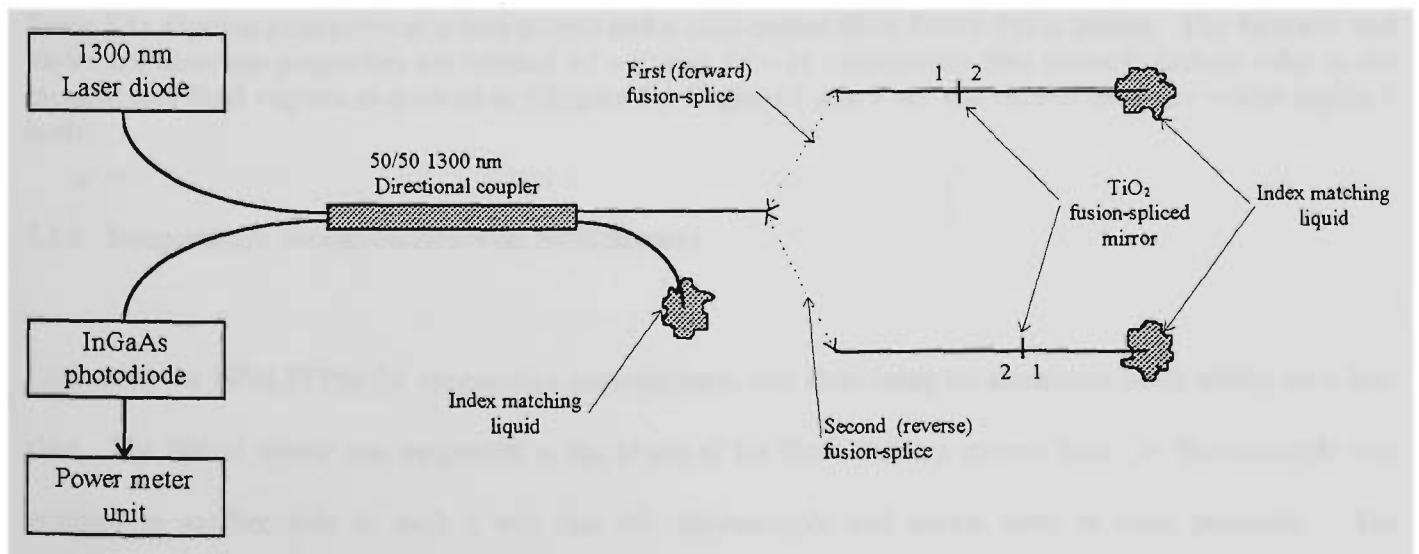


Figure 7.1: Schematic diagram for evaluating the optical properties of in-fibre fusion-spliced reflectors.

In general the optical properties of the proximal reflectors for either the face-coated or core-coated sensors were similar as presented in Table 7.1. This result was expected since only the film in the region of the core was effective in reflecting the light. In addition Table 7.1 shows that the forward-and backward-direction optical properties of the face-coated or the core-coated fusion-spliced mirrors were slightly different. Both face-coated and core-coated in-fibre fusion-spliced mirrors exhibited some non-reciprocal properties. When addressed in transmission, the best direction to illuminate these sensors is in the direction which exhibits the least amount of single-pass loss.

Parameters	Face-Coated Fabry-Pérot <i>ComFace</i>		Core-Coated Fabry-Pérot <i>ComCore</i>	
	$bd = 12$	$bd = 21$	$bd = 12$	$bd = 21$
Reflectance (first mirror): $R_{bd} = r_{bd} ^2$	11.5 %	7.0 %	3.6 %	5.4 %
Transmittance (first mirror): $T_{bd} = t_{bd} ^2$	52.5 %	53.5 %	59 %	59 %
Excess loss (first mirror): $L_{bd} = 1 - R_{bd} - T_{bd}$	36.0 %	39.5 %	37.4 %	35.6 %
Reflectance (second mirror): $R_{23} = r_{23} ^2$	~ 30 %		~ 30 %	
Effective Reflectance (second): $ r_{23} ^2 t_{12} ^2 t_{21} ^2$	8.4 %		10.4 %	
Cavity length	5.5 mm		5.0 mm	

Table 7.1: Optical properties of a face-coated and a core-coated fibre Fabry-Pérot sensor. The forward and backward direction properties are labeled $bd = 12$ and $bd = 21$ respectively [the numeric indices refer to the incident and final regions as defined in Chapter 3]. Regions 1 and 2 are the core of the fibre whilst region 3 is air.

7.1.2 Temperature Measurements with NPM Sensors

Calibrating the NPM FFPSs for temperature measurements was done using an aluminum block sitting on a hot-plate. The optical sensor was suspended at the centre of the block inside a narrow hole. A thermocouple was mounted in another hole in such a way that the thermocouple and sensor were in close proximity. The thermocouple was thermally contacted to the aluminum block using silicone heat-sink compound. The FFPS was not in direct contact with the block and equilibrated via cavity radiation. The assumption made is that the block, thermocouple and the FFPS were in thermal equilibrium at a uniform temperature.

Figure 7.2 shows the experimental arrangement used. The FFPS was addressed with an arrangement similar to that shown in Figure 7.1 whilst the type-K thermocouple was read with a Fluke 52 K/J thermometer (resolution of 0.1 °C and an accuracy of ± 1 °C in the range between 0 °C and 260 °C). Fringe shifts in the output of the FFPS were evident from the peaks and troughs in the detected intensity as the temperature was altered.

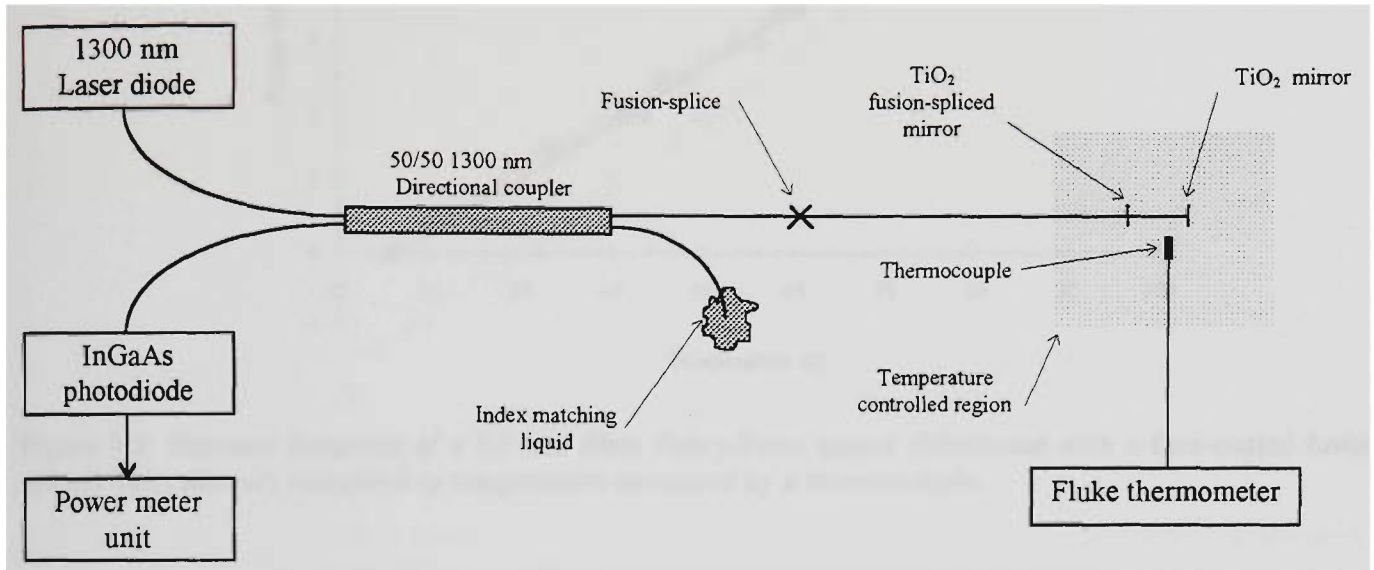


Figure 7.2: Schematic diagram of the system used for evaluating the performance of an in-fibre fusion-spliced Fabry-Pérot interferometer as a temperature sensor.

A typical experimental measurement run involved slowly increasing the temperature of the hot-plate (heating cycle) and subsequently allowing the block to naturally cool to room temperature (cooling cycle). The hot-plate was turned off to begin the cooling cycle after several fringe shifts have been observed in the interferometric output of the Fabry-Pérot sensor. A heating cycle typically took about 2 hours while the cooling cycle about 3 hours.

The linearity of FFPS interferometric fringe shifts with temperature for both *ComFace* and *ComCore* sensors may be seen in Figure 7.3 and Figure 7.4. The points plotted in the figures are the maxima and minima of the corresponding interferometric outputs. The lines of best fit in Figure 7.3 and Figure 7.4 have a 0.998 correlation coefficient (r^2). The absolute temperature sensitivities were calculated from the slopes of these lines and the associated errors were obtained from the least squares fit.

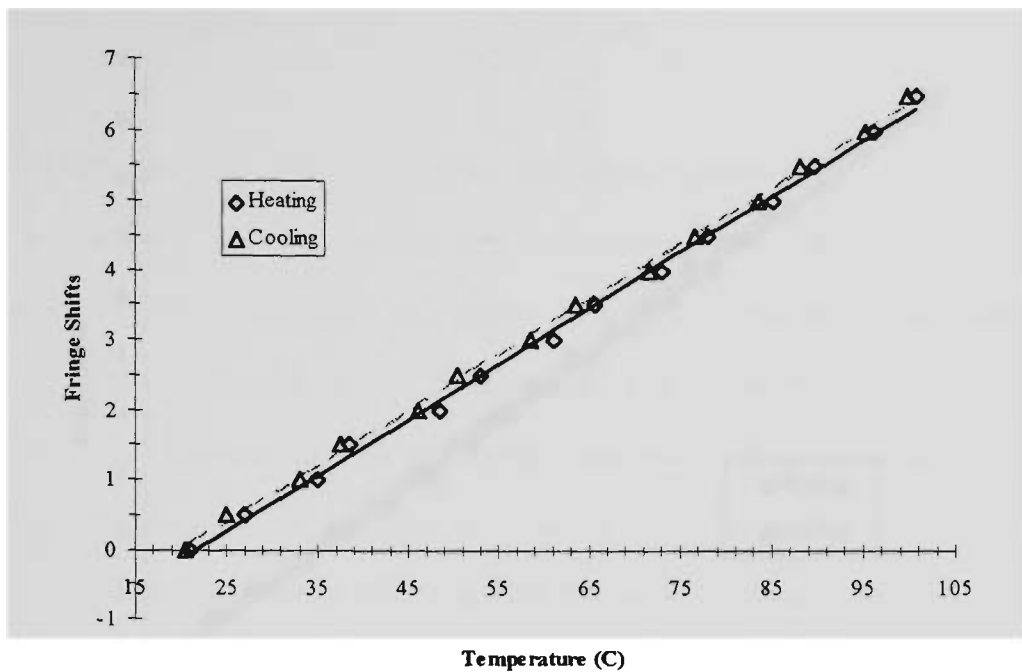


Figure 7.3: Thermal Response of a 5.5 mm fibre Fabry-Pérot sensor (fabricated with a face-coated fusion-spliced TiO_2 mirror) compared to temperature measured by a thermocouple.

The fractional phase-temperature sensitivity of the sensors was also calculated. The uncertainties in this parameter were substantially due to a dominant contribution from the large uncertainty in determining the length of the sensor. Nevertheless, the optical sensors exhibited an average fractional phase sensitivity of about $6.7 \pm 1.0 \times 10^{-6} / ^\circ\text{C}$ which was lower than the expected value of $8.04 \times 10^{-6} / ^\circ\text{C}$ (evaluated at ~ 780 nm, see Chapter 4). Any difference can be attributed to the crude method of detecting the interferometric fringe shifts and possibly to a small temperature difference between the thermocouple and the FFPS. Table 7.2 summarises the temperature performance of the NPM sensors.

Hysteresis between the heating and cooling cycles is evident in Figure 7.3 and Figure 7.4 and may be explained by a thermal lag between the radiation coupled FFPS and the direct contact thermocouple. For the purpose of taking initial temperature measurements, however, the arrangement of the aluminum block was sufficient to demonstrate the performance of FFPS as temperature sensors. In the subsequent temperature measurements, improved experimental arrangements were employed minimising thermal hysteresis.

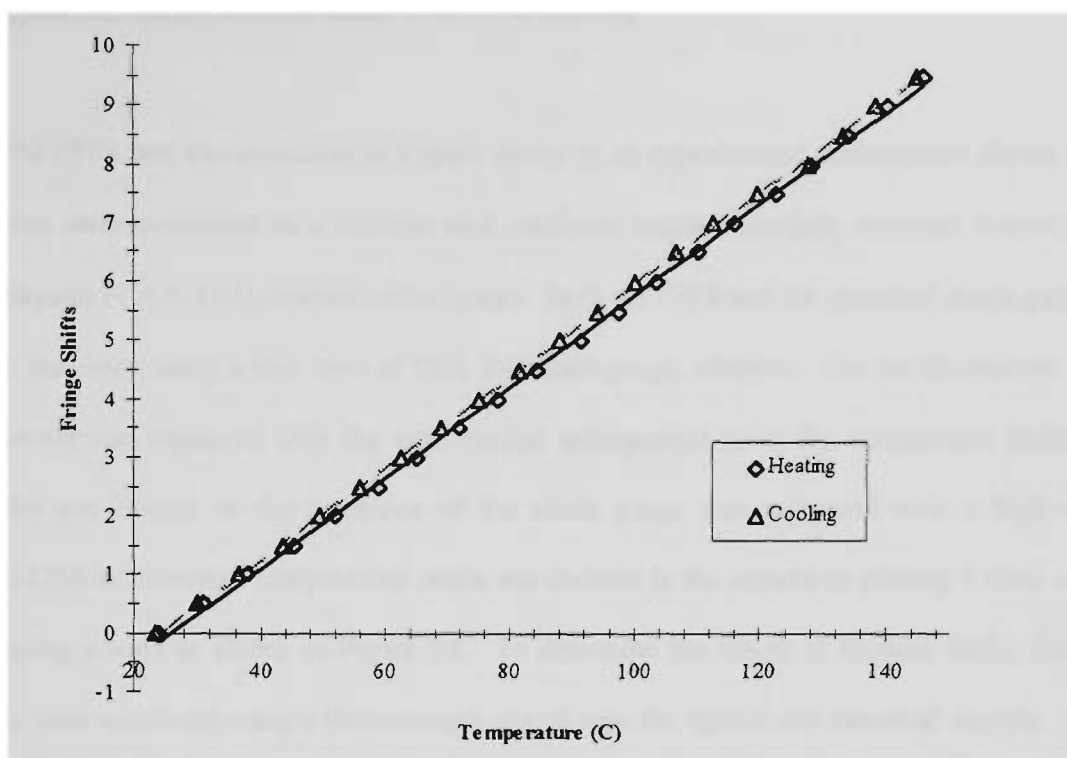


Figure 7.4: Fringe shifts of a 5 mm fibre Fabry-Pérot sensor (fabricated with a core-coated fusion-spliced TiO₂ mirror) against temperature determined with a thermocouple.

Parameters	Units	<i>ComFace</i>	<i>ComCore</i>
Unambiguous measurand range (heating)	°C / fringe	12.4 ± 0.2	12.79 ± 0.09
Unambiguous measurand range (cooling)	°C / fringe	12.5 ± 0.1	12.75 ± 0.04
Unambiguous measurand range (average)	°C / fringe	12.4 ± 0.2	12.8 ± 0.1
Average fractional phase-temperature sensitivity	10 ⁻⁶ / °C	6.5 ± 0.5	6.9 ± 0.5
Free spectral range	GHz	19 ± 0.7	20 ± 0.8
cavity length	mm	5.5 ± 0.2	5.0 ± 0.2

Table 7.2: Experimental temperature sensitivities of fibre Fabry-Pérot sensors with either a face- or core-coated spliced mirror.

In summary, there was no major difference in the optical performance of NPM fibre Fabry-Pérot sensors with either a face- or core-coated-spliced TiO₂ mirror as temperature sensors. Both sensors gave excellent phase-temperature linearity over a temperature range of around 100 °C.

7.1.3 Static Longitudinal Strain Measurement with NPM Sensors

The *ComCore* NPM FFPS was also evaluated as a strain sensor in an experimental arrangement shown in Figure 7.5. The sensor was surface-mounted on a stainless steel cantilever beside a similarly mounted 5-mm-long TML (Tokyo Sokki Kenkyujo) FLA-5-11-1L resistive strain gauge. Both the FFPS and the electrical strain gauge (ESG) were glued on the cantilever using a thin layer of TML P-2 strain-gauge adhesive. The interferometric output of the Fabry-Pérot sensor was measured with the same optical arrangement as in the temperature measurements (Figure 7.2) whilst any change in the resistance of the strain gauge was measured with a high-resolution Hewlett-Packard 3478A multimeter. Longitudinal strain was induced in the sensors by placing a mass at the free end, thereby inducing a bend as shown in Figure 7.6. To determine the extent of thermal drifts, the ambient thermal variations were monitored using a thermocouple placed near the optical and electrical sensors. A typical measurement run involved gradual loading followed by a gradual unloading of the free end of the cantilever.

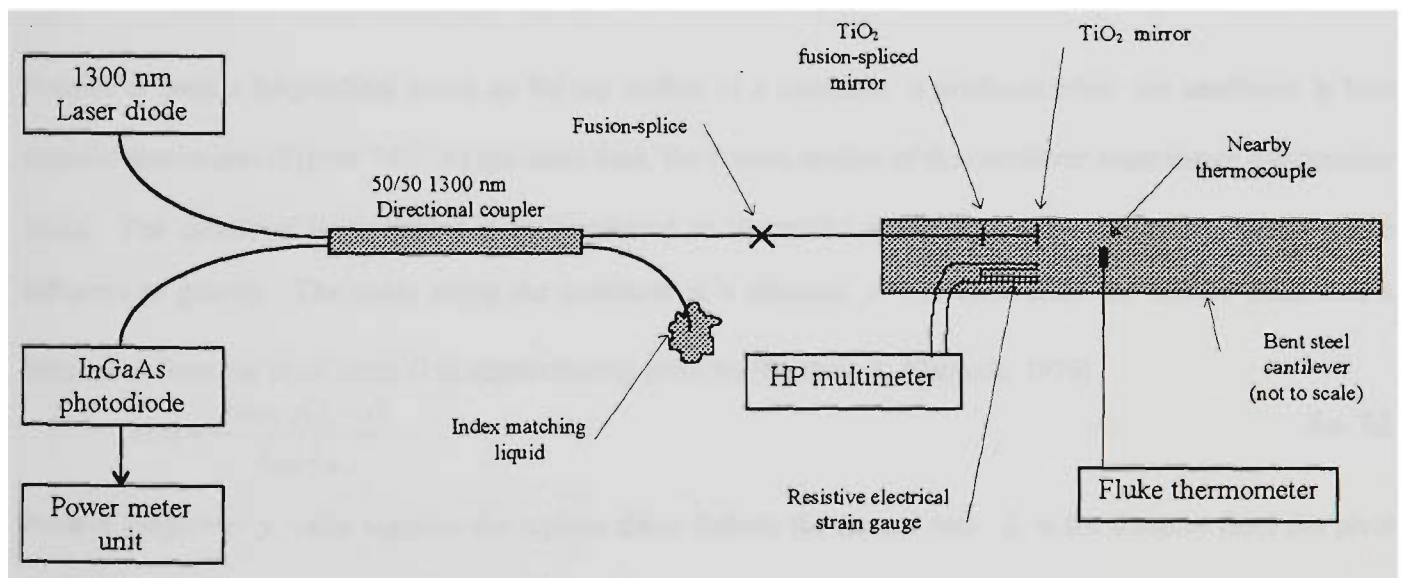


Figure 7.5: Schematic diagram of the system used for evaluating the performance of an in-fibre fusion-spliced Fabry-Pérot interferometer as a strain sensor.

Although the refractive index of the cured glue used to fix the sensors on the cantilever was not measured, it was previously observed that the reflectance of an ordinarily cleaved end embedded in cured glue was greatly reduced from its air value. In this circumstance, it was important for the distal end of the FFPS to be coated for high reflectance before being glued.

The resistive strain gauge had an average resistance of $\sim 120 \Omega$ and a gauge factor of 2.14. The gauge factor is the ratio between the fractional change in the resistance of the ESG and strain. The Hewlett-Packard 3478A multimeter had an accuracy of $\pm 4 \Omega$ and a resolution of $1 \text{ m}\Omega$. This resistance resolution implied a strain resolution of about $\sim 3.9 \mu\epsilon$ which was adequate for the purpose of initial strain measurements.

Typically, a Wheatstone bridge amplifier is used to measure variations in the resistance of an ESG. Such an amplifier involved four strain gauges configured such that at least one of these strain gauges can compensate for temperature-induced drifts in the primary ESG. However, the use of four strain gauges was unnecessary provided that the strain measurements were taken in a thermally stable environment. Based on the manufacturer's test results for the TML FLA-5-11-1L strain gauge, the worst case value for the change in the gauge factor due to temperature is about 2 % per 4°C . The laboratory temperature seldom changed by more than 4°C over short periods because of the built-in climate control.

Positive or tensile longitudinal strain on the top surface of a cantilever is produced when the cantilever is bent concave downwards (Figure 7.6). At the same time, the bottom surface of the cantilever experiences compressive strain. The cantilever in its unbent state is assumed to be parallel to the horizontal, *i.e.* perpendicular to the influence of gravity. The strain along the cantilever at a distance y transverse from the neutral plane and a distance z from the pivot point O is approximately given by [Benham & Warnock, 1976]

$$\epsilon(z) \approx \frac{y m_{WT} g (L - z)}{Y_{can} I_m} \quad \text{Eq. 7.1}$$

Positive (negative) y value signifies the regions above (below) the neutral axis. L is the distance from the pivot point where the bending weight is applied and Y_{can} the Young's Modulus of the cantilever beam. I_m is the second moment of the cross-sectional area of the cantilever about the neutral plane, m_{WT} is the mass hanging from the free end and g is the acceleration due to gravity. For a cantilever beam with rectangular cross-section of thickness a_{can} and of width b_{can} ,

$$I_m = \frac{(a_{can})^3 b_{can}}{12} \quad \text{Eq. 7.2}$$

Eq. 7.1 predicts that strain increases linearly along the cantilever, reaching a maximum tensile or compressive strain near the pivot point O . This linear relationship implies that the average strain measured by either an FFPS

or an ESG is the strain at the centre of these sensors. The error in Eq. 7.1 increases with increasing curvature of the cantilever and in order to avoid the sensors measuring different average strain values, both the z -coordinate of their centres and their gauge lengths need to be the same.

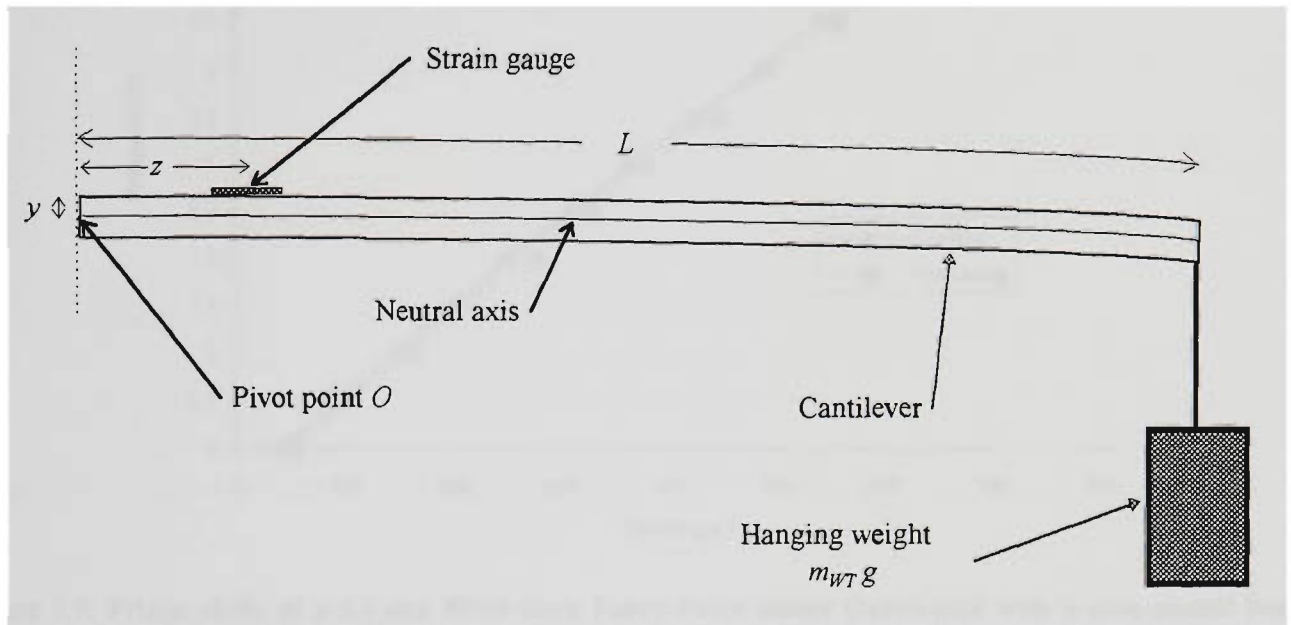


Figure 7.6: Bending arrangement used to induce strain in surface-mounted sensors.

In subsequent discussions, the strain measurement refers to result from *ComCore* and an electrical sensor whose centres were both located at about 95 mm from the pivot point on the top surface of the cantilever. The cantilever had a 9 mm side square cross-section and hence the sensors 4.5 mm above the neutral axis. The cantilever was made of 304-type stainless steel bar which had a thermal expansion coefficient of $17.2 \times 10^{-6} / ^\circ C$, a Young's modulus of 193 GPa and a weight of 4 N. The weight of the cantilever provided a bending moment which gave the cantilever an initial curvature in addition to other deformations.

Figure 7.7 shows the fringe shifts of *ComCore* against the strain measured by the electrical strain gauge. The points on the graph are the peaks and troughs of the interferometric outputs relative to the peak at around $50 \mu\epsilon$ (*i.e.* the chosen zero reference value). From the line of best fit of the data for the loading and unloading cycles, the strain sensitivity of *ComCore* at 1300 nm was about $112.8 \mu\epsilon / \text{fringe}$. Only the data up to $600 \mu\epsilon$ was used to calculate the strain sensitivity since above this value the temperature variations began to increase (see Figure 7.8). The average fractional strain sensitivity (optical gauge factor) was 0.79 ± 0.06 which was in excellent agreement with the expected value of 0.78 (Chapter 4). The strain sensitivities of *ComCore* are summarised in Table 7.3.

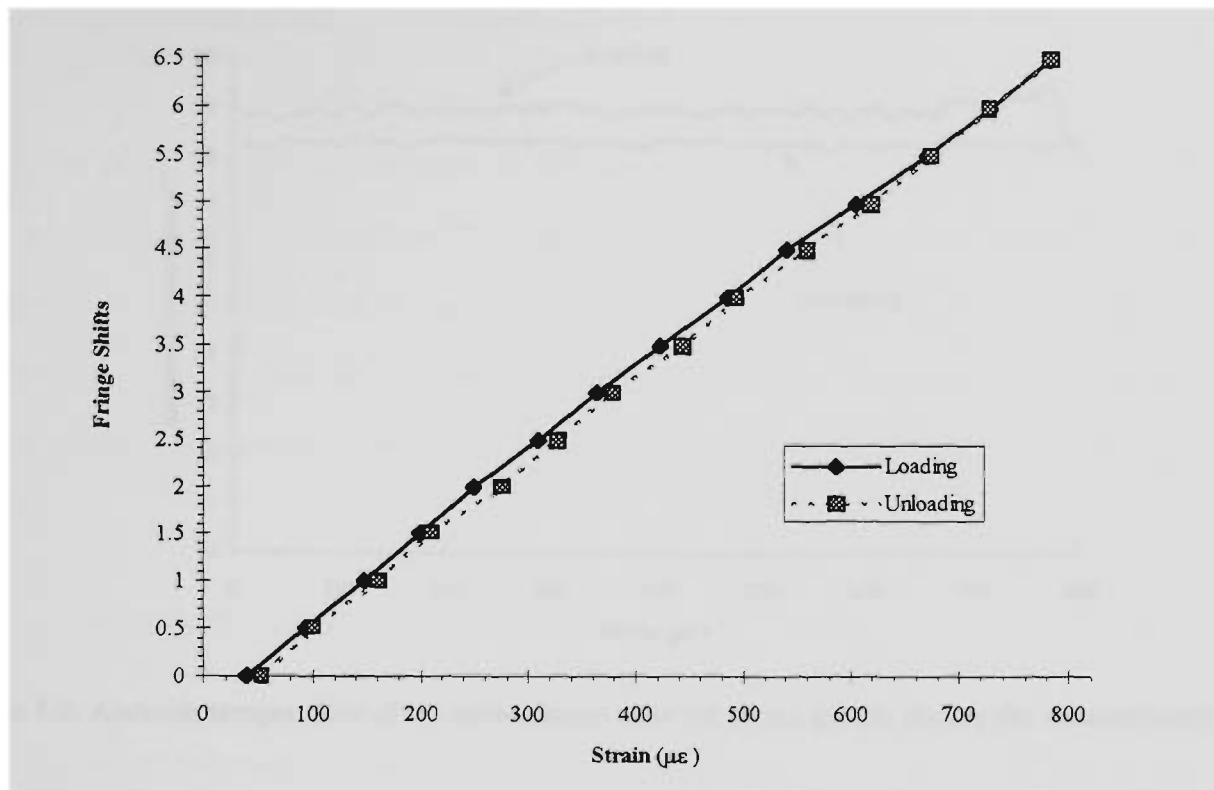


Figure 7.7: Fringe shifts of a 5.0 mm NPM fibre Fabry-Pérot sensor (fabricated with a core-coated fusion-spliced TiO_2 mirror) placed on the top surface of a $645 \times 9 \times 9 \text{ mm}^3$ stainless steel cantilever beam against the ESG strain. The sensor was 95 mm from the pivot point.

During the measurement run, no attempt was made to stabilise the temperatures of the cantilever beam and the sensors. However, the ambient temperature of their immediate environments was monitored using a thermocouple.

Figure 7.8 shows the ambient temperature during the measurement run described in Figure 7.7.

Parameters	Units	ComCore
Unambiguous measurand range (loading)	$\mu\epsilon$	112.2 ± 1.1
Unambiguous measurand range (unloading)	$\mu\epsilon$	113.0 ± 1.0
Unambiguous measurand range(average)	$\mu\epsilon$	112.6 ± 2.0
Average optical gauge factor		0.79 ± 0.06
Free spectral range (FSR)	GHz	20 ± 0.8
Cavity length	mm	5.0 ± 0.2

Table 7.3: Experimental strain sensitivities of an NPM fibre Fabry-Pérot sensor with a core-coated splice mirror (measured at 1300 nm).

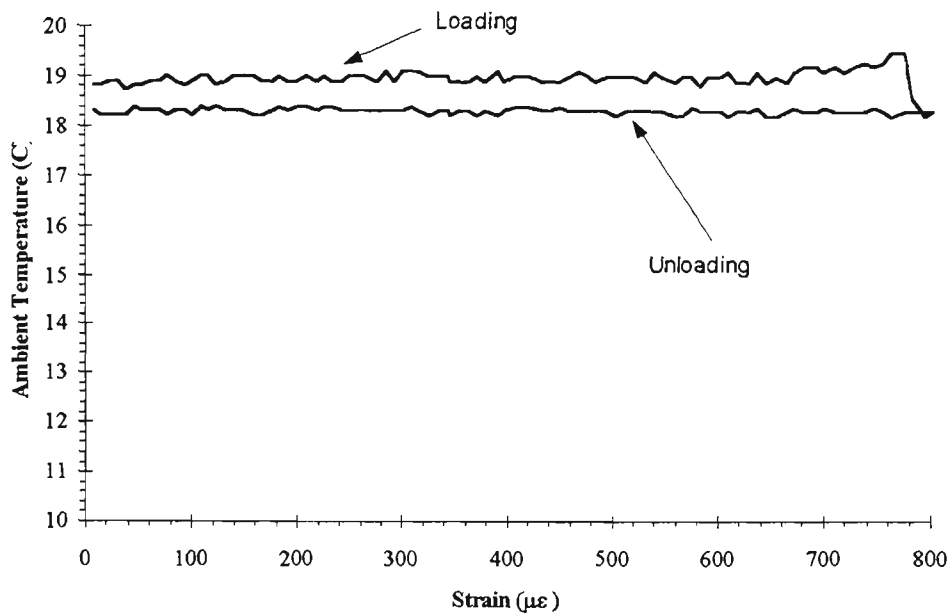


Figure 7.8: Ambient temperature of the environment near the strain gauges during the measurement run.

The average temperature during the loading run was $\sim 19^\circ\text{C}$ whilst during the unloading run $\sim 18.3^\circ\text{C}$. For an unbonded sensor, this temperature difference of -0.7°C during the measurements would correspond to a shift of ~ -0.05 of a fringe (using the measured temperature sensitivity of *ComCore* when the sensor was free to expand). For a bonded sensor, the thermally induced strain must also be taken into account. This thermally-induced strain (differential thermal expansion) on the sensor was about $-12\ \mu\epsilon$ which was equivalent to about -0.11 of a fringe based on the measured phase-strain sensitivity of the sensor as shown earlier in Table 7.3. Thus the aggregated shift is expected to be about -0.16 fringe. Figure 7.7 shows that the unloading cycle lags the loading cycle by some 0.14 of a fringe. Thus, it can be concluded that the phase difference between the cycles was predominantly due to the thermal expansion of the cantilever.

In summary, a 5 mm NPM fusion-spliced fibre Fabry-Pérot sensor has performed in a broadly comparable manner to a 5 mm resistive strain gauge over an $800\ \mu\epsilon$ range. The main advantage of the optical sensor is that it has a small footprint compared to a typical resistive strain gauge although the UMR of the optical sensor was small and it was necessary to count fringes to obtain measurements up to $800\ \mu\epsilon$. Since temperature- and strain-induced effects are indistinguishable in the output of an FFPS, the temperature must be kept constant or at least determined by some other means for unambiguous strain measurements.

7.2 Performance of Fusion-Spliced Birefringent Fibre Fabry-Pérot Sensors

Following the fabrication and characterisation of NPM fusion-spliced FPPSs, the more challenging polarisation-maintaining or birefringent fusion-spliced FFPSs were fabricated (second generation of sensors). The fabrication of the latter was similar to that of NPM fusion-spliced FPPSs with the additional requirement of alignment of the polarisation axes of the birefringent FFPS with those of the lead-in fibre. Accurate post-fusion alignment of the polarisation axes was necessary in order to obtain satisfactory independent measurements using the two axial interferometers.

7.2.1 Characteristics of the Fusion-Spliced Birefringent Sensors

Several birefringent fusion-spliced fibre Fabry-Pérot sensors were fabricated using 3M FS-HB-4211 birefringent fibre which had an internal elliptical cladding (IEC-fibres). Typically, these fusion-spliced sensors had long cavities compared to the NPM sensors. There are several reasons for this but one of the main ones was that the construction of fusion-spliced mirrors with aligned polarisation axes was not easy and it was decided not to risk successfully spliced mirrors by having them subject to tension during future cleaving to produce the second mirror surface. These fibres had a cladding outer diameter (OD) of 80 μm compared to 125 μm for the NPM fibres. Hence they would be subjected to greater stress than was the case with NPM fusion-spliced mirrors. The birefringent sensor (labeled “*HibiFace*”) for which subsequent data is presented had a 44 mm cavity length. The TiO_2 film used in the fusion-spliced mirrors had an initial thickness of 92 nm (before splicing). The distal mirror was simply the cleaved end of the fibre which had a reflectance of about 3.6 %.

The eventual performance of the sensor critically depended on the polarimetric and optical properties of the reflective fusion splice. These properties were determined during the fabrication of the fusion-spliced TiO_2 mirror (Chapter 5). For *HibiFace*, the post-fusion transmission along one polarisation axis was approximately 16% and the polarisation extinction ratio was approximately 1%. This extinction value represented a good figure of merit as it was close to the extinction ratio of the analyser used (0.65%). The polarisation extinction ratio value indicated excellent post-fusion angular alignment between the polarisation axes of the lead-in fibre and the Fabry-Pérot

cavity. Because the core diameter of the birefringent fibres was $4.5\ \mu\text{m}$, even a slight misalignment of the cores can yield a high insertion loss in addition to other loss mechanisms at the splice. Since, when addressed in reflection, the double pass transmission through the reflective splice would be about 2.5 %, this sensor was more suitable for transmission measurements.

The high transmission loss prevented accurate determination of the bi-directional reflection properties of the splice. Experimentally the reflected beam from the splice was not sufficiently distinguishable from the beam reflected from the other optical components. However, the reflection properties can be indirectly obtained from the fringe visibility of the sensor (Chapter 3). The transmission fringe visibility of *HibiFace* was measured to be $V = 0.014$. This low visibility implies a combined reflectance of the Fabry-Pérot mirrors of $R = 0.7\ \%$ (Eq. 3.58) and thus the sensor certainly satisfies the condition for low-finesse. The reflectance of the TiO_2 reflective fusion splice was estimated to be about 0.15 %.

In a typical experimental run, the transmitted intensity was measured to be about $40\ \mu\text{W}$. Assuming the axes were equally excited, about $20\ \mu\text{W}$ was available along each polarisation axis. Even though the fringe visibility was low, the peak-to-peak value of the axial interferometer signals was about $560\ \text{nW}$ which is about two-order of magnitude larger than the noise floor of the photodiode circuit (see Appendix C).

7.2.2 Temperature Measurements with Fusion-Spliced Birefringent Sensors

Figure 7.9 shows a schematic diagram of the experimental arrangement employed to determine the phase-temperature sensitivity of each axial interferometer of *HibiFace*. The sensor was suspended in a drilled hole within an aluminum block which was enclosed with a styrofoam box. The finite thickness of the styrofoam box meant that approximately 1 cm of the Fabry-Pérot cavity was suspended outside the aluminum block. This allowed the distal end of the sensor to be brought close to a $\times 10$ microscope objective lens which collimated the exit beam (Figure 7.9). Since not all of the sensor was inside the aluminum block, the effective sensing length for temperature measurements was less than the physical sensor length. The average temperature of the sensor was dependent on the temperature gradient along the cavity. For the temperature measurements results shown in

Figure 7.11, the length suspended within the aluminum block was estimated to be 34 ± 1 mm, some 75% of the 44-mm cavity of the sensor.

The temperature of *HibiFace* was varied using resistors embedded in the aluminum block as shown in Figure 7.10. An AD 590 semiconductor device was used to provide independent temperature measurements.

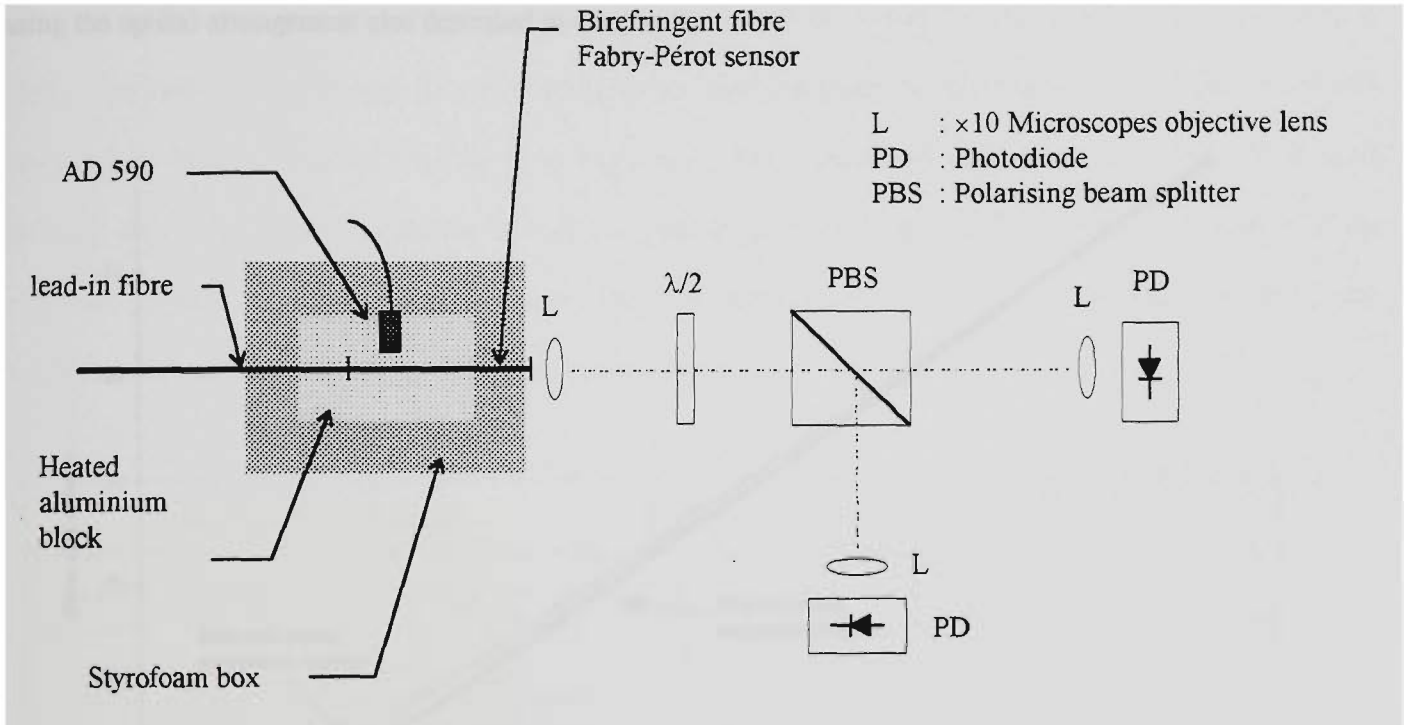


Figure 7.9: Experimental arrangement used to measure the transmission output of a birefringent Fabry-Pérot sensor (*HibiFace*).

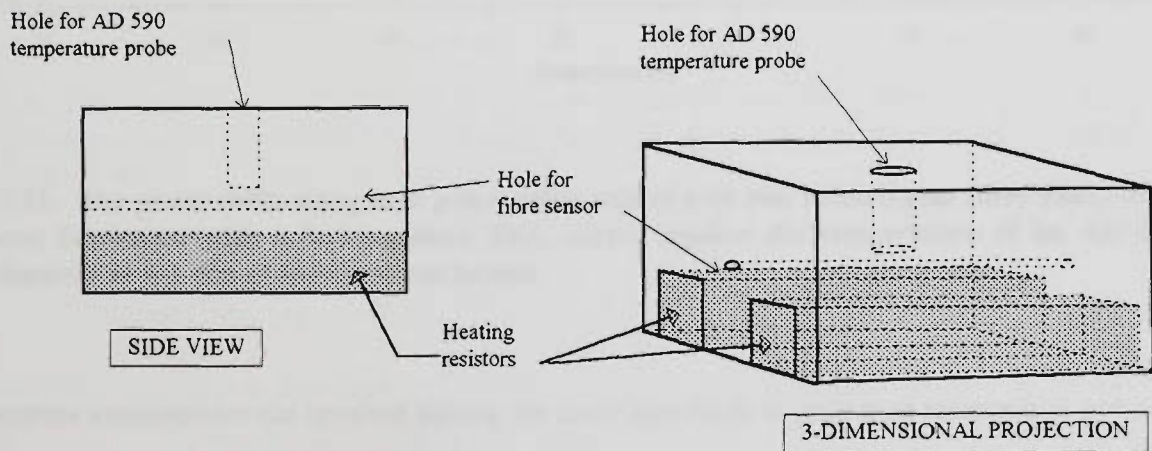


Figure 7.10: Heating arrangement used to determine the thermal sensitivity of a birefringent Fabry-Pérot sensor.

The AD 590 gave an output change of about $1 \mu\text{A}/^\circ\text{C}$ which was converted to a voltage sensitivity of about $100 \text{ mV}/^\circ\text{C}$ using a transconductance amplifier. The accuracy of the AD 590 temperature readings was $\pm 1.5^\circ\text{C}$ between of -55°C to $+150^\circ\text{C}$ with a repeatability of 0.1°C . The optical sensor was illuminated with the output of a 785 nm LD whose drive current was modulated in a sawtooth manner to implement the pseudo-heterodyne signal processing scheme described in Chapter 6. The resulting optical signal along each polarisation axis was detected using the optical arrangement also described in Chapter 6.

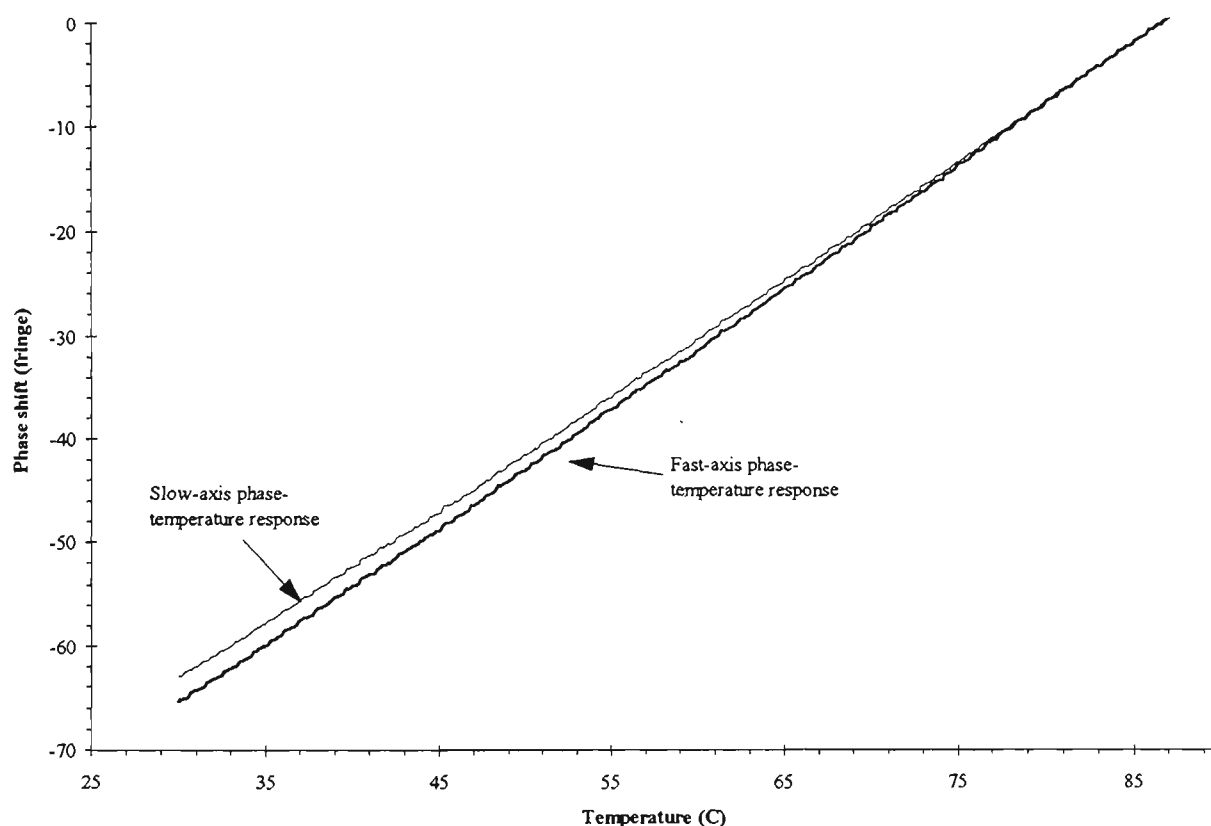


Figure 7.11: The phase shifts along each polarisation axis of a 44 mm birefringent fibre Fabry-Pérot sensor (*HibiFace*) fabricated with a fusion-spliced TiO_2 mirror against the temperature of an AD 590 device. Approximately $34 \pm 1 \text{ mm}$ of *HibiFace* was heated.

A temperature measurement run involved heating the aluminum block to some high temperature and subsequently allowing the block to slowly cool. During the cooling cycle, the phase shifts of each axial interferometer of the sensor and the temperature determined by the AD 590 were monitored and recorded. Data gathering commenced after the block had begun to slowly cool. These circumstances were such that the temperature of the block and the

AD 590 were expected to be very similar. Because a fraction of *HibiFace* was outside the insulated aluminum block, the average temperature along the sensor was expected to be lower than that of the aluminum block.

The automated monitoring system recorded the fringe shifts of the fast- and slow-axis interferometers of the sensor for every 0.1 °C change in the temperature of the AD 590 during cooling from 87 °C to 30 °C. The results are displayed in Figure 7.11. The aluminum block cooled in about 3 hours and the automated system was useful in monitoring such a long process. The monitoring system was essentially the same as the final measuring system described in Chapter 6 except that the electronic circuits which were used to process the optical signals were different from those that were employed with the grating-based birefringent FFPSs. The performance of the electronic circuits used with *HibiFace* were found to significantly contribute to the phase noise in the measurements. This phase noise is discussed later in this section.

Temperature parameter	Fast-axis	Slow-axis	Differential
Phase-temperature sensitivity (fringe/°C)	1.1649 ± 0.0009	1.1212 ± 0.0008	0.044 ± 0.002
Unambiguous measurand range (°C)	0.8584 ± 0.006	0.8919 ± 0.0007	23 ± 1
Fractional temperature sensitivity (10 ⁻⁶ /°C)	9.2 ± 0.3	8.9 ± 0.3	0.35 ± 0.03
Linear correlation coefficient (r ²)	0.9997	0.9997	0.9817
UMR extension factor ($E_{UMR,T}$)	26.8		

Table 7.4: The temperature sensitivities of a 44-mm birefringent fibre Fabry-Pérot sensor (*HibiFace*) fabricated with a fusion-spliced TiO₂ mirror. Approximately 34 ± 1 mm of *HibiFace* was directly exposed to thermal variations.

Table 7.4 summarises the phase-temperature sensitivities of *HibiFace*. The fractional phase-temperature sensitivity was slightly higher than those for NPM FFPSs (Table 7.2). The slight difference can be attributed to the slight difference in $\frac{dn}{dT}$ for the fibres and the different operation wavelengths of the sensors. The NPM sensors were operated with a 1300 nm LD whilst the birefringent sensors used a 785 nm LD.

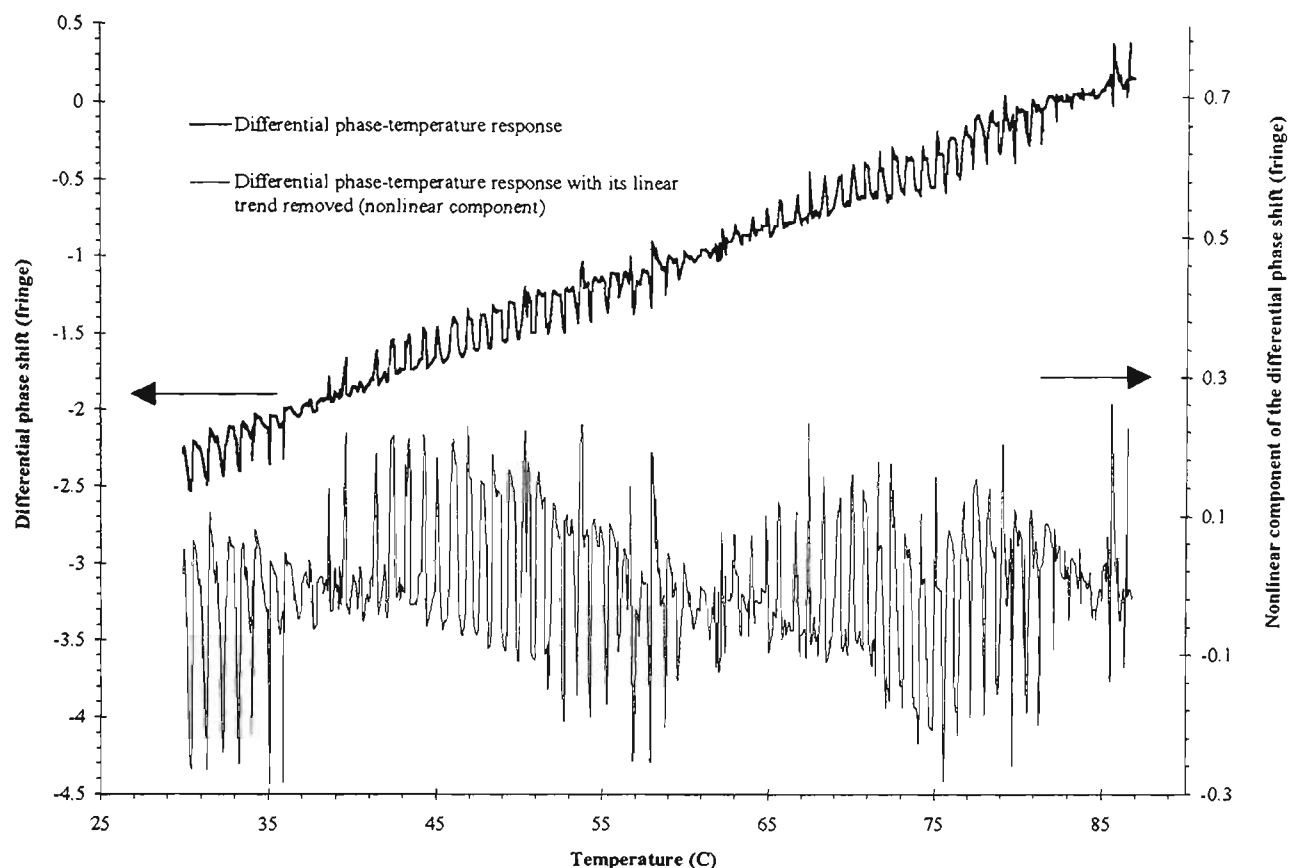


Figure 7.12: The differential (between the fast-axis and slow-axis) phase shifts of a 44-mm birefringent fibre Fabry-Pérot sensor (*HibiFace*) against the temperature of an AD 590 device. Approximately 34 ± 1 mm of the sensor was heated.

The phase-temperature responses of both axial interferometers were reasonably linear as seen in Figure 7.11 and confirmed by the correlation coefficients of 0.9997 (Table 7.4). It was expected that the differential phase-temperature response (fast-axis response relative to that of the slow-axis) would be linear as well. A general linear variation was in fact observed except that the correlation coefficient for the differential phase-temperature response, 0.9817, was lower than either of the fast- or slow-axis values as presented in Table 7.4. Figure 7.12 highlights this discrepancy by showing the differential phase response (left vertical scale in the figure) as the temperature of the centre of the block was varied. In addition to a linear trend, the differential phase also exhibited a phase noise which appears periodic with respect to temperature. To focus on this periodic feature, the general linear behaviour in the differential phase can be removed to highlight the nonlinear component of the differential phase (right vertical axis) as shown in Figure 7.12. This nonlinear (not linear with respect to temperature) phase “noise” showed some high thermal-frequency periodic structure together with a periodic phase-amplitude envelope

modulation. This modulation envelope is consistent with a beating effect produced when two periodic noise signals with slightly different thermal-frequencies are subtracted.

In Figure 7.12, the temperature-period of the envelope in the differential phase-temperature response was about 23 °C whilst that of the higher thermal-frequency periodic variations was approximately 0.9 °C. Interestingly, these values were very similar to the unambiguous measurand (temperature) range values for the axial and differential information summarised in Table 7.4. A detailed examination of the high frequency nonlinear component of the differential phase response shows that it involved at least 10 data points per period and thus any aliasing effects may be discounted. If these effects are systematic rather than random, it is not strictly correct to refer to them as noise. However, since they are mixed with genuine noise and they represent a form of “noise” as far as the measurements are concerned, then this term will continue to be used in the following discussion.

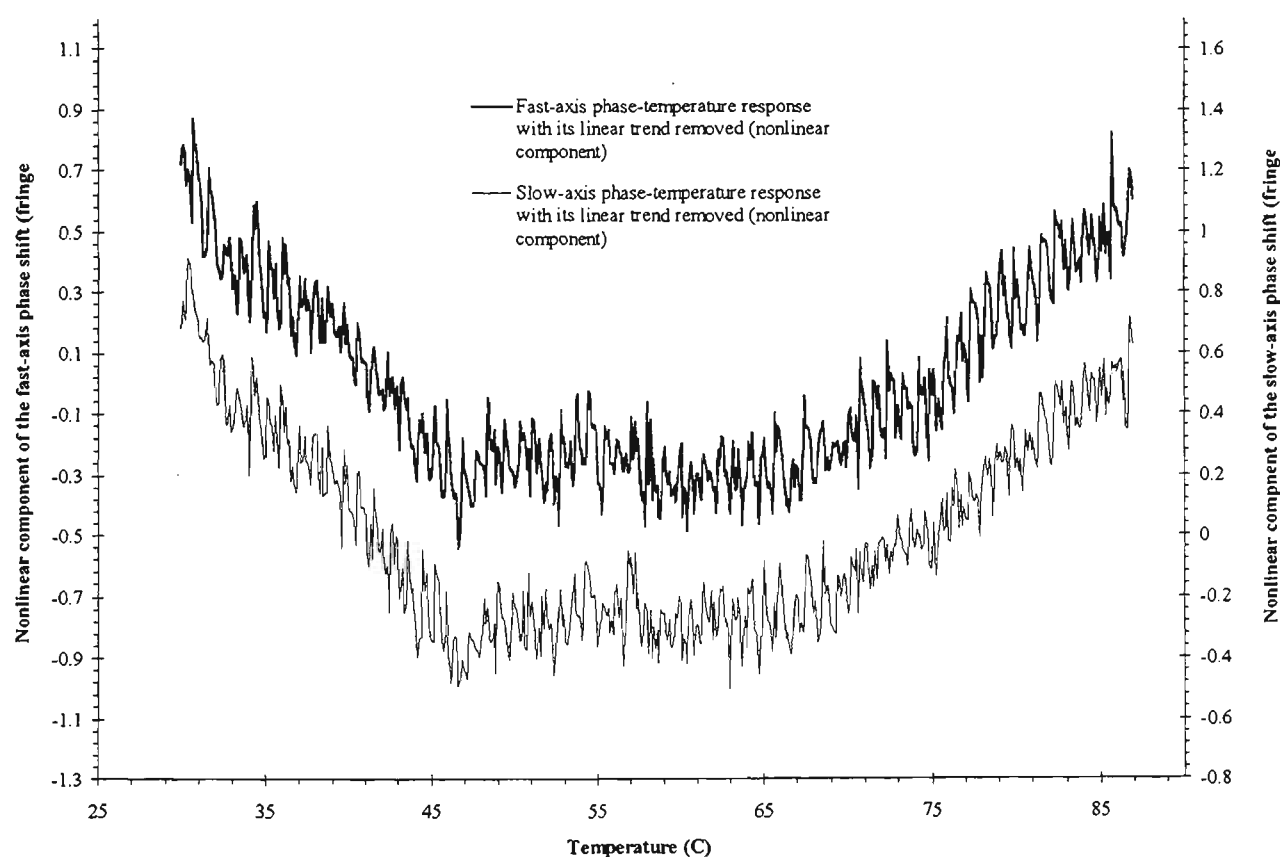


Figure 7.13: The phase shifts for each polarisation axis, with its linear trend removed, for a 44 mm birefringent fibre Fabry-Pérot sensor (fabricated with a face-coated splice mirror) against temperature measured by an AD 590 device. Approximately 34 ± 1 mm of the sensor was heated. The fast- and slow-axis responses are presented with the same vertical scale but different vertical offset values.

These effects in the differential phase prompted a more careful examination of the individual polarisation axis responses shown in Figure 7.11. The linear thermal trend of the fast- and slow-axis phase responses in Figure 7.11 can be removed to highlight any nonlinear effects in these individual axial responses. Figure 7.13 shows the fast- and slow-axis responses with their linear trends removed (nonlinear component). The figure shows that the nonlinear component of either axial response exhibits two main features, an approximately (concaved upward) parabolic variation with a span of ~ 58 °C and a high frequency periodic variation with a period of ~ 0.9 °C.

These parabolic features were a very small fraction of the total phase change (~ 1 fringe in 60 fringes) and hence not easily seen in Figure 7.11. They were present only in the axial responses (Figure 7.13) but not in the differential response (Figure 7.12). This observation implies the parabolic features may have been caused by a common source. The quadratic dependence of each axial phase-temperature response could arise from two sources. The first of these possible sources was the first-order term in the dependence of the refractive index on temperature. Lee *et al.* [1988] have measured this term using a fusion-spliced Fabry-Pérot interferometer technique over the range -200 °C to $+1050$ °C. They found substantial quadratic nonlinearity in the phase change as a function of temperature, particularly over the range -200 °C to $+100$ °C. Over this range the slope of the curve changed by a factor of 3.2. Using the data of Lee *et al.* to obtain estimates of the phase nonlinearity over the temperature range shown in Figure 7.13 is not easy because of the way the data was presented and the limited number of data points over the temperature range of interest. However we re-plotted their data and estimated the phase nonlinearity to be about 3 %. While this value is not considered highly reliable it is clearly of the same order of magnitude and form as the nonlinearity we have observed (~ 2 %). Hence the first-order term in the thermal dependence of refractive index may well be the origin of the quadratic phase feature shown in Figure 7.13.

The second possibility which we considered for the origin of the quadratic phase nonlinearity arises from the non-uniform temperature along the sensor length. If the temperature gradient at points along the sensor varies in a nonlinear way with increasing aluminum block temperature, then the total phase change will include a term which is quadratic in temperature rise above ambient. Such a nonlinear gradient could arise if the temperature of the free end of the fibre increased in a nonlinear way with aluminum block temperature or if the width of the region over

which there existed a substantial temperature gradient changed with temperature. This effect while plausible is not easy to reliably quantify. Whatever the origin of the quadratic nonlinearity in the phase change it is clear that it arises from an effect which is common to both interferometer axes.

Figure 7.14 shows the remaining component of each axial phase-temperature response of *HibiFace* after the linear and quadratic trends have been removed. Both axial responses shown in Figure 7.14 exhibit slowly varying changes with respect to the temperature of the block. These slowly varying features were not observed in the differential response (Figure 7.12) and so may also have been caused by a common source. Most likely, these phase variations may have been caused by thermally induced drifts in the LD emission frequency since the temperature measurements were taken over a long period of time. Unfortunately this effect could not be verified because the temperature and consequently the wavelength changes of the LD were not recorded during the measurement run.

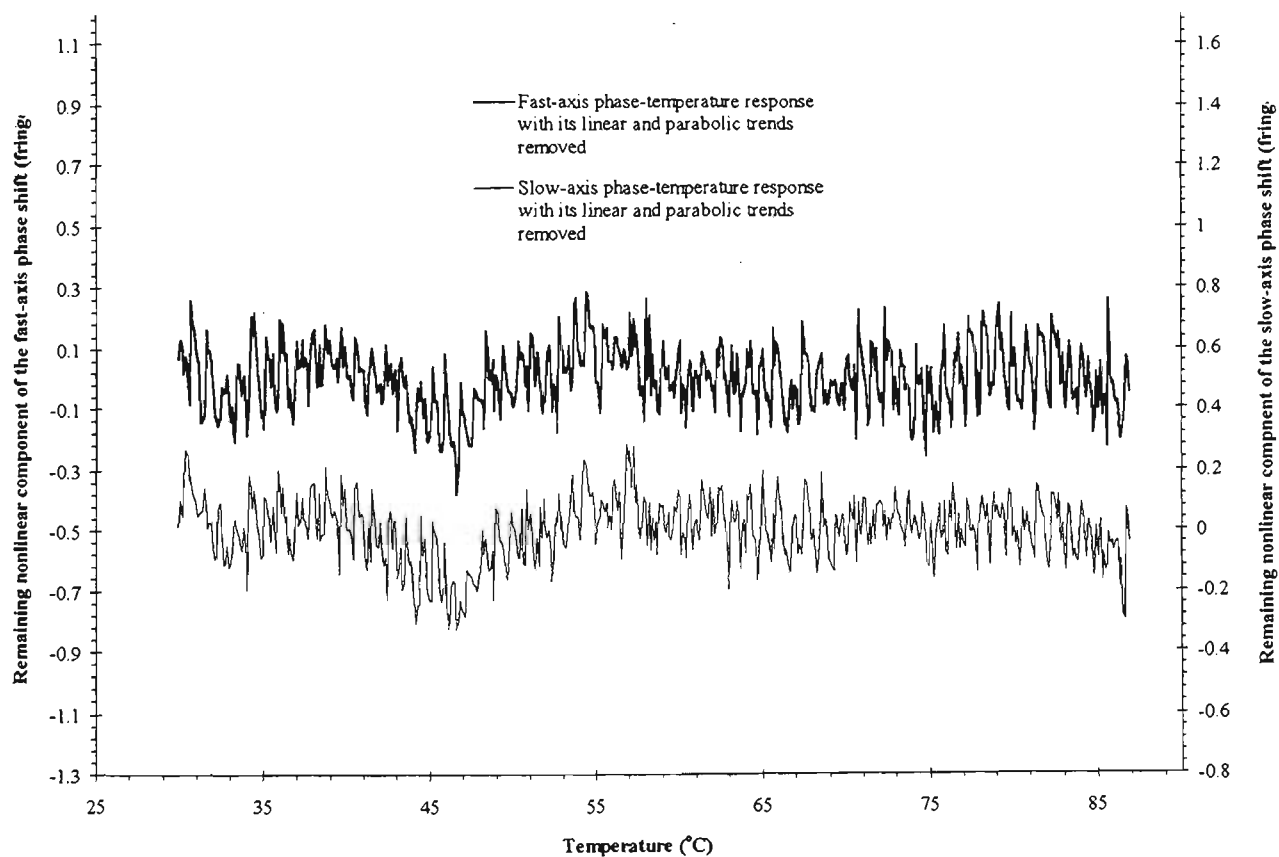


Figure 7.14: The phase shifts of each polarisation axis with its linear and parabolic trends removed for a 44 mm birefringent fibre Fabry-Pérot sensor (fabricated with a face-coated splice mirror) against temperature measured by an AD 590 device. Approximately 34 ± 1 mm of the sensor was heated. The fast- and slow-axis responses are presented with the same vertical scale but different vertical offset values.

Figure 7.13 and Figure 7.14 confirm the presence of some periodic phase noise (spikes) on both the fast and slow axial responses. This periodic phase noise on either axial response of the sensor was not sinusoidal but definitely periodic. The phase-amplitudes of these periodic signals appeared to be very similar although the phase-amplitude for the fast axis exhibited a slightly larger value than that of the slow axis. On average the peak-to-peak phase-amplitude of the periodic phase noise was about $0.2 \times 2\pi$ radian. A closer examination of these phase noise features revealed their behaviour had some similarity to that of a negatively sloping sawtooth signal. Using the fast Fourier transform algorithm, the fundamental harmonic variations on the fast-axis and slow-axis curves shown in Figure 7.14 were determined to be 1.17 ± 0.01 /°C and 1.11 ± 0.01 /°C for the fast and slow axes respectively. The corresponding thermal period of these sawtooth-type phase noise were 0.855 ± 0.009 °C and 0.901 ± 0.009 °C for the fast and slow axes respectively. Interestingly these thermal period values were essentially the same as the UMR for the corresponding axial interferometer of the sensor (Table 7.4). Unlike the parabolic features, the periodic phase noise on the fast- and slow-axis responses did not cancel each other when the differential phase response was determined. Moreover, because these periodic phase noise in the fast- and slow-axis responses had different thermal periods, a beating effect is observed in the differential phase-temperature response (Figure 7.12).

Initially the periodic phase noise on each axial response was simply considered as unavoidable noise of the entire measurement arrangement. However, the periodic nature and the relatively large amplitude of the periodic phase noise along either the fast- or slow-axis response suggest it needs further investigation if the performance of this sensor is to be fully understood. The possible causes of this phase noise are discussed in the following paragraphs.

The periodic phase noise in each axial response can be attributed to effects in the signal processing electronics for the raw interferometric output of each axial interferometer. The effectiveness of a pseudo-heterodyne signal processing scheme implemented using a modulated LD hinges on two important characteristics of the optical frequency ramp modulation. First, the amplitude of the optical frequency ramp needs to be exactly equal to (or an integer-multiple of) the free spectral range of the interferometer. Second, the optical frequency scan of the ramp needs to be perfectly linear. Deviations from the ideal adjustment of the amplitude and the linearity of the ramp were found to contribute to the phase noise in each axial response. There is one other factor which is also

involved. The modulation of the current through the LD produces an unwanted intensity modulation of the output which also needs to be removed by the signal processing scheme. In fact that is the real reason for the difference between the signal processing scheme used with *HibiFace* and that described in chapter 6 and then used with the Bragg grating-based sensor described later in this chapter. The signal processing used with *HibiFace* is rather simpler than that described in chapter 6 as the sensor length was long enough for very small LD modulation to be sufficient to scan the system through one FSR.

Before the *HibiFace* interferometric phase shifts were measured, two signal-processing-related adjustments had to be made. The first adjustment involved choosing the amplitude of the sawtooth drive current into the LD such that the resulting total optical frequency change in the output of the LD, $\Delta\nu$, was equivalent to the average free spectral range of the sensor, $\Delta\nu_{FSR}$. During each period of the linear sawtooth modulation, this adjustment produced a signal involving a factor (*c.f.* the corresponding ideal expression given by Eq. 6.37)

$$V \cos(d_\omega \omega_m t - \phi_{int}), \quad \text{Eq. 7.3}$$

$$\text{where } d_\omega = \frac{\Delta\nu}{\Delta\nu_{FSR}}, \quad \text{Eq. 7.4}$$

V is the fringe visibility, ω_m the angular modulation frequency and ϕ_{int} is the total round-trip phase change for the Fabry-Pérot cavity (excluding changes produced by the ramp modulation). Eq. 7.3 assumes that the optical frequency of the LD output varies linearly during each ramp period. The ideal adjustment requires

$$d_\omega = 1. \quad \text{Eq. 7.5}$$

The sawtooth drive current induced a sawtooth modulation in the intensity of LD output and also of the interferometric signals. The second adjustment is related to the scheme used to isolate the $V \cos(d_\omega \omega_m t - \phi_{int})$ term from the raw intensity-modulated pseudo-heterodyne signal I_{raw} (*c.f.* the corresponding ideal expression given by Eq. 6.40):

$$I_{raw} = K' [1 + r(t)] [1 + V \cos(d_\omega \omega_m t - \phi_{int})]. \quad \text{Eq. 7.6}$$

Here K' is a constant of proportionality which includes the quantum efficiency of the photodiode and the gain of its transimpedance amplifier. The scheme used with *HibiFace* to separate $V \cos(d_\omega \omega_m t - \phi_{int})$ involved subtracting from I_{raw} a term proportional to $r(t)$ followed by band-pass filtering the resulting signal about the

modulation frequency. ($r(t)$ is the AC component (with respect to time t) of the sawtooth ramp divided by the DC component of the ramp). We can represent the action of the circuit elements in mathematical terms and include the effects of non-ideal adjustments by expanding the discussions of Chapter 6. The amount subtracted from the raw signal can be described by $K'[1 - d_e]r(t)$ where d_e is some small number. This signal $K'[1 - d_e]r(t)$ can be derived from the output of the sawtooth generator used to modulate the LD. In these terms, the processed interferometric signal can be readily obtained as

$$\begin{aligned} I'_{raw,sub} &= K' \left\{ d_e r(t) + V[1 + r(t)] \cos(d_\omega \omega_m t - \phi_{int}) \right\} + K' \\ &= K' V \left\{ d_V r(t) + [1 + r(t)] \cos(d_\omega \omega_m t - \phi_{int}) \right\} + K' \end{aligned} \quad \text{Eq. 7.7}$$

where

$$d_V = \frac{d_e}{V}. \quad \text{Eq. 7.8}$$

If the signal derived from the sawtooth generator can be adjusted such that

$$d_V = d_e = 0, \quad \text{Eq. 7.9}$$

then the action of a narrow band-pass filter is to remove the DC term K' and the unwanted $r(t) \cos(d_\omega \omega_m t - \phi_{int})$ term in Eq. 7.7. This leaves a processed output proportional to $V \cos(d_\omega \omega_m t - \phi_{int})$. If the band-pass filter is not sufficiently narrow, then residual effects due to $r(t) \cos(d_\omega \omega_m t - \phi_{int})$ will appear in the output even if $d_V = d_e = 0$. However if $r(t) \ll 1$ these effects are expected to be small.

Unfortunately the 100Hz - 10KHz band-pass filter used with *HibiFace* was obviously far too wide to avoid these effects and hence they are expected to be present in the measured data. The expected phase errors were simulated using Mathematica. The simulation determined the positively-sloping zero-crossings of the AC component of $I'_{raw,sub}$. This was done by using the first term of Eq. 7.7 (without K') and allowing for ϕ_{int} -dependent zero-offsets arising from $r(t) \cos(d_\omega \omega_m t - \phi_{int})$ in calculating the zero-crossings. The results of these simulations are shown in Figure 7.15. The first curve plotted in the figure is the ideal phase reading obtained from the location of the positively-sloping zero-crossings of $V \cos(\omega_m t - \phi_{int})$ (which has no dependence on d_ω). The second curve in Figure 7.15 is the non-ideal phase reading similarly obtained from the location of the positively-sloping zero-crossings of the $I'_{raw,sub}$ for the case when $d_V = d_e = 0$, $d_\omega = 1$ and the (peak-to-peak) amplitude of $r(t)$ was 0.08 which was similar to the normalised sawtooth current of the LD used to obtain the temperature measurements

with *HibiFace*. The third curve in Figure 7.15 is the phase difference between the ideal and the non-ideal phase readings.

The ideal phase reading shown in Figure 7.15 behaved linearly with ϕ_{int} and lags ϕ_{int} by 0.25 fringe because of the cosine dependence. Figure 7.15 shows that the ideal and the non-ideal phase readings were essentially the same and thereby confirming the usefulness of the signal processing procedures described above to give an output which is essentially $V \cos(\omega_m t - \phi_{\text{int}})$. The phase difference between the ideal and the simulated (non-ideal) phase readings sinusoidally varies with ϕ_{int} and exhibits a peak-to-peak amplitude of 0.004 of a fringe. This sinusoidal phase error had a discontinuity at the beginning (or end) of each ramp modulation. This discontinuity can be attributed to the step change in $r(t)$ during flyback.

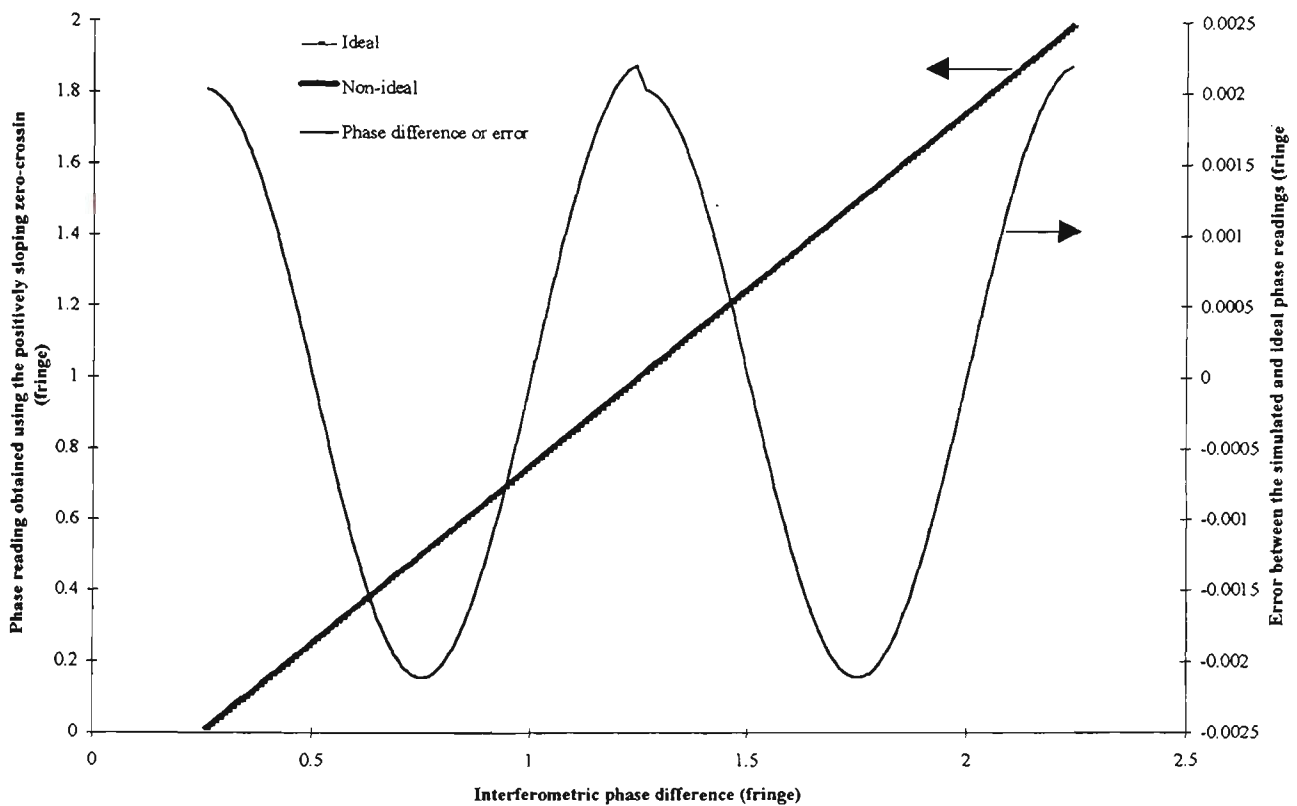


Figure 7.15: The simulated phase readings obtained from the positively sloping zero-crossing of the ideal and the processed (non-ideal) interferometric functions. The processed interferometric function is $K'V\{d_V r(t) + [1 + r(t)]\cos(d_\omega \omega_m t - \phi_{\text{int}})\}$ with $d_V = d_e = 0$, $d_\omega = 1$ whilst the ideal interferometric function is $V \cos(\omega_m t - \phi_{\text{int}})$. The (peak-to-peak) amplitude of $r(t)$ is 0.08. *NB:* The ideal and non-ideal curves are almost on top of each other.

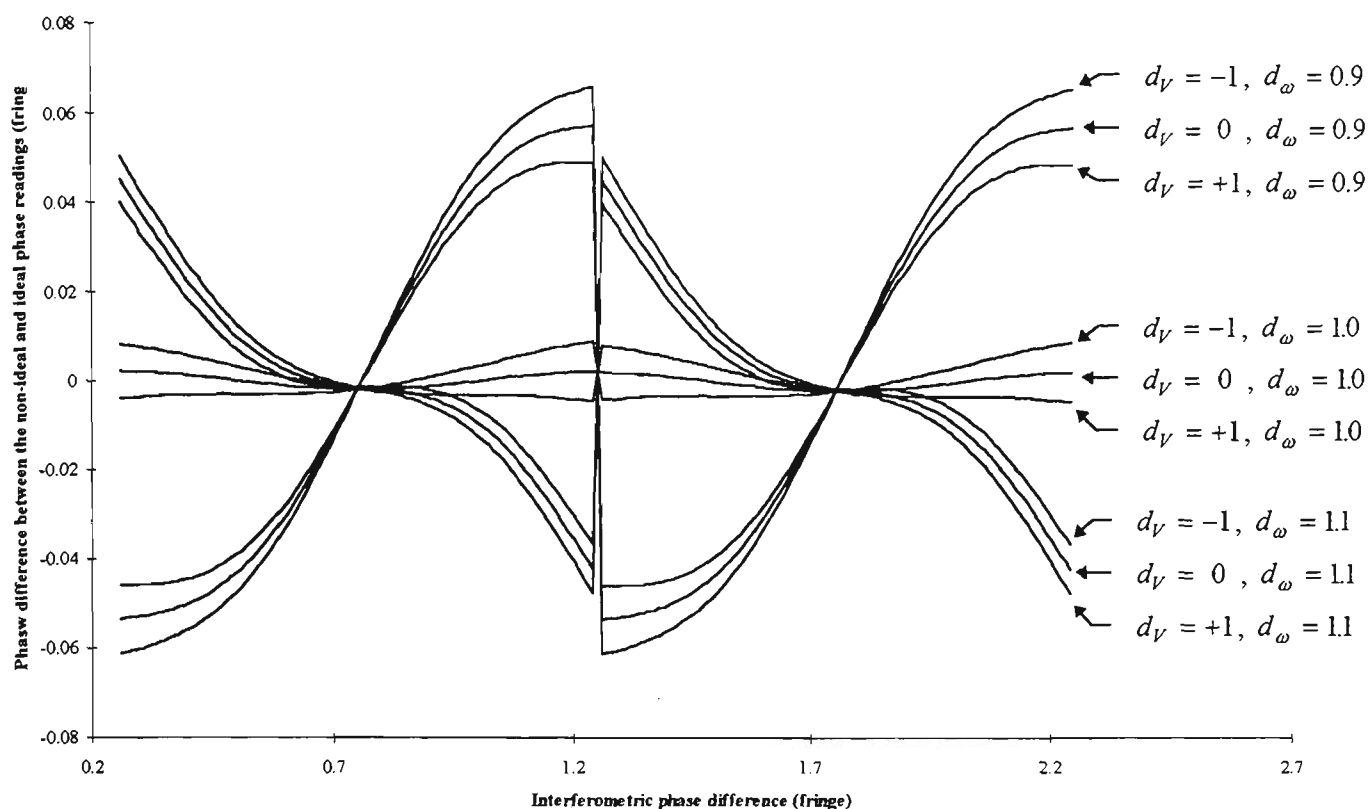


Figure 7.16: The difference in the phase readings obtained from the positively sloping zero-crossing of the ideal and the processed (non-ideal) interferometric functions. The processed interferometric function is $K'V\{d_V r(t) + [1+r(t)]\cos(d_\omega \omega_m t - \phi_{\text{int}})\}$ whilst the ideal interferometric function is $V \cos(\omega_m t - \phi_{\text{int}})$. The (peak-to-peak) amplitude of $r(t)$ is 0.08.

Although the period of the simulated phase noise presented in Figure 7.15 can explain the experimentally observed period of the periodic phase noise in the fast- and slow-axis responses of *HibiFace*, the results shown in the figure (for the case when Eq. 7.5 and Eq. 7.9 hold) still can not explain the sawtooth nature and the magnitude of the phase-amplitude noise observed in Figure 7.13 and Figure 7.14. Similarly-behaving sawtooth-type phase noise was subsequently simulated when $d_V \neq 0$ and $d_\omega \neq 1$. Figure 7.16 shows the difference between the non-ideal and the ideal phase readings for the cases indicated in the figure. For all the cases shown in Figure 7.16, the normalised ramp amplitude was 0.08. The cases presented in Figure 7.16 are believed to span the likely upper and lower bounds in the values d_V and d_ω for *HibiFace*. Although when temperature measurements with *HibiFace* were obtained, d_e was believed to be small, d_V can easily become significant because the transmission fringe visibility of *HibiFace* was low ($V \sim 0.014$). Nevertheless, during the experiments, d_V could be assumed to lie between -1 and +1 because there was no dominant background ramp feature in the intensity of the optical signal detected by the photodiode. Also it was believed that the maximum deviation of the optical frequency chirp of the

LD differed from the free spectral range of *HibiFace* by no more than $\pm 10\%$, i.e. $0.9 \leq d_\omega \leq 1.1$. Deviations larger than this would be expected to be visible in the output waveform.

Figure 7.16 illustrates that for the case when $d_\omega > 1$ the phase error behaves in a manner which is broadly similar to a negatively sloping nonlinear sawtooth ramp whilst for the case when $d_\omega < 1$, to a positively sloping nonlinear ramp. Furthermore examining each group of curves corresponding to $d_\omega = 1.1$, $d_\omega = 1.0$ and $d_\omega = 0.9$ reveals that the phase error slopes more negatively (or less positively) as d_V increases. Figure 7.16 shows that deviation of d_ω from the ideal condition of $d_\omega = 1$ had a greater contribution to the phase error compared with the contribution of the deviation of d_V from the ideal condition of $d_V = 0$. This observation implies that adjusting the amplitude of the optical frequency ramp to equal the free spectral range of the sensor was critical in order to effectively reduce the phase noise during the measurements.

Table 7.5 summarises the difference between the value of the phase error at the beginning and at the end of each ramp. The value for the case when $d_V = d_e = 0$ and $d_\omega = 1$ is simply the value of the peak-to-peak phase error amplitude because in such a case the phase error behaved sinusoidally as shown in Figure 7.15. Table 7.5 essentially shows that a ± 0.1 change in d_ω produces an error of about ± 0.1 fringe whilst $d_V = \pm 1$ yields a beginning-to-end-of-ramp phase error of about ± 0.01 fringe. Figure 7.16 and Table 7.5 indicate within the assumed limits on the value of d_V and d_ω , only about 50% of the magnitude of the observed phase errors on each axial phase response can be attributed to $d_V \neq 0$ and $d_\omega \neq 1$.

	$d_\omega = 1.1$	$d_\omega = 1.0$	$d_\omega = 0.9$
$d_V = +1$	+0.098	+0.013	-0.095
$d_V = 0$	+0.087	+0.004	-0.111
$d_V = -1$	+0.076	-0.013	-0.121

Table 7.5: The difference (as a fraction of a fringe) between the values of the phase error at the beginning and at the end of each ramp for the cases shown in Figure 7.16. The phase difference value for the case when $d_V = d_e = 0$ and $d_\omega = 1$ was the peak-to-peak amplitude value for the corresponding phase error.

A second possible source for the phase noise in each axial response of *HibiFace* is a nonlinearity in the optical frequency ramp modulation of the LD output. This nonlinearity is produced by the slow thermal response of the emission frequency of the LD to variations in drive current (i_{LD}). Such an effect would be most prominent during the ramp flyback where $\frac{di_{LD}}{dt}$ is relatively high. Appendix C will describe an experiment which measured the instantaneous optical frequency chirp of the LD as its current was varied in a linear sawtooth ramp fashion. These measurements quantified the deviations from ideal behaviour in the optical frequency of the LD output. Figure 7.17 shows the variation in the optical frequency normalised to the amplitude of the optical frequency ramp together with the ideal linear optical frequency ramp. The maximum optical frequency of the actual ramp lags that of the ideal ramp by about 0.07 of the ramp period.

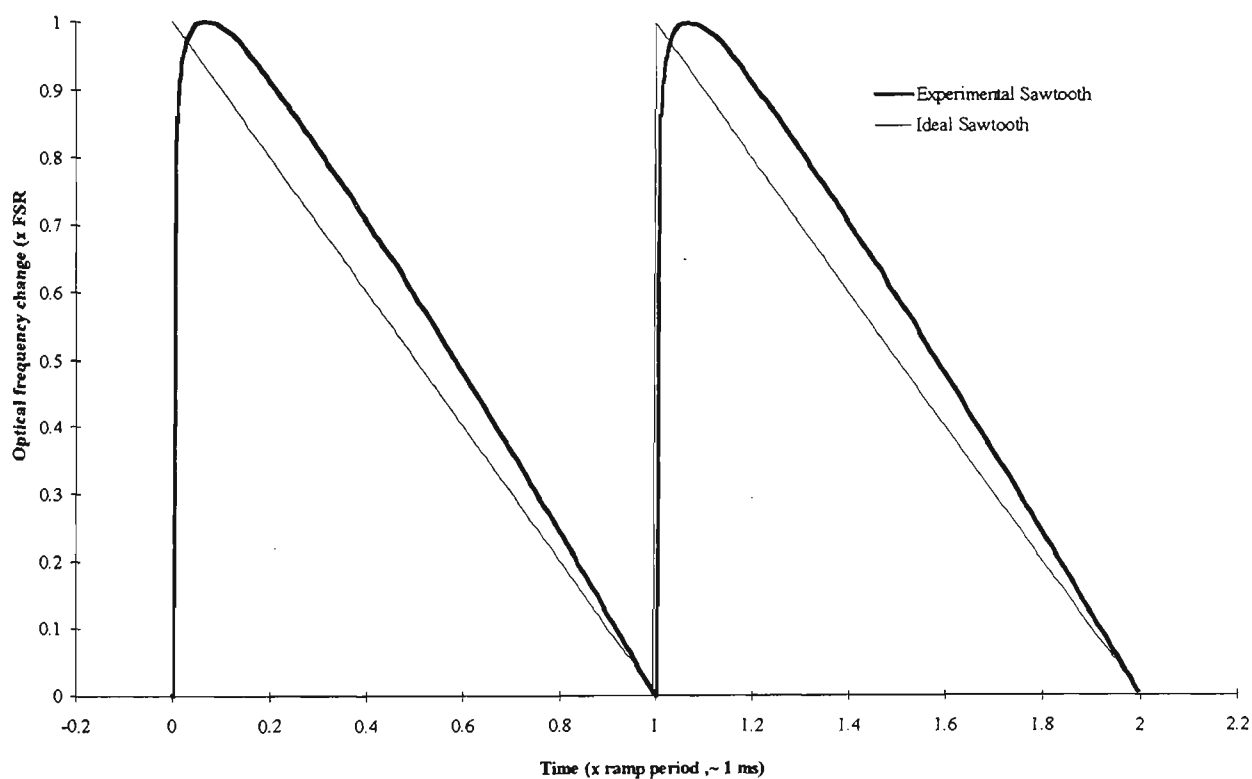


Figure 7.17: Experimentally measured (thicker line) nonlinear optical frequency ramp of an LD normalised to the free spectral range of a fibre Fabry–Pérot sensor. The second curve (thinner line) represents the ideal optical frequency sawtooth ramp.

For the data presented in this section, the peak-to-peak current modulation was about 2 mA and the DC current was about 50 mA. This sawtooth current modulation can be considered as a small-signal modulation. Hence, Figure 7.17 can be used as the normalised transfer function from ramp current modulation to optical frequency modulation for any ramp amplitude which satisfies the small-signal condition [Petermann, 1988].

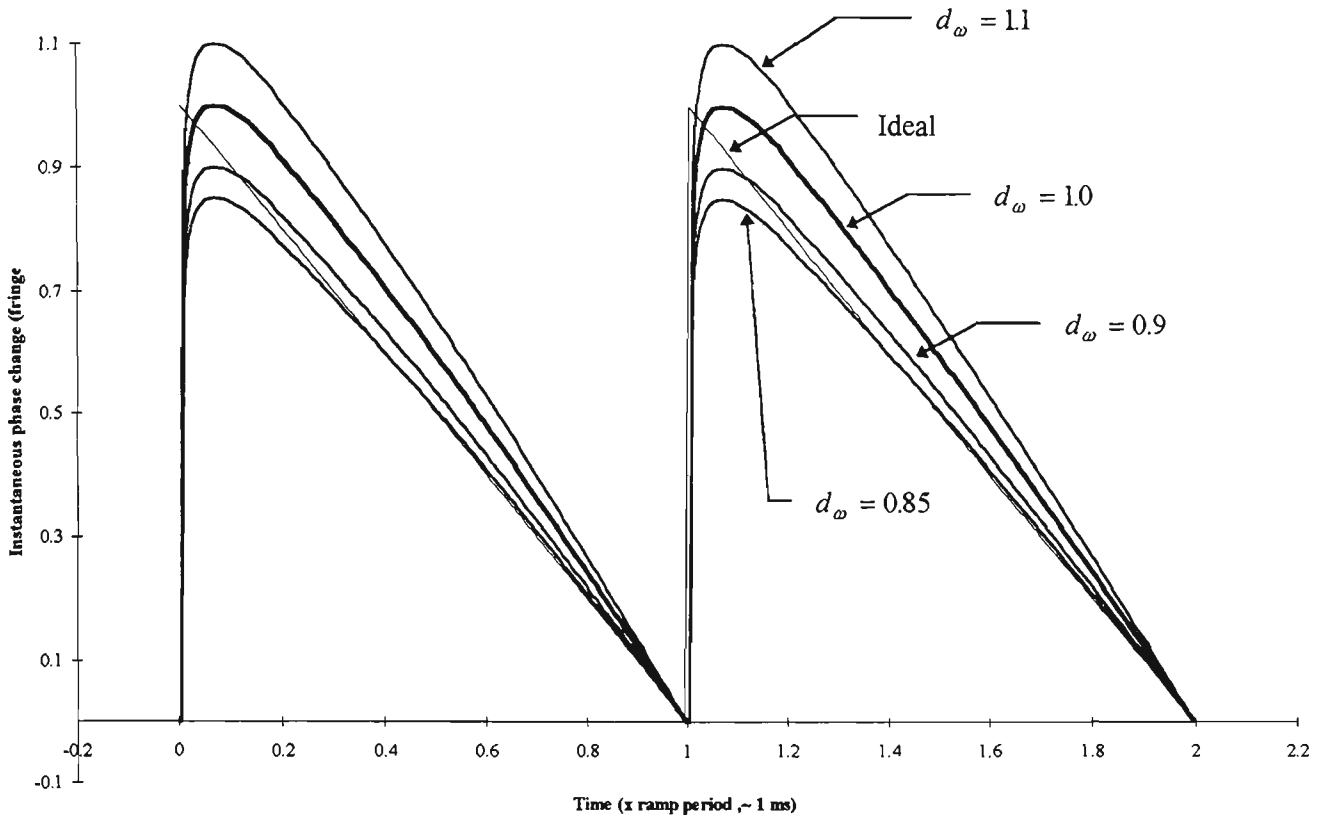


Figure 7.18: The time-varying phase produced by a nonlinear optical frequency ramp for different ratios of the optical frequency ramp amplitude and the free spectral range.

To simulate the effect of the nonlinear optical frequency ramp, the normalised transfer function depicted in Figure 7.17 was multiplied by $d_\omega \omega_m$. The resulting product was used to replace the $d_\omega \omega_m t$ term in Eq. 7.6 and Eq. 7.7 to yield nonlinear instantaneous phase variations during the ramp period. Consequently the actual experimental pseudo-heterodyne signal can be described as

$$I'_{raw,sub} = K'V \left\{ d_V r(t) + [1+r(t)] \cos(\phi_{sig} - \phi_{int}) \right\} + K' \quad \text{Eq. 7.10}$$

where $\phi_{sig} = \phi_{sig}^0 + \phi_{sig}^{nl}$ Eq. 7.11

describes the instantaneous time-varying phase of $I'_{raw,sub}$.

$$\phi_{sig}^0 = d_\omega \omega_m t \quad \text{Eq. 7.12}$$

is the linear variation (with respect to time) of ϕ_{sig} whilst ϕ_{sig}^{nl} represents all the nonlinear components. ϕ_{sig}^{nl} is the phase error function of ϕ_{sig} with respect to ϕ_{sig}^0 . Figure 7.18 shows ϕ_{sig} as a function of time and Figure 7.19 shows ϕ_{sig}^{nl} against time for several values of d_ω .

Figure 7.19 shows that each ϕ_{sig}^{nl} function is periodic with a period equal to the sawtooth modulation period. From the figure, it can be seen that the magnitude of ϕ_{sig}^{nl} depends on d_ω . When $d_\omega \approx 0.85$, the values of ϕ_{sig}^{nl} for times (relative to the beginning of the ramp) greater than 40 % of the ramp period are negligible. In fact for all values of d_ω , the largest value of ϕ_{sig}^{nl} occurs in the first 20% of the ramp period. In hindsight, possibly a better way to operate the sensor may involve only measuring zero-crossings occurring during the latter half of the ramp period and switching between positive- and negative-going crossings according to the phase of the signal.

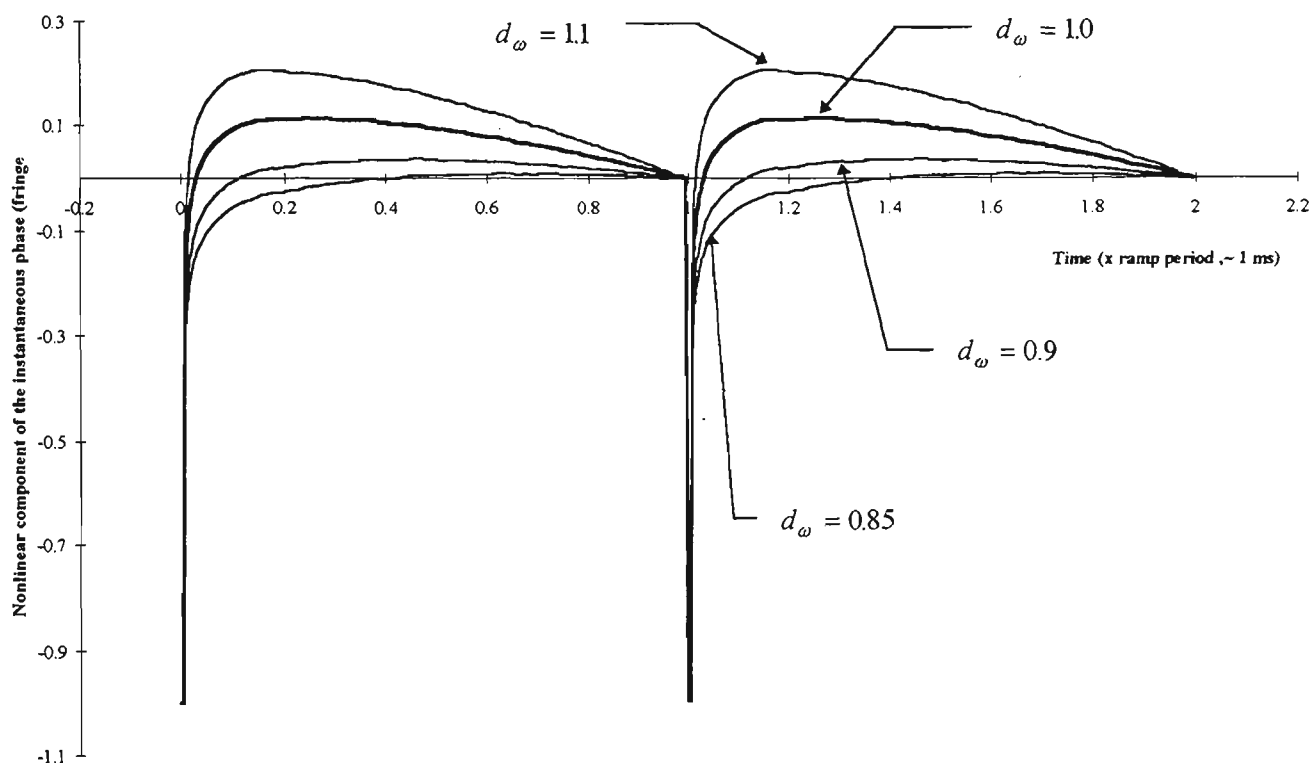


Figure 7.19: The nonlinear component of the time-varying phase produced by a nonlinear optical frequency ramp for different ratios of the optical frequency ramp amplitude to the free spectral range.

Since ϕ_{sig}^{nl} is periodic, it can be expressed as a Fourier series of harmonics of the modulation frequency. ϕ_{sig}^{nl} can be interpreted as an extra phase modulation in the processed signal $I'_{raw,sub}$ which is in addition to that introduced by the measurand. This extra phase modulation produces higher harmonics in the power spectrum of $I'_{raw,sub}$. Because the fundamental frequency of ϕ_{sig}^{nl} is the same as the sawtooth modulation frequency, the first sidebands in the power spectrum of $I'_{raw,sub}$ produced by the phase modulation ϕ_{sig}^{nl} are at DC and at $\pm 2\omega_m$. Thus if $I'_{raw,sub}$ is band-pass filtered around the sawtooth modulation frequency and the bandwidth of the filter is narrow enough, the

effect introduced by ϕ_{sig}^{nl} can be greatly reduced. Clearly the characteristics of the band-pass amplifier play an important role in the strength of the phase noise attributed to the nonlinear optical frequency ramp. In the case of the measurements obtained with *HibiFace*, a band-pass amplifier with a pass-band from 100 Hz to 10 kHz was used. This filter had little effect on ϕ_{sig}^{nl} which has a fundamental frequency of 1 kHz.

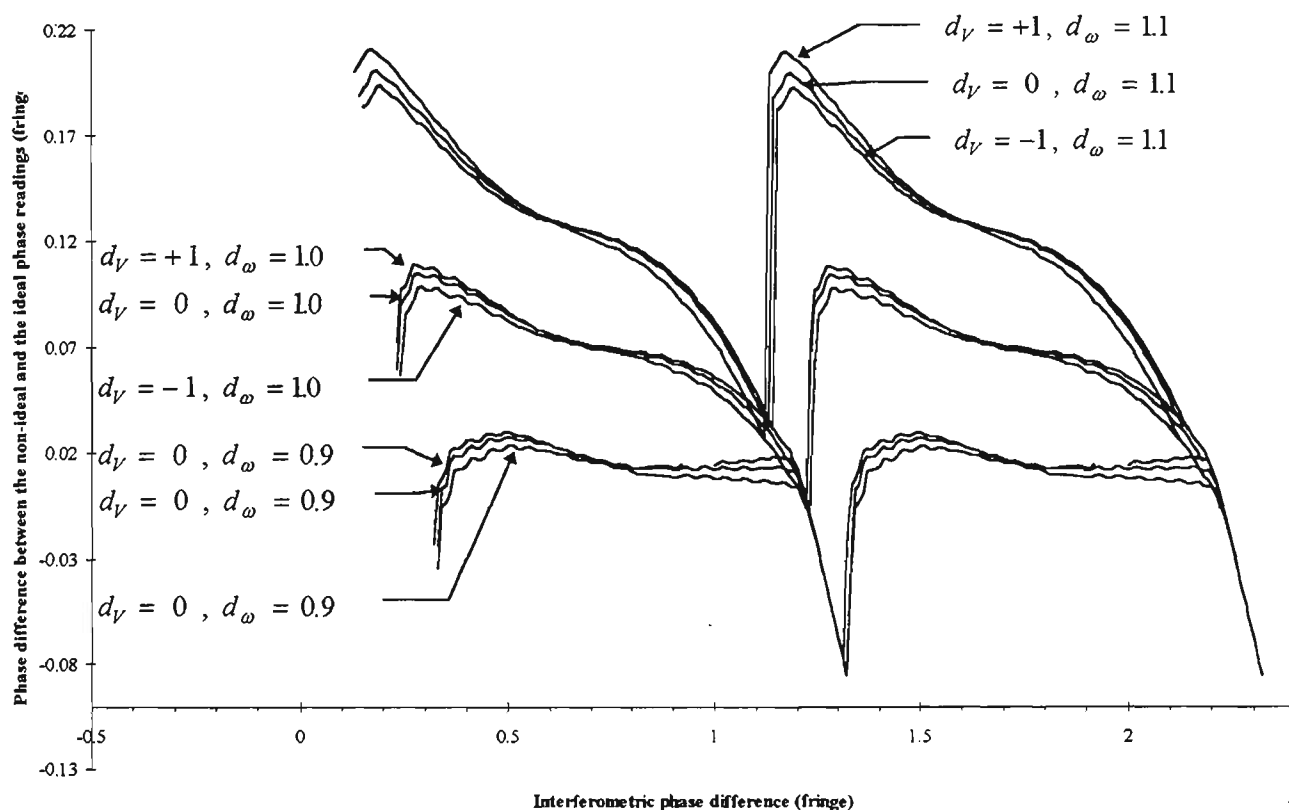


Figure 7.20: The difference in the phase readings obtained from the positively sloping zero-crossing of the ideal and the processed interferometric functions. The processed interferometric function is $K'V\{d_V r(t) + [1+r(t)]\cos(d_\omega \omega_m t + \phi_{sig}^{nl} - \phi_{int})\}$. This was subsequently filtered with a simulated 100 Hz to 10 kHz band-pass amplifier. The ideal interferometric function is assumed to be $V \cos(\omega_m t - \phi_{int})$. The (peak-to-peak) amplitude of $r(t)$ is 0.08.

Figure 7.20 shows the simulated phase noise for the same cases as presented in Figure 7.16 but including the nonlinear phase variations due to a nonlinear optical frequency ramp. Table 7.6 summarises the peak-to-peak phase amplitude for the phase noise corresponding to the different cases. The effect of the band-pass amplifier used with *HibiFace* was also considered. There are several similarities between the graphs shown in Figure 7.20 and Figure 7.16. First, in general the graphs in Figure 7.20 and Figure 7.16 for the different cases behaved very broadly like periodic sawtooth signals. Second, as the value of d_ω increases, the sawtooth-type phase ramp

exhibits a more negative slope. Third, the magnitude of the effect due to variations in the values of d_V is similar for the case when the optical frequency ramp is linear (compare Table 7.5 and Table 7.6).

	$d_\omega = 1.1$	$d_\omega = 1.0$	$d_\omega = 0.9$
$d_V = +1$	0.184	0.115	0.106
$d_V = 0$	0.169	0.109	0.113
$d_V = -1$	0.163	0.109	0.109

Table 7.6: The peak-to-peak amplitude values (as a fraction of a fringe) of the phase noise curves for the cases shown in Figure 7.20. The optical frequency of the LD output varies in a nonlinear ramp manner.

As well as similarities, there are several differences between the graphs shown in Figure 7.20 and Figure 7.16. First, one of the phase noise curves depicted in the figures was approximately flat for the cases when $d_\omega = 0.9$ for the nonlinear ramp case whilst the same was true for $d_\omega = 1.0$ for the linear ramp case. Comparing the graphs shown in Figure 7.20 and Figure 7.16, the contribution of the nonlinear optical frequency ramp induced the sawtooth-type phase noise to slope more negatively by an extra peak-to-peak phase value of about 0.1 fringe. The second main difference between the curves in Figure 7.20 and Figure 7.16 is that the corresponding phase noise for different values of d_ω exhibits a phase shift in Figure 7.20 and not in Figure 7.16. This phase shift in Figure 7.20 changes by 0.1 fringe for a change in d_ω of 0.1. This phase shift is simply a consequence of the fact that the zero-crossings of $\cos(d_\omega \omega_m t + \phi_{sig}^{nl} - \phi_{int})$ will vary with d_ω .

Examining the values presented in Table 7.6, the case when $d_\omega = 1.1$ (and $|d_V| < 1$) can best explain the negatively-sloping sawtooth-type periodic phase noise observed on each axial response of *HibiFace* as shown in Figure 7.13 and Figure 7.14. Comparing Figure 7.20 and Figure 7.16, for the case when $d_\omega = 1.1$, about half the magnitude of the phase noise was due to the extent of the optical frequency scan and the other half was due to the nonlinearity of this scan. The contribution of the latter was large because of the large bandwidth of the band-pass amplifier used with *HibiFace*. The reason for using such a large bandwidth filter was to reduce the electronic phase shift introduced by the band-pass filter. In hindsight, this characteristic for the filter was a poor choice. In other measurements obtained in this work, a narrower bandwidth band-pass filter was used. The phase noise

shown in the simulations of Figure 7.20 has approximately the same magnitude, the same period and roughly the same shape as the phase noise observed experimentally. The exact shape clearly varies with d_ω and d_ν and so it is quite conceivable that the form of the experimentally-observed phase noise can be obtained for an appropriate combination of d_ω , d_ν and nonlinear form of the optical frequency ramp.

Up to this stage, it has been assumed that the transmission interferometric functions of *HibiFace* behaved sinusoidally (Eq. 7.3) and that no polarisation cross-coupling occurred. The first assumption is justifiable because *HibiFace* exhibited very low combined Fabry-Pérot mirror reflectance of 0.7 %. The second assumption would not hold if there was some misalignment in the polarisation axes of the sensor and the lead-in fibre, misalignment or incomplete cross-polarisation extinction of the polarising beam splitter or misalignment of the lead-in fibre polarisation axes with respect to the non-polarising beam splitter. If any of these effects occur to any significant extent, the resulting optical signal can be extremely complicated. However, in the case of the measurements made with *HibiFace*, no obvious polarisation beating effect were observed in the axial interferometer responses. Some small amount of polarisation cross-coupling may be responsible for the observed variation in the spikes in the individual axial responses from one period to another.

Summarising this section, fusion-spliced birefringent FFPSs were constructed and have performed reasonably well as temperature sensors. These sensors were preferentially addressed in transmission because of the high optical loss at the splice. Over a temperature measurement range of about 60 °C, the individual axial interferometric phase shifts depended linearly on temperature. A parabolic feature with a magnitude of about 1 fringe in 60 was observed in both axial interferometer responses but not in the differential response. This feature appeared to be associated with the optical fibre itself and was consistent with the magnitude of the second-order term in $\frac{dn}{dT}$ which was observed by Lee *et al.* [1988]. In addition to the parabolic feature, the individual axial interferometer responses showed other effects which were not present in the differential phase response. These effects were attributed to drifts in the LD during the extended time required for measurements.

The differential phase showed periodic phase noise features at the UMR of the individual axial interferometers together with beating effects associated with the slight difference in UMR of the interferometers. These effects were simulated and found to be consistent with non-ideal adjustments of the signal processing system together with a nonlinearity in the optical frequency ramp.

No strain measurements were performed on fusion-spliced birefringent FFPSs because the sensors were fragile. Many of these sensors were accidentally broken even with careful handling. To obtain sensors exhibiting greater tensile strength, birefringent FFPSs with in-fibre Bragg gratings were subsequently fabricated. Temperature or strain measurements obtained with these grating-based sensors are presented in the next section.

7.3 Performance of Grating-Based Birefringent-Fibre In-Fibre Fabry-Pérot Sensors

7.3.1 Description of the Sensor

The third generation of sensors developed in this work were birefringent fibre Fabry-Pérot sensors (FFPSs) with in-fibre Bragg grating mirrors. These sensors were subsequently used to measure temperature, static strain and dynamic (time varying) strain. In this section, the performance of one of these grating-based birefringent FFPSs, labelled "*HibiGrat*," is described. *HibiGrat* was fabricated with an in-fibre Bragg grating as the proximal mirror and a cleaved end as the distal mirror. The fibre grating used with *HibiGrat* was *Grating1*. The optical transmission spectrum of *Grating1* has been described in Chapter 5 (Figure 5.22). Since *Grating1* was formed in a birefringent fibre, it exhibited effectively two gratings, one along each polarisation axis. The maximum reflectance of each axial grating of *Grating1* was approximately 17.5 % and 20.7 % for the fast and slow axis respectively.

In the case of temperature measurements, the cleaved distal end of the sensor was not coated and thus had a Fresnel fibre-air reflectance of about 3.6 %. In the case of strain measurements, the distal end of *HibiGrat* was coated with a TiO₂ thin film having a quarter-wave optical thickness and a reflectance of 32.4 % at the monitoring wavelength of 840 nm. Assuming that the refractive indices of the TiO₂ film at 840 nm and 785 nm were about the same, the reflectance of the film (fibre-film-air) was also about 32 % at 785 nm. The use of an optical

thickness close to a quarter-wave at 785 nm meant that the distal cleaved end would exhibit a high reflectance for a single-layer film. This property of the film was important since *HibiGrat* was later immersed in a bonding epoxy which had a refractive index similar to that of the core of the fibre.

In either temperature or strain measurements, the fast- and slow-axis interferometers of *HibiGrat* can be considered as low-finesse interferometers. Furthermore, the effective cavity length of *HibiGrat* was measured to be 15 ± 0.2 mm - the distance from the middle of *Grating1* to the cleaved end (Chapter 5). This cavity length is small enough for a reasonable approximation to localised measurements in many situations.

7.3.2 The Characteristics of In-Fibre Bragg Grating

The optical, thermal and mechanical properties of fibre Bragg gratings (FBGs) were important considerations in determining the limits of the fibre Fabry-Pérot sensor fabricated with them. Prior to forming *HibiGrat*, the optical and thermal characteristics of *Grating1* were first determined. Spectrally, the main features of the transmission spectrum of *Grating1* were two Bragg peaks with central wavelengths of about 783.23 nm and 783.69 nm (at room temperature) and each with a bandwidth of about 0.17 nm (Figure 5.22).

Temperature parameter	Units	Fast-axis	Slow-axis
Bragg wavelength sensitivity	pm/°C	6.4 ± 0.2	5.5 ± 0.2
Fractional temperature sensitivity	$10^{-6}/^{\circ}\text{C}$	8.2 ± 0.2	7.0 ± 0.2

Table 7.7: The temperature sensitivities of the shifts in the fast- and slow-axis Bragg wavelengths of a grating written in a birefringent fibre.

The spectrum of each axial grating can shift with temperature or strain. Table 7.7 summarises the temperature sensitivities of the Bragg wavelength shifts of each axial grating. These values were obtained by measuring the axial Bragg wavelength shifts using an optical spectrum analyser. *Grating1* was illuminated with a white-light source and its temperature varied. In general the results for the wavelength shifts of both axial gratings as tabulated in Table 7.7 were in agreement with the expected value of ~ 0.6 nm/°C (Chapter 4). However the relative

errors in the results were large because the signal-to-noise ratio was poor due to the low spectral density of the white-light source and the inefficient coupling of light into the birefringent fibre which had a core-radius of 2.25 μm .

No strain measurements were performed on the fibre gratings because there were only a few gratings available at the time the experiment was conducted. If strain measurements were done, there was a risk of destroying them. Other Bragg gratings in standard communications fibres had shown strain sensitivities very close to the expected values (Chapter 4) and so it was decided that there was little point in making such measurements.

The light source used with this sensor was an index-guided LD driven with a bias current high enough to ensure that it operated on a single-mode. For a single LD to be used for both axial interferometers, the wavelength of the LD must fall within the reflectance spectrum of both axial gratings. Since the spectrum of each axial grating shifts with temperature or strain, the natural choice is a wavelength between the two Bragg wavelengths. This wavelength shifts, together with the narrow reflection bandwidths, restricted the range of operation of *HibiGrat*. Consequently, to obtain a strong reflection fringe visibility of *HibiGrat*, the temperature change should not be more than $\sim 30^\circ\text{C}$ or $\sim 15^\circ\text{C}$ for single-axis or dual-axes operation of *HibiGrat*, respectively. This is not a fundamental limitation with the use of Bragg grating mirrors but at the time when the sensors were made, our laboratory was unable to fabricate wider chirped gratings. In the measurements with *HibiGrat*, the signal-to-noise ratios of the measurements were quite high and the detector gain available was also high and so we were in fact able to operate the dual-axis sensor over a much wider range than the $\sim 15^\circ\text{C}$ mentioned above.

7.3.3 Temperature Measurements with Grating-Based Sensors

Figure 7.21 shows the schematic diagram of the experimental arrangement employed to determine the thermal sensitivities of *HibiGrat*. In order for this sensor to thermally expand without any mechanical constraints, it was suspended within a hollow cavity in the centre of an aluminum block. The block was formed by pressing together two 4 mm thick aluminum plates. On one side of each plate, a 3 mm wide and 1 mm deep region was milled off

such that when these milled surfaces of the two plates were made to face each other, an air cavity was formed. The top plate of the block had a provision at its centre for the placement of an AD 590 which monitored the temperature of the block. The underside of the bottom plate rested on two Peltier devices which were used to control the temperature of the block. The Peltier device sat on a large stainless steel table which acted as a heat reservoir. The temperature of the block was controlled using a temperature controller similar to that used to control the temperature of the LD. The arrangement was insulated by enclosing it within a styrofoam box. By controlling the temperature of the block and allowing adequate time for the arrangement to reach thermal equilibrium, the AD 590, *HibiGrat* and the centre of the block can be assumed to have very similar temperatures.

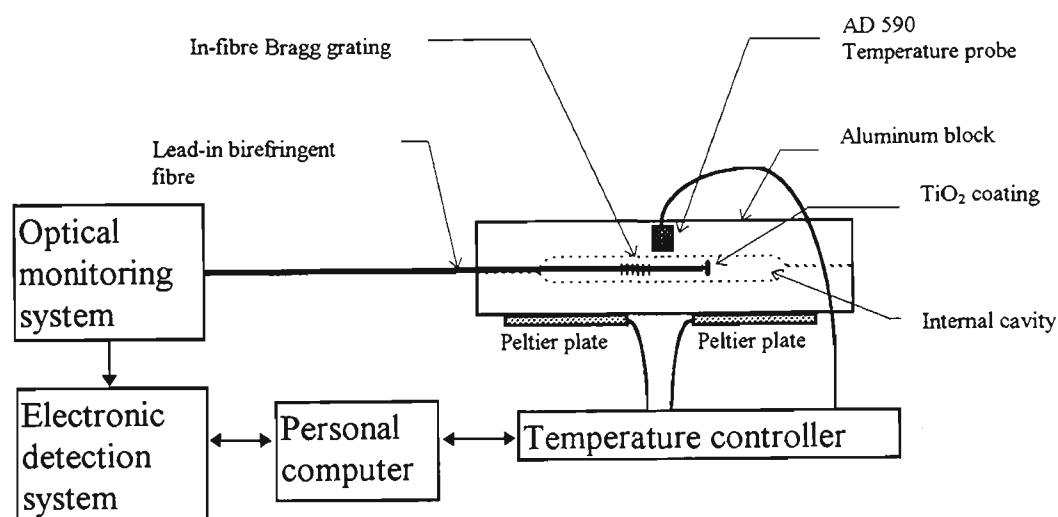


Figure 7.21: Schematic diagram of the experimental arrangement for determining the thermal sensitivities of a birefringent Fabry-Pérot sensor (*HibiGrat*) with an in-fibre Bragg grating.

A personal computer was used to regulate and monitor the temperature of the aluminum block. After all the initialisation procedures have been completed (see Chapter 6), a typical temperature measurement cycle involved three steps: first, the computer incremented the reference temperature for the block; second, the block was allowed to equilibrate at the new temperature and lastly, the computer gathered the phase of each axial interferometer, the temperature of the LD and the temperature of the aluminum block. In other measurement runs, the peak-to-peak AC voltage output of the photodiode circuits (see Chapter 6) were also recorded. When the final desired temperature had been reached, the data obtained were stored as computer text files.

The reflectance of the grating-based birefringent FFPSs was at least an order of magnitude higher than that of the fusion-spliced birefringent FFPSs. Such high reflectance values allowed the grating-based birefringent FFPSs to be addressed in reflection. The optical system used to address the sensors has been described in Chapter 6.

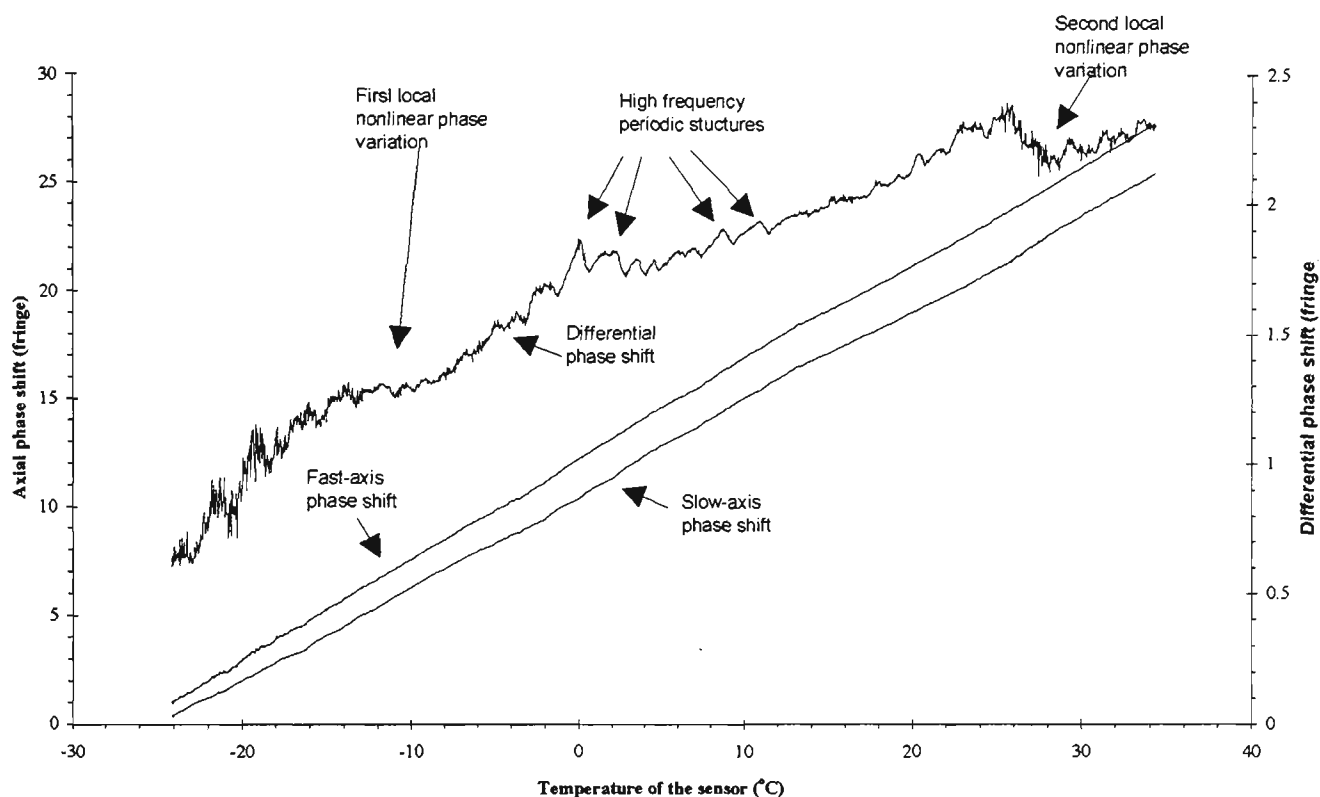


Figure 7.22: The axial and differential phase shifts of a birefringent fibre Fabry-Pérot sensor (*HibiGrat*) with a fibre Bragg grating proximal reflector against the temperature of the sensor (Measurement run 1). Each data point corresponded to a 0.04°C change. The total duration of this measurement run was about 16 hours.

Figure 7.22 presents one of the initial temperature measurement results obtained with *HibiGrat* (Measurement run 1). The figure shows the phase shifts along each axial interferometer of the sensor as well as the differential or polarimetric phase response as the temperature of the sensor was incremented in steps of 0.04°C . The differential phase-temperature response was the difference between the fast-axis and slow-axis phase-temperature responses. From the figure it can be seen that the fast-axis response was slightly more sensitive to temperature change than that of the slow-axis. Both axial responses exhibited reasonable linearity with temperature. Table 7.8 summarises the temperature sensitivities of *HibiGrat* calculated from the results shown in Figure 7.22. The uncertainties quoted in the table were obtained from the least squares fits to the data.

Temperature parameter	Fast-axis	Slow-axis	Differential
Phase-temperature sensitivity (fringe/°C)	0.4637 ± 0.0002	0.4352 ± 0.0003	0.00285 ± 0.0005
Unambiguous measurand range (°C)	2.157 ± 0.001	2.298 ± 0.002	35.1 ± 0.6
Fractional temperature sensitivity ($10^{-6}/^{\circ}\text{C}$)	8.3 ± 0.2	7.8 ± 0.2	0.5 ± 0.02
Linear correlation factor (r^2)	0.9998	0.9993	0.7080

Table 7.8: The temperature sensitivities of a birefringent fibre Fabry-Pérot sensor (*HibiGrat*) with a fibre Bragg grating proximal reflector (Measurement run 1).

There are several notable features of the differential response of *HibiGrat* as shown in Figure 7.22. First, it exhibited a general linearity with temperature as in the case of the differential response of *HibiFace*. Second, the differential response of *HibiGrat* exhibited also some high frequency features or phase noise as was the case with *HibiFace*. In the case of *HibiGrat*, these mode structures occurred about every 2 °C which corresponded to the average temperature UMR of the sensor (Table 7.8). Similar correspondence was observed in the temperature measurements with *HibiFace*. However there is no obvious beating envelope in the differential phase response of *HibiGrat* as was evident in *HibiFace* (Figure 7.12). The origin of the high frequency periodic phase noise in *HibiGrat* will be discussed in the latter part of this sub-section. Third, the differential response of *HibiGrat* shows two localised nonlinear phase variations as indicated in Figure 7.22. These nonlinear phase variations occurred in the region of - 10 °C and + 30 °C.

Although it was highly improbable, the nonlinear behaviour in the differential response of *HibiGrat* may have been caused by drifts in the temperature of the LD. Figure 7.23 shows the variations in the temperature of the LD and the differential phase shifts of *HibiGrat* during measurement run 1. The figure clearly indicates that the variations in the temperature of the LD do not coincide with the changes in the differential phase response. However the drifts in the temperature of the LD could explain the deviation from linear behaviour of each of the individual axial phase-temperature responses of *HibiGrat*. Figure 7.22 shows that the axial responses appeared to exhibit lower phase-temperature slope or sensitivity between 15 °C to 30 °C. This decrease in sensitivity can be attributed to the temperature rise of about 0.25 °C in the LD temperature as shown in Figure 7.23. Previous measurements on the characteristics of the LD used in this work gave a spectral thermal sensitivity of 56 pm/°C or - 29 GHz/°C. The

FSR of *HibiGrat* was measured to be about 6.4 GHz (section 7.4). Consequently the $+0.25\text{ }^{\circ}\text{C}$ change in the temperature of the LD corresponded to a phase change of about -1 fringe. This observation implied the need to better stabilise the temperature of the LD. The stability requirement for the temperature of the LD is discussed in section 7.4.

The noise in the temperature of the LD as shown in Figure 7.23 was due to some voltage noise during the measurement and not due to the actual variations in the LD temperature which can not abruptly change. This voltage noise can be reduced by employing some suitable averaging techniques and the final averaged value was limited by the $0.04\text{ }^{\circ}\text{C/bit}$ resolution of the digital-to-analog conversion.

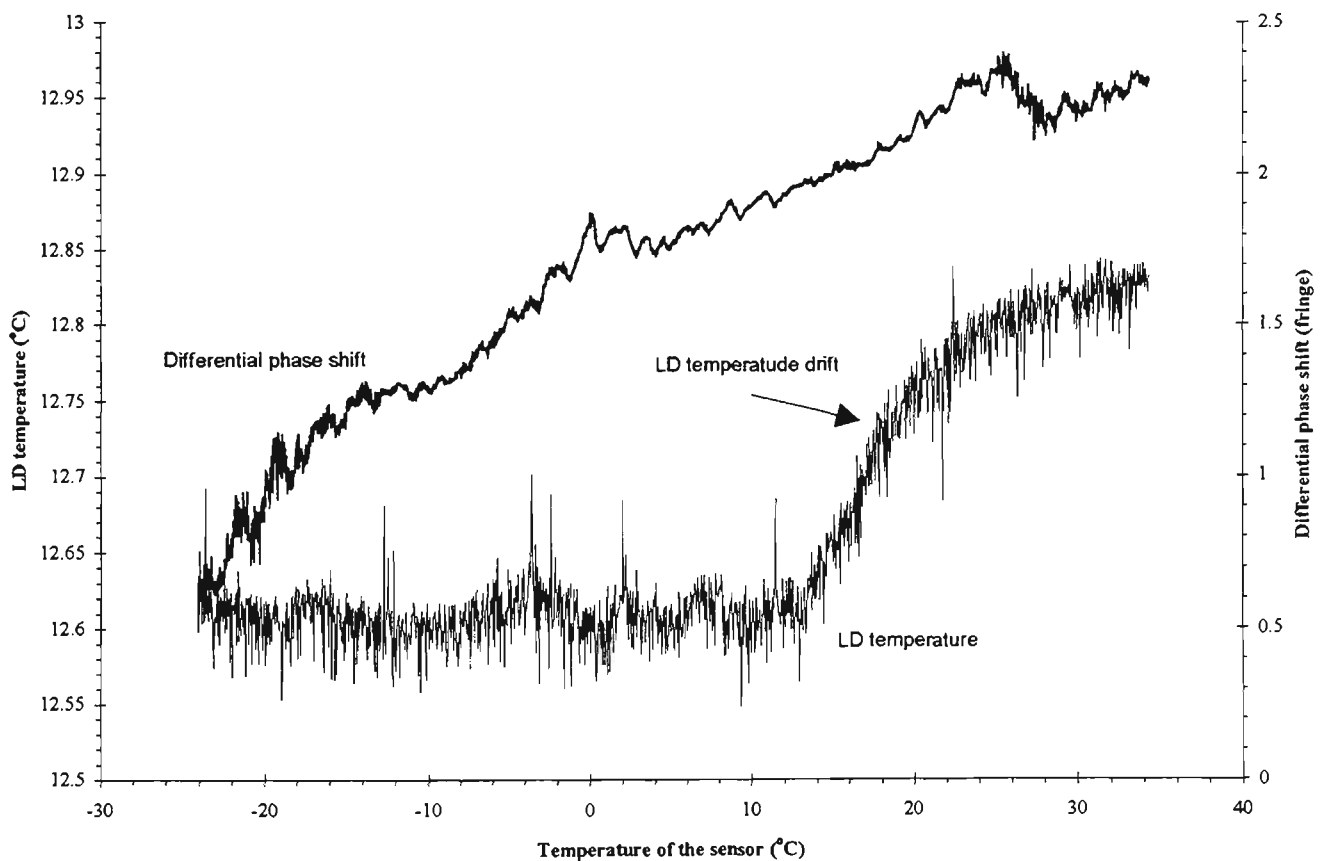


Figure 7.23: The differential phase shifts of a birefringent fibre Fabry-Pérot sensor (*HibiGrat*) with a fibre Bragg grating proximal reflector and the temperature of the laser diode plotted against the temperature of the sensor (Measurement run 1). Each data point corresponded to a 0.04°C change. The total duration of this measurement run was about 16 hours.

Several other measurement runs with *HibiGrat* were obtained and in each of these runs, the drifts in the temperature of the LD were avoided or occurred at a different point in the measurement range. All of these

measurement runs revealed features similar to those in Figure 7.22 and the major features occurred at the same point in the measurement range. In general the nonlinear phase variations in the differential response of *HibiGrat* can not be attributed to drifts in the temperature of the LD and the locations of these nonlinear effects were always about -10°C and $+30^{\circ}\text{C}$.

No similar nonlinear phase variations were observed in the differential response of *HibiFace*. For this reason it was suspected that the source of these nonlinear phase variations was some property of the Bragg grating. The temperature difference between the positions of the nonlinear phase variations was about 40°C . Using the average temperature sensitivity of *Grating1* (Table 7.7), this temperature difference corresponded to about ~ 0.36 nm wavelength shift which was about the same value as the spectral separation of the Bragg wavelengths of the two axial gratings.

In order to confirm that the nonlinear effects in the differential phase response were due to the grating, the peak-to-peak values of the AC output voltage of each photodetector amplifier circuit were recorded at different values of the temperature of *HibiGrat*. The fast- and slow-axis interferometers of the sensor were low finesse. From the discussion presented in Chapter 3, it can be concluded that for a low finesse Fabry-Pérot interferometer, the amplitude of the reflectance of the interferometer is proportional to the square root of the reflectance of the Fabry-Pérot mirrors (see Eq. 3.53). Thus the square of the amplitude of the fringe signal (half the recorded peak-to-peak voltage values) was approximately proportional to the reflectance of *Grating1* because the reflectance of the distal TiO_2 thin film of *HibiGrat* can be assumed to be constant.

Several temperature measurement runs were made which also recorded the peak-to-peak values of the AC output voltage of each photodiode amplifier circuit. The temperature range was wider than that shown in Figure 7.22 in order to cover as much as possible the bandwidths of both axial gratings. Figure 7.24 shows the phase shifts experienced by the axial interferometers of *HibiGrat* over an 80°C range. Again, the individual axial phase shifts show reasonable linear phase-temperature responses. Table 7.9 summarises the temperature sensitivities of *HibiGrat* during the measurement run shown in Figure 7.24.

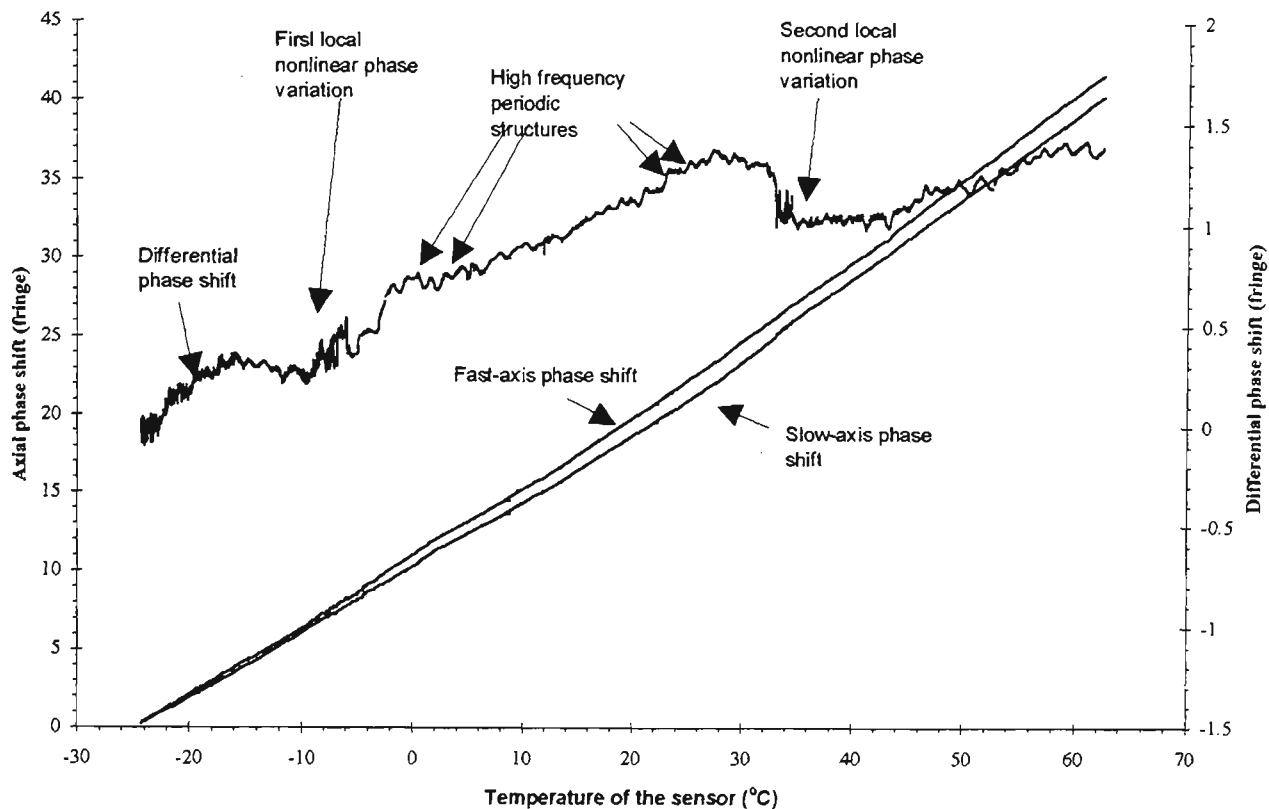


Figure 7.24: The axial and differential phase shifts of a birefringent fibre Fabry-Pérot sensor (*HibiGrat*) with a fibre Bragg grating proximal reflector against the temperature of the sensor (Measurement run 2). Each data point corresponded to a 0.04°C change. *NB*: There is an offset between the differential phase shift scales of figures 7.22 and 7.24. This offset is due to a difference in the phase of the individual axial interferometers at the start of the run.

Temperature parameter	Fast-axis	Slow-axis	Differential
Phase-temperature sensitivity (fringe/ $^{\circ}\text{C}$)	0.474 ± 0.003	0.421 ± 0.002	0.053 ± 0.003
Unambiguous measurand range ($^{\circ}\text{C}$)	2.11 ± 0.01	2.37 ± 0.01	19 ± 1
Fractional temperature sensitivity ($10^{-6}/^{\circ}\text{C}$)	8.5 ± 0.4	7.5 ± 0.2	0.9 ± 0.05
linear correlation factor (r^2)	0.9956	0.9985	0.7786

Table 7.9: Temperature sensitivities of a birefringent fibre Fabry-Pérot sensor (*HibiGrat*) with a fibre Bragg grating proximal reflector (Measurement run 2).

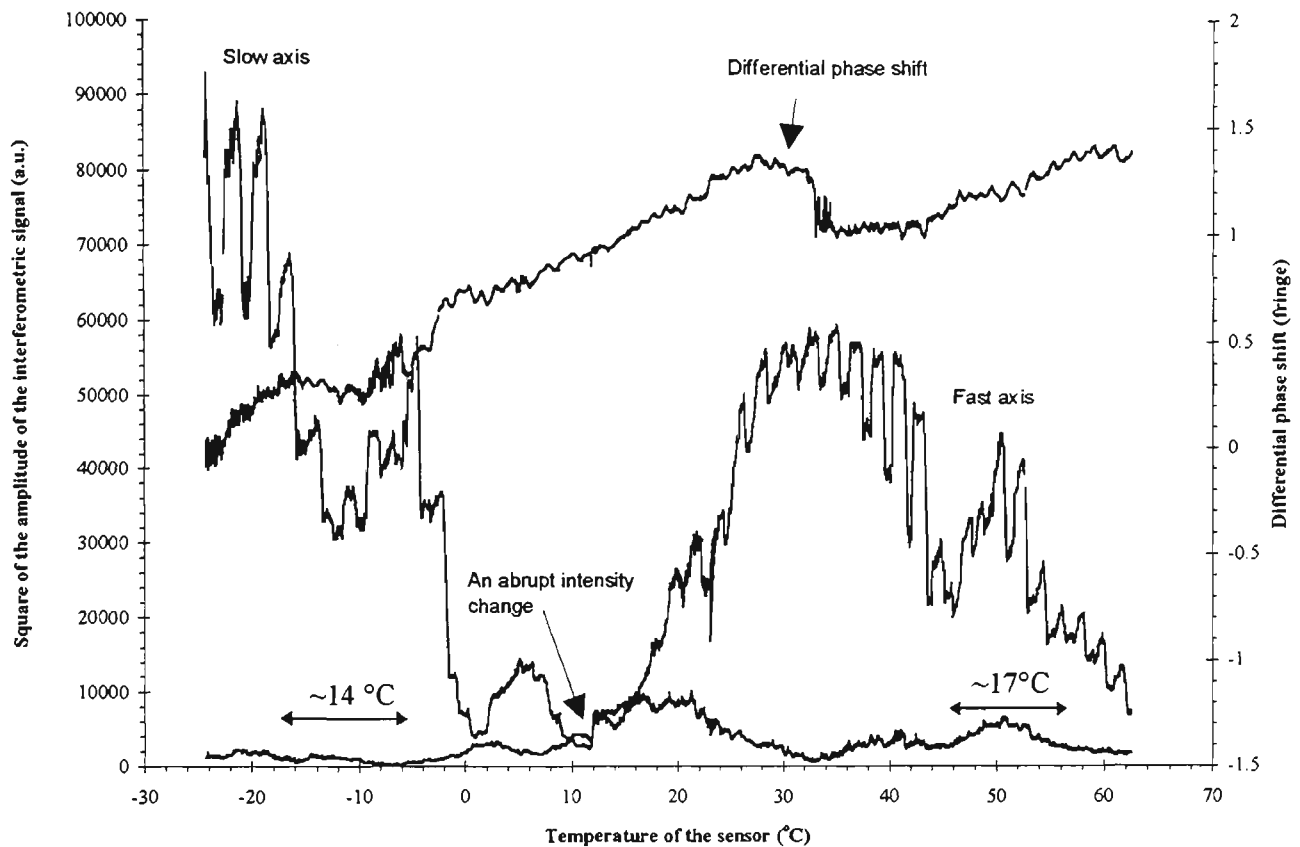


Figure 7.25: The differential phase shifts of a birefringent fibre Fabry-Pérot sensor (*HibiGrat*) with a fibre Bragg grating proximal reflector and the square of the intensity (voltage) amplitude of the fast- and slow-axis interferometric signal against the temperature of the sensor (Measurement run 2). Each data point corresponded to a 0.04°C change.

Figure 7.25 shows a plot of the square of the amplitude of the interference signal and the differential phase response of the sensor against temperature for the measurement run shown in Figure 7.24. Figure 7.25 clearly shows that the location of each localised nonlinear phase effect occurred at the temperature when the average wavelength of the LD was close to the Bragg wavelength of the corresponding axial grating. The phase features in the differential phase response of the sensor at about -10°C and $+30^{\circ}\text{C}$ appear consistent with the anomalous dispersion of the axial gratings. The evidence for this is much clearer for the fast axis than for the slow axis. In fact the temperature scan did not go low enough to include the central peak of the slow-axis grating. For this reason and also because of the somewhat complicated reflectance of the grating in the region of -25°C to 0°C , it was really not possible to make any conclusion about the differential phase in this temperature range. However, the reflectance of the fast-axis grating was well covered within the temperature scan and the differential phase feature at $+30^{\circ}\text{C}$ is clearly centred at the peak reflectance of the fast-axis grating. The peak-to-peak phase change

of this feature was about 0.35 of a fringe. This is about 18 times the expected phase change of 0.02 of a fringe for a grating with a reflectance of 17.5 % (calculated in a manner similar to the anomalous dispersion curve of Figure 3.8). Despite the somewhat greater than expected magnitude of the phase change, the location and shape of the feature make it difficult not to conclude that it is due to anomalous dispersion. To highlight the essential features of the differential phase effects, Figure 7.26 shows a filtered version of the differential phase with its linear trend removed.

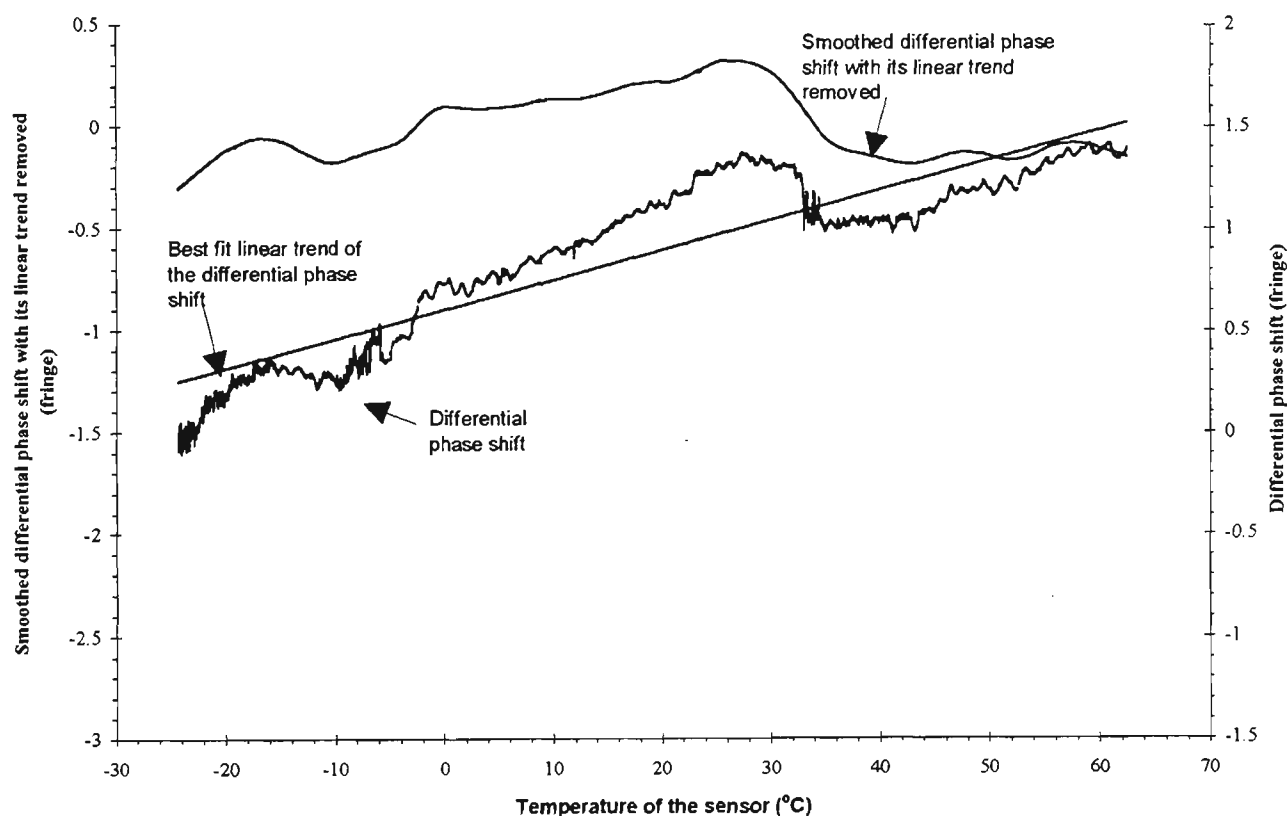


Figure 7.26: The measured differential phase shift of Figure 7.25, best fit linear trend and smoothed version of the differential phase shift with its linear trend removed.

We had not expected to see any effect due to anomalous dispersion as the rate of change of anomalous dispersion phase with temperature was expected to be a very small fraction of the total rate of phase change with temperature. The total rate of phase change can be calculated from Eq. 4.139 which essentially says that the total rate of phase change is equal to ω_T times total round-trip phase change in the cavity including the Bragg reflector. Using approximate values of $\omega_T = 8 \times 10^{-6} / ^\circ\text{C}$ and a total phase change of 2000 fringes in the Bragg grating and 53000 fringes in the rest of the cavity, this gives a total rate of phase change with temperature of about 0.44 fringe/ $^\circ\text{C}$.

The rate of change of anomalous dispersion phase can be estimated to be about 0.0006 fringe/°C from the expected phase shifts of about 0.02 fringe over a bandwidth of about 0.2 nm together with a rate of Bragg wavelength shift with temperature of 6 pm/°C. As expected we did not see any anomalous dispersion effect in each individual axial response. However, the differential phase provides a very sensitive avenue for detecting small phase change effects.

There are three main reasons why the anomalous dispersion can be observed in the differential phase response of *HibiGrat*. Firstly, the total phase noise in the measurement was below the magnitude of the anomalous dispersion of each axial grating. Secondly, the phase-resolution of the phase-detection scheme used in this work was high (10^{-4} of a fringe). Finally the sensor was short and so the difference in the total round trip phase of the two axial interferometers was small. Hence small phase change effects such as anomalous dispersion could still give significant fractional changes in the differential phase measurement. The issue of anomalous dispersion effects in the differential phase measurements will arise again later in this chapter when strain measurements are reported.

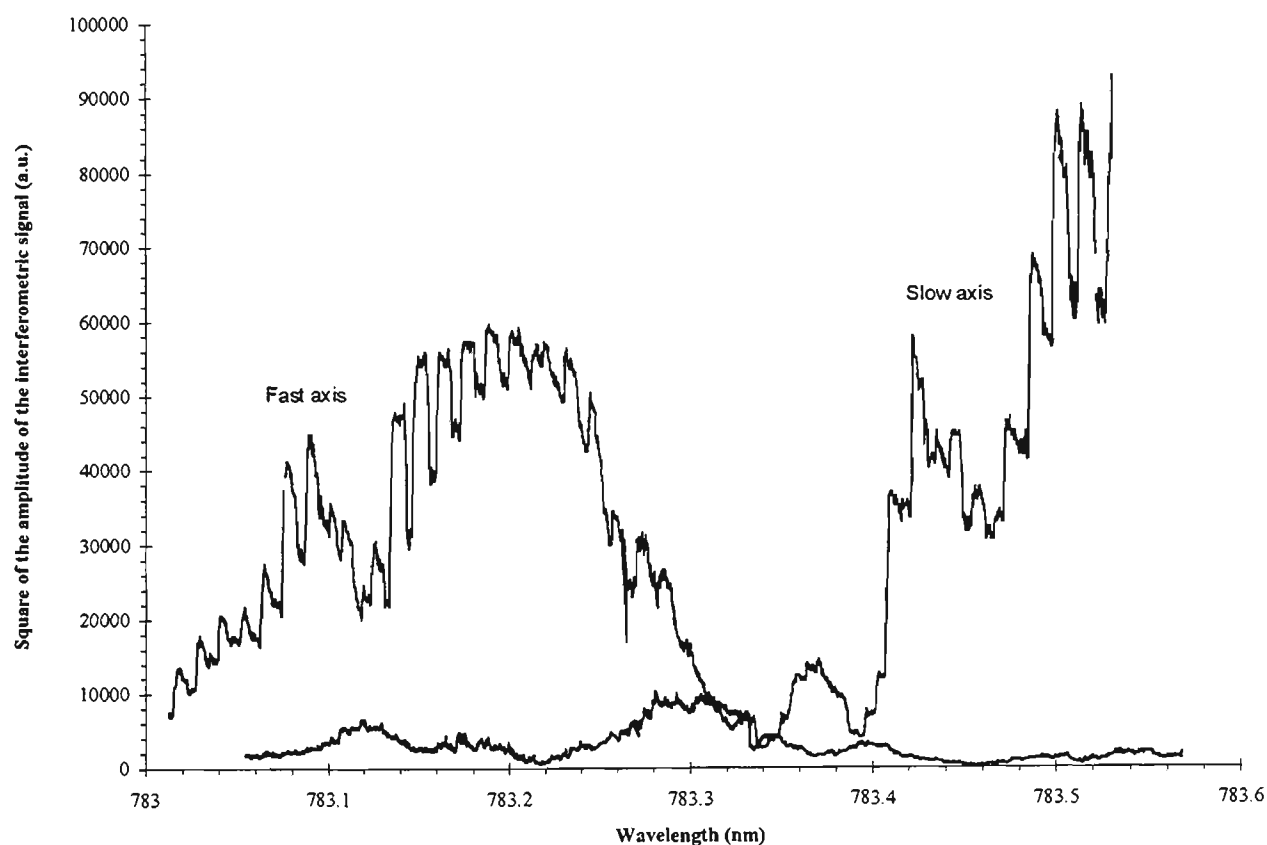


Figure 7.27: Reconstructed reflection spectrum of a fibre Bragg grating at 16 °C (*Grating1*).

There are other comments that can be made regarding the results presented in Figure 7.25. By noting the wavelength of the LD at the beginning of the measurement run, the reflectance-temperature spectrum shown in Figure 7.25 can be converted into a reflectance spectrum of the grating by simply re-scaling the temperature axis using the wavelength-temperature sensitivity of each axial grating (Table 7.7). Figure 7.27 shows the reconstructed spectrum of the birefringent grating at a temperature of 16 °C. The reference wavelength of the LD was 783.31 nm at a temperature of 12.2 °C.

Although the reflection spectrum of *Grating1* shown in Figure 7.27 is not complete, the main features in the figure were certainly very similar to the transmission spectrum obtained using an optical spectrum analyser (Figure 5.22). Both spectra show a FWHM bandwidth of the fast-axis grating to be 0.17 nm.

The spectrum in Figure 7.27 is in fact obtained with much higher signal-to-noise ratio and much better spectral resolution than the previous spectrum using a white-light source and spectrum analyser. In the latter case the spectral resolution was nominally 0.1 nm and for Figure 7.27 the spectral resolution 0.25 pm (0.04 °C × 6 pm/°C). Figure 7.27 suggests that the Bragg grating reflection peaks are in fact more complicated than previously assumed with a subsidiary peak on the short wavelength side of each axial peak in the spectrum. In addition it is possible to estimate the length of the Bragg grating using the spacing of the minima of the small ringing features in the spectrum well away from the Bragg wavelength. The spacing of these minima can readily be shown to be given by

$$\Delta\lambda_{b,mode} \approx \frac{(\lambda_b)^2}{2n_b \ell_b} \quad \text{Eq. 7.13}$$

Using the two spacings indicated by 17 °C and 14 °C in Figure 7.25, the length of the Bragg grating can be estimated to be ~ 2.36 mm and ~2.27 mm respectively. This is somewhat longer than the 1.2 mm estimated by fitting the optical spectrum analyser trace. It is not easy to estimate the magnitude of the peak reflectance in the fast-axis spectrum of Figure 7.27 since this involves a number of different factors including the coupling efficiency of light into the fibre, the sensitivity of the detectors and the amplifier gains and these were not carefully measured. Nevertheless it does appear that there are grounds for believing that the Bragg grating characteristics may be somewhat different to those obtained in Chapter 3. The reason for including the coupling efficiency in the items

listed above is that this can drift during the long period required for the temperature measurement run. In fact there is an intensity discontinuity which occurs simultaneously in the data from both axial interferometers (Figure 7.25) which we attribute to a coupling effect.

One of the most obvious features of the spectra in Figure 7.27 is the intensity modulation evident in the waveforms. This is not simply noise. The modulation occurs at the temperature UMR (about 2 °C) of the individual axial interferometers. This modulation is not a result of a $\cos(\phi)$ term but rather a modulation of intensity of the fringes caused by the interaction of two effects. The current modulation of the LD sweeps the wavelength in a ramp period by an amount which is something like a tenth of the bandwidth of the grating. This produces an intensity modulation dependent on the slope of the grating reflectance in the operating region. Hence, in Figure 7.27, the modulation occurs principally as one scans the region of high reflectivity of the grating. The modulation is further complicated by the un-removed intensity variations of the LD during each scan period. This causes a variation in the peak-to-peak amplitude of the modulation which is dependent on the position of the maximum and minimum of the modulation within the ramp period. Thus, for example, a maximum occurring early in the ramp period will be little affected by the intensity modulation of the LD and a maximum occurring late in the ramp period will be further increased because of the increased LD output. The interaction of these two effects produces a modulation in the intensity of the interference signal which varies according to the interferometer phase (position of maxima within the ramp period) and position within the grating reflectance spectrum.

Figure 7.28 shows the temperature of the LD during measurement run 2. In this case, the temperature drift occurred at a different position in the differential phase response (*c.f.* Figure 7.23). This re-affirms the non-correlation between the differential phase response and the temperature of the LD. Furthermore, if one compares the individual axial interferometer responses for measurement runs 1 and 2 (Figure 7.22 and Figure 7.24) with their corresponding LD temperature graphs (Figure 7.23 and Figure 7.28), there is a strong suggestion that the kinks in linear response of the axial interferometers may result from temperature variations of the LD.

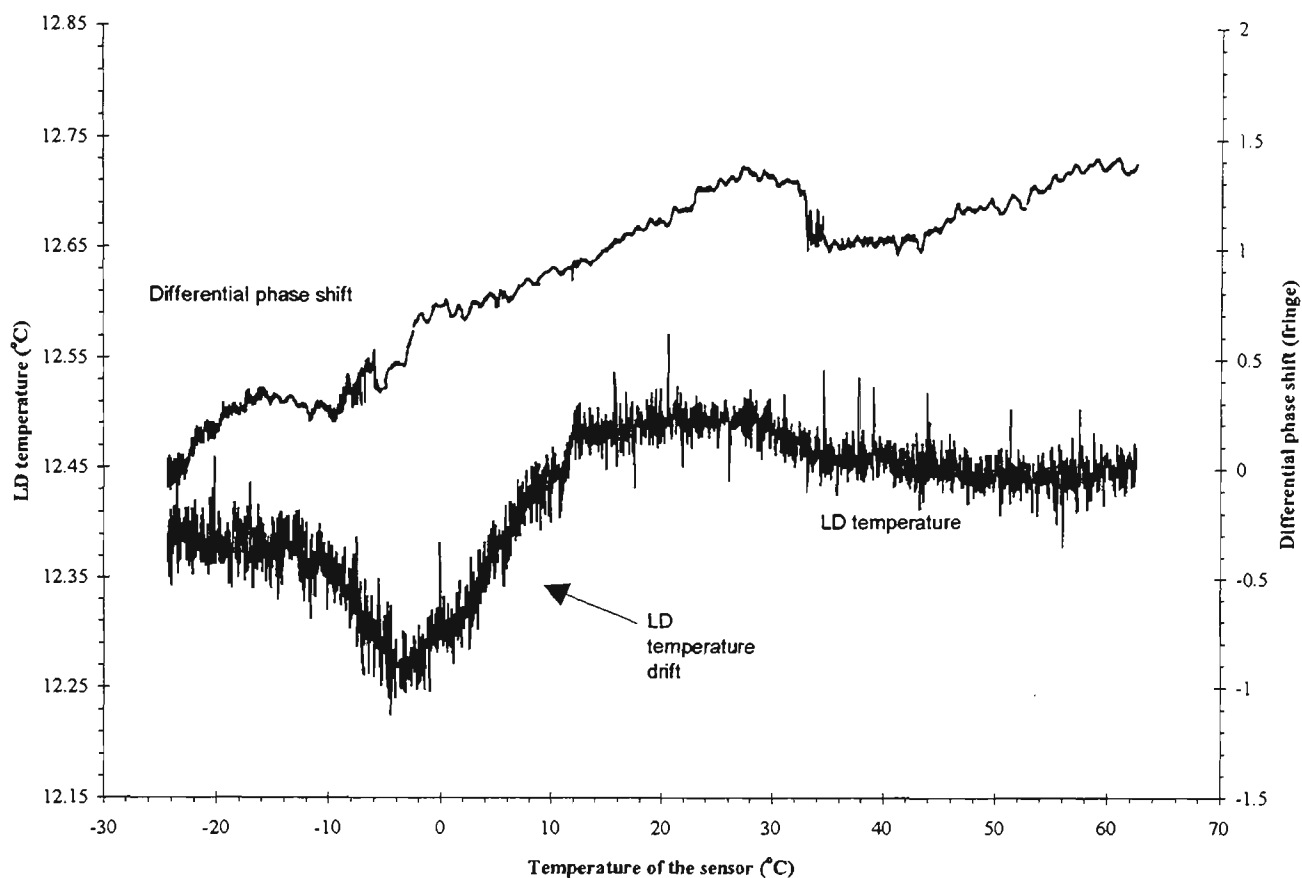


Figure 7.28: The differential phase shifts of a birefringent fibre Fabry-Pérot sensor (*HibiGrat*) with a fibre Bragg grating proximal reflector and the temperature of the laser diode plotted against the temperature of the sensor (Measurement run 2). Each data point corresponded to a 0.04°C change.

The differential phase-temperature response of *HibiGrat* as shown in Figure 7.22 and Figure 7.24 exhibited some other high frequency noise which is not completely random and is here described as periodic phase noise. The peak-to-peak phase-amplitude of this periodic feature was about 0.075 of a fringe. The possible origin of this high frequency periodic phase noise will be discussed in the remainder of this section.

Polarisation cross-coupling effects can be discounted as a possible source of the periodic phase noise because the observed temperature-period for this phase noise was similar to the UMR of either axial interferometer rather than the UMR of the differential response (axial beat period) as would be expected for polarisation cross-coupling.

The possibility was also considered that this noise could arise from a non-cosine interferometer response. Although the finesse of either the fast- or slow-axis interferometer was expected to be low, the corresponding

fineness value can be significant enough that the two-beam approximation for the axial interferometer signals may strictly not be valid. In this situation the Fabry-Pérot response looks more like an Airy function rather than a cosine function. In fact this Airy function is periodic with the round-trip interferometer phase shift and the zero crossings of this function (or for that matter any specific point in this function) still moves linearly with round-trip phase shift. Hence the shape of the interferometer function is not important as long as it is a periodic function. This assertion was verified for a perfectly linear LD optical frequency ramp using Mathematica.

As in the case of *HibiFace*, the characteristics of the signal processing used with *HibiGrat* may also be responsible for the period phase noise in the differential phase response. The intermediate signal processing used with *HibiGrat* was different from that of *HibiFace*. Because the FSR of *HibiGrat* was at least three times that of *HibiFace*, a sawtooth current ramp modulation with a larger ramp amplitude was required. Consequently, the corresponding sawtooth intensity modulation in the interferometric output was substantially greater than that of *HibiFace*. This greater amount of intensity modulation meant that if the ramp-subtraction technique used with *HibiFace* (to isolate the interferometric function from the raw interferometric signal) was also employed with *HibiGrat*, a great amount of phase error or noise was to be expected. Therefore, a normalisation technique (divide circuit) was used to remove the intensity modulation in the raw interferometric output of *HibiGrat*. The normalisation technique was more superior than the ramp-subtraction technique because the former eliminated any error in the determining the zero-crossing transitions due to intensity (sawtooth) variations.

As in the case of *HibiFace*, the nonlinear ramp optical frequency modulation produced by a linear ramp sawtooth current was finally believed to have caused the high frequency periodic phase noise in the differential phase response of *HibiGrat*. The peak-to-peak phase-amplitude value for periodic phase noise in *HibiGrat* was lower than the corresponding value observed in the results with *HibiFace*. This lower phase-noise amplitude value can be attributed to the narrower bandwidth of the 500 Hz-1500 Hz band-pass amplifier used with *HibiGrat* (a 100 Hz - 10 kHz band-pass filter was used with *HibiFace*). As discussed in the previous section, a narrow bandwidth reduces the effect of the periodic variations introduced by the nonlinear ramp optical frequency modulation.

The expected AC component of a pseudo-heterodyne-type reflected intensity signal from a Fabry-Pérot sensor with properties similar to *HibiGrat* was simulated. To simulate as close as possible the experimental signals obtained with *HibiGrat*, the simulation employed a nonlinear optical frequency ramp as depicted in Figure 7.17 and included the effect of the 1 kHz bandwidth filter used with *HibiGrat*. Figure 7.29 shows the difference or error between the actual (non-ideal) and ideal phase readings obtained from the positively sloping zero-crossing transitions of the intensity signal. The phase error or noise was periodic with the change in ϕ_{int} (which is the total phase difference associated with a round-trip across the cavity).

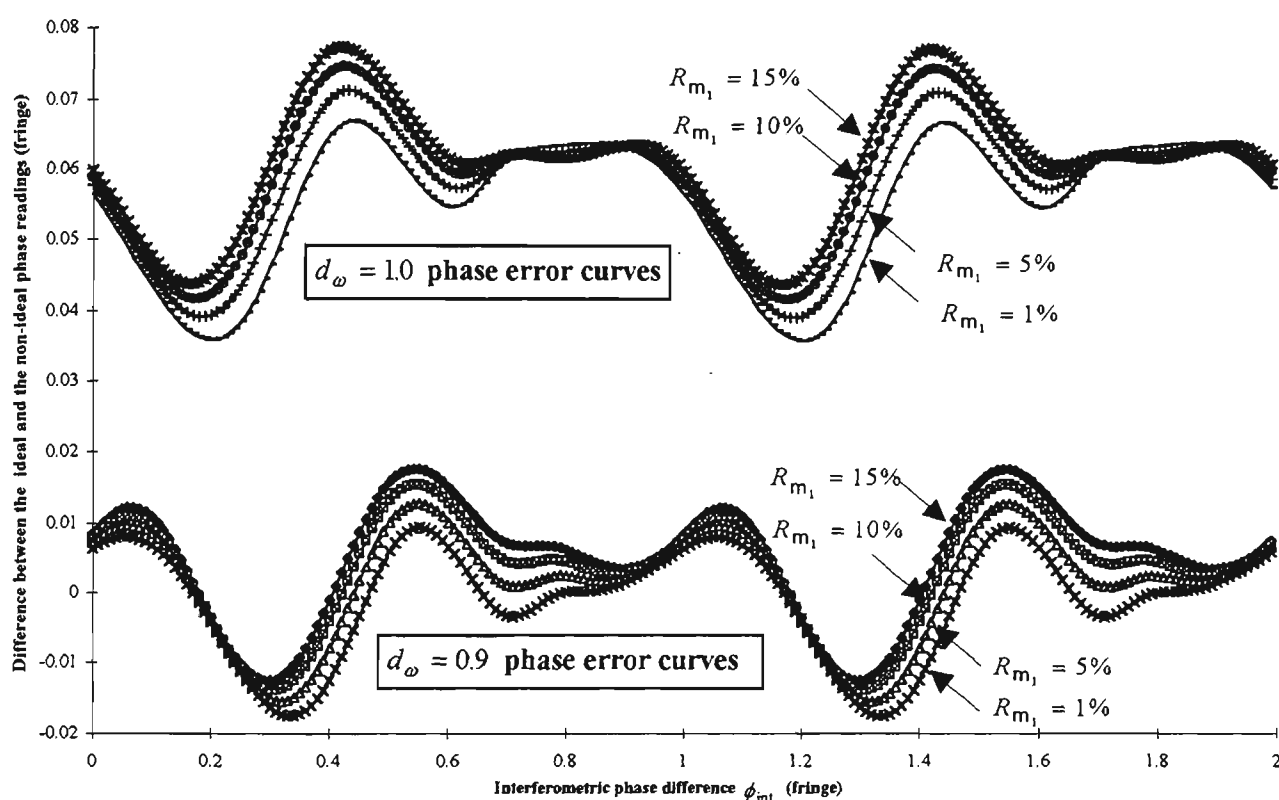


Figure 7.29: The simulated difference between the phase readings obtained from the positively sloping zero-crossing of the ideal and the non-ideal pseudo-heterodyne-type signals. This phase difference or error was calculated using the reflection transfer for a Fabry-Pérot interferometer. The ideal and non-ideal signals refer to the case when linearly or nonlinearly ramped optical frequency sawtooth modulation was used (see Figure 7.17). For the ideal linear-ramp signal, $d_\omega = 1.0$. The cases when $d_\omega = 1.0$ and $d_\omega = 0.9$ for the nonlinear frequency ramp are shown in the figure. The reflectance of the proximal Fabry-Pérot mirror (R_{m_1}) was also varied.

Figure 7.29 shows two sets of phase error curves corresponding to $d_\omega = 1.0$ and $d_\omega = 0.9$ (where d_ω is the ratio between the amplitude of the nonlinear optical frequency ramp modulation and the FSR of the sensor (Eq. 7.4)).

The curves for $d_\omega = 1.0$ were vertically shifted by about 0.06 of a fringe with respect to the $d_\omega = 0.9$ curves. Incidentally, the offset value for the latter was approximately zero. This low offset can be attributed to the fact that a nonlinear optical frequency ramp with $d_\omega = 0.9$ closely resembles the ideal optical frequency ramp (Figure 7.18).

Because the reflectance of the proximal grating (R_{m_1}) at the wavelength of the LD can vary with temperature or strain, different reflectance values (indicated in the figure) were used in the simulations. The simulation revealed that the amplitude and behaviour of the phase noise were relatively independent of R_{m_1} . However, the effect of increasing the values of R_{m_1} was to slightly increase the offset value of the corresponding phase noise and to slightly shift the position of the maxima of the phase noise (along the ϕ -axis).

The peak-to-peak phase error in Figure 7.29 is about 0.03 of a fringe. This is therefore the magnitude of the peak-to-peak error expected on either of the two axial interferometers of *HibiGrat*. The phase noise in the differential phase response would depend on the phase difference between the two axial signals (and hence would vary during a temperature scan) but could be as great as 0.06 of a fringe at places where the phase difference is 180° . This value agrees reasonably well with the observed maximum phase noise of about 0.75 of a fringe (see Figure 7.22 and Figure 7.24).

Effects similar to the nonlinear phase variations which we have observed and which we attribute to the nonlinear optical frequency ramp have been observed in several related papers by Brady *et al.* [1995], Rao *et al.* [1996] and Rao *et al.* [1997b]. In each of these cases they used a pseudo-heterodyne optical detection scheme for measuring the wavelength changes in strained Bragg grating sensors. A bulk-optic PZT-scanned Michelson interferometer was used to produce a wavelength-modulated optical signal which illuminates strained and unstrained Bragg gratings. The heterodyne signals were band-pass filtered and the phase shift produced by the wavelength shift in the reflectance spectrum of the strained grating was obtained by measuring the phase difference of the two reflected signals. In the third of these papers a further PZT-scanned Michelson interferometer with different free spectral range was incorporated into the detection system in order to increase the UMR of the sensor. Their published waveforms and measured phase shifts show very similar features to the individual axial phase signals described in

this thesis and they ascribe the nonlinearities in their results to a very similar cause. In their case they associated the phase nonlinearities to the nonlinear response of the PZT to the sawtooth voltage waveform applied. The mechanical response of the PZT in their work was analogous to the thermal response of the change in the emission frequency of the LD in this thesis. The above papers did not attempt to quantitatively analyse the observed nonlinearities and did not report any observation of the anomalous dispersion phase shifts. This is perhaps not surprising as anomalous dispersion effects are only made more obvious in the results of this thesis because of the existence of two similar interferometric signals and the ability to measure differential phase shifts.

Summarising the results of this sub-section, birefringent Fabry-Pérot sensors with fibre Bragg grating reflectors were fabricated and used to measure temperature. These sensors gave reasonably linear phase-temperature response along each polarisation axis over a range of about 90 °C. However the differential phase response exhibited two additional features in addition to their expected linear trend. These additional features were periodic phase noise and localised nonlinear phase variations. The former has been established to be due to the nonlinear ramp of the optical frequency of the LD output whilst the latter was consistent with the anomalous dispersion of the Bragg grating. The method of measurement of the nonlinearity in the optical phase modulation to obtain the results that was used in this section will be described in section 7.4. Table 7.10 summarises the average temperature sensitivity of *HibiGrat* over ten measurement runs.

Temperature parameter	Fast-axis	Slow-axis	Differential
Phase-temperature sensitivity (fringe/°C)	0.477 ± 0.003	0.447 ± 0.002	0.029 ± 0.003
Unambiguous measurand range (°C)	2.10 ± 0.01	2.24 ± 0.01	34 ± 1
Fractional temperature sensitivity ($10^{-6}/^{\circ}\text{C}$)	8.5 ± 0.4	8.0 ± 0.4	0.5 ± 0.1
UMR extension factor	16		

Table 7.10: Temperature sensitivities of a birefringent fibre Fabry-Pérot sensor (*HibiGrat*) with a fibre Bragg grating proximal reflector (average of 10 measurement runs).

7.3.4 Static Longitudinal Strain Measurements with Grating-Based Sensors

The phase-strain sensitivities of grating-based birefringent fibre Fabry-Pérot sensors were also measured. Both static and dynamic strain measurements were made. In this sub-section, the results of the static strain measurements with *HibiGrat* are presented whilst in the next sub-section dynamic strain results are given.

A 304-type stainless steel cantilever beam was used in the strain measurements. The experimental arrangement (*c.f.* Figure 7.11) and the procedures were similar to those measurements with non-polarisation-maintaining fibre Fabry-Pérot sensors (Section 7.1.3). However the dimensions of the cantilever were different ($343 \times 9 \times 9$ mm). A 5 mm TML FLA-5-11-1L resistive strain gauge was placed side-by-side with the grating-based sensor. The centre of the resistive electrical strain gauge (ESG) was 15 mm from the pivot end and the centre of the effective cavity of *HibiGrat* was 17.5 mm. This centre separation was not ideal. Ideally the sensors would have been the same distance from pivot so that they experience the same average strain. The current placement was made because originally *HibiGrat* was wrongly believed to have a cavity length of 10 mm. The distal end of *HibiGrat* had to be coated with a reflective TiO_2 film because the adhesive employed to attach the Fabry-Pérot sensor would otherwise reduce the reflectance of this end.

The change in the resistance in the resistive strain gauge was measured using a high-resolution Hewlett-Packard 3478A multimeter (described in section 7.1) whilst the optical sensor used the arrangement described in Chapter 6. During the strain measurements, the whole cantilever assembly was enclosed with air-bubble wrapping sheets. These sheets were extremely useful in thermally insulating the cantilever from variations in room temperature. The measuring system also recorded the ambient temperature near the cantilever, the temperature of the LD and the (voltage) peak-to-peak amplitude of the interferometric intensity signals from the sensors.

The average strain experienced by the grating was different from that experienced by the Fabry-Pérot cavity. This difference was because the physical centre of the grating was 25 mm from the pivot end. However, following from Eq. 7.1, the average strain experienced by the grating and the sensor differed only by about 2 % ($\sim(25-17.5) \text{ mm}/343 \text{ mm}$).

Two types of static measurement were made. The first involved tensile (positive) strain with the resistive and optical strain gauges placed on the top surface of the cantilever whilst the second involved compressive (negative) strain with the sensors on the bottom surface. The cantilever beam was bent using weights hanging at the free end. Measurements were made with mass increments of 0.05 kg until a total mass of 2.7 kg reached. For each measurement run data was recorded during both loading and unloading.

Figure 7.30 and Figure 7.31 show the fringe shifts of typical static strain measurements with *HibiGrat* for the cases when the strain sensors were on top or on the bottom of the cantilever respectively. After each mass increment, it was necessary to wait for the beam oscillations to damp out. For this reason, the complete set of loading and unloading measurements for both tensile and compressive strain took about 3 hours. Under these circumstances, it would be possible for measurements to be affected by ambient temperature changes and LD drift. However, cantilever and LD temperatures were monitored and changes were negligible.

These results were obtained one after another in order that both axial gratings were equivalently scanned by the LD light source as the strain on *HibiGrat* was varied. The zero strain value indicated in Figure 7.30 and Figure 7.31 refers to the average value of the unloaded ESG strains when this sensor was on the top and on the bottom surface of the cantilever. The small strain values for no added mass at the start of the runs are due to the weight of the cantilever which produces a slight tensile or compressive strain depending on whether the sensor is on the top or bottom of the cantilever.

Figure 7.30 and Figure 7.31 show that the fast- and slow-axis responses of *HibiGrat* exhibited reasonably good linearity with the strain detected by the ESG. The figures show the fast- or slow-axis responses had very similar slopes. In addition, Figure 7.30 and Figure 7.31 show that there was little difference in the increasing and decreasing strain cases. This latter observation implied negligible mechanical hysteresis between the loading or unloading half-cycles of the measurement run. Table 7.11 and Table 7.12 summarise the results for the measurement run shown in Figure 7.30 and Figure 7.31 respectively. Comparing the values for the cases when the strain sensors were on the top and bottom of the cantilever beam in Table 7.11 and Table 7.12, the values indicate

that the corresponding phase-strain sensitivity were different (by up to 2 %). The differences between values for the top-surface and bottom-surface cases are explained shortly.

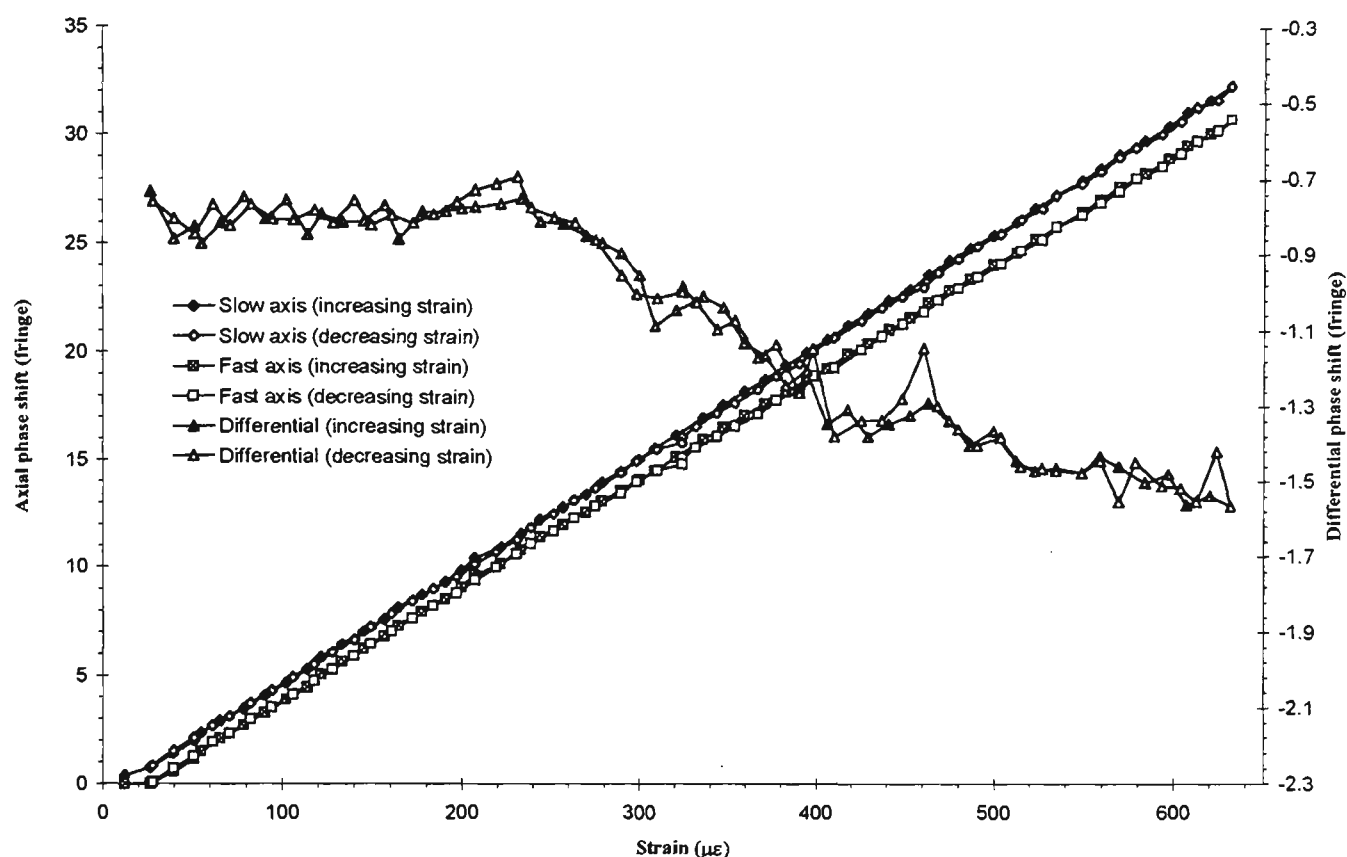


Figure 7.30: The phase shifts of the axial interferometers of a 15 mm birefringent Fabry-Pérot sensor (*HibiGrat*) with one Bragg grating reflector against the strain determined with a 5 mm resistive strain gauge. The sensors were placed on the top surface of a $343 \times 9 \times 9$ mm stainless cantilever beam. The centre of the optical sensor was 17.5 mm from the pivot end of the beam whilst that of the electrical sensor, 15 mm. Each data point corresponds to about $12 \mu\epsilon$ or a 50 g change in the mass hanging at the free end of the cantilever beam. The loading and unloading axial phase shift data are overlapping.

Parameter (tensile strain)	Fast-axis	Slow-axis
Phase-strain sensitivity (fringe/ $\mu\epsilon$)	0.0504 ± 0.0001	0.0520 ± 0.0001
Unambiguous measurand range ($\mu\epsilon$)	19.80 ± 0.04	19.22 ± 0.03
Optical gauge factor	0.91 ± 0.07	0.93 ± 0.07
linear correlation coefficient (r^2)	0.9998	0.9999

Table 7.11: Strain sensitivities of a birefringent fibre Fabry-Pérot sensor (*HibiGrat*) for the data shown in Figure 7.30, the case when the strain gauges were on the top surface of the cantilever. The values shown in the table were calculated based on the least squares line fit for the whole data (loading and unloading).

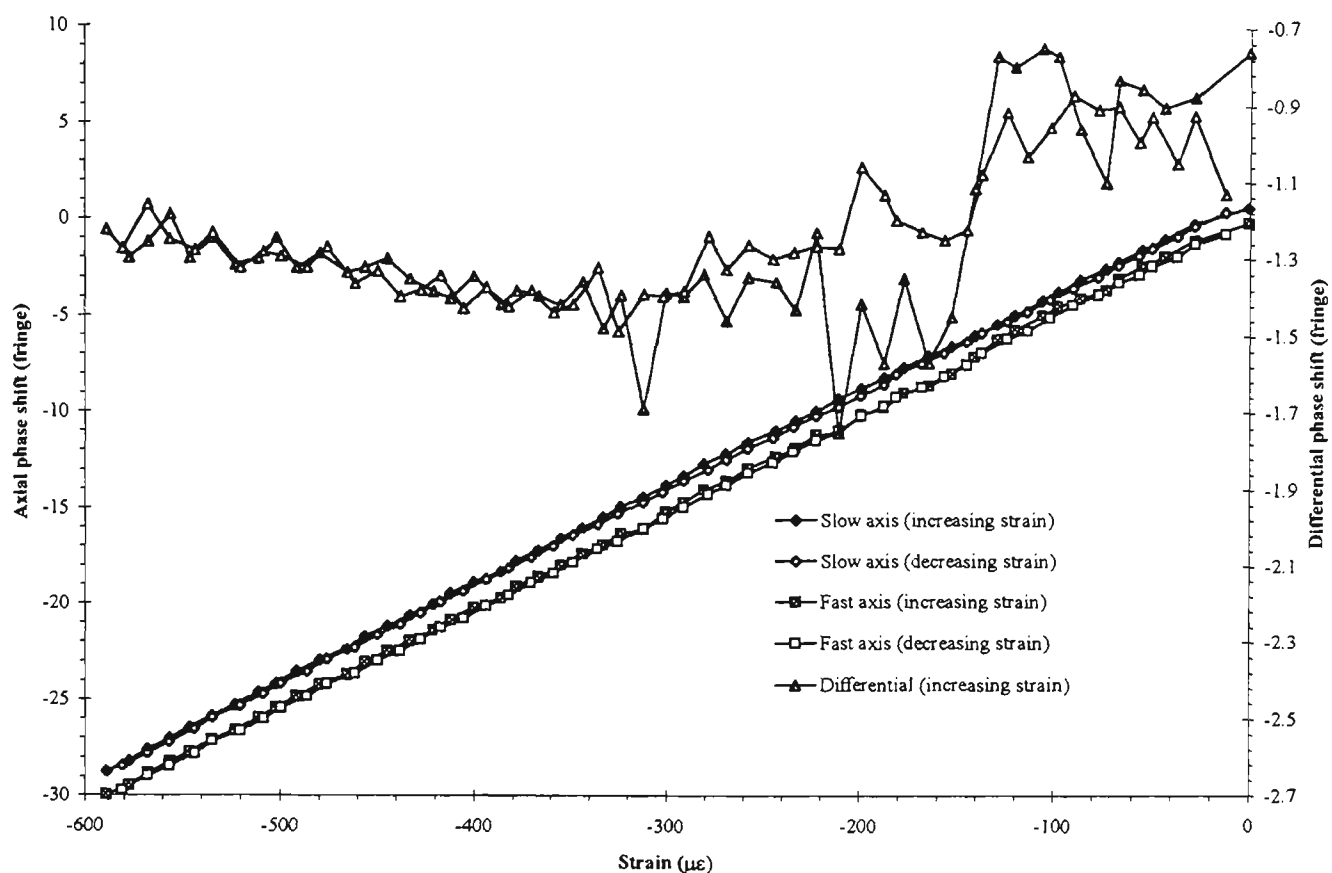


Figure 7.31: The phase shifts of the axial interferometers of a 15 mm birefringent Fabry-Pérot sensor (*HibiGrat*) with one Bragg grating reflector against the strain determined with a 5 mm resistive strain gauge. The sensors were placed on the top surface of a $343 \times 9 \times 9$ mm stainless cantilever beam. The centre of the optical sensor was 17.5 mm from the pivot end of the beam whilst that of the electrical sensor, 15 mm. Each data point corresponds to about $12 \mu\epsilon$ or a 50 g change in the mass hanging at the free end of the cantilever beam. The loading and unloading axial phase shift data are overlapping.

Parameter (compressive strain)	Fast-axis	Slow-axis
Phase-strain sensitivity (fringe/ $\mu\epsilon$)	0.0515 ± 0.0001	0.0508 ± 0.0001
Unambiguous measurand range ($\mu\epsilon$)	19.42 ± 0.04	19.67 ± 0.03
Optical gauge factor	0.92 ± 0.07	0.91 ± 0.07
linear correlation coefficient (r^2)	0.9997	0.9998

Table 7.12: Strain sensitivities of a birefringent fibre Fabry-Pérot sensor (*HibiGrat*) for the data shown in Figure 7.31, the case when the strain gauges were on the bottom surface of the cantilever. The values shown in the table were calculated based on the least squares line fit for the whole data (loading and unloading).

The differential response also exhibited similar characteristics to those evident in the temperature measurements (section 7.3.3). The differential responses shown in Figure 7.30 and Figure 7.31 exhibit some high frequency

phase(-strain) noise structures. These structures, especially in certain segments of the differential response, appear to be periodic with strain and to have a period equivalent to the strain UMR of the axial interferometers. These structures were believed to have a similar origin to those observed in the temperature measurements. However, the period of these structures could not be measured because the incremental change in strain during the measurement was comparable to the strain-UMR of each axial interferometer.

Since the axial response exhibited linearity with strain, the differential response was also expected to be linear with strain. Although some general linear trend can be inferred, the observed differential response was predominantly not linear with strain as depicted in Figure 7.30 and Figure 7.31. As was the case with the temperature measurements, the origin of this nonlinear phase variations was suspected to be some property of the grating. In Figure 7.32 and Figure 7.33, the variations in the square of the amplitude of the interferometric signal detected by the photodetectors and the differential response of *HibiGrat* during the measurement runs shown in Figure 7.30 and Figure 7.31 are compared. The modulation evident in the squared signal amplitude curves is believed to have the same origin as that described for the corresponding modulation of the curves in the temperature measurements. Figure 7.32 and Figure 7.33 show that the inflection point of the nonlinear phase variations in the differential response occurred very close to the centre of the peak reflectance of both the fast- and slow-axis grating. The results shown in Figure 7.32 and Figure 7.33 give further evidence that indeed the nonlinear phase variations in the differential response can be attributed to the anomalous dispersion of the axial gratings. In this case, the data range was sufficient for both axial gratings to be covered.

The nonlinear phase variation features in the differential response of the strain measurements are more pronounced than those of the corresponding temperature measurements. This could be due to fact that the phase-strain sensitivities of the fast and slow axes were more similar than the phase-temperature sensitivities and hence the linear trend in the strain data is less. Figure 7.30 and Figure 7.32 show that the features which we believed are due to the anomalous dispersion dominated the differential response. This dominance can explain the slight difference between the phase-strain sensitivities of the corresponding axial interferometers shown in the results summarised in Table 7.11 and Table 7.12. For tensile and compressive strain measurements, the LD scans through the fast-

and slow-axis gratings respectively. Because the phase of the fast axis is affected in one scan and that of the slow axis in the other, the slopes of corresponding axial phase changes are different in the two scans. With the linear trend removed from the fast-axis-grating differential phase data, the magnitude of the peak phase change across the anomalous dispersion feature is about 0.4 fringe and the corresponding value for the slow-axis grating is about 0.5 fringe. Phase changes of this magnitude over a $600 \mu\epsilon$ range translate to an average slope change of about $0.0007 - 0.0008 \text{ fringe}/\mu\epsilon$. These numbers agree reasonably with the $0.0011 - 0.0012 \text{ fringe}/\mu\epsilon$ differences in the table sensitivities.

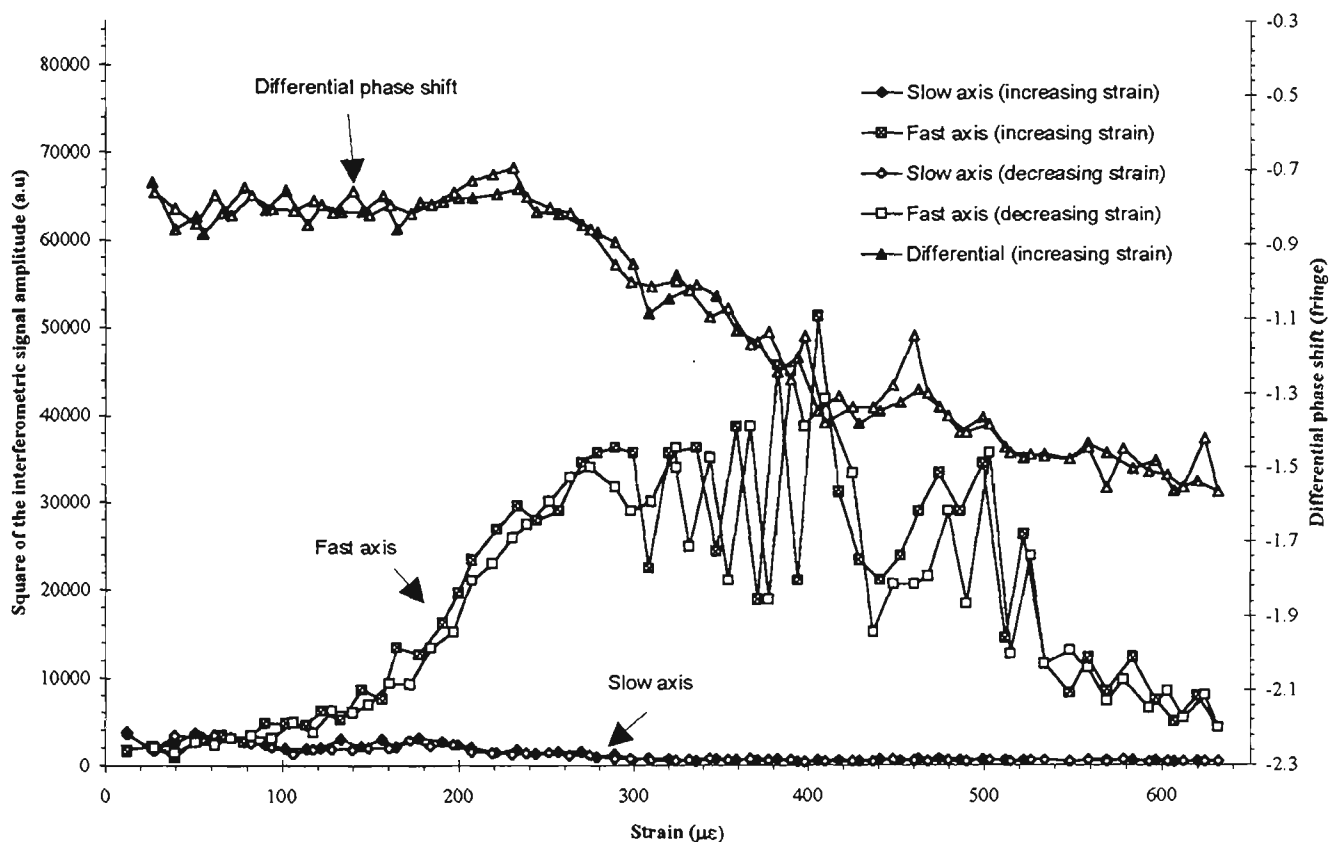


Figure 7.32: Differential phase shifts and the square of the signal amplitude of a birefringent Fabry-Pérot sensor (*HibiGrat*) against the strain determined with a resistive strain gauge for the data shown in Figure 7.30, the case when the strain gauges were on the top surface of the cantilever.

Because of the dominance of the anomalous dispersion of the axial gratings in the differential response of *HibiGrat*, and the limited scan range, the underlying linear trend of the differential phase response can not be easily determined from the data. In an attempt to get some idea of this trend and also to compare the behaviour of the differential phase changes in the region of the two axial gratings, the differential phase response shown in

Figure 7.32 and Figure 7.33 were divided into three segments (left, middle and right) and the slopes calculated. These segments were approximately 0 to 240 $\mu\epsilon$, 240 to 400 $\mu\epsilon$ and 400 to 630 $\mu\epsilon$ for Figure 7.32; and -600 to 450 $\mu\epsilon$, -450 to -140 $\mu\epsilon$, -140 to 0 $\mu\epsilon$ for Figure 7.33. Table 7.13 summarises the phase-strain sensitivities of each of the segments.

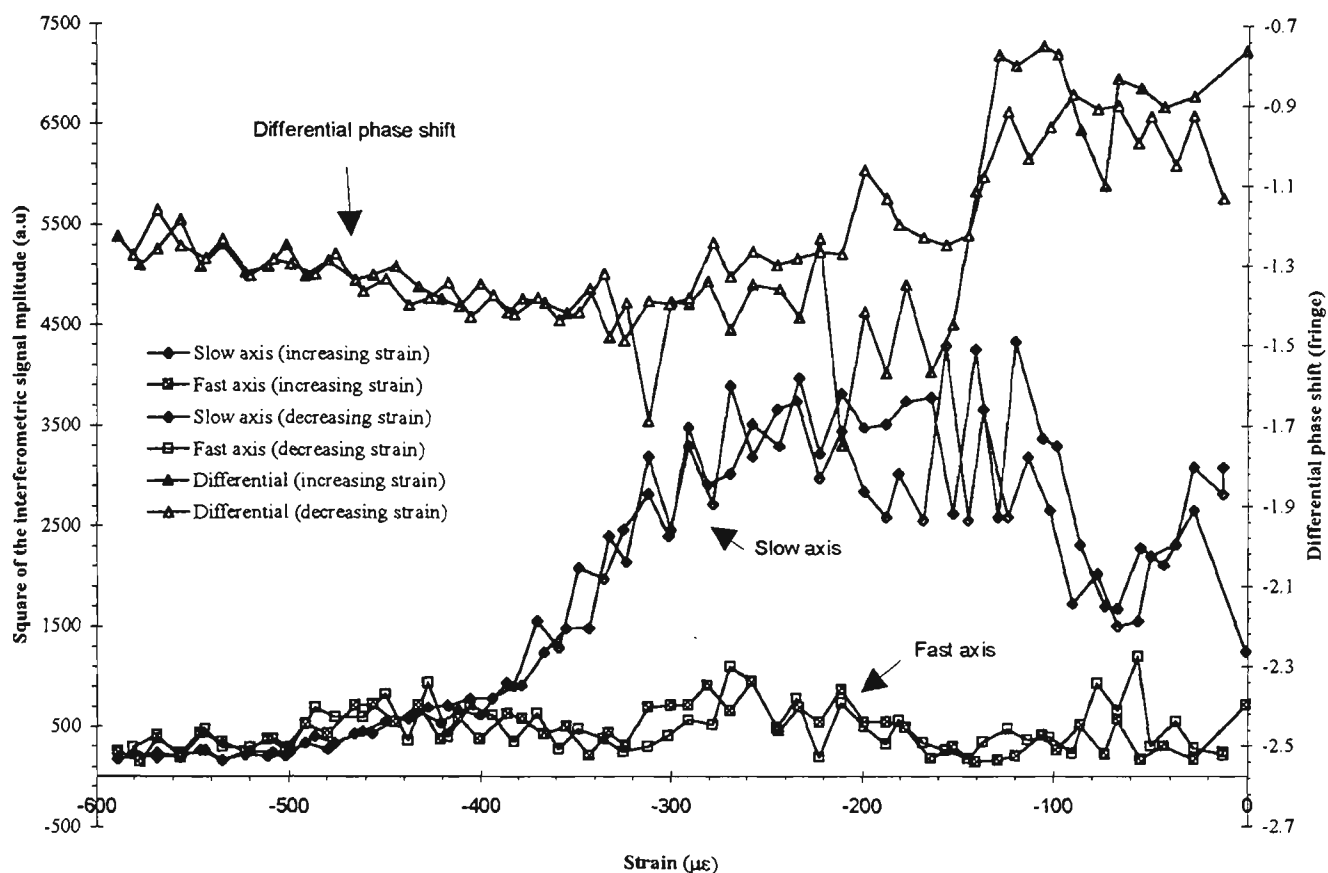


Figure 7.33: Differential phase shifts and the square of the signal amplitude of a birefringent Fabry-Pérot sensor (*HibiGrat*) against the strain determined with a resistive strain gauge for the data shown in Figure 7.30, the case when the strain gauges were on the bottom surface of the cantilever.

Differential Phase-Strain Sensitivity	Top surface	Bottom surface
Right segment (10^{-4} fringe/ $\mu\epsilon$)	-8.9	-2
Middle segment (10^{-4} fringe/ $\mu\epsilon$)	-28.6	22
Left segment (10^{-4} fringe/ $\mu\epsilon$)	1.7	-8.6

Table 7.13: Phase-strain sensitivities of different segments of the differential phase response of a birefringent fibre Fabry-Pérot sensor (*HibiGrat*).

The differential phase-strain sensitivity of the right segment for the bottom-surface case and the left segment for the top-surface case were small. If these two sets of data are put side-by-side to form a continuous record from about $-600 \mu\epsilon$ to $+600 \mu\epsilon$ (as in Figure 7.34), then these two differential phase curves should be continuous. Their average sensitivity in the region between the two axial grating effects was $\sim 0.14 \times 10^{-4}$ fringe/ $\mu\epsilon$ which is close enough to zero considering the uncertainties involved.

The phase-strain sensitivities in the middle segments where anomalous dispersion phase shifts dominate are also similar in magnitude. The opposite sign of these sensitivities is expected since slow-axis data is subtracted from the fast-axis data to obtain the differential phase shift.

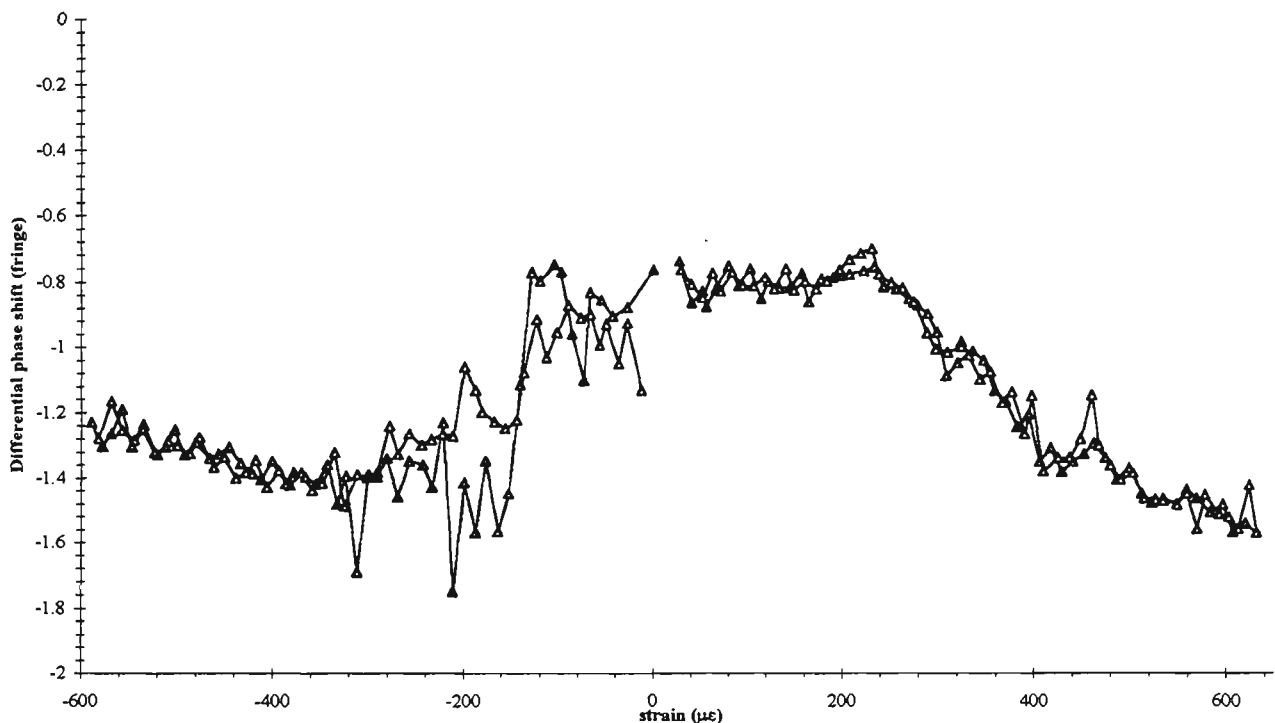


Figure 7.34: Combined differential phase responses (fast axis minus slow axis) of Figure 7.32 and Figure 7.33. Four separate curves are plotted for tensile and compressive strain during both loading and unloading of the cantilever.

The differential phase-strain sensitivity of the left segment for the bottom-surface case and the right segment for the top-surface case were similar. These segments were furthest away from the effects of the axial gratings and thus these segments were less affected by the anomalous dispersion of the gratings. Their average phase-strain sensitivity was about -8.8×10^{-4} fringe/ $\mu\epsilon$. This value is the best estimate which can be obtained from the data of

the non-resonant differential phase-strain sensitivity of the fibre Fabry-Pérot cavity. Since this value is negative, the slow-axis interferometer had a greater strain sensitivity than the fast-axis interferometer.

As mentioned earlier, a typical strain measurement took about 3 hours for both tensile and compressive strain measurement runs. During this time it is conceivable that extraneous effects such as LD drift may have occurred and may be responsible for the phase changes we have ascribed to anomalous dispersion. This is unlikely since these phase changes occurred at the same point during both loading and unloading cycles. In order to further demonstrate that drifts were not the causes of these phase changes, the LD temperature and the cantilever temperature were monitored during the strain runs and this data is plotted together with the differential phase shift in Figure 7.35 and Figure 7.36. Clearly there were no significant changes in the cantilever or LD temperature during the runs. The average temperature of the LD was about 12.20 ± 0.02 °C whilst the cantilever temperature near the strain gauges was 19.17 ± 0.02 °C. The stability of these temperatures may be responsible for the excellent overlap of the loading and unloading data.

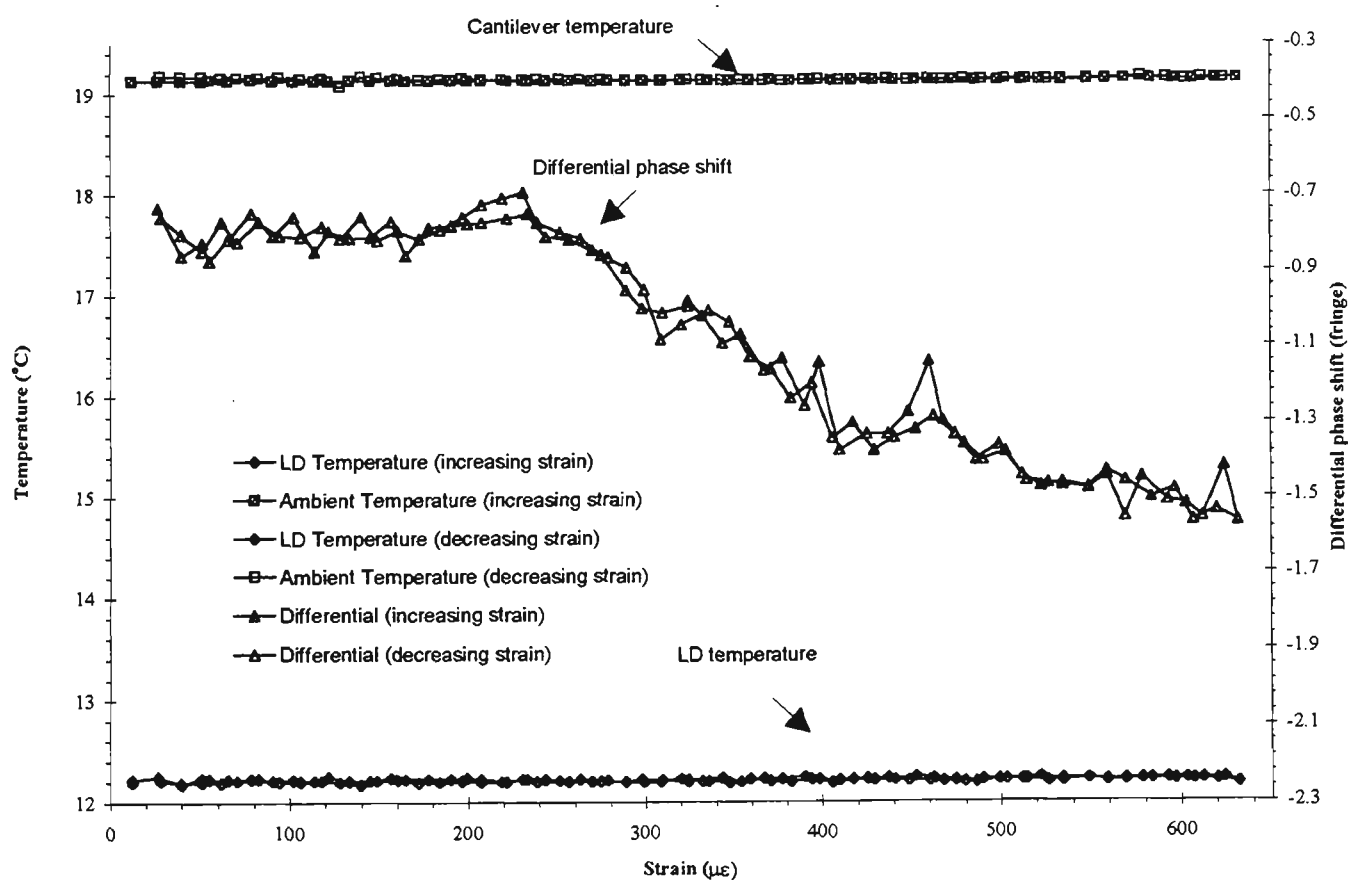


Figure 7.35: Differential phase shift together with cantilever temperature and the LD temperature during tensile strain measurements.

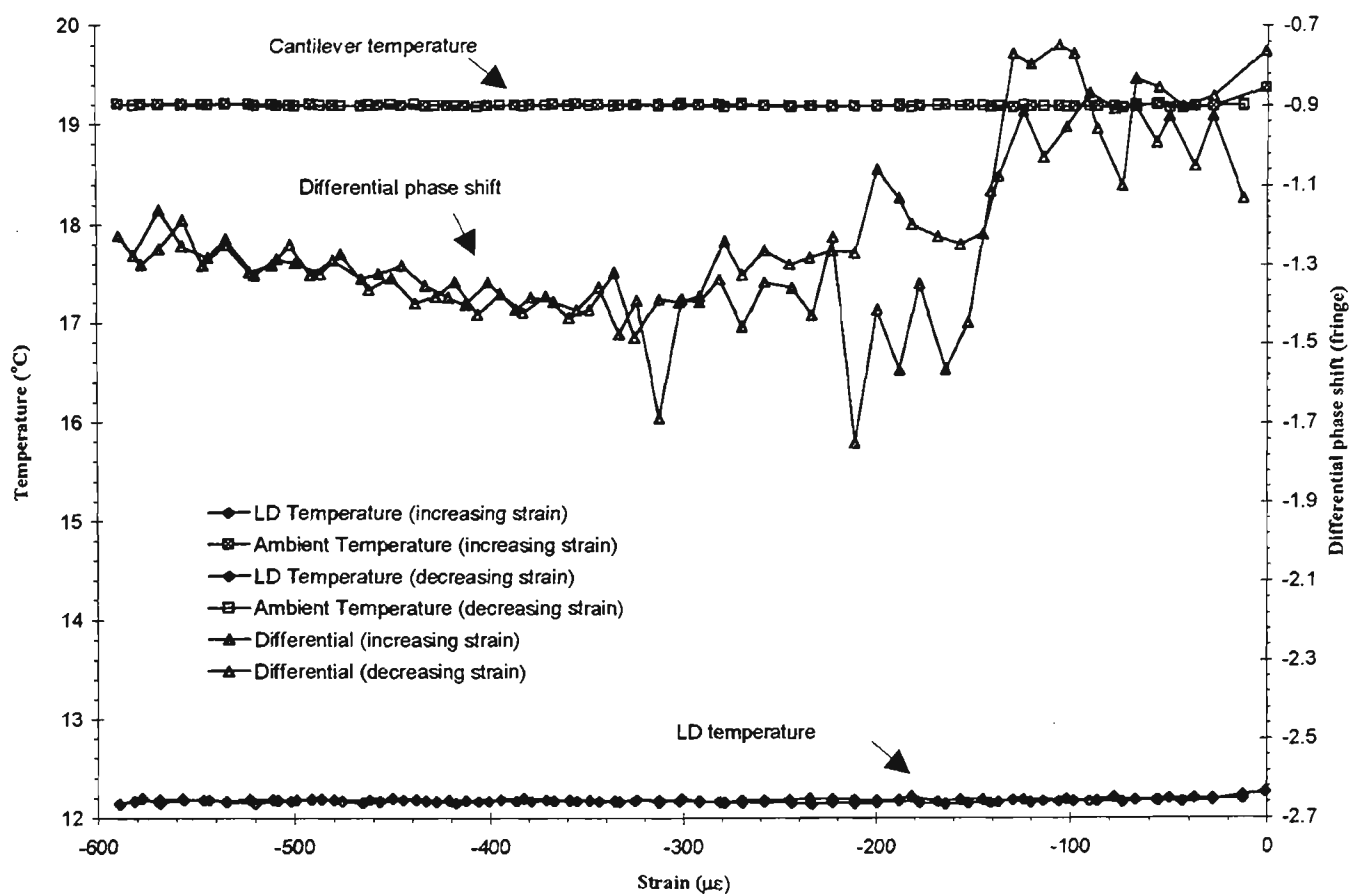


Figure 7.36: Differential phase shift together with cantilever temperature and the LD temperature during compressive strain measurements.

In summary, static strain measurements have been made in a birefringent fibre Fabry-Pérot sensor incorporating a Bragg grating as one of its mirrors. Both the fast-axis and slow-axis responses were quite linear. The differential response of this sensor exhibited similar features to those observed in the fast axis response during temperature measurements. In the strain case the measurement range, sensor sensitivity and system stability were such that the features were very clearly evident for both axial interferometers (via the differential phase shift) and the features could clearly be identified as due to anomalous dispersion in the gratings. This method is clearly a direct experimental approach of measuring the anomalous dispersion effects in a Bragg grating. Since it is normally necessary to operate a sensor in the region of reasonable reflectance of the grating, these anomalous dispersion effects represent a limitation to the linearity which is possible with the sensor.

Table 7.14 summarises the average strain sensitivities of *HibiGrat*. These figures were obtained by averaging the tensile and compressive strain figures.

Parameter	Fast-axis	Slow-axis	Differential
Phase-strain sensitivity (fringe/ $\mu\epsilon$)	0.0508 ± 0.0002	0.0516 ± 0.0002	0.0008 ± 0.0002
Unambiguous measurand range ($\mu\epsilon$)	19.69 ± 0.05	19.38 ± 0.06	1250 ± 0.03
Optical gauge factor	0.91 ± 0.05	0.93 ± 0.05	0.014 ± 0.004
UMR extension factor ($E_{UMR,\epsilon}$)	64.5		

Table 7.14: Average strain sensitivities of a birefringent fibre Fabry-Pérot sensor (*HibiGrat*). Average of the data of 6 strain runs.

Despite the significant difference in the details of their sensor configuration compared to that described in this sub-section, perhaps the most comparable paper reporting results for UMR extension in strain measurements is the recent paper by Rao *et al.* [1997b]. The results reported in this sub-section compare favourably with those of Rao *et al.* and perhaps the simplest way to illustrate the significance of the strain performance we have achieved is to look at the details of this comparison. Table 7.15 below compares the principal performance characteristics of the two sensors. In terms of construction and operation, the sensor described in this thesis is more difficult to construct as alignment of polarisation axes is involved. However the optics and electronics of the detection system is considerably simpler than that of Rao *et al.* In addition, the sensor described in this thesis is far more amenable to construction in all-fibre form.

Parameter	This thesis	Rao <i>et al.</i>
Phase noise at constant strain	$\sim 3^\circ$	$\sim 2^\circ$
Phase-strain sensitivity	$\sim 18^\circ/\mu\epsilon$	up to $9.6^\circ/\mu\epsilon$
Unambiguous measurand range	$1250 \mu\epsilon$	$1500 \mu\epsilon$
Dynamic range	6.45×10^5	4×10^4
UMR extension factor ($E_{UMR,\epsilon}$)	64.5	40

Table 7.15: Comparison of the strain performance of the sensor described in this thesis and that of a Bragg grating sensor [Rao *et al.*, 1997b] which used a pseudo-heterodyne detection scheme for measuring Bragg wavelength shifts based on cascaded two-beam interferometers.

In practical applications it is likely that a sensor of the type described in this thesis may be used in an environment in which both temperature and strain may vary. Hence it is of interest to compare the temperature and strain sensitivity. From Table 7.10 and Table 7.14, one fringe corresponds to a temperature change of approximately 2 °C or to a strain change of about 20 $\mu\epsilon$.

From Table 7.10 and Table 7.14 also show a large difference between the UMR extension factor for temperature and strain. This result was of not surprising because the temperature rate of change of the linear birefringence in elliptically clad birefringent fibres is high and so the UMR extension factor is low.

7.3.5 Dynamic Strain Measurements with Grating-Based Sensors

Temporally varying strain (between 1 Hz and 10 Hz) measurements were also made with *HibiGrat* and were compared with resistive strain gauge data. The same cantilever arrangement as in the last sub-section was used and the strain sensors were on the top surface. Since these dynamic strain measurements involved a relatively small range of strain, a classical Wheatstone Bridge amplifier circuit was used to measure the resistance changes of the ESG. The resistive bridge network was formed by two 1%-precision 120 Ω resistors together with a sensing and a reference 120 Ω ESG. The reference gauge was bonded near the sensing ESG but was not strained. The purpose of this second gauge was to provide automatic compensation whenever the ambient temperature near the cantilever varied. The voltage output of the Wheatstone Bridge circuit was digitised and stored in the computer using a 12-bit analogue-to-digital converter. *HibiGrat* was addressed and interrogated in reflection as in the previous measurements. The average wavelength of the LD was set between the two axial Bragg wavelengths.

Two types of dynamic strain measurement are described in this sub-section. The first type involved allowing the free end of the cantilever to vibrate naturally after this end had been initially displaced (natural damping experiment). The second type involved a mass attached to the free end of the cantilever and to the experimental table using two springs (coupled block experiment).

The natural damping experiment began by first bending the beam to initially concave downward. This bend was achieved by pulling the free end downward using a large mass hanging with a piece of thick soldering lead wire. With this arrangement, reasonably repeatable vibration could be initiated by touching the solder wire with a high-temperature iron. The whole measurement was performed inside an air-bubble wrapper bag as was done with the static strain measurements in order to reduce variations in the cantilever temperature.

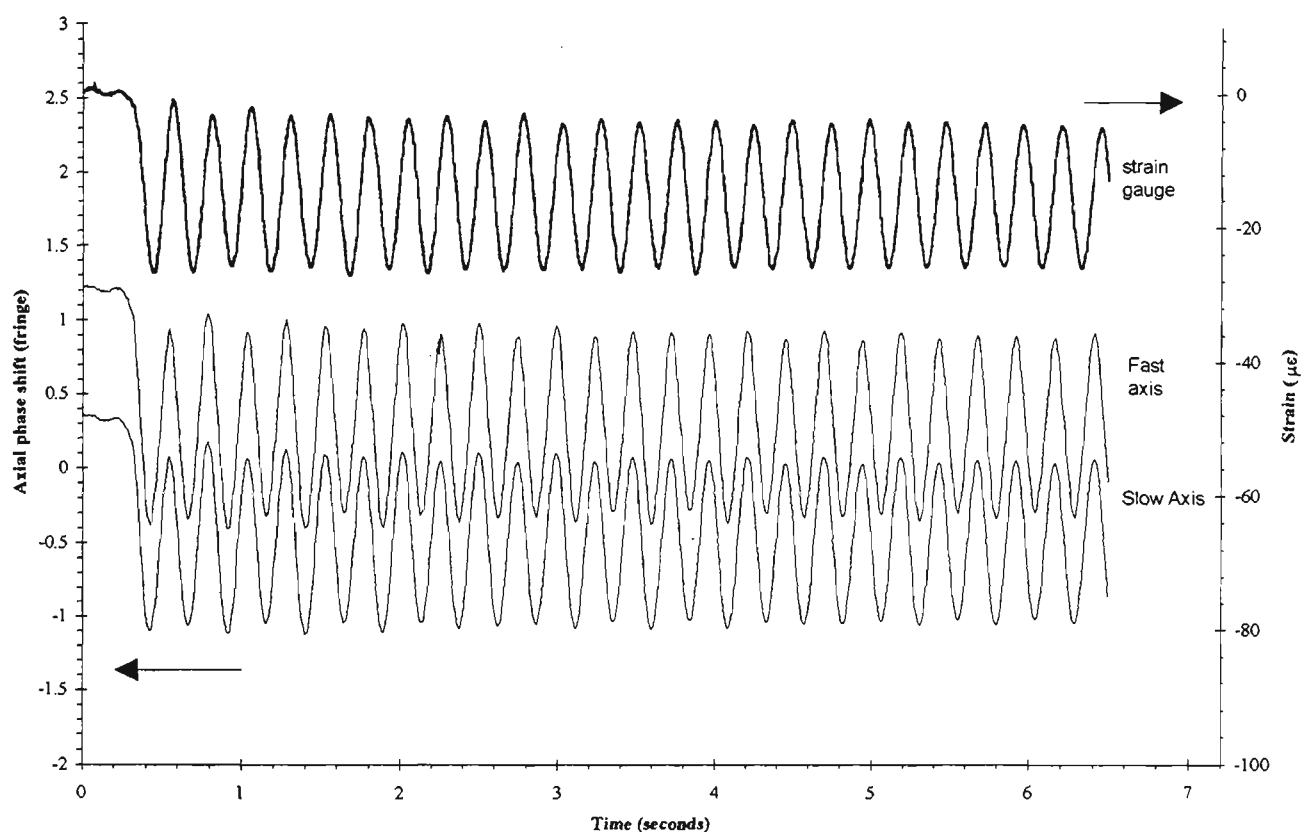


Figure 7.37: Axial phase shifts of a birefringent Fabry-Pérot sensor (*HibiGrat*) together with the strain measurements with a resistive strain gauge over time as the cantilever beam vibrated (natural damping). The initial phase offset between the fast- and slow-axis response is adjusted to separate the two curves.

Figure 7.37 compares the performance of a resistive strain gauge and *HibiGrat* over time as the free end of the cantilever vibrated. The initial curvature of the cantilever produced a positive strain on the optical and electrical strain gauges. The zero for electrical strain measurements was chosen as the point of maximum strain (just before release of cantilever). Hence, when the cantilever was allowed to vibrate, negative strain was registered by the electrical strain gauge. The period of the vibrating cantilever beam was about 0.25 s.

Figure 7.37 shows that the fast- and slow-axis response of *HibiGrat* essentially followed the response of the ESG. Both sensors show that there is some small amplitude modulation of the vibration which may indicate some non-planar vibration. The optical and electrical sensors were about 20° out of phase and this difference could be caused by phase shifts in the strain gauge amplifier electronics.

The coupled-block experiment involved a 0.4 kg block of mass attached to the free end of the cantilever and also to the experimental table using two springs with spring constants of 138 N/m. The free end, the springs and the block were vertically aligned by eye. The block was displaced vertically by hand and when released, it vibrated vertically but with some side-to-side wobble. The expected mechanical response was a regular oscillation with a low-frequency modulation of its amplitude. This arrangement was chosen simply to give a more complicated waveform than that of the previous figure. Figure 7.38 shows the performance of the optical and electrical sensors during vibration using this coupled-block arrangement. The fundamental period of oscillation of the free end was 0.49 second whilst the period of the envelope about 7.7 seconds.

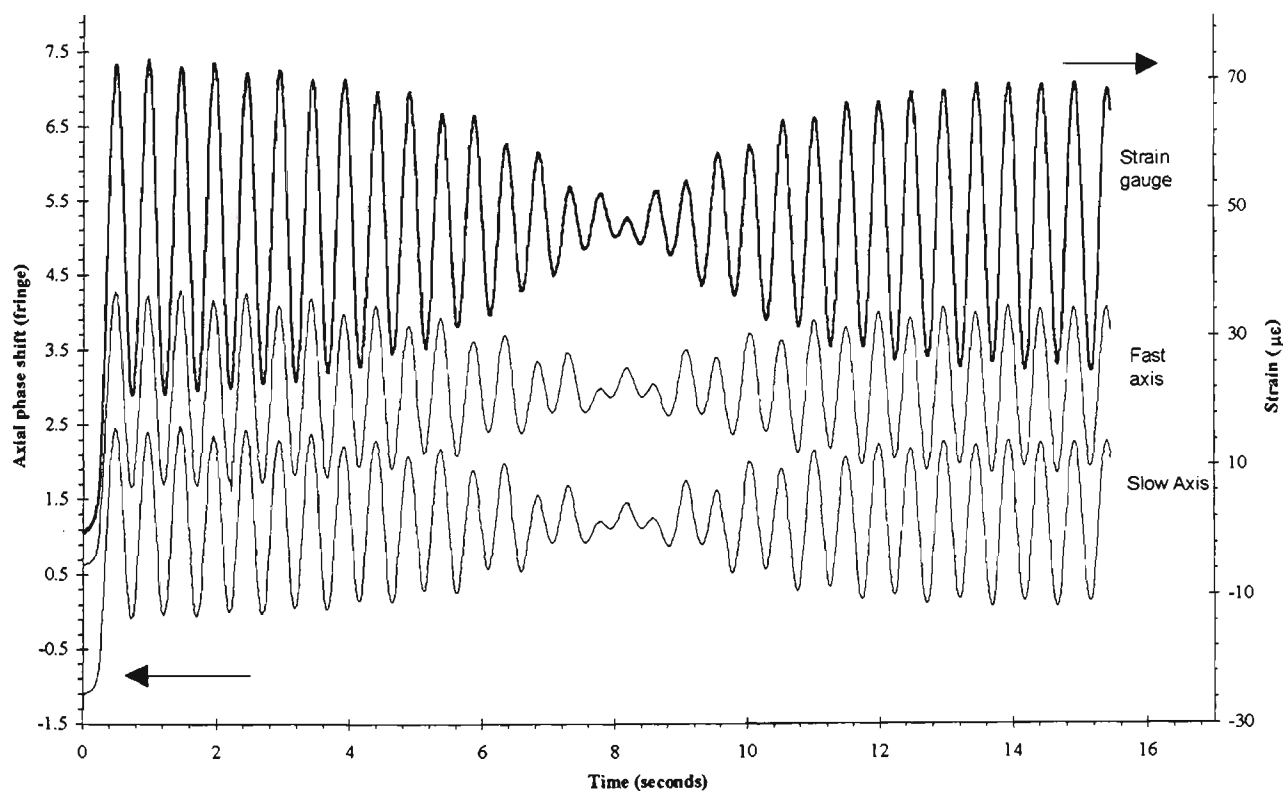


Figure 7.38: The axial phase shifts of a birefringent Fabry-Pérot sensor (*HibiGrat*) together with the strain measured with a resistive strain gauge over time as the free end of a stainless steel cantilever beam vibrated (coupled block). The offset between the fast- and slow-axis data was increased for clarity of display.

It is clear from Figure 7.38 that the optical and electrical sensors behaved very similarly. However, the unintentional wobble of the cantilever did produce a phase shift which complicates the comparison. This is particularly evident in the region of the node of the amplitude modulation.

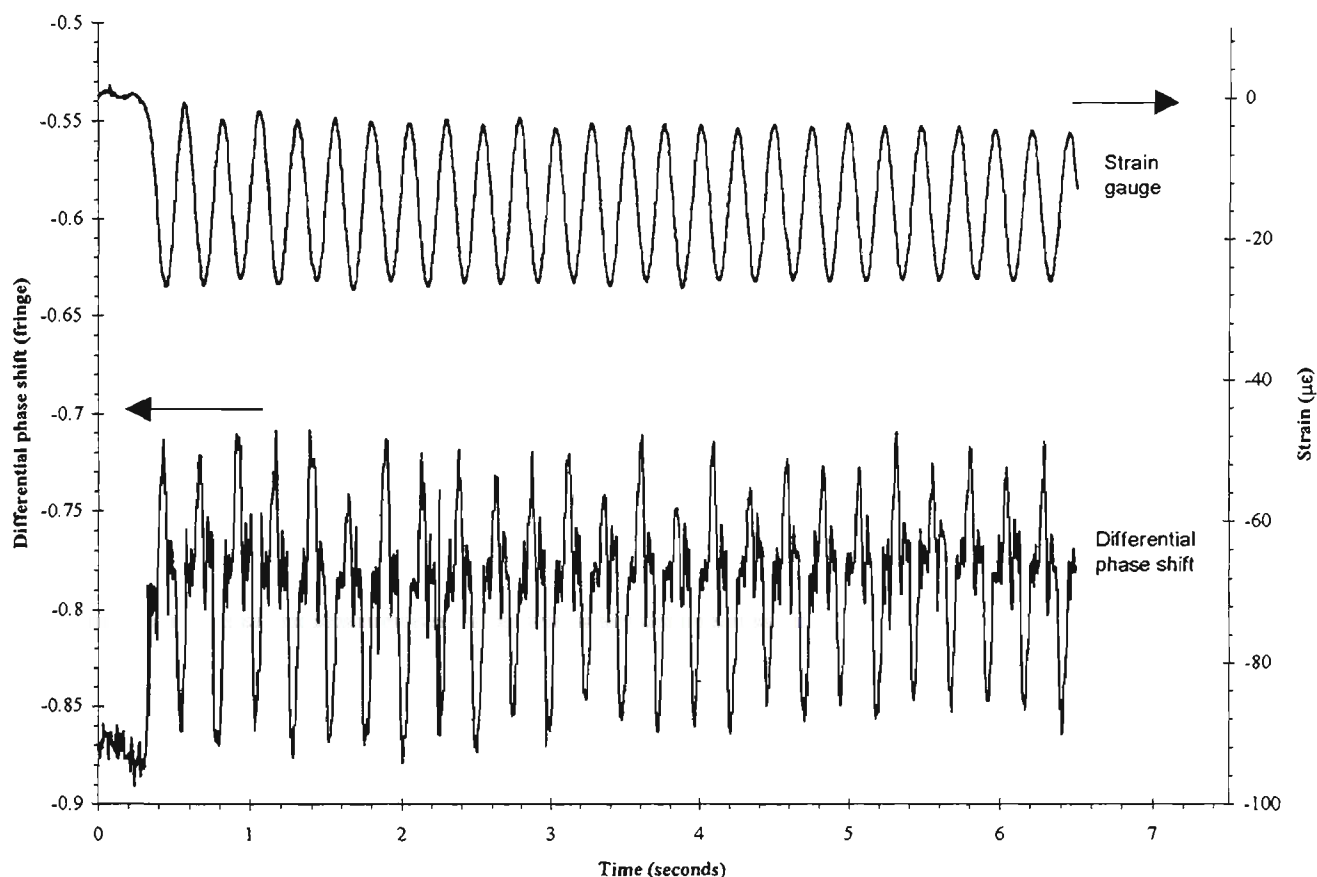


Figure 7.39: The differential phase shift of a birefringent Fabry-Pérot sensor (*HibiGrat*) together with the strain measured with a resistive strain gauge over time as the free end of a stainless steel cantilever beam vibrated (natural damping).

Figure 7.39 and Figure 7.40 compare the differential phase response of *HibiGrat* with the response of the ESG for the case shown in Figure 7.37 and Figure 7.38 respectively. These figures show that the peak-to-peak differential phase amplitude was about 0.1 - 0.15 fringe, which is about 10% of the peak-to-peak axial phase amplitudes. It is also evident that the differential phase shows nonlinear effects and therefore does not follow a sinusoidal variation.

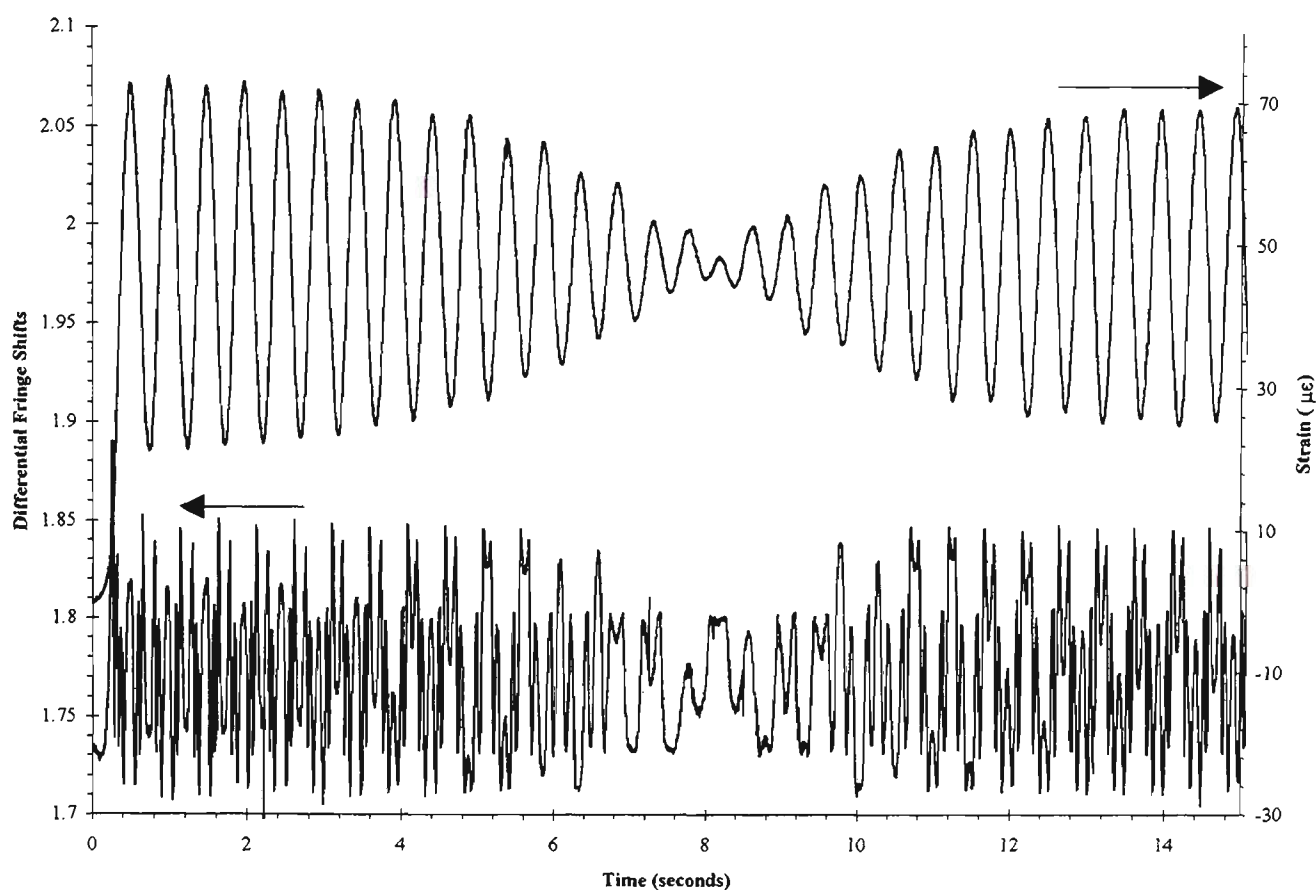


Figure 7.40: The differential phase shift of a birefringent Fabry-Pérot sensor (*HibiGrat*) together with the strain measured with a resistive strain gauge over time as the free end of a stainless steel cantilever beam vibrated (coupled block).

Figure 7.41 shows the first two seconds of data recorded during the coupled-block experiment (Figure 7.40). The individual data points are marked with circles. This figure shows that the additional modulation seen in the differential response was not some random noise effect but rather a regular periodic one. Furthermore, Figure 7.41 shows that the higher frequency phase-modulated structures in the differential response were regular and periodic. The Fourier transform of this differential phase signal gave two main peaks which corresponded to the strain-UMR of each axial interferometer. Both the magnitude of the effect and the characteristic frequencies indicate that the origin of these differential phase effect is the nonlinearity in the optical frequency ramp.

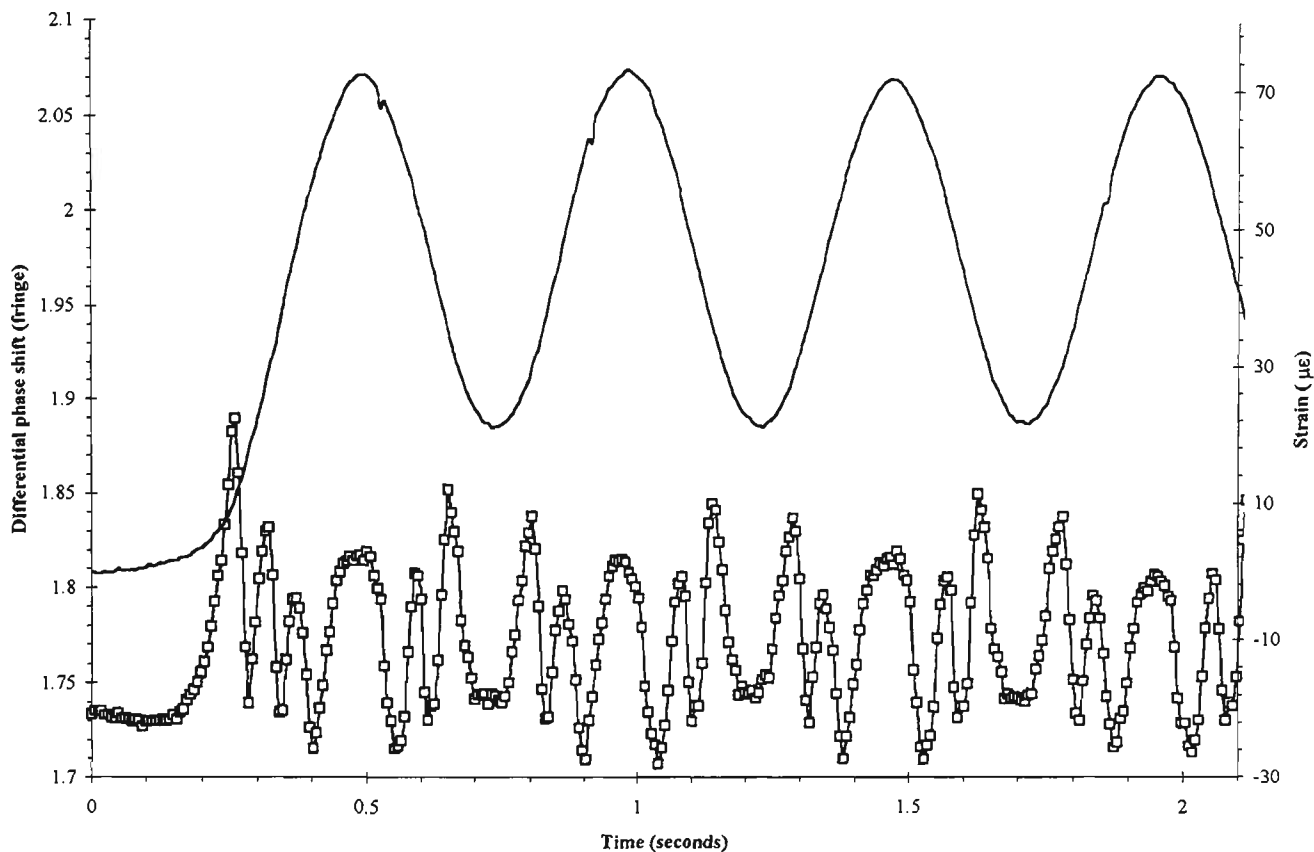


Figure 7.41: The differential phase shift of a birefringent Fabry-Pérot sensor (*HibiGrat*) together with the strain measured with a resistive strain gauge over time as the free end of a stainless steel cantilever beam vibrated (coupled block - first two seconds).

Figure 7.42 shows the fast- and slow-axis response of *HibiGrat* plotted against the strain as measured by the ESG for the data of Figure 7.38 from $t=1$ s to 3 s. This axial response data was made monotonic by only using the positive sloping parts of the data. Also shown in the figure is the differential phase. The plots show some bifurcation at higher strain levels since there is some variation in the amplitudes of the peaks in the figure which arises due to the non-planar vibrations. The individual axial response plot show a sinusoidal-like variation with ESG strain. This sinusoidal variation is very clearly shown in the differential phase data. The period of this variation agrees well with strain-UMR of the axial interferometers. This, and the differential peak-to-peak amplitude of about 0.1 fringe provide further very strong evidence that these features are the result of a nonlinearity in the optical frequency ramp.

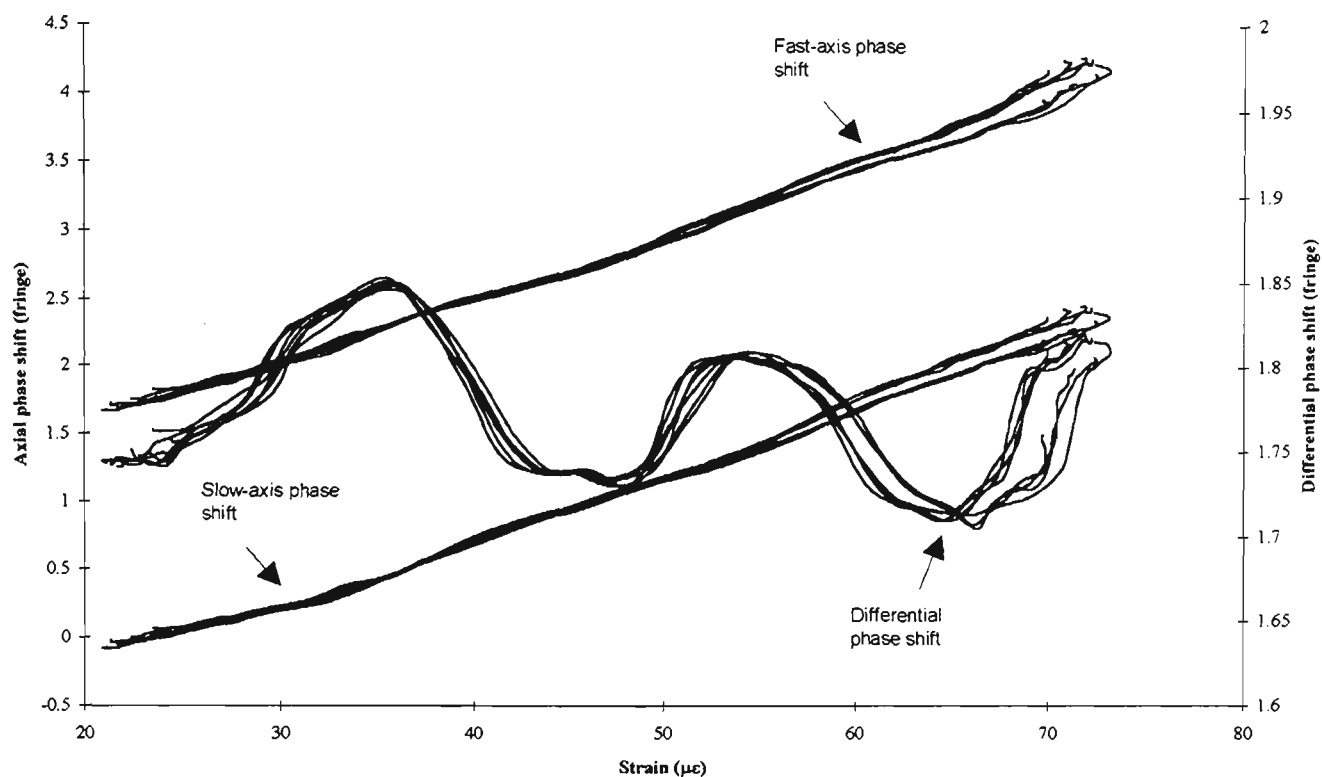


Figure 7.42: The axial and differential phase shift of a birefringent Fabry-Pérot sensor (*HibiGrat*) plotted against the strain measured with a resistive strain gauge. Only the positively sloping parts of the data from $t=1$ s to 3 s in Figure 7.38 is plotted. The offset between the fast- and slow-axis data was increased for clarity of display.

In summary, this sub-section has shown that in addition to the static strain measurements reported earlier, the grating-based sensor is also suitable for dynamic strain measurements. To achieve its performance potential, the sensor would need careful adjustment and a linear optical frequency ramp. This ramp could perhaps be produced using a nonlinear sawtooth current modulation for the LD. Data of the type shown in Figure 7.42 clearly reveal the existence of any nonlinearity in the optical frequency ramp. Perhaps this type of experiment could be used during adjustments to the current modulation to indicate when the optical frequency ramp is sufficiently linear.

Chapter 8:

Conclusion

8.1 Synthesis

In this work we have investigated an optical fibre sensing arrangement which can be operated in an all-fibre form and can measure both temperature change and strain with high sensitivity and large unambiguous measurand range. The chosen sensor configuration is that of a polarisation-maintaining (birefringent) fibre Fabry-Pérot interferometer. This sensor effectively has two Fabry-Pérot interferometers - one for each polarisation axis. The sensitivity of this birefringent sensor is provided by the sensitivities of the axial interferometers whilst its UMR is determined by the differential phase response.

A pseudo-heterodyne signal processing scheme implemented with a sawtooth-modulated LD was chosen to determine the phase shifts of each axial interferometer. This scheme allows the detection of moderately fast variations in temperature or strain up to half the frequency of the sawtooth modulation. The delay (relative to the start of the ramp) of the zero-crossings of each interferometric output was determined using a high-frequency clock signal and changes in this delay is proportional to the interferometric phase shift. The ratio of the frequencies of the sawtooth and the clock signals was chosen to give a phase resolution of $2\pi \times 10^{-4}$ radian.

We have developed a range of FFPSs. Fusion-spliced non-polarisation-maintaining FFPSs were first fabricated to provide initial measurements of the sensitivities of FFPSs and more importantly to perfect the technique of producing fusion-spliced FFPSs. The NPM sensors performed well as temperature and static strain sensors.

Fusion-spliced birefringent FFPSs were next fabricated. These fusion-spliced sensors exhibited high loss and were difficult to construct primarily because of the need to align the polarisation axes of a lead-in fibre and those of the sensor. In addition, these sensors were very fragile and hence were not suitable for strain measurements. Subsequently grating-based birefringent FFPSs were also made. These grating-based sensors exhibited high tensile strength and minimal transmission loss at the grating. Furthermore, they were easy to construct since the polarisation axes of the lead-in fibre and those of the sensor are naturally aligned. However, there are complications associated with the use of FBGs as Fabry-Pérot mirrors. The optical length of a grating implies a phase change between its ends. This phase change can be accounted for by using an effective cavity length of the sensor calculated from the centres of the gratings. The grating also exhibits anomalous dispersion which is small for low Bragg reflectance. The finite optical bandwidth of the spectrum of FBGs and their sensitivities to temperature and strain imply that the fringe visibility depends on these measurands. Consequently, the overall measurand range of the sensors would be limited by intensity noise in the interferometric output as the fringe visibility decreases.

The fusion-spliced sensors gave reasonably linear phase responses. The magnitude of the phase sensitivities depends on the sensing length. For a sensing length of about 34 mm, the average phase-temperature sensitivities (in the range from 0°C to 100°C) are about 1.1649 fringe/°C and 1.1212 fringe/°C for the fast- and slow-axis interferometers respectively. These values give a temperature-UMR of about 23 °C and a noise-free temperature resolution of about 8.7×10^{-5} °C. The high resolution measurements have allowed the detection of other nonlinear phase effects common to both axes of the sensor. These effects were slowly-varying phase drifts, a parabolic phase feature, and a periodic phase noise effect. When the differential phase was calculated, the parabolic feature and the slowly-varying drifts in both axial responses practically canceled each other whilst the periodic phase noise produced a beating waveform since the periods of these phase noises were slightly different. The parabolic feature was attributed to the second-order dependence of the core refractive index with temperature and to the non-uniform heating of the ends of the sensor. The slowly-varying drifts were due to thermally-induced drifts in the LD output.

In this work, the shape, magnitude and period of the periodic phase noise in each axial response were simulated and subsequently the mis-adjustments in the signal processing and the nonlinear optical frequency ramp were identified as the origin of this phase noise. These axial phase noises were not a fundamental limitation and in principle they can be significantly reduced by using proper signal-processing adjustments, a linearly-ramped optical frequency sawtooth modulation and a narrow band-pass filter.

The grating-based sensors gave reasonably linear phase responses as well. For a sensing length of about 15 mm, the average phase-temperature sensitivities (in the range from 0°C to 100°C) are about 0.477 fringe/°C and 0.447 fringe/°C for the fast- and slow-axis interferometers respectively whilst the average phase-strain sensitivities (in the range from -1000 $\mu\epsilon$ to +1000 $\mu\epsilon$) are about 0.0508 fringe/ $\mu\epsilon$ and 0.0516 fringe/ $\mu\epsilon$ for the fast- and slow-axis interferometers respectively. From these values, the temperature- and strain-UMR are about 34 °C and 1250 $\mu\epsilon$ respectively whilst the noise-free temperature and strain resolutions are 2.1×10^{-4} °C and 2.0×10^{-3} $\mu\epsilon$ respectively.

As in the case of the phase measurements with the fusion-spliced sensors, periodic phase variations were also observed in the phase responses of the grating-based sensors. These phase noises were likewise modeled and were attributed mainly to the nonlinear optical frequency ramp. However, the magnitude of the periodic phase noises due to the nonlinear optical frequency ramp in the grating-based sensors was less than that of the fusion-spliced sensors because the band-pass filter used with the grating-based sensors had a narrower bandwidth compared with that employed with the fusion-spliced sensors.

In addition to the periodic phase noise in the differential phase response, additional localised nonlinear phase variations were observed. These variations were only seen with the grating-based sensors and subsequently were attributed to the dispersion of the axial grating-mirrors. By measuring the fringe visibility of each axial interferometer as the measurand was varied, an extremely high-resolution (~ 0.4 pm) reflectance spectrum of the grating was obtained. Comparing the high-resolution spectrum and the differential phase response, the position and shape of these nonlinear variations were similar to those of the anomalous dispersion of a grating. The high-resolution spectrum was similar to that obtained with an optical spectrum analyser with a resolution of 0.1 nm.

More importantly the high-resolution spectrum revealed a secondary peak in each axial grating. Although not predicted by the coupled-mode theory of FBGs, the presence of a secondary peak can account for the fact that the magnitude of the observed dispersion effect in each axial grating was about 20 times larger than the expected value. Clearly the exact structure of the grating needs to be further investigated. To begin with, the reflectance spectrum of the grating can be re-measured directly instead of indirectly using the method described in this work. Because effects common to both axial responses cancel one another when the differential phase is calculated, uncommon effects like the dispersion of the axial gratings can be highlighted. Thus, to the best of our knowledge, we have developed a direct method of experimentally measuring the dispersion of a grating written in an optical fibre.

8.2 Further work

The capability to obtain high resolution phase measurements using the arrangement described in this thesis can not be fully exploited because of the large phase noise due to a variety of sources. As a major improvement to future measurements with the birefringent sensors, the signal-processing-related noise can be reduced by producing a linearly-ramped optical frequency sawtooth modulation with its amplitude properly adjusted to equal the (average) FSR of the sensor. The linearly-ramped optical frequency modulation can be produced by using an appropriate nonlinear current ramp. As the linearity of the optical frequency ramp improves, its amplitude can be easily adjusted to equal the FSR of the sensor with greater accuracy because the intensity-modulation-free interferometric signals approach the ideal behaviour of continuous sinusoids.

It may not be possible to produce an optical frequency sawtooth modulation which is linearly ramped over the whole duration of the ramp period because of the limited frequency response of the current-to-emission frequency transfer function. In such cases, the use of a narrow band-pass filter is further suggested in order to attenuate the effects due to deviations from the ideal sawtooth optical frequency ramp. However, the side-effect of this filter is that the maximum frequency of the measurand change is limited to roughly half the bandwidth of the filter.

After producing an approximately linearly-ramped optical frequency modulation, a better mode of operation of the sensor is recommended. This involves measuring alternately the positively- and negatively-sloping zero-crossings of the interferometric outputs occurring in the most linear region of the linearised optical frequency ramp. Although this mode of operation requires additional circuits, it can certainly reduce the noise associated with the nonlinearity in the optical frequency ramp.

Unless the LD temperature is stabilised, thermally-induced drifts in the LD output (~ 29 GHz/ $^{\circ}$ C) can produce large phase drift (~ 5.4 fringe/ $^{\circ}$ C for a 15-mm FFPS). Since there were problems with the LD temperature controller used in this work, an alternative temperature controller is suggested for future measurements. This alternative controller is based on a proportional-integrating-differentiating (PID) feedback control circuit. This controller is more suitable in regulating the current across the Peltier devices because Peltier devices require a bias current to properly operate.

Since the LD temperature controller may not completely stabilise the LD temperature, slight drifts in the average emission frequency of the sawtooth-current-modulated LD can be further reduced using a technique reported by Tsuchida & Mitsuhashi [1987]. In their work, a fraction of the beam from their sawtooth-current-modulated LD was diverted towards a high-finesse reference Fabry-Pérot etalon which had one of its mirrors slightly dithered at 800 Hz. A feedback control arrangement varied the DC drive current of the LD such that the minimum value of the 800 Hz dithered signal in the interferometric output occurred at the same instant relative to the start of the ramp period. The unused beam reflected by the non-polarising beam splitter in the arrangement shown in Figure 6.1 is suggested to be used for the purpose of stabilising the average emission frequency of the LD.

With the above mentioned recommendations in improving the signal processing arrangement and in reducing the LD frequency noise, there can be some usefulness in improving the current value of the phase-resolution of $2\pi \times 10^{-4}$ radian. The phase resolution can be increased by increasing the reference clock rate, e.g. 100 MHz, while keeping the sawtooth frequency constant.

Chirped gratings which have a wider bandwidth than linearly-spaced gratings can be also used with the birefringent sensors described in this work. A wider bandwidth implies a wider measurand range in which the fringe visibility remains strong and also implies less constraints in using a single narrow linewidth source to excite both polarisation axes of the sensor. However, the expected dispersion of the chirped grating need to be strongly considered since they contribute to the differential phase measurements.

When extending the UMR of a birefringent sensor, its differential phase is used to identify the fringe of the more-sensitive axial response. Unique fringe identification, however, requires that the differential phase varies monotonically with the measurand change. Clearly the UMR of a birefringent sensor is limited to the measurand range for which the differential phase varies monotonically with measurand change. Thus, the UMR of a grating-based sensor is limited by the magnitude of the dispersion of the grating which can yield a non-monotonic differential phase response as was the case with strain measurements. However the inflection points of the dispersion of the grating can be used to self-calibrate the sensor since they correspond to unique points in the spectrum of the grating.

In the light of the observation of the dispersion of a grating in the differential phase response of the grating-based sensors developed in this work, we propose a novel method of observing the dispersion of FBGs which ordinarily are not easily observed. In this method, two FFPIs need to be fabricated. The proximal and distal reflectors of the first FFPI are the grating being investigated and a dielectric thin film respectively whilst those of the second FFPI are a reflective fusion-spliced in-line mirror and a dielectric thin film respectively. These single-grating-based and fusion-spliced FFPIs need to have equal effective cavity lengths. Hence when these FFPIs are exposed to the same average amount of measurand change, the differential phase between the interferometric phase change in these FFPIs approximately gives the dispersion of the grating.

The short-cavity birefringent fibre Fabry-Pérot interferometric sensors developed in this work have been demonstrated as promising sensors for localised measurement of temperature or strain with high measurand resolution and large unambiguous measurand range.

Appendix A:

Measurement of the Group Refractive Index of a Single-Mode Optical Fibre

Neil Caranto and Alex Shelamoff

(A reprint of the Internal Newsletter of the Dept. of Applied Physics, VUT, Volume 1, number 3, 11 October 1994)

Recently, in the course of developing a facility for the production of fibre Bragg gratings, we required the value of the effective refractive index of the fundamental guided mode of particular single-mode optical fibres to an accuracy of three decimal places. Manufacturers, in general, do not divulge this figure, and, as we discovered, is difficult to measure. The only value manufacturers quote is the refractive index step between core and cladding.

In OTDRs, a value of "refractive index" needs to be inputted for the instrument to convert time into distance. This is the *group* refractive index. At communications wavelengths (1300 and 1550 nm) a nominal value of 1.47 is often used. Stated like this, to 2 decimal places, it has proven adequate for most OTDR applications. However, in our application, this figure would, firstly, not have been accurate enough, and secondly would not have been applicable to the wavelength of interest, namely 785 nm.

The relationship between effective refractive index, n , and the group refractive index, n_g , is:

$$n_g = n - \lambda \frac{dn}{d\lambda} \quad (1)$$

where λ is the wavelength of the light source.

By measuring the value of n_g at a number of closely spaced wavelengths the value of n could be derived. (See Neil for the method).

The technique we used for accurately measuring the group refractive index was from the measurement of electrical phase shifts introduced by an optical fibre when inserted in an electrical path.

When two in-phase electrical sine wave travel separately along two co-axial cables of lengths ℓ_s and ℓ_r ($\ell_s > \ell_r$) and are compared at B (Figure 1), the wave arriving from ℓ_s would lag that on the reference path by

$$\phi_{\alpha} = 2\pi \frac{n_{\alpha}(\ell_s - \ell_r)f}{c} \quad (2)$$

where n_{α}/c is the speed of propagation of an electrical signal in a co-axial cable, c the speed of light in vacuum and f is the modulation frequency. Effectively, Figure 1 describes a Mach-Zehnder interferometer at RF frequencies.

A piece of optical fibre can be inserted along the signal arm. In this case, E/O (Electrical-to-Optical) and O/E converters are employed to interface the two different media (Figure 2). The phase difference detected at B is given by

$$\phi_k = 2\pi \frac{f}{c} \left[n_{\alpha}(\ell_s - \ell_r) + n_g \ell_k + \theta_{E/O}(f) + \theta_{O/E}(f) \right] \quad (3)$$

where ℓ_k is the length of the optical fibre and $2\pi \frac{f}{c} \theta_{E/O}(f)$ and $2\pi \frac{f}{c} \theta_{O/E}(f)$ are the electrical phase shifts introduced by the converters. These phase shifts are in general functions of the modulation frequency f .

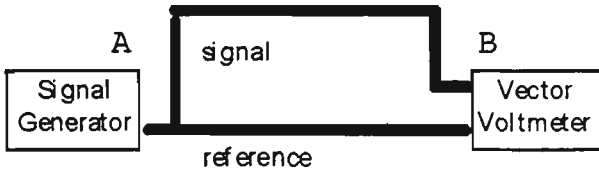


Figure 1: A Schematic diagram of an all-electrical Mach-Zehnder Interferometer

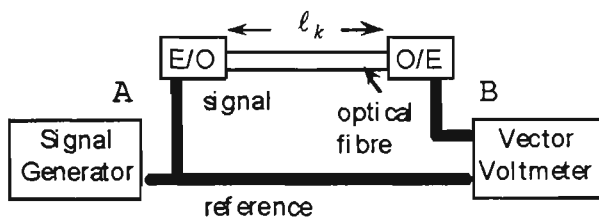


Figure 2: A Schematic diagram of an electrical Mach-Zehnder Interferometer with an optical waveguide inserted in the signal arm.

By subtracting the electrical phase difference measured using two different fibre lengths ℓ_1 and ℓ_2 , and at the same frequency f , a useful expression independent of any contributions from the co-axial cables or the converters is derived:

$$\begin{aligned} \phi(f) &= \phi_2 - \phi_1 \\ &= 2\pi \frac{n_g(\ell_2 - \ell_1)f}{c} = m \cdot f \end{aligned} \quad (4)$$

Thus, from the slope m of $\phi(f)$ the group refractive index is given by

$$n_g = \frac{m \cdot c}{2\pi(\ell_2 - \ell_1)} \quad (5)$$

The experimental arrangement employed a Wavetek 3510 signal generator capable of setting the rf frequency to within 0.001 MHz over a range of 1 GHz and a Hewlett Packard vector voltmeter capable of measuring phase with a 0.1 degree

resolution. The E/O converter was an OTRL light source using a Sharp LT022-PS 780 nm laser diode which was modulated by a signal from the signal generator. The O/E converter was an OTRL silicon detector module.

Figure 3 shows the aggregate phase shift difference against the frequency of modulation stepped from 10 MHz to 800 MHz for two set of measurements: one using a 226 mm (top line) and another using a 2854 mm (bottom line) of 3M FS-HB-4211 single-mode birefringent optical fibre inserted in the signal arm. Stepping the frequency enables the order (multiple of 360 degrees) of $\phi(f)$ to be determined (e.g. from the zero phase crossings) thus greatly increases the accuracy of the phase measurement. Clearly the accurate instruments used has contributed to the excellent linearity of $\phi(f)$ evident in Figure 3 (middle line). The coefficient of linear regression of the best fit line for $\phi(f)$ is $r = 0.9999997!$

The accuracy of measuring the group refractive index is limited by the accuracy of measuring $(\ell_2 - \ell_1)$. In the case of the current example, the group refractive index of the birefringent fibre is 1.476 ± 0.001 . Because this fibre is birefringent, this value is the average of the group refractive index along each eigen-polarisation axis. The linear birefringence of the fibre from the manufacturer's data is 0.0004 and it is hence outside the resolution of the measurement to determine the group refractive index along each axis.

Using the dispersion of pure silica, the effective refractive index was calculated to be 1.462 ± 0.002 from Equation 1.

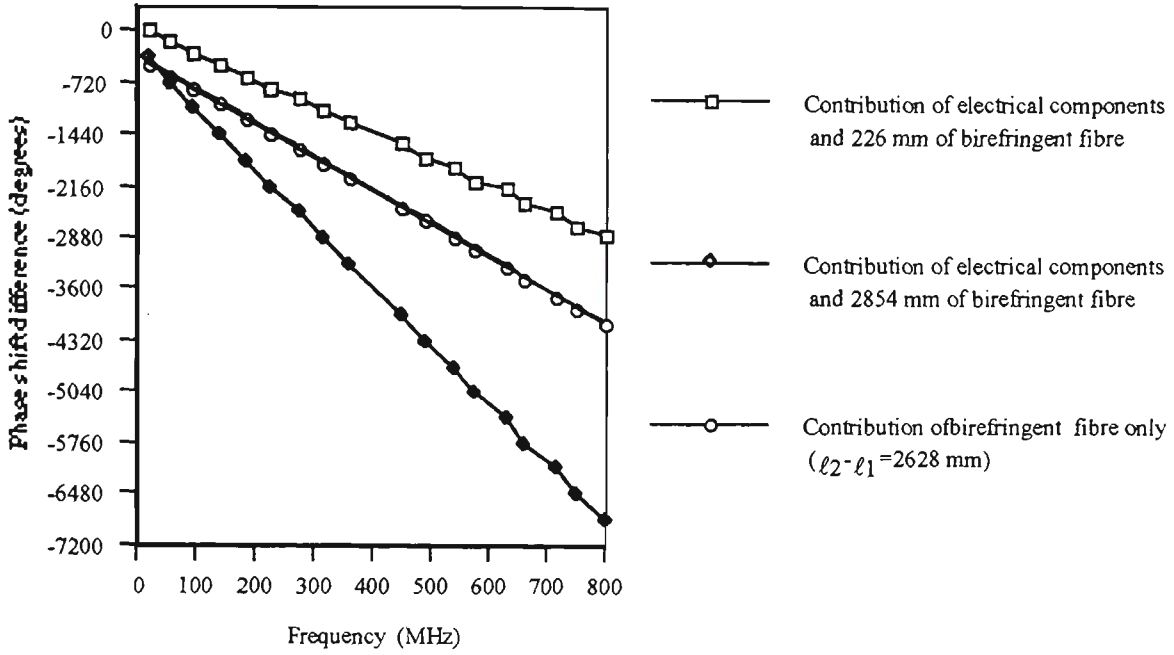


Figure 3: The phase shift difference as a function of frequency

The technique has also been applied to measure the group refractive index of other single-mode fibres with an error of ± 0.001 (Table 1). The technique described can convincingly give the group refractive index of a single-mode optical fibre. However

from the group refractive index, the effective refractive index can be deduced from the dispersion of the core of the fibre. Likewise, the actual core refractive index can also be indirectly estimated although other techniques might be more appropriate.

Fibre/Manufacturer	Group Refractive Index	Wavelength of source (nm)
3M FS-HB-4211	1.476	780
Corning Flexcor-780	1.477	780
Corning Flexcor-780	1.463	1320
Sumitomo/Olex 1300	1.465	1320

Table 1: Group refractive index of different types of optical fibres.

Appendix B:

Descriptions of the Experimental Circuits and Computer Interfaces

This appendix describes in detail the experimental circuits and the computer interface used in this work. The final circuits developed are described first followed by the computer interface.

B.1 Experimental Circuits

In this work, phase shifts of two axial interferometers of a birefringent FFPS are obtained simultaneously. These are referred to as Channel 1 and Channel 2. In this section, the experimental circuits for a single channel/axis (Channel b where $b = 1$ or 2) processing are described since the processing of each channel is the same. To be able to appreciate more the relationship between the circuits, it may be useful to refer back to the schematic diagram (Figure 6.8) and the corresponding intermediate waveforms (Figure 6.9) of the signal processing scheme and phase determination scheme.

B.1.1 Sawtooth Generator Circuit

Figure B.1 shows the schematic diagram for the sawtooth generator used in this work. An Analog Device AD7541A 12-Bit Digital-to-Analog-Converter (DAC) was used to generate the sawtooth ramp. The digital inputs of the DAC were derived from a continuously clocked 12-bit counter composed of three National Semiconductor CD4520 Synchronous Up Counters. Their clock inputs were connected to a common 4.000 MHz square-wave

synchronous clock signal derived from an oscillating crystal. As a result the period of the sawtooth ramp was 1,024 ms (frequency = 976.5625 Hz) and was very stable because of the excellent stability of crystal oscillations. Furthermore the fly-back period of the sawtooth generator was very short, $\sim 0.5 \mu\text{s}$. This short period was due to the fast response of the output of the counters and the DAC. In particular the DAC was designed to quickly change its output voltage without any ringing. Also, the generated ramp exhibited very good linear trend because the ramp voltage was incremented by a fix amount every clock period.

A disadvantage of this method of generating a sawtooth voltage ramp was the staircase nature of the ramp composed of 4096 voltage "steps". However this staircase feature did not introduce any undesirable effects because the response of the intermediate circuit immediately after the input lead of the LD drive circuit effectively smoothed these steps. This smoothing effect was accomplished first by the effective voltage divider circuit formed by the variable resistor T3 and the series capacitor-resistor pair C1 and R8 and second by the frequency response of the coupling transistor P1 and diode D2 as shown in Figure B.2.

The circuit shown in Figure B.1 produced three outputs of the same frequency: The first output was a sawtooth ramp rising from 0 Volt to +5 Volts, the second a ramp decreasing from 0 Volt to - 5 Volts, and the third a symmetric TTL-compatible square wave. Due to the design of the LD drive circuit, the negatively sloping ramp output was used to modulate the LD current in order to obtain a negatively-sloping sawtooth modulation of LD emission frequency. This type of optical frequency modulation was chosen so that the sense of interferometric phase shifts is the same as the sense of the measurand variations (see section 6.5). The symmetric square wave was simply the behaviour of the most significant bit (msb) of the continuously running 12-bit counter. The rising edge of this square wave signified the start of the sawtooth ramp. Hence, this square wave was suitable as the reference signal for determining the temporal position of the zero-crossings of the interferometric signal during each ramp period.

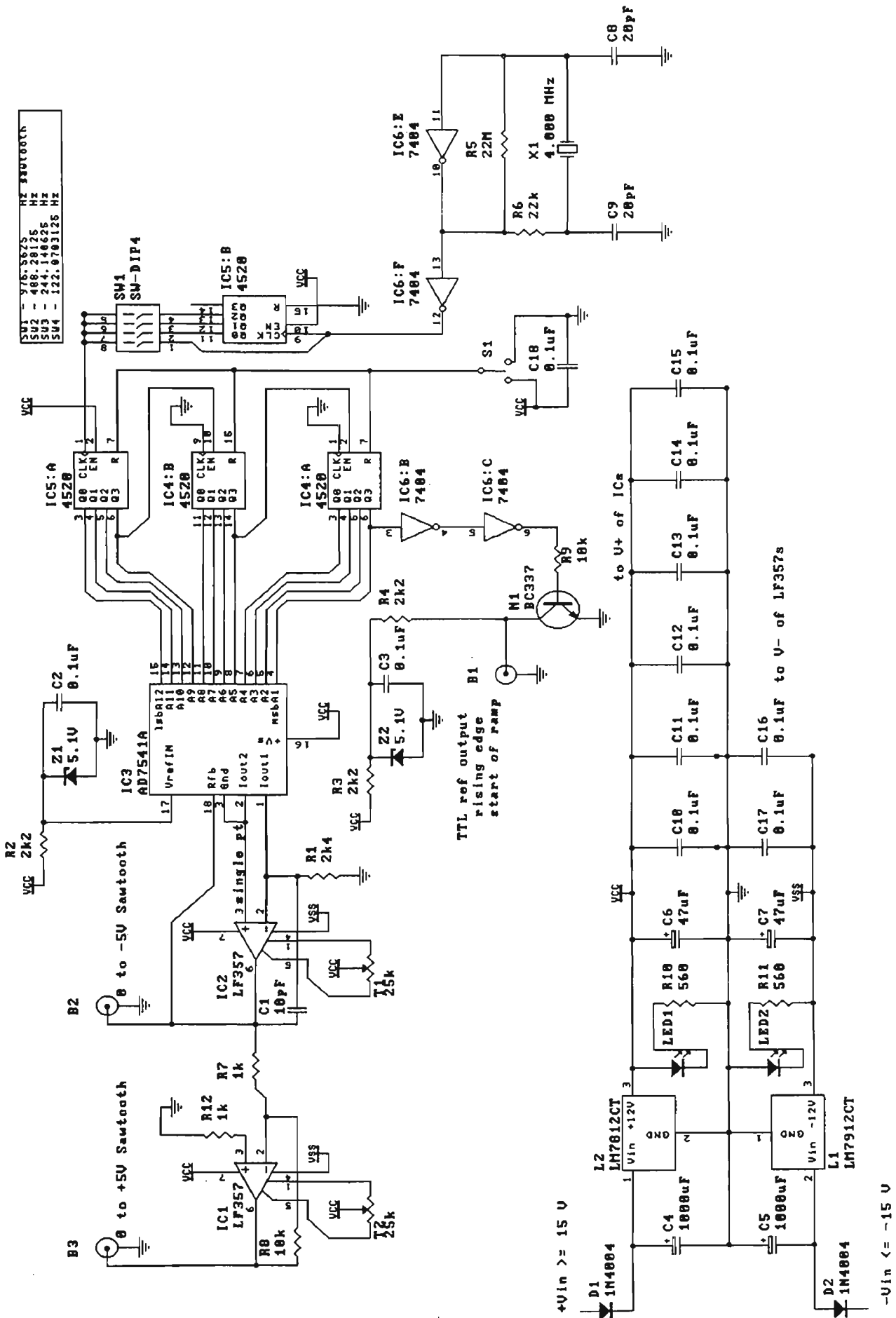


Figure B.1: Schematic diagram of the sawtooth generator.

If desired the circuit shown in Figure B.1 can generate a sawtooth wave with a frequency of 488.28125 Hz, 244.140625 Hz or 122.0703125 Hz by appropriately closing the corresponding switches of the DIP switch SW1. This feature was not necessary but was simply included to utilise the unused 4-bit counter after the 12-bit counter was formed using two 4520 chips. Switch S1 allowed or inhibited the generation of the sawtooth wave. This feature was useful in temporarily suspending the sawtooth modulation without disconnecting the lead between the sawtooth generator and the LD driver circuit.

The generator was powered with a different electric power source from the LD. This arrangement ensures proper isolation of the LD drive circuit from the sawtooth generator assuming proper electrical shielding techniques have been employed and electrical ground current loops have been avoided.

B.1.2 Laser Diode Drive Circuit

Figure B.2 shows the schematic diagram for the LD drive circuit used to operate a Hitachi HL7806G device. This circuit diagram shows several components, however, the basic LD drive circuit consisted of two transistor current-mirror circuits. The first (based on transistor N1) circuit provided the primary constant DC bias current to the LD whilst the second transistor (based on transistor N2) circuit provided secondary DC current. Dividing the source of the DC current in such a manner allowed for coarse and fine adjustments of the bias current via the variable resistors T1 and T2. The fine adjustment was an important safety feature. Since the output-power/current conversion ratio is high above the threshold condition, the fine adjustments avoid large increases in the LD current which may produced an output power greater than the maximum allowed value. In addition to a DC current, the second current-mirror provided as well an AC current proportional to the AC modulation voltage present at the input connector B5. The strength of the AC current modulating the LD was primarily controlled by the variable resistor T3 and secondarily by T2. The resistor R8 was chosen such that the modulation voltage at the base of transistor N2 was 1/5 of that present at the modulation input and thereby protecting the LD from excessive modulation. The low-noise operational amplifier O1 (op-amp) monitored the total current across the LD and was calibrated to give an output of -100 mV/mA.

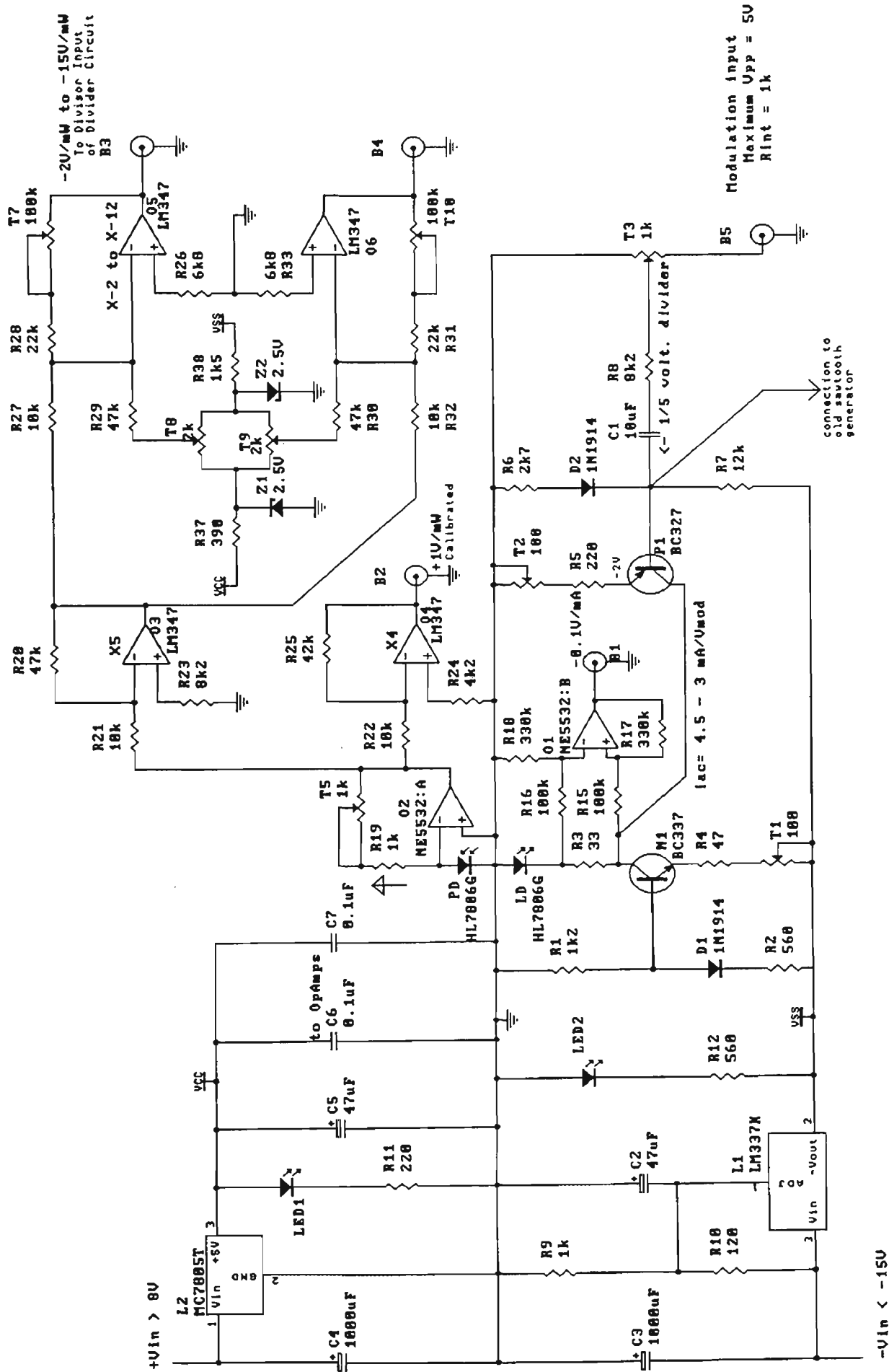


Figure B.2: Schematic diagram of the LD drive circuit used with a Hitachi HL7806G device.

The HL7806G had a built-in PD directly behind the back facet of the LD. Using a low-noise trans-impedance amplifier, this PD determined the output the intensity of the LD. The output of the trans-impedance amplifier was further connected to two voltage amplifiers; the first of which (based on the op-amp O3) gave a direct reading of the LD intensity whilst the output of second (based on the op-amp O4) was further amplified (Figure B.2). The variable resistor T5 of the trans-impedance amplifier was adjusted such that the effective output of the op-amp O3 was calibrated to give + 1,000 mV per 1 mW of output intensity. The (additional) amplifier (O5) provided the required signal used to remove the intensity modulation in the interferometric output. The division circuit required that only negative voltage values are present at its divisor input in order to avoid positive feedback. It was also important to eliminate any offset voltage at the output of the amplifier O5. This offset voltage can be canceled by adjusting the variable resistor T8 such that the output voltage is zero when the intensity of the LD is zero. The gain of amplifier O5 can be controlled using the variable resistor T7 but its actual value was not a critical parameter. The remaining unused op-amp in the quad-op-amp LF347 chip was used to assemble amplifier O6 which had similar characteristics as amplifier O5.

To avoid supply voltage noise translating into current noise and hence phase and intensity noise in the LD output, the whole circuit in Figure B.2 was powered from low-noise voltage-regulated supplies. In addition, low-noise NE5532 op-amps were selected for amplifier O1 and amplifier O2 because they were directly connected to the LD and PD of the HL7806G device.

B.1.3 Temperature Controller Circuit

To avoid thermally-induced drifts in the LD output, the LD temperature had to be kept constant. This constant temperature was achieved using a temperature controller which adjusts the current flowing into some peltier devices. One surface of the peltier device was in thermal contact with the case of the HL7806G while the other to a large heat sink. Figure B.3 shows the schematic diagram of the temperature controller. For “LOAD” which involved peltier devices, switch SW2 was closed in order both positive and negative current can flow across the

peltier devices. The current driving the peltier devices were derived from a separate power source to avoid disturbing the feedback circuitry.

The feedback circuitry involved producing a control voltage which was proportional to the difference between the set (or stabilisation) temperature and the actual temperature of the LD. This control voltage in turn produced a proportional current into the peltier device. The actual LD temperature was determined using an AD 590 device. This device produced a current proportional to temperature. A trans-impedance amplifier with its gain adjusted using the variable resistor VR2, produced an output of 100 mV/°C. The set temperature was determined from a reference voltage derived from the voltage divider R7-VR3-R8 (Figure B.3).

There were other features of the temperature controller. The controller had a digital display which shows either the actual or set temperature depending on the state of SW1. The light emitting diodes, LED1 and LED2, signaled whether the controller was cooling or heating the LD respectively.

Although the temperature controlled circuit was found to stabilise the temperature of the LD over a short period of time, the temperature controller circuit in its current form has a major drawback when peltier devices are used as heating/cooling elements. Because a current is required for a peltier device to operate, the equilibrium temperature reached was not that stipulated by the set temperature value. The equilibrium temperature exhibited a temperature offset with respect to the set temperature such that the temperature offset produced a constant current through the peltier devices. The value of this current is determined by the thermal equilibrium among the LD, the peltier device and the ambient environment. Consequently, the equilibrium temperature obtained is strongly dependent on the ambient temperature as was observed in the results (Chapter 7).

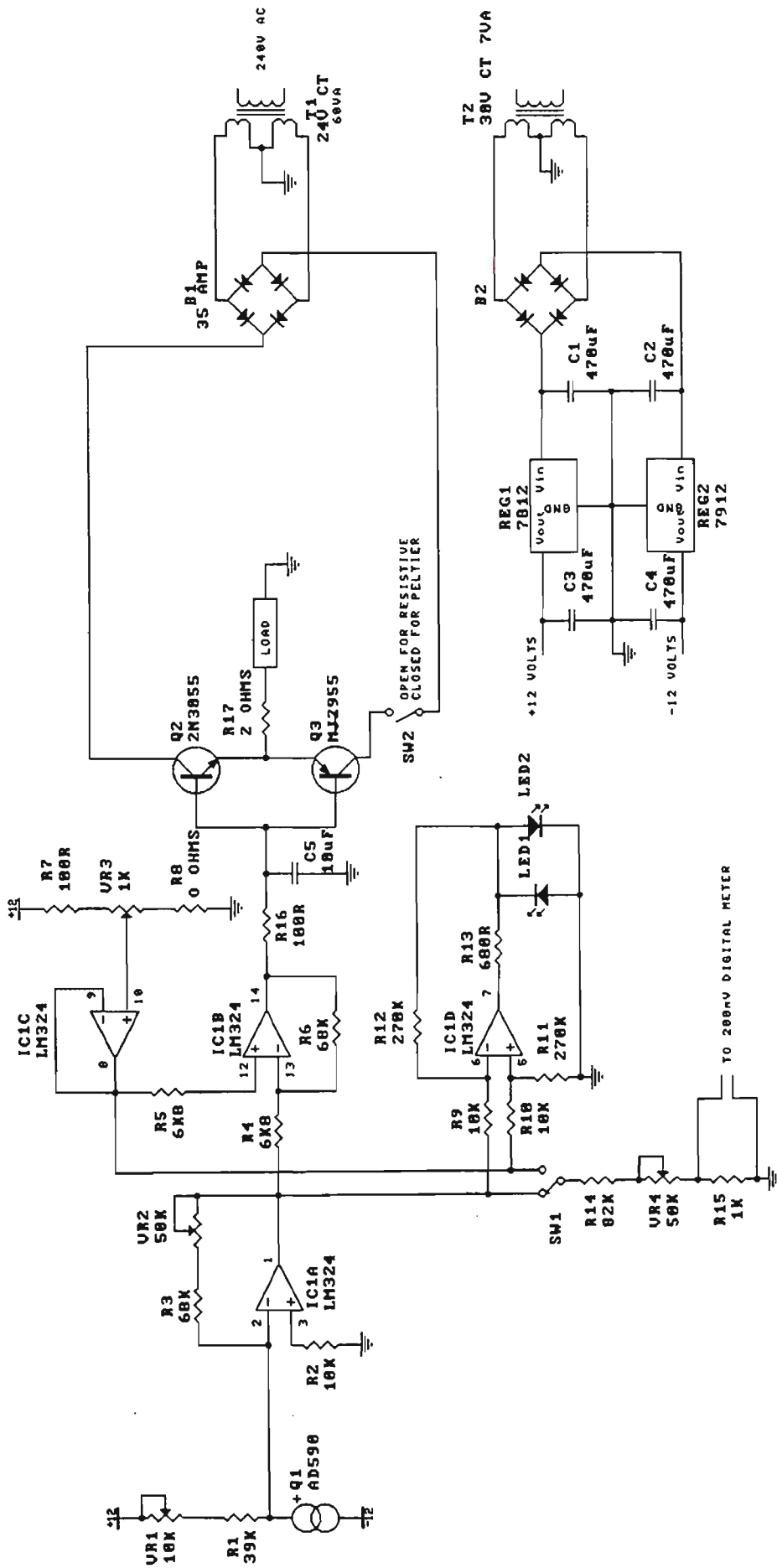


Figure B.3: Schematic diagram of the temperature controller circuit.

B.1.4 Division Circuit

Figure B.4 shows the schematic diagram for the division circuit used in the experimental arrangement. This circuit was simply an Analog Devices AD532 four-quadrant multiplier/divider chip configured as an analogue divider. The interferometric signal detected by the PD (dividend input Z) is divided by a voltage proportional to the LD intensity (divisor input X) to produce an intensity-modulation-free interferometric signal (PD “simplified” signal). The signal presented at the divisor input was limited to negative voltage values in order to avoid positive feedback. This implied that the resulting quotient output was an inverted version of the interferometric intensity signal (see Figure 6.9).

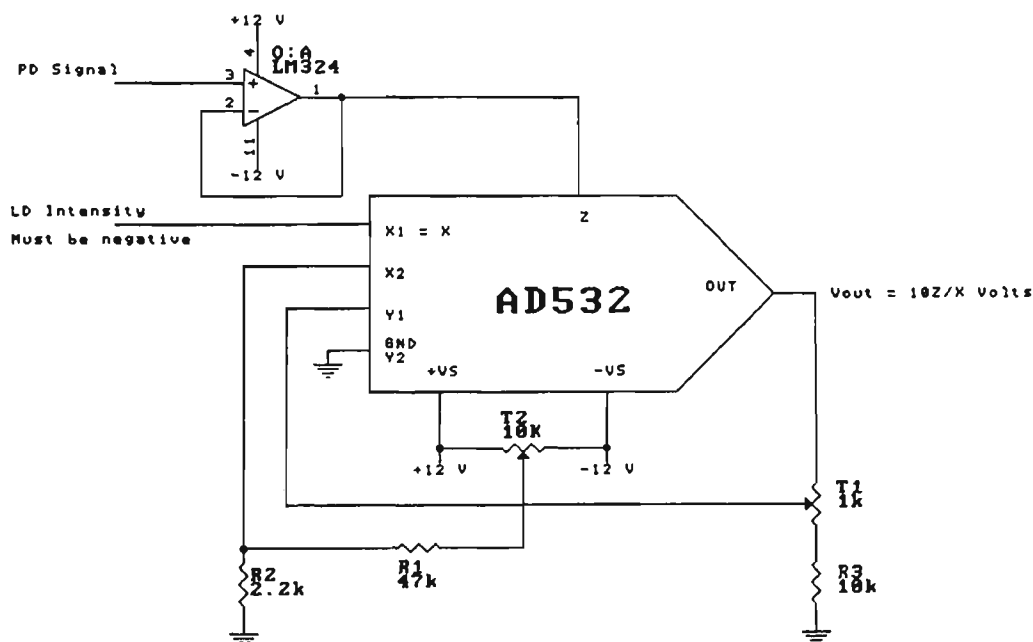


Figure B.4: Schematic diagram of the division circuit.

B.1.5 Photodiode Circuit

Figure B.5 shows the schematic diagram for the amplifier used to convert the optical intensity signal into an electrical voltage suitable for subsequent processing. This circuit was composed of a trans-impedance amplifier and a negative-gain amplifier. The negative-gain amplifier ensured that the final output had the same polarity as the optical intensity. The PD used was a silicon detector (OPTEK OPF 480) which had a quantum efficiency of about ~ 0.5 A/W at 785 nm. Hence the effective trans-impedance gain of the whole circuit can be varied from 0.6

to 6.6 mV/nW. Typically the variable resistor T2 in Figure B.5 was adjusted such that the total gain resistance of the trans-impedance amplifier was $\sim 250\text{k}\Omega$, giving an equivalent gain of 3 mV/nW. The use of such high resistance did not limit the frequency response of the PD since the minimum overall system bandwidth requirement was about 2 kHz. To reduce the noise in the amplifier, the whole circuit was powered from two 9 V batteries and used low-noise NE5532 op-amps.

In general the final output voltage for the circuit in Figure B.5 was not zero even when the no optical power was present at the PDs. This offset voltage can be generated by the input offset current, input offset voltage of the op-amp used and by the PD dark current. Although this offset voltage can be minimised by ensuring that the op-amp input legs encounter the same amount of impedance, this offset voltage was eliminated by introducing an equivalent voltage at the input end of the last stage amplifier such that the total output offset voltage was zero. This equivalent voltage was derived from a voltage divider (variable resistor T1) across two reference zener diodes. The zener diodes was used as voltage references because over time the terminal potential difference across the batteries gradually diminished. The need to produce a zero offset voltage was extremely important because the final PD output was to be divided with respect to the LD intensity which was varying in a sawtooth manner.

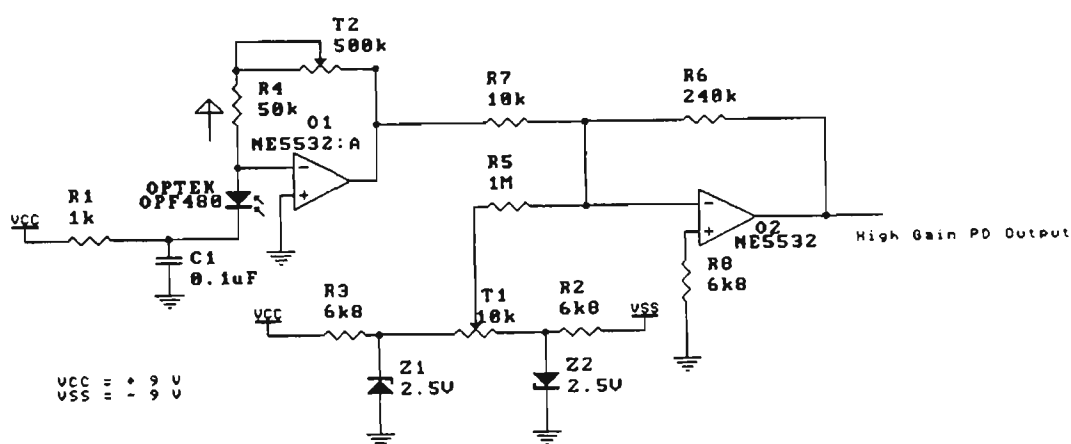


Figure B.5: Schematic diagram of the PD circuit to detect the interferometric signal from each axial interferometer of the sensor.

The effect of a non-zero PD output offset voltage is illustrated in Figure B.6. The figure shows that a non-zero output offset voltage undesirably include an additional non-linear ($1/x$) ramp in the time domain to the quotient output. Clearly this additional signal will undermine the temporal position of the zero-crossing of the interferometric signal and hence the determination of the actual interferometric phase as well. On the other hand, Figure B.6 also illustrates that only situation when the output of the division circuit was a horizontal line was when the output offset voltage of the PD circuit was zero. Thus, before the start of each experiment, the output of the division circuit was made constant to avoid the undesirable effect of a non-zero PD output offset voltage.

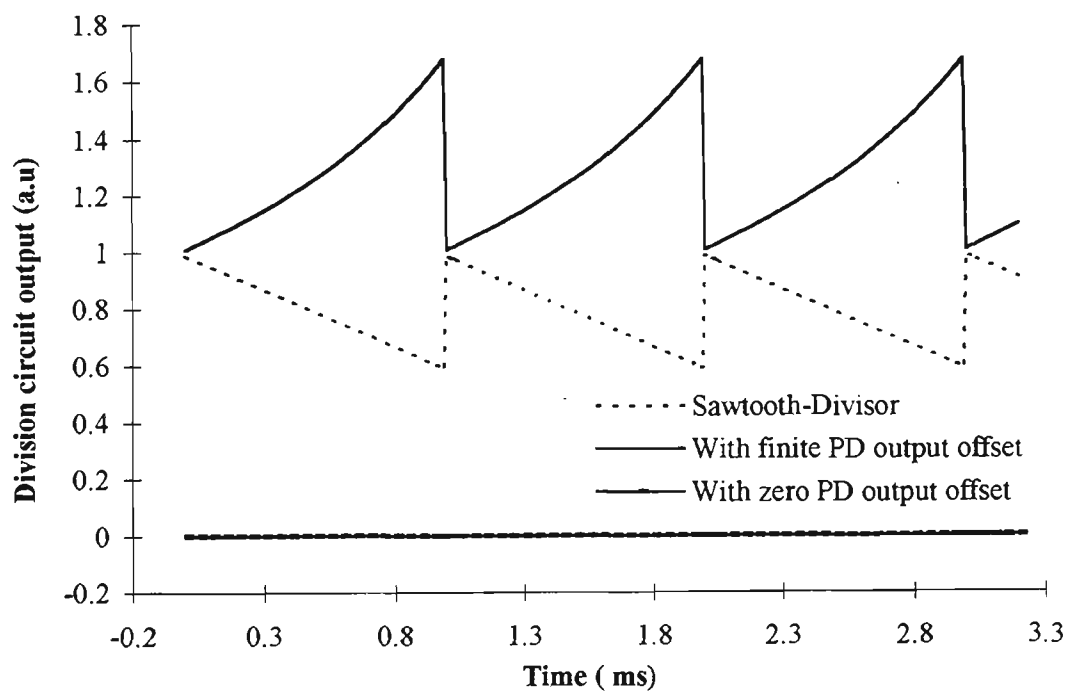


Figure B.6: The effect of a non-zero PD output offset voltage to the output of the division circuit.

B.1.6 Band-pass Amplifier Circuit

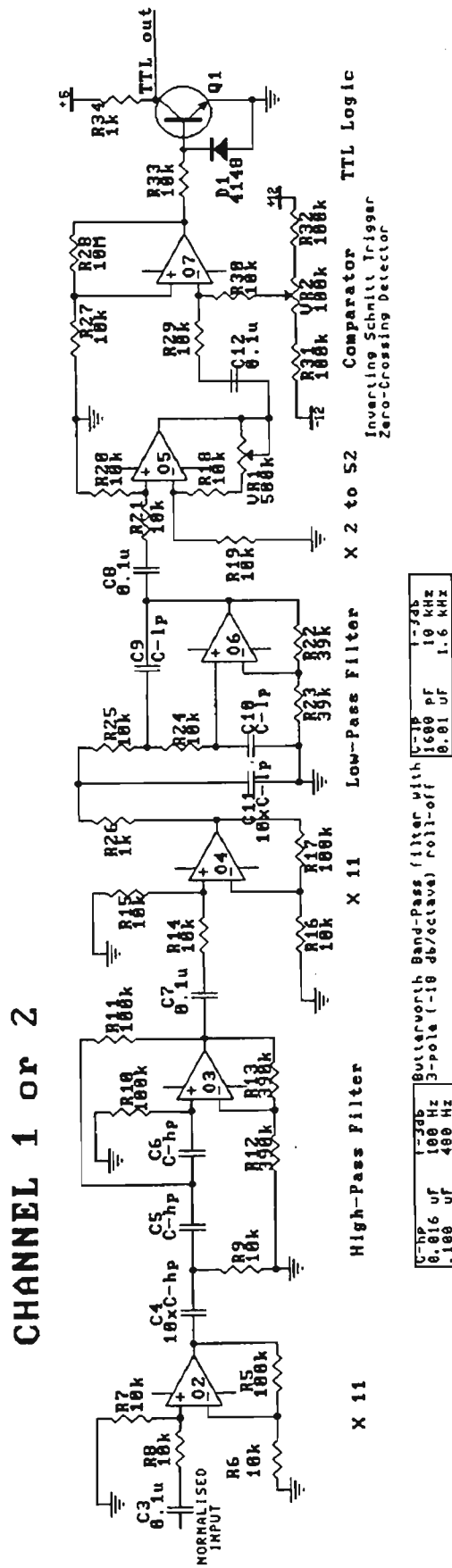


Figure B.7: Schematic diagram of the band-pass amplifier and harmonic squaring circuits.

Figure B.7 shows the schematic diagram for the band-pass amplifier and the squaring circuits. The primary purpose of the band-pass filter was to amplify only the periodic component of the intensity-modulation-free signal (PD “simplified” signal). The band-pass filter designed with a central frequency of ~ 1 kHz was constructed by cascading a 3rd-order high-pass and a 3rd-order low-pass Butterworth filters. These Butterworth filters were chosen for their amplitude response which exhibited the flattest response among the different type of filters [Lancaster, 1975]. The components of these filters were selected using the equal-component-value Sallen-Key circuit as building blocks. Employing 3rd-order response meant 18 dB/octave roll-off amplitude edge responses. The -3 -dB (70.7%) frequency edge of the filters can be selected by values of the capacitors C-hp and C-lp for the high-pass and low-pass filters respectively. Table B.1 and Table B.2 summarise the characteristic capacitance values used in the experiments.

The entire band-pass amplifier employed three other AC-coupled amplifiers (op-amps O2, O4 and O5) interleaved between the high-pass and low-pass filters. The first two had a gain of 11 whilst the final stage had a gain which can be varied from 2 to 52. Thus, the effective voltage gain at the central frequency can be between 29.8 dB and 44 dB since the high-pass and low-pass filters had a voltage gain of about 2 well into their pass regions.

-3 dB Frequency	C-hp
100 Hz	16 nF
480 Hz	0.1 μ F

Table B.1: Capacitance of the characteristic capacitor for the high-pass filter.

-3 dB Frequency	C-lp
10 kHz	1.6 nF
1.6 kHz	0.01 μ F

Table B.2: Capacitance of the characteristic capacitor for the low-pass filter.

Initially, the filter was configured such that it had a pass-band from 100 Hz to 10 kHz. This filter was used with the fusion-spliced birefringent Fabry-Pérot sensors. The idea behind such a large bandwidth was to minimise the electronic phase shift introduced by the filter. From the initial experimental results, such a large bandwidth was unnecessary because either the temperature or strain measurements were practically DC-type measurements (< 1 Hz). Furthermore, such a large pass-bandwidth was found to contribute some periodic phase noise in the axial response of fusion-spliced birefringent fibre Fabry-Pérot sensor (see Section 7.2). To reduce the phase noise, the pass-band of the combined amplifier was modified to be 480 Hz to 1.6 kHz. This band-pass amplifier gave a

quality factor Q of ~ 1 . Figure B.8 shows the amplitude and phase response of this unity- Q filter. The actual -3 dB high-pass and low-pass frequency edges and the central frequency of the filter was 530 Hz, 1530 Hz and 950 Hz respectively. This filter response eliminated any high frequency variations expected in the interferometric signal immediately during the flyback period of the sawtooth ramp (Figure 6.9).

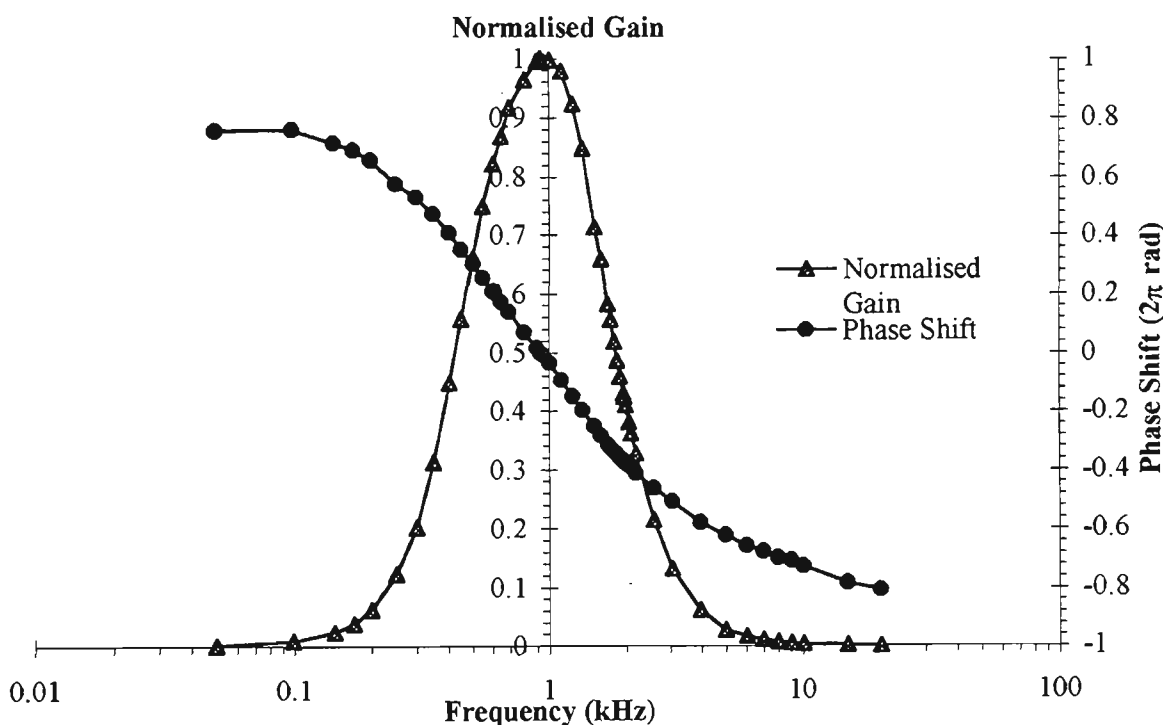


Figure B.8: The amplitude and phase response of the band-pass amplifier (unity Q).

B.1.7 Squaring Circuit

The squaring circuit was composed of an inverting Schmitt Trigger comparator and a TTL-compatible-output transistor NOT circuit (last two stages in Figure B.7). The classic inverting Schmitt Trigger circuit was chosen as a voltage-reference-crossing detector for its excellent noise immunity against rapid variations of the input voltage around the reference voltage [Malvino, 1989]. The reference voltage can be adjusted with the variable resistor VR2. The voltage reference was set to be zero in order that the phase determination procedure became independent of the amplitude of amplified interferometric signal. This feature allowed the operation of the measuring system even when the optical signal from the birefringent sensor was inherently low because of either the high loss at a fusion-spliced mirror or in the drifting of the grating reflectance spectrum away from the LD emission wavelength.

Finally, the TTL-compatible-output transistor NOT circuit converted the square wave output of the Schmitt Trigger into a TTL square wave (Channel *b* Zero-Crossing TTL signal) which was in phase with the output of the band-pass amplifier. Effectively the rising edges of this TTL signal corresponded to the positively-sloping zero-crossing transitions of the “simplified” PD signal and hence to the negatively-sloping zero-crossing transitions of the unprocessed interferometric signal. The Channel *b* TTL signal was subsequently exploited to determine its relative phase with respect to the sawtooth modulation.

B.1.8 Phase Determination Circuit

The relative temporal phase of a sinusoidal (interferometric) signal can be determined from a variety of ways. In this work, a digital synchronous-asynchronous phase-detection (D-SAPD) technique was employed in determining this temporal phase. This temporal phase was inferred from the temporal position of the first positively-sloping zero-crossing of the Channel *b* TTL signal. Prior to processing, a reference signal was required for each basic (single-channel single-processing-half) phase-determination circuit. This reference signal can be of two types. Either type can be obtained from the two outputs of a TTL edge-triggered Toggle Flip-Flop (FF), formed from an ordinary D-type FF ($\frac{1}{2}$ of a 74LS74 chip). The clock input of the Toggle FF was connected to the trigger signal output of the sawtooth generator (Figure B.17). These outputs, labeled HIGH and LOW in Figure B.4, were symmetric TTL square waves at half the sawtooth modulation frequency and their high value signified the two halves of the processing cycle for each channel. These reference signals effectively allowed the simultaneous control of two counters which alternately measure the width of the current pulse or to retain the width of the recently concluded pulse.

The basic phase determination circuit employed another Toggle FF and an AND gate (Figure B.9). The clock input of this edge-triggered Toggle FF was connected to the Channel *b* TTL signal whilst its asserted-low set input was connected to one of the reference signals. (Asserted-low means that when the voltage is low at the set input of the Toggle FF, the output of the FF becomes high, *i.e.* set state). This reference signal can be considered as an enabling signal which allows the Toggle FF to change its state from high to low.

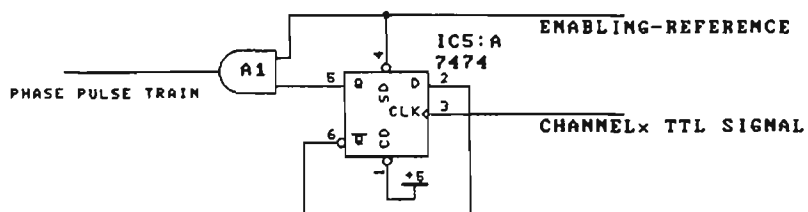


Figure B.9: Schematic diagram of the basic phase determination circuit for processing a single channel or axial interferometer and for one of the two possible signal processing half-cycles.

Figure B.10 and Figure B.11 show the timing diagram for the phase determination algorithm applied to both halves of the processing cycle for a single channel. Since each of the 74LS74 FFs changes state on the rising transition of its clock input, the Q output of the zero-crossing Toggle FF (for each processing cycle) synchronously changed from a high state to a low state whenever a rising edge transition of the Channel b TTL signal connected to this Toggle FF. This arrangement describes the synchronous aspect of the phase-determination. The Q output remained low until the end of the (processing) cycle when it asynchronously returned to its high state because of the connection to the set input described recently. This Q output remained high until the next rising-edge transition of the Channel b TTL signal in the next enabled period of the reference signal. Effectively, the Q output of the Toggle FF produced an asserted-low pulse train with a frequency half the sawtooth modulation frequency and with each falling edge of each pulse signified the occurrence of a rising edge transition of the Channel b TTL signal during each processing half (HIGH or LOW).

Subsequently performing an AND-logic operation between the Q output of the zero-crossing Toggle FF and corresponding enabling-reference signal (either the HIGH-half or LOW-half reference signals) produced a complementary pulse train with each pulse exhibited during the high state of the enabling-reference signal. As shown in Figure B.10 and Figure B.11, the rising edge of each resulting pulse corresponded to the start of each processing cycle and the falling edge, the first negatively-sloping zero-crossing of the original interferometric signal during each processing cycle (HIGH or LOW). The width of each pulse was proportional to the “phase” of interferometric signal modulo 2π .

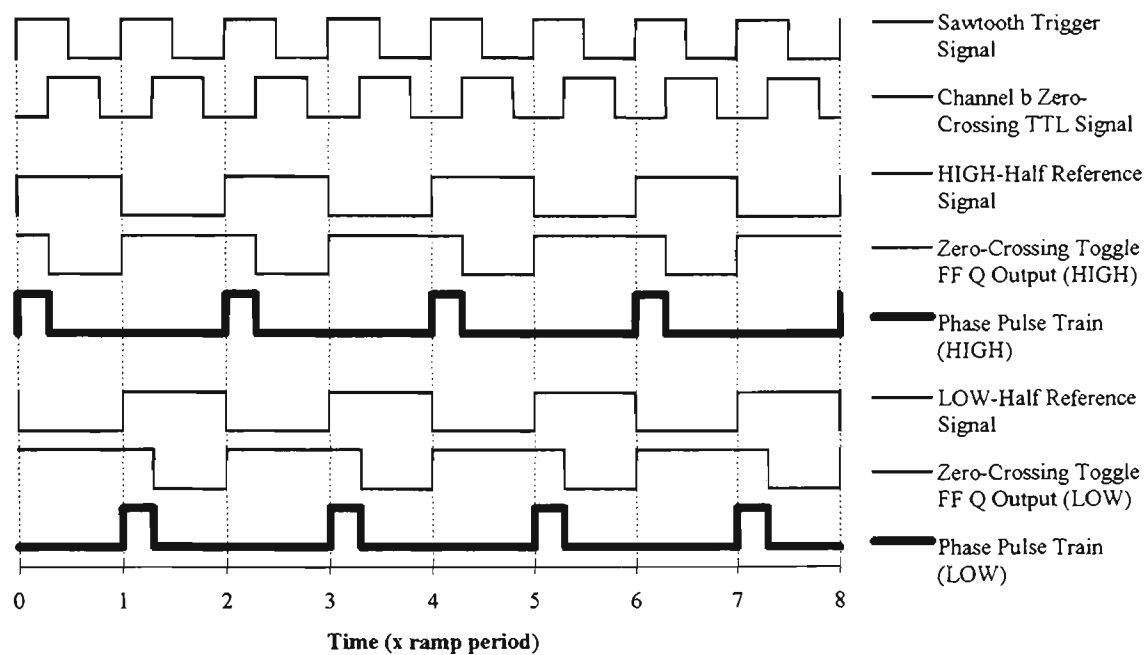


Figure B.10: Timing diagram for the phase determination circuit for the case when the width of the pulses is less than $\frac{\tau_{saw}}{2}$. Channel b ($b=1$ or 2) refers to each axial interferometer of the sensor.

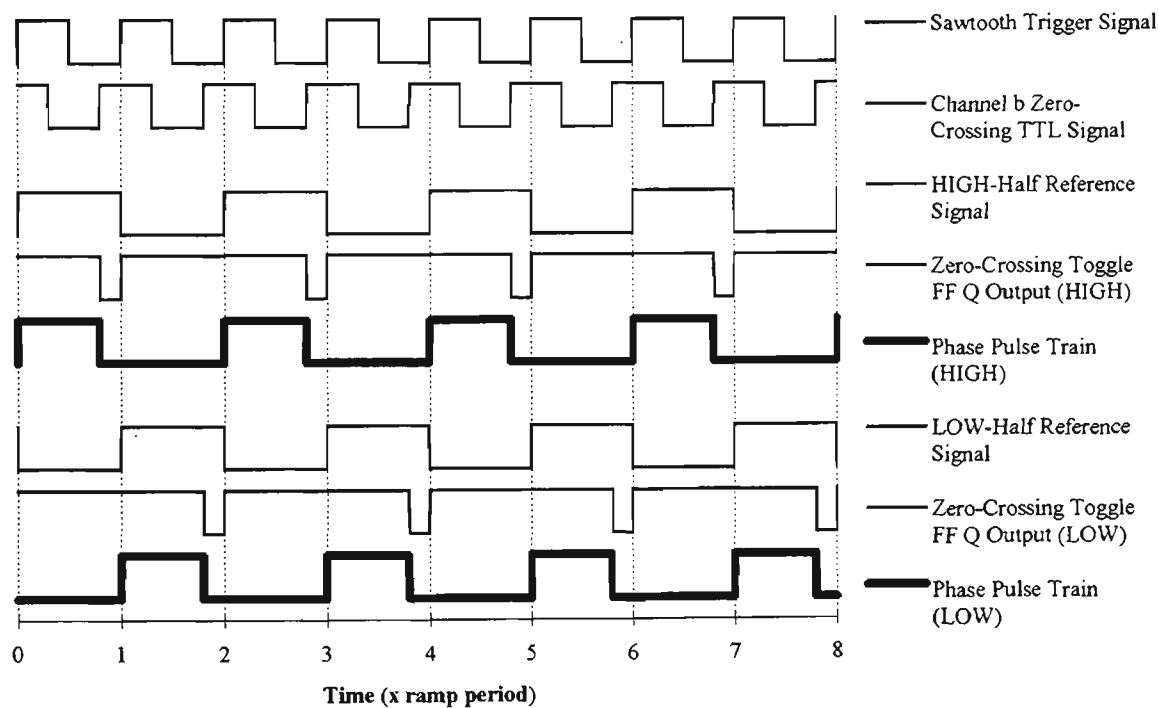


Figure B.11: Timing diagram for the phase determination circuit for the case when the width of the pulses is greater than $\frac{\tau_{saw}}{2}$. Channel b ($b=1$ or 2) refers to each axial interferometer of the sensor.

The width of each pulse can be determined in a number of ways. For example, the DC component of the pulse train can be measured simply with a DC voltmeter. The DC component is clearly proportional to the pulse width of each pulse. Therefore the phase resolution and signal bandwidth is determined by the resolution and bandwidth of the DC voltmeter. However in this work, the pulse width was measured using a digital counter based on a high-frequency clock signal. This technique offered high phase resolution and large measurand signal bandwidth compared with the low-pass filter method. In this work, a phase resolution of about $1/10,000^{\text{th}}$ of a fringe was obtained.

An alternative method to the D-SAPD method of producing phase pulse trains described above is that of the Exclusive-OR (XOR) method. Figure B.12 shows the schematic diagram of the XOR technique. In this technique, the Channel *b* Zero-Crossing TTL signal and the sawtooth modulation were converted into a symmetric square waves at half their original frequencies. The resulting signals were XOR-ed to produce a pulse train with each pulse exhibiting a width proportional their relative phase. Figure B.12 shows the schematic diagram of the XOR technique whilst Figure B.13 the corresponding relevant timing diagram.

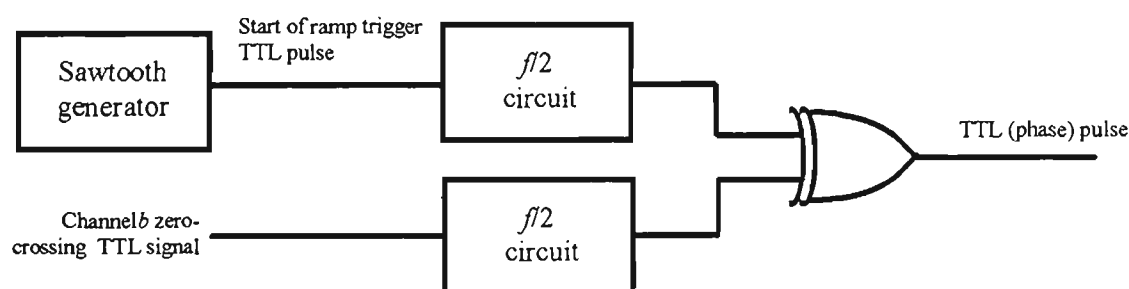


Figure B.12: Schematic diagram for exclusive-OR (XOR) phase determination technique.

At first glance the final output of the D-SAPD and XOR techniques seemed to be equivalent. Comparing the outputs of these techniques (compare Figure B.12 with Figure B.10 and Figure B.11), the XOR output was simply the combination of the HIGH and LOW processing half-cycles (for each channel) of the D-SAPD method. However, it had been experimentally observed that when the Channel *b* TTL signal become instantaneously in phase with the sawtooth modulation, the subsequent pulses of the XOR output suffered from a TTL-logic inversion as opposed to the correct sense of the pulses of the D-SAPD outputs.

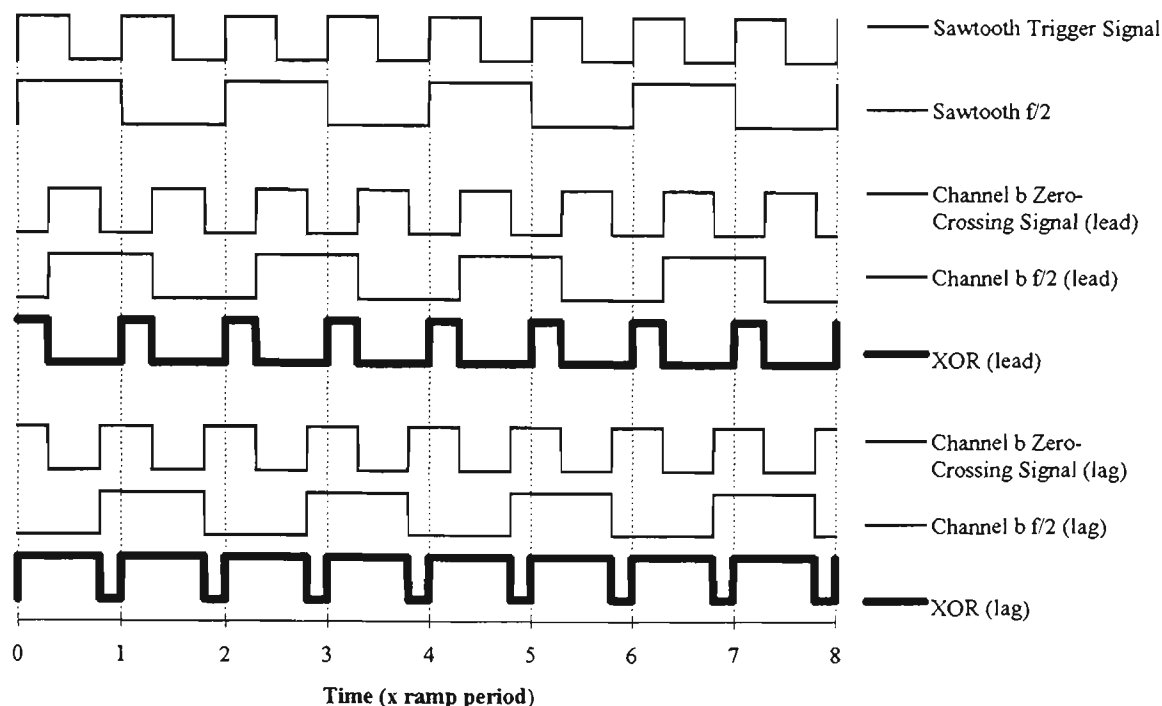


Figure B.13: Timing diagram for exclusive-OR (XOR) phase determination technique.

Figure B.14 shows in the detail the comparison between the output pulse trains of the D-SAPD and XOR techniques. At time index 5 and time index 14, the rising edges of the sawtooth trigger signal and the Channel *b* TTL signal coincided. Between these time indices, the XOR pulses for each ramp period was the complement of the corresponding output in either the HIGH- or LOW-half processing cycle pulses obtained using the D-SAPD technique. On the other hand, the only effect when the rising edges of these two signals coincided to the D-SAPD outputs was a missing pulse at time index 5 and 14. This was not an anomaly but simply described that the relative phase between the two signals was zero. Further examination of Figure B.14 concluded that D-SAPD output pulse trains do not suffer any TTL-logic and gives the correct pulse widths to describe the relative phase shifts between the interferometric and sawtooth signals. For these properties, the D-SAPD method of producing phase pulse trains described above was more suitable for measuring phase shifts greater than 2π compared with the simpler Exclusive-OR (XOR) method of phase determination.

The production of two pulse trains in the D-SAPD technique may seem to be a disadvantage because half of the time of each pulse train does not exhibit any information. If a DC voltmeter is used to measure the DC component of these pulse trains, the sensitivity is reduced by half. However in the case of measuring the width of the pulses

using a counter, these signals have facilitated the measurement of phase. Since an ordinary counter cannot count and at the same time memorise the count value for the last pulse, the “dead” period of each pulse train clearly allowed the contents of the counter to be read by another register, *e.g.* a memory location in a computer, before the value of the counter is updated.

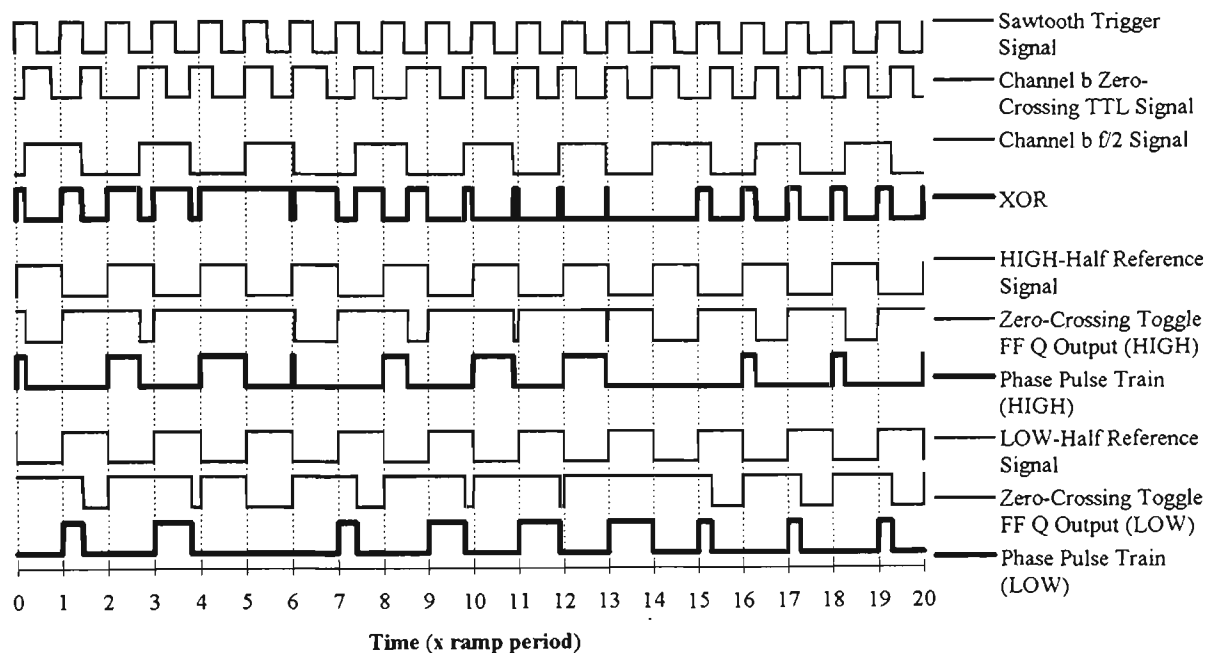


Figure B.14: Comparison between D-SAPD and XOR phase determination techniques.

B.2 Computer Interfaces

In this work, the whole measuring system was interfaced with an IBM-compatible AT personal computer. This digital interface involved a multi-channel Analogue-to-Digital-Converter (ADC) interface card and a general purpose commercial Input/Output (I/O) card. This I/O card contained 3 digital counters and programmable I/O ports. Because four counters were required in this work, the I/O card was slightly modified to accommodate the additional counter.

The general-purpose I/O card used an Intel 8255, a programmable peripheral interface chip. This chip had three programmable ports, Port A, B and C. Port A was designated to be an output port and was wired to select the clock frequency for the phase-determination counters. Table B.3 indicates bit definitions of Port A and the

associated clock frequency. Port B was designated to be an output port and was wired to select the gain of a strain gauge amplifier and its calibration resistors. Table B.4 and Table B.5 indicate the bit definitions of Port B. Port C was designated as an input port which allowed a computer program to poll the state of the phase-determination circuits. The empty cells in the tables mean that the actual values of the corresponding bits do not matter (don't cares).

P O R T A								Clock frequency
A7	A6	A5	A4	A3	A2	A1	A0	
A	INH	B						
	1							0 MHz
0	0	0						9.8304 MHz
1	0	0						2.4576 MHz
0	0	1						1.2288 MHz
1	0	1						4.9152 MHz

Table B.3: T Port A (of the 8255 PPI chip) bit definitions used to select the clock frequency for the phase determination counters.

P O R T B								Calibration resistor
A7	A6	A5	A4	A3	A2	A1	A0	
INH	C	B	A					
1	x	x	x					None connected
0	0	0	0					5.63 M Ω
0	0	0	1					2.22 M Ω
0	0	1	0					1.004 M Ω
0	0	1	1					557 k Ω
0	1	0	0					219 k Ω
0	1	0	1					119.8 k Ω
0	1	1	0					50.6 k Ω
0	1	1	1					11.92 k Ω

Table B.4: Port B bit definitions used to select the calibration resistor for the strain gauge amplifier.

P O R T B								Strain gauge gain
A7	A6	A5	A4	A3	A2	A1	A0	
						B	A	
						0	0	5 mV/ $\mu\epsilon$
						0	1	10 mV/ $\mu\epsilon$
						1	0	50 mV/ $\mu\epsilon$
						1	1	100 mV/ $\mu\epsilon$

Table B.5: Port B bit definitions used to select the gain of the strain gauge amplifier.

P O R T C							
A7	A6	A5	A4	A3	A2	A1	A0
				LOW/2	HIGH/2	LOW	HIGH

Table B.6: Port C bit definitions used to poll the processing cycle.

B.2.1 Measurand Detection Circuits

The performance of the birefringent FFPSs developed as temperature and strain sensors were compared with an AD 590 device and a resistive strain gauge. The output of the sensors were digitised with an ADC and stored together with the phase measurements obtained with the FFPSs.

B.2.1.1 Temperature Detection Circuit

Figure B.15 shows schematic diagram for the temperature detection circuit and its corresponding interface with the ADC card via the connector CN2. The zener diodes at the output pin were include to protect the ADC from excessive voltage. The AD 590 was a current source device which produced an output proportional to temperature ($1 \mu\text{A}/^\circ\text{C}$). The voltage output of the trans-impedance amplifier IC4:A can be subsequently calibrated using two known temperature. First, the variable resistor VR4 was adjusted to remove any output offset voltage when the temperature was 0°C . After nulling the output offset voltage, the resistor VR3 was adjusted so that the final output had a gain of $+100 \text{ mV}/^\circ\text{C}$.

TEMPERATURE DETECTION CIRCUIT

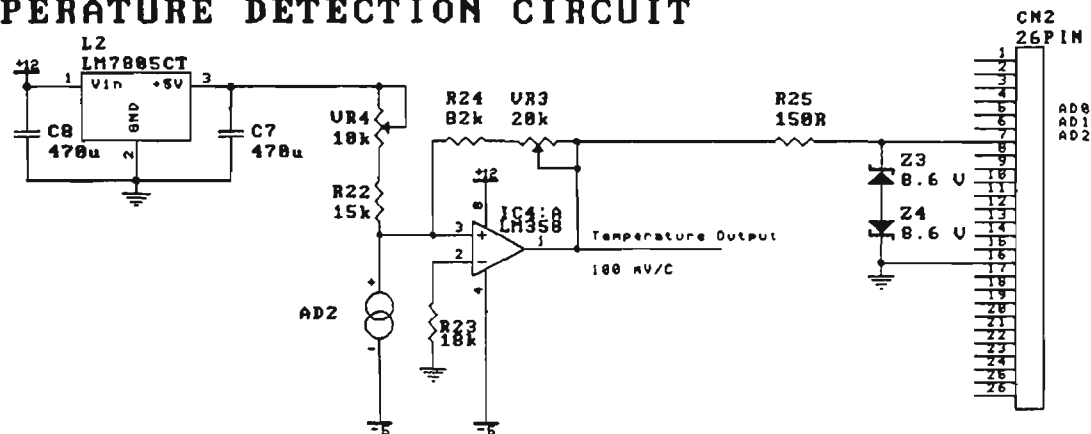


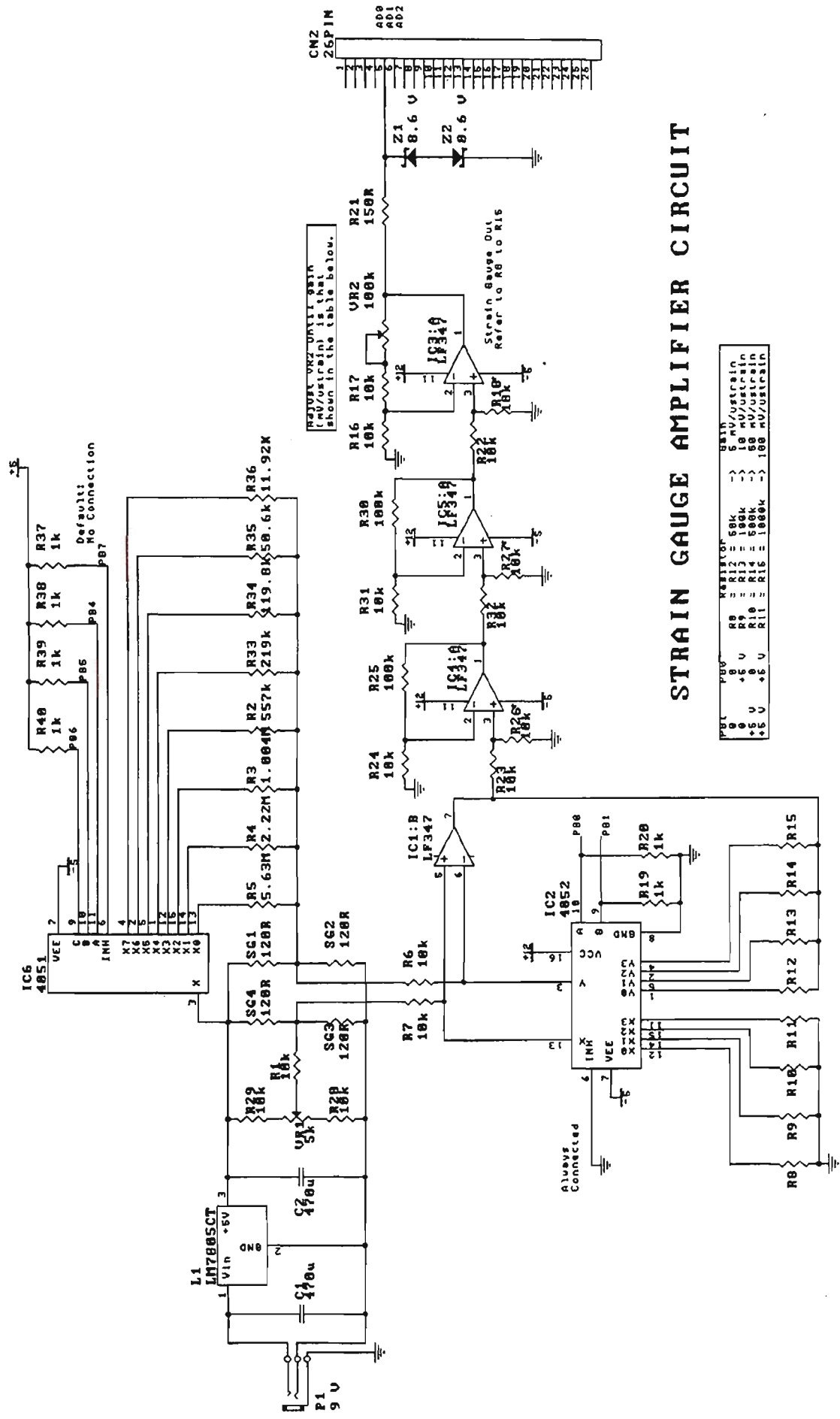
Figure B.15: Schematic diagram of the temperature detection circuit.

B.2.1.2 Electrical Strain Gauge Amplifier

Figure B.16 shows the schematic diagram for the classic strain gauge bridge amplifier circuit and its corresponding interface with the ADC card via the connector CN2. The labels PB_x, referred to connections to x-bit of Port B of the 8255. These bits were made available using the connector CN1 (Figure B.17). The overall gain of the circuit can be selected via bits 1 and 0 of Port B of the 8255 chip (Table B.5). Likewise zener diodes were incorporated at the final stage of the amplifier to protect the ADC. The circuit also had provisions for nulling the output voltage by adjusting the variable resistor VR1.

The bridge resistors SG1 to SG4 referred to the resistors of the amplifier. All of these resistors can be electrical strain gauges (ESGs) connected in a variety of configurations [Neubert, 1967]. In this work, only two these resistors were actual ESGs, SG4 and SG2. One of these ESGs was bonded on to a cantilever beam whilst the other was placed close to the first but not strained. This arrangement compensated for thermal drifts in the ESGs.

The circuit shown in Figure B.16 also had provision for calibrating the amplifier. Before including into the circuit, the resistance of one of the bridge resistors (SG1) was previously measured. When a resistor of known resistance is connected in parallel to SG1, the effective resistance of the SG1 changes by a calculable amount. This change simulates the effect of strain. The calibration resistors was connected to the bridge amplifier using a CMOS 4051 8-1 analogue multiplexer which can be programmed using bits 7 to 5 of port B as defined in Table B.4.



STRAIN GAUGE AMPLIFIER CIRCUIT

Figure B.16: Schematic diagram of the strain gauge amplifier.

B.2.2 Continuous Monitoring of the Interferometric Phase Shifts

Figure B.17 shows the schematic diagram of four phase determination circuits (two axial interferometric signals times two types of reference signal (HIGH-half or LOW-half) and the subsequent digital interface to a personal computer. The output of these four determination circuits were subsequently connected to the gate input of four separate digital counters via a wire connector (CN1).

The counters used in this work are 16-bit programmable counters available with the Intel 8253-2 chip which was part of the general purpose I/O card. Each counter was programmed such that the content of its register was reset to zero during the rising edge of its gate input. Subsequently the counter counted down from 0 until the falling edge of input gate pulse. The rate at which the content of each count register was decremented was determined by the selected clock frequency (Table B.3). After counting, the contents of its register was kept until the arrival of the next pulse at the gate input. During this inactive "dead" period, a computer program can read the contents of the count register. This dead period can be determine by polling the state of each reference cycle.

The clock signal for the counters was derived from a 19.6608 MHz oscillating crystals (Figure B.17). Using a 4-bit synchronous counter, 74LS93, the clock signal be any of the next 4 sub-harmonic of the crystal frequency. The selection can digitally be made by controlling the INH, A and B inputs of a CMOS 4052 4-to-1 analogue multiplexers. These inputs were wired to bit 7 to bit 5 of Port A of an Intel 8255 incorporated in the general purpose I/O card. Hence a computer program can select the clock frequency of the counters by suitable controlling Port A whose bit definitions are indicated in Table B.3.

In this work, the 9.8304 MHz clock signal was typically used for the counters. Since the sawtooth period was 1024 ms, this clock rate implied a resolution of $1/10,066$ th of a fringe or 0.624 mrad. This resolution defined the accuracy of each measurement. From the phase shift measurements (Chapter 7), such resolution was more than adequate since the total phase noise of the measuring system was larger than this value (Appendix C).

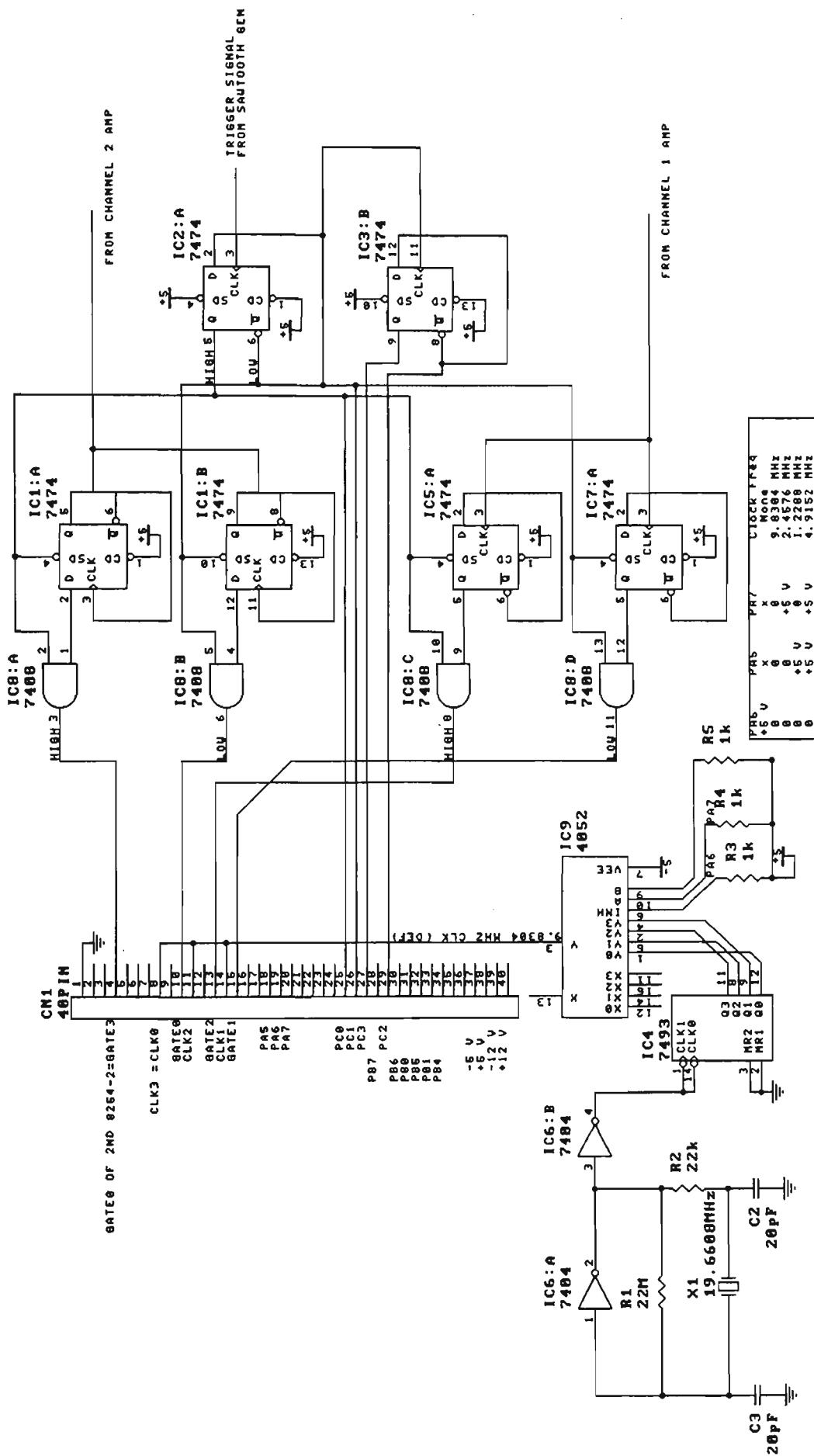


Figure B.17: Schematic diagram of the phase recording and computer interface circuit.

Figure B.18 shows the flow diagram describing the steps encompassing the continuous and simultaneous monitoring of the interferometric phase shifts along two polarisation axis of a birefringent Fabry-Pérot sensor. Prior to the execution of the phase monitoring program, the optical and signal processing components were adjusted such two independent interferometric signals from the sensor arrived at two PDs and that the amplitude of the sawtooth current ramp suitably adjusted to provide the desired pseudo-heterodyne signals as described previously (Section 6.5).

The continuous computer program begin with some initialisation routines. These routines include:

- initialising of the ADC interface card and other components interfaced with the IBM-compatible AT computer,
- selecting of the operation mode of Port A, Port B and Port C of the 8255 chip as described in Table B.3 to Table B.6,
- specifying the operation mode for each counters,
- selecting the clock rate used with the counters (selected by initialising the value of Port A),
- determining which polling signal (one of the defined bits of Port C) to be used, and
- setting the program for processing either only one of both halves of the processing cycle which has been selected by the user.

Since there are basically two types of reference signals (either having a frequency half or one-fourth of the sawtooth modulation frequency) and either one or both halves of each reference signal can processed, the possible sampling rate which can either be equal, half or one-fourth of the sawtooth frequency.

For minimal operation, only two counters were required, one for each axial channel. However such arrangement reduced the sampling frequency to half the sawtooth modulation frequency. Clearly when another pair of counters was used during the LOW-half of the process cycle, the combined alternate operation of both pairs of counters gave a data acquisition rate of equal to the ramp frequency. Since this arrangement was not difficult to produce, such a quad-counter operation was implemented in this work.

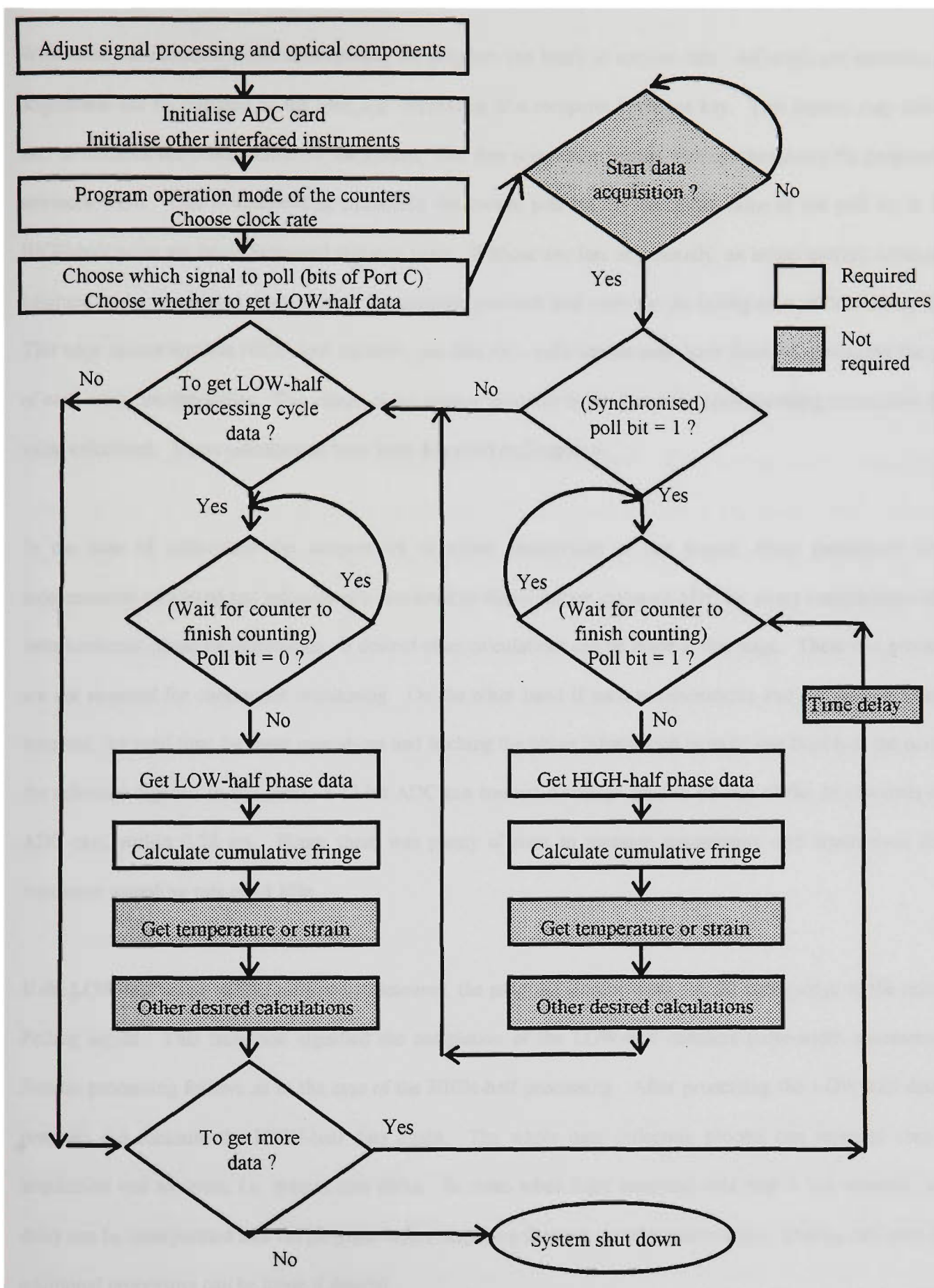


Figure B.18: Flow diagram for continuous and simultaneous monitoring of the phase interferometric phase from a birefringent fibre Fabry-Pérot sensor .

With these initialisation routines completed, the program can begin to acquire data. Although not necessary, data acquisition can be initiated by the user, *e.g.* depressing of a computer keyboard key. This feature may allow the user to re-check the configuration of the system. The data acquisition begins with synchronising the program with sawtooth wave. This is achieved by inspecting the chosen poll bit. If the initial value of the poll bit is 1, the HIGH-half pulse are being measured and vice versa. Without any loss of generality, an initial poll bit value of 1 is assumed in the succeeding discussions. The program proceeds and waits for the falling edge of the Polling signal. This edge means that the HIGH-half counters, one for each polarisation axis, have finished measuring the phase of each axial interferometer. The values of the counter can now be read and the corresponding cumulative fringe value calculated. These calculations have been described in Chapter 6.

In the case of calibration the temperature or strain sensitivities of the sensor, these parameters can be independently measured and subsequently converted to digital format using an ADC for direct comparison with the interferometric phase measurements. If desired other calculations can be made at this stage. These two procedures are not required for continuous monitoring. On the other hand if such measurements and calculation would be involved, the total time for these procedures and fetching the phase information must be less than half the period of the reference signal. In this work, a 12-bit ADC can convert a voltage present on one of the 16 channels of the ADC card within 0.28 ms. Hence there was plenty of time to measure temperature and strain even for the maximum sampling rate of ~ 1 kHz.

If the LOW-half pulse widths were to be measured, the program similar waits for the rising edge of the reference Polling signal. This transition signified the completion of the LOW-half counters pulse-width measurements. Similar processing follows as in the case of the HIGH-half processing. After processing the LOW-half data, the program can measure the HIGH-half data again. The whole data collecting process can repeated until data acquisition was to cease, *i.e.* system shut down. In cases when high sampling data rate is not required, a time delay can be incorporated into the program before acquiring the next set of measurements. During this time delay, additional processing can be made if desired.

Appendix C:

System Noise and Limitations

In chapter 7, the performance of birefringent fibre Fabry-Pérot temperature and strain sensors were discussed. The phase shifts of each axial interferometer of the sensors were found to change reasonably linear with either temperature or strain. The deviation from this linear phase-measurand relationship (nonlinear phase variations) were attributed to signal-processing-related phase noise. In the case of the grating-based sensors, the dispersion of the axial Bragg gratings contributed as well to the nonlinear phase noise. In this appendix, the inherent intensity and phase noise in the components of the measuring system are discussed. These inherent noise can be associated with the electronic noise at the detector and signal processing electronics, the various optical components of the measuring arrangement described in Chapter 6, the electronic noise in the LD drive current or the thermal drifts in the LD output.

C.1 Phase Noise Due to Intensity-Related Noise

C.1.1 Detection Electronics Noise: Electrical Noise in the Photodiode Circuit

Although the phase of the interferometric signal from each axial interferometer of a birefringent sensor was of interest, the intensity of the signal must be sufficiently strong so that the signal can be distinguished from any noise signal at the detector. A complete noise analysis of the signal detection electronics would be somewhat uninformative and tedious because of the numerous components involved. It is sufficient to examine the noise at the PD since this noise term is amplified the most amongst the other electronic noise contributions in the circuit.

Figure B.5 shows the schematic diagram of the PD circuit used in this work. There are three main sources of noise in this first stage circuit:

- the shot noise of the PD,
- the thermal noise of the trans-impedance gain resistors, and
- the Root-Mean-Square (RMS) voltage V_{ans} and current I_{ans} noise per unit square root of the electronic signal frequency bandwidth Δf present at the input of the operational amplifier.

The shot noise, which is the statistical noise associated with the photo-generated I_{sig} and dark I_{dark} currents in the PD can be expressed as

$$I_{shot}^2 = 2e(I_{sig} + I_{dark})\Delta f \quad \text{Eq. C.1}$$

where e is the charge of an electron. The photo-generated current is given by

$$I_{sig} = \eta_{PD} P_{sig} \quad \text{Eq. C.2}$$

where P_{sig} is the optical intensity of the interferometric signal and η_{PD} the responsivity of the PD. The thermal noise which is generated by the random thermal agitation of the charge carriers in the trans-impedance gain resistors can be expressed as

$$I_{thrm}^2 = \frac{4kT}{R_{gain}}\Delta f \quad \text{Eq. C.3}$$

where k is the Boltzmann's constant, T the absolute temperature (in Kelvin) and R_{gain} the trans-impedance gain (resistance) value. The power signal-to-noise ratio (SNR) of first stage of PD circuit can be given by

$$SNR = \frac{I_{sig}^2 R_{gain}}{2e(I_{sig} + I_{dark})\Delta f R_{gain} + 4kT\Delta f + \frac{V_{ans}^2 \Delta f}{R_{gain}} + I_{ans}^2 R_{gain} \Delta f} \quad \text{Eq. C.4}$$

The noise equivalent photo-generated current (*i.e.* $SNR=1$) is

$$I_{sig=noise} = e\Delta f + \sqrt{(e\Delta f)^2 + 2eI_{dark}\Delta f + \frac{4kT}{R_{gain}}\Delta f + \frac{V_{ans}^2 \Delta f}{R_{gain}^2} + I_{ans}^2 \Delta f} \quad \text{Eq. C.5}$$

Using the noise figures for the NE5532 op-amp provided by the manufacturer, the PD circuit is limited primarily by the noise contribution of the amplifier and secondarily by the thermal noise for a low input power signal. The shot noise contribution becomes significant only at high input power. Figure C.1 shows the relationship of $I_{sig=noise}$ with R_{gain} and Δf . The relevant parameters are summarised in Table C.1.

$\eta_{PD} = 0.55 \text{ A/W}$	$k = 1.380658 \cdot 10^{-23} \text{ J/K}$
$I_{dark} = 0.2 \text{ nA}$	$T = 293 \text{ K}$
$e = 1.60217733 \cdot 10^{-19} \text{ C}$	
$V_{ans} = 5 \text{ nV} / \sqrt{\text{Hz}}$	$I_{ans} = 0.7 \text{ pA} / \sqrt{\text{Hz}}$
$\Delta f = 1 \text{ KHz}$	$R_{gain} = 50 \text{ k}\Omega \text{ to } 550 \text{ k}\Omega$

Table C.1: Noise-parameters of the components of the first-stage PD circuit.

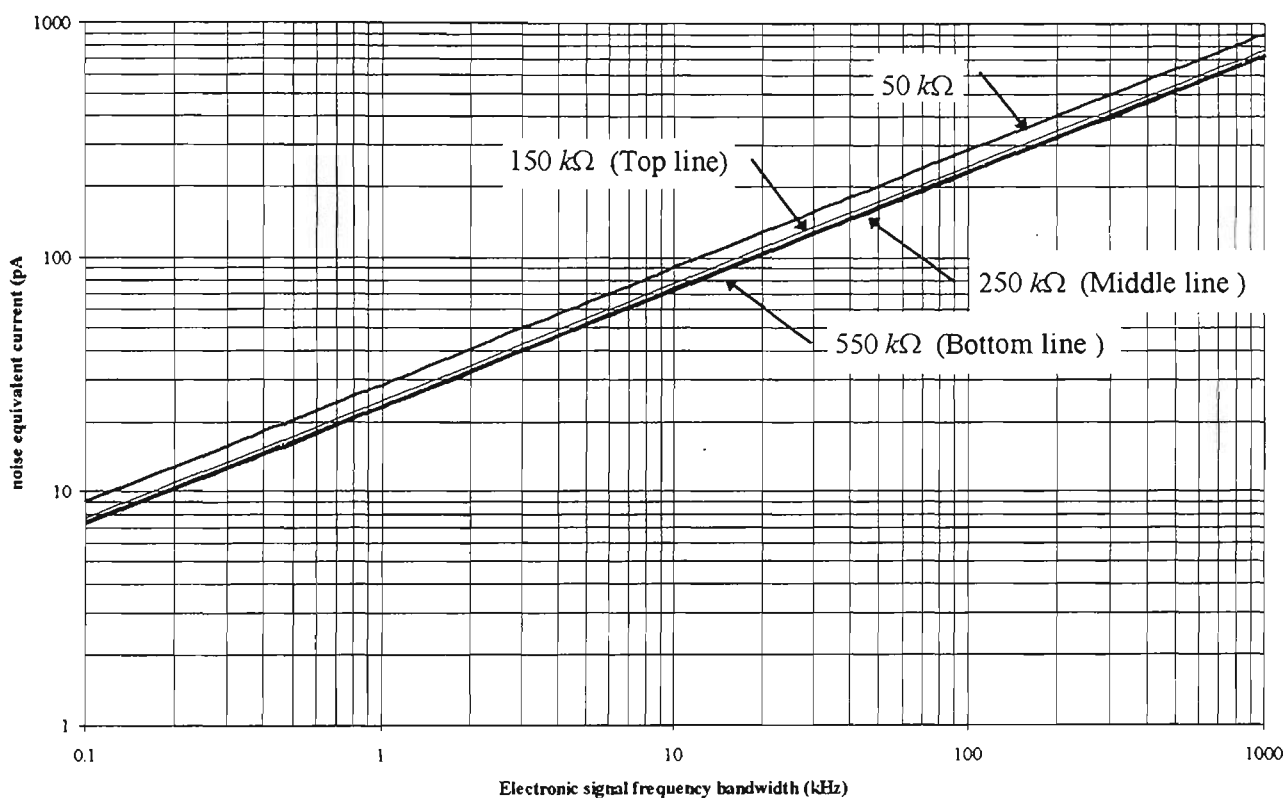


Figure C.1: Dependence of the noise equivalent photo-generated current, $I_{sig=noise}$ with the trans-impedance gain (resistance) R_{gain} and electronic signal frequency bandwidth, Δf .

Figure C.1 shows that for $R_{gain} > 150 \text{ k}\Omega$, $I_{sig=noise}$ no longer depends on R_{gain} . For a bandwidth of $\Delta f \sim 1 \text{ kHz}$ and $R_{gain} = 250 \text{ k}\Omega$, Figure C.1 indicates a noise equivalent photo-generated current $I_{sig=noise}$ of 22 pA which is equivalent to 40 pW of optical RMS intensity. Experimentally, $I_{sig=noise}$ was determined to be 35 pA (or 63 pW of optical power) in a bandwidth of about 1 kHz around sawtooth modulation frequency of 976.5625 Hz. Although this experimental noise figure was about 50% higher than the expected figure depicted in Figure C.1, the experimental noise figure agreed well with the expected noise value considering that only a partial noise analysis was made.

C.2 Phase Error in the Detection of the Zero-Crossing Edges

A Schmitt Trigger Circuit (STC) can perform well in detecting the occurrence of a zero-crossing voltage transition of the AC component of a voltage signal (Chapter 6). For as long as the absolute value of the noise voltage in the signal was below the Trigger level voltage, the output of the STC does unnecessarily change its values. The trade-off of this high noise immunity meant that the STC was strictly not a zero-crossing detector. Hence there is a phase error between the location of the zero-crossing detected by the STC and the ideal zero-crossing detector. Assuming a sinusoidal input voltage signal, this phase error can be calculated. Figure C.2 shows the absolute phase error as a function of the ratio between the Signal and Trigger voltage. As this signal-to-trigger voltage ratio increases, the STC approximates the behavior of an ideal zero-crossing detector which determines the occurrence of zero-crossings independent of the amplitude of its input signal.

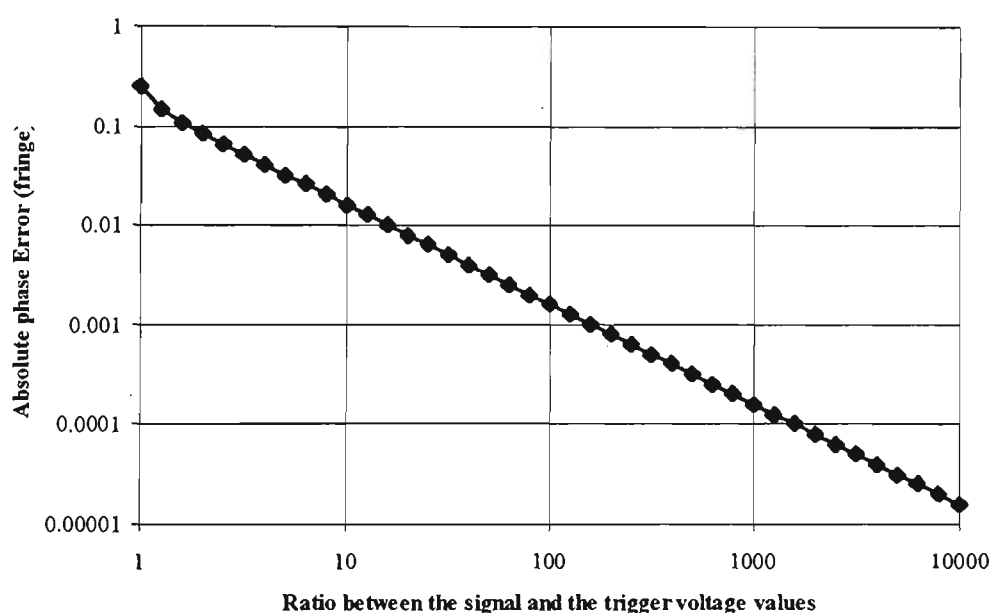


Figure C.2: The absolute phase introduced by the Schmitt trigger circuit due to the finite value of the trigger voltage. The x-axis in the figure is the ratio of between the signal and trigger voltage values.

For the experimental results discussed in the last two sections, the signal-to-trigger voltage ratio for the fusion-spliced birefringent sensors was generally low. The value of this ratio was then constant during the temperature measurements and consequently the corresponding phase error was also a constant. This phase error did not constitute as an experimental error in the measurand-induced phase measurements. On the other hand, for the grating-based sensor, the signal-to-trigger voltage ratio changed as temperature or strain varied. Hence there was a

corresponding phase error associated with a varying signal-to-trigger voltage ratio. Figure C.2 shows that for as long as the signal-to-trigger voltage ratio was greater than 160, the phase error was less than 0.001 of a fringe. In the case of the measurements with the grating sensors, such high Signal-to-Trigger voltage ratio was easily obtained because of the minimal transmission loss exhibited by the grating.

C.3 Phase Noise Due to Some of the Optical Components

C.3.1 Fresnel Reflection From the Proximal Face of the Lead-In Fibre

In Chapter 6, it has been established that the Fresnel reflection from the proximal end-face of the lead-in fibre concatenated with a birefringent Fabry-Pérot sensor, has to be minimised in order to avoid additional Fabry-Pérot interference between the beam reflected from this proximal end-face and the reflected beams from the sensor.

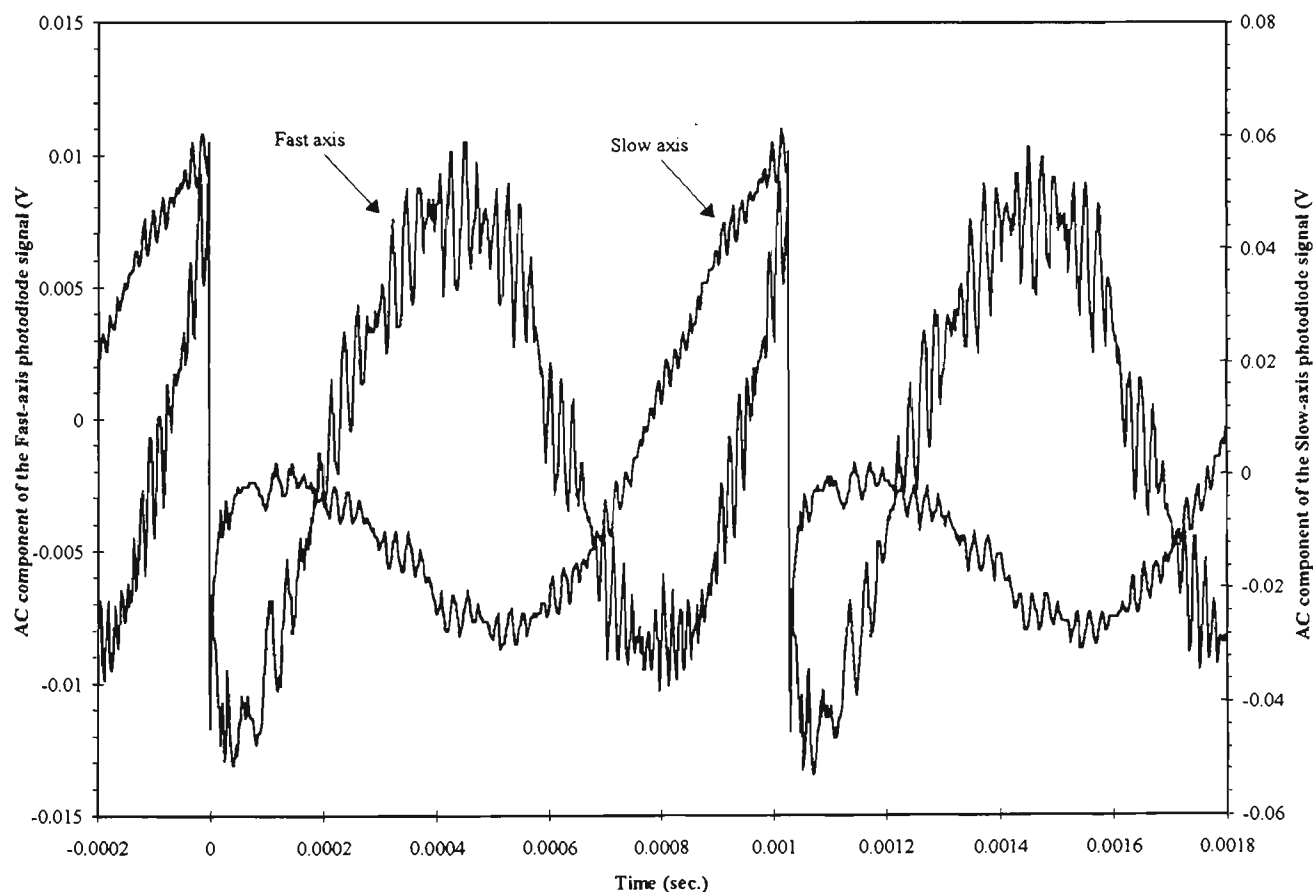


Figure C.3: The effect on the interferometric outputs of a single-grating-based birefringent fibre Fabry-Pérot sensor (*HibiGrat*) when the Fresnel reflection from the proximal face of the lead-in fibre was not negligible. *NB:* Each axial response has a different voltage scale and offset.

Figure C.3 shows the effect produced in the total reflected beam when the reflection from the proximal-face Fresnel was not negligible. The two set of waveforms in the figure are the intensities detected by two PDs and corresponded to each axis of *HibiGrat* (described in Chapter 5). Figure C.3 clearly indicates higher frequency fringes which corresponded to the additional Fabry-Pérot interference between reflection from this end-face and the internal mirrors of the Fabry-Pérot sensors. This additional Fabry-Pérot effect was verified by a simple procedure - when the lead-in fibre was slightly strained, the higher frequency fringes were found to shift whilst the lower frequency fringe remained undisturbed. Interestingly, this simple experiment also verified the excellent alignment of the polarisation axes of the lead-in fibre and *HibiGrat*.

Although the additional higher frequency Fabry-Pérot interference fringes caused by the Fresnel reflection can be theoretically eliminated using a narrow-band-pass filter, this Fresnel reflection still had to be reduced. Since the Fresnel reflected beam was not coupled into the fibre, the amplitude of these higher frequency fringes was sometimes large enough to obscure the (lower frequency) Fabry-Pérot interference fringes of the sensor or even to saturate the output of the normalisation circuit. In such cases, the phase of each axial interferometer of the sensor can not be suitably measured. Moreover, a real band-pass filter can still pass a fraction of signal associated with these higher frequency fringes. Consequently this residual signal can contribute to the noise in determining the zero-crossing of the interferometric output. Several methods were used in this work to eliminate the Fresnel reflected beam from the proximal end-face of the lead-in fibre.

The first method employed was to coat this face with an anti-reflection thin film. Typically a quarter-wave layer of MgF_2 was used giving a reflectance of around 1%. This procedure was insufficient to remove the problem as the residual reflectance value of the anti-reflection coating was of the same order of magnitude as the beam returning from sensor (Chapter 6). In many cases, the former had a greater contribution than the latter.

An alternatively method was to angle-polish the proximal end of the lead-in fibre. To produce such angle-polished end, the proximal end of the lead-in fibre was glued within a fibre chuck which had an angled end. This end was polished in order that the proximal face of the lead-in fibre had the same angle as the end face of the fibre chuck.

An angled proximal face can also be obtained by using a bad fibre cleaver. The latter procedure was implemented more often than not since it gave the same result as the polishing technique.

The whole idea of intentionally angle-cleaving the proximal face of the lead-in fibre was to direct the Fresnel reflected beam away from the optical axis of the optical arrangement of the measuring system. Subsequently the Fresnel reflected beam can be blocked with an aperture which only permitted the returning beam from the sensor to reach the PDs (Figure C.4). In this work, a circular aperture with a 1 mm diameter was used. The size of this aperture was chosen such that most of the beam from the sensor passed through with minimal diffraction whilst the Fresnel reflected beam was mostly spatially blocked.

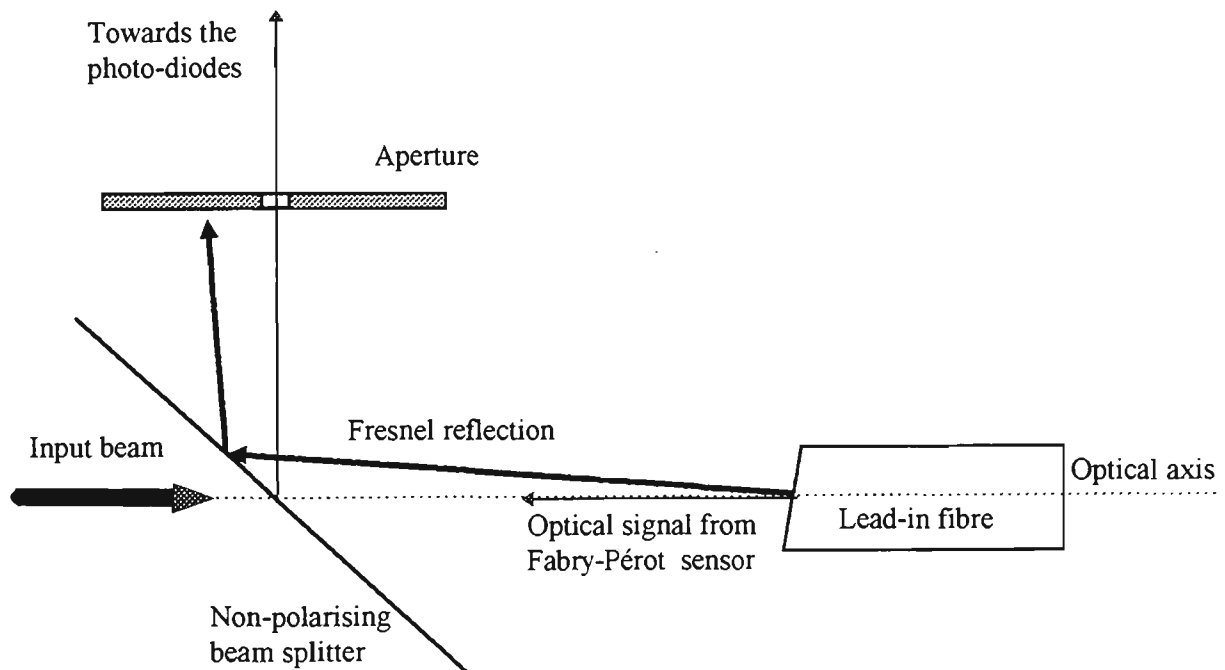


Figure C.4: Spatial blocking of the Fresnel reflection from an angled-face (proximal) of the lead-in fibre.

C.3.2 Lead-In Fibre Insensitivity

The insensitivity to environmental perturbation of the lead-in fibre is one of the most promising features of the optical fibre sensing system described in this work. Figure C.5 shows the interferometric phase along each axis of *HibiGrat* while the temperature of 10 cm of the lead-in fibre was drastically varied. This temperature variations simulated any other effects which perturbed the optical length of the lead-in fibre. Figure C.5 shows that the phase

shifts do not resemble the functional behavior of the change in the optical length of the 10 cm section of the lead-in fibre. The slow-varying trends in the each axial response of the sensor shown in Figure C.5 can be attributed to drifts in the LD temperature rather than that in the sensor temperature which was relatively constant as illustrated in Figure C.6.

However, there was an observable effect of the perturbation in the lead-in fibre in the total phase noise. Prior to the onset of the perturbation, the RMS phase noise on either axis was about 0.007 fringe ($\times 2\pi$) whilst during presence of the perturbation, it was increased to 0.014 of a fringe. This RMS noise were simply the residual phase variations after removing the slowly varying trends (due to temperature change in the LD or in the sensor) in each axial phase measurements. The RMS phase noise contributed only by the perturbations in optical length of the lead-in fibre was calculated to be 0.012 of a fringe.

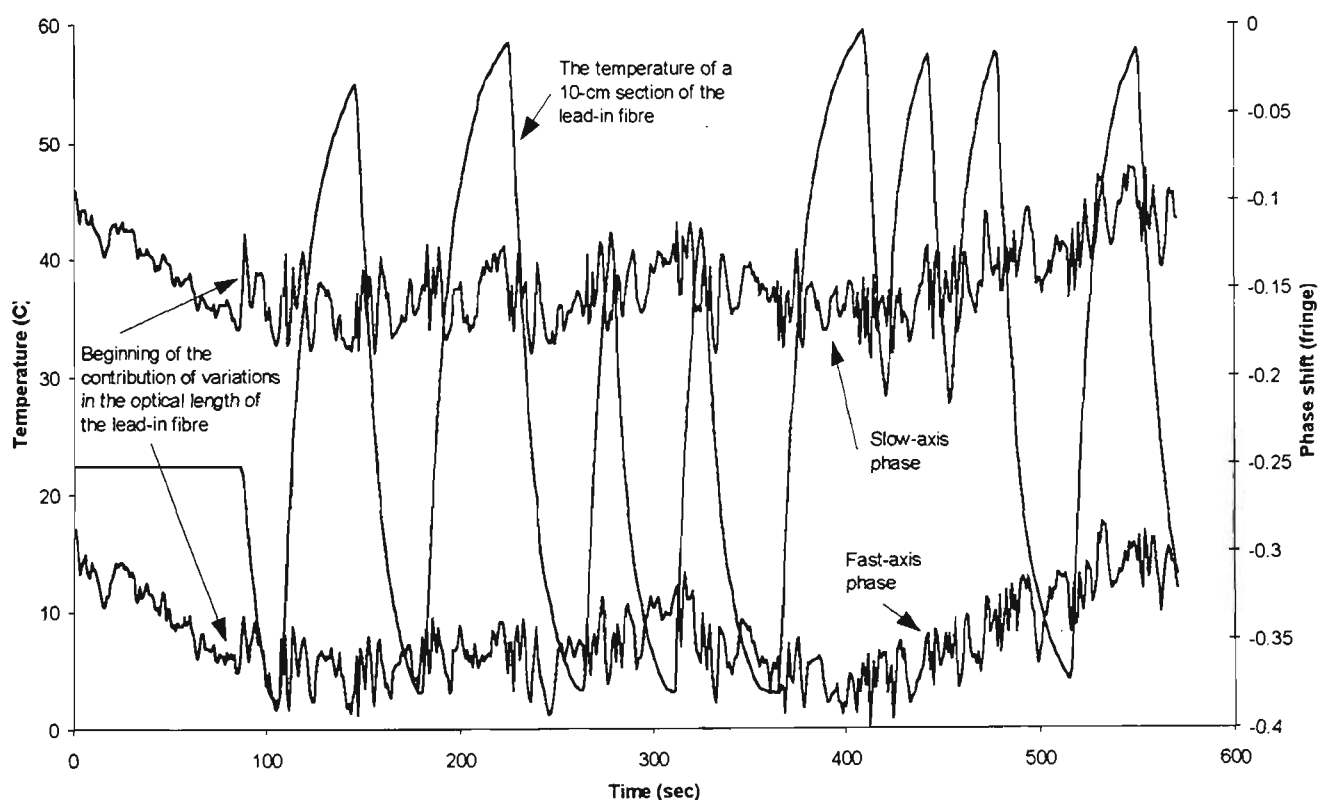


Figure C.5: The phase shifts along each polarisation axis of *HibiGrat* as the optical length of the lead-in fibre was thermally perturbed. The right vertical axis corresponds to the temperature of a 10 cm section of the lead-in fibre. The left vertical axis corresponds to the interferometric phase of each axial interferometer of the sensor.

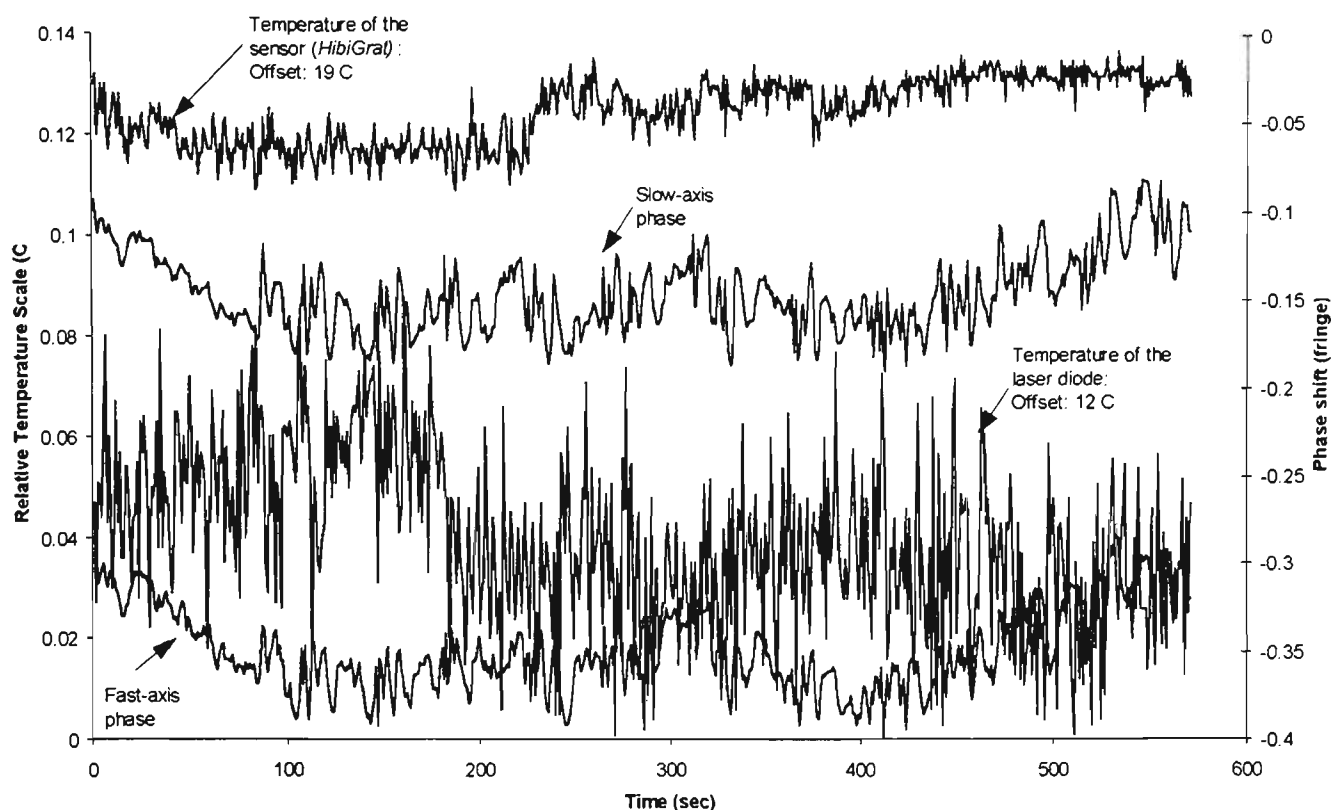


Figure C.6: The phase shifts along each polarisation axis of *HibiGrat* as the optical length of the lead-in fibre was thermally perturbed. The right vertical axis corresponds to the temperature of the laser diode and sensor relative to their corresponding offsets. The left vertical axis corresponds to the interferometric phase of each axial interferometer of the sensor.

The additional phase noise on each axial interferometer of *HibiGrat* depicted in Figure C.5 can be attributed to the effect produced by any slight mis-alignment between the polarisation axes of the different components of the optical arrangement, the finite extinction ratio of the polarising beam splitter (Chapter 6) or photo-induced birefringence in the grating (Chapter 5). In any one of these cases, the final intensity signal obtained by the PDs would contain harmonics of the optical path lengths of both polarisation axes of the lead-in fibre and harmonics of the sum and difference of these path lengths as well. This conclusion can be elucidated by calculating the general Jones Matrix of the sensing arrangement without any of the simplifications discussed in Chapter 6. The additional phase noise due to perturbations in the optical length of the lead-in fibre can actually be interpreted as a maximum phase noise simply because this phase effect was expected to be periodic with respect to variations in the optical path length along each axis of the lead-in fibre. In spite of the phase noise described above, Figure C.5 and Figure C.6 shows that the interferometric phase difference of each axial interferometer of the sensor did not change significantly. Such situations confirm the excellent alignment of the polarisation axes of the lead-in fibre and *HibiGrat*.

C.4 Phase Noise Due to the Characteristics of the Laser Diode

One limitation to the use of direct current modulation was the induced phase noise due to fluctuations in the optical frequency of the LD output [Dandridge *et al.*, 1981]. These phase noise increases with optical path difference or decreasing free spectral range of an interferometric sensor. The main mechanisms for these phase noise were temperature and carrier density fluctuations in the laser cavity [Dandridge & Tveten, 1981; Petermann, 1988]. The effects of these two parameters on the Hitachi HL78006G LD used in this work are investigated in order to appreciate the limitations of the sensing arrangement described in Chapter 6.

C.4.1 DC Current Characteristics and Noise

Figure C.7 shows the output power of a Hitachi HL7806G LD against its drive current for different values of its case temperature. The slope efficiency was approximately 0.27 mW/mA. Figure C.7 clearly shows the strong dependence of the threshold current of the LD on the temperature of the LD.

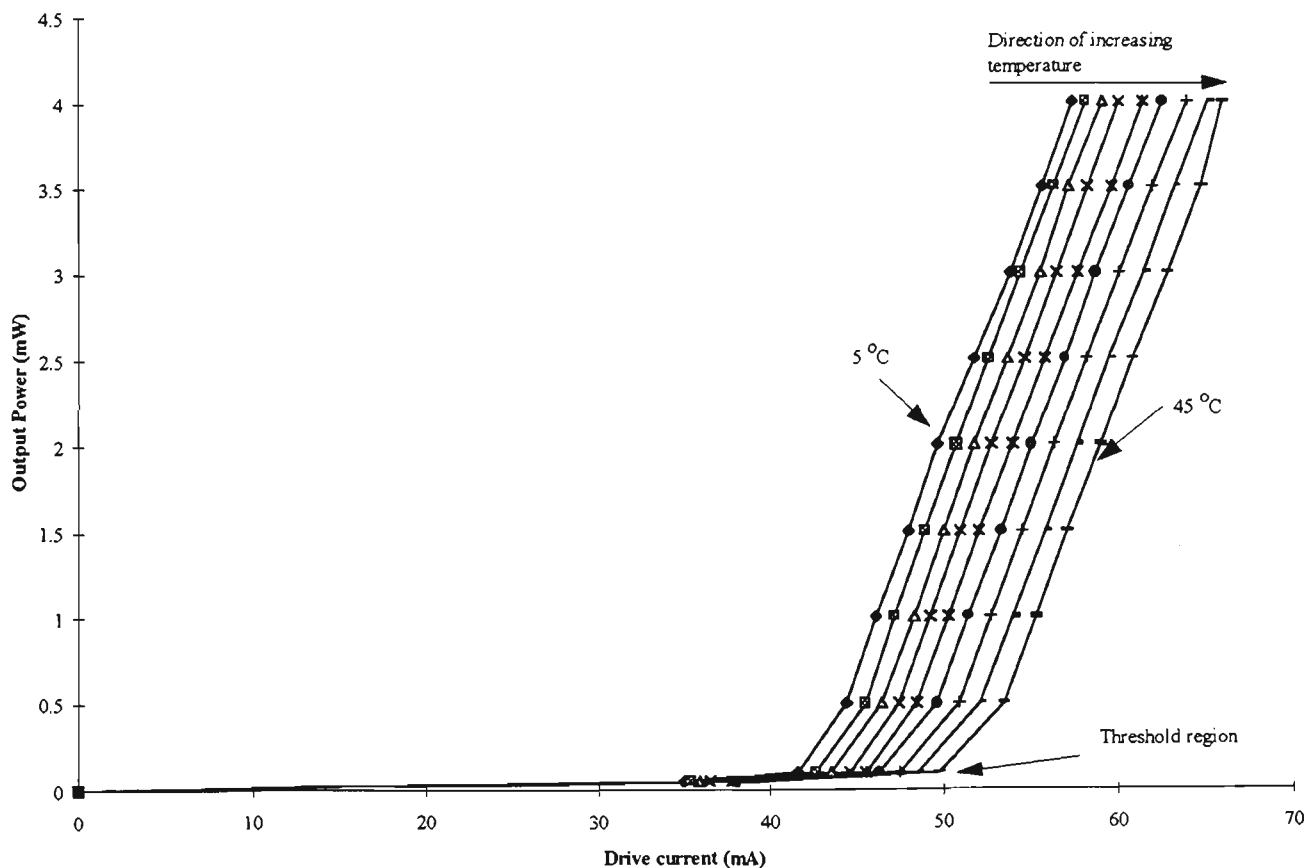


Figure C.7: The output power of a Hitachi HL78006G laser diode as a function of its drive current for different constant values of its cases temperature.

Figure C.8 shows the emission wavelength of a Hitachi HL7806G LD against its drive current for different constant values of its case temperature. The figure clearly shows that as the drive current and the temperature were varied the LD emission wavelength can abruptly change, *i.e.* mode-hop. Usually a mode-hop involves a pair of adjacent longitudinal modes. For an HL7806G LD, the longitudinal mode spacing was measured to be approximately 0.3 nm or 147 GHz (Figure C.9). Figure C.8 shows that for a constant temperature, the LD emission wavelength will typically mode-hop by about 0.3 nm. Mode-hopping limits the maximum usable optical frequency chirp for subsequent pseudo-heterodyne signal processing. This limitation dictates the minimum possible cavity length of a fibre Fabry-Pérot sensor that can be illuminated with a sawtooth-modulated LD. Diode laser mode-hopping needs to be avoided during the sawtooth current ramp because of the resulting abrupt phase shift which is proportional to the mode-hop frequency shift. In the non-mode-hop region of the curves shown in Figure C.8, the shift in emission wavelength of the LD due to changes in the DC current was about ~ 7.1 pm/mA (~ 3.5 GHz/mA). This sensitivity also implied that a noise current of ± 1 μ A introduced an RMS optical frequency noise of ± 3.5 MHz which in turn can be exhibited as interferometric phase noise in the output of the sensor.

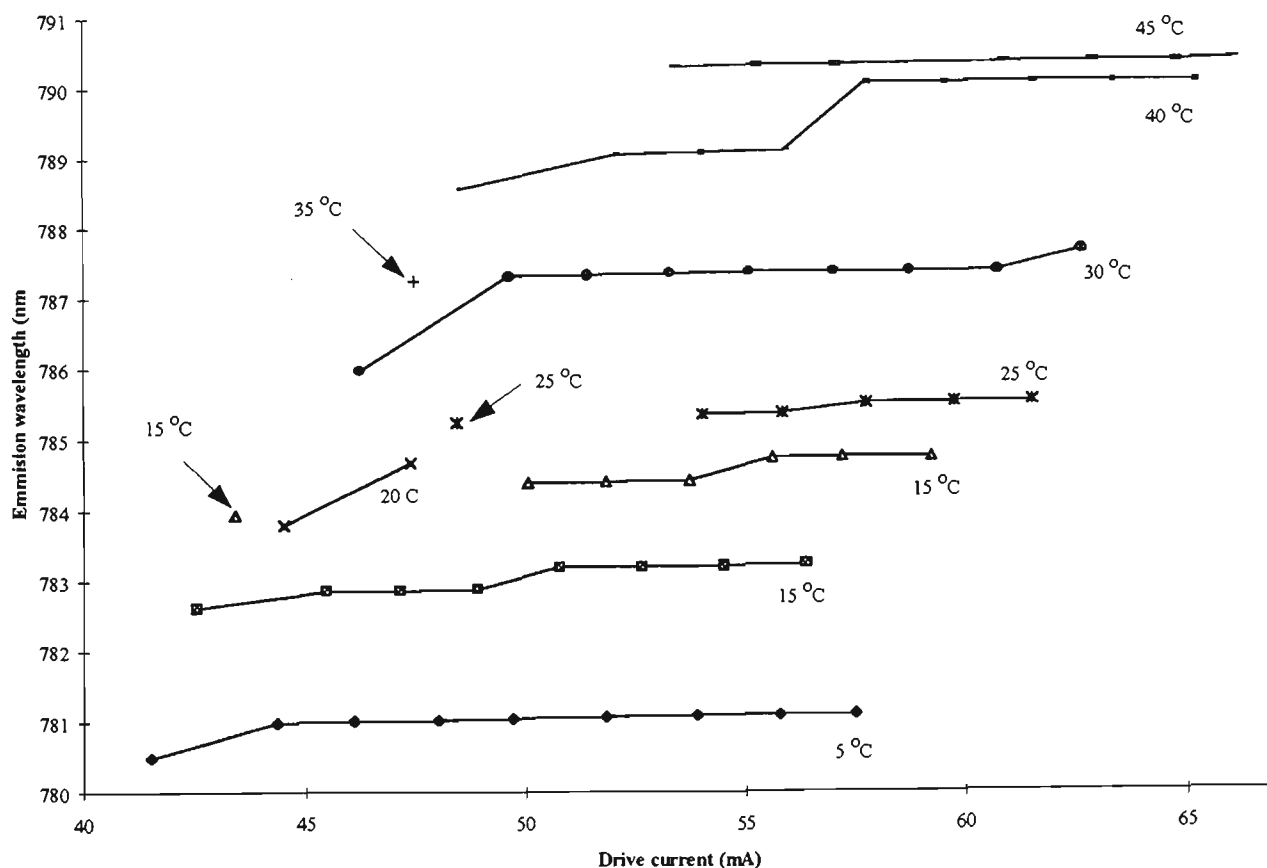


Figure C.8: The emission wavelength of a Hitachi HL7806G laser diode as a function of its drive current and its case temperature.

Noise in the LD drive current produces some intensity and phase noise in an interferometric output [Uttam & Culshaw, 1985; Economou *et al.*, 1986; Petermann, 1988]. To identify all the sources of noise in the LD drive circuit used in this work can be cumbersome since the LD drive circuit (Figure B.2) involved many components. However, the most critical components are the power supply voltage and the resistors responsible of producing the drive currents. These resistors were the series combination of T2 and R5 and T1 and R4. The expected (shot and thermal) noise contributions of these resistors were found to be negligible compared with the contribution of the supply voltage. The LM337 voltage regulator which was connected to give an output of - 12 V had a line regulation of about ± 0.6 mV. This regulation noise translated to about ± 9 μ A drive current noise, or ± 2 μ W intensity noise and ± 30 MHz optical frequency noise. Since the typical output power of the LD was in the mW range, the ± 2 μ W intensity noise can be neglected but the frequency noise can not. In the case of *HibiGrat*, this optical frequency noise implied about ± 0.005 fringe phase noise.

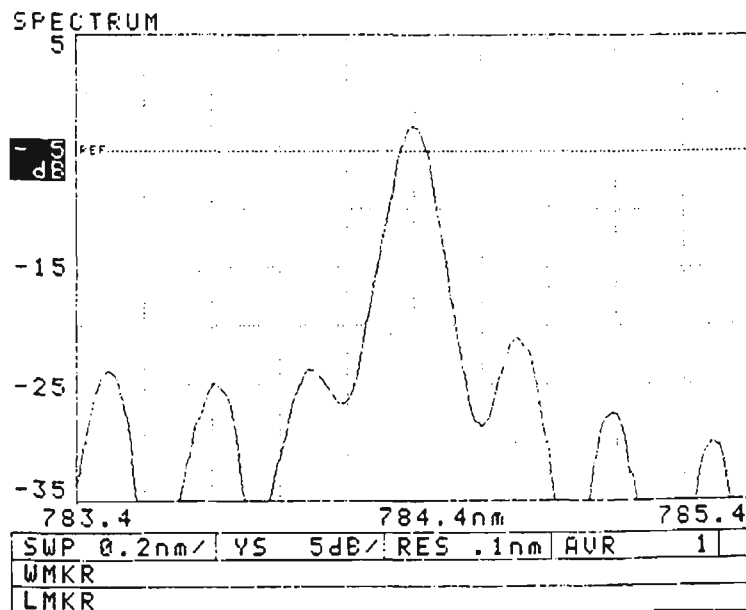


Figure C.9: The optical spectrum of a modulated Hitachi HL7806G laser diode (0.1 nm resolution).

C.4.2 Coherence Length of the Laser Diode Operated With A Small-Signal AC Sawtooth Current Modulation

The coherence length of the LD output was an important parameter in determining the operational characteristics of the sensors investigated in this work. The modulation of the LD may cause its output line-width to broaden compared with the unmodulated case. The line-broadening of the modulated LD output can introduce

interferometric phase noise in addition to reducing the fringe visibility of the interferometric output of interferometer [Economou *et al.*, 1986]. The effect of a sawtooth current modulation to the coherence length of the output beam of the Hitachi HL7806G LD used in this work was investigated.

First, the optical spectrum of the sawtooth-modulated LD was measured using an ANDO AQ3610B optical spectrum analyser (OSA). Figure C.9 shows the typical spectrum obtained with the OSA. The figure illustrates that even under current modulation the LD output was single-mode at ~ 785 nm and its intensity was 20 dB (power) stronger than the immediately adjacent modes on either the blue or red end of the spectrum. Unfortunately the OSA has a maximum resolution of the 0.1 nm which can not give the true line-width of the LD output. Alternatively the LD coherence length was estimated using an interferometric technique.

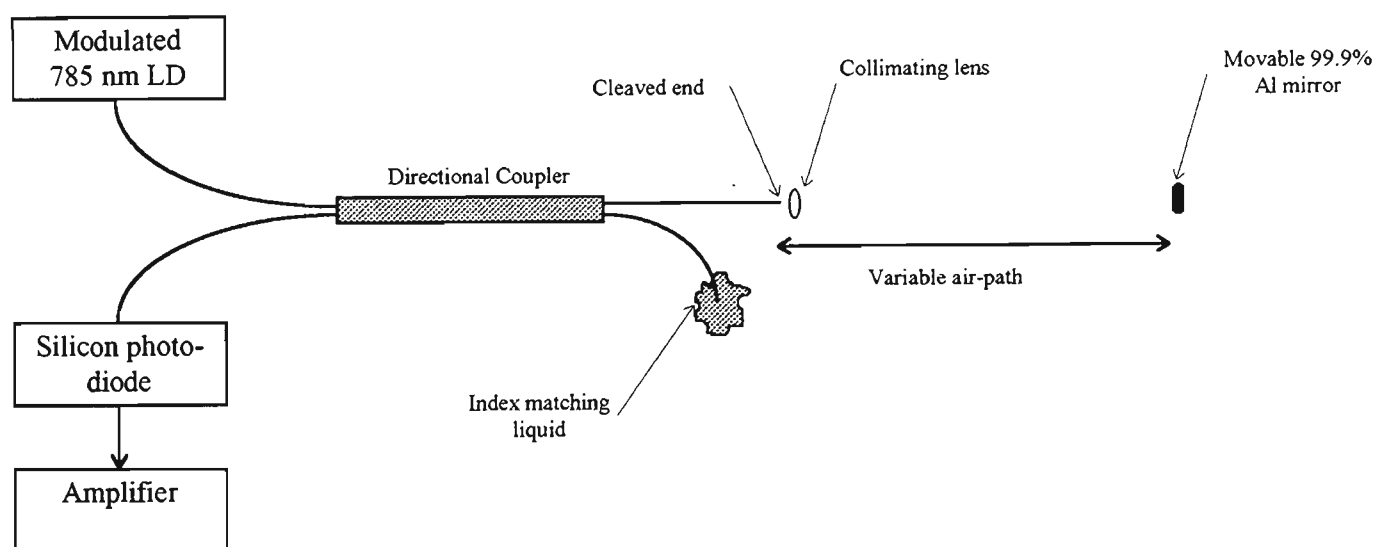


Figure C.10: Schematic diagram of the experimental arrangement employed to determine the current-to-optical frequency response of a modulated Hitachi HL7806G LD.

Figure C.10 shows the experimental arrangement to determine the coherence length of the LD under current modulation. The coherence length was inferred from the fringe visibility in the resulting optical signal from a Fabry-Pérot interferometer cavity formed by the cleaved end of a fibre and the highly reflecting and movable aluminum (Al) plane mirror as shown in Figure C.10. The beam emerging from the cleaved end was collimated in order to minimise the re-insertion loss experienced by the beam reflected from the Al mirror. The bulk-optic Fabry-Pérot interferometer was addressed in reflection using the classical fibre directional coupler arrangement.

Light from the 785 nm LD was launched into one of the legs of the coupler and excited the opposite legs one of which was concatenated with the Fabry-Pérot interferometer. The reflected beam from the interferometer was detected using an appropriately placed PD. The unused leg of the coupler was index-matched to avoid reflections back to the PD and the LD.

The LD current was modulated in a sawtooth manner in order to produce a set of moving fringes in time at the PD. For the same sawtooth current modulation, the length of the Fabry-Pérot cavity was varied from 40 mm to 3000 mm in order to adjust the FSR of the cavity. Subsequently the fringe visibility of the interference and the corresponding instantaneous change in the optical frequency of the LD was measured. The results of latter set of measurements are discussed in section D.4.3. Typical interferometric signals from the bulk-optic Fabry-Pérot interferometer are shown in Figure C.12 and Figure C.13.

The coherence length of the LD was estimated to be around 2 m when the LD was operated far from any mode-hop region. This coherence length value implied a line-width of 0.15 pm or 75 MHz. An estimate was only possible because the intensity of the beam injected back into the directional coupler was dependent on the coupling efficiency of the collimating lens and the divergence of reflected beam from the Al mirror. An accurate determination of any coherence length greater than 1 m was not critical because this work deals with low-finesse and short cavity-length FFPSs.

Qualitatively, the fringe visibility was found to decrease either when the LD was operated close to a mode-hop region or when the optical output power was between 1.5 and 2.0 mW. In these unstable operation regimes, phase noise can be expected. Subsequently the pragmatic choice of operating the LD far from these unstable regimes was made.

C.4.3 AC Current Characteristics And Noise

To effectively implement the pseudo-heterodyne signal processing scheme using a modulated LD, the drive current and the emission frequency of the LD needs to linearly correspond. To obtain a linear sawtooth optical frequency

ramp from a linear sawtooth current ramp, the frequency response of the current-to-optical-frequency transfer function needs to be relatively flat over several harmonics of the sawtooth current ramp. Figure C.11 shows the typical small-signal current-to-optical-frequency response of a Channel-Substrate-Planar (CSP) LD, similar to a Hitachi HL7806G device.

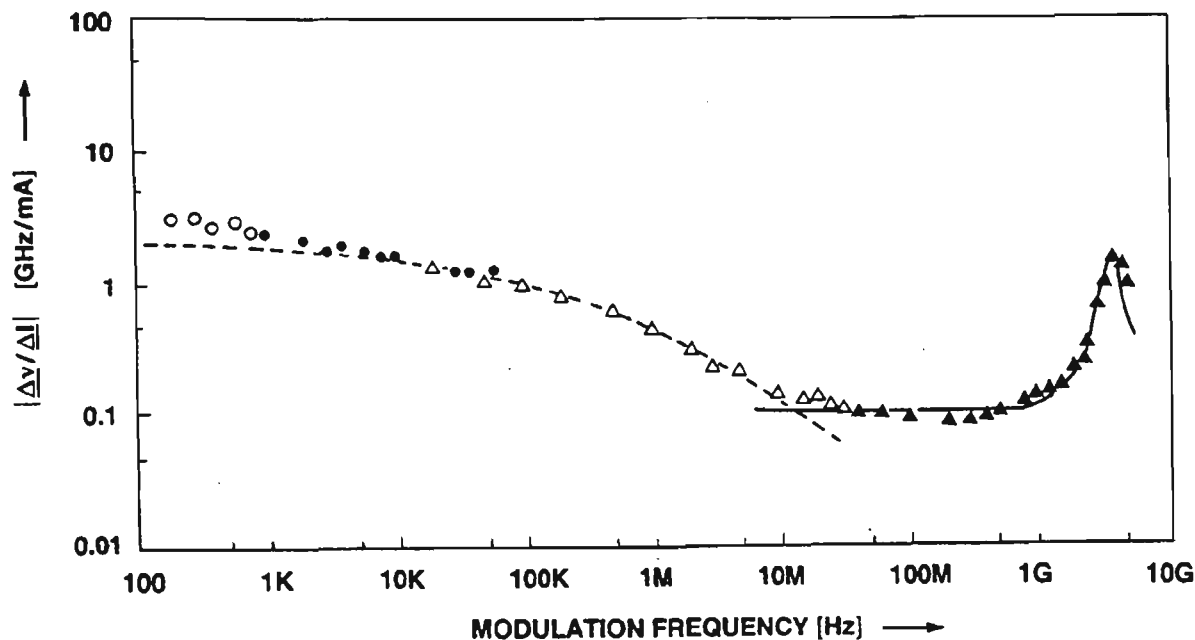


Figure C.11: Modulus of the small-signal current-to-optical frequency transfer function of a GaAlAs-CSP laser diode. The dash line denotes the thermal effect whilst as the solid line the carrier effect [p. 124: Petermann, 1988].

The nonlinear (modulation) frequency response of the current-to-emission-frequency conversion is caused by the interplay between thermal and carrier density effects. At lower modulation frequencies, the optical frequency chirp is due to thermal effects whilst at higher modulation frequencies due to carrier density effects [Kobayashi *et al.*, 1982; Jacobsen *et al.*, 1982; Clark *et al.*, 1982; Welford & Alexander, 1985; Petermann, 1988]. The nearly flat response between 10 MHz and 1 GHz in Figure C.11 is due to wide difference in the cut-off modulation frequency for the thermal and carrier-density effects [Petermann, 1988].

The flat region between 10 MHz and 1 GHz is clearly an ideal region to implement the pseudo-heterodyne signal processing scheme. However, the corresponding current-to-optical-frequency response in this region is about an order of magnitude less than that at the lower modulation frequencies. This situation implies that the amplitude of the current modulation needs to be increased substantially in order to obtain the same amount of optical frequency

chirp at lower modulation frequencies. However the maximum amplitude of the current modulation is limited by mode-hopping in the LD output.

Although the current-to-optical-frequency sensitivity is high and relatively flat for frequencies less than 10 KHz, the frequency chirp is dominantly a thermal effect. The cut-off frequency of this thermal effect, ~ 100 kHz (see Figure C.11), limits the fly-back response of the LD emission frequency [Economou *et al.*, 1986]. The fly-back period is characterised by a relatively slow turn-off cycle preventing any rapid restart of the ramp [Goldberg *et al.*, 1981]. On the other hand, the intensity of the output which is strongly dependent on the current density can change very quickly (Figure 6.9).

Figure C.12 and Figure C.13 shows output of the PD circuit (Figure B.5) and the division circuit (Figure B.4) during one period and during the fly-back period of the sawtooth modulation when arrangement shown in Figure C.10 was illuminated with a sawtooth-current modulated Hitachi HL7806G LD. The division circuit divides the output of the PD circuit with a signal proportional to the intensity of the output of the LD. For the data shown in Figure C.12 and Figure C.13, the bulk Fabry-Pérot interferometer (Figure C.10) had a cavity length of 750 mm, or an FSR of 2 MHz.

Figure C.13 shows that at the start of the ramp, the optical frequency continued to decrease and only began to rise after $2 \mu\text{s}$ from the start of the ramp. This observation means that the temperature of the LD had continued to increase even after the LD current had decreased during the fly-back edge of the current sawtooth modulation. During the next $66 \mu\text{s}$, the cavity of the LD continued to cool, *i.e.* turn-off cycle. In the meantime this cooling process was counteracted by the heating effect of the rising current ramp. $68 \mu\text{s}$ after the start of the ramp, the heating effect begins to dominate and the optical frequency began to decrease again, *i.e.* turn-on cycle. This period, $\sim 7\%$ of the ramp period, represents the fly-back period for the optical frequency sawtooth modulation. After this fly-back period, the frequency shift behaved quadratically with respect to the ramp but becomes practically linear during the second half of the ramp period.

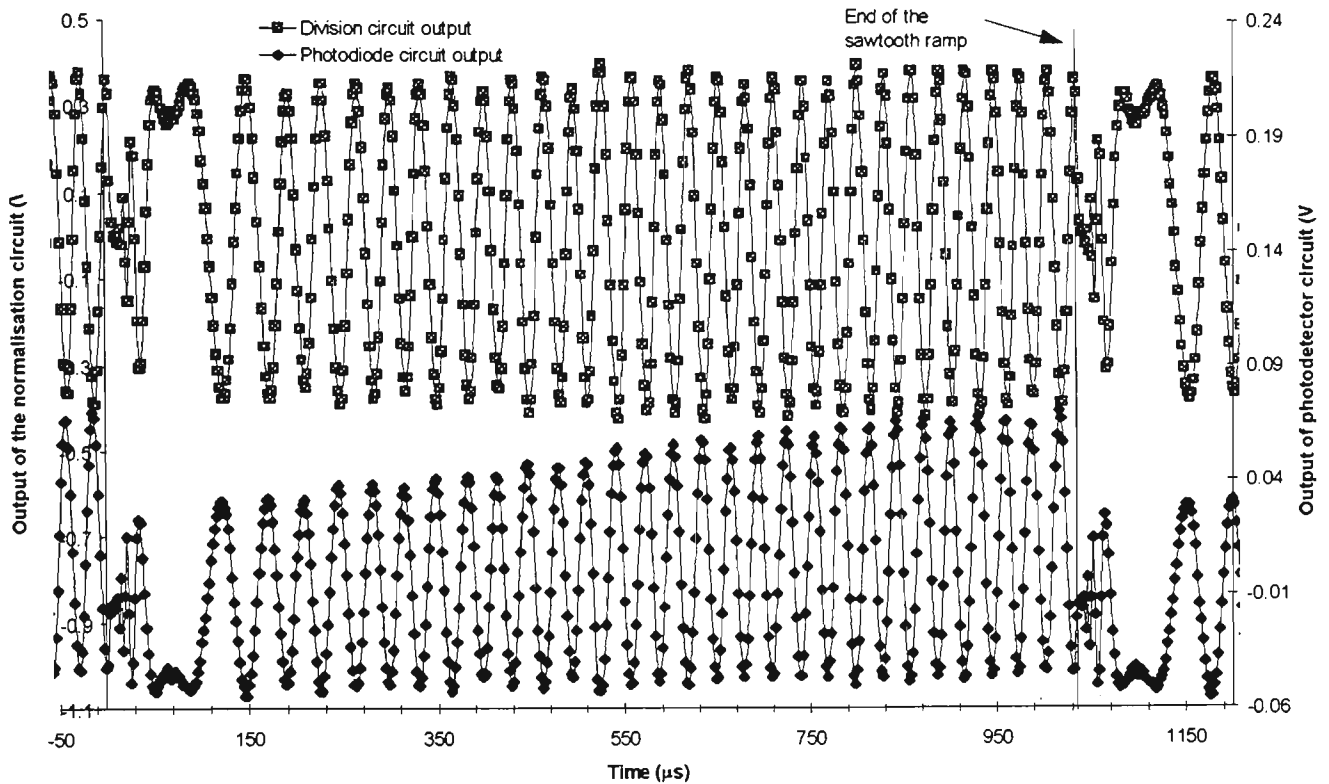


Figure C.12: The unprocessed and intensity-modulation free PD signals used to measure the LD emission frequency sawtooth modulation. Air-cavity length = 750 mm.

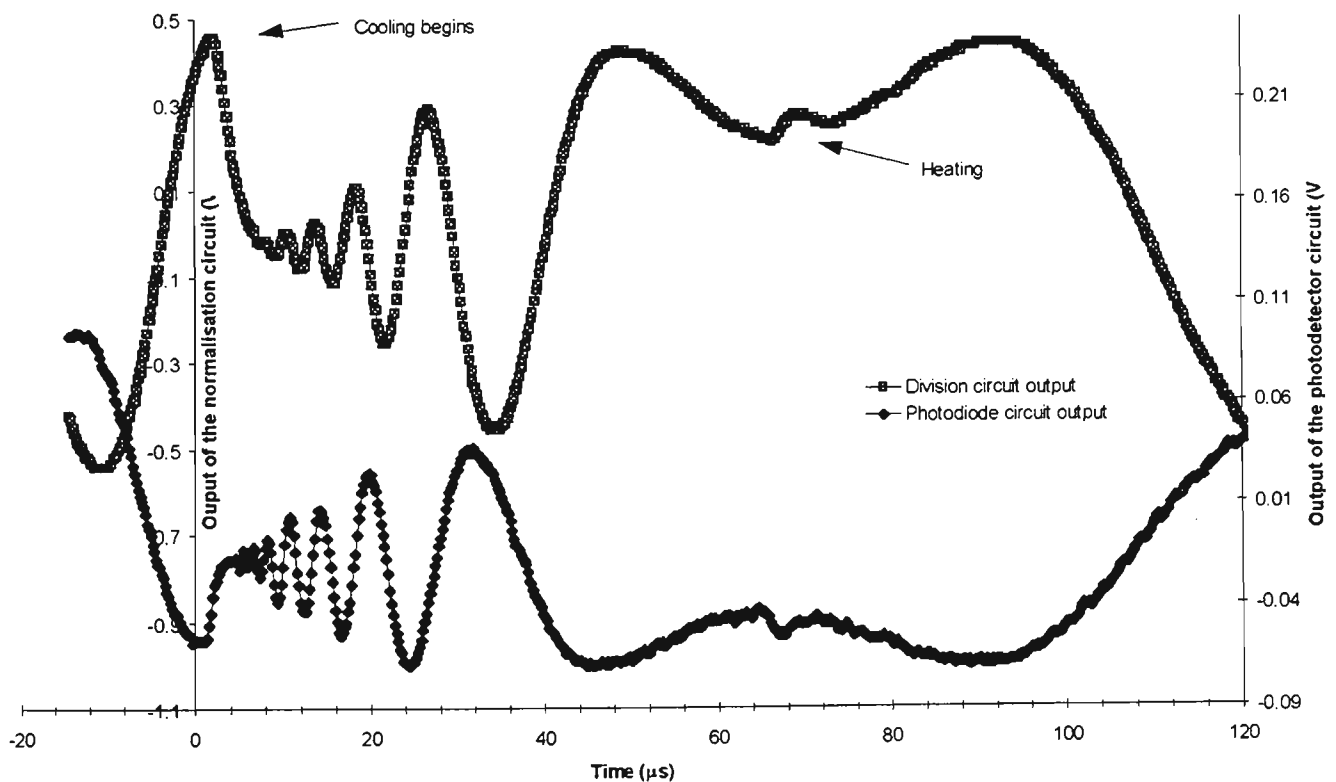


Figure C.13: The unprocessed and intensity-modulation free PD signals used to measure the LD emission frequency sawtooth modulation (fly-back period). Air-cavity length = 750 mm.

From the measurements shown in Figure C.12 and Figure C.13, Figure C.14 shows the calculated shifts in the LD emission frequency modulation within one sawtooth cycle. The behaviour of the LD frequency modulation clearly deviated from a linear sawtooth. Consequently, this nonlinear optical frequency ramp produced a similarly varying change in the interferometric phase of an FFPS. Using the measurements presented in Figure C.14, it was possible to measure the FSR of an FFPS since the FSR of the bulk interferometer in Figure C.10 was known. In particular the average FSRs of axial interferometers of *HibiGrat* was measured to be 6.4 GHz using this method. This FSR value implied a cavity length of 16 mm which was in agreement from the value inferred from the distance between the centre of the grating to the cleaved end of *HibiGrat* (15 ± 1 mm).

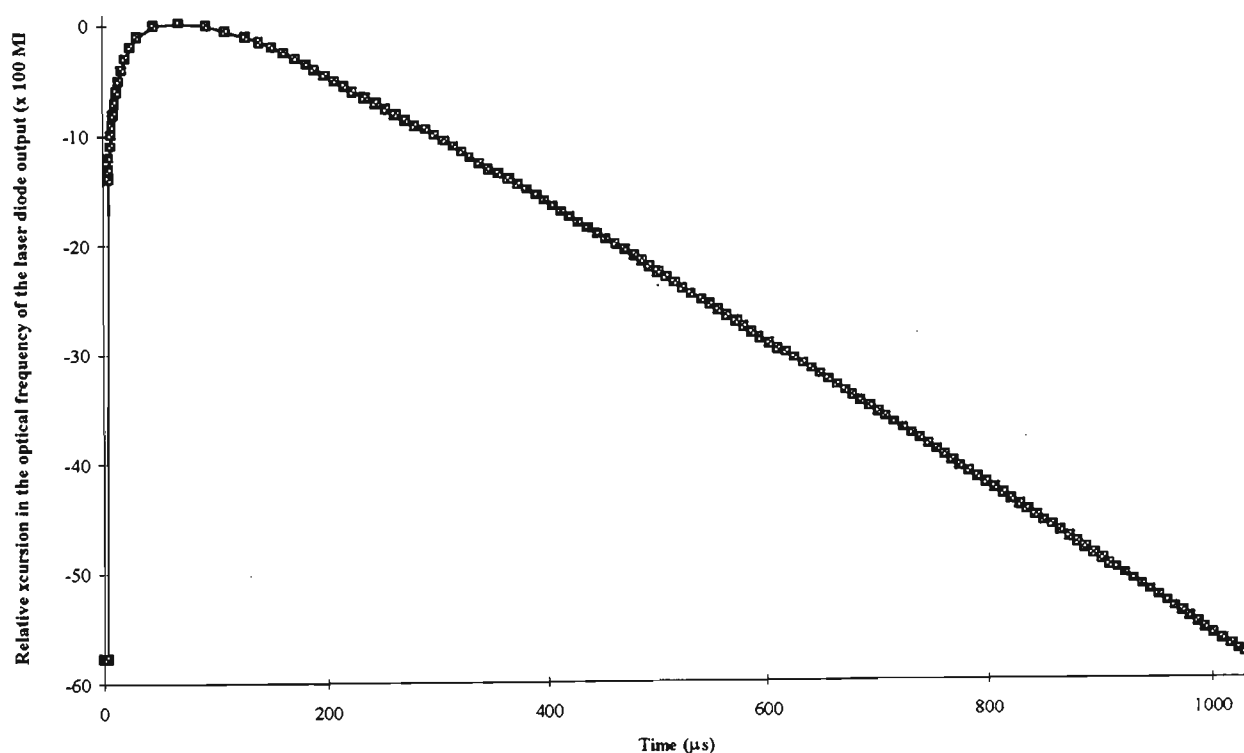


Figure C.14: The instantaneous optical frequency chirp within one sawtooth period of LD current modulation.

Analysis of the interferometric signals shown in Figure C.12 and Figure C.13 confirmed the single-mode output of the LD since no other fringe pattern was observed. Furthermore, the stability of the fringe pattern even for small FSR air-path implied that the thermally induced noise resulting from the limitations of the LD temperature-controller was much less than that previously expected. Hence the LD temperature stability can be further estimated to be about $\pm 0.0001^\circ\text{C}$ over a period of 15 minutes. This excellent short term temperature stability

assured accurate phase and hence temperature or strain measurements over a very short period of time in spite of a design flaw in the temperature controller for the LD (Appendix B)

The same optical frequency ramp measurement described above can also provide a measurement of the AC optical-frequency/current sensitivity. The ratio between the amplitudes of the optical frequency and drive current sawtooth ramps was determined to be -2.4 GHz /mA . This AC sensitivity was similar to those measured by others for a Hitachi HL7801E which was similar in construction to the HL7806G (Table C.2). Also, this sensitivity value was in agreement to that depicted in Figure C.11. The AC optical-frequency-current sensitivity was less than the corresponding DC characteristics measured previously for the LD. This difference between the AC and DC sensitivities was attributed to the thermal nature of the dependence of the LD optical frequency with its drive current (Figure C.11).

This high AC optical-frequency/current sensitivity of the LD suggested another possible source of optical frequency noise can be due the noise in the modulation current. One possible current noise source was the staircase-type sawtooth modulation. The RMS noise due to this staircase ramp was calculated to be 3.524×10^{-5} of ramp current amplitude. Since the ramp amplitude was adjusted to correspond to the FSR of the sensor, the expected noise was expected to be 3.524×10^{-5} of a fringe. The actual noise value would be less than 3.524×10^{-5} of a fringe because the staircase steps were expected to be smoothen out by the input stage of the LD drive circuit. Nevertheless, the 3.524×10^{-5} of a fringe was an order of magnitude less than the resolution of the measuring system (10^{-4} of a fringe). Thus the assumption that the staircase nature of the voltage sawtooth ramp modulation signal do not introduce any undesirable effects holds ground.

Another possible current noise source was the components of the LD drive circuit (Figure 6.12). The LM337 voltage regulator used in the circuit had a worst-case RMS noise of $360 \mu\text{V}$ between 10 Hz and 10 kHz which translated to about $5 \mu\text{A}$ (RMS) in the same frequency range. Subsequently this value implied an optical frequency noise of 12 MHz (RMS). In particular for *HibiGrat*, this current noise implied about 0.002 fringe (RMS) phase noise.

C.4.4 Temperature Sensitivity of the Laser Diode and Limitations of the LD Temperature Controller

Figure C.15 shows the dependence of the optical output power against temperature at different constant drive current which were greater than the threshold value. The dependence was clearly not linear. Interestingly the output power appeared to fluctuate between 1.5 mW to 2 mW of optical power output. This instability was not completely understood. However, it was definitely clear that the LD must be operated away from this instability region. In the work, optical output power was preferentially chosen to be greater than 2 mW. This conveniently implied a lower value for relative amplitude of the sawtooth intensity modulation with respect to DC intensity value. This condition meant the intensity modulation in the interferometric signal was less severe.

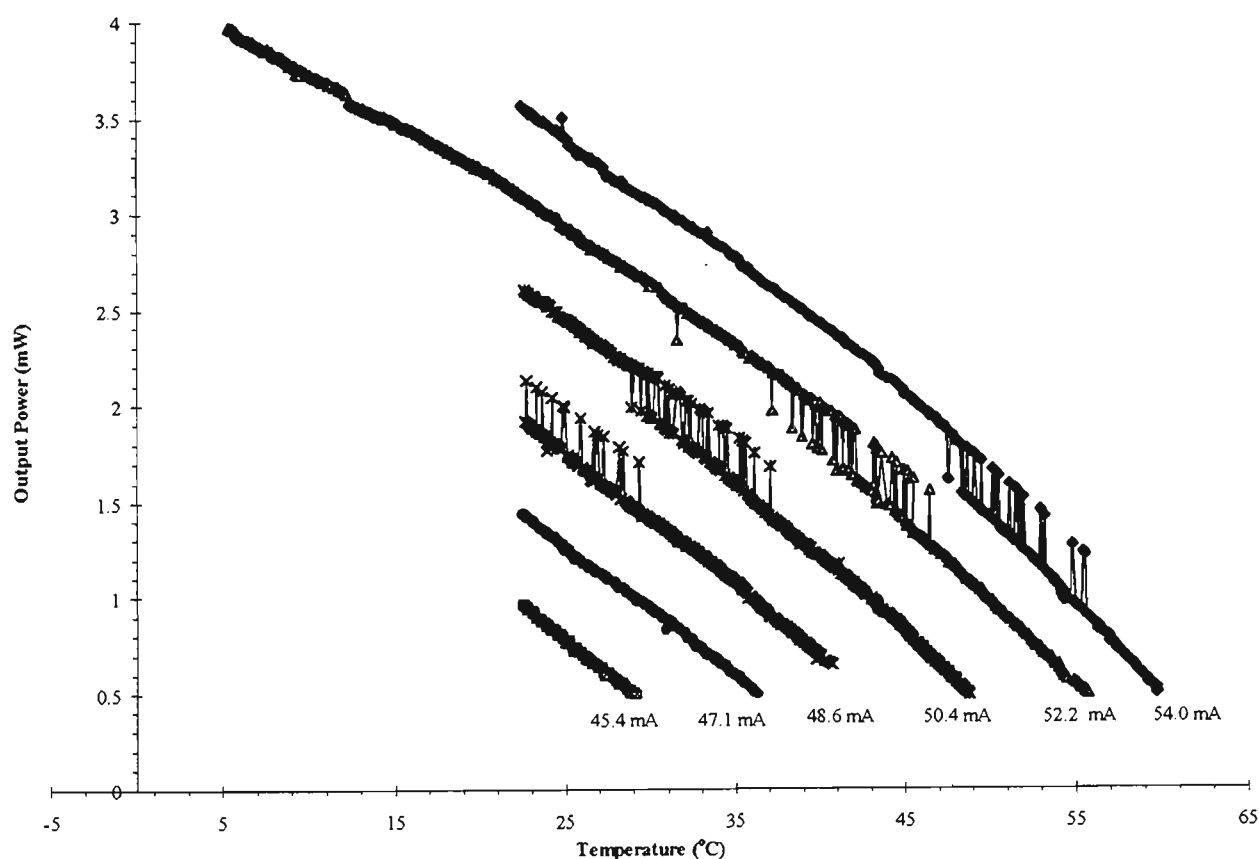


Figure C.15: The dependence of the output power of a Hitachi HL7806G LD with its case temperature for different values of its DC drive currents.

Figure C.16 shows the LD emission wavelength as the case temperature of the LD was varied. The figure clearly illustrates the mode-hopping behaviour of the LD output. Furthermore, The figure indicates the emission wavelength had a greater dependence on temperature than the DC drive current. Figure C.16 shows that the most

stable region of operation for the LD was between 790 nm to 791 nm. In this wavelength range, the LD output didn't not appear to mode-hop as the temperature and the drive current of the LD was varied.

In each of the non-mode-hop regions shown in Figure C.16, the wavelength(frequency)/temperature sensitivity was measured to be about 0.06 nm/°C (or -29 GHz/°C). This sensitivity was similar to those measured by others (Table C.2). This high sensitivity demanded excellent stabilisation of the LD temperature. In this work, the LD was temperature-controlled using Peltier devices with the best long-term stability (~ 3 hrs) of about ± 0.02 °C provided that the ambient temperature was relatively constant. Unfortunately ± 0.02 °C translated into thermally-induced drift of ± 0.58 GHz in the LD optical frequency. In the case of *HibiGrat*, this large frequency drift produced a significantly large phase drift of about ± 0.1 of a fringe. Only for sensors with a physical cavity length less than 1.75 mm would the equivalent phase drift be less than ± 1 %. Incidentally such large-FSR sensors may not be suitably processed by the pseudo-heterodyne technique implemented with a modulated LD.

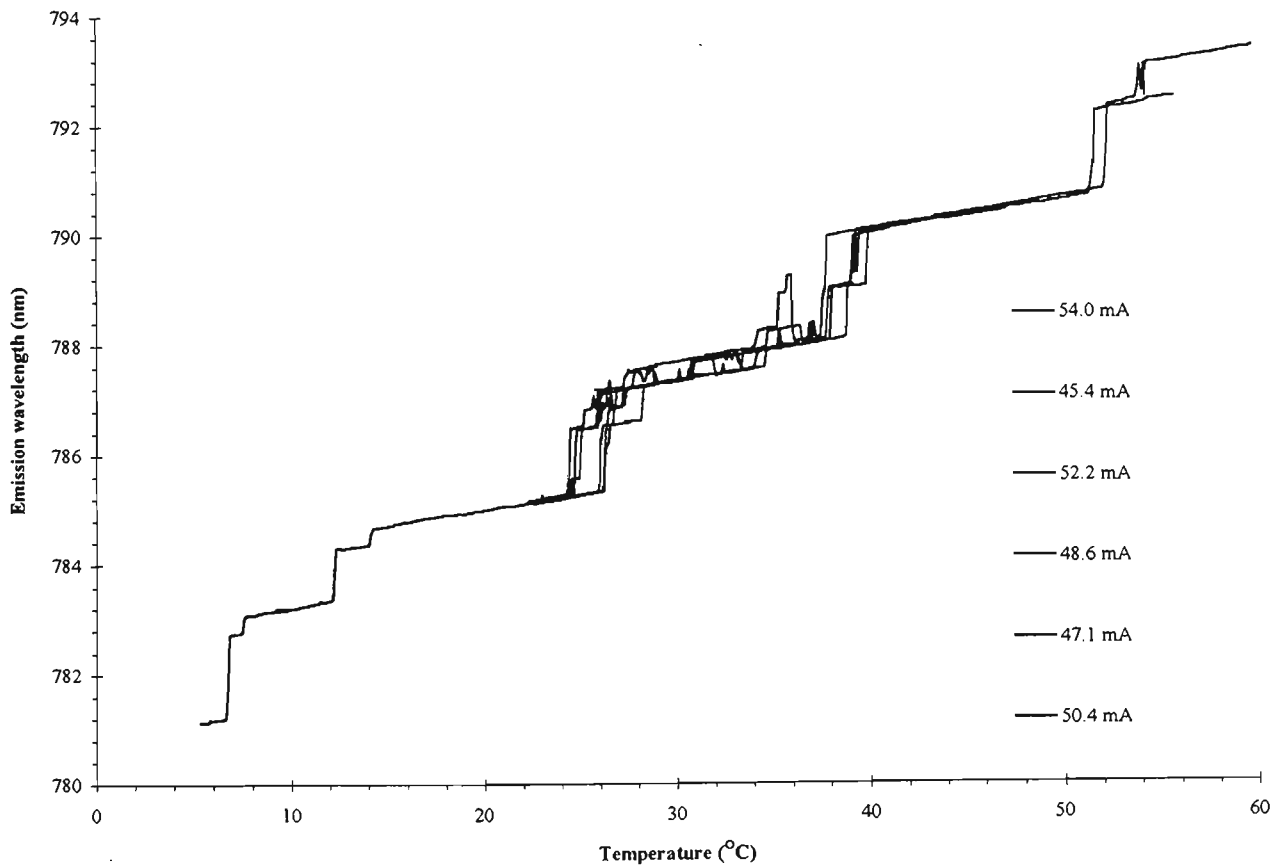


Figure C.16: The dependence of the emission wavelength of a Hitachi HL7806G LD with its case temperature for different values of its DC drive currents. Each curve in the figure was formed by connecting data points separated by 0.1 °C.

Figure C.17 shows the effect of drifts in the LD output wavelength on the interferometric fringe shifts. The polarisation axes indicated in were those of *HibiGrat*. Each data point in the figure was an average of 20 data points sampled every 5 seconds. The figure shows that interferometric phase of the sensor was strongly affected by the LD temperature drifts : $-5.4 \text{ fringe}/^{\circ}\text{C}$. This thermally induced phase shift was consistent with that obtained from direct wavelength shift measurements of the LD (Figure C.16). This thermal sensitivity was expected to be a negative value because an increase in the LD temperature decreases the LD emission frequency. Figure C.17 also shows that the total phase shifts along each polarisation axes were slightly different. Since the FSR of each axis of the sensor was very similar, the difference was attributed to drifts in the temperature of the sensor itself.

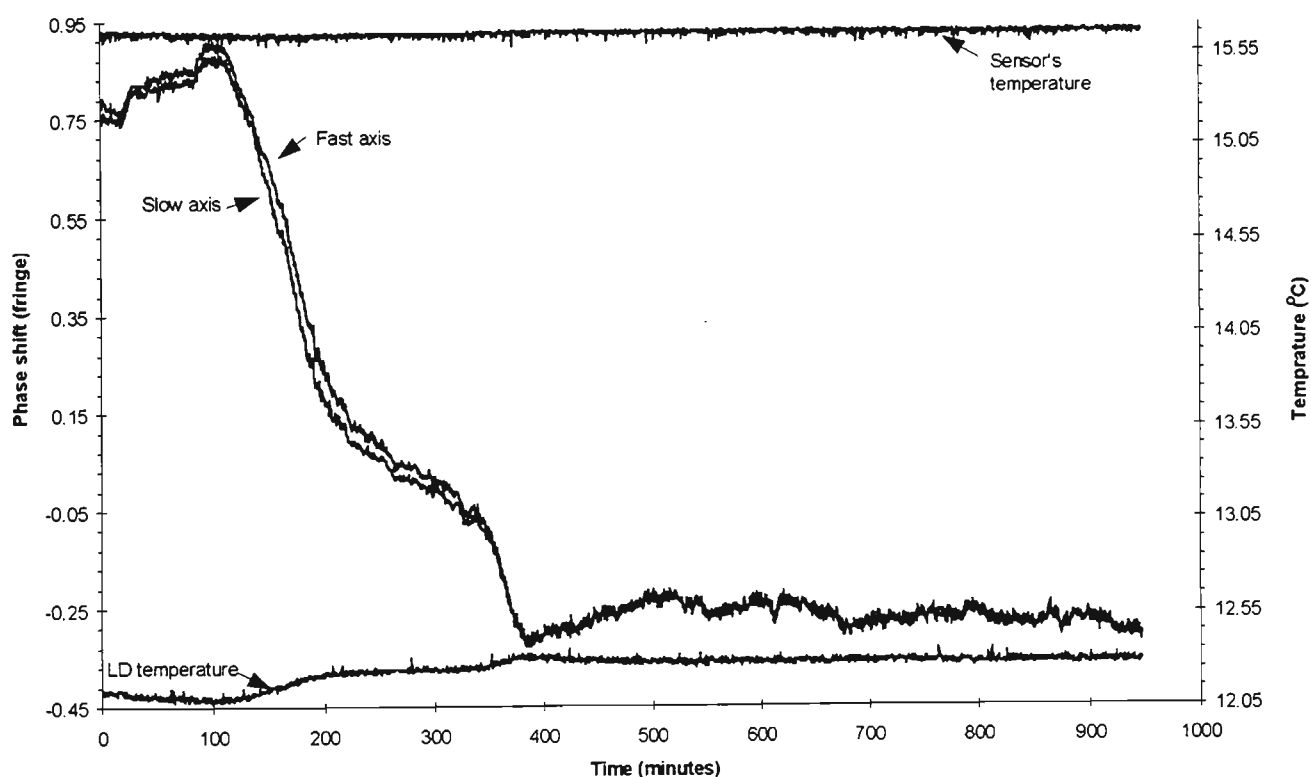


Figure C.17: The phase drifts of each interferometer of *HibiGrat* due to thermally induced variations in the LD emission wavelength.

The drift in the LD temperature depicted in Figure C.17 was a direct consequence of a design flaw in the typical temperature controller available in the laboratory (Figure 2.13). Since the feedback current produced by the temperature controller was proportional to the difference between some set (stabilisation) temperature and the actual temperature of the LD, this design was not suitable to control the Peltier devices which require a continuous flow of current to produce the Peltier effect. Consequently the present thermal stabilisation scheme can drift as the

ambient temperature changes. The rather good temperature stabilisation reported was because the laboratory temperature did not change drastically during the course of the experiments. In hindsight, a more suitable temperature controller was required.

To summarize this sub-section, Table C.2 summarises the different parameters of the HL7806G relevant in defining both the operational range and limits of the LD when employed to implement the pseudo-heterodyne-signal processing scheme.

Parameter	HL7806G experimental values	Other Hitachi laser diodes	Values obtained by others	References
DC spectral current dependence	7.1 pm/mA (-3.5 GHz/mA)			
AC spectral current dependence	4.9 pm/mA (-2.4 GHz/mA) at 1 kHz	HL7801E	4.6 pm/mA (-2.3 GHz/mA)	Chen et al., 1988
DC spectral temperature dependence	0.06 nm/°C (-29 GHz/°C)	HL7801E	0.07 nm/°C (-34 GHz/°C)	Chen et al., 1988
			0.06 nm/°C (-29 GHz/°C) 10°C-30°C range	Ohba et al., 1989
Coherence length	~2 m	HL7801	~5 m (from 20 MHz line-width)	Maystre & Dändliker, 1989

Table C.2: The measured parameters for the HL7806G laser diode used in this work compared with similar laser diodes used by others.

C.5 Phase Noise Due to the Band-Pass Filter

The band-pass filtering an electronic signal inadvertently introduced an additional phase to the input signal. Without loss of generality, assuming a two-beam approximation of the input optical signal, the electronic signal, prior to filtering can be expressed as

$$I_{r,AC} = A \cos(\omega_m t - \phi(t)_{\text{int}}) \quad \text{Eq. C.6}$$

where A is some voltage signal amplitude, ω_m the sawtooth angular modulation frequency and t time.

$$\phi(t)_{\text{int}} = \phi_{0,M} + \phi_M^A \sin(\omega_M t) \quad \text{Eq. C.7}$$

is the phase signal associated with the measurand M with $\phi_{0,M}$ as some initial time-independent phase, ϕ_M^A the phase-amplitude of the signal (depth of modulation) and ω_M angular frequency of the measurand-induced phase shifts. Using the identity,

$$\exp\left(i \cdot \left(r \cdot \sin[\phi]\right)\right) = \sum_{q=-\infty}^{+\infty} J_q(r) \exp\left(i \cdot \left(q \cdot [\phi]\right)\right) \quad \text{Eq. C.8}$$

where $J_q(r)$ are the Bessel function of the first kind of order q . Eq. C.6 can be expanded in terms of its Fourier components:

$$I_{r,AC} = \sum_{q=-\infty}^{+\infty} J_q(\phi_M^A) \cos\left[(\omega_m - q \omega_M)t - \phi_{0,M}\right] \quad \text{Eq. C.9}$$

Eq. C.9 indicates that the measurand-induced phase signal, $\phi(t)_{\text{int}}$, is manifested in the side bands around the modulation frequency. These side bands will consequently encounter different electronic phase shift due to the band-pass filter depending on its distance in the frequency domain from the modulation frequency, expressed by $\omega_{\text{saw}} - q \omega_M$. Typically the first harmonic of the measurand-induced phase signal dominated the other harmonics and hence usually only two major sidebands in $I_{r,AC}$ were important

In a bandwidth of about 100 Hz around the centre of the pass-band of the for the unity-Q 1-kHz band-pass amplifier described in Chapter 6, the amount of electronic phase shift was approximately linear with changes in frequency. The phase/frequency sensitivity for the unity Q band-pass amplifier was about $4 \times 10^{-4} \times 2\pi/\text{Hz}$. The phase shift introduced by the band-pass filter can be considered constant for as long as the frequency spectrum of the measurand-induced phase signal was constant. Hence, when the dominant signal frequency varied from one situation to another, additional phase error can be expected. This phase error can be below 10^{-3} of a fringe for a signal frequency change of up to 2 Hz. This frequency change can be more than adequate for temperature measurements but not necessarily for strain measurements. Using a band-pass filter with a wider bandwidth and with lower electronic-filter-order can reduced the associated phase shift. However enlarging the bandwidth increased the noise in the photo-detector and thereby reducing the minimum detectable optical intensity (Figure C.1).

C.6 Overall Phase Noise

Although the resolution of the phase recording scheme employed in this work was about 10^{-4} of a fringe, the actual useful phase resolution was limited by phase noise. The sources of phase noise have been described above. The amount of phase noise depends on the FSR of the sensor. In the case of *HibiGrat*, the total expected phase noise was calculated to be 0.007 RMS of a fringe. This calculated value was obtained by assuming an RMS 0.001 °C variation in the LD temperature (0.005 of a fringe), moderate variation in the optical length of the lead-in fibre (0.001 RMS of a fringe - 10 % of the maximum value described in section 2), typical power supply noise in the LD drive circuit (0.005 RMS + 0.002 RMS of a fringe), and about 2 Hz variation in the dominant frequency of measurand-induced phase variations (0.001 RMS of a fringe). The experimentally measured phase noise varied from 0.005 to 0.009 (RMS) of a fringe for *HibiGrat* and was in agreement with the expected RMS phase noise.

The typical RMS phase noise for *HibiGrat* recently described was predominantly due to that induced by the electronic noise in the LD power supply and variations in the LD temperature. Reduced phase noise can be achieved with low-noise LD power supply and with greater stability of the LD temperature. Achieving greater stability in the LD temperature over long periods of time reduced the long-term phase drifts as well.

Appendix D:

Publications Resulting From This Thesis

Caranto, N. R. Y., Murphy, M. M. and Booth, D. J. (1994).

A Fusion-Spliced Birefringent Fabry-Pérot Interferometric Temperature Sensor, *Proc. 19th Australian Conference on Optical Fibre Technology (Melbourne, Victoria, Australia, December)*.

Caranto, N. R. Y., Murphy, M. M. and Booth, D. J. (1994).

A Birefringent Fabry-Pérot Interferometer for Temperature Sensing, *Proc. 6th Asia Pacific Physics Conference & 11th Australian Institute of Physics Congress: BrisPhys '94 (Brisbane, Queensland, Australia, July)*.

Kaddu, S. C., Caranto, N. R. Y., Murphy, M. M., Collins, S. F. and Booth, D. J. (1993).

Construction of Fibre Fabry-Pérot Sensors for Temperature or Strain Measurement, *Proc. 18th Australian Conference on Optical Fibre Technology, 245 - 248 (Wollongong, New South Wales, Australia, December)*.

Caranto, N. R. Y., Kaddu, S. C., Szajman, J., Murphy, M. M., Collins, S. F. and Booth, D. J. (1993).

An optical fibre thin film thickness monitor, *Measurement Science and Technology*, 4(8), 865 - 869.

Caranto, N. R. Y., Kaddu, S. C., Szajman, J., Murphy, M. M., Collins, S. F. and Booth, D. J. (1993).

An optical fibre thin film thickness monitor, *Engineering Optics*, 6(4), 451 - 455 (1993).

Caranto, N. R. Y., Kaddu, S. C., Szajman, J., Murphy, M. M., Collins, S. F. and Booth, D. J. (1992).

An optical-fibre-based thin film thickness monitor, *Proc. International Conference on Physics and Technology in the 1990's (Quezon City, Philippines)*.

Appendix E:

References

- Alavie, A. T., Karr, S. E., Othonos, A. and Measures, R. M. (1993).**
A Multiplexed Bragg Grating Fiber Laser Sensor System, *IEEE Photonics Technology Letters*, 5(9), 1112-1114.
- Alcoz, J. J., Lee, C. E. and Taylor, H. F. (1990).**
Embedded Fiber-Optic Fabry-Pérot Ultrasound Sensor, *IEEE Transactions on Ultrasonics, Ferroelectrics and Frequency Control*, 37(4), 302-306.
- An, S. and Sipe, J. E. (1992).**
Polarization Aspects of Two-Photon Photosensitivity in Birefringent Optical Fibers, *Optics Letters*, 17(7), 490-492.
- Anderson, D. J. and Jones, J. D. C. (1992).**
Optothermal Modulation of Diode Lasers, *Proceedings of the 8th International Conference on Optical Fiber Sensors, Monterey, U.S.A., 22-25.*
- Anderson, D. Z., Mizrahi, V., Erdogan, T. and White, A. E. (1993).**
Production of In-Fibre Gratings Using a Diffractive Optical Element, *Electronics Letters*, 29(6), 566-588.
- Atkinson, K. E. (1989).**
An Introduction to Numerical Analysis, 2nd edn., John Wiley & Sons, New York.
- Baldini, F. and Mignani, A. G. (1994).**
In-Vivo Biomedical Monitoring by Fiber Optic Systems, *Proceedings of the 10th International Conference on Optical Fiber Sensors, Glasgow, Scotland, 80-89.*
- Ball, G. A., Morey, W. W. and Cheo, P. K. (1993).**
Single- and Multipoint Fiber-Laser Sensors, *IEEE Photonics Technology Letters*, 5(2), 267-270.
- Ballard, S. S. and Browder, J. S. (1986).**
Thermal Properties of Optical Crystals, *CRC Handbook of Laser Science and Technology: Volume 4: Optical Materials, Part 2: Properties*, Weber, M. J. (ed.), CRC Press, Florida.
- Bardal, S., Kamal, A. and Russell, P. St. J. (1992).**
Photo-induced Birefringence in Optical Fibers: A Comparative Study of Low-Birefringence and High-Birefringence Fibers, *Optics Letters*, 17(6), 411-413.
- Barlow, A. J. and Payne, D. N. (1983).**
The Stress-Optic Effect in Optical Fibers, *IEEE Journal of Quantum Electronics*, QE-19(5), 834-839.

Beals, M. D. (1970).

Single-Crystal Titanates and Zirconates, *High Temperature Oxides: Part II*, Alper, A. M. (ed.), Academic Press, New York, U. S. A.

Beheim, G., Fritsch, K., Flatico, J. M. and Massood, T. A. (1989).

Silicon-Etalon Fiber-Optic Temperature Sensor, *Proceedings of the Society of Photo-Optical Instrumentation Engineers*, 1169, 504-511.

Benham, P. P. and Warnock, F. V. (1976).

Mechanics of Solids and Structures, Pittman Publishing, London, U. K.

Bennett, J. M., Pelletier, E., Albrand, G., Borgogno, J. P., Lazarides, B., Carniglia, C. K., Schmell, R. A., Allen, T. H., Tuttle-Hart, T., Guenther, K. H. and Saxer, A. (1989).

Comparison of the Properties of Titanium Dioxide Films Prepared by Various Techniques, *Applied Optics*, 28(15), 3303-3317.

Berkoff, T. A. and Kersey, A. D. (1992).

Passive Phase Interrogation and Multiplexing of Two-Mode Fiber Strain Sensors for Smart Structures Systems, *Proceedings of the First European Conference on Smart Structures and Materials, Glasgow, Scotland*, 39-43.

Berkoff, T. A., Kersey, A. D. and Moeller, R. P. (1990).

Novel Analog Phase Tracker for Interferometric Fiber Optic Sensor Applications, *Proceedings of the Society of Photo-Optical Instrumentation Engineers*, 1367, 53-57.

Bertholds, A. and Dändliker, R. (1987).

Deformation of Single-Mode Optical Fibers Under Static Longitudinal Stress, *Journal of Lightwave Technology*, LT-5(7), 895-900.

Bertholds, A. and Dändliker, R. (1988).

Determination of the Individual Strain-Optic Coefficients in Single-Mode Optical Fibers, *Journal of Lightwave Technology*, 6(6), 17-20.

Bhatia, V., Campbell, D., Claus, R. O. and Vengsarkar, A. M. (1997).

Simultaneous Strain and Temperature Measurement with Long Period Gratings, *Optics Letters*, 22(9), 648-650.

Bhatia, V., Murphy, K. A., Claus, R. O., Jones, M. E., Grace, J. L., Tran, T. A. and Greene, J. A. (1996).

Optical Fibre Based Absolute Extrinsic Fabry-Pérot Interferometric Sensing System, *Measurement Science and Technology*, 7, 58-61.

Bock, W. J. and Eftimov, T. A. (1994).

Simultaneous Hydrostatic Pressure and Temperature Measurement Employing an LP₀₁-LP₁₁ Fiber-Optic Polarization-Sensitive Intermodal Interferometer, *IEEE Transactions on Instrumentation and Measurement*, 43(2), 337-340.

Bock, W. J., Urbanczyk, W., Buczynski, R. and Domanski, A. W. (1994).

Cross-Sensitivity Effect in Temperature-Compensated Sensors Based on Highly Birefringent Fibers, *Applied Optics*, 33(25), 6078-6083.

Bohnert, K. and Nehring, J. (1989).

Fiber-Optic Sensing of Voltages by Line Integration of the Electric Field, *Optics Letters*, 14(5), 290-292.

Born, M. and Wolf, E. (1980).

Principles of Optics: Electromagnetic Theory of Propagation, Interference and Diffraction of Light, 6th edn., Pergamon Press.

Borrelli, N. F. and Miller, R. A. (1968).

Determination of the Individual Strain-Optic Coefficients of Glass by an Ultrasonic Technique, *Applied Optics*, 7(5), 745-750.

Brady, G. P., Kalli, K., Webb, J. D., Jackson, D. A., Reekie, L. and Archambault, J. L. (1995).

Simultaneous Interrogation of Interferometric and Bragg Grating Sensors, *Optics Letters*, 20(11), 1340-1242.

Brady, G. P., Kalli, K., Webb, J. D., Jackson, D. A., Reekie, L. and Archambault, J. L. (1997).

Simultaneous Measurement of Strain and Temperature Using First- and Second-Order Diffraction Wavelengths of Bragg Grating, *IEE Proceedings: Optoelectronics*, 144(3), 156-161.

Butter, C. D. and Hocker, G. B. (1978).

Fiber Optics Strain Gauge, *Applied Optics*, 17(18), 2867-2869.

Campbell, M., Zheng G., Wallace, P. A. and Holmes-Smith, A. S. (1996).

Reflectometric Birefringent Fiber Sensor for Absolute and Relative Strain Measurement, *Proceedings of the Society of Photo-Optical Instrumentation Engineers*, 2839, 254-259.

Caranto, N. R. Y., Kaddu, S. C., Szajman, J., Murphy, M. M., Collins, S. F. and Booth, D. J. (1993).

An Optical Fibre Thin Film Thickness Monitor, *Measurement Science and Technology*, 4(8), 865-869.

Carrara, S. L. A. (1990).

Birefringent-Fiber Splice Alignment, *Proceedings of the Society of Photo-Optical Instrumentation Engineers*, 1267, 24-28.

Carrara, S. L. A., Kim, B. Y. and Shaw, H. J. (1986).

Elasto-Optic Alignment of Birefringent Axes in Polarization-Holding Optical Fiber, *Optics Letters*, 11(7), 470-472.

Chardon, D. and Huard, S. J. (1988).

Simultaneous Measurement of Temperature and Pressure with a Single-Mode Fiber, *Proceedings of the 5th International Conference on Optical Fiber Sensors, New Orleans, U.S.A.*, Postconference edn., Optical Society of America Technical Digest Series, vol. 2, parts 1 & 2, 495-501.

Chen, J., Ishii, Y. and Murata, K. (1988).

Heterodyne Interferometry With a Frequency-Modulated Laser Diode, *Applied Optics*, 27(1), 124-128.

Chiang, K. S. and Tsuchida, H. (1988).

Dual-Sensor Technique for Extending the Dynamic Range of a Fiber-Optic Interferometric Sensor, *Optics Letters*, 13(10), 850-852.

Chien, P. Y. (1992).

Open-Loop Fiber Optic Gyroscope With Wide Dynamic Range, *Review of Scientific Instruments*, 63(7), 3783-3784.

Clark, G. L., Heflinger, L. O. and Roychoudhuri, C. (1982).

Dynamic Wavelength Tuning of Single-Mode GaAlAs Lasers, *IEEE Journal of Quantum Electronics*, QE-18(2), 199-204.

Cole, J. H., Danver, B. A. and Bucaro, J. A. (1982).

Synthetic-Heterodyne Interferometric Demodulation, *IEEE Journal of Quantum Electronics*, QE-18(4), 694-697.

- Corke, M., Kersey, A. D. and Jackson, D. A. (1985).**
Combined Michelson and Polarimetric Fibre-Optic Interferometric Sensor, *Electronics Letters*, 21(4), 148-149.
- Corke, M., Kersey, A. D., Jackson, D. A. and Jones, J. D. C. (1983).**
All-Fibre 'Michelson' Thermometer, *Electronics Letters*, 19(13), 471-373.
- Corke, M., Kersey, A. D., Jackson, D. A. and Jones, J. D. C. (1984).**
Remote Temperature Sensing Using Polarisation-Preserving Fibre, *Electronics Letters*, 20(2), 67-69.
- Crossley, S. D. (1994).**
Commercially Available Fibre Optic Sensors - 10 Years of Progress?, *Proceedings of the 10th International Conference on Optical Fiber Sensors, Glasgow, Scotland*, 249-252.
- Dakin, J. and Culshaw, B. [eds.] (1988).**
Optical Fiber Sensors: Principles and Components, Vol. I & II, Artech House, Boston.
- Dakin, J. P., Ecke, W., Rothardt, M., Schauer, J. Usbeck, K. and Willsch, R. (1997).**
New Multiplexed Scheme for Monitoring Fiber Optic Bragg Grating Sensors in the Coherence Domain, *Proceedings of the 12th International Conference on Optical Fiber Sensors, Williamsburg, Virginia, U.S.A.*, 31-34.
- Dandridge, A. and Goldberg, L. (1982).**
Current-Induced Frequency Modulation in Diode Lasers, *Electronics Letters*, 18(7), 302-304.
- Dandridge, A. and Tveten, A. B. (1981).**
Phase Noise of Single-Mode Diode Lasers in Interferometric Systems, *Applied Physics Letters*, 38(7), 530-532.
- Dandridge, A., Tveten, A. B. and Giallorenzi, T. G. (1983).**
Homodyne Demodulation Scheme for Fiber Optic Sensors Using Phase Generated Carrier, *IEEE Journal of Quantum Electronics*, QE-18(10), 1647-1653.
- Dandridge, A., Tveten, A. B., Miles, R. O., Jackson, D. A. and Giallorenzi, T. G. (1981).**
Single-Mode Diode Laser Phase Noise, *Applied Physics Letters*, 38(2), 77-78.
- Davis, M. A. and Kersey, A. D. (1995).**
Application of a Fiber Fourier Transform Spectrometer to the Detection of Wavelength-Encoded Signals from Bragg Grating Sensors, *Journal of Lightwave Technology*, 13(7), 1289-1295.
- Davis, M. A. and Kersey, A. D. (1997).**
Simultaneous Measurement of Temperature and Strain Using Fibre Grating and Brillouin Scattering, *IEE Proceedings in Optoelectronics*, 144(3), 151-155.
- Day, G. W. and Rose, A. H. (1988).**
Faraday Effect Sensors: The State of the Art, *Proceedings of the Society of Photo-Optical Instrumentation Engineers*, 985, 138-150.
- del Pozo, J. M. and Díaz, L. (1992).**
Method for the Determination of Optical Constants of Thin Films: Dependence on Experimental Uncertainties, *Applied Optics*, 31(22), 4474-4481.

- Domanski, A. W., Gorecki, A. and Swillo, M. (1995).**
Dynamic Strain Measurements by Use of the Polarimetric Fiber Optic Sensors, *Proceedings of the IEEE Instrumentation/Measurement Technology Conference. Integrating Intelligent Instrumentation and Control (IMTC) Proceedings (Cat. No.95CH35783)*, 816-819.
- Dunphy, J., Ball, G., D'Amato, F., Ferraro, P., Inserra, S., Vannucci, A. and Varasi, M. (1993).**
Instrumentation Development in Support of Fibre Grating Sensor Arrays, *Proceedings of the Society of Photo-Optical Instrumentation Engineers*, 2071, 2-11.
- Economou, G., Youngquist, R. C. and Davies, D. E. (1986).**
Limitations and Noise in Interferometric Systems Using Frequency Ramped Single-Mode Diode Lasers, *Journal of Lightwave Technology*, LT-4(11), 1601-1608.
- Egalon, C. O. and Rogowski, R. S. (1992).**
A Model of an Axially Strained Weakly Guiding Optical Fiber Modal Pattern, *Optical Engineering*, 31(6), 1332-1339.
- Egorov, S. A., Mamaev, A. N. and Polyantsev (1995).**
Spectral Signal Processing in Intrinsic Interferometric Sensors Based on Birefringent Polarization-Maintaining Optical Fibers, *Journal of Lightwave Technology*, LT-3(1), 83-92.
- Eickoff, W. (1981).**
Temperature Sensing by Mode-Mode Interference in Birefringent Optical Fibers, *Optics Letters*, 6(4), 204-205.
- Eickoff, W. (1982).**
Stress-induced Single-Polarization Single-Mode Fiber, *Optics Letters*, 7(12), 629-631.
- Erdogan, T. and Mizrahi, V. (1994).**
Characterization of UV-Induced Birefringence in Photosensitive Ge-Doped Silica Optical Fibers, *Journal of the Optical Society of America B*, 11(10), 2100-2105.
- Farahi, F., Jones, J. D. C. and Jackson, D. A. (1988b).**
An Extended Range Fibre-Optic Temperature Sensor, *International Journal of Optoelectronics*, 3(3), 237-245.
- Farahi, F., Newson, T. P., Leilabady, P. A., Jones, J. D. C. and Jackson, D. A. (1988a).**
A Multiplexed Remote Fibre Optic Fabry-Pérot Sensing System, *International Journal of Optoelectronics*, 3(1), 79-88.
- Farahi, F., Webb, D. J., Jones, J. D. C. and Jackson, D. A. (1990b).**
Simultaneous Measurement of Temperature and Strain Using Fibre Optic Interferometric Sensors, *Journal of Lightwave Technology*, 8(2), 138-142.
- Farahi, F., Webb, D. J., Jones, J. D. C. and Jackson, D. A. (1990a).**
Simultaneous Measurement of Temperature and Strain Using Fibre Optic Interferometric Sensors, *Proceedings of the Society of Photo-Optical Instrumentation Engineers*, 1314, 270-277.
- Feng, T., YiZun, W. and PeiDa, Y. (1990).**
Random Coupling theory of Single-Mode Optical Fibers, *Journal of Lightwave Technology*, 8(8), 1235-1242.
- Ferreira, L. A., Lobo Ribiero, A. B., Santos, J. L. and Farahi, F. (1996).**
Simultaneous Measurement of Displacement and Temperature Using Low Finesse Cavity and a Fiber Bragg Grating, *IEEE Photonics Technology Letters*, 8(11), 1519-1521.

- Flavin, D. A., McBride, R. and Jones, J. D. C. (1993).**
Simultaneous Measurement of Temperature and Strain by Dispersive Fourier Transform Spectroscopy, *Proceedings of the 9th International Conference on Optical Fiber Sensors, Florence, Italy*, 333-336.
- Flavin, D. A., McBride, R. and Jones, J. D. C. (1997).**
Absolute Measurement of Wavelengths From a Multiplexed In-Fibre Bragg Grating Array by Short-Scan Interferometry, *Proceedings of the 12th International Conference on Optical Fiber Sensors, Williamsburg, Virginia, U.S.A.*, 24-27.
- Flavin, D. A., McBride, R., Jones, J. D. C., Burnett, J. G. and Greenaway, A. H. (1994).**
Combined Temperature and Strain Measurement with a Dispersive Optical Fibre Fourier Transform Spectrometer, *Optics Letters*, 19(24), 2167-2169.
- Fleming, J. W. (1986).**
Optical Glasses, *CRC Handbook of Laser Science and Technology: Volume 4: Optical Materials, Part 2: Properties*, Weber, M. J. (ed.), CRC Press, Florida.
- Franks, R. B., Torruellas, W. and Youngquist, R. C. (1985).**
Birefringent Stress Location Sensor, *Proceedings of the Society of Photo-Optical Instrumentation Engineers*, 586, 84-89.
- Franks, R. B., Torruellas, W. and Youngquist, R. C. (1986).**
An Extended Fibre Optic Stress Location Sensor, *Optica Acta*, 33(12), 1505-1518.
- Fürstenau, N., Schmidt, W. and Goetting, H. C. (1992).**
Simultaneous Interferometric and Polarimetric Strain Measurements on Composites using a Fiber-Optic Strain Gauge, *Applied Optics*, 31(16), 2987-2993.
- Gauthier, R. C. and Turgeon, S. (1993).**
Birefringent Sensor Enhancement by Wavelength Multiplexing, *Optics and Laser Technology*, 26(6), 377-381.
- Gerges, A. S., Farahi, F., Newson, T. P., Jones, J. D. C. and Jackson, D. A. (1987).**
An Interferometric Fiber Optic Sensor Using a Short Coherence Length Source, *Electronics Letters*, 23(21), 1110-1111.
- Giallorenzi, T. G., Bucaro, J. A., Dandridge, A., Sigel, G. H. Jr., Cole, J. H., Rashleigh, S. C. and Priest, R. G. (1982).**
Optical Fiber Sensor Technology, *IEEE Journal of Quantum Electronics*, QE-18(4), 626-665.
- Giles, I. P., Uttam, D., Culshaw, B. and Davies, D. E. N (1983).**
Coherent Optical-Fibre Sensors with Modulated Laser Sources, *Electronics Letters*, 19(1), 14-15.
- Giulianelli, L. C., Buckman, A. B., Walser, R. M. and Becker, M. F. (1994).**
Digital Demodulation Scheme for Wide Dynamic Range Measurements of a Fiber Optic Interferometer, *Proceedings of the Society of Photo-Optical Instrumentation Engineers*, 2191, 314-323.
- Goldberg, L., Taylor, H. F. and Weller, J. F. (1981).**
Time-Dependent Thermal Effects in Current-Modulated Semiconductor Lasers, *Electronics Letters*, 17(14), 497-499.
- Gottlieb, M. (1986).**
Elasto-optic Materials, *CRC Handbook of Laser Science and Technology: Volume 4: Optical Materials, Part 2: Properties*, Weber, M. J. (ed.), CRC Press, Florida.

Grossman, B. and Costandi, W. (1992).

Fiber Optic Sensor for the Simultaneous Detection of Strain and Temperature, *Proceedings of the Society of Photo-Optical Instrumentation Engineers*, 1798, 175-185.

Gusmeroli, V. and Martinelli, M. (1994).

Non-Incremental Interferometric Fiber-Optic Measurement Method for Simultaneous Detection of Temperature and Strain, *Optics Letters*, 19(24), 2164-2166.

Hecht, E. (1987)

Optics, 2nd edn., Addison-Wesley Publishing Company, Reading, Massachusetts, U.S.A.

Henderson, P. J., G. F., Rao, Y. J., Jackson, D. A., Zhang, L. and Bennion, I. (1997).

Simultaneous Dynamic-Strain and Temperature Monitoring Using a Wavelength Multiplexed Fibre- Fabry-Pérot Array with Low-Coherence Interrogation, *Proceedings of the 12th International Conference on Optical Fiber Sensors, Williamsburg, Virginia, U.S.A.*, 56-43.

Herzog, J. P. and Meyrueis, P. (1990).

Interferometric Optical Fiber Pressure Sensor with Temperature Compensation, *Proceedings of the Society of Photo-Optical Instrumentation Engineers*, 1267, 134-141.

Hill, K. O., Bilodeau, F., Malo, B. and Johnson, D. C. (1991).

Birefringent Photosensitivity in Monomode Optical Fibres: Application to External Writing of Rocking Filters, *Electronics Letters*, 27(11), 1548-1550.

Hill, K. O., Malo, B., Bilodeau, F., Johnson, D. C. and Albert, J. (1993).

Bragg Gratings Fabricated in Monomode Photosensitive Optical Fiber by UV Exposure Through a Phase Mask, *Applied Physics Letters*, 62(10), 1035-1037.

Hocker, G. B. (1979).

Fiber-Optic Sensing of Pressure and Temperature, *Applied Optics*, 18(9), 1445-1448.

Hogg, D., Janzen, D., Valis, T. and Measures, R. M. (1991).

Development of a Fiber Fabry-Pérot Strain Gauge, *Proceedings of the Society of Photo-Optical Instrumentation Engineers*, 1588, 300-307.

Hogg, W. D., Turner, R. D. and Measures, R. M. (1989).

Polarimetric Fiber Optic Structural strain Sensor Characterisation, *Proceedings of the Society of Photo-Optical Instrumentation Engineers*, 1170, 542-549.

Huang, S. Y., Blake, J. N. and Kim, B. Y. (1990).

Perturbation Effects on Mode Propagation in Highly Elliptical Core Two-Mode Fibers, *Journal of Lightwave Technology*, 8(1), 23-33.

Hughes, R. and Priest, R. (1979).

Thermally Induced Optical Phase Effects in Fiber Optic Sensors, *Applied Optics*, 19(9), 1477-1483.

Hurwitz, H. Jr. and Jones, R. C. (1941).

A New Calculus for the Treatment of Optical Systems: I. Proof of Three General Equivalence Theorems, *Journal of the Optical Society of America*, 31, 493-503.

Hymans, A. J. and Lait, J. (1960).

Analysis of a Frequency-Modulated Continuous-Wave Ranging Systems, *Proceedings of the Institute of Electrical Engineers*, (Paper No. 3264 E, July), 365- 372.

Inci, M. N., Kidd, S. R., Barton, J. S. and Jones, J. D. C. (1992).
Fabrication of Single-Mode Fibre Optic Fabry-Pérot Interferometers, Using Fusion Spliced Titanium Dioxide Optical Coatings, *Measurement Science and Technology*, 3, 678-684.

Inci, M. N., Kidd, S. R., Barton, J. S. and Jones, J. D. C. (1993).
High Temperature Miniature Fibre Optic Interferometric Thermal Sensors, *Measurement Science and Technology*, 4, 382-387.

Ito, M. and Kimura, T. (1980).
Carrier Density Dependence of Refractive Index in AlGaAs Semiconductor Lasers, *IEEE Journal of Quantum Electronics*, QE-16(9), 910-911.

Izumita, H., Horiguchi, T. and Kurashima, T. (1997).
Distributed Sensing Techniques Using Brillouin Scattering, *Proceedings of the 12th International Conference on Optical Fiber Sensors, Williamsburg, Virginia, U.S.A.*, 316-319.

Jackson, D. A. (1994).
Fibre Optic Sensors, *Measurement Science and Technology*, 5, 612-638.

Jackson, D. A. and Jones, J. D. C. (1986).
Fibre Optic Sensors, *Optica Acta*, 33(12), p1469-1503.

Jackson, D. A., Kersey, D. A., Corke, M. and Jones, J. D. C. (1982).
Pseudo-Heterodyne Detection Scheme for Optical Interferometers, *Electronics Letters*, 18(25), 1081-1083.

Jackson, J. D. (1975).
Classical Electrodynamics, 2nd edn., John Wiley and Son, Inc., New York, U.S.A.

Jacobsen, G., Olesen, H., Birkedahl, F. and Tromborg (1982).
Current/Frequency-Modulation Characteristics for Directly Optical Frequency-Modulated Injected Lasers at 830 nm and 1.3 μm , *Electronics Letters*, 18(20), 874-876.

James, S. W., Dockney, M. L. and Tatam, R. P. (1996).
Simultaneous Independent Temperature and Strain Measurement Using In-Fibre Bragg Grating Sensors, *Electronic Letters*, 32(12), 1133-1134.

Jerrard, H. G. (1982).
Modern Description of Polarized Light: Matrix Methods, *Optics and Laser Technology*, 14(6), 309-319.

Jeunhomme, L. B. (1990).
Single-Mode Fiber Optics: Principles and Applications, 2nd edn., Marker Dekker, New York, U.S.A.

Jin, W., Mitchie, W. C., Thursby, G., Konstantaki, M. and Culshaw, B. (1996).
Simultaneous Strain and Temperature Recovery: Error Analysis, *Proceedings of the 11th International Conference on Optical Fiber Sensors, Sapporo, Japan*, 116-119.

Jin, X. D., Sirkis, J. S. and Venkateswarn. (1997).
Simultaneous Measurement of Two Strain Components in Composite Structures Using Embedded Fiber Sensors, *Proceedings of the 12th International Conference on Optical Fiber Sensors, Williamsburg, Virginia, U.S.A.*, 44-47.

Jones, J. D. C. (1997).
Review of Fibre Sensors Techniques for Temperature-Strain Discrimination, *Proceedings of the 12th International Conference on Optical Fiber Sensors, Williamsburg, Virginia, U.S.A.*, 316-319.

Jones, R. C. (1941).

A New Calculus for the Treatment of Optical Systems: I. Description of the Calculus, *Journal of the Optical Society of America*, 31, 488-493.

Kaddu, S. C. (1996).

Low-Coherence Fibre Fabry-Pérot Sensors Suitable for Multiplexed Strain Measurement, *Ph. D. Thesis, Victoria University of Technology, Melbourne, Australia*.

Kaddu, S. C., Caranto, N. R. Y., Murphy, M. M., Collins, S. F. and Booth, D. J. (1993).

Construction of Fibre Fabry-Pérot Sensors for Temperature or Strain Measurement, *Proceedings of the 18th Australian Conference on Optical Fibre Technology, Wollongong, NSW, Australia*, 245-248.

Kaminow, I. P. (1981).

Polarization in Optical Fibers, *IEEE Journal of Quantum Electronics*, QE-17(1), 15-22.

Kaminow, I. P. and Ramaswamy, V. (1979).

Single-Polarization Optical Fibers: Slab Model, *Applied Physics Letters*, 34(4), 268-270.

Kanellopoulos, S. E., Handerek, V. A. and Rogers, A. J. (1994).

Simultaneous Strain and Temperature Sensing Employing a Photogenerated Polarisation Coupler and Low-Order Modes in an Elliptically Cored Optical Fibre, *Electronics Letters*, 30(21), 1786-77.

Kanellopoulos, S. E., Handerek, V. A. and Rogers, A. J. (1995).

Simultaneous Strain and Temperature Sensing with Photogenerated In-Fibre Gratings, *Optics Letters*, 20(3), 333-335.

Kanellopoulos, S. E., Valente, L. C. G., Handerek, V. A. and Rogers, A. J. (1991).

Photorefractive Polarisation Couplers in Elliptical Core Optical Fibres, *IEEE Photonics Technology Letters*, 3(9), 806-809.

Katsuyama, T., Matsumura, H. and Suganuma, T. (1983).

Propagation Characteristics of Single Polarization Fibers, *Applied Optics*, 22(11), 1748-1753.

Kersey, A. D. (1990).

Recent Progress in Interferometric Fibre Sensor Technology, *Proceedings of the Society of Photo-Optical Instrumentation Engineers*, 1367, 2-12.

Kersey, A. D. and Morey, W. W. (1993).

Multi-Element Bragg-Grating Based Fibre-Laser Strain Sensor, *Electronics Letters*, 29(11), 964-966.

Kersey, A. D., Berkoff, T. A. and Morey W. W. (1992).

Fiber-Grating Based Strain Sensor With Phase Sensitive Detection, *Proceedings of the First European Conference on Smart Structures and Materials, Glasgow, U.K.*, 61-67.

Kersey, A. D., Dandridge, A. and Burns, W. K. (1986).

Two-Wavelength Fibre Gyroscope With Wide Dynamic Range, *Electronics Letters*, 22(18), 935-937.

Kersey, A. D., Davis, M. A. and Marrone, M. J. (1989).

Differential Polarimetric Fiber-Optic Sensor Configuration with Dual Wavelength Operation, *Applied Optics*, 28(2), 204-206.

Kersey, A. D., Davis, M. A., Patrick, H. J., LeBlanc, M., Koo, K. P., Askins, C. G., Putnam, M. A. and Friebele, E. J. (1997).

Fiber Grating Sensors, *Journal of Lightwave Technology*, 15(8), 1442-1463.

- Kersey, A. D., Jackson, D. A. and Corke, M. (1984).**
Linearised Polarimetric Optical Fibre Sensor Using a 'Heterodyne-Type' Signal Recovery Scheme, *Electronics Letters*, 20(5), 209-211.
- Kidd, S. R., Barton, J. S., Inci, M. N. and Jones, J. D. C. (1994).**
Unsteady Gas Temperature Measurement Using an Ultra-Short Optical Fibre Fabry-Pérot Interferometer, *Measurement Science and Technology*, 5, 816-822.
- Kihara, T. and Yokomori, K. (1992).**
Simultaneous Measurement of the Refractive Index and Thickness of Thin Films by s-polarized Reflectances, *Applied Optics*, 31(22), 4482-4487.
- Kim, B. K., Yun, S. H., Hwang, I. K. and Kim, B. Y. (1996).**
Nonlinear Response of Two-Mode Fibre-Optic Interferometer to Strain, *Proceedings of the 11th International Conference on Optical Fiber Sensors, Sapporo, Japan*, 112-115.
- Kim, B. Y., Blake, J. N., Huang, S. Y. and Shaw, H. J. (1987).**
Use of Highly Elliptical Core Fibers for Two-Mode Fiber Devices, *Optics Letters*, 12(9), 729-731.
- Kim, K., Ismail, Y. and Springer, G. S. (1993b).**
Measurement of Strain and Temperature with Embedded Intrinsic Fabry-Pérot Optical Fiber Sensors, *Journal of Composite Materials*, 27(17), 1663-1677.
- Kim, K., Kollár, L. and Springer, G. S. (1993a).**
A Model of Embedded Fiber Optic Fabry-Pérot Temperature and Strain Sensors, *Journal of Composite Materials*, 27(17), 1618-1662.
- Kim, Y. and Neikirk. (1995).**
Micromachined Fabry-Pérot Cavity Pressure Transducer, *IEEE Photonics Technology Letters*, 7(12), 1471-1473.
- Kliger, D. S., Lewis, J. W. and Randall, C. E. (1990).**
Polarized Light in Optics and Spectroscopy, Academic Press, San Diego, U.S.A.
- Kobayashi, S., Yamamoto, Y., Ito, M. and Kimura, T. (1982).**
Direct Frequency Modulation in AlGaAs Semiconductor Lasers, *IEEE Journal of Quantum Electronics*, QE-18(4), 582-595.
- Koch, A. and Ulrich, R. (1991).**
Fiber-Optic Displacement Sensor with 0.02 μm Resolution by White-Light Interferometry, *Sensors and Actuators A*, A25-A27, 201-207.
- Koo, K. P. and Kersey, A. D. (1995).**
Bragg Grating-Based Laser Sensors Systems with Interferometric Interrogation and Wavelength Division Multiplexing, *Journal of Lightwave Technology*, 13(7), 1243-1249.
- Krause, J. T., Kurkjian, C. R. and Paek, U. C. (1981a).**
Strength of Fusion Splices for Fibre Lightguides, *Electronics Letters*, 17(6), 232-233.
- Krause, J. T., Kurkjian, C. R. and Paek, U. C. (1981b).**
Tensile Strengths > 4 GPa for Lightguide Fusion Splices, *Electronics Letters*, 17(21), 812-813.

Krug, P. A., Eggleton, B. and Coll, P. (1993).

Growth of Holographically Written Optical Fibre Bragg Gratings, *Proceedings of the 18th Australian Conference on Optical Fibre Technology, Wollongong, NSW, Australia*, 59-62.

Kuroda, Y., Abe Y., Kuwahara, H. and Yoshinaga K. (1985).

Field-Test of Fiber-Optic Voltage and Current Sensors, *Proceedings of the Society of Photo-Optical Instrumentation Engineers*, 586, 30-37.

Lagakos, N. Bucaro, J. A. and Jarzynski, J. (1981).

Temperature-Induced Optical Phase Shifts in Fibres, *Applied Optics*, 20(13), 2305-2308.

Lam, D. K. W. and Garside, B. K. (1981).

Characterisation of Single-Mode Optical Fiber Filters, *Applied Optics*, 20(3), 440-445.

Lancaster, D. (1975).

Active Filter Cookbook, Howard W. Sams & Co., Indianapolis, U.S.A.

Lauzon, J., Gagnon, D., LaRoche, S., Blouin, A. and Ouellette, F. (1992).

Dynamic Polarization Coupling in Elliptical-Core Photosensitive Optical Fibres, *Optics Letters*, 17(23), 1664-1666.

Lee, C. E. and Taylor, H. F. (1988).

Interferometric Sensors Using Internal Fiber Mirrors, *Proceedings of the 5th International Conference on Optical Fiber Sensors, New Orleans, U.S.A.*, 48-51.

Lee, C. E., Atkins, R. A. and Taylor, H. F. (1987).

Reflectively Tapped Optical Fibre Transverse Filters, *Electronics Letters*, 23(11), 596-598.

Lee, C. E., Atkins, R. A. and Taylor, H. F. (1988).

Performance of a Fiber-Optic Temperature Sensor from -200 to 1500 °C, *Optics Letters*, 13(11), 1038-1040.

Lee, C. E., Gibler, W. N., Atkins, R. A. and Taylor, H. F. (1992a).

In-line Fiber Fabry-Pérot Interferometer with High-Reflectance Internal Mirrors, *Proceedings of the 8th International Conference on Optical Fiber Sensors, Monterey, U.S.A.*, 105-108.

Lee, C. E., Gibler, W. N., Atkins, R. A., Alcoz, J. J., Taylor, H. F. and Kim, K. S. (1992b).

Fiber Optic Fabry-Pérot Sensors Embedded in Metals and in a Composite, *Proceedings of the 8th International Conference on Optical Fiber Sensors, Monterey, U.S.A.*, 368-371.

Lee, C. E., Taylor, H. F., Markus, A. M. and Udd, E. (1989).

Optical-Fiber Fabry-Pérot Embedded Sensor, *Optics Letters*, 14(21), 1225-1227.

Lefèvre, H. C., Desforges, F. X., Martin, P. and Simonpietri, P. (1990).

"Two-Mode²" Fiber Gauge for Dual Measurement of Temperature and Strain, *Proceedings of the 7th International Conference on Optical Fiber Sensors, Sydney, Australia*, 387-390.

Legoubin, S., Douay, M., Bernage, P., Niay, P., Boj S. and Delevaque E. (1995).

Free Spectral Range Variations Fabry-Pérot Filters Photowritten in Optical Fibres, *Journal of Optical Society of America A*, 12(8), 1687-1694.

Leilabady, P. A. (1987).

Optical Fiber Point Temperature Sensor, *Proceedings of the Society of Photo-Optical Instrumentation Engineers*, 838, 231-237.

Leilabady, P. A. and Corke, M. (1987).

All-Fiber-Optic Remote Sensing of Temperature Employing Interferometric Techniques, *Optics Letters*, 12(10), 772-774.

Leilabady, P. A., Jones, J. D. C. and Jackson, D. A. (1985).

Monomode Fiber-Optic Strain Gauge with Simultaneous Phase- and Polarization-State Detection, *Optics Letters*, 10(11), 576-578.

Leilabady, P. A., Jones, J. D. C. and Jackson, D. A. (1986a).

Combined Interferometric-Polarimetric Fibre Optic Sensor Capable of Remote Operation, *Optics Communications*, 57(2), 77-80.

Leilabady, P. A., Jones, J. D. C. and Jackson, D. A. (1986b).

A Dual Interferometer Implemented in Parallel on a Single Birefringent Monomode Optical Fibre, *Journal of Physics E: Scientific Instruments*, 19(2), 143-146.

Lemaire, P. J., Atkins, R. M., Mizrahi, R. M. and Reed, W. A. (1993).

High Pressure H₂ Loading as a Technique for Achieving Ultrahigh UV Photosensitivity and Thermal Sensitivity in GeO₂ Doped Optical Fibres, *Electronics Letters*, 29(13), 1191-1192.

Lequime, M. (1997).

Fiber Sensors for Industrial Applications, *Proceedings of the 12th International Conference on Optical Fiber Sensors, Williamsburg, Virginia, U.S.A.*, 66-71.

Lewin, A. C., Kersey, A. D. and Jackson, D. A. (1985).

Practical Sagnac Interferometer Based Fibre Optic Current Sensor, *IEE Proceedings: Part J*, 132(5), 271-275.

Liu, X. P., Spooncer, R. C. and Jones, B. E. (1991).

An Optical Fibre Displacement Sensor with Extended Range Using Two-Wavelength Referencing, *Sensors and Actuators A*, 25-27, 197-200.

Lui, T., Fernando, G. F., Zhang, L., Bennion, L, Rao, Y. J. and Jackson, D. A. (1997).

Simultaneous Strain and Temperature Measurement Using a Combined Fibre Bragg Grating/Extrinsic Fabry-Pérot Sensor, *Proceedings of the 12th International Conference on Optical Fiber Sensors, Williamsburg, Virginia, U.S.A.*, 40-43.

Luke, D. G., McBride, R., Lloyd, P., Burnett, J. G., Greenamway, A. H. and Jones, J. D. C. (1996).

Strain and Temperature Measurement in Composite-Embedded Highly-Birefringent Optical Fibre Using Mean and Differential Group Delay, *Proceedings of the 11th International Conference on Optical Fiber Sensors, Sapporo, Japan*, 200-203.

Ma, J., Tang, W. and Zhou, W. (1996).

Optical-Fiber-Sensor for Simultaneous Measurement of Pressure and Temperature: Analysis of Cross Sensitivity, *Applied Optics*, 35(25), 5206-5210.

Malvino, A. P. (1989).

Electronic Principles, 4th edn., McGraw-Hill Book. Co., New York, U.S.A.

Martens, G., Helzel, T. and Kordts, J. (1985).

Optical Detection of Respiration Motion and Heart Beats for Magnetic Resonance Imaging (MRI) Applications, *Proceedings of the Society of Photo-Optical Instrumentation Engineers*, 586, 250-259.

Martin, J. and Ouellette, F. (1994).

Novel Writing Technique of Long and Highly Reflective In-Fiber Gratings, *Electronics Letters*, 30(10), 811-812.

Martinelli, M. and De Maria, L. (1988).

Non-Incremental Coherent Optical Fiber Sensor, *Optics Letters*, 13(9), 779-781.

Mason, B., Valis, T. and Hogg, D. (1992).

Commercialization of Fiber-Optic Strain Gauge Systems, *Proceedings of the Society of Photo-Optical Instrumentation Engineers*, 1795, 215-222.

Matthews, C. T. and Sirkis, J. S. (1990).

The Interaction Mechanics of Interferometric Optical Fiber Sensors Embedded in a Monolithic Structure, *Proceedings of the Society of Photo-Optical Instrumentation Engineers*, 1370, 142-153.

Maystre, F. and Dändliker, R. (1989).

Polarimetric Resonator Sensor with High Sensitivity and Large Dynamic Ranges, *Optical Fiber Sensors*, Springer Proceedings in Physics, Arditty *et al.* (eds.), 44, 44-47.

McGarrity, C. and Jackson, D. A. (1996).

Determining Quasi-Static Measurands Without a Receiving Interferometer Using a Simple Dual-Wavelength Technique, *Proceedings of the Society of Photo-Optical Instrumentation Engineers*, 2839, 122-132.

McGarrity, C. and Jackson, D. A. (1998).

A Network for Large Numbers of Interferometric Sensors and Fiber Bragg Gratings with High Resolution and Extended Range, *Journal of Lightwave Technology*, 16(1), 54-65.

Measures, R. M. (1992).

Advances Toward Fiber Optic Based Smart Structures, *Optical Engineering*, 31(1), 34-47.

Meggitt, B. T., Palmer, A. W. and Grattan, K. T. V. (1988).

Fibre-Optic Sensors Using Coherence Properties: Signal Processing Aspects, *International Journal of Optoelectronics*, 3(6), 451-464.

Meltz, G. and Dunphy, J. R. (1988).

Twin-Core Fiber-Optic Strain and Temperature Sensor, *Proceedings of the 5th International Conference on Optical Fiber Sensors*, New Orleans, U.S.A., paper THFF6, 142.

Meltz, G., Morey, W. W. and Glenn, W. H. (1989).

Formation of Bragg Gratings in Optical Fibers by a Transverse Holographic Method, *Optics Letters*, 14(15), 823-825.

Meunier, C., Guerin, J. J., Lequime, M., Rioual, M., Noel, E., Eguiazabal, D., Gluery, D., Maurin, J. and Mongin R. (1994).

Industrial Prototype of a Fiber Optic Sensor Network for the Thermal Monitoring of the Turbogenerators of a Nuclear Power Plant, *Proceedings of the 10th International Conference on Optical Fiber Sensors*, Glasgow, Scotland, 238-244.

Michalske, T. A. and Bunker, B. C. (1984).

Slow Fracture Model Based on Strained Silicate Structure, *Journal of Applied Physics*, 58(10), 2686-2693.

Michie, W. C., Culshaw, B., Roberts, S. S. J. and Davidson, R. (1991).

Fibre Optic Technique for Simultaneous Measurement of Strain and Temperature Variations in Composite Materials, *Proceedings of the Society of Photo-Optical Instrumentation Engineers*, 1588, 342-355.

Mitchel, G. L. (1989).

A Review of Fabry-Pérot Interferometric Sensors, *Optical Fiber Sensors*, Springer Proceedings in Physics, Arditty *et al.* (eds.), 44, 450-457.

Miyajima, Y., Ishihara, K., Kakii, T., Toda, Y and Tanaka, S. (1981).

Long-Length Fibre Containing High-Strength Splices, *Electronics Letters*, 17(18), 670-672.

Mizrahi, V., Lemaire, P. J., Erdogan, T., Reed, W. A., DiGiovanni, D. J. and Atkins, R. M. (1993).

Ultraviolet Laser Fabrication of Ultrastrong Optical Fiber Gratings and of Germania-Doped Channel Waveguides, *Applied Physics Letters*, 63(13), 1727-1729.

Morey, W. W., Bailey, T. J., Glenn, W. H. and Meltz, G. (1992a).

Fiber Fabry-Pérot Interferometer Using Side Exposed Fiber Bragg Gratings, *Digest of Conference on Optical Fiber Communications*, 1992 Optical Society of America Technical Digest Series, 5, 96.

Morey, W. W., Meltz, G. and Weiss, J. M. (1992b).

Evaluation of a Fibre Bragg Grating Hydrostatic Pressure Sensor, *Proceedings of the 8th International Conference on Optical Fiber Sensors*, Monterey, U.S.A., Postdeadline paper: PD-4.

Muhs, J. D. (1989).

Multiplexed, High- and Low-Sensitivity Fiber-Optic Strain/Temperature Sensor, *Proceedings of the Society of Photo-Optical Instrumentation Engineers*, 1169, 172-176.

Murphy, K. A. (1996).

Practical Applications of Extrinsic Fabry-Pérot Interferometric (EFPI) Sensors, *Proceedings of the Society of Photo-Optical Instrumentation Engineers*, 2839, 82-92.

Murphy, K. A., Gunther, M. F., Wang, A., Claus, R. O. and Vengsarkar, A. M. (1992).

Extrinsic Fabry-Pérot Optical Fiber Sensor, *Proceedings of the 8th International Conference on Optical Fiber Sensors*, Monterey, U.S.A., 193-196.

Murphy, K. A., Miller, M. S., Vengsarkar, A. M. and Claus, R. O. (1990).

Elliptical-Core Two-Mode Optical-Fiber Sensor Implementation Methods, *Journal of Lightwave Technology*, 8(11), 1688-1696.

Navarette, M. C. and Bernabeu, E. (1994).

Three-Branch Optical Fibre Interferometer for Simultaneous Measurement of Two Physical Measurands, *Optics Communications*, 110, 55-59.

Neubert, H. K. P. (1967).

Strain Gauges: Kinds and Uses, Macmillan, London.

Newson, T. P., Farahi, F., Jones, J. D. C. and Jackson, D. A. (1988).

Combined Interferometric and Polarimetric Temperature Sensor with a Short Coherence Length Source, *Optics Communications*, 68(3), 161-165.

Ning, Y. N., Wang, Z. P., Palmer, A. W. and Grattan, K. T. V. (1995).

Recent Progress in Optical Current Sensing Techniques, *Review of Scientific Instruments*, 66(5), 3097-3111.

Nishii, J., Kitamura, N., Yamanaka, H., Hosono, H. and Kawazoe, H. (1995).

Ultraviolet-Radiation-Induced Chemical Reactions Through One- and Two-Photon Absorption Process in GeO₂-SiO₂ Glasses, *Optics Letters*, 20(10), 1184-1186.

- Noda, J., Okamoto, K. and Sasaki, Y. (1986).**
Polarization-Maintaining Fibers and Their Applications, *Journal of Lightwave Technology*, LT-4(8), 1071-1089.
- Noda, J., Shibata, N., Edahirao, T. and Sasaki, Y. (1983).**
Splicing of Single Polarisation-Maintaining Fibers, *Journal of Lightwave Technology*, LT-1(1), 61-66.
- Norman, S. R., Payne, D. N., Adams, M. J. and Smith, A. M. (1979).**
Fabrication of Single-Mode Fibres Exhibiting Extremely Low Polarisation Birefringence, *Electronics Letters*, 15(11), 309-311.
- Ohba, R., Kakuma, S., Yamane, H. and Uehira, I. (1989).**
Static Strain Monitoring OFS Using an FM Laser Diode, *Optical Fiber Sensors*, Springer Proceedings in Physics, Arditty *et al.* (eds.), 44, 400-407.
- Okamoto, K., Sasaki, Y. and Shibata N. (1982).**
Mode Coupling Effects in Stress-Applied Single Polarization Fibers, *IEEE Journal of Quantum Electronics*, QE-18(12), 1890-1899.
- Ono, K., Nishiura Y. and Nishikawa M. (1991).**
Phase-Modulated Fiber Optic Gyroscope with Wide Dynamic Range and Linear Scale Factor, *Applied Optics*, 30(9), 1070-1073.
- Othonos, A., Alavie, A. T., Melle, S., Karr, S. E. and Measures, R. M. (1993).**
Fibre Bragg Grating Laser Sensors, *Optical Engineering*, 32(11), 2841-2846.
- Parker, T. R., Farhadiroushan, M., Handerek, V. A. and Rogers, A. G. (1997).**
A Fully Distributed Simultaneous Strain and Temperature Sensor Using Spontaneous Brillouin Backscatter, *IEEE Photonics Technology Letters*, 9(7), 979-981.
- Patrick, H. J., Williams, G. M., Kersey, A. D., Pedrazzani, J. R. and Vengsarkar, A. M. (1996).**
Hybrid Fiber Bragg Grating/Long Period Fiber Grating Sensor for Strain/Temperature Discrimination, *IEEE Photonics Technology Letters*, 8(9), 1223-1225.
- Petermann, K. (1988).**
Laser Diode Modulation and Noise, Kluwer Academic Publishers, Dordrecht, the Netherlands.
- Pitt, C. W., Kirk, I. H. and Stevens, R. J. (1975).**
Automatic Monitoring of Deposition Conditions During RF Sputtering of Dielectric Materials, *Vacuum*, 25(6), 265-271.
- Poirier, M., Thibault, S., Lauzon, J. and Ouellette, F. (1993).**
Dynamic and Orientational Behavior of UV-Induced Luminescence in Ge-doped Silica Optical Fiber, *Optics Letters*, 18(11), 870-872.
- Pulker, H. K., Paesold, G. and Ritter, E. (1976).**
Refractive Indices of TiO₂ Films Produced by Reactive Evaporation of Various Titanium-Oxygen Phases, *Applied Optics*, 15(12), 2986-2991.
- Ramaswamy, V., Stolen, R. H., Divino, M. D. and Pleibel, W. (1979).**
Birefringence in Elliptically Clad Borosilicate Single-Mode Fibers, *Applied Optics*, 18(24), 4080-4084.
- Rao, Y. J. (1997).**
In-Fibre Bragg Grating Sensors, *Measurement Science and Technology*, 8, 355-375.

Rao, Y. J. and Jackson, D. A. (1996).

Recent Progress in Fibre Optic Low-Coherence Interferometry, *Measurement Science and Technology*, 7(7), 981-999.

Rao, Y. J., Henderson, P. J., Jackson, D. A., Zhang, L. and Bennion, I. (1997c).

Simultaneous Strain, Temperature and Vibration Measurement Using a Multiplexed In-Fibre-Bragg-Grating/Fibre-Fabry-Pérot Sensor System, *Electronics Letters*, 33(24), 2063-2064.

Rao, Y. J., Jackson, D. A., Zhang, L. and Bennion, I. (1996).

Dual-Cavity Interferometric Wavelength-Shift Detection for In-Fiber Grating Sensors, *Optics Letters*, 21(19), 1556-1558.

Rao, Y. J., Jackson, D. A., Zhang, L. and Bennion, I. (1997b).

Extended Dynamic Range Detection System for In-Fibre Bragg Grating Strain Sensors Based on Two Cascaded Interferometric Wavelength Scanners, *Measurement Science and Technology*, 8, 1043-1049.

Rao, Y. J., Webb, D. J., Jackson, D. A., Zhang, L. and Bennion, I. (1997a).

In-Fiber Bragg-Grating Temperature Sensor System for Medical Applications, *Journal of Lightwave Technology*, 15(5), 779-785.

Rashleigh, S. C. (1981).

Magnetic Field Sensing with a Single-Mode Fiber, *Optics Letters*, 6(1), 19-21.

Rashleigh, S. C. (1983).

Origins and Control of Polarisation Effects in Single-Mode Fibers, *Journal of Lightwave Technology*, LT-1(2), 312-331.

Rashleigh, S. C. and Marrone, M. J. (1983).

Temperature Dependence of Stress Birefringence in an Elliptically Clad Fiber, *Optics Letters*, 8(2), 127-129.

Ren, Z. B. and Robert, Ph. (1989).

Discrimination Between Linear Birefringence and Faraday Rotation in Optical Fiber Current Sensors by Polarization Multiplexing, *Proceedings of the Society of Photo-Optical Instrumentation Engineers*, 1169, 226-232.

Richardson, M. L. and Gangolli, S. [eds.] (1994).

The Dictionary of Substances and Their Effects, The Royal Society of Chemistry, Cambridge, U.K.

Rourke, H. N., Baker, S. R., Byron, K. C., Baulcomb, R. S., Ojha, S. M. and Clements, S. (1994).

Fabrication and Characterisation of Long, Narrowband Fibre Gratings by Phase Mask Scanning, *Electronics Letters*, 30(16), 1341-1342.

Russell, P. St. J. and Hand, D. P. (1990).

Rocking Filter Formation in Photosensitive High Birefringence Optical Fibres, *Electronics Letters*, 26(22), 1846-1858.

Sakai, J. and Kimura, T. (1981).

Birefringence and Polarization Characteristics of Single-Mode Optical Fibers Under Elastic Deformations, *IEEE Journal of Quantum Electronics*, QE-17(6), 1041-1051.

Schultheis, L. (1988).

A Simple Fiber-Optic Fabry-Pérot Temperature Sensor, *Proceedings of the 5th International Conference on Optical Fiber Sensors, New Orleans, U.S.A.*, Postconference edn., Optical Society of America Technical Digest Series, vol. 2, parts 1 & 2, 506-509.

Schultheis, L., Amstutz, H. and Kaufmann, M. (1988).

Fiber-Optic Temperature Sensing with Ultrathin Silicon Etalon, *Optics Letters*, 13(9), 782-784.

Severin, P. J. and Severijns, A. P. (1990).

In Situ Film Thickness Monitoring in CVD Processes, *Journal of the Electrochemical Society*, 137(4), 1306-1309.

Sharma, A. and Posey, R. (1995).

Dual-Mode Fiber-Optic Interferometer: A Novel Design, *Optics Letters*, 20(22), 2345-2347.

Sharma, A. and Posey, R. (1996).

Multiwavelength LP₀₂ - LP₂₁ Intermodal Interferometric Temperature Sensing Using Stimulated Raman Scattering, *Proceedings of the 11th International Conference on Optical Fiber Sensors, Sapporo, Japan.*, 240-243.

Shlyagin, M., Khomenko, A. and Tentori, D. (1994).

Remote Measurement of Mode-Coupling Coefficients in Birefringent Fiber, *Optics Letters*, 19(12), 913-915.

Shlyagin, M., Miridonov, S. V., Tentori, D. and Castillo, J. (1997).

Twin Grating-Based Interferometric Fiber Sensor, *Proceedings of the 12th International Conference on Optical Fiber Sensors, Williamsburg, Virginia, U.S.A.*, 472-474.

Simon, A. and Ulrich, R. (1977).

Evolution of Polarization Along a Single-Mode Fiber, *Applied Physics Letters*, 31(8), 517-520.

Simpson, J. R., Stolen, R. H., Sears, F. M., Pleibel, W., Macchesney, J. B. and Howard, R. E. (1983).

A Single-Polarization Fiber, *Journal of Lightwave Technology*, LT-1(2), 370-373.

Singh, H. and Sirkis, J. S. (1997).

Simultaneously Measuring Temperature and Strain Using Optical Fiber Microcavities, *Journal of Lightwave Technology*, LT-15(4), 647-655.

Sirkis, J. S. (1993a).

Unified Approach to Phase-Strain-Temperature Models for Smart Structure Interferometric Optical Fiber Sensors: Part 1, Development, *Optical Engineering*, 32(4), 752-761.

Sirkis, J. S. (1993b).

Unified Approach to Phase-Strain-Temperature Models for Smart Structure Interferometric Optical Fiber Sensors: Part 2, Applications, *Optical Engineering*, 32(4), 762-773.

Sirkis, J. S. (1991).

Phase-Strain-Temperature Model for Structural Embedded Interferometric Optical Fiber Strain Sensors and Applications, *Proceedings of the Society of Photo-Optical Instrumentation Engineers*, 1588, 26-43.

Sirkis, J. S. and Haslach, H. W. Jr. (1990).

Complete Phase-Strain Model for Structural Embedded Interferometric Optical Fiber Sensors, *Proceedings of the Society of Photo-Optical Instrumentation Engineers*, 1370, 248-259.

Sirkis, J. S. and Lo, Y. (1994).

Simultaneous Measurement of Two strain Components Using 3 x 3 and 2 x 2 Coupler-Based Passive Demodulation of Optical Fiber Sensors, *Journal of Lightwave Technology*, 12(12), 2153-2161.

- Sirkis, J. S., Berkoff, T. A., Jones, R. T., Singh, H., Kersey, A. D., Friebele, E. J. and Putman, M. A (1995).**
In-Line Fiber Étalon (ILFE) Fiber-Optic Strain Sensors, *Journal of Lightwave Technology*, 13(7), 1256-1263.
- Sirkis, J. S., Kersey, A. D., Berkoff, T. A. and Friebele, E. J. (1996).**
Extended Range Pseudo-Heterodyne Demodulation for Fiber Optic Sensors, *Experimental Mechanics*, 30(2), 135-141.
- Smith, A. M. (1980).**
Birefringence Induced by Bends and Twists in Single-Mode Optical Fiber, *Applied Optics*, 19(15), 2606- 2611.
- Snyder, A. W. and Love, J. D. (1983).**
Optical Waveguide Theory, Chapman & Hall, London.
- Song, M., Lee, B., Lee, S. B. and Choi, W. S. (1997).**
Interferometric Temperature-Insensitive Strain Measurement with Different-Diameter Fiber Gratings, *Optics Letters*, 22(11), 790-792.
- Stagg, B. J. and Charalampopoulos, T. T. (1992).**
Sensitivity of the Reflection Technique: Optimum Angles of Incidence to Determine the Optical Properties of Materials, *Applied Optics*, 31(22), 4420-4429.
- Stolen, R. H. (1983).**
Calculation of Stress Birefringence in Fibers by an Infinitesimal Element Method, *Journal of Lightwave Technology*, LT-1(2), 297-301.
- Stone, J. and Stulz, L. W. (1993).**
Passively Temperature-Compensated Nontunable Fibre Fabry-Pérot Etalons, *Electronics Letters*, 29(18), 1608-1609.
- Sudo, M., Nakai, M., Himeno, K., Suzuki, S., Wada, A. and Yamauchi, R. (1997).**
Simultaneous Measurement of Temperature and Strain Using PANDA Fiber Grating, *Proceedings of the 12th International Conference on Optical Fiber Sensors, Williamsburg, Virginia, U.S.A., 24-27.*
- Suzuki, F., Kikuchi, Y., Shiota, T., Fukuda, O. and Inada, K. (1988).**
Magnetic-Field Sensor with Polarization-Maintaining Optical Fiber, *Proceedings of the 5th International Conference on Optical Fiber Sensors, New Orleans. U.S.A., 292-302.*
- Tachikura, M. and Haibara, T. (1985).**
Devitrification Effect on Optical-Fiber Strength Reduction by Fusion Splicing, *Journal of Lightwave Technology*, LT-3(3), 662-668.
- Tang, D., Rose, A. H., Day, G. W. and Etzel, S. M. (1991).**
Annealing of Linear Birefringence in Single-Mode Fiber Coils: Application to Optical Fiber Current Sensors, *Journal of Lightwave Technology*, 9(8), 1031-1037.
- Taylor, R. M., Webb, D. J., Jones, J. D. C. and Jackson, D. A. (1987).**
Extended-Range Fiber Polarimetric Strain Sensor, *Optics Letters*, 12(9), 744-746.
- Thomas, N. L. (1986).**
Optical Thin Film Monitoring Using Optical Fibers, *Proceedings of the Society of Photo-Optical Instrumentation Engineers*, 678, 123-129.

- Thursby, G., Michie, W. C., Walsh, D., Konstantaki, M. and Culshaw, B. (1995).**
Simultaneous Recovery of Strain and Temperature Fields by the Use of Two-Moded Polarimetry with an In-Line Mode Splitter/Analyzer, *Optics Letters*, 20(18), 1919-1921.
- Timoshenko, S. P. and Goodier, J. N. (1970).**
Theory of Elasticity, 3rd edn., McGraw-Hill.
- Tsai, K., Kim, K. and Morse, T. F. (1991).**
General Solutions for Stress-Induced Polarization in Optical Fibers, *Journal of Lightwave Technology*, 9(1), 7-17.
- Tseng, S. and Chen, C. (1988).**
Optical Fiber Fabry-Pérot Sensors, *Applied Optics*, 27(3), 547-551.
- Tsubokawa, M., Higashi, T. and Sasaki, Y. (1989).**
Measurement of Mode Couplings and Extinction Ratios in Polarization-Maintaining Fibers, *Journal of Lightwave Technology*, 7(1), 45-50.
- Tsubokawa, M., Shibata, N. and Seikai, S. (1985).**
Evaluation of Polarization Mode Coupling Coefficient from Measurement of Polarization Mode Dispersion, *Journal of Lightwave Technology*, LT-3(4), 850-854.
- Tsuchida, H. and Mitsuhashi, Y. (1987).**
Frequency Stabilisation of a Modulated Semiconductor Laser, *Electronic Letters*, 23(21), 1147-1148.
- Turner, R. D., Laurin, D. G. and Measures, R. M. (1992).**
Localized Dual-Wavelength Fiber-Optic Polarimeter for the Measurement of Structural Strain and Orientation, *Applied Optics*, 31(16), 2994-3003.
- Udd, E., Nelson, D. and Lawrence, C. (1997).**
Multiple Axis Strain Sensing Using Fiber Gratings Written onto Birefringent Single-Mode Optical Fiber, *Proceedings of the 12th International Conference on Optical Fiber Sensors, Williamsburg, Virginia, U.S.A.*, 48-51.
- Udd, E., Nelson, D., Lawrence, C., Spingarn, J. R. and Ferguson, B. (1996).**
Three Axis Strain and Temperature Sensor, *Proceedings of the 11th International Conference on Optical Fiber Sensors, Sapporo, Japan*, 244-247.
- Ulrich, R. (1979).**
Polarization Stabilization on Single-Mode Fiber, *Applied Physics Letters*, 35(11), 840-842.
- Ulrich, R. and Simon, A. (1979).**
Polarization Optics of Twisted Single-Mode Fibers, *Applied Optics*, 18(13), 2241-2251.
- Ulrich, R., Rashleigh, S. C. and Eickhoff, W. (1980).**
Bending-Induced Birefringence in Single-Mode Fibers, *Optics Letters*, 5(6), 273-275.
- Uttam, D. and Culshaw, B. (1985).**
Semiconductor Lasers in Advanced Interferometric Optical-Fibre Sensors, *Proceedings of the Institute of Electrical Engineers J*, 132(3), 184-190.
- Uttam, D. and Culshaw, B. (1985b).**
Precision Time Domain Reflectometry in Optical Fiber Systems Using a Frequency Modulated Continuous Wave Range Technique, *Journal of Lightwave Technology*, LT-3(5), 971-977.

Valis, T., Hogg, D. and Measures, R. M. (1990a).

Fiber Optic Fabry-Pérot Strain Gauge, *IEEE Photonics Technology Letters*, 2(3), 227-228.

Valis, T., Hogg, D. and Measures, R. M. (1990b).

Composite Material Embedded Fiber-Optic Fabry-Pérot Strain Rosette, *Proceedings of the Society of Photo-Optical Instrumentation Engineers*, 1370, 154-161.

van Oort, J. M. and ten Kate, H. J. (1994).

A Fiber Optics Sensor for Strain and Stress Measurements in Superconducting Accelerator Magnets, *IEEE Transactions on Magnetics*, 30(4), 2600-2603.

Varnham, M. P., Barlow, A. J., Payne, D. N. and Okamoto, K. (1983).

Polarimetric Strain Gauges Using High-Birefringence Fibre, *Electronics Letters*, 19(17), 699-700.

Vaughan, J. M. (1989).

The Fabry-Pérot Interferometer: History, Theory, Practice and Applications, Adam Hilger Series on Optics and Optoelectronics, IOP Publishing, Bristol, England.

Vengsarkar, A. M., Michie, W. C., Jankovic, L., Culshaw, B. and Claus, R. O. (1990).

Fiber Optic Sensor for Simultaneous Measurement of Strain and Temperature, *Proceedings of the Society of Photo-Optical Instrumentation Engineers*, 1367, 249-260.

Vengsarkar, A. M., Michie, W. C., Jankovic, L., Culshaw, B. and Claus, R. O. (1994).

Fiber-Optic Dual-Technique Sensor for Simultaneous Measurement of Strain and Temperature, *Journal of Lightwave Technology*, 12(1), 170-177.

Vengsarkar, A. M., Michie, W. C., Jankovic, L., Culshaw, B. and Claus, R. O. (1996).

Fiber-Optic Dual-Technique Sensor for Simultaneous Measurement of Strain and Temperature, *Journal of Lightwave Technology*, 14(1), 58-64.

Voges, E., Ostwald, O., Schiek, B. and Neyer A. (1982).

Optical Phase and Amplitude Measurement by Single Sideband Homodyne Detection, *IEEE Journal of Quantum Electronics*, QE-18(1), 124-129.

Vossen, J. L. and Cuomo, J. J. (1978).

Glow Discharge Sputter Deposition, *Thin Film Processes*, Vossen, J. L. and Kern, W. (eds.), Academic Press, Orlando, U. S. A.

Waits, R. K. (1978).

Planar Magnetron Sputtering, *Thin Film Processes*, Vossen, J. L. and Kern, W. (eds.), Academic Press, Orlando, U. S. A.

Wang, A. B., Wang, G. Z., Vengsarkar, A. M. and Claus, R. O. (1991b).

Demodulation Techniques for Two-Mode Elliptical-Core Fiber Sensors, *Electronics Letters*, 27(16), 1454-1456.

Wang, A. B., Wang, G. Z., Vengsarkar, A. M. and Claus, R. O. (1991a).

Two-Mode Elliptical-Core Fiber Sensors for Measurement of Strain and Temperature, *Proceedings of the Society of Photo-Optical Instrumentation Engineers*, 1584, 294-303.

Wang, G. Z., Wang, A. B., Murphy, K. A. and Vengsarkar, A. M. (1991).

Two-Mode Fabry-Pérot Optical Fibre Sensors for Strain and Temperature Measurement, *Electronics Letters*, 27(20), 1843-1845.

- Watanabe, T., Osaka, K., Sasaoka, E., Tanaka, S. and Asano, Y. (1988).**
Splicing of Polarization-Maintaining Fibers, *Optical Fiber Sensors*, Springer Proceedings in Physics, Arditty *et al.* (eds.), 44, 346-352.
- Webb, D. J., Jones, J. D. C., Taylor, R. M. and Jackson, D. A. (1988a).**
Extended Range Monomode Fibre-Optic Sensors: Spectral and Polarisation Techniques, *International Journal of Optoelectronics*, 3(3), 213-224.
- Webb, D. J., Jones, J. D. C., Taylor, R. M. and Jackson, D. A. (1988b).**
Extended-Range Interferometry Using a Coherence-Tuned, Synthesised Dual-Wavelength Technique with Multimode Fibre Links, *Electronics Letters*, 24(18), 1173-1175.
- Weber, M. J. (1986).**
Optical Crystals, *CRC Handbook of Laser Science and Technology: Volume 4: Optical Materials, Part 2: Properties*, Weber, M. J. (ed.), CRC Press, Florida.
- Weis, R. S., Kersey, A. D. and Berkoff, T. A. (1994).**
A Four Element Fiber Grating Sensor Array with Phase-Sensitive Detection, *IEEE Photonics Technology Letters*, 6(12), 1469-1472
- Welford, D. and Alexander, S. B. (1985).**
Magnitude and Phase Characteristics of Frequency Modulation in Directly Modulated GaAlAs Semiconductor Diode Lasers, *Journal of Lightwave Technology*, LT-3(5), 1092-1099.
- Wickersheim, K. A. and Hyatt, W. D. (1990).**
Commercial Applications of Fiber-Optic Temperature Measurement, *Proceedings of the Society of Photo-Optical Instrumentation Engineers*, 1267, 84-96.
- Window, A. L. [ed] (1992).**
Strain Gauge Technology, 2nd edn., Elsevier Science Publishers, England.
- Wolinski, T. R., Domanski, A. W. and Galazka, P. (1996).**
Polarimetric Fiber Optic Sensing for Smart Structures, *Proceedings of the Society of Photo-Optical Instrumentation Engineers*, 2839, 265-271.
- Wosinski, L., Bétend-Bon, J. P., Breidne, M., Sahlgren, B. and Stubbe, R. (1992).**
Quasi-Distributed Fiber-Optic Sensor for Simultaneous Absolute Measurement of Strain and Temperature, *Proceedings of the First European Conference on Smart Structures and Materials, Glasgow, Scotland*, 53-56.
- Wosinski, L., Breidne, M., Stubbe, R., Sahlgren, B. and Bétend-Bon, J. P. (1994).**
Experimental System Considerations for Distributed Sensing with Grating Fabry-Pérot Interferometers, *Proceedings of the 10th International Conference on Optical Fiber Sensors, Glasgow, Scotland*, 146-149.
- Xu, M. G., Archambault, J. L., Reekie, L. and Dakin, J. P. (1994).**
Discrimination Between Strain and Temperature Effects Using Dual-Wavelength Fibre Grating Sensors, *Electronics Letters*, 30(13), 1085-1087.
- Yariv, A. (1973).**
Coupled-Mode Theory for Guided-Wave Optics, *IEEE Journal of Quantum Electronics*, QE-9(9), 919-933.
- Yariv, A. and Nakamura, M. (1977).**
Periodic Structures for Integrated Optics, *IEEE Journal of Quantum Electronics*, QE-13(4), 233-253.

Yeh, Y., Lee, C. E., Atkins, R. A., Gibler, W. N. and Taylor, H. F. (1990).

Fiber Optic Sensor for Substrate Temperature Monitoring, *Journal of Vacuum Science and Technology A*, 8(4), 3247-3250.

Yeh, Y., Lee, J. H., Lee, C. E. and Taylor, H. F. (1991).

In-line Fabry-Pérot Interferometric Temperature Sensor with Digital Signal Processing, *Proceedings of the Society of Photo-Optical Instrumentation Engineers*, 1584, 72-78.

Yu, A. and Siddiqui, A. S. (1994).

Practical Sagnac Interferometer Based Fibre Optic Current Sensor, *IEE Proceedings in Optoelectronics*, 141(4), 249-256.

Zhang, Q., Brown, D. A., Reinhart, L., Morse, T. F., Wang, J. Q. and Xiao, G. (1994b).

Tuning Bragg Wavelength by Writing Gratings on Prestrained Fibers, *IEEE Photonics Technology Letters*, 6(7), 839-841.

Zheng, G., Campbell, M. and Wallace, P. (1996).

Reflectometric Frequency-Modulation Continuous-Wave Distributed Fiber-Optic Stress Sensor with Forward Coupled Beams, *Applied Optics*, 35(28), 5722-5726.

Zhou, C. and Letcher, S. V. (1995).

Fiber-Optic Microphone Based on a Combination of Fabry-Pérot Interferometry and Intensity Modulation, *Journal of Acoustical Society of America*, 98(2), Part 1, 1042-1046.

Zhou, X., Iiyama, K. and Hayashi, K. (1996).

Extended-Range FMCW Reflectometry Using an Optical Loop with a Frequency Shifter, *IEEE Photonics Technology Letters*, 8(2), 248-250.

Appendix F:

Symbols Used In This Thesis

Symbol	Meaning of the symbol
a	The semi-major axis of the internal elliptical cladding of an elliptically-cladded birefringent fibre
a_{can}	Thickness of a cantilever beam
$\arg(e^{i x})$	Argument function: returns x in the function $e^{i x}$
A	Constant voltage amplitude
$A(\phi)$	The Fabry-Pérot Airy function
b	The semi-minor axis of the internal elliptical cladding of an elliptically-cladded birefringent fibre
b_{can}	Width of a cantilever beam
b_{fib}	Normalised propagation constant of an optical fibre
B	Birefringence of an optical fibre
B'	Apparent birefringence of a birefringent fibre with a Bragg grating
\bar{B}	Change in the optical indicatrix (second-rank) tensor $\left[\left(\frac{1}{n^2} \right)_i \right]$ of an optical fibre
B_i	i -th element of \bar{B}
B_G	Birefringence due to geometry (<i>i.e.</i> asymmetry in the dimensions of the core of an optical fibre)
B_S	Stress-induced birefringence due to the stress-applying components in the cladding
B_{So}	Self-induced birefringence due to the difference in the thermal expansion of an

Symbol	Meaning of the symbol
	asymmetric core of an optical fibre and its surrounding cladding
c	Speed of light in free space
\bar{c}	Elastic compliance (fourth-rank) tensor
$\cos(x)$	Cosine function
$\cosh(x)$	Hyperbolic cosine function
C_1, C_2	Photo-elastic stress constants
C_E	Strain-optic coefficient
C_σ	Stress-optic coefficient
d_e	Some small number
d_g	Molar concentration of the doping material g
d_ω	Ratio between the sawtooth optical frequency ramp amplitude and the FSR of the sensor
d_V	Ratio between d_e and the fringe visibility V
$\frac{d(\Delta\phi_{j,M})}{dt}$	Derivative of $\Delta\phi_{j,M}$ with respect to time t
$\left \frac{d(\Delta\phi_{j,M})}{dt} \right _{\max}$	Maximum absolute value of $\frac{d(\Delta\phi_{j,M})}{dt}$
D_1, D_2	Some constants
e	$= 1.60217733 \times 10^{-19}$ C, charge of an electron
e_{ic}	Ellipticity of the internal elliptical cladding of an elliptically-cladded fibre
$\exp(x)$	Exponential function e^x
$E_{UMR,M}$	UMR extension factor
$E_{UMR,P}$	UMR extension factor for the measurement of pressure
$E_{UMR,T}$	UMR extension factor for the measurement of temperature

Symbol	Meaning of the symbol
$E_{UMR,\epsilon}$	UMR extension factor for the measurement of strain
$\tilde{\mathbf{E}}_o$	Time-dependent complex electric field
\tilde{E}_o	Time-independent complex electric field
$(\tilde{\mathbf{E}}_o)^*$	Complex conjugate of $\tilde{\mathbf{E}}_o$
$ \tilde{E}_o $	The magnitude (absolute value) of \tilde{E}_o
E_o	Amplitude of the electric field \tilde{E}_o
$\tilde{\mathbf{E}}_b$	Time-independent complex electric field strength of the beam incident from region b ($=1,2$ or 3)
$\tilde{\mathbf{E}}_d^r$	Time-independent complex electric field strength of the reflected beam entering region d ($=1,2$ or 3)
$\tilde{\mathbf{E}}_d^t$	Time-independent complex electric field strength of the transmitted beam entering region d ($=1,2$ or 3)
$\tilde{\mathbf{E}}_r$	Fabry-Pérot reflection complex electric field
$\tilde{\mathbf{E}}_t$	Fabry-Pérot transmission complex electric field
$\tilde{\mathbf{E}}_r^m$	m -th component of $\tilde{\mathbf{E}}_r$
$\tilde{\mathbf{E}}_t^m$	m -th component of $\tilde{\mathbf{E}}_t$
$\tilde{\mathbf{E}}_r^{1+2}$	Two-beam-approximation Fabry-Pérot reflection complex electric field
$\tilde{\mathbf{E}}_t^{1+2}$	Two-beam-approximation Fabry-Pérot transmission complex electric field
\mathbf{E}_{in}	Normalised input electric field
E_x	Component of \mathbf{E}_{in} along the x -axis
E_y	Component of \mathbf{E}_{in} along the y -axis
\mathbf{E}'_{in}	Electric field launched into the lead-in fibre
\mathbf{E}_{out}	Output electric field

Symbol	Meaning of the symbol
$\mathbf{E}_{out,b}$	Output electric field incident on photodiode b ; If all the required adjustments have been made, $\mathbf{E}_{out,b}$ describes the electric field polarised along the b -axis (x - or y -axis) of the birefringent FFPS
$\mathbf{E}_{returning,Fresnel}$	Electric field of the beam reflected from the proximal face of the lead-in fibre and returning to the laser diode
f	Frequency
f_{beat}	Characteristic beat frequency
f_L	Focal length of a lense
f_{saw}	Frequency of the sawtooth ramp
f_{FS}	Single-pass frequency shift introduced by an acousto-optic modulator
\mathcal{F}	Finesse of a Fabry-Pérot interferometer
F	Coefficient of finesse
F_{ij}	Elements of the Jones matrix \mathbf{J}_{FP}
F_{xx}	Fabry-Pérot reflection transfer function along the x -axis
F_{yy}	Fabry-Pérot reflection transfer function along the y -axis
F_{xy}	Coupling the y -axis Fabry-Pérot reflection transfer function into that of the x -axis
F_{yx}	Coupling the x -axis Fabry-Pérot reflection transfer function into that of the y -axis
g	Acceleration due to gravity
\tilde{G}	A complex term ($= \tilde{r}_{12}\tilde{r}_{21} - \tilde{t}_{12}\tilde{t}_{21}$) used expressing the Fabry-Pérot reflectance function
G	The magnitude of \tilde{G}
h	Polarisation holding parameter: (Intensity) cross-talk between the polarisation modes per unit coupling length z
H	Angle between the x -axis of the half-wave plate and that of the PBS of the sensing system
i	The imaginary number $\sqrt{-1}$
i_{LD}	Drive current of a semiconductor laser diode

Symbol	Meaning of the symbol
I_o	Irradiance or time-averaged intensity of the electric field $\tilde{\mathbf{E}}_o$
I_m	Second moment of the cross-sectional area of a cantilever about the neutral plane
I_r	Reflection irradiance of a Fabry-Pérot interferometer address by a beam with electric field $\tilde{\mathbf{E}}_o$
I_t	Transmission irradiance of a Fabry-Pérot interferometer address by a beam with electric field $\tilde{\mathbf{E}}_o$
I_x	Irradiance along the x -axis of an optical fibre
I_y	Irradiance along the y -axis of an optical fibre
$\langle I_x \rangle$	Average irradiance along the x -axis of an optical fibre
$\langle I_y \rangle$	Average irradiance along the y -axis of an optical fibre
I_{ans}	Root-Mean-Square (RMS) current noise per unit square root of the electronic signal frequency bandwidth Δf present at the input of an operational amplifier
$I_{out,b}$	Intensity detected by photodiode b (derived from $\mathbf{E}_{out,b}$), ($b = x$ or y)
I_{max}	Maximum intensity value
I_{min}	Minimum intensity value
I_{raw}	Raw pseudo-heterodyne signal with the intensity-modulated associated with a current-modulated laser diode
$I_{raw,sub}$	I_{raw} less the background AC sawtooth modulation
$I'_{raw,sub}$	I_{raw} with some residual background AC sawtooth modulation
I'_{raw}	Band-pass filtered signal of $I_{raw,sub}$
I_{dark}	Dark current in a photodiode
I_{sig}	Photo-generated current in a photodiode
I_{shot}	Shot-noise current
$I_{sig=noise}$	Noise equivalent current (noise current yielding an $SNR = 1$)

Symbol	Meaning of the symbol
I_{thrm}	Thermal-noise current
$I_{r,AC}$	The electronic signal prior to filtering
$J_q(r)$	Bessel function of the first kind of order q
$\mathbf{J}_{P,b}$	The Jones matrix representation for a PBS polarising along the b -axis (either x - or y -axis)
\mathbf{J}	Characteristic Jones matrix representation for an optical element
J_{ij}	Elements of \mathbf{J} ($i, j = x$ or y)
\mathbf{J}_m	The Jones matrix representation for the m -th optical element
\mathbf{J}_t	The final Jones matrix representation for an optical arrangement composed of several optical devices or interfaces
\mathbf{J}_{FP}	The Jones matrix representation for a birefringent fibre Fabry-Pérot sensor. Its elements are the Fabry-Pérot reflection or transmission functions.
\mathbf{J}_{NPr}	The Jones matrix representation for a Non-Polarising Beam Splitter (reflection)
\mathbf{J}_{NPt}	The Jones matrix representation for a Non-Polarising Beam Splitter (transmission)
\mathbf{J}_{half}	The Jones matrix representation for a half-wave plate
\mathbf{J}_{lead}	The Jones matrix representation for the lead-in fibre of the sensing system
$\mathbf{J}_{Fresnel}$	The Jones matrix representation for the Fresnel reflection from the proximal face of the lead-in fibre
$\mathbf{J}_{in-fibre}$	The Jones matrix representation for the optical fibre components of the sensing system
$\mathbf{J}_{launching}$	The Jones matrix representation for the launching optical sub-system
$\mathbf{J}_{quarter}$	The Jones matrix representation for a quarter-wave plate
$\mathbf{J}_{detection,b}$	The Jones matrix representation for the detection optical sub-system (Photodiode b)
k	$= 1.380658 \times 10^{-23}$ J / K, Boltzmann's constant
k_o	$= \frac{2\pi}{\lambda}$, wavenumber

Symbol	Meaning of the symbol
k_b	Effective wave-number along the b -axis (either x - or y -axis) of a birefringent fibre
K	Some constant of proportionality
K'	Constant of proportionality which includes the quantum efficiency of the photodiode and the gain of its transimpedance amplifier
\tilde{K}	Sensitivity matrix
\tilde{K}^{-1}	Inverse of the matrix \tilde{K}
$ \tilde{K} $	Determinant of matrix \tilde{K}
K_{lM}	Phase-measurand sensitivity of interferometer l to measurand M
K_{aM}	Phase-measurand sensitivity of interferometer a to measurand M
K_{bM}	Phase-measurand sensitivity of interferometer b to measurand M
K_{rM}	Ratio of the absolute values K_{aM} and K_{bM}
K'_{lM}	Wavelength-measurand sensitivity of the l -th fibre Bragg grating to measurand M
$K_{dual, M}$	Phase-measurand sensitivity of a dual-mode sensor
$K_{pol, M}$	Phase-measurand sensitivity of a polarimetric sensor
ℓ	Physical cavity length of a Fabry-Pérot interferometer
ℓ_b	Physical length of a fibre Bragg grating
ℓ_f	Physical thickness of a thin film
L	Distance from the pivot point where the bending weight is applied
L_B	Distance between two locations along the fibre whereby the incident beam has the same SOP
L_c	Distance within which the incident light remains polarised and depends on the optical bandwidth $\Delta\lambda$ of the light source
L_T	Temperature sensing length: segment of the Fabry-Pérot cavity exposed to temperature change
L_M	Sensing length

Symbol	Meaning of the symbol
L_ε	Gauge length: segment of the Fabry-Pérot cavity exposed to strain
L_1	Sensing length of interferometer 1
L_2	Sensing length of interferometer 2
L_{bd}	Loss term which incorporates all the energy losses in the mirror between media b and d
L_{ij}	The elements of matrix J_{lead} ($i, j = x$ or y)
L_{OPD}	Optical path difference of an interferometer
$L_{OPD,1}$	Optical path difference of interferometer 1
$L_{OPD,2}$	Optical path difference of interferometer 2
LP_{01} and LP_{11}	The first few guided modes of an optical fibre
LP_{11}^{even}	Even LP_{11} modes
LP_{11}^{odd}	Odd LP_{11} modes
m	An integer
m_{WT}	Mass hanging from the free end of a cantilever
M	Measurand, in general either temperature T or strain ε
\vec{M}	Measurand vector
m_1	Fabry-Pérot mirror 1 (proximal mirror) which can either be a dielectric thin film or a fibre Bragg grating
m_2	Fabry-Pérot mirror 2 (distal mirror) which can either be a dielectric thin film or a fibre Bragg grating
n	Refractive index of mode guided in the un-stressed core; refractive index of the fibre
n_1	Refractive index of region 1, the incident region
n_2	Refractive index of region 2; index of refraction of the Fabry-Pérot cavity
n_3	Refractive index of region 3, the distal region
n_b	Average effective refractive index of the mode guided within a fibre Bragg grating

Symbol	Meaning of the symbol
n_c	Refraction of the core of an optical fibre
n_f	Refractive index of a thin film
n_x	Reflective index of the x -axis (slow-axis) of a birefringent fibre
n_y	Reflective index of the y -axis (fast-axis) of a birefringent fibre
n_{co}	Refractive index of the material used in the core of an optical fibre
n_{cl}	Refractive index of the material used in the cladding of an optical fibre
n_{sf}	Average refractive index between the polarisation axes of a birefringent FFPS
n_{LD}	Refractive index of the cavity of a semiconductor laser diode
n_{fast}	Refractive index along the fast axis of a birefringent fibre
n_{slow}	Refractive index along the slow axis of a birefringent fibre
N	Some constant integer
N_b	Number of periodic refractive index (grating) planes composing a fibre Bragg grating
O	Pivot point
OPD_{fibre}	Optical path difference between the sensing beam and the zeroth-order beam in the fibre Michelson interferometer in the work of Zhou <i>et al.</i> , [1996]
OPL_{loop}	Optical path length of an optical fibre loop
\bar{p}	Elasto-optic (fourth-rank) tensor
P_{sig}	Optical intensity of an interferometric signal
P	Pressure
p_{11}, p_{12} and p_{44}	Pockels strain-optic coefficients for a homogeneous optical fibre
q	An integer
Q	Quality Factor of a band-pass filter
Q	Angle between the x -axis of the input beam and that of the quarter-wave plate of the sensing system

Symbol	Meaning of the symbol
r^2	Correlation coefficient associated with a least squares fit
r_b	Electric field reflection coefficient of a fibre Bragg grating
r_f	The electric field reflection coefficient of a Fresnel interface
r_x	The electric field reflection coefficient along the x -axis of an NPBS
r_y	The electric field reflection coefficient along the y -axis of an NPBS
r^+	The electric field reflection coefficient along the x - and y -axis of an NPBS when $r_x = r_y$
$r(t)$	AC component (with respect to time t) of the sawtooth ramp divided by the DC component of the ramp
\tilde{r}_{film}	Electric field reflection coefficient of a dielectric thin film embedded in an optical fibre
r_{co}	Radius of the core of an optical fibre
\tilde{r}_{bd}	Complex electric field reflection coefficient of the interface between media b and d
r_{bd}	Electric field reflection amplitude coefficient; amplitude of \tilde{r}_{bd}
R	Reflection coefficient (intensity); reflectance
R	Combined internal reflectance of the Fabry-Pérot mirrors
$\mathbf{R}(Q)$	Matrix transformation due to an angular rotation of Q
R_b	Reflectance function of a fibre Bragg grating
R_b^0	Bragg reflectance of a fibre Bragg grating
R_f	Reflectance of a Fresnel optical interface
R_{m_1}	Reflectance of the proximal Fabry-Pérot mirror
R_{1+2}	Two-beam approximation of the reflectance of a Fabry-Pérot interferometer
R_{gain}	Photodiode trans-impedance gain resistance
R_{film}	Reflectance of a dielectric thin film embedded in an optical fibre

Symbol	Meaning of the symbol
$R_{film}^{\lambda/4}$	Reflectance of a quarter-wave thick dielectric thin film embedded in an optical fibre
R_{bd}	Reflectance of the mirror between media b and d
\bar{s}	Elastic stiffness (fourth-rank) tensor
$\operatorname{sech}(x)$	Hyperbolic secant function
$\sin^{-1}(x)$	Inverse sine function
$\sin(x)$	Sine function
$\sinh(x)$	Hyperbolic sine function
S	Angle between the x -axis of the NPBS and that of the lead-in fibre of the sensing system
S_b	$= \sqrt{\kappa^2 - (\delta\beta_b)^2}$, a complex term used in the transfer function of a fibre Bragg grating (coupled-mode theory solution)
SNR	Power signal-to-noise ratio
t	Time
t_b	Electric field transmission coefficient of a fibre Bragg grating
t_x	The electric field transmission coefficient along the x -axis of a NPBS
t_y	The electric field transmission coefficient along the y -axis of a NPBS
t^+	The electric field transmission coefficient along the x - and y -axis of an NPBS when $t_x = t_y$
\tilde{t}_{film}	Electric field transmission coefficient of a dielectric thin film embedded in an optical fibre
\tilde{t}_{bd}	Complex electric field transmission coefficient of the interface between media b and d
t_{bd}	Electric field transmission amplitude coefficient; amplitude of \tilde{t}_{bd}
$\tan(x)$	Tangent function
$\tan^{-1}(x)$	Inverse tangent function

Symbol	Meaning of the symbol
$\tanh(x)$	Hyperbolic tangent function
T	Transmission coefficient (intensity); transmittance
T	Temperature
T_b	Transmittance function of a fibre Bragg grating
T_b^0	Bragg transmittance of a fibre Bragg grating
T_f	Transmittance of a Fresnel optical interface
T_s	Effective temperature when thermal stress in the fibre has begun to build up
T_{1+2}	Two-beam approximation of the transmittance of a Fabry-Pérot interferometer
T_{bd}	Transmittance of the mirror between media b and d
T_{fwd}	Combined forward transmittance of the Fabry-Pérot mirrors
T_{film}	Transmittance of a dielectric thin film embedded in an optical fibre
T_{max}	Maximum transmittance of an ideal Fabry-Pérot interferometer
U	Angle between the x-axis of the lead-in fibre and of the Fabry-Pérot sensor of the sensing system
V	Fringe visibility
V_R	Reflection fringe visibility of a Fabry-Pérot interferometer
V_T	Transmission fringe visibility of a Fabry-Pérot interferometer
V_R^{1+2}	Two-beam-approximation of the reflection fringe visibility of a Fabry-Pérot interferometer
V_T^{1+2}	Two-beam-approximation of the transmission fringe visibility of a Fabry-Pérot interferometer
V_{ans}	RMS voltage noise per unit square root of the electronic signal frequency bandwidth Δf present at the input of an operational amplifier
V_{fb}	Normalised frequency of an optical fibre
V_{sig}	Electronic (voltage) signal

Symbol	Meaning of the symbol
V'_{sig}	Frequency-down-shifted version of V_{sig}
W	Angle between the x-axis of the NPBS and that of the half-wave plate of the sensing system
y	Value of the regions above (below) the neutral axis(/plane) of a cantilever
Y	Young's modulus of an optical fibre
Y_{can}	Young's modulus of a cantilever
z	coupling length along a fibre Bragg grating; represents the longitudinal axis of an optical fibre; distance along an optical fibre
Z	Angle between the x-axis of quarter-wave plate and that of the NPBS of the sensing system
α	Linear thermal expansion coefficient of an optical fibre; Linear thermal expansion coefficient of the core of an elliptically-cladded birefringent fibre
α_e	Linear thermal expansion coefficient of the inner cladding of an elliptically-cladded birefringent fibre
α_s	Linear thermal expansion coefficient of the outer cladding of an elliptically-cladded birefringent fibre
α_{LD}	Thermal expansion coefficient of the cavity of a semiconductor laser diode
α_{SiO_2}	Linear thermal expansion coefficient of silicon dioxide
$\alpha_{B_2O_3}$	Linear thermal expansion coefficient of boron oxide
α_{GeO_2}	Linear thermal expansion coefficient of germanium dioxide
$\alpha_{P_2O_5}$	Linear thermal expansion coefficient of phosphate
β	Single-pass Fabry-Pérot cavity phase shift
$\beta(\epsilon_j, \Delta T)$	The effective propagation constant of an electro-magnetic wave polarised along the j -axis (either x -axis or y -axis) of an optical fibre
β_f	Single-pass phase change associated with the optical length of a thin film
β_b	Phase change associated with the optical length of a fibre Bragg grating

Symbol	Meaning of the symbol
β_b^0	β_b evaluated at the Bragg wavelength
β_X	Phase change associated with the optical length of the mirror X ($= m_1$ or m_2)
β_{m_1}	Phase change associated with the optical length of the mirror m_1
β_{m_2}	Phase change associated with the optical length of the mirror m_2
χ_{co}	Waveguide effect due to Δn_{co}
δ_{kz}	Kronecker delta function
δn	Fractional difference between the refractive indices of the core and cladding of an optical fibre
δn_x	The stress-induced change in the refractive index along the x -axis of the core of an elliptically-cladded birefringent fibre
δn_y	The stress-induced change in the refractive index along the y -axis of the core of an elliptically-cladded birefringent fibre
$\delta\phi'$	Half of the FWHM bandwidth of a Lorentzian (line-shape) function
$\delta\alpha_1$	Thermal coefficient mismatch between the inner cladding and the core of an elliptically-cladded birefringent fibre
$\delta\alpha_2$	Thermal coefficient mismatch between the outer and inner claddings of an elliptically-cladded birefringent fibre
$\delta\beta_b$	Bragg phase mismatch
$\delta\bar{M}$	Uncertainty of the vector \bar{M}
$\delta\bar{\Phi}$	Uncertainty of the vector $\bar{\Phi}$
Δ	Change
Δf	Electronic signal frequency bandwidth
Δn_b	Amplitude of the refractive index modulation of a fibre Bragg grating
Δn_b^f	Amplitude of the refractive index modulation along the fast axis of a birefringent Bragg grating
Δn_b^s	Amplitude of the refractive index modulation along the slow axis of a birefringent Bragg grating

Symbol	Meaning of the symbol
Δn_b^{sf}	Birefringence exhibited in the refractive index modulation
Δn_{sf}	Apparent birefringence of a birefringent fibre with a Bragg grating
$(\Delta n)_\varepsilon$	Elasto-optic change in the effective refractive index of the mode guided in an optical fibre
$(\Delta n)_{\varepsilon T}$	Change in n produced by thermal strain $\bar{\varepsilon}^T$
$\Delta n_{i,T}$	Temperature-induced phase change along the i -th (x -or y -) polarisation axis of a birefringent FFPS
$\Delta n_{x,T}$	The temperature-induced change in the x -axis refractive index of an elliptically-cladded birefringent fibre
$\Delta n_{y,T}$	The temperature-induced change in the y -axis refractive index of an elliptically-cladded birefringent fibre
$\Delta n_{x,\varepsilon}$	The strain-induced change in the x -axis refractive index of an elliptically-cladded birefringent fibre
$\Delta n_{y,\varepsilon}$	The strain-induced change in the y -axis refractive index of an elliptically-cladded birefringent fibre
Δr_{co}	Change in r_{co}
ΔM	Measurand change
ΔM_{UMR}	Unambiguous measurand range for measurand M
ΔT	Temperature change
$\Delta \varepsilon_{EM}$	Amplitude modulation of the electric permittivity
$\Delta \lambda_b$	Bragg wavelength shift
$\Delta \lambda_{b,mode}$	Approximate wavelength separation between consecutive minima of the reflectance transfer function of a fibre Bragg grating (far from the central Bragg wavelength)
$\Delta \lambda_b^{sf}$	Bragg wavelength separation of a Bragg grating written on a birefringent fibre
$\Delta \nu$	Amplitude of the laser diode emission frequency sawtooth ramp
$\Delta \nu_{beat}$	Optical beat frequency
$\Delta \nu_{FSR}$	Free spectral range

Symbol	Meaning of the symbol
$\Delta\nu_{FSR,f}$	Free spectral range along the fast-axis of a birefringent FFPS
$\Delta\nu_{FSR,s}$	Free spectral range along the slow-axis of a birefringent FFPS
$\Delta\nu_{FSR,sf}$	Average of the free spectral ranges of the polarisation axes of a birefringent FFPS
$\Delta\nu_{FSR,max\ error}$	Maximum error in $\Delta\nu_{FSR}$
$\Delta\nu_{FWHM}$	Frequency Full-Width-at-Half-Maximum bandwidth
$\Delta\phi$	Change in Fabry-Pérot cavity phase ϕ
$\Delta\phi_{j,M}$	Measurand-induced phase shifts along the j -axis
$\Delta\phi$	Interferometric phase change
$\Delta\phi_a$	Total phase change produced in interferometers a
$\Delta\phi_b$	Total phase change produced in interferometers b
$\Delta\phi_{i,\varepsilon}$	Strain-induced phase change along the i -th (x -or y -) polarisation axis of a birefringent FFPS
$\Delta\rho_c$	Change in current carrier density ρ_c
$\frac{\Delta\phi}{\Delta M}$	Phase-measurand sensitivity
$\left \frac{\partial\theta_f^{nl}}{\partial\beta_f} \right $	Absolute value of $\frac{\partial\theta_f^{nl}}{\partial\beta_f}$
$\left \frac{\partial\theta_f^{nl}}{\partial\beta_f} \right _{\max}$	Maximum value of $\left \frac{\partial\theta_f^{nl}}{\partial\beta_f} \right $
$\left \frac{\partial\theta_b^{nl}}{\partial\beta_b} \right _{\max}$	Maximum value of $\left \frac{\partial\theta_b^{nl}}{\partial\beta_b} \right $
ε	Strain in general: Axial (or longitudinal) strain
$\bar{\varepsilon}$	(Total) strain expressed as a second-rank tensor
ε_j	Strain along the j -axis of an optical fibre

Symbol	Meaning of the symbol
$\bar{\varepsilon}^T$	Thermal strain
$\varepsilon(z)$	Strain along the surface of a cantilever a distance z from the pivot point O
ε_{EM}	Electric permittivity
ε_{jb}	The ratio between the transmission along the j -axis and the b -axis of the PBS
ϕ	Total Fabry-Pérot cavity phase difference, optical phase shift
ϕ'	Phase near the centre of a longitudinal mode of the Fabry-Pérot Airy function $A(\phi)$
ϕ^{nl}	Nonlinear measurand-induced variations in ϕ : ϕ with its linear trend with respect to a measurand M removed
$\phi_{1/2}$	The distance in ϕ -space from a longitudinal mode giving half the maximum output for high finesse Fabry-Pérot transmission output
ϕ_r	Difference between the combined transmission and reflection phase shifts of the proximal mirrors
ϕ_G	$\arg(r_{12}r_{21} - t_{12}t_{21} \exp[i\phi_r])$, this phase value is determined by the properties of the proximal mirror of a Fabry-Pérot interferometer
ϕ_j	j -axis interferometric phase either that of the fast-axis, slow-axis or differential phase responses
$2\pi\phi_j$	Modulo 2π value of ϕ_j
$2\pi\phi_{j,current}$	Current value of $2\pi\phi_j$
$2\pi\phi_{j,previous}$	Previous value of $2\pi\phi_j$
$\phi_{j,Order}$	Fringe order of ϕ_j
ϕ_{sig}	Instantaneous time-varying phase of $I'_{raw,sub}$
ϕ_{sig}^0	Linear variation (with respect to time) of ϕ_{sig}
ϕ_{sig}^{nl}	Phase term representing all the nonlinear components in ϕ_{sig}
ϕ_{int}	The round-trip phase change due to the Fabry-Pérot cavity less the phase change due to $\Delta\nu$

Symbol	Meaning of the symbol
$\phi(t)_{\text{int}}$	ϕ_{int} explicitly expressed as a function of time; the sinusoidal phase signal associated with the measurand M
$\phi_{0,M}$	Some initial time-independent phase of the sinusoidal signal $\phi(t)_{\text{int}}$
ϕ_M^A	(Depth of modulation) phase-amplitude of the sinusoidal signal $\phi(t)_{\text{int}}$
$\phi_{j,M}^A$	Amplitude (depth of modulation) of the measurand-induced phase shifts along the j -axis $\Delta\phi_{j,M}$
$ \phi_{j,M}^A $	Absolute value of $\phi_{j,M}^A$
$\bar{\Phi}$	Interferometric phase change vector
φ	Interferometric phase (due only to the optical path difference of an interferometer)
φ_j	Effective propagation constant of an electro-magnetic wave polarised along the j -axis
φ_ε	Component of the Fabry-Pérot phase contributed by a round-trip of the gauge length L_ε (strain measurement)
φ_T	Component of the Fabry-Pérot phase contributed by a round-trip of the temperature sensing length L_T
φ_{int}	The round-trip phase change due only to the optical length Fabry-Pérot cavity ($n\ell$)
φ_{pol}	Phase of a polarimetric sensor
φ_{dual}	Phase of a dual-mode sensor
$\varphi_{x,T}$	Component of the Fabry-Pérot phase along the x -axis of a birefringent fibre contributed by a round-trip of the temperature sensing length L_T
$\varphi_{y,T}$	Component of the Fabry-Pérot phase along the y -axis of a birefringent fibre contributed by a round-trip of the temperature sensing length L_T
$\varphi_{x,\varepsilon}$	Component of the Fabry-Pérot phase along the x -axis of a birefringent fibre contributed by a round-trip of the gauge length L_ε (strain measurement)
$\varphi_{y,\varepsilon}$	Component of the Fabry-Pérot phase along the y -axis of a birefringent fibre contributed by a round-trip of the gauge length L_ε (strain measurement)
γ	Intensity coupling efficiency into the lead-in fibre of the sensing system
Γ	(Sensing) length of the fibre exposed to a temperature change and total strain

Symbol	Meaning of the symbol
$\langle \eta \rangle$	Extinction ratio between the two polarisation mode of a birefringent fibre
η_b	Fraction of the total power of the mode guided in the core of an optical fibre
η_{PD}	Responsivity of a photodiode
κ	(Bragg) coupling phase
κ_b	Value of κ at λ_b
λ	Optical wavelength in vacuum
$\bar{\lambda}$	Averaged wavelength value
λ_1	Wavelength of light source 1
λ_2	Wavelength of light source 2
$\lambda/2$	Half-wave plate
$\lambda/4$	Quarter-wave plate
λ_b	Bragg wavelength
$\lambda_{b,l}$	Bragg wavelength of fibre Bragg grating l
$\lambda_{b,1}$	Bragg wavelength of fibre Bragg grating 1
$\lambda_{b,2}$	Bragg wavelength of fibre Bragg grating 2
Λ	Spatial period of the grating (pitch length)
μ	Poisson's ratio of an optical fibre
ν	Optical frequency of a light source; laser diode emission frequency
ν_1	Optical frequency of light source 1
ν_2	Optical frequency of light source 2
π	$=3.141592654$; ratio of the circumference and diameter of a circle
θ_b	Characteristic phase response of a fibre Bragg grating
θ_c	Phase shift due to two successive internal cavity reflections (incident from the cavity);

Symbol	Meaning of the symbol
	Sum of the phase change upon internal reflections from the Fabry-Pérot mirrors
θ_b^r	Phase change upon reflection of a fibre Bragg grating
θ_b^t	Phase change upon transmission of a fibre Bragg grating
θ_b^r	Phase change due to reflection from a fibre Bragg grating
θ_X^r	Phase change upon reflection on either surface of the reflector X ($= m_1$ or m_2)
$\theta_{m_1}^r$	Phase change upon reflection on either surface of the reflector m_1
$\theta_{m_2}^r$	Phase change upon reflection on either surface of the reflector m_2
θ_{film}^r	The phase shift upon reflection from a dielectric thin film
θ_{film}^t	The phase shift upon transmission from a dielectric thin film
θ_{bd}^r	Electric field reflection phase difference; argument of \tilde{r}_{bd}
θ_{bd}^t	Electric field transmission phase difference; argument of \tilde{t}_{bd}
θ_b^{nl}	(Residual) nonlinear phase component of θ_b with respect to β_b
θ_f^{nl}	(Residual) nonlinear component of θ_{film}^r with respect to β_f
θ_X^{nl}	(Residual) nonlinear phase component of θ_X^r with respect to β_X ($X = m_1$ or m_2)
$\theta_{m_1}^{nl}$	(Residual) nonlinear phase component of $\theta_{m_1}^r$ with respect to β_{m_1}
$\theta_{m_2}^{nl}$	(Residual) nonlinear phase component of $\theta_{m_2}^r$ with respect to β_{m_2}
ϑ	Relative phase between the two linearly polarised beams of a birefringent fibre
ρ_c	Current carrier density in a semiconductor laser diode
$\vec{\sigma}$	Stress (force per unit area) expressed as a second-rank tensor
${}^1\vec{\sigma}$	Thermal stress between the core and the inner cladding of an elliptically-cladded birefringent fibre
${}^2\vec{\sigma}$	Thermal stress between the outer circular and the inner elliptical cladding of an

Symbol	Meaning of the symbol
	elliptically-cladded birefringent fibre
$[\sigma_k]$	Initial stress producing the birefringence
τ	Period; multiple of the period $2\pi/\omega$
τ_c	Coherence time of a light source
τ_{saw}	Period of a sawtooth modulation
$\tau_{Sampling}$	Sampling period
ω	Angular frequency
ω_c	Carrier angular frequency
ω_m	Angular modulation frequency: m -th order of the sawtooth modulation frequency
ω_M	Angular frequency of the measurand-induced phase shifts
$\omega_{j,M}$	Angular frequency of the measurand-induced phase shifts along the j -axis $\Delta\phi_{j,M}$
$\omega_{Nyquist}$	Angular Nyquist frequency
ϖ_T	Fractional phase-temperature sensitivity of a fibre interferometer
ϖ_M	Fractional phase-measurand sensitivity of a fibre interferometer
ϖ_ε	Fractional phase-strain sensitivity of a fibre interferometer
$\varpi_{x,T}$	Fractional phase-temperature sensitivity along the x -axis of a birefringent fibre interferometer
$\varpi_{y,T}$	Fractional phase-temperature sensitivity along the y -axis of a birefringent fibre interferometer
$\varpi_{x,\varepsilon}$	Fractional phase-strain sensitivity along the x -axis of a birefringent fibre interferometer
$\varpi_{y,\varepsilon}$	Fractional phase-strain sensitivity along the y -axis of a birefringent fibre interferometer
$\varpi_{\varepsilon T}$	Fractional cross-sensitivity of a fibre interferometer
$\varpi_{x,\varepsilon T}$	Fractional cross-sensitivity of a fibre interferometer along the x -axis
$\varpi_{y,\varepsilon T}$	Fractional cross-sensitivity of a fibre interferometer along the y -axis

Symbol	Meaning of the symbol
ω_T^{film}	Fractional phase-temperature sensitivity of a thin film
ω_ϵ^{film}	Fractional phase-strain sensitivity of a thin film
ω_M^{film}	Fractional phase-measurand sensitivity of a thin film
$\omega_M^{m_1}$	Fractional phase-measurand sensitivity of mirror \mathfrak{M}_1
$\omega_M^{m_2}$	Fractional phase-measurand sensitivity of mirror \mathfrak{M}_2

Appendix G:

Abbreviations Used In This Thesis

Notation	Description
AC	Alternating Current
ADC	Analog-to-Digital Converter
Ag	Silver
Al	Aluminium
AOM	Acousto-Optic Modulator
Ar	Argon
B ₂ O ₃	Boron Dioxide
BBO	Beta Barium Borate
CCD	Charge-Coupled Device
CMOS	Complementary Metal-Oxide Silicon
CO ₂	Carbon Dioxide
<i>ComCore</i>	A fibre Fabry-Pérot (interferometric) sensor using communications-grade fibre for its cavity and having a core-coated TiO ₂ fusion-spliced in-line reflector
<i>ComFace</i>	A fibre Fabry-Pérot (interferometric) sensor using communications-grade fibre for its cavity and having a face-coated TiO ₂ fusion-spliced in-line reflector
CSP	Channel-Substrate-Planar
CW	Continuous Wave
DAC	Digital-to-Analog Converter
DFB	Distributed Feedback
DFTS	Dispersive Optical Fourier Transform Spectroscopy
D-SAPD	Digital Synchronous-Asynchronous Phase-Detection

Notation	Description
DC	Direct Current
e-core	Elliptical-core
ESG	Electrical Strain Gauge
FBG	In-fibre Bragg Grating
FF	Flip-Flop
FFPI	Fibre Fabry-Pérot Interferometer
FFPS	Fibre Fabry-Pérot (interferometric) Sensor
FM	Frequency-Modulated
FMCW	Frequency-Modulated-Continuous-Wave
FSR	Free Spectral Range
FWHM	Full Width at Half Maximum
Ge	Germanium
GeO ₂	Germanium Dioxide
<i>Grating1</i>	First of two fibre Bragg gratings written on birefringent fibre fabricated at OFTC. This grating was used as the proximal Fabry-Pérot mirror of <i>HibiGrat</i> .
<i>Grating2</i>	Second of two FBGs written on birefringent fibre fabricated at OFTC.
<i>Grating3</i>	One of the initial FBGs written on birefringent fibre fabricated at OTRL.
HeNe	Helium Neon
<i>HibiFace</i>	A fibre Fabry-Pérot (interferometric) sensor using HiBi fibre for its cavity and having a face-coated TiO ₂ fusion-spliced in-line reflector
<i>HibiGrat</i>	A fibre Fabry-Pérot (interferometric) sensor using HiBi fibre for its cavity and having an in-fibre Bragg grating
HiBi	Highly Birefringent or High-Birefringence
I/O	Input/Output
IEC	Internal Elliptical Cladding
ILFE	In-line Fabry-Pérot Etalon

Notation	Description
InGaAs	Indium Gallium Arsenide
<i>InlineFP1</i>	First of the two initial in-line FFPSs developed in this work. The sensor used HiBi fibre for its cavity and had two in-fibre two FBGs as Fabry-Pérot mirrors.
<i>InlineFP2</i>	Second of the two initial in-line FFPSs developed in this work. The sensor used HiBi fibre for its cavity and had two in-fibre two FBGs as Fabry-Pérot mirrors.
LD	Laser Diode
LED	Light-Emitting Diode
LoBi	Low-Birefringence
LPG	Long-Period (Fibre) Grating
MgF ₂	Magnesium Flouride
MOPO	Master Oscillator Power Oscillator
msb	Most significant bit
Nd:YAG	Neodymium Yttrium Aluminum Garnet
NPBS	Non-Polarising Beam Splitter
NPM	Non-Polarisation-Maintaining
O ₂	Gaseous oxygen
OD	Outer Diameter
OFS	Optical Fibre Sensor
OFTC	Optical Fibre Technology Centre
OH	Hydroxide ion
op-amp	Operational Amplifier
OPD	Optical Path Difference
OPO	Optical Parametric Oscillator
OSA	Optical Spectrum Analyser
OTRL	Optical Technology Research Laboratory
P ₂ O ₅	Phosphate

Notation	Description
PBS	Polarising Beam Splitter
PD	Photodiode
PID	Proportional-Integral-Derivative controller
PM	Polarisation-Maintaining or Phase-Modulated
PZT	Lead Zirconate Tantalate
RMS	Root-Mean-Square
SiO ₂	Silicon Dioxide
SLED	Super-luminescence LED
SMTS	Simultaneous Measurement of Temperature and Strain
SNR	Signal-to-Noise Ratio
SOP	State of Polarisation
SRS	Stimulated Raman Scattering
STC	Schmitt Trigger Circuit
Ti	Titanium
Ti ₂ O ₅	Titanium Pentaoxide
TiO	Titanium Monoxide
TiO ₂	Titanium Dioxide
TML	Tokyo Sokki Kenkyuji (manufacturer of strain gauges)
TTL	Transistor-Transistor Logic
UMR	Unambiguous Measurand Range
UV	Ultraviolet
WLI	White-Light Interferometry
XOR	Exclusive-OR logic